Annalen der Meteorologie

Nr. 25

10th International Cloud Physics Conference Preprints

Volume I

Bad Homburg v. d. H.

15. – 20. August 1988

Offenbach am Main 1988

Im Selbstverlag des Deutschen Wetterdienstes

Die für die Veröffentlichung als Vorabdruck zur 10. Internationalen Konferenz für Wolkenphysik 1988 eingesandten Manuskripte stellen erweiterte Zusammenfassungen der Vorträge dar. Für ihren Inhalt sind die Verfasser verantwortlich. Die Wiedergabe dieser Zusammenfassungen nimmt eine spätere ausführliche Veröffentlichung durch die Autoren an anderer Stelle nicht vorweg.

ISSN 0072-4122
ISBN 3-88148-240-7

Herausgeber und Verlag:
Deutscher Wetterdienst
Frankfurter Str. 135
D-6050 Offenbach am Main

Redaktionsschluß: 10. Mai 1988

International Sponsors

International Association of Meteorology and Atmospheric Physics (IAMAP)

International Commission on Cloud Physics (ICCP)

USAF European Office of Aerospace Research and Development, London

US Army Research Office, London

Sponsors in the Federal Republic of Germany

Ministry for Research and Technology (BMFT)

German Weather Service (DWD)

German Meteorological Society (DMG)

German Aerospace Research Establishment (DFVLR)

The City of Bad Homburg

International Program Committee

Prof. Dr. P. V. Hobbs	(USA), (Chairman)
Dr. A. A. Chernikov	(USSR)
Dr. A. J. Heymsfield	(USA)
Dr. P. Jonas	(UK)
Prof. Dr. Z. Levin	(Israel)
Prof. Dr. R. List	(Canada)
Prof. Dr. H. D. Orville	(USA)
Prof. Dr. H. R. Pruppacher	(FRG)
Prof. Dr. R. G. Soulage	(France)
Dr. T. Takeda	(Japan)
Prof. Dr. B. Zhao	(PRC)

National Organizing Committee

Prof. Dr. H. R. Pruppacher (Chairman)

Prof. Dr. H. W. Georgii

Prof. Dr. H. Grassl

Prof. Dr. F. Herbert

Prof. Dr. E. Raschke

Dr. H. Reiser

Prof. Dr. U. Schumann

TABLE OF CONTENTS

Page

Author Index XXIV

Preface 1

SESSION 1: CLOUD MICROPHYSICS I: LABORATORY STUDIES

THE EFFECT OF CHARGE ON THE COALESCENCE OF SMALL PRECIPITATION DROPS AT TERMINAL VELOCITY 4
H. T. Ochs III, R. R. Czys and J. Q. Feng, Illinois State Water Survey, Champaign, IL, USA

WAKE-EXITED RAINDROP OSCILLATIONS 7
K. V. Beard and H. T. Ochs, Illinois State Water Survey, Champaign, IL, USA

TEMPORAL VARIATIONS OF SNOW CRYSTAL GROWTH PARAMETERS. 9
T. Takahashi, N. Fukuta**, T. Endoh* and G. Wakahama*, *The Institute of Low Temperature Science, Hokkaido University, Sapporo, JAPAN, **University of Utah, Salt Lake City, UT, USA*

EMPIRICAL EQUATIONS OF ICE CRYSTAL GROWTH MICROPHYSICS FOR MODELLING AND ANALYSIS 12
C. R. Redder and N. Fukuta, University of Utah, Salt Lake City, UT, USA

THE CONTRAST STUDY OF NEW MODEL ON ICE CRYSTAL GROWTH. 15
A.-S. Wang, Institute of Atmospheric Physics, Academia Sinica, Beijing, PRC

A WIND TUNNEL STUDY ON THE MELTING OF SNOW FLAKES. 18
S. K. Mitra, O. Vohl, H. R. Pruppacher, Johannes Gutenberg-Universität, Mainz, FRG

EVAPORATION AND MELTING OF ICE CRYSTALS: A LABORATORY STUDY 22
R. G. Oraltay and J. Hallett, Desert Research Institute, Reno, NV, USA

A NEW MECHANISM FOR ICE INITIATION IN WARM-BASED MIDWESTERN CUMULI 25
R. R. Czys, Illinois State Water Survey, Champaign, IL, USA

SPREADING OF SUPERCOOLED WATER DROPLETS ON AN ICE SURFACE 28
Y. Dong and J. Hallett, Desert Research Institute, Reno, NV, USA

A MODEL OF THE ELECTROSTATIC-AERODYNAMIC SHAPE OF RAINDROPS 31
C. Chuang and K. V. Beard, University of Illinois, Urbana, IL, USA

SESSION 2: CLOUD MICROPHYSICS II: FIELD MEASUREMENTS AND THEORY

MEASUREMENTS OF THE PARTITIONING OF AEROSOL MASS AND NUMBER BETWEEN CLOUD DROPLETS AND INTERSTITIAL AIR 34
J. Ogren, J. Heintzenberg and K. Noone, University of Stockholm, Stockholm, SWEDEN

THE CALCULATION OF SUPERSATURATIONS AND GROWTH OF DROPLETS IN CONTINENTAL CUMULUS CLOUDS 37
K. N. Bower and T. W. Choularton, UMIST, Manchester, UK

ON THE OBSERVATIONS OF CLOUD TEMPERATURE AND LIQUID WATER CONTENT USING A LYMAN-α AND AN FSSP SENSOR. 40
J. B. Jensen and D. Baumgartner, NCAR, Boulder, CO, USA and G. B. Raga, University of Washington, Seattle, WA, USA

EVALUATION OF DROPLET GROWTH RATES IN HAWAIIAN OROGRAPHIC CLOUDS. 43
D. Baumgartner, NCAR, Boulder, CO, USA

STUDIES OF WARM-RAIN DEVELOPMENT..... 46
W. A. Cooper, NCAR, Boulder, CO, USA

RADAR OBSERVATIONS AND MODELLING OF WARM RAIN INITIATION..... 49
A. J. Illingworth and I. J. Caylor, UMIST, Manchester, UK

A TEST OF ICE CRYSTAL PRODUCTION BY AIRCRAFT..... 52
G. Vali, R. D. Kelly and F. Serrano, University of Wyoming, Laramie, WY, USA

AIRBORNE STUDIES OF THE ICE PHASE IN MARITIME CLOUDS AROUND THE BRITISH ISLES..... 55
P. R. A. Brown, Meteorological Office, Bracknell, Berkshire, UK and T. W. Choularton, UMIST, UK

PRECIPITATION INITIATION MECHANISMS IN CLOUDS OVER NORTH INDIA..... 58
R. N. Chatterjee, P. Prakash, G. Singh and R. K. Kapoor, Indian Institute of Tropical Meteorology, Pune, INDIA

EVIDENCE OF PREFERENTIAL ZONES OF ICE MULTIPLICATION BY SPLINTERING IN CONVECTIVE CELLS..... 62
J.-F. Gayet, C. Duroure and R. G. Soulage, LAMP, Aubière, FRANCE

MICROPHYSICAL CHARACTERISTICS OF WARM-BASED CUMULI: OBSERVATIONS AT −10° C..... 64
R. R. Cyzs, Illinois State Water Survey, Champaign, IL, USA

SESSION 3: CLOUD MICROPHYSICS III. ENTRAINMENT AND MIXING

A COMPARATIVE STUDY OF LABORATORY THERMALS AND ATMOSPHERIC CLOUDS..... 67
H. Johari, G. Taylor**, M. Baker** and R. Breidenthal*, *Dept. of Aeronautics and Astronautics, **Geophysics Program, University of Washington, Seattle, USA*

ENTRAINMENT AND FINE-SCALE (MOLECULAR) MIXING..... 70
I. R. Paluch and D. G. Baumgardner, NCAR, CO, USA

AIRBORNE STUDIES OF THE INFLUENCE OF ENTRAINMENT ON THE VERTICAL AND HORIZONTAL MICROPHYSICAL STRUCTURE OF SMALL CUMULUS CLOUDS..... 73
J. Latham, UMIST, Manchester, UK, and A. M. Blyth, New Mexico Institute of Mining & Technology, Socorro, NM, USA

ENTRAINMENT SITES, MIXING PROCESSES IN WARM CONVECTIVE CLOUDS. EFFECT ON DROPLET GROWTH..... 76
E. Hicks, A. Rigaud, J. Gagneux, C. Pontikis, Météorologie Nationale EERM/CRPA, Magny les Hameaux, FRANCE

STRUCTURE OF UPPER CLOUDS BOUNDARY USING THE LIDAR DATA..... 79
V. E. Zuev, V. S. Shamanaev, I. E. Penner and I. V. Samokhvalov, Institute of Atmospheric Optics, Siberian Branch USSR Academy of Sciences, Tomsk, USSR

TURBULENT TRANSPORT PROCESSES WITHIN AND BELOW SMALL CUMULUS CLOUDS..... 82
A. M. Jochum, Institut für Physik der Atmosphäre, DFVLR, Oberpfaffenhofen, FRG

INSTABILITY THEORY IN CLOUDS AND THE PARAMETRIZATION OF EDDY VISCOSITY COEFFICIENTS..... 85
Y. Takaya, Meteorological Research Institute, Tsukuba, JAPAN

THREE DIMENSIONAL CUMULUS ENTRAINMENT STUDIES..... 88
T. L. Clark, P. K. Smolarkiewicz and W. D. Hall, NCAR, Boulder, CO, USA

HETEROGENEOUS MIXING MEASUREMENTS IN SMALL NON PRECIPITATING CUMULI..... 91
J. L. Brenguier, Direction de la Météorologie National EERM/CNRM, Toulouse Cedex, FRANCE

SESSION 4: CLOUD MICROPHYSICS IV: NUMERICAL MODELING

THE CASE FOR SUBGRID-SCALE CONDENSATION IN NUMERICAL CLOUD MODELS..... 94
F. B. Lipps and R. S. Hemler, Princeton University, Princeton, NJ, USA

THE EFFECT OF TURBULENCE ON THE COLLECTION OF CLOUD DROPS: A STOCHASTIC MODEL..... 97
G. W. Reuter, McGill University, Montreal, CANADA

THE EFFECT OF ICE PHYSICAL PROCESSES ON THE NUMERICAL SIMULATION OF WEST AFRICAN SQUALL LINES..... 100
W. D. Hall, NCAR, Boulder, CO, USA, and J. P. Lafore, CNRM, Toulouse, FRANCE

NUMERICAL SIMULATION OF MICROPHYSICAL PROCESSES IN CUMULONIMBUS..... 103
Z. Hu and G. He, Academy of Meteorological Sciences, Beijing, PRC

A COMPARATIVE STUDY OF TWO MICROPHYSICAL SCHEMES IN A β MESOSCALE MODEL..... 106
E. Richard and N. Chaumerliac, LAMP, OPGC, Clermont-Ferrand, FRANCE

GENERALIZED MICROPHYSICS SCHEME FOR USE IN MESOSCALE/CLOUD MODELS..... 109
G. J. Tripoli, University of Wisconsin, Madison, WI, USA, and P. J. Flatau and W. R. Cotton, Colorado State University, Fort Collins, CO, USA

THE STUDY OF NUMERICAL SIMULATION ON THE FORMATION OF THE CLOUD DROPLET SPECTRA IN CUMULUS CLOUDS..... 112
H. Xiao, H. XU, and M. Huang, Institute of Atmospheric Physics, Academia Sinica, Beijing, PRC

SESSION 5: CLOUDS AND RADIATION

SOME OUTSTANDING PROBLEMS ON THE INFLUENCE OF CLOUDS ON RADIATION..... 115
G. L. Stephens, Colorado State University, Fort Collins, CO, USA

THEORY ON THE UNCERTAINTY IN CLOUD MICROPHYSICAL PROCESSES AND CLIMATE..... 118
K. N. Liou and S. C. Ou, University of Utah, Salt Lake City, UT, USA

IN SITU MEASUREMENTS OF "SHIP TRACKS"..... 121
L. F. Radke, J. H. Lyons and P. V. Hobbs, University of Washington, Seattle, USA, and J. E. Coakley, NCAR, Boulder, CO, USA

RADIATION INDUCES GROWTH AND EVAPORATION OF DROPLETS IN BOUNDARY LAYER CLOUDS..... 124
R. Davies, McGill University, Montreal, Quebec, CANADA

CLOUD AND AEROSOL OPTICAL DEPTHS: PRELIMINARY RESULTS FROM FIFE..... 125
R. F. Pueschel, P. B. Russell*, T. P. Ackerman**, D. S. Colburn*, R. C. Wrigley*, M. A. Spanner***, and J. M. Livingston****,*
**NASA, Ames Research Center, Moffett Field, CA, USA,*
***Pennsylvania State University, PA, USA,*
****TGS Technology, Moffett Field, CA, USA,*
*****SRI International, Menlo Park, CA, USA*

AN OBSERVATIONAL STUDY OF RADIATIVELY DRIVEN CONVECTION..... 127
S. Nicholls, Meteorological Office, Bracknell, Berkshire, UK

RADIATIVE INFLUENCES ON PRECIPITATING MESOSCALE SYSTEMS..... 130
W. R. Cotton and S. Chen, Colorado State University, Fort Collins, CO, USA, and G. Tripoli, University of Wisconsin, Madison, WI, USA

CIRRUS MICROPHYSICS AND INFRARED RADIATIVE TRANSFER: A CASE STUDY. 133
T. P. Ackerman, A. J. Heymsfield**, F. P. J. Valero*** and St. Kinne****
**Dept. of Meteorology, Pennsylvania State University, PA, USA*
***NCAR, Boulder, CO, USA,*
****NASA, Ames Research Center, Space Science Division Moffett, CA, USA*

POSTER SESSION A: CLOUD MICROPHYSICS AND CHEMISTRY

THE COLLECTION EFFICIENCY OF A MASSIVE FOG COLLECTOR. 135
R. S. Schemenauer and P. I. Joe, Atmospheric Environment Service, Downsview, Ontario, CANADA

THE USE OF AUTOMATIC PARTICLE RECOGNITION TO IMPROVE THE DETERMINATION OF BULK QUANTITIES FROM PMS 2-D PROBE DATA IN CIRRUS. 138
A. G. Darlison and P. R. A. Brown, Meteorological Office, Bracknell, Berkshire, UK

THE COMPARISON OF HOLOGRAPHIC AND 2-D PROBE MEASUREMENTS OF ICE CRYSTALS. 141
P. R. A. Brown and A. G. Darlison, Meteorological Office, Bracknell, Berkshire, UK

DEVELOPMENT OF HYDROMETEOR VIDEO SONDE. 144
M. Murakami and T. Matsuo, Meteorological Research Institute, Tsukuba, JAPAN

THE STUDY OF THE INTERSTITIAL AEROSOL PARTICLES AND CLOUD DROPLETS WITH DIGITAL IMAGE ANALYSIS OF DIFFRACTION IMAGES. 148
R. Jaenicke and R. Sörensen, University of Mainz, Mainz, FRG

ON THE DETERMINATION OF DROPLET SIZE DISTRIBUTIONS WITH THE CONTERFLOW VIRTUAL IMPACTOR. 151
B. Johansson and J. Heintzenberg, University of Stockholm, Stockholm, SWEDEN

MULTIPARAMETER CHARACTERIZATION OF RAINDROP SIZE DISTRIBUTION BY THE POLARIMETRIC DFVLR RADAR: FIRST RESULTS. 154
M. Chandra, A. Schroth and E. Lüneburg, DFVLR, Institut für HF-Technik, Weßling, FRG

AN INVESTIGATION OF THE EFFECT OF ELECTRICAL CHARGES ON THE COLLISION EFFICIENCY OF CLOUD DROPS. 158
V. M. Kim, Institute of Experimental Meteorology, Obninsk, USSR

MICROPHYSICAL AND ELECTRICAL PHENOMENA DURING FREEZING OF WATER DROPS. 161
A. Kh. Adzhiev and S. T. Tomazov, High Mountain Geophysical Institute, Nalchik, USSR

A DESCRIPTION OF CONDENSATION PROCESSES IN A TURBULENT THREE-PHASE CLOUD. 164
L. N. Novosyolov and A. S. Stepanov, Institute of Experimental Meteorology, Obninsk, USSR

EFFECT OF THE ELECTRIC FIELD ON THE RAINDROP SHAPE. 166
G. G. Magradze, Academy of Sciences of the Georgian SSR, Tbilisi, USSR

DAMPED OSCILLATION REPRESENTATION OF DROP-SPECTRUM EVOLUTION DUE TO COALESCENCE AND BREAKUP. 169
P. S. Brown, Trinity College, Hartford, CT, USA

KINETIC EQUATION FOR POLLUTED CLOUD DROPLET SPECTRUM. 172
I. M. Enukashvily, Israel Meteorological Service, Bet-Dagan, ISRAEL

LIQUID WATER CONTENT, MEDIAN VOLUME DIAMETER, AND TEMPERATURE IN DEPENDENCE ON THE HEIGHT ABOVE THE CLOUD BASE FOR DIFFERENT TYPES OF CLOUDS. 175
H.-E. Hoffmann and R. Roth, DFVLR-Oberpfaffenhofen, Institut Physik der Atmosphäre, Weßling, FRG

A DETAILED EXAMINATION OF DISCONTINUITIES IN NATURAL RAIN SPECTRA. 178
H. C. Vaughan, Iowa State University, Ames, IA, USA

CRYSTALLIZATION OF SUPERCOOLED SOLUTIONS. 180
K. Harrison and J. Hallett, Desert Research Institute, Reno, NV, USA

KINETICS OF ICE CRYSTAL FORMATION ON AEROSOL PARTICLES IN SUPERCOOLED FOG. 183
B. Z. Gorbunov, A. E. Paschenko and H. Kakutkina, Institute of Chem. Kinetics and Combustion, Novosibirsk, USSR

ABOUT SECONDARY ICE CRYSTAL PRODUCTION. 185
T. G. Gzirishvili and V. G. Khorguany, Academy of Sciences of the Georgian SSR, Tbilisi, USSR

EXPERIMENTAL STUDIES ON SECONDARY ICE PARTICLE PRODUCTION. .. 188
A. Yamashita, H. Konishi, W. Shimada, M. Miyatake and K. Tani, Osaka Kyoiku University, Osaka, JAPAN

PROPORTION OF RIMING GROWTH PROCESS IN SNOWFALL PHENOMENA. 190
T. Harimaya and M. Sato, Hokkaido University, Sapporo, JAPAN

THREE-DIMENSIONAL STRUCTURES OF SNOW CRYSTALS SHOWN BY STEREO-PHOTOMICROGRAPHS. 193
K. Iwai, Shinshu University, Nagano, JAPAN

ON THE VARIATION OF FALLING VELOCITY OF EARLY SNOWFLAKES. 196
M. Kajikawa, Akita University, Akita, JAPAN

A PARAMETERIZATION SCHEME FOR THE COALESCENCE OF WATER DROPS USING THE STOCHASTIC COLLECTION EQUATION. 199
C. Lüpkes, K. D. Beheng and G. Doms, Johann Wolfgang Goethe-Universität, Frankfurt am Main, FRG

ON THE DYNAMICS OF THE FALLING ICE CRYSTAL ZONE. 202
J. Podzimek, University of Missouri, Rolla, MO, USA

A NEW DATABASE OF ICE PARTICLE SIZE SPECTRA FOR ALTITUDES UP TO 10 KM, (30,000 FT). 205
R. K. Jeck, Naval Research Laboratory, Washington, DC, USA

A VERTICAL WIND TUNNEL FOR THE STUDY OF SNOWFLAKES AND EFFECTS OF ACCUMULATED SNOW ON MATERIALS. 208
K. Isono, Nagoya University, Tokyo, JAPAN; J. Kobayashi, Japan Weather Association, Tokyo; JAPAN; T. Gonda, Science University of Tokyo, Chiba, JAPAN; Y. Sasyo, and T. Mori, Suga Test Instruments Co. Ltd.; JAPAN

PROPERTIES OF THE PRECIPITATION EMBRYOS EVOLUTION IN CHARACTERISTIC HAWAIIAN BANDCLOUDS. 211
A. Rigaud, E. Hicks, J. Gagneux and C. Pontikis, Direction Météorologique Nationale EERM/CRPA, Magny les Hameaux, FRANCE

PATTERN OF AIR BUBBLE INCLUSIONS IN ATMOSPHERIC ICE FORMED DURING ACCRETION GROWTH. 214
P. Gribelin, P. Personne and H. Isaka, LAMP, Aubière, FRANCE

ANALYSIS OF HAILSTONES FROM A SEVERE STORM AND THEIR SIMULATED EVOLUTION. 217
L. Levi, Consejo Nacional de Investigaciones Cientificas y Tĕcnicas, ARGENTINA, and L. Lubart, Servicio Meteorológico Nacional, Buenos Aires, ARGENTINA

THE COLLECTION EFFICIENCIES OF SOFT-HAILSTONES FOR SUPER-COOLED WATER DROPLETS AND ICE CRYSTALS. 220
W. D. Keith and C. P. R. Saunders, UMIST, Manchester, UK

SIMULATION OF CONICAL GRAUPEL BY USING A BALLISTIC MODEL. 223
P. Personne, Chr. Duroure and H. Isaka, LAMP, Aubière, FRANCE

COMPARISON OF MODEL RESULTS FOR MODELS OF DIFFERING MICROPHYSICAL DETAIL..... 226
R. D. Farley and H. D. Orville, South Dakota School of Mines and Technology, Rapid City, SD, USA

AIRBORNE "CLOUD SIEVING"..... 229
E. E. Hindman, Physics and Atmospheric Science Department, Drexel University, PA, USA

CLOUD CAPTURE BY A MOUNTAIN TOP FOREST: ACIDITY AND DOSAGE DURATION. 232
V. K. Saxena and N.-H. Lin, North Carolina State University, Raleigh, NC, USA

DETERMINATION OF CHEMICAL REACTION RATES IN FOG. 235
R. Dlugi and W. Seidl, Meteorologisches Institut der Universität München, Munich, FRG

INSOLUBLE PARTICLES IN HYDROMETEORS. 238
M. Krämer and L. Schütz, University of Mainz, FRG

BELOW CLOUD SCAVENGING BY RAIN AND DRIZZLE. 241
B. T. McGann and S. G. Jennings, University College, Galway, IRELAND

STUDIES OF CLOUD MICRO-CHEMICAL PHYSICS. 243
R. L. Pitter and W. G. Finnegan, Desert Research Institute, Reno, NV, USA

KINETICS AND MECHANISM OF THE Fe-CATALYZED AUTO-OXIDATION OF S(IV)-OXIDES IN AQUEOUS SOLUTION. 246
J. Kraft, M. Dellert, P. Braun and R. Van Eldik, University of Witten/Herdecke, FRG

THE EFFECT OF AEROSOLS ON THE pH OF SNOWFALLS..... 249
M. Kumai, U.S. Army Cold Regions Research and Engineering Laboratory, Hannover, NH, USA

IONIC CONCENTRATIONS OF RIME ICE AND SNOW AND BERGERON PROCESS..... 251
S. H. Huang, Nanjing University, Nanjing, PRC, R. A. Castillo, Western Connecticut State University, Danbury, CT, USA, and V. A. Monhen, ASCR, SUNY, NY, USA

CHEMICAL NATURE OF PRECIPITATION AT VISAKHAPATNAM..... 254
S. Nizamuddin, Andhra University, Waltair, INDIA

A ONE-DIMENSIONAL NUMERICAL MODEL TO SIMULATE LIQUID PHASE CHEMICAL REACTIONS WITHIN RADIATION FOG. 255
R. Forkel and W. Seidl, Meteorologisches Institut der Universität München, Munich, FRG

SESSION 6: CLOUD CHEMISTRY AND ACIDIC PRECIPITATION I: MEASUREMENTS

THE EFFECT OF FREEZING ON THE COMPOSITION OF CLOUD DROPLETS. 258
J. V. Iribarne and T. Pyshnov, University of Toronto, Toronto, Ontario, CANADA

SOME EFFECTS OF CLOUD MICROPHYSICS ON CLOUD CHEMISTRY..... 261
D. A. Hegg and P. V. Hobbs, University of Washington, Seattle, WA, USA

PROCESSES DETERMINING CLOUDWATER COMPOSITION: FIELD EVIDENCE FOR INCLOUD REACTIVE SCAVENGING OF SO_2..... 264
P. H. Daum, Brookhaven National Laboratory, Upton, NY, USA

ACIDIFICATION OF STRATIFORM CLOUDS AND THEIR AEROSOL SCAVENGING PROPERTIES. 267
R. A. Castillo, Western Connecticut State University, Danbury, CT, USA, and J. Deluisi, NOAA, Boulder, CO, USA

MICROPHYSICAL, DYNAMICAL AND CHEMICAL ASPECTS OF SCAVENGING PROCESSES DURING WINTER PRECIPITATION. 270
A. Waldvogel, T. Schumann and B. Zinder, Atmospheric Physics ETH, Zürich, SWITZERLAND

VERTICAL PROFILES OF POLLUTANTS INSIDE AND OUTSIDE OF CLOUD. .. 273
G. A. Isaac and W. R. Leaitch, Atmospheric Environment Service, Downsview, Ontario, CANADA

RESULTS OF TIME AND HEIGHT RESOLVED SCAVENGING EXPERIMENTS. 276
L. Kins, Universität München, Munich, FRG, and F. X. Meixner, Fraunhofer Institut für Atmosph., Garmisch-Partenkirchen, FRG, and K. P. Müller, Kernforschungsanlage Jülich, Institut für Atmosph. Chemie, Jülich, FRG

OXIDATION REGIMES IN OROGRAPHIC CAPPING CLOUD. 279
P. A. Clark, G. P. Gervat, T. A. Hill, and A. R. W. Marsh, Central Electricity Research Laboratories, Leatherhead, Surrey, UK, and A. S. Chandler, T. W. Choularton, and M. J. Gay, UMIST, Manchester, UK

AN EXAMINATION OF THE CHEMICAL AND PHYSICAL VARIABILITY OF CLOUDS AT A MOUNTAIN-TOP SITE IN CENTRAL SWEDEN. 282
K. J. Noone, J. A. Ogren and J. Heintzenberg, Stockholm University, Stockholm, SWEDEN

INFLUENCES OF CLOUD MICROPHYSIC ON CONTINENTAL AND MARINE PRECIPITATION CHEMISTRY. 285
F. Parungo and C. Nagamoto, NOAA/ERL, Boulder, CO, USA

CONCENTRATIONS IN RAIN EVENTS COLLECTED SEQUENTIALLY: MEASUREMENTS VERSUS RESULTS OF A SIMPLE SCAVENGING MODEL. 288
J.-L. Jaffrezo and J.-L. Colin, Université Paris, Paris Cedex, FRANCE

EXPERIMENTS ON MICROPHYSICS AND CHEMISTRY OF RADIATION FOGS. 291
K. H. Enderle, H. Obenland, and W. Jaeschke, Johann Wolfgang-Goethe Universität, Frankfurt am Main, FRG

SESSION 7: CLOUD CHEMISTRY AND ACIDIC PRECIPITATION II: NUMERICAL MODELING

CHEMICAL EVOLUTION WITHIN A CLOUD MODEL FEATURING A POLYDISPERSE DROPLET SIZE SPECTRUM. 294
T. A. Hill, UMIST, Manchester, UK

MODELING STUDIES ON THE FORMATION, GROWTH, DISSIPATION, AND ACIDIFICATION OF CUMULUS CLOUDS. 297
S. K. Nair and L. K. Peters, University of Kentucky, Lexington, KY, USA

A NUMERICAL INVESTIGATION OF SULFATE PRODUCTION AND DEPOSITION IN MIDLATITUDE CONTINENTAL CUMULUS CLOUDS. 300
G. Taylor, University of Washington, Seattle, WA, USA

A NUMERICAL SIMULATION OF THE ACIDIFICATION PROCESS OF RAIN WATER BELOW THE CLOUD AND THE MECHANISM OF ACID RAIN FORMATION IN AREA OF CHONGQING. 303
M. Huang and S. Liu, Institute of Atmospheric Physics, Academia Sinica, Beijing, PRC

EFFECTS OF CLOUD MICROPHYSICAL PROCESSES ON TRACE CHEMICAL REMOVAL EFFICIENCIES. 306
D. Lamb and J. P. Chen, The Pennsylvania State University, University Park, PA, USA

DYNAMIC, RADIATIVE AND CHEMICAL EFFECTS OF CLOUDS ON TROPOSPHERIC TRACE GASES. 309
C. J. Walcek, SUNY, Albany, NY, USA

PARAMETERIZATIONS OF MICROPHYSICAL PROCESSES IN CLOUDS FOR APPLICATION IN MODELS OF REGIONAL ATMOSPHERIC DEPOSITION..... 312
I. Y. Lee, Argonne National Laboratory, Argonne, IL, USA

A MODEL OF WET DEPOSITION TO COMPLEX TERRAIN BY THE SEEDER-FEEDER PROCESS..... 316
A. Jones and T. W. Choularton, UMIST, Manchester, UK

METEOROLOGICAL AND CHEMICAL INFLUENCING FACTORS ON ACIDITY PRODUCTION IN A MESOSCALE MODEL WITH QUASI-SPECTRAL MICROPHYSICS..... 319
N. Chaumerliac and R. Rosset, LAMP, Aubière, FRANCE

SESSION 8: INSTRUMENTATION

A COMPARISON OF RADIOMETRIC AND IMMERSION TEMPERATURE MEASUREMENTS IN WATER CLOUDS..... 322
S. Nicholls, E. L. Simmons, N. C. Atkinson and S. D. Rudman, Meteorological Office, Bracknell, Berkshire, UK

CALIBRATION OF PMS FSSP AND 1D-C PROBES FOR CLOUD DROPLET MEASUREMENTS..... 325
J.-F. Gayet, LAMP, Aubière, FRANCE

RADAR OBSERVATIONS OF PRECIPITATION MICROSTRUCTURE: THE MORPHOLOGY OF LINEAR DEPOLARIZATION MEASUREMENTS IN CLOUD..... 328
P. H. Herzegh, NCAR, Boulder, CO, USA, and A. R. Jameson, Applied Research Corporation, Landover, MD, USA

MULTIPARAMETER DOPPLER RADAR OBSERVATIONS OF A SQUALL LINE WITH THE POLARIMETRIC DFVLR RADAR..... 330
P. Meischner, V. N. Bringi and T. Jank; DFVLR-Oberpfaffenhofen, Weßling, FRG

A POOR MANS OPTICAL FOG DETECTOR..... 333
R. K. A. M. Mallant, Netherlands Energy Research Foundation, ECN, Petten, THE NETHERLANDS

APPLICATIONS OF THE NCAR ELECTRA DOPPLER RADAR FOR THE STUDY OF PHYSICAL PARAMETERS OF CLOUDS..... 335
C. Walther, C. Frush and P. Hildebrand, NCAR, Boulder, CO, USA

INTERCOMPARISONS OF AIRCRAFT MEASUREMENTS WITH LIDAR RETURNS FROM AEROSOL, ICE CRYSTALS, AND WATER DROPLETS..... 338
W. R. Leaitch and R. M. Hoff, Atmospheric Environment Service, Downsview Ontario, CANADA, and A. I. Carswell, S. Pal and G. A. Cunningham, York University, Downsview, Ontario, CANADA

A NEW AIRBORNE DEVICE FOR MEASUREMENT OF CLOUD PARTICLES USING VIDEO-MICROSCOPE..... 341
T. Tanaka, T. Matsuo, K. Okada, and I. Ichimura, Meteorological Research Institute, Ibaraki, JAPAN, and S. Ichikawa and A. Tokuda, Sankei Co. Ltd., JAPAN

SESSION 9: OROGRAPHIC CLOUDS

ON THE SMALL SCALE TOPOGRAPHICAL INFLUENCES ON PRECIPITATION..... 344
W. W. Grabowski, Polish Academy of Science, Warsaw, POLAND

A NUMERICAL INVESTIGATION OF AN OROGRAPHIC PRECIPITATION EVENT..... 347
M. P. Meyers and W. R. Cotton, Colorado State University, Fort Collins, CO, USA

COMPLEX MICROPHYSICAL INTERACTIONS WITHIN A CENTRAL SIERRA NEVADA OROGRAPHIC CLOUD SYSTEM..... 350
R. M. Rauber, University of Illinois, Urbana, IL, USA

COMPARISON OF OROGRAPHIC CLOUD AND PRECIPITATION DEVELOPMENT OF THREE DIFFERENT GEOGRAPHIC LOCATIONS USING A 3-D NESTED GRID CLOUD MODEL 353
R. M. Rasmussen, Bureau of Reclamation, Denver, CO, USA, and P. Smolarkiewicz, W. D. Hall and T. Clark, NCAR, Boulder, CO, USA

MICROPHYSICAL OBSERVATIONS OVER THE ATLAS MOUNTAINS IN MAROCCO 356
O. Baddour, Météorologie Nationale, Casablanca, Royaume du Maroc, and R. M. Rasmussen, Bureau of Reclamation, Denver, CO, USA

MICROPHYSICAL AND DYNAMICAL INTERACTIONS IN COLORADO FRONT RANGE UPSLOPE STORMS 359
D. A. Wesley, M. J. Weisbluth, R. A. Pielke and W. R. Cotton, Colorado State University, Fort Collins, CO, USA

CHARACTERISTICS OF RADAR ECHO OF A SNOWBAND FORMED IN THE LEE SIDE OF A MOUNTAIN 362
Y. Fujiyoshi, T. Endoh and G. Wakahama, Institute of Low Temperature Science, Hokkaido University, Sapporo, JAPAN

POSTER SESSION B: CLOUD MACROPHYSICS

STUDY ON CLOUD AND RAIN PROCESS BY MICROWAVE RADIOMETER OBSERVATION 364
B. Zhao, Peking University, Beijing, PRC

A NEW DROPSONDE FOR CLOUD PROBINGS 366
D. E. Gaytandjiev, Hydrometeorological Service, Sofia, BULGARIA

HUMIDITY MEASUREMENTS DURING CLOUD FORMATION USING INFRARED HYGROMETRY 369
P. J. DeMott and D. C. Rogers, Colorado State University, Fort Collins, CO, USA

IDENTIFICATION OF PRECIPITATION PARTICLES USING DUAL POLARIZATION RADAR 372
A. J. Illingworth and I. J. Caylor, UMIST, Manchester, UK

Z-R RELATIONS FORM AIRBORNE 2D-P MEASUREMENTS IN HAWAIIAN SHOWERS 375
R. J. Kubesh, K. V. Beard and D. B. Johnson, Illinois State Water Survey, Champaign, IL, USA

COMPARISON BETWEEN AIRCRAFT AND DOPPLER RADAR MEASUREMENTS DURING ENCC (VOVES 1983) 378
H. Sauvageot, Laboratoire Aérologie Campistrous, FRANCE, and A. Rigaud, E. Hicks and C. Pontikis, Météorologie Nationale EERM/CRPA, Magny les Hameaux, FRANCE

EHF ATTENUATION THROUGH THE MELTING LAYER 380
A. J. Barnes, Jr., Air Force Geophysics Laboratory, Hanscom AFB, MA, USA

SIZE DISTRIBUTION OF PRECIPITATION PARTICLES IN MIDLATITUDE MESOSCALE CONVECTIVE COMPLEXES 383
J. D. Yeh, B. F. Fan and W. R. Cotton, Colorado State University, Fort Collins, CO, USA

A PRELIMINARY RESEARCH ON THE RADIATION FOG IN XISHUANG BANNA 386
Y. Huang, W. Xu, Meteorological Bureau of Yunnan Province, Yunnan, PRC, Z. Li, W. Huang, L. Fan, Nanjing Institute of Meteorology, Nanjing, PRC

THE BASIC CHARACTERISTICS OF THE WINTER NORTHERN XINJIANG STRATIFORM CLOUD SYSTEM 389
Z. Gao and J. Zhang, Weather Modification Office, Xinjiang, PRC

THE RAINFALL ENHANCEMENT BY TWO LAYER CLOUD STRUCTURE OBSERVED AT OROFURE MOUNTAIN RANGE, HOKKAIDO, JAPAN 393
K. Kikuchi, K. Iwanami and T. Taniguchi, Hokkaido University, Sapporo, Japan

MULTIPLE DOPPLER RADAR OBSERVATIONS OF AIRFLOW FIELDS DURING CONVECTIVE ECHO MERGERS 443
P. C. Kennedy, Illinois State Water Survey, Champaign, IL, USA

RESULTS FROM WARM RAIN STUDIES IN PENANG, MALAYSIA 446
R. List, D. Hudak and R. Nissen, University of Toronto, Toronto, Ontario, CANADA, and N. P. Tung, S. K. Soo and T. S. Kang, Malaysian Meteorological Service, Petaling Jaya, MALAYSIA

THE KINEMATICS OF MESO-GAMMA SCALE PRECIPITATION SYSTEMS 449
P. I. Joe, C. L. Crozier and T. R. Nichols, Atmospheric Environment Service, Downsview, Ontario, CANADA

THE ORIGIN OF AIR MASSES LEADING TO SEVERE HAILSTORMS IN SOUTHWESTERN FRANCE 452
J. Dessens, Centre de Recherches Atmosphériques, Lannemezan, FRANCE, and Fournier d'Albe, Dormont, Saint-Pierre de Bailleul, FRANCE

RADAR REMOTE SENSING OF MELTING HAIL 455
V. N. Bringi and P. Meischner, DFVLR, Institut für Physik der Atmosphäre, Weßling, FRG

TEST OF PARAMETERIZATION SCHEMES FOR CLOUD MICROPHYSICAL PROCESSES IN A 3-D MESOSCALE MODEL 458
L. Levkov, D. Jacob, D. Eppel and H. Graßl, Forschungszentrum Geesthacht, Geesthacht, FRG

DEVELOPMENT OF ANALYTICAL METHODS FOR THE INVESTIGATION OF CLOUDS, FOG AND RAIN, TOGETHER WITH THE GASEOUS PHASE, AND RESULTS OF FIELD MEASUREMENTS 461
K. Bächmann, U. Sprenger, G. R. Fuchs-Pohl, W. Schmied, and P. Zeißler, Technische Hochschule Darmstadt, FRG

RAIN AEROSOL COUPLING IN MARITIME, URBAN AND RURAL AREA. SCAVENGING RATIOS MEASUREMENTS IN RELATION WITH TRANSPORT 463
J. L. Colin and J. L. Jaffrezo, Université Paris, Paris Cedex, FRANCE

THE RAINOUT REMOVAL OF SULFUR DIOXIDE AND ACIDIFICATION OF PRECIPITATION FROM STRATIFORM CLOUDS 466
Q. Yu, Peking University, Beijing, PRC

SESSION 10: CIRRUS CLOUDS

STRUCTURAL AND TEXTURAL CHARACTERISTICS OF CIRRUS CLOUDS 468
K. S. Kuo, R. M. Welch and S. K. Sengupta, South Dakota School of Mines and Technology, Rapid City, SD, USA

CIRRUS CLOUDS AND MESOSCALE ATMOSPHERIC PROCESSES 471
E. P. Borisenkov and T. A. Bazlova, Main Geophysical Observatory, Leningrad, USSR

MESOSCALE AND MICROSCALE STRUCTURE OF CIRRUS CLOUDS: THREE CASE STUDIES 473
K. Sassen and M. Griffin, University of Utah, Salt Lake City, UT, USA

VERTICAL VELOCITIES WITHIN A CIRRUS CLOUD FROM DOPPLER LIDAR AND AIRCRAFT MEASUREMENTS DURING "FIRE": IMPLICATIONS FOR PARTICLE GROWTH 476
I. Gultepe and A. Heymsfield, NCAR, Boulder, CO, USA

HYDROMETEOR DEVELOPMENT IN COLD CLOUDS IN "FIRE" 479
A. J. Heymsfield and N. C. Knight, NCAR, Boulder, CO, USA

NUMERICAL SIMULATION OF COASTAL CLOUDS WHEN SOLAR RADIATION IS BLOCKED BY SMOKE 396
C. R. Molenkamp, Lawrence Livermore National Laboratory, Livermore, CA, USA

LONG-LIVED HAWAIIAN RAIN BANDS 398
P. Smolarkiewicz, and T. L. Clark, NCAR, Boulder, CO, USA, and R. Rasmussen, Bureau of Reclamation, Denver, CO, USA

A LONG-LASTING RAINSTORM TRAVELLING ALONG A STATIONARY FRONT 401
H. Sakakibara and A. Tabata, Meteorological Research Institute, Ibaraki, JAPAN

THREE-DIMENSIONAL AIRFLOW AND VORTICITY BUDGET OF RAINBANDS IN A WARM OCCLUSION 404
O. Hertzman and P. V. Hobbs, University of Washington, Seattle, WA, USA

DOPPLER RADAR OBSERVATION OF CONVERGENCE BAND CLOUD FORMED ON THE WEST COAST OF HOKKAIDO ISLAND, JAPAN 407
Y. Fujiyoshi, K. Tsuboki and G. Wakahama, Institute of Low Temperature Science, Hokkaido University, Sapporo, JAPAN

THE USE OF OXYGEN ISOTOPES IN STUDIES OF ICE PHASE PRECIPITATION FROM WINTER STORMS 410
B. Demoz, J. A. Warburton and R. L. Stone, Desert Research Institute, Reno, NV, USA

NUMERICAL SENSITIVITY STUDY OF THE MORPHOLOGY OF LAKE-EFFECT SNOW STORMS OVER LAKE MICHIGAN 413
M. Hjelmfelt, NCAR, Boulder, CO, USA

DOPPLER RADAR OBSERVATIONS OF SNOW PARTICLES IN WINTER CONVECTIVE CLOUDS 416
H. Konishi, Osaka Kyoiku University, Osaka, Japan, and T. Endoh and G. Wakahama, Institute of Low Temperature Science, Hokkaido University, Sapporo, JAPAN

THE RELATIONSHIP BETWEEN ENTRAINMENT RATE AND SOME PRODUCTS OF 1-D Cb MODEL 419
M. Curic and D. Janc, University of Belgrad, Beograd, YUGOSLAVIA

ON THE ENTRAINMENT IN CUMULI – A CONTRIBUTION TO A CASE STUDY 422
I. Nemesova, Institute of the Physics of the Atmosphere, Prague, CZECHOSLOVAKIA

A FINE RESOLUTION TWO-DIMENSIONAL NUMERICAL STUDY OF A CLOUD-CAPPED BOUNDARY LAYER 425
M. K. MacVean and S. Nicholls, Meteorological Office, Bracknell, Berkshire, UK

A NUMERICAL METHOD FOR INTEGRATING THE THERMAL CONVECTION EQUATIONS IN THE ATMOSPHERE 428
I. M. Enukashvily, Israel Meteorological Service, Bet-Dagan, ISRAEL

A DIAGNOSTIC STUDY OF VERTICAL FLUXES IN CUMULUS CLOUDS USING MODEL OUTPUT DATA 431
M. J. Weissbluth and W. R. Cotton, Colorado State University, Fort Collins, CO, USA

EFFICIENCY OF DEEP CONVECTIVE CLOUDS RELATED WITH SOME PARAMETERS OF OCCURRENCE OVER THE ARGENTIN TERRITORY 434
M. E. Saluzzi, Universidad de Buenos Aires, Conicet, Buenos Aires, ARGENTINA

CHARACTERISTICS OF MESOSCALE CLOUD SYSTEMS DEVELOPED IN THE MARITIME SUBTROPICS 437
M. Ishihara, A. Tabata, K. Akaeda, T. Yokoyama and H. Sakakibara, Meteorological Research Institute, Ibaraki, JAPAN

ON THE MERGER OF TWO SMALL CONVECTIVE RADAR ECHOES 440
B. Ackerman and P. C. Kennedy, Illinois State Water Survey, Champaign, IL, USA

MICROPHYSICAL STRUCTURE OF JAPANESE WARM-FRONTAL CLOUDS OBSERVED WITH A NEW TYPE SONDE (HYVIS) 521
M. Murakami, T. Matsuo, H. Mizuno and Y. Yamada, Meteorological Research Institute, Ibaraki, JAPAN

COLD FRONTAL PASSAGE OVER THE SIERRA BARRIER 525
J. D. Marwitz, University of Wyoming, Laramie, WY, USA

A NUMERICAL MODELING STUDY OF COLD-FRONTAL RAINBANDS 527
D. J. Knight and P. V. Hobbs, University of Washington, Seattle, WA, USA

NUMERICAL SIMULATION OF RAINBANDS CAUSED BY MESO-ß SCALE POTENTIAL VORTICITY ANOMALIES 529
H. R. Cho and D. S. T. Chan, University of Toronto, Toronto, Ontario, CANADA

SIMULATION OF FRONTAL CLOUDS AND PRECIPITATION USING A MESOSCALE WEATHER PREDICTION MODEL 532
E. Müller and U. Wacker, Deutscher Wetterdienst, Offenbach/M., FRG

LONG LASTING TRADE WIND RAINBANDS 535
T. Takahashi, Kyushu University, Fukuoka, JAPAN

CHARACTERISTICS OF CUMULUS BANDCLOUDS OFF THE COAST OF HAWAI 538
G. B. Raga, J. B. Jensen**, J. Wettlaufer*, and M. B. Baker*, *University of Washington, Seattle, WA, USA, **NCAR Boulder, CO, USA*

STRUCTURE OF LAYER CLOUDS AS OBSERVED SIMULTANEOUSLY BY A MICROWAVE RADIOMETER AND AN 8.6 MM RADAR 541
G. Liu and T. Takeda, Water Research Institute, Nagoya University, Nagoya, JAPAN

ANALYSIS OF SINGLE DOPPLER RADAR DATA: WIND FIELD AND PRECIPITATION OBSERVATIONS DURING A FRONTAL PASSAGE 544
M. Hagen, Institut für Physik der Atmosphäre – DFVLR, Oberpfaffenhofen, FRG

THE OCCURRENCE OF ICE IN CLOUDS ASSOCIATED WITH EXTRATROPICAL CYCLONES 547
R. T. Bruintjes, South African Weather Bureau, Pretoria, REPUBLIC OF SOUTH AFRICA

SESSION 13: GRAUPEL AND HAIL

THE SUPERCOOLING OF SURFACE WATER SKINS OF SPHERICAL AND SPHEROIDAL HAILSTONES 551
R. List, F. Garcia-Garcia, R. Kuhn and B. Greenan, University of Toronto, Toronto, Ontario, CANADA

MICROPHYSICAL CONCEPT OF HAIL FORMATION 554
M. I. Tlisov and V. G. Khorguani, High-Mountain Geophysical Institute, Nalchik, USSR

STUDIES OF ARTIFICIAL HAILSTONES UNDER DIFFERENT EXPERIMENTAL CONDITIONS 557
F. Prodi, Istituto FISBAT-CNR, Bologna, ITALY, and A.-S. Wang, Institute of Atmospheric Physics, Academia Sinica, Beijing, PRC

WIND TUNNEL HAILSTONE GROWTH USING DOPPLER RADAR DERIVED TRAJECTORIES 560
G. B. Lesins, University of Oklahoma, Norman, OK, USA

THE EFFECT OF SUPERCOOLED DROPLET ELECTRICAL CHARGES ON THE HAIL GROWTH COAGULATIVE PROCESS 563
T. G. Bliadze, A. I. Kartsivadze, A. M. Okudjava and T. N. Saliashvili, Institute of Geophysics, Georgian Academy of Sciences, Tbilisi, USSR

GROWTH OF HAILSTONES IN CONVECTIVE CLOUDS. RESULTS OF MEASUREMENTS AND NUMERICAL EXPERIMENTS 566
S. Stoyanov, Hydrometeorological Service, Sofia, BULGARIA, M. Tlisov, High Mountain Geophysical Institute, Nalchik, USSR, and I. Geresdi, Cs. Zoltán, Cs. Székely, K. Molńar, Meteorological Service, Szaláanta, HUNGARY

HAIL IMPACTS, HAIL NETS AND DAMAGE..... 569
D. Roos, Council for Scientific and Industrial Research, Pretoria, SOUTH AFRICA, and S. F. Durrant, University of Surrey, Guildford, UK

COMPARISON OF THE SHAPE AND SIZE DISTRIBUTIONS OF RAINDROPS AND HAILSTONES..... 572
P. K. Wang, University of Wisconsin, Madison, Wisconsin, USA

TWO STAGE HAILSTONE GROWTH IN THE AUGUST 1, 1981 CCOPE STORM 574
J. C. Pflaum, University of Oklahoma, Norman, OK, USA, and R. M. Rasmussen, Bureau of Reclamation, Denver, CO, USA

ON SOME CHARACTERISTICS DETERMINING THE DEVELOPMENT OF HAIL PROCESSES IN BULGARIA 576
P. Simeonov, Hydrometeorological Service, Sofia, BULGARIA, and D. Sirakov, Sofia University, Sofia, BULGARIA

SESSION 14: CONVECTIVE CLOUDS I: MEASUREMENTS

MEASUREMENTS OF CLOUD DROPS; THEIR AEROSOL CONTENT AND CLOUD INTERSTITIAL NUCLEI NEAR THE BASES OF CONVECTIVE CLOUDS IN ISRAEL..... 579
Z. Levin, E. Ganor, C. Price and D. Pardess, Tel Aviv University, Ramat Aviv, ISRAEL

MICROPHYSICAL CHARACTERISTICS OF CONVECTIVE CLOUDS OVER THE SOUTH-CENTRAL UNITED STATES 582
M. R. Poellot, University of North Dakota, Grand Forks, ND, USA, and J. C. Pflaum, University of Oklahoma, Norman, OK, USA

INVESTIGATION BY TRACER METHOD OF THE CONVECTIVE CELLS OF CUMULONIMBUS CLOUDS 585
L. A. Dinevich, State Hydrometeorological Committee, USSR, and S. S. Salavejus, Institute of Physics of the Academy of Sciences, Lithuanian SSR

INVESTIGATING MIXING AND THE ACTIVATION OF ICE WITH GASEOUS TRACER TECHNIQUES..... 588
J. L. Stith, University of North Dakota, Grand Forks, ND, USA, M. K. Politovich and R. F. Reinking, NOAA/ERL, Boulder, CO, USA, and A. Detwiler and P. L. Smith, South Dakota School of Mines and Technology, Rapid City, SD, USA

FIRST FORMATION OF PRECIPITATION IN AN ISOLATED CONCECTIVE CLOUD..... 591
C. A. Knight, NCAR, Boulder, CO, USA

RETRIEVAL OF DYNAMIC VARIABLES IN DOPPLER-OBSERVED CONVECTIVE CLOUD SYSTEMS 594
C. E. Hane, National Severe Storms Laboratory NOAA, Norman, OK, USA

THE EFFECTS OF THE EXISTENCE OF STRATIFORM CLOUD ON THE DEVELOPMENT OF CUMULUS CLOUD AND ITS PRECIPITATION..... 597
M. Huang, Y. Hong, H. Xu and H. Zhou, Institute of Atmospheric Physics, Academia Sinica, Beijing, PRC

A CASE STUDY OF A SLOW-MOVING CONVECTIVE BAND OBSERVED BY A DOPPLER RADAR..... 600
K. Akaeda, M. Ishihara, A. Tabata, T. Yokoyama and H. Sakakibara, Meteorological Research Institute, Ibaraki, JAPAN

SESSION 15: CONVECTIVE CLOUDS II: THEORY AND NUMERICAL MODELING

ANALYSIS OF DIFFERENT APROACHES TO MATHEMATICAL DESCRIPTION OF CONVECTION 603
M. V. Buikov, Ukrainian Regional Research Institute, Kiev, USSR

ORGANIZATION OF CLOUD CONVECTION BY GRAVITY WAVES IN THE LOWER TROPOSHERE 606
J. M. Radziwill, University of Warsaw, POLAND

DRAG EFFECT IN CONVECTIVE DRAFTS 609
K. E. Haman and S. P. Malinowski, University of Warsaw, Warsaw, POLAND

MOISTURE CONVERGENCE AS A SOURCE OF EXPLOSIVE GROWTH IN MODELED CUMULUS CLOUDS 612
J. H. Helsdon, Jr., H. D. Orville, R. D. Farley and F. J. Kopp, South Dakota School of Mines and Technology, Rapid City, SD, USA

THE EFFECTS OF COLD WATER SURFACE ON WARM CUMULUS CLOUDS-NUMERICAL EXPERIMENT 615
F. Kong, M. Huang and H. Xu, Institute of Atmospheric Physics, Academia Sinica, Beijing, PRC

COMPREHENSIVE RESEARCH OF CONVECTIVE CLOUD DYNAMICS FROM THE DATA OF AIRCRAFT AND NUMERICAL EXPERIMENTS 618
J. A. Dovgaljuk, V. P. Drachova, A. D. Egorov, A. A. Sinkevich, E. N. Stankova, V. D. Stepanenko, Main Geophysical Observatory, Leningrad, USSR

A STUDY ON NUMERICAL SIMULATION OF CLOUD MERGERS AND INTERACTIONS 621
M. Huang, H. Xu and W. Ji, Institute of Atmospheric Physics, Academia Sinica, Beijing, PRC

SMOOTH PARTICLE HYDRODYNAMICS AS APPLIED TO 2-D CUMMULUS TYPE CONVECTION 624
A. Gadian, UMIST, Manchester, UK

CONVECTION WAVES AND THEIR STRUCTURAL IMPACT ON CLOUD FIELDS 626
T. Hauf and T. L. Clark, NCAR, Boulder, CO, USA

COMPARISON BETWEEN NUMERICAL CLOUD RESULTS AND OBSERVATIONS 629
B. Mitzeva and V. Andreev, University of Sofia, Sofia, BULGARIA

SESSION 16: THUNDERSTORMS

LOCAL ENVIRONMENTAL CONDITIONS INFLUENCING THE GROWTH AND INTERNAL STRUCTURE OF NON SEVERE THUNDERSTORMS 632
N. E. Westcott, Illinois State Water Survey, Champaign, IL, USA

DOPPLER RADAR STUDY OF A WEAKLY SHEARED THUNDERSTORM 635
D. J. Raymond and A. M. Blyth, New Mexico Institute of Mining & Technology, Socorro, NM, USA

INTERIOR CHARACTERISTICS AT MID LEVELS OF THUNDERSTORMS IN THE SOUTHEASTERN UNITED STATES 638
D. F. Musil and P. L. Smith, South Dakota School of Mines and Technology, Rapid City, SD, USA

ELECTRIFICATION OF THE 31 JULY 1984 NEW MEXICO MOUNTAIN THUNDERSTORM 641
C. L. Ziegler, National Severe Storms Laboratory, Norman, OK, USA, and P. S. Ray and S. L. Lang, Florida State University, Tallahassee, FL, USA

RETRIEVAL OF MICROPHYSICAL VARIABLES IN NEW MEXICAN MONTAIN THUNDERSTORMS FROM DOPPLER RADAR DATA..... 644
P. S. Ray, C. L. Ziegler**, and S. L. Lang*, *Florida State University, Tallahassee, FL, USA, **National Severe Storms Laboratory, Norman, OK, USA*

ON THE ROLE OF PRECIPITATION IN MAINTENANCE OF DOWNDRAFTS IN CUMULONIMBUS CLOUDS 647
H. Pawloska-Mankiewicz, University of Warsaw, POLAND

INFLUENCE OF THUNDERSTORM-GENERATED ACOUSTIC WAVE ON COAGULATION..... 650
M. Curic, University of Belgrad, Beograd, YUGOSLAVIA, and Z. Vukovic, Hydrometeorological Institute of Serbia, Beograd, YUGOSLAVIA

SESSION 17: SATELLITE STUDIES

SATELLITE-SURFACE LINKAGE TO ESTIMATE MID-LATITUDINAL PRECIPITATION FEATURES..... 653
M. Scholl, Freie Universität Berlin, Berlin, FRG

RESULTS FROM THE RAINFALL ESTIMATION STUDIES BASED ON METEOSAT DATA..... 656
O. M. Turpeinen, European Space Operations Centre, Darmstadt, FRG

COMPARISON OF SATELLITE DATA WITH SURFACE-BASED REMOTE SENSING MEASUREMENTS IN UTAH WINTER OROGRAPHIC STORMS..... 659
D. C. Rogers, Colorado State University, Fort Collins, CO, USA, and K. Sassen and G. C. Dodd, University of Utah, Salt Lake City, UT, USA

PASSIVE MICROWAVE OBSERVATIONS OF THUNDERSTORMS FROM HIGH-ALTITUDE AIRCRAFT 662
G. M. Heymsfield, NASA Goddard Space Flight Center, Greenbelt, MD, USA, and R. Fulton, General Sciences Corporation, Laurel, MD, USA

NUMERICAL FRONTAL ANALYSIS SCHEME FOR OPERATIONAL INTERPRETATIONS OF SATELLITE PICTURES AND PRECIPITATION ESTIMATIONS..... 665
L. Lesch, Institut für Meteorologie, Freie Universität Berlin, Berlin, FRG

SESSION 18: SEVERE STORMS AND HURRICANES

A MIDDLE LATITUDE SQUALL LINE IN FRANCE..... 666
G. Jaubert, M. Chong and J. M. Giudicelli, Direction de la Météorologie Nationale (EERM/CNRM), Toulouse Cedex, FRANCE

A STUDY OF THE DYNAMICS OF SQUALL LINES USING A NON-HYDROSTATIC CLOUD MODEL 669
D. B. Parsons, R. Rotunno, J. B. Klemp and M. L. Weisman, NCAR, Boulder, CO, USA

PHYSICAL PROCESSES AND OBSERVED FEATURES IN MICROBURST-PRODUCING STORMS 672
M. Hjelmfelt and C. Kessinger, NCAR, Boulder, CO, USA

ON THE MICROPHYSICS OF MICROBURSTS..... 675
H. D. Orville, F. J. Kopp, R. D. Farley and Y. C. Chi, South Dakota School of Mines and Technology, Rapid City, SD, USA

OBSERVATION OF MICROBURSTS FROM SNOW CLOUDS IN WINTER MONSOON SEASON 678
H. Uyeda, R. Shirooka and K. Kikuchi, Hokkaido University, Sapporo, JAPAN

EVOLUTION OF CONVECTIVE STORM ALONG BOUNDARY LAYER CONVERGENCE LINES..... 681
J. Wilson and C. Müller, NCAR, Boulder, CO, USA

THE STRUCTURE OF THE CONVECTIVE CELLS AND THE DYNAMICS OF HAILSTORM DEVELOPMENT IN ALAZANI VALLEY 684
A. I. Kartsivadze, T. G. Salukvadze, R. I. Doreuli, E. I. Khelaya, and A. Sh. Balavadze, Institute of Geophysics, Georgian Academy of Sciences, Tbilisi, USSR

EVOLUTION OF MESOCYCLONIC CIRCULATION IN SEVERE STORMS 687
P. I. Joe and C. L. Crozier, Atmospheric Environment Service, Toronto, Ontario, CANADA

A NUMERICAL STUDY OF MULTICELLULAR SEVERE CONVECTIVE STORMS FOLLOWED BY LONG-LASTING HEAVY RAINFALL 690
J. Shiino, Meteorological Research Institute, Ibaraki, JAPAN

3-D NUMERICAL MODELING AND RADAR OBSERVATIONS OF DEEP CONVECTIVE CLOUDS 693
H. Höller, Institut für Physik der Atmosphäre, DFVLR-Oberpfaffenhofen, Weßling, FRG

OBSERVED STRUCTURE AND EVOLUTION OF A MESOVORTEX IN THE TRAILING STRATIFORM REGION OF A MCC 696
J. Verlinde and W. R. Cotton, Colorado State University, Fort Collins, CO, USA

MELTING LAYER STRUCTURE IN MCC STRATIFORM PRECIPITATION 699
P. T. Willis, Atlantic Oceanographic and Meteorological Laboratories, Miami, FL, USA, and A. J. Heymsfield, NCAR, Boulder, CO, USA

DUAL-DOPPLER AND AIRBORNE MICROPHYSICAL OBSERVATIONS IN THE STRATIFORM REGION OF THE 10-11 JUNE MCS OVER KANSAS DURING PRESTORM 702
S. A. Rutledge, R. A. Houze Jr.**, A. J. Heymsfield***, and M. I. Biggerstaff** *Oregon State University, Corvallis, OR, USA, **University of Washington, Seattle, WA, USA, ***NCAR, Boulder, CO, USA*

VERTICAL DRAFTS IN THE CONVECTIVE REGIONS OF MESOSCALE CONVECTIVE SYSTEMS IN KANSAS 705
M. I. Biggerstaff and R. A. Houze, Jr., University of Washington, Seatlle, WA, USA, and S. A. Rutledge, Oregon State University, Corvallis, OR, USA

MESOSCALE PATTERNS OF ICE PARTICLE CHARACTERISTICS IN HURRICANE NORBERT 708
R. A. Houze, Jr., University of Washington, Seattle, WA, USA, and F. D. Marks, Jr., and R. A. Black, Hurricane Research Division NOAA/AOML, Miami, FL, USA

THE BULK WATER BUDGET OF HURRICANE NORBERT (1984) AS DETERMINED FROM THERMODYNAMIC AND MICROPHYSICAL ANALYSES RETRIEVED FROM AIRBORNE DOPPLER RADAR 711
J. F. Gamache, F. D. Marks, Jr. and R. A. Black, Hurricane Research Division, NOAA/AOML, Miami, FL, USA, and R. A. Houze, Jr., University of Washington, Seattle, WA, USA

MICROPHYSICS IN A CONVECTIVE CLOUD SYSTEM ASSOCIATED WITH A MESOSCALE CONVECTIVE COMPLEX – AND NUMERICAL SIMULATION 714
B. F. Fan, J. D. Yeh and W. R. Cotton, Colorado State University, Fort Collins, CO, USA, annd G. J. Tripoli, University of Wisconsin, Madison, WI, USA

OBSERVATIONAL ANALYSIS OF MESOSCALE CONVECTIVE SYSTEM GROWTH AND STRUCTURE 717
K. R. Knupp, University of Alabama, Huntsville, AL, USA

INVESTIGATION OF THUNDER AND HAIL CLOUDS USING REMOTE METHODS 719
M. R. Vatyan, M. G. Bakhsoliani, N. E. Lomidze, G. B. Brylev, B. E. Peskov, USSR

STUDIES OF CONVECTIVE CLOUDS DEVELOPMENT IN CENTRAL ASIA 723
A. D. Dzhuraev, H. A. Imamdzhanov, B. Sh. Kadyrov and V. P. Kurbatkin, The Bugaev Central Asian Regional Research Institute, Tashkent, USSR

Ackerman, B. 440
Ackerman, T.P. 125, 133,
Adzhiev, A.Kh. 161
Akaeda, K, 437, 600
Andreev, V. 629
Atkinson, N.C. 322
Azarov, A.S. 518

Baddour, O. 356
Baechmann, K. 461
Baker, M. B. 67, 538
Bakhsoliani, M.G. 719
Balavadze, A.Sh. 684
Barnes jr., A.J. 380
Baumgardner, D.G. 40, 43, 70
Bazlova, T.A. 471
Beard, K.V. 7, 31, 375
Beheng, K.D. 199
Bezrukova, N.A. 518
Biggerstaff, M.I. 702, 705
Black, R.A. 708, 711
Bliadze, T.G. 563
Blyth, A.M. 73, 635
Borisenkov, E.P. 471
Bott, A. 490
Bower, K. 37
Braun, P. 246
Breidenthal, R. 67
Brenguier, J.L. 91
Bringi, V.N. 330, 455
Brown jr., Ph. S. 169
Brown, P.R.A. 55, 138, 141
Bruintjes, R.T. 547
Brylev, G.B. 719
Biukov, M.V. 6o3
Buranbaev, N.F. 518

Carswell, A.I. 338
Castillo, R.A. 251, 267
Caylor, I.J. 49, 372
Chan, D.S.T. 529
Chandler, A.S. 279
Chandra, M. 154
Chatterjee, R.N. 58
Chaumerliac, N. 106, 319
Chen, J.P. 306
Chen, S. 130
Chernikov, A.A. 518
Chi, Y.C. 675
Cho, H.R. 529
Chong, M. 666
Choularton, T.W. 37, 55, 279, 316
Chuang, C. 31
Clark, P.A. 279
Clark, T.L. 88, 353, 398, 626
Coakley, J.E. 121
Colburn, D.C. 125
Coldaev, A.V. 518
Colin, J.-L. 288, 463
Cooper, W.A. 46
Cotton, W.R. 109, 130, 347, 359, 383, 431, 699, 714
Crozier, C.L. 449, 687, 696
Cunningham, G.A. 338
Curic, M. 419, 650
Czys, R.R. 4, 25, 64

Darlison, A.G. 138, 141, 485
Daum, P.H. 264
Davies, R. 124
Dellert, M. 246
Deluisi, J. 267
DeMott, P.J. 369
Demoz, B. 410
Dessens, J. 452
Detwiler, A. 588
Dinevich, L.A. 585
Dlugi, R. 235
Dodd, G.C. 659
Doms, G. 199
Dong, Y. 28
Doreuli, R.I. 684
Dovgaljuk, J.A. 618
Drachova, V.P. 618
Duroure, Chr. 62, 223
Durrant, S.F. 569
Duynkerke, P.G. 511
Dzhuraev, A.D. 723

Egorov, A.D. 618
Eldik, R. v. 246
Enderle, K.H. 291
Endoh, T. 9, 362, 416
Enukashvily, I.M. 172, 428
Eppel, D. 458

Fan, B.F. 383, 714
Fan, L. 386
Farley, R.D. 226, 612, 675
Feng, J.Q. 4
Finger, J.E. 509
Finnegan, W.G. 243
Fitzjarrald, D. 493
Flatau, P.J. 109
Forkel, R. 255
Fournier d'Albe, E.M. 452
Franken, F. 514
Friederich, B. 514
Frush, C. 335
Fuchs-Pohl, G.R. 461

Fujiyoshi, Y. 362, 407
Fukuta, N. 9, 12
Fulton, R. 662

Gadian, A. 624
Gagneux, J. 76, 211
Gamache, J.F. 711
Ganor, E. 579
Gao, Z. 389
Garcia-Garcia, F. 551
Gay, M.J. 279
Gayet, J.-F. 62, 325
Gaytandjiev, D.E. 366
Geresdi, I. 566
Gervat, G.P. 279
Giudicelli., J.M. 666
Gonda, T. 208
Gorbunov, B. 183
Grabowski, W.W. 344
Grassl, H. 458
Greenan, B. 551
Gribelin, P. 214
Griffin, M. 473
Gutelpe, I. 476
Gzirishvili, T. 185

Hagen, M. 544
Hall, W.D. 88, 100, 353
Hallett, J. 22, 28, 180
Haman, K.E. 609
Hane, C.E. 594
Harimaya, T. 190
Harrison, K. 180
Hauf, T. 626
He, G. 103
Hegg, D.A. 261
Heintzenberg, J. 34, 151, 282
Helsdon jr., J.H. 612
Hemler, R.S. 94
Hertzman, O. 404
Herzegh, P.H. 328
Heymsfield, A.J. 133, 476, 479, 699, 702
Heymsfield, G.M. 662
Hicks, E. 76, 211, 378
Hildebrand, P. 335
Hill, T.A. 279, 294
Hindman, E.E. 229
Hjelmfelt, M. 413, 672
Hobbs, P.V. 1, 121, 261, 404, 527
Hoeller, H. 693
Hoff, R.M. 338
Hoffmann, H.-E. 175
Hong, Y. 597
Houze jr., R.A. 702, 705, 708, 711
Hu, Z. 103
Huang, M. 112, 303, 597, 615, 621
Huang, S.H. 251
Huang, W. 386
Huang, Y. 386
Hudak, D. 446

Ichikawa, S. 341
Ichimura, I. 341
Illingworth, A.J. 49, 372
Imamdzhanov, H.A. 723
Iribarne, J.V. 258
Isaac, G.A. 273
Isaka, H. 214, 223
Ishihara, M. 437, 600
Isono, K. 208
Iwai, K. 193
Iwanami, K. 393

Jacob, D. 458
Jaenicke, R. 148
Jaeschke, W. 291
Jaffrezo, J.-L. 288, 463
Jameson, A.R. 328
Janc, D. 419
Jank, T. 330
Jaubert, G. 666
Jeck, R. 205
Jennings, S.G. 241
Jensen, J.B. 40, 538
Ji, W. 621
Jin, D.-Z. 507
Jochum, A.M. 82
Joe, P.I. 135, 449, 687
Johansson, B. 151
Johari, H. 67
Johnson, D.B. 375
Jones, A. 316

Kadyrov, B.Sh. 723
Kajikawa, M. 196
Kakutkina, H. 183
Kang, T.S. 446
Kapoor, R.K. 58
Kartsivadze, A.I. 563, 684
Keith, W.D. 220
Kelly, R.D. 52
Kennedy, P.C. 440, 443
Kessinger, C. 672
Khelaya, E.I. 684
Khorguani, V. 185
Kikuchi, K. 393, 678
Kim, V.M. 158
Kinne, St. 133, 488
Kins, L. 276
Klemp, J.B. 669
Knight, C.A. 591
Knight, D.J. 527
Knight, N.C. 479
Knupp, K.R. 717
Kobayashi, J. 208

Kolev, I.N. 515
Kolev, S.I. 515
Kong, F. 615
Konishi, H. 188, 416
Kopp, F.J. 612, 675
Kosarev, A.L. 482
Kostadinov, L.A. 515
Kraemer, M. 238, 514
Kraft, J. 246
Kubesh, R.J. 375
Kuhn, R. 551
Kumai, M. 249
Kuo, K.S. 468
Kurbatkin, V.P. 723

Lafore, J.P. 100
Lamb, D. 306
Lang, S.L. 641, 644
Latham, J. 73
Leaitch, W.R. 273, 338
Lee, I.Y. 312
Lei, X. 503
Lesch, L. 665
Lesins, G.B. 560
Levi, L. 217
Levin, Z. 579
Levkov, L. 458
Li, Y.-Z. 507
Li, Z. 386
Lin, N.-H. 232
Liou, K.-N. 118, 488
Lipps, F.B. 94
List, R. 446, 551
Liu, G. 541
Liu, S. 303
Livingston, J.M. 125
Lomidze, N.E. 719
Lubart, L. 217
Lueneburg, E. 154
Luepkes, C. 199
Lyons, J.H. 121

MacVean, M.K. 425
Magradze, G. 166
Malinowski, S.P. 609
Mallant, R.K.A.M. 333
Marks jr., F.D. 708, 711
Marsh, A.R.W. 279
Marwitz, J.D. 525
Matsuo, T. 144, 341, 521
Mazin, I.P. 482
McGann, B.T. 241
Meischner, P. 330, 455
Meixner, F.X. 276
Meyers, M.P. 347
Mitra, S.K. 18
Mitzeva, B. 629
Mitzuno, H. 521
Miyatake, M. 188
Molenkamp, C.R. 396
Molnar, K. 566
Monhen, V.A. 251
Mori, T. 208
Mueller, C. 681
Mueller, E. 532
Mueller, K.P. 276
Murakami, M. 144, 521
Musil, D.F. 638

Nagamoto, C. 285
Nair, S.K. 297
Nemesova, I. 422
Nevzorov, A.N. 482
Nicholls, S. 127, 322, 425
Nichols, T.R. 449
Nissen, R. 446
Nizamuddin, S. 254
Noone, K. 34, 282
Novosyolov, L.N. 164

Obenland, H. 291
Ochs, H.T. 4, 7
Ogren, J. 34, 282
Okada, K. 341
Okudjava, A.M. 563
Oraltay, R.G. 22
Orville, H.D. 226, 612, 675
Ou, S.C. 118

Pal, S. 338
Paluch, I.R. 70
Pardess, D. 579
Parsons, D.B. 669
Parungo, F. 285
Parvanov, O.P. 515
Paschenko, A. 183
Pawloska-Mankiewicz, H. 647
Penner, I.E. 79
Personne. P. 214, 223
Peskov, B.E. 719
Peters, L.K. 297
Pflaum, J.C. 574, 582
Pielke, R.A. 359
Pitter, R.L. 243
Podzimek, J. 202
Poellot, M.R. 582
Politovich, M.K. 588
Pontikis, C. 76, 211, 378
Prakash, P. 58
Price, C. 579
Prodi, F. 557
Pruppacher, H.R. 18
Pueschel, R.F. 125
Pyshnov, T. 258

Qian, M.-W. 503

Radke, L.F. 121
Radziwill, J.M. 606
Raga, G. 40, 538
Rasmussen, R.M. 353, 356, 398, 574
Rauber, R.M. 350
Ray, P.S. 641, 644
Raymond, D.J. 635
Redder, C.R. 12
Reinking, R.F. 588
Reuter, G. 97
Richard, E. 106
Rigaud, A. 76, 211, 378
Rogers, D.C. 369, 659
Roos, D. 569
Rosset, R. 319
Roth, R. 175
Rotunno, R. 669
Rudman, S.D. 322
Russel, P.B. 125
Rutledge, S.A. 702, 705

Sakakibara, H. 401, 437, 600
Salavejus, S.S. 585
Saliashvili, T.N. 563
Salukvadze, T.G. 684
Saluzzi, M.E. 434
Samokhvalov, I.V. 79
Sassen, K. 473, 659
Sasyo, Y. 208
Sato, M. 190
Saunders, C.P.R. 220
Sauvageot, H. 378
Saxena, V.K. 232
Schemenauer R.S. 135
Schmied, W. 461
Scholl, M. 653
Schroth, A. 154
Schuetz, L. 238, 514
Schumann, T. 270
Seidl, W. 235, 255
Sengupta, S.K. 468
Serrano, F. 52
Shamanaev, V.S. 79
Shiino, J. 690
Shimada, W. 188
Shirooka, R. 678
Sievers, U. 490
Simeonov, P. 576
Simmons, E.L. 322
Singh, G. 58
Sinkevich, A.A. 618
Sirakov, D. 576
Smith, P.L. 588, 638
Smolarkiewicz, P.K. 88, 353, 398, 493
Soerensen, R. 148
Soo, S.K. 446
Soulage, R.G. 62
Spanner, M.A. 125
Sprenger, U. 461
Stankova, E.N. 618
Stepanenko, V.D. 618
Stepanov, A.S. 164
Stephens, G.L. 115
Stith, J.L. 588
Stone, R.L. 410
Stoyanov, S. 566
Szekely, Cs. 566

Tabata, A. 401, 437, 600
Takahashi, T. 9, 535
Takaya, Y. 85
Takeda, T. 341, 541
Tanaka, T. 341
Tani, K. 188
Taniguchi, T. 393
Taylor, G. 67, 300
Tjernstroem, M. 499
Tlisov, M.I. 554, 566
Tokuda, A. 341
Tomazov, S.T. 161
Tripoli, G.J. 109, 130, 714
Tsuboki, K. 407
Tung, N.P. 446
Turpeinen, O.M. 656

Uyeda, H. 678

Valero, F.P.J. 133
Vali, G. 52
Vatyan, M.R. 719
Vaughan, H.C. 178
Verlinde, J. 696
Vohl, O. 18
Vukovic, Z. 650

Wacker, U. 532
Wakahama, G. 9, 362, 407, 416
Walcek, C.J. 309
Waldvogel, A. 270
Walther, C. 335
Wang, A.-S. 15, 557
Wang, P.K. 572
Wang, X.-L. 507
Warburton, J.A. 410
Weisman, M.L. 669
Weissbluth, M.J. 359, 431
Welch, R.M. 468
Wendling, P. 509
Wesley, D.A. 359
Westcott, N.E. 632
Wettlaufer, J. 538
Willis, P.T. 699
Wilson, J. 681
Wobrock, W. 496
Wrigley, R.C. 125

Xiao, H. 112
Xu, H. 112. 597, 615, 621
Xu, W. 386

Yamada, Y. 521
Yamashita, A. 188
Yeh, J.D. 383, 714
Yokoyama, T. 437, 603
Yu, Q. 466

Zdunkowski, W. 490
Zeissler, P. 461
Zhang, J. 389
Zhao, B. 364
Zheng, C.R. 507
Zhou, H. 597
Ziegler, C.L. 641, 644
Zinder, B. 270
Zoltan, Cs. 566
Zuev, V.E. 79

P R E F A C E

RESEARCH ON CLOUDS AND PRECIPITATION: PAST, PRESENT AND FUTURE

Peter V. Hobbs
President, International Commission on Cloud Physics, and Chairman
International Program Committee for the 10th International Conference on Cloud Physics

It is now thirty-four years since the 1st International Conference on Cloud Physics was held in Switzerland. The 1988 Conference marks the tenth in this series of conferences. On this occasion it is, perhaps, appropriate to glance back to our origins, to reflect on the current situation, and to look to the future.

1. EARLY HISTORY*

Questions concerning the nature of clouds, why it rains, will it rain tomorrow, what is thunder etc., must have been asked by prehistoric humans. Certainly, the ancient Greeks theorized on these matters; Aristotle appears to have known that clouds consist of water, and he speculated on the origins of hail. However, another two thousand years was to pass before it was realized that liquid water evaporates as water vapor and not air.

Chinese writings of the 2nd century B.C. associated the number six with water, and the first recorded observation that snow crystals exhibit hexagonal symmetry was made in China in 135 B.C.. Not until 1611 was the same observation made (by Kepler) in Europe. Correlations between the shapes of snow crystals and meteorological conditions were noted by Martens in 1675. By the 1760's, Wilcke was nucleating snow crystals with idoform and camphor, thereby anticipating artificial cloud seeding by 200 years!

Newton knew that moist air is less dense than dry air, but this concept was not generally understood until the latter half of the 18th century. In 1715 Barlow elaborated on an idea, the origins of which can be traced back to the 10th century, that raindrops form due to larger cloud drops overtaking and colliding with smaller drops.

Hamberger (1743) and Franklin (1749) noted that heating can cause air to rise, although it was not until 1834 that the term convection was introduced by Prout. Le Roy (1752) made great strides in clarifying ideas on dry and moist air and condensation. Du Carla (1780) had the general idea that expansion cools rising air and produces condensation, and, remarkably, he even stated that the precipitation rate is proportional to the rate of ascent. However, it was Erasmus Darwin who first stated clearly the connection between expansion, cooling and condensation (1788). Darwin also extended to the atmosphere Black's ideas on latent heat release, although it was not until the 1830's that its importance in clouds was generally recognized.

The 19th century opened with the first useful classification of clouds by Howard (1803). Cooling and warming of air by expansion and compression were described mathematically by Poisson (1823). Dove (1828) discussed cooling due to orographic ascent and to the upward flow of warm air over colder air.

The middle of the 19th century saw great activity in the studies of tornados, hurricanes and (what were later to be called) cyclones. Redfield (1836) showed that tropical storms are vortices. Espy (1841) put forward the idea that air in large weather systems may converge along a line; an idea that was developed by Loomis (1841). Over half a century was to pass before these ideas were taken up in the Norwegian frontal model of a cyclone.

Espy (1835) noted that latent heat release due to condensation reduces the rate of cooling by expansion of rising air parcels. Maille (1836) estimated the magnitude of this effect; he also calculated the precipitable water in a column and showed it could explain heavy rain. Thomson (later Lord Kelvin) derived analytical expressions for the dry and saturated lapse rates (1862). By 1868 Peslin had produced a clear description of stability and instability in the vertical displacement of air parcels.

* Much of this material is abstracted from "A History of the Theories of Rain" by W. E. K. Middleton (Franklin Watts Inc., New York, 1965). Both Middleton's account, and my own, are biased toward contributions from the western hemisphere.

The question of cloud droplet growth was tackled in earnest in the latter half of the 19th century. Following Thomson's (1870) theoretical determination of equilibrium vapor pressure as a function of drop size, Reynolds (1877) showed that growth by condensation is too slow to explain the formation of raindrops. By the turn of the century, Lenard (1904) and Defant (1905) had deduced that collisions between droplets play an important role in the growth of raindrops.

As early as 1672, Guericke had hinted at the role of particles in the formation of drops by condensation, but this idea was not confirmed until the elegant experiments of Coulier (1875) and Aitken (1881).

Fahrenheit (1724) noted that ice appeared in a flask of cold water when it was shaken, but it was de Saussure (1783) who first pointed out that water in clouds resists freezing even at low temperatures. The suggestion that hailstones may grow by collecting supercooled drops followed shortly after (Nöllner, 1853; Maille, 1853). Maille also noted that the different layers in hailstones might be due to their recycling in a cloud.

In 1789 Franklin suggested "... much of what is rain, when it occurs at the surface of the earth, might have been snow, when it began its descent ...". But it was not until the 20th century that this conjecture was put on a firm foundation by Wegener (1911), Bergeron (1933) and Findeisen (1938). Bergeron also realized that ice particles from high clouds might grow by collection as they fall through lower clouds (the "seeder-feeder" mechanism), although this idea can be traced back to Renou (1866).

This brief review of the early history of cloud physics research serves to remind us, to paraphrase Newton, that we "... stand on the shoulders of giants".

2. THE MODERN ERA

Bergeron marked the beginning of the "modern era" of cloud physics research. During this period the pace of research accelerated enormously, but we are probably too close to it to assess its overall importance. We can, however, obtain an idea of changes in the level and types of research activity by briefly reviewing the contents of the international conferences on cloud physics.

A measure of the growth in the subject is provided by the number of papers at these conferences (Fig. 1). The 1954 Conference consisted of just 20 invited papers. Since then the numbers of papers has increased sharply. At this conference (1988), 376 papers were submitted and 284 accepted. This growth is even more remarkable when it is realized that during this same period cloud physics spawned international conferences in Atmospheric Aerosols and Nucleation, Atmospheric Electricity, Weather Modification and Cloud Modeling.

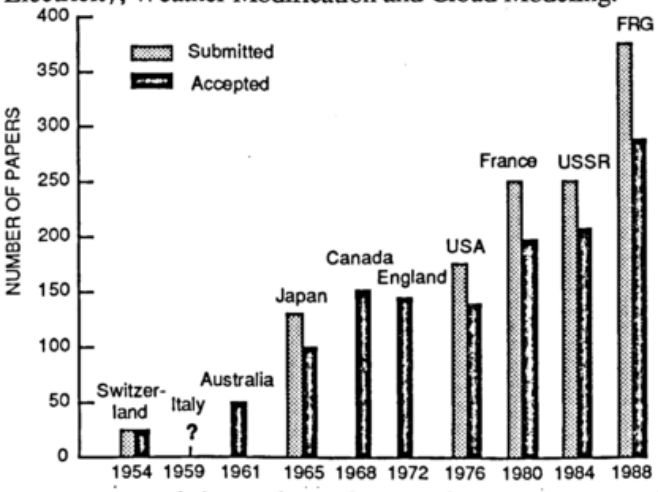


Figure 1. *Trends in numbers of papers for the International Cloud Physics Conferences.*

Shifts in research emphasis are reflected in the papers presented at the conferences. In the 1968 Conference about 75% of the papers were concerned with cloud microphysics, and the rest with larger-scale processes. In the 1988 Conference about 56% of the papers are concerned with microphysics and 44% with macrophysics. If the papers presented in 1968 are divided into field, laboratory, theoretical and numerical modeling studies, the respective percentages are 36, 33, 23 and 8. The corresponding percentages for the 1988 Conference are 51, 7, 15 and 27. Clearly, in the past 20 years a more reasonable balance has evolved between microphysical and macrophysical studies, and numerical modeling has come on very strongly. Laboratory studies, on the other hand, have fallen off sharply, to what might be less than an optimum level.

Another important development in recent years has been a broadening of the subject. The 1988 Conference contains sessions on clouds and radiation, cloud chemistry and acidic precipitation, boundary-layer processes and satellite studies. At this conference we have assembled a group of scientists with a broader range of interests in clouds than has probably ever before collected in one place.

Yet, despite these signs of significant progress, one might characterize the present period by Dickens' phrase: "... the best of times, ... the worst of times". The best of times, because we have at hand the tools to unravel complex cloud and precipitation processes. The worst of times, perhaps, because we must strive harder than ever before to obtain the resources to pursue these tasks in the face of mounting competition from many other areas of science and from societal needs in general.

3. THE FUTURE

The 13th International Conference on Cloud Physics should be held in year 2000. How will the subject have evolved by that time?

My first prediction is that the conference will not be entitled "Cloud Physics". This is a misnomer even now, as we can see from the 1988 Conference which contains many papers that are not well described by this title. For this reason alone, the conference might be called something like "International Conference on Cloud and Precipitation Processes". However, I believe the title will be even broader than this, for the reasons given below.

Wiscombe and Ramanathan (1985) have pointed out that since the 1940's meteorology has been dominated by dynamic and synoptic meteorology, but that it is now moving into an era that requires a multidisciplinary approach involving meteorology, geophysics, chemistry and biology. This realization has culminated in the International Geosphere-Biosphere Program: A Study of Global Change (IGBP), which focuses on cross-disciplinary studies related to changes in the global environment. I anticipate that the concept of the IGBP will dominate atmospheric research for the remainder of this century.

Clouds play a significant role in global change. For example, a few percent increase in low-level global cloud cover, or their optical properties, could offset the warming of the earth due to a doubling in CO_2. A recent theory proposes that a relatively small change in DMS emissions from phytoplankton in the oceans could affect the optical properties of marine clouds. Studies of the Antarctic ozone hole point to the crucial role played by polar stratospheric clouds. Cloud chemistry and precipitation scavenging contribute significantly to acid deposition. Clouds affect the vertical distribution of trace species. The effects of clouds are being incorporated into numerical forecasting models. Tropical clouds play a key role in the general circulation of the atmosphere. The list could go on, but the message is clear: cloud studies should form an integral component of the IGBP.

What can we do to meet the challenge of the future? First, we must look outward from our discipline. To be sure, we must continue to work on unsolved core problems; we must better integrate observational, theoretical and modeling studies and, in particular, we must work on the scale-interaction problem. However, we must give increasing attention to tilling the fertile fields that border our discipline. This latter task will require a broad educational base. Cloud physics evolved as much from classical physics as it did from meteorology, but in the past twenty years it has rightly shifted firmly into meteorology. In the next twenty years it will need to widen even further, to include overlapping areas with chemistry, biology and geophysics. A goal for future researchers might be to have, in addition to a core discipline, at least one interdisciplinary interface.

Predictions are fraught with danger. Perhaps, in the year 2000, the president of the ICCP will amuse the 13th Conference by recalling my crystal-ball gazing.

4. ACKNOWLEDGEMENTS

Planning for this conference began four years ago, while the 9th Conference was still in progress. Since then, the planning has increased in pace each year and involved increasing numbers of individuals. Unfortunately, it is not possible for me to list all those that have helped bring the conference to fruition. I must, however, express my sincere thanks to Professor Hans R. Pruppacher, not only for the most efficient way in which he has organized the local and national arrangements, but also for raising funds without which the conference would be much the poorer. It has been a great pleasure to work with him. I also thank the members of the International Program Committee and the National Organizing Committee for their help and support.

The work of these committees is now nearing an end. It remains for the conferees, through their presentations and discussions, to make the 10th Conference a success.

The Effect of Charge on the Coalescence of Small Precipitation Drops at Terminal Velocity

Harry T. Ochs III, Robert R. Czys and James Q. Feng

Climate and Meteorology Section
Illinois State Water Survey
Champaign, Illinois USA

It has long been recognized that charge can affect the results of collisions in streams of drops (Rayleigh, 1879; Goyer, *et al.*, 1960), between drops and a flat water surface (Jayaratne and Mason, 1964), between two drop streams (Park, 1970; Sartor and Abbott, 1972; Brazier-Smith, *et al.*, 1972), and for drops fired at suspended drops (List and Whelpdale, 1969; Whelpdale and List, 1971). We present the first observations of the effect of charge on the coalescence of colliding water drops that were initially falling freely at terminal velocity. Other experiments using uncharged drops show large discrepancies between drop stream or suspended drop results and free fall, terminal velocity results (Beard and Ochs, 1983; Ochs and Beard, 1984; Ochs, *et al.*, 1986). Therefore, it is probable that previous work on charge affects should not be directly applied to cloud situations. The present findings support this contention, because the charge required to induce complete coalescence differs from previous results at similar drop sizes and size ratios by an order of magnitude. The following new features of charged drop interactions were observed: a unique impact angle dividing the coalescence from the non-coalescence region that is independent of charge; a two-order of magnitude range of relative charge between drop bounce and complete charge-induced coalescence; a wide range of charge where a satellite drop occurs with temporary coalescence; and, at higher charge levels, the beginning of charge-induced permanent coalescence at the most grazing collisions.

The range of charges used in this experiment coincide closely with charges observed in nature: about 1.0×10^{-16} C for drops in developing cumulus clouds to about 1.0×10^{-12} C for drops in thunderstorms (Takahashi, 1972). Observations were taken with eight positive charges and three negative charges on the large drop with a constant small drop positive charge for more than 5000 interactions between a 340 μm and a 190 μm radius drop. These drop sizes are typical of drizzle drops or small precipitation drops. Charges of like sign were emphasized since drizzle drops in clouds are likely to have the same polarity (Pruppacher and Klett, 1978).

A unique computer controlled apparatus was developed to permit the study of repetitive isolated pairs of freely falling drops with independently controllable drop charge. The computer operated two drop generators, positioned the drop collisions in the camera field of view, and synchronized camera and strobe operations. The drop generators used hollow cylindrical piezoelectric transducers that vibrated radially to induce capillary waves on a jet caused by forcing water through a pin hole. The jet broke up into a stream of uniformly sized drops. Most of the drops were highly charged using a cylindrical electrode around the point of jet breakup. These drops were deflected into a gutter as they fell through a strong horizontal electric field. A switching circuit controlled by the computer periodically imposed a pulse on the drop charging voltage. This produced individual drops with lower charge which fell through the horizontal electric field and into the experiment chamber. The charge on the large and small drops was measured frequently and adjustments were made to maintain desired drop charges. Two cameras were used to record the collisions from orthogonal directions in a horizontal plane. Incandescent lamps located behind and 30° above each camera's optical axis illuminated the falling drops and produced streaks on the film. The impact angle for each collision was obtained from the distance separating the streaks.

The examples of streak signatures shown in Fig. 1 are from one orthogonal camera view. When the two drops don't collide the image in Fig. 1a resulted. Coalescence (Fig. 1b) occurred when two falling drops collided, made contact and united to form a single drop. Oscillation of the newly coalesced drop caused the waviness of the streak below the collision-coalescence point. Bounce is shown in Fig. 1c. Temporary coalescence is shown in Fig. 1d and the short streak extending to the right was caused by a satellite drop. An average satellite radius of about 80 μm (about

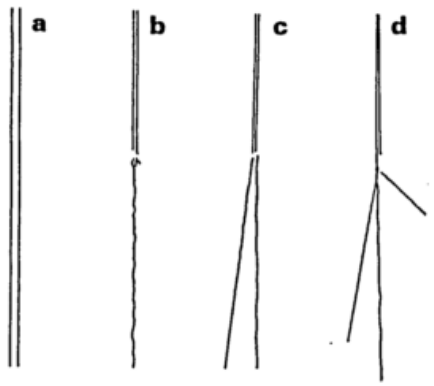


Figure 1. Tracings of streak photography images: (a) miss, (b) coalescence, (c) bounce and (d) temporary coalescence. Each image corresponds to a single frame of film. Examples without the strobe flash were chosen to better illustrate the streak images.

Table 1. Summary of Experiment Parameters.

Experiment	N	R μm	r μm	Q_R x10^{-14} C	Q_r x10^{-14} C	Q_R-Q_r x10^{-14} C	Φ_c deg.
1	66	329	193	1.0	-0.1	1.1	44
2	37	340	191	3.9	3.0	0.9	42
3	45	341	193	0.2	2.1	-2.0	44
4	81	342	192	11.0	2.3	8.7	42
5	42	331	186	35.2	1.8	33.4	44
6	77	336	192	41.0	1.7	39.4	44
7	93	340	191	84.4	2.8	81.5	43
8	50	341	197	129.7	3.8	125.4	--
9	160	339	192	208.0	2.9	205.0	--
10	47	339	198	-3.5	2.3	-5.7	40
11	45	338	197	-19.6	2.3	-21.9	42
12	42	351	195	-99.2	3.0	-102.1	44
13	130	341	194	40.1	23.4	16.7	42

7% of the small drop mass) was measured on low intensity strobe exposures superimposed on the streak images.

The parameters used are shown in Table 1. Collision results for the positively charged drops (Runs 2-9) are displayed in Fig. 2 as a function of impact angle and magnitude of difference in mean drop charge. The small drop charge, Q_r, averaged 2.5x10^{-14} C (with a standard deviation of 0.5x10^{-14} C) while the large drop charge, Q_R, ranged from 2.0x10^{-15} to 2.1x10^{-12}. We observed an abrupt transition at a critical impact angle of 43° ± 1° from a coalescence to a non-coalescence region. Collisions occurring for impact angles < 43° *always* resulted in coalescence regardless of drop charge. For impact angles > 43°, the magnitude of the mean relative charge in Fig. 3 must exceed 1.9x10^{-14} C (Q_r = 2.1x10^{-14} and Q_R = 2.0x10^{-15} for the experiment in which this minimum was observed) before charge influenced the result of collisions. Once a relative charge of about 3.0x10^{-13} C was exceeded bounce was completely suppressed and temporary coalescence resulted. Interestingly, the probability of satellite production decreased with further increases in relative charge. At higher charge, coalescence was induced when the relative charge exceeded about 8.0x10^{-13} C. Fig. 3 shows that coalescence begins at large impact angles (about 90°) and "creeps in" as charge increases. Permanent coalescence at all impact angles resulted when the relative charge exceeds 2.0x10^{-12} C. The results in Fig. 2 show that coalescence is promoted by charge even though both drops carry positive charge.

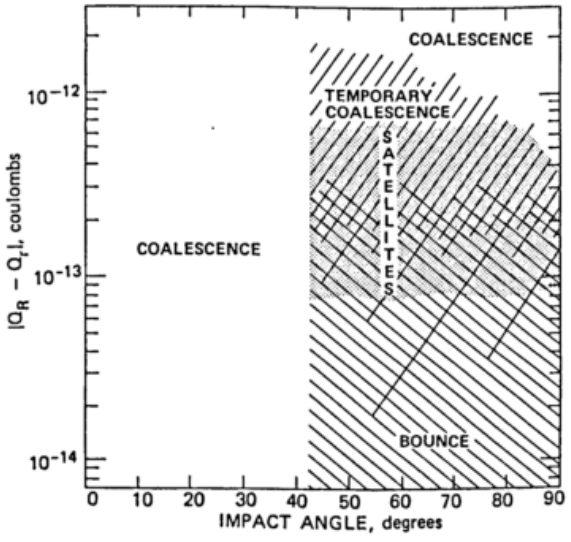


Figure 2. Collision outcome as a function of impact angle and mean relative charge. The charge on the small drop was fixed at 2.5x10^{-14} C and the large drop charge varied from 1.5x10^{-15} to 2.1x10^{-12} C in eight irregular steps. Coalescence occurs in the clear area. The hatched area sloping down from left to right indicates the area where bouncing occurs. The hatched area sloping up from left to right delineates the region of temporary coalescence. The stippled area covers the drop charges and impact angles for which satellite production is likely if temporary coalescence occurs. The concentration of hatched area overlap suggests the probability of bounce and temporary coalescence in the transition region.

Three runs were conducted using about the same mean charge on the small drop as in Runs 2-9, but with negative charge on the large drop. The collision results using oppositely charge drops were found to be generally consistent with the results using positively charged drops. Runs 10 thru 12 have the same critical impact angle, fit the overall trend for bounce to be replaced initially by temporary coalescence and do not contradict the tendency for charge induced coalescence to begin for the most glancing collisions. The only inconsistency found in the data was in Run 12 which showed satellite production when the data for positively charged drops suggested none.

Run 1 was conducted with minimum charge on each drop. The results of this run clearly indicated that the collision results for "uncharged" drops are no different from the results for weakly charged drops.

Finally, Run 13 was conducted with an increased charged on the small drop and intermediate charge on the large drop to provide further information on using $|Q_R-Q_r|$ to generalize the results. From Table 1 $|Q_R-Q_r|$ for Run 13 falls in a region where the data suggest a transition from mostly bounce to mostly temporary

coalescence with a satellite. Data from Run 13 had a critical impact angle of 43° and had a mixture of temporary coalescence and bounce that could be expected from the trends in the data from Runs 4, 5 and 11.

Previous laboratory investigations using suspended drops or drop streams have determined threshold relative charges for complete coalescence that have ranged over three orders of magnitude. A charge of 3.0×10^{-14} C caused a stream of drops to coalesce with a flat water surface (Jayaratne and Mason, 1964). Drops in continuous streams have been induced to coalesce by charges of about 2.0×10^{-13} C (Park, 1970; Sartor and Abbott, 1972) and 4.0×10^{-11} C (Brazier-Smith, *et al.*, 1972). A charge of 3.0×10^{-12} C (List and Whelpdale, 1969) and 3.0×10^{-11} C (Whelpdale and List, 1971) caused coalescence in suspended drop experiments. The first value is close to ours, however, their drop sizes and size ratios (0.07) are significantly different and thus comparisons are probably invalid. Charge-induced temporary coalescence has been reported (Jayaratne and Mason, 1964; Park, 1970; Whelpdale and List, 1971) but satellites have not. The wide range of charge required to induce coalescence in previous experiments ($3\text{-}4000 \times 10^{-14}$ C) suggests that data on charge effects cannot be reliably extrapolated to drop interactions in clouds unless the conditions of the natural interactions are well simulated. This conclusion is supported by measurements using uncharged drops at terminal velocity (Beard and Ochs, 1983; Ochs and Beard, 1984; Ochs, *et al.*, 1986) in which results were found to differ significantly from drop stream and suspended drop experiments. The wide range of previous results from supported drops and drop streams and our unique ability to study drop interactions under free fall at terminal velocity give impetus to further research.

Our new data demonstrate that effects of charge on drop coalescence are significantly more complicated than had been previously thought. Several new phenomena were uncovered that remain unexplained. Of particular interest is the constant critical impact angle dividing permanent coalescence from bounce or temporary coalescence. Since drops colliding at angles < 43° coalesce, one might expect that drops colliding at angles just > 43° almost coalesce. Using this reasoning, as charge increases, coalescence should be induced for these collisions first, and the critical angle should steadily increase with increasing charge until permanent coalescence finally occurs for the largest impact angle. Figure 2 shows this logic to be incorrect. In addition, Fig. 2 shows that the lowest charge-induced permanent coalescence occurs at the largest impact angles where the drops follow grazing trajectories. These collisions have the least interaction time and, after coalescence, the largest angular momentum which should be most conducive to temporary coalescence (Brazier-Smith, *et al.*, 1972). Another interesting aspect of our results is that satellites form at the intermediate relative charges required for temporary coalescence and are suppressed at higher relative charges. Although more refined experiments may help to explain these observations, an adequate understanding will probably require complex modeling of coalescing drops.

Our data indicates that the outcome of drop collisions varies considerably over the natural range of electrical environment found in clouds. Such variability suggests important consequences for precipitation evolution. Traditionally, for lack of better information, calculations of precipitation drop spectra have assumed that every collision results in coalescence (Berry and Reinhardt, 1974). Recent experimental results suggest that this assumption is invalid for weakly charged drops since many collisions result in bounce rather than coalescence (Ochs, *et al.*, 1986). Comparisons between the computed evolution of precipitation utilizing the traditional assumption of coalescence and a more realistic assumption including drop bounce, have shown significant differences in the concentration at which large precipitation drops are produced (Ochs and Beard, 1985). Thus we expect that a transition between bounce and coalescence induced by charge will significantly impact subsequent precipitation development. The observations presented here indicate that, in addition, moderate amounts of charge will induce satellites which, in turn, can serve as embryos for new precipitation drops. Thus the electrical state of the cloud can influence the subsequent evolution of precipitation.

Acknowledgement. This research was supported by the National Science Foundation under grant NSFATM 8314072 and NSFATM 8601549.

References

Beard, K. V; Ochs, H. T.: *J. Atmos. Sci.* **40** (1983) 146-153.
Berry, E. X; Reinhardt, R. L.: *J. Atmos. Sci.* **31** (1974) 1814-1831, 2118-2135.
Brazier-Smith, P. R.; Jennings, S. G.; Latham, J.: *Proc. Roy. Soc. London* **A326** (1972) 393-408.
Goyer, G. G.; McDonald, J. E.; Baer, F.; Braham, R. R.: *J. Meteor.* **17** (1960) 442-445.
Jayaratne, O. W.; Mason, B. J.: *Proc. Roy. Soc. London* **A280** (1964) 545-565.
List, R.; Whelpdale, D. M.: *J. Atmos. Sci.* **26** (1969) 305-308.
Ochs, H. T.; Beard, K. V.: *J. Atmos. Sci.* **40** (1984) 863-867.
Ochs, H. T.; Beard, K. V.: *J. Atmos. Sci.* **42** (1985) 1451-1454.
Ochs, H. T.; Czys, R. R.; Beard, K. V.: *J. Atmos. Sci.* **43** (1986) 225-232.
Park, R. W.: Ph.D. Thesis, University of Wisconsin (1970) 108-111.
Pruppacher, H. R.; Klett, J. D.: Reidel (1978) 714 pp..
Rayleigh, Lord: *Proc. Roy. Soc. London* **28** (1879) 406-409.
Sartor, J. D.; Abbott, C. E.: *J. Rech. Atmos.* **6** (1972) 479-493.
Takahashi, T.: *J. Geophys. Res.* **77** (1972) 3869-3878.
Whelpdale, D. M.; List, R.: *J. Geophys. Res.* **76** (1971) 2836-2856.

WAKE-EXITED RAINDROP OSCILLATIONS

Kenneth V. Beard and Harry T. Ochs

Climate and Meteorology Section, Illinois State Water Survey
2204 Griffith Drive, Champaign, Illinois 61820

1. INTRODUCTION

The notion that raindrop oscillations can be excited by eddies detaching from the drop originated with Gunn (1949) who postulated that the lateral drift behavior of 1 mm diameter drops might be caused by a mechanical distortion at resonance between the eddy shedding frequency and the oscillation frequency. In spite of the wide acceptance of this hypothesis as fact, the resonance phenomenon had not been observed. The major difficulty in studying wake-excited oscillations for water drops falling in air is the coincidental drift behavior; such drops cannot be contained within a wind tunnel or an acceleration column. We designed a special experiment to determine the effect of wake forcing on drop shape under free-fall conditions. The experimental approach minimized the lateral drift problem by generating drops at terminal velocity in still air whereby wake-excited oscillations were investigated over relatively short distances.

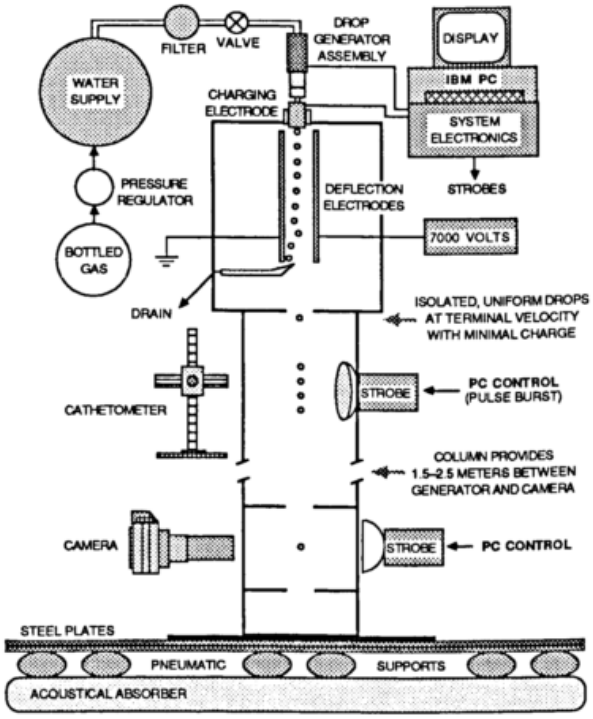


Fig. 1. Diagram of experimental apparatus.

2. METHOD

Details of the design of our one-story experiment for measuring the axis ratio of small raindrops are given in Fig. 1. The upper third of equipment is the system for producing isolated, uniform drops (consisting of pressurized water supply, drop generator assembly, charging electrode, electrostatic deflection chamber and PC controls). The lower 2 chambers are for measuring drop velocity using a cathetometer and strobe (dark-field), and for bright-field photography drop silhouettes. The fall columns that extend the generator to camera distance from 1.5 to 2.5 m are not shown. The chambers and water reservoir are on separate platforms to isolate the experiment from vibrations. The camera, cathetometer and strobes are supported by a metal frame around the experiment that rests on the floor.

3. RESULTS

The major phase of our experimentation on wake forcing has been completed with results that are summarized by Fig. 2 where the axis ratio for small raindrops is given as a function of drop diameter. For the smaller drops ($d \leq 1$ mm) our observations of axis ratios agree well with the perturbation theory (Pruppacher and Pitter, 1971) based on the numerical pressure

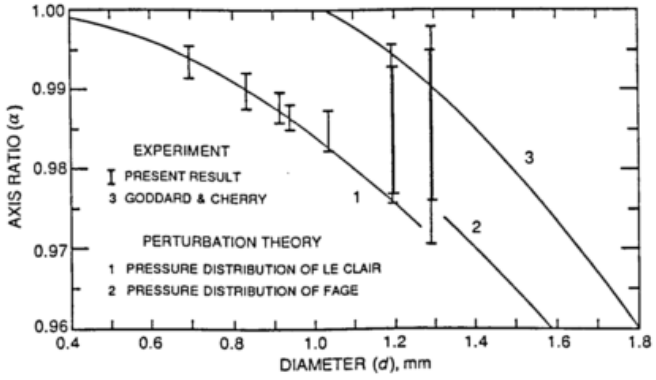


Fig. 2 Axis ratio as a function of raindrop diameter. Data are shown from present experiment as 95% confidence intervals for the mean axis ratio for smaller drops without oscillations (d = 0.7–1.03 mm), and two standard deviations for axis ratios for larger drops with oscillations (d = 1.2–1.3 mm).

distributions for steady state flow around a sphere. Above d = 1 mm the axis ratios scatter *above* the theoretical curve. [Note: the data near d = 1.2 and 1.3 mm are based on 58 observations of axis ratios.] We discovered that this one-sided scatter above the equilibrium axis ratios is consistent with oscillations only for the transverse mode of the two lower harmonics (frequencies). We also found that the transverse mode was the only oscillation response matching the forcing pattern expected from pressure changes as eddies detach from alternate sides of the upper pole.

The result of Goddard and Cherry (1984), shown as curve 3, is based on Z_{DR} measurements in rain, using the Chilbolton (UK) high resolution (1/4° beam, 0.5 μs pulse) dual-polarization radar and measurements of raindrops sizes using distrometers. The axis ratios given by curve 3 were used to rectify calculated values of Z_{DR} from the raindrop size distributions with the measured values of Z_{DR}. It seems plausible that raindrop oscillations of the type observed in our experiment might have been responsible for the shift in axis ratio, especially if oscillations also occurred at larger sizes.

It is clear from our experimental results that we have verified the long-standing hypothesis—*small raindrops oscillate because of resonant interaction with eddy shedding*—but for larger sizes, and possibly higher harmonics, than originally proposed by Gunn (1949). We plan to make additional measurements to extend the axis ratio measurements to about d = 1.5 mm using the present apparatus [Experiments for larger drops will require a multi-story experiment.] Measurements will also be made near d = 1.1 mm to help establish the transition size for resonant oscillations. We also plan to make frequency measurements to distinguish between the two possible harmonics using streak photographs of refracted and reflected light similar to the method shown in Ochs *et al.* (1986).

4. ACKNOWLEDGMENTS

This material is based upon work supported by the National Science Foundation under Grants ATM84-19490 and ATM86-01549. Any opinions, findings, and conclusions or recommendations expressed in this material are those of the authors and do not necessarily reflect the views of the National Science Foundation.

5. REFERENCES

Goddard, J. W. F., and S. M. Cherry, 1984, The ability of dual-polarization radar (copolar linear) to predict rainfall rate and microwave attenuation. *Radio Sci., 19*, 201-208.

Gunn, R., 1949: Mechanical resonance in freely falling drops. *J. Geophys. Res., 54*, 383-385.

Ochs, H. T., R. R. Czys, and K. V. Beard, 1986: Laboratory measurements of coalescence efficiencies for small precipitation drops. *J. Atmos. Sci., 43*, 225-232.

Pruppacher, H. R., and R, L. Pitter, 1971: A semi-empirical determination of the shape of cloud and raindrops. *J. Atmos Sci., 28*, 86-94.

TEMPORAL VARIATIONS OF SNOW CRYSTAL GROWTH PARAMETERS

Tsuneya Takahashi*, Norihiko Fukuta**, Tatsuo Endoh* and Gorow Wakahama*

* The Institute of Low Temp. Sci., Hokkaido Univ., Sapporo, 060 Japan
** Dept. of Meteor., Univ. of Utah, Salt Lake City, Utah 84112, U.S.A.

1. INTRODUCTION

Accurate growth behavior of free-falling snow crystals reproduced under clearly controlled laboratory conditions is indispensable not only for studying snowfall mechanisms but also for planning cloud seeding and assessing the result.

Although there exists some information in the literature on relations between snow crystal growth parameters such as crystal masses, dimensions and velocities, temporal variations of these parameters are not sufficient (Fukuta, 1969; Ryan et al., 1976). Fukuta et al. (1982) succeeded in suspending and growing a snow crystal for 10 min using a newly devised supercooled cloud tunnel which applied an aerodynamical mechanism for horizontal stability and determined crystal growth parameters. Fukuta et al. (1984) experimentally showed that the isometric crystals grown around -10°C have fast falling velocities and a tendency to develop appendages and become graupel.

In this paper, we shall report the results of measurements on temporal variations of snow crystal growth parameters by (1) vapor diffusion under water saturation and (2) riming around -10°C. The present study was carried out using the improved version of the tunnel; the growth time in our measurements was up to 30 min.

2. RESULTS AND DISCUSSION

2-1 TEMPORAL VARIATIONS OF GROWTH PARAMETERS BY VAPOR DIFFUSION UNDER WATER SATURATION

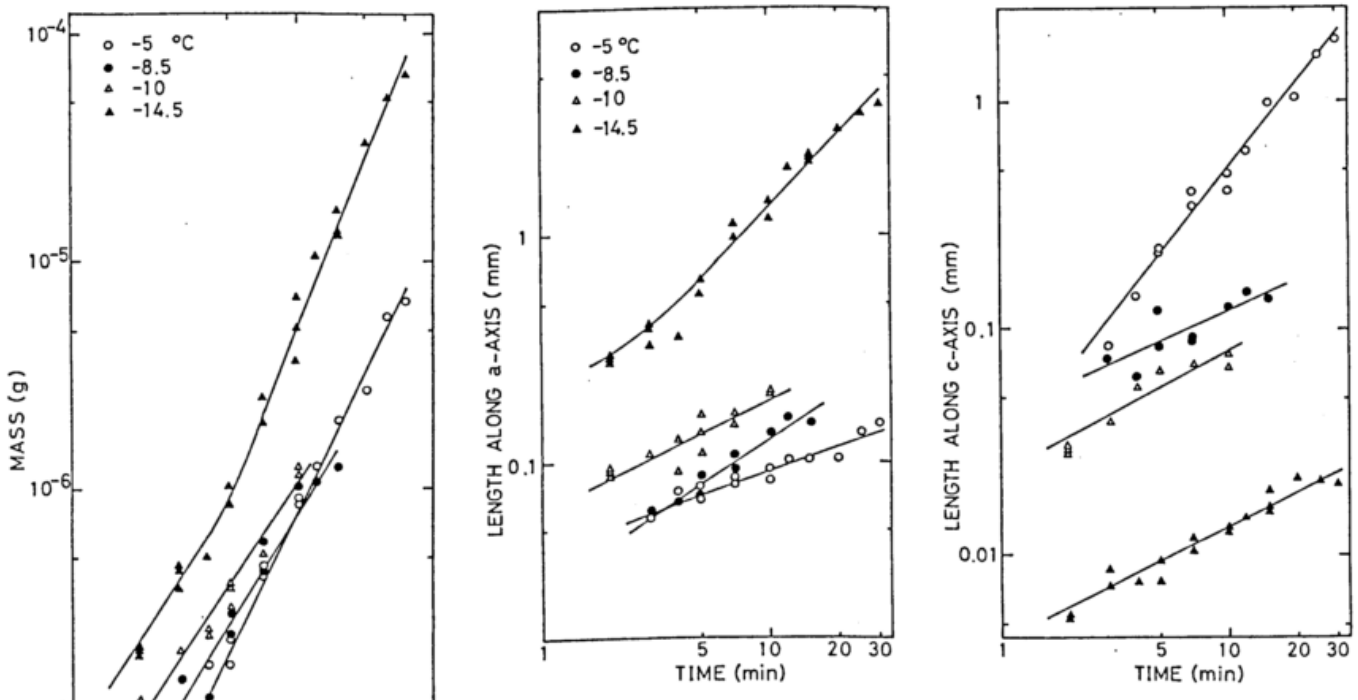


Fig. 2 Temporal variations of crystal dimensions.

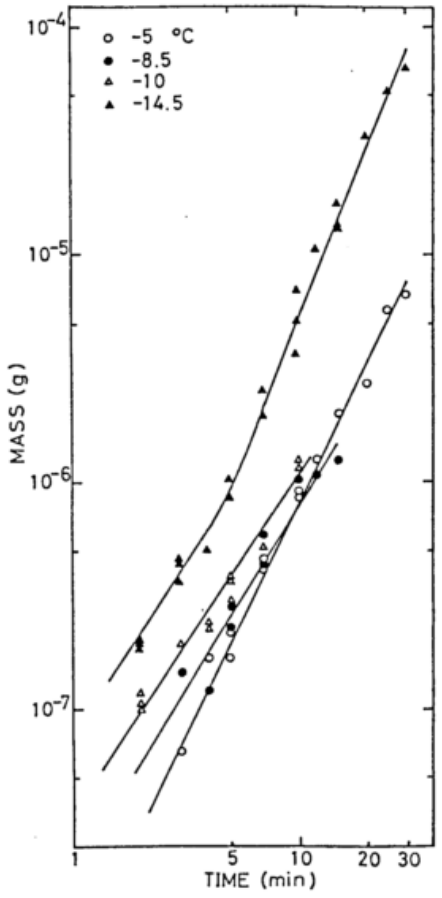


Fig. 1 Temporal variations of crystal masses.

The observed crystal habits were needles at -5°C, columns at -8.5°C and double plates at -10°C. At -14.5°C, the crystal shape changed from sector to dendrite after 5 min of growth. At -8.5 and -10°C, the crystal shapes were isometric.

Figure 1 shows temporal variations of crystal masses. The slopes of isometric crystals were approximately Maxwellian value of 1.5. Those at -5 and -14.5°C were 2.0 and 1.6 (growth time < 5 min) to 2.4 (growth time > 5 min), respectively. Water vapor was deposited effectively on the dendrites and needles compared with plates and columns. Thus, the masses at -5°C became greater than those at -8.5°C after 10 min of growth.

Figure 2 shows temporal variations of crystal dimensions. At -8.5 and -10°C, 2a and c were approximately propotional to $t^{0.5}$ respectively. Those relations can be explained by solving the vapor diffusion equation around a crystal face spreading out concentrically. When side stretching occurred, i.e. needles and dendrites grew, $a \propto t^{0.36}$, $c \propto t^{1.26}$ and $a \propto t^{0.93}$, $c \propto t^{0.51}$, respectively.

Next, we discuss the ventilation factors (f_v) of needles and dendrites (see Fig. 3). f_v was obtained using the following mass growth equation:

$$f_v = (dm/dt)(A+B)/4\pi C(S_i-1)$$

where m is the crystal mass, C the crystal shape factor, S_i the ambient saturation ratio with respect to ice, A the heat conduction term and B the vapor diffusion term. dm/dt = (d log m/d log t)(m/t): d log m/d log t was obtained using Fig. 1 and m/t the experimental values. f_v was underestimated to be less than 1 in the early growth stage because the shape factors calculated for prolate or oblate spheroids having the same maximum dimensions were a little large than those of the real crystals (McDonald, 1963). The ventilation effect became noticeable after the growth time of 5 min in case of dendrites. On the other hand, it was not evident in case of needles. These results were probably related with the experimental fact that dendrites grow only over several percents of the supersaturation with respect to water, although needles develop even under water saturation in the static chamber (Kobayashi, 1961). That is, dendrites grew due to the increased apparent vapor density at the crystal edges by the ventilation effect; this result was similar to Keller and Hallett's (1982) result under the forced ventilation.

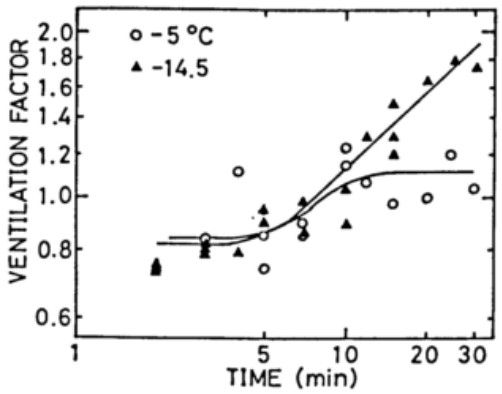


Fig. 3 Temporal variations of ventilation factors at -5 and -14.5°C.

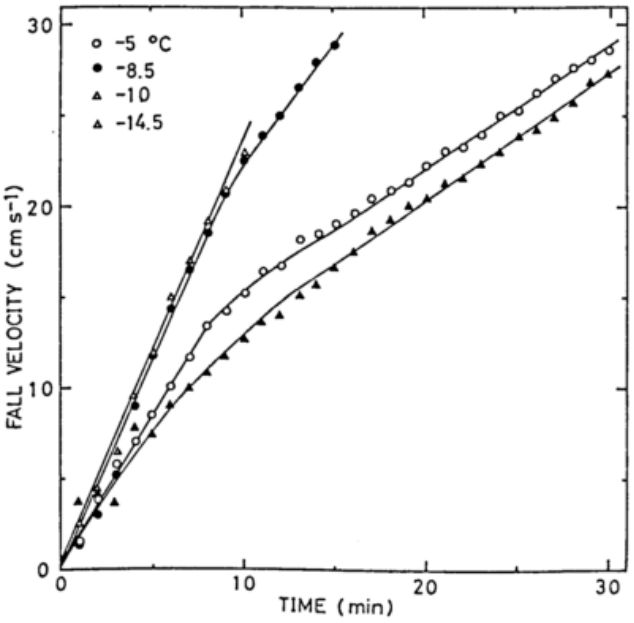


Fig. 4 Temporal variations of crystal fall velocities.

Figure 4 shows temporal variations of crystal fall velocities. The relations can be represented by a straight line at -10°C, two straight lines at -5 ang -8.5°C and a convex curve and a straight line at -14.5°C. The relation that fall velocity became constant when a dendrite grew beyond 1 mm in diameter (Nakaya and Terada, 1935), was not observed.

2-2 TEMPORAL VARIATIONS OF CRYSTAL GROWTH PA-

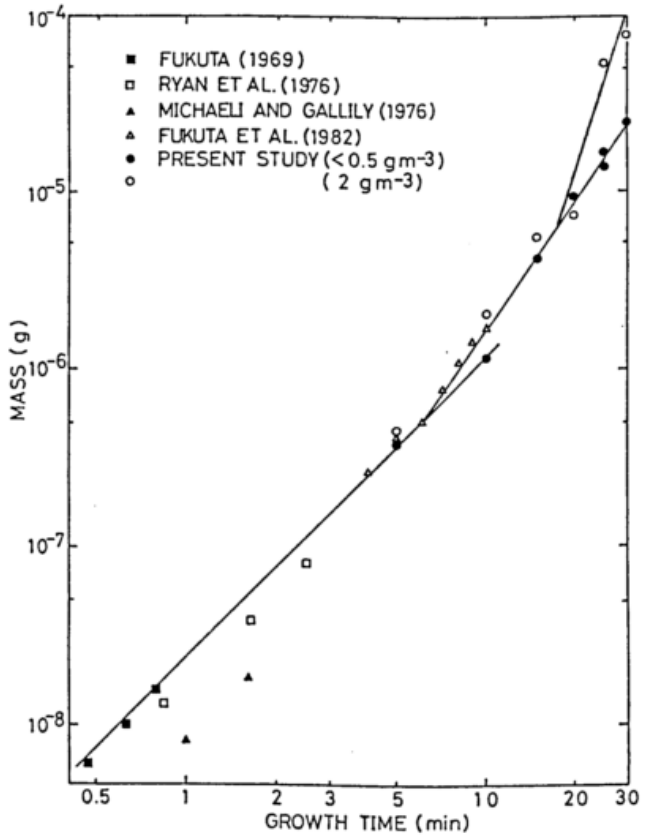


Fig. 5 Temporal variation of crystal masses at -10°C.

RAMETERS BY RIMING AROUND -10°C

Temporal variation of crystal masses for -10°C on the liquid water content below 0.5 g m^{-3} and of 2 g m^{-3} was plotted in Fig. 5. The figure also gives the results obtained by Fukuta (1969), Ryan et al. (1976), Michaeli and Gallily (1976) and Fukuta et al. (1982). The variation was represented by three stages:

Stage I: Vapor diffusional growth stage
(d log m / d log t = 1.6)

Stage II: Transitional growth stage
(d log m / d log t = 2.3)

Stage III: Graupel growth stage
(d log m / d log t = 6.2)

In stage III, the slope was nearly equal to the theoretical value of graupel growth, 6, obtained by Fukuta (1980). The particle shape was nearly spherical: this was probably indication of particle rotation. In stage II, droplets were captured only on the edges of crystal surfaces perpendicular to flow. In stage I and III, the particles followed Stokes' law and Newton's law of resistance, respectively.

ACKNOWLEDGMENTS This work was partially supported by the Division of Atmospheric Sciences, National Science Fundation under Grant ATM-82-18966 and Scientific Research Funds, Japan Ministry of Education under Grant 61020001.

REFERENCES

Fukuta, N.: Experimental studies on the growth of small ice crystals. J. Atmos. Sci. 26 (1969), 522-531.

___: Development of fast falling ice crystals in clouds at -10°C and its consequence in ice phase processes. Proc. 8th. Internat. Conf. on Cloud Phys. (1980), 97-100.

___, M. W. Kowa and N. H. Gong: Determination of ice crystal growth parameters in a new supercooled cloud tunnel. Preprints Conf. on Cloud Phys. (1982), 325-328.

___, N. H. Gong and A. S. Wang: A microphysical origin of graupel and hail. Proc. 9th Internat. Conf. on Cloud Phys. (1984), 257-260.

Keller, V. W. and J. Hallett: Influence of air velocity on the habit of ice crystal growth from the vapor. J. Crystal Growth 60 (1982), 91-106.

Kobayashi, T. : The growth of snow crystals at low supersaturations. Phil. Mag. 6 (1961), 1363-1370.

McDonald, J. E. : Use of the electrostatic analogy in studies of ice crystal growth. Z. Angew. Math. Phys. 14 (1963), 610-619.

Michaeli, G. and I. Gallily: Growth rates of freely falling ice crystals. Nature 259 (1976), 110.

Nakaya, U. and T. Terada: Simultaneous observations of the mass, falling velocity and form of individual snow crystals. J. Fac. Sci., Hokkaido, Univ. Ser. II, 1 (1935), 191-201.

Ryan, B. F., E. R. Wishart and D. E. Shaw: The growth rates and densities of ice crystals between -3°C and -21°C. J. Atmos. Sci. 33 (1976), 842-850.

EMPIRICAL EQUATIONS OF ICE CRYSTAL GROWTH MICROPHYSICS FOR MODELING AND ANALYSIS

C.R. Redder and N. Fukuta

Department of Meteorology, University of Utah
Salt Lake City, Utah 84112, U.S.A.

1. INTRODUCTION

Microphysical behaviors of ice crystals growing in supercooled clouds are an indispensable knowledge to understand subsequent ice phase processes. Existing theories are limited in their applicable ranges and need to be verified with experimental data. Using a unique, vertical, supercooled cloud tunnel, we have been measuring microphysical parameters of ice crystal growth. By comparing the cloud tunnel data (Fukuta et al., 1979; Kowa, 1981; Gong and Fukuta, 1985; Takahashi and Fukuta, to be published) and others (Fukuta, 1969; Ryan et al., 1976) with existing theories of ice crystal growth, we have recently deduced empirical expressions as a function of time up to 30 min at different temperatures in the range from -4 to -20°C, suitable for use in modeling and analysis. The expressions preserve the functional styles while being made to best match the experimental data. This paper reports the results.

2. EMPIRICAL EQUATIONS

When a small particle grows in a supersaturated environment, it is known that accommodation coefficients for mass and heat exchanges play an important role (diffusion-kinetic equation, Fukuta and Walter, 1970). For a spherical ice crystal, the mass may be expressed as

$$m = m_0 [(1 + C_{m1}t)^{1/2} - 1]^3, \qquad (1)$$

where

$$m_0 = \frac{\pi \rho_i}{3} \left(\frac{C_1}{C_2}\right)^3 ,$$

$$C_{m1} = \frac{4C_2}{C_1^2} ,$$

$$C_1 = \frac{\rho_i}{(S - 1)} \left(\frac{L^2 l_\alpha}{K R_v T_\infty^2} + \frac{l_\gamma}{D \rho_{\infty,sat}}\right) ,$$

$$C_2 = \frac{\rho_i}{2(S - 1)} \left(\frac{L^2}{K R_v T_\infty^2} + \frac{1}{D \rho_{\infty,sat}}\right),$$

$$l_\alpha = \frac{(2 - \alpha) K (2\pi R_a T)^{1/2}}{2\alpha p (c_v + R_a/2)} ,$$

$$l_\gamma = \frac{(2 - \gamma) D}{2\gamma} \left(\frac{2\pi}{R_v T_\infty}\right)^{1/2} ,$$

and t the time, ρ_i the density of ice, S the saturation ratio of the environment with respect to ice, L the latent heat of deposition per unit mass, K the thermal conductivity of air, R_v and R_a the specific gas constant for water vapor and air, respectively, T_∞ and $\rho_{\infty,sat}$ the absolute temperature and the saturation vapor density in the environment, p the pressure, c_v the specific heat at constant volume, D the diffusivity of water vapor in air, α the thermal accommodation coefficient of air and γ the deposition coefficient of water vapor.

Equation (1) gives $m \propto t^3$ when $t \to 0$ which is the mass increase under free-molecular flows, and $m \propto t^{1.5}$ when $t \to \infty$, which is the growth condition of the Maxwellian theory. When the crystal grows under the influences of coexisting supercooled cloud droplets and the fall, additional effects of fog vapor field, ventilation and riming have to be considered. Experimental data for long growth period (Gong and Fukuta, 1985; Takahashi and Fukuta, to be published) show that the exponent of t increases towards 6 (Fukuta, 1980), which is the ideal case of graupel and hail growth. Then raising the value of the exponent to the half way to accommodate the above effects except for the graupel and hail process, equation (1) may be modified to

$$m = m_0'[(1 + C_{m1}t)^{1/2} - 1] + C_{m2}t^3, \qquad (2)$$

where m_0' is equivalent to m_0 but includes additional effects such as fog and ventilation, and C_{m2} a constant to be determined empirically.

For ice crystals whose shapes are nearly independent of time, the diameter, 2a, and the c-axial length, c, may be expressed in a manner similar to equation (2). However, for very short growth time zone, data are scarce and it does not affect the behavior of ice crystal growth in the long time zone. Therefore, we ignore the former or the diffusion-kinetic effect dominated zone caused by thermal accommodation and deposition coefficients in the corresponding free molecular transportation. Then, we can write

$$2a = C_{a1}t^{1/2} + C_{a2}t, \qquad (3)$$

Table 1. Constants for empirical equations of m, 2a, c and w determined from experimental data.

T	m'_o	C_{m1}	C_{m2}	C_{a1}	C_{a2}	C_{c1}	C_{c2}	w_o	C_{w1}
°C	μg	s^{-1}	$\mu g/s^3$	$mm/s^{1/2}$	mm/s	$mm/s^{1/2}$	mm/s	cm/s	s^{-1}
-4	6.22e-4	1.78e-1	5.35e-10	2.94e-3	2.42e-5	1.77e-3	3.30e-4	8.88e0	7.76e-3
-5	3.99e-3	9.10e-2	6.85e-10	2.88e-3	3.52e-5	1.49e-3	9.39e-4	5.23e0	1.46e-2
-6	2.22e-4	4.85e-1	1.71e-9	2.84e-3	4.65e-5	2.24e-3	9.03e-4	6.40e0	1.21e-2
-7	8.58e-5	8.62e-1	1.62e-9	2.69e-3	6.91e-5	5.27e-3	4.24e-4	1.98e1	3.75e-3
-8	1.70e-4	5.60e-1	1.89e-9	2.16e-3	1.45e-4	6.48e-3	1.34e-4	5.68e1	1.35e-3
-9	2.86e-4	4.30e-1	2.52e-9	1.96e-3	2.35e-4	5.21e-3	9.29e-5	5.98e1	1.44e-3
-10	2.25e-4	5.32e-1	3.06e-9	2.33e-3	3.00e-4	4.05e-3	6.72e-5	2.38e1	4.39e-3
-11	7.25e-5	1.19e0	2.82e-9	4.00e-3	3.24e-4	2.70e-3	5.77e-5	1.37e1	8.37e-3
-12	4.59e-5	1.76e0	2.96e-9	5.40e-3	4.20e-4	2.17e-3	3.33e-5	7.22e0	1.68e-2
-13	8.06e-5	1.42e0	5.05e-9	5.44e-3	8.41e-4	1.70e-3	1.01e-5	2.26e0	6.17e-2
-14	5.03e-6	8.98e0	1.25e-8	1.58e-3	1.84e-3	1.54e-3	1.93e-6	7.98e-1	2.19e-1
-15	3.46e-4	7.28e-1	1.62e-8	4.32e-4	2.32e-3	1.40e-3	3.74e-6	3.97e-1	5.44e-1
-16	9.16e-5	1.57e0	5.80e-9	6.89e-3	1.33e-3	1.40e-3	5.20e-6	3.95e-1	5.75e-1
-17	1.31e-6	2.18e1	1.71e-9	1.08e-2	4.74e-4	1.64e-3	1.74e-5	9.30e-1	1.99e-1
-18	2.89e-8	2.54e2	1.36e-9	9.21e-3	3.37e-4	3.26e-3	6.92e-5	1.56e0	1.06e-1
-19	3.72e-9	9.97e2	1.30e-9	7.07e-3	3.20e-4	5.98e-3	3.54e-4	2.77e0	4.98e-2
-20	1.84e-4	8.73e-1	1.81e-9	5.46e-3	3.68e-4	4.79e-3	5.63e-4	4.25e0	2.81e-2

$$c = C_{c1}t^{1/2} + C_{c2}t, \qquad (4)$$

where C_{a1}, C_{a2}, C_{c1}, and C_{c2} are constants to be determined by fitting these functions to experimental data.

Equations (2) through (4) give apparent density of the crystals. The density values thus obtained create no serious inconsistencies.

For relatively small crystals, combination of the Maxwellian theory of growth and the Stokes law of fall velocity for a spherical ice gives the fall velocity $w \propto t$. Whereas, for graupel growth combined with Newton's parabolic law of terminal velocity under turbulent resistance also leads to $w \propto t$ (Fukuta, 1980). However, between these two extremes, there exists ice crystal shape enhancing zone mainly due to the ventilation effect where the fall velocity development is expected to be slower. Towards the end of this zone, riming will become more and more noticeable. For this zone before strong riming to take place, we may describe

$$w = w_o[(1 + C_{w1}t)^{2/3} - 1], \qquad (5)$$

where w_o and C_{w1} are empirical constants to be determined from the experimental data. The shape enhancing effect is small for isometric crystals at around -10°C (Fukuta, 1980).

Table 1 shows constants determined for empirical equations (2) through (5) from experimental data for m, 2a, c and w as a function of t under constant temperatures.

3. COMPARISON BETWEEN THE EMPIRICAL EQUATIONS AND EXPERIMENTAL DATA

Figure 1 compares the computed (solid lines) values with experimental data of the four growth parameters as a function of time at -11°C. Since this is the temperature close to the zone of isometric crystal growth, the shape enhancement is minimal and velocity development does not appreciably slow down.

Figure 2 gives the comparison in temperature plot. The inverted triangles indicate the computed values. a and c values are for 10 min growth and m and w values for 20 min, without correction of pressure effect which is small compared with other errors. The computed values show deviation mostly less than 30% from the respective averages of experimental data in the time range up to 30 min. For further information, see Redder (1988).

Acknowledgments. This work was jointly supported by the Division of Atmospheric Sciences, N.S.F. under Grant ATM-8616568 and Utah/NOAA Weather Modification Program under Contract No. 87-1999.

REFERENCES

Fukuta, N., 1969: Experimental studies on the small ice crystals. J. Atmos. Sci., 26, 522 - 531.

Fukuta, N., L.R. Neubauer and D.D. Erickson, 1979: Laboratory studies of organic ice nuclei smoke under simulated seeding conditions: Ice crystal growth. Final Rept. to NSF under Grant No. ENV77-15346, January 1979.

Fukuta, N., 1980: Development of fast falling ice crystals in clouds at -10°C and its consequence in ice phase processes. Preprints 8th International Conference Cloud Physics, Clermont-Ferrand, France, 97 - 100.

Fukuta, N. and L.A. Walter, 1970: Kinetics of hydrometeor growth from a vapor-spherical model. J. Atmos. Sci., 27, 1160 - 1172.

Gong, N.-H. and N. Fukuta, 1985: Supercooled cloud tunnel studies of ice crystal growth for extended periods of time. Plateau

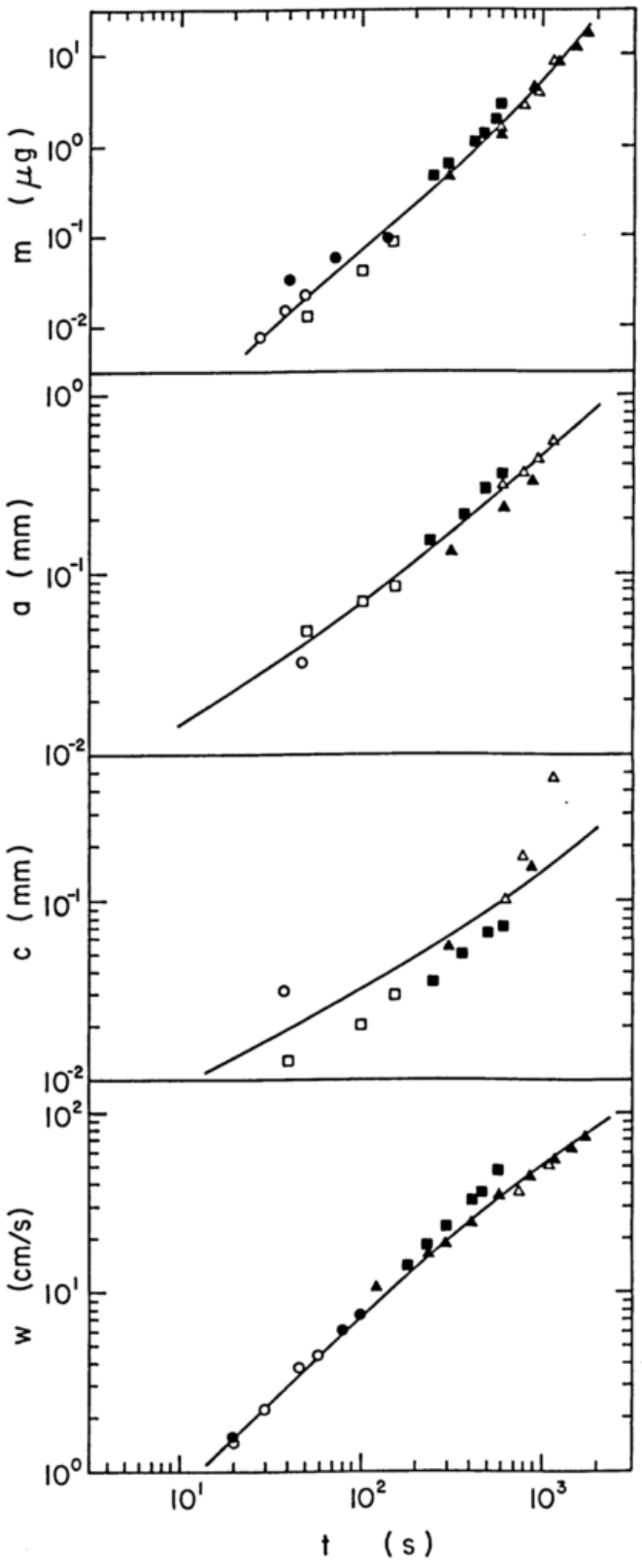


Fig. 1. Ice crystal growth parameters plotted as a function of time at -11°C. The solid curves represent the empirical equations. The geometric symbols correspond to data from the following investigations: O-Fukuta (1969), ●-Fukuta et al. (1979), □-Ryan et al. (1976), ■-Kowa (1981), △-Gong and Fukuta (1985), ▲-Takahashi and Fukuta (to be published).

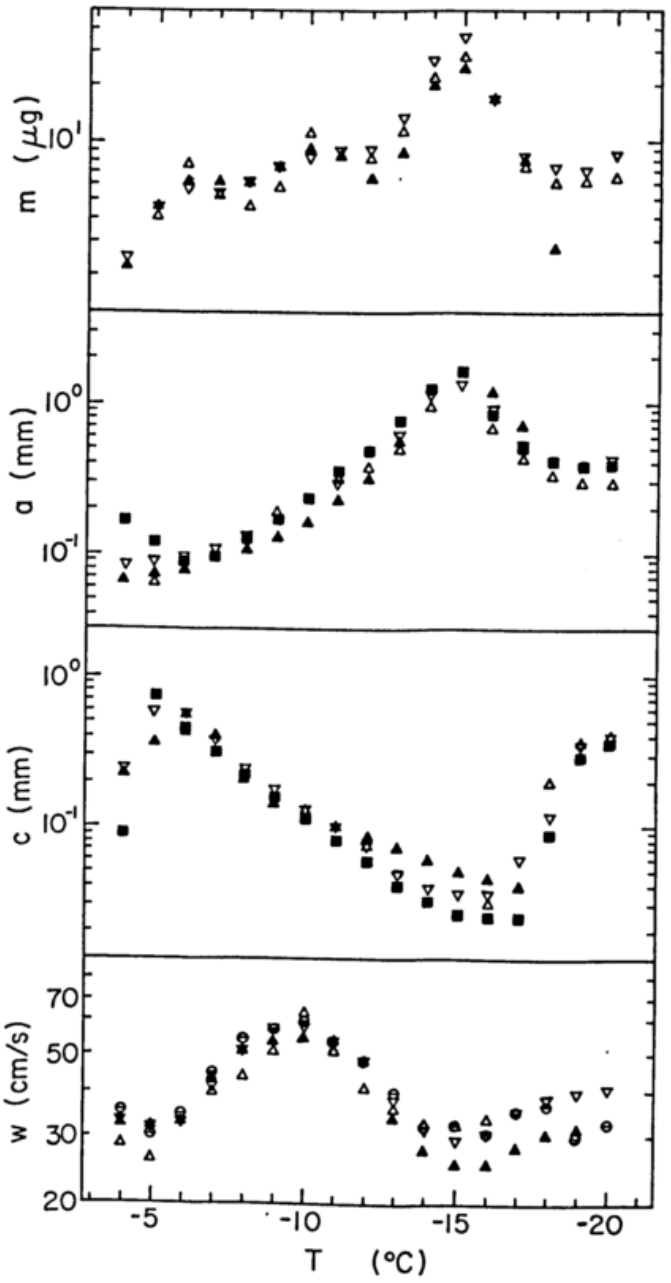


Fig. 2. Ice crystal growth parameters plotted as a function of temperature. Growth time for a and c is 10 min and that for m and w 20 min. For symbols, see Fig. 1 except that ▽- calculated from empirical equation, ⊖- calculated by another method to be published.

Meteorology, 4, 293 - 302.

Kowa, M.W., 1981: Determination of ice crystal growth parameters in a supercooled cloud tunnel. M.S. Thesis, Univ. of Utah, 1981.

Redder, C.R., Development of ice crystal growth microphysics for modeling and analysis. M.S. Thesis, Univ. of Utah, 1988, (in preparation).

Ryan, B.F., E.R. Wishart and E.W. Holroyd, III, 1976: The growth rates and densities of ice crystals between -3°C and -21°C. J. Atmos. Sci., 33, 842 - 850.

Takahashi, T. and N. Fukuta: Supercooled cloud tunnel studies on the growth of snow crystals between -4 and -20°C (in preparation).

THE CONTRAST STUDY OF NEW MODEL ON ICE CRYSTAL GROWTH

Wang Ang-Sheng

Institute of Atmospheric Physics, Academia Sinica
Beijing, The People's Republic of China

1. INTRODUCTION

The growth and shape variation of ice crystals under different environmental conditions are the most important and basic problems in atmospheric physics. In this field, the works of U. Nakaya (1954), J. Hallett and B. J. Mason (1958),and T. Kobayashi (1961) were important. But there were several flaws which need to improve and modify; and many scientists engaged this work (Wang Ang-Sheng, 1984).

Since new law of ice crystal growth was found in a wedge shaped chamber and new model was presented by Wang Ang-Sheng and N. Fukuta (1984), and Wang Ang-Sheng (1984), the quantitative growth law and Wang-Fukuta's model were payed wide attention. As a deeply study, authors will study the comparisons between new results with qualitative study, with Kobayashi's model, with dynamic experiment and with field data of natural ice crystal etc. They will presented in this paper.

2. THE CONTRAST WITH QUALITATIVE STUDY

It is well known that since 1949, the law of ice crystal growth was studied. There were some famous models in this field, for example, M. Hamajima (1949), U. Nakaya (1954), J. Hallett and B. J. Mason (1958), and T. Kobayashi (1961) et al. They are qualitative results. Due to these model were wide used in atmospheric physics, so it is very important to contrast new model with them.

Firstly we must point out that in the qualitative studied, there is no quantitative concept, so the boundery lines between different kinds of ice crystals (for example, plate and prism or prism and needle and so on) were decided by the shapes of ice crystal, of course, it is not clear. In new quantitative result, the forms of ice crystal were decided by 2a/c (Wang Ang-Sheng, 1984). In there, 2a is the longest dimension of basal plane, and c is the height of ice crystal. Their boundery lines between different kinds of ice crystal are very clear and decided by quantitative value 2a/c. This is best result. Now, the contrast of Wang-Fukuta's result with above qualitative model is shown in Table 1. From this Table, we can find that there have a best similarity between new result and above famous model in the shapes of ice crystal. When we use Wang-Fukuta's model (Wang Ang-Sheng, 1984; and 1987) to contrast with old models (M. Hanajima, 1949; U. Nakaya, 1954; J. Hallett and B. J. Mason, 1958; and T. Kobayashi, 1961), it is very clear that all results are close in the region where is higher than water saturation. This means new result has good unanimity with above models in above region. But there are different from above old models below water saturation region (Wang Ang-Sheng, 1984, and 1987). This is new important development of new work which will be given in the next section.

3. THE CONTRAST WITH KOBAYASHI-PRUPPACHER'S MODEL

Among the above models, Kobayashi's model has been frequently quoted, and Pruppacher improved it in some parts by using several results (H. R. Pruppacher and J.D. Klett, 1978). But, we pointed out that there have some flaws in the Kobayashi-Pruppacher's model (Wang Ang-Sheng and Fukuta, 1985; and Wang Ang-Sheng, 1987).

As a important advance, we contrast new result with Kobayashi-Pruppacher's model. In Fig. 1 and Fig. 2, we give Wang-Fukuta's result (Fig. 1, 1984) and Kobayashi's model (Fig. 2, 1961). Because they have same size in the figures, the comparison is easily. As mentioned above, it is clear that most situations are close in the region where is over water saturation. But they are different each other in another part which is below water saturation. Due to the limit of experimental data, the shapes of ice crystal are decided by temperature and vapor density excess in the Kobayashi-Pruppacher's model. But there were only few data in the region below water

A WIND TUNNEL STUDY ON THE MELTING OF SNOW FLAKES

S.K. Mitra, O. Vohl and H.R. Pruppacher
Johannes Gutenberg-Universität, Mainz, FRG

1. INTROCUCTION

The process of snow flake melting plays an important role in precipitation physics considering that in many midlatitude spring-, fall-, and winter storms precipitation develops as a result of individual snow crystals aggregating to larger snow crystal-aggregates or snow flakes which, on their way from the cloud to the ground, melt into raindrops. The process of melting is also of considerable significance to the dynamic behaviour of clouds as the latent heat released during melting becomes added to the buoyancy of the cloud air.

Melting in atmospheric precipitating clouds is indicated very prominently on Radar RHI displays as a zone of increased intensity of the backscattered radiation. This so called "bright band" is of typical vertical extent between 100 and 500 m with an average extent of about 300 m. This bright band, investigated by many Radar studies (for a summary see Stewart *et al.*, 1984) is essentially a result of four mechanisms acting: Between about -5°C and 0°C snow crystals of different sizes and fall velocities exhibit strong aggregation to form flakes of very similar fall velocity, thus increasing the size of the precipitation particles and decreasing their number concentration. As these flakes pass through the 0°C level they become wet, causing the dielectric constant of the particle to become almost that of water which strongly enhances the Radar reflectivity. Following a change of shape the flakes, upon completion of melting, collapse to raindrops of sizes much smaller than those of the snow flakes but with widely different fall speeds which are much larger than those of the originial flakes. This acts to decrease the concentration of the precipitation particles and thus the Radar reflectivity. Above the melting level snow crystal aggregates were found to have diameters reaching 5 to 11 mm with fall velocities between 1 and 1.5 m/sec. They were found to melt between 0 and +5°C to raindrops of equivalent diameters reaching 1.1 to 2.6 mm with terminal velocities at sea level reaching 4.3 to 7.6 m/sec, depending on the density of the individual snow flakes (see Locatelli and Hobbs, 1974; Matsuo and Sasyo, 1981a). Of specific interest for calculating the precipitation intensity *below* the melting layer from snow flake size distributions *above* the melting layer is the question as to whether the equivalent drop size distribution derived from the masses of the snow flakes above the melting layer changes as the flakes pass through the melting layer. Such changes could be the result of breakup of the flakes as they melt, or due to the coalescence of melting flakes. Past Radar studies present diverging points of view. Some support the idea that melting flakes break up or believe that melting snow flakes grow by coalescence within the melting layer, while others appear to have evidence that neither coalescence growth, nor breakup occurs in the melting layer.

In order to approach these problems, Matsuo and Sasyo (1981b) undertook a laboratory study in which they melted individual snow flakes, collected during natural snow falls. During melting the flakes were held on a net of thin nylon threads exposed to an air stream of fixed velocity of 1 m/sec and

+5.5°C. From photographic records they deduced the rate of melting of the flakes.

Unfortunately nylon threads considerably influence the melting behaviour in attracting the water to the string binding the flake to the net. In an attempt to improve on the drawbacks of the experimental set-up of Matsuo and Sasyo (1981a) we undertook our own laboartory study.

2. THE EXPERIMENTAL SET-UP

Our study was carried out with the help of a recenty completed vertical wind tunnel at the University of Mainz. This wind tunnel represents a second generation of the type, built at the University of California in 1968, and described in detail by Beard and Pruppacher (1969). The present wind tunnel built at Mainz incorporates several important improvements over the earlier tunnel built at UCLA. One of these improvements consists of a positive control of the rate of cooling and warming of the air in the tunnel, such that these rates are independent of the vertical velocity of the air in the observation section of the tunnel. This feature allows to study in detail the melting behaviour of atmospheric ice particles which can be kept at their terminal velocity freely "floating" in the tunnel air while the tunnel air is warmed or cooled at a desired rate.

For our melting studies three experimental set-ups were used. In the *first set-up*, natural or "artificial" snow flakes from laboratory grown snow crystals were placed on a net of nylon threads of 0.1 mm diameter mounted inside the vertical observation section of the tunnel. The tunnel air was adjusted to the terminal velocity of the flake such that it almost hovered on the net. This set-up was chosen to study the flake surface during the initial stages of the snow flake melting. In the *second set-up* natural or "artificial" snow flakes were held into the tunnel air while being suspended on a thin nylon fiber. In this set-up, the tunnel air was continously adjusted such that the nylon fiber was completely loose and without tension, thus insuring that the flake was at its terminal velocity. Sideways motions of the flake were, however, restricted. In the *third set-up* the snow flakes were freely suspended in the air stream of the wind tunnel. During melting of the flake the speed of the air stream was continually adjusted to keep the melting flake at its terminal velocity such that the flake remained at a fixed vertical position in the observation section. Unfortunately, in free fall, it was not possible to observe the melting of the flake to the very end of the melting since the fall speed increased rather abruptly during the final transition to a drop, and the erratic sailing motions of the flake became very intense.

The air speed of the tunnel was calibrated by means of a calibrated TSI hot wire anemometer system. The dew point, i.e. the relative humidity of the tunnel air was monitored by a Cambridge systems dew point hygrometer. The relative humidity was about 90% during all experiments. The temperature of the tunnel air was monitored by calibrated thermocouples and Platinum resistance thermometers. The rate of warming of the tunnel air was about 1.5°C/min coresponding to temperature gradients between 1.25°C/100 m and 0.35°C/100 m for the falling snow flake, considering its changing fall speed as it melted. The natural snow flakes were obtained from freshly fallen snow captured on mink fur just outside the laboratory. The "artificial" snow flakes were formed by a specially developed technique from individual dendritic and needle crystals grown from the vapor in our large walk-in cold chamber. Most of the experiments were carried out with flakes of about 10 mm diameter, corresponding to masses of about 2 mg to 11 mg, depending on the density of the individual flakes. These flakes melted into drops of 1.5 mm to 2.0 mm diameter with fall velocities of 5.4 m/sec to 7.6 m/sec. The sizes, masses and fall velocities of the present flakes correspond well to those given by Locatelli and

Hobbs (1974) and by Matsuo and Sasyo (1981a). All observations on the melting snow flakes were documented by still- and motion picture photography.

3. RESULTS

The results of our observations on melting snow flakes can be summarized as follows:

(1) All snow flakes studied melted within a fall distance of 500 m from the 0°C level for typical atmospheric temperature gradients encountered by the flakes. Most flakes melted, however, within a 300 m fall. Thus the flakes were melted into raindrops before they reached a temperature level of 2 to maximally 5°C.

(2) "Dry" snow flakes exercise a spinning, helical and shaking motion whose frequency of rotation and oscillation depends much on the overall size and on the porosity of the flake. As soon as melting starts, the frequency of rotation and oscillation changes and sideways-sailing sets in. During continued melting the way of turning of the flake may change abruptly, and one or the other motion may interupt for a brief period, all resulting from a rearrangement of the flake's internal structure. Upon the collapse of the ice framework of the flake's uncontrollable erratic downward and sideways motion sets in. Tumbling over, however, was never observed. The intense erratic sideways motions of melting flakes suggest that the growth of melting flakes by coalescence continues in the upper portion of the melting layer, the liquid portion of the flake guaranteeing a 100% coalescence efficiency upon collision.

(3) In agreement with the observation of Matsuo and Sasyo (1981a) and Knight (1979) we found that the melting of a snow flake may be divided into four stages:

(a) *Stage 1*: Small drops of tens of microns in diameter appear at the tips of the crystal branches which make up a flake, melting being most intense at the periphery and lower side of the flake.

(b) *Stage 2*: By capillary action and by surface tension effects which attempt to minimize the total surface energy, the melted water flows from the periphery effectively to the intersections of the snow crystal branches. There the water accumulates, leaving the "surface" of the flake essentially uncovered of water. Since the main ice frame remains intact a "ragged" surface of the flake is maintained. Thus, the water acts as a powerful "cement" for the flake during the melting, helping to keep the aggregate together, but at the same time attempting to collapse the particle into a more compact shape.

(c) *Stage 3*: The smallest branches of the flake's inside melt and the water also flows to the intersection of the main branches. This allows structural rearrangement to take place since the main framework is now less confined. Thus the main branches may bulge out or be flipped inward. The crystal mesh of the flake changes from one with many small openings to one with few large ones.

(d) *Stage 4*: The main ice frame collapses suddenly. The water covers it and pulls its shape together into that of a drop.

(4) Although the breakup of melting snow flakes was found not to occur as a rule, particularly not for flakes smaller than about 5 mm in diameter, three types of breakup were observed:

(a) Small pieces of ice or micron sized drops left the melting flake.

(b) Larger flakes with an off-center mass distribution, whose connecting small crystal branches melted during stage 3 broke mechanically apart into pieces.

(c) Larger flakes whose off-center mass distribution melted locally lost this water through drop shedding. In these cases the drop terminal velocities were larger than those of the flakes (e.g., a drop of about 300 µm diameter may have a terminal velocity larger than that of a flake).

(5) Rough estimates from our film and still pictures give for air of *90% relative humidity*, typical atmospheric temperature gradients, and snow flakes of about 10 mm diameter the following relations:

(a) 0, 30 70, 90% water in flake after 30, 50, 70 and 90% "melt distance", resp.

(b) 0, 15, 40, 80% of total size change taken place after 30, 50, 70, and 90% "melt distance", resp.

(c) 0, 15, 30, 50, 75% of the terminal velocity of the drop into which the flake melted after 30, 50, 70, 90, 95% "melt distance", resp.

As "melt distance" we considered the distance between the *0°C level* and the level at which the flake had melted completely into a drop. The above numbers appear to verify qualitatively the results derived by Matsuo and Sasyo (1981 a,b) from their semi-empirical heat transfer theory for snow flakes.

REFERENCES:

BEARD, K.V., and H.R. PRUPPACHER, 1969: A wind tunnel determination of the terminal velocity and drag of small water drops. *J. Atmos. Sci.*, **26**, 1066-1072

KNIGHT, C.A., 1979: Observations of the morphology of melting snow. *J. Atmos. Sci.*, **36**, 1123-1130

LOCATELLI, J.D., and P.V. HOBBS, 1974: Fall speeds and masses of solid precipitation particles. *J. Geophys. Res.*, **79**, 2185-2197

MATSUO, T., and Y. SASYO, 1981a: Melting of snow flakes below freezing levels in the atmosphere. *J. Meteor. Soc. Japan*, **59**, 10-25

MATSUO, T., and Y. SASYO, 1981b: Empirical formulas for the melting rate of snow flakes. *J. Meteor. Soc. Japan*, **59**, 1-8.

STEWART, R.E., J.D. MARWITZ and I.C. PACE, 1984: Characteristics through the melting layer of stratiform clouds. *J. Atmos. Sci.*, **41**, 3227-3236

EVAPORATION AND MELTING OF ICE CRYSTALS: A LABORATORY STUDY

Riza G. Oraltay and John Hallett
Desert Research Institute
Reno, Nevada 89506

1. INTRODUCTION

Melting and evaporation of ice crystals during free fall are important in interpretation of the radar bright band, understanding the thermodynamics of the melting layer and the ice crystal economy of cloud systems. Information on the morphology of melting relies on a limited number of observational and experimental studies (KNIGHT 1971, p.1123; MATSUO and SASYO 1981, p.1; RASMUSSEN ET AL. 1983, p.381; FUJIYOSHI 1986, p.307) while little laboratory work is available on the morphology of evaporation. We used a thermal diffusion chamber (KELLER and HALLETT 1982, p.91) to grow ice crystals (dendrites, columns and plates) as a function of supersaturation, temperature and air flow velocity and studied melting or evaporation under controlled relative humidity, temperature and fall velocity.

2. EXPERIMENTAL STUDY

After the crystals were grown the air flow was reversed through separate temperature and moisture conditioners. The temperature of the air was raised to a fixed value at controlled relative humidity. Air flow velocity was adjusted approximately equal to the fall velocity of the ice crystals. The morphology of evaporation and melting was observed through a video camera.

3. RESULTS AND DISCUSSION

3.1 MORPHOLOGY OF DENDRITIC CRYSTALS:

At low relative humidity and ice bulb temperature only evaporation was observed. As the ice bulb temperature approached ~ -0.5°C, evaporation caused breakup of ice particles (Fig. 1). A crystal of 5 mm in size produced 7 to 10 ice particles in a range 50μm to 1mm.

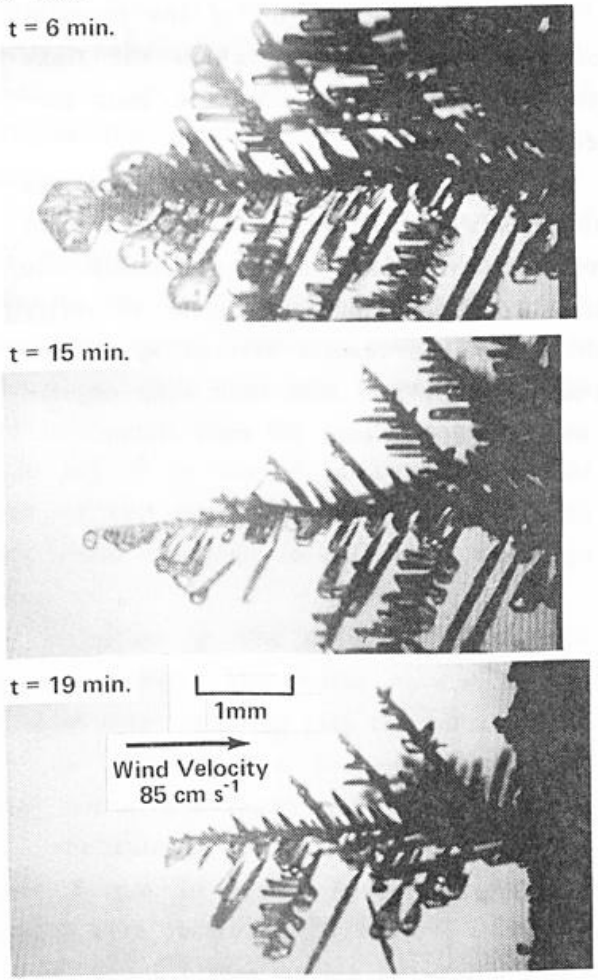


Fig. 1: Evaporation of a dendrite at T_a = +1°C, T_I = ~ 0°C, Relative Humidity 80%.

With increasing ambient air temperature, the wet bulb temperature exceeded 0°C and melting occurred. At low relative humidity (RH < 80%), melted water accumulated in the interstices. The ice pieces between them eroded very quickly, leading to shedding of water droplets containing ice pieces (about five drops 25μm to 400μm in diameter). At higher relative humidities, melted water

covered most of the crystal and water shedding took place at the later stages of melting (Fig. 2). At high relative humidity and temperature (RH > 90%, T_a > 4°C), crystals were moulded aerodynamically in the air flow and no shedding was observed.

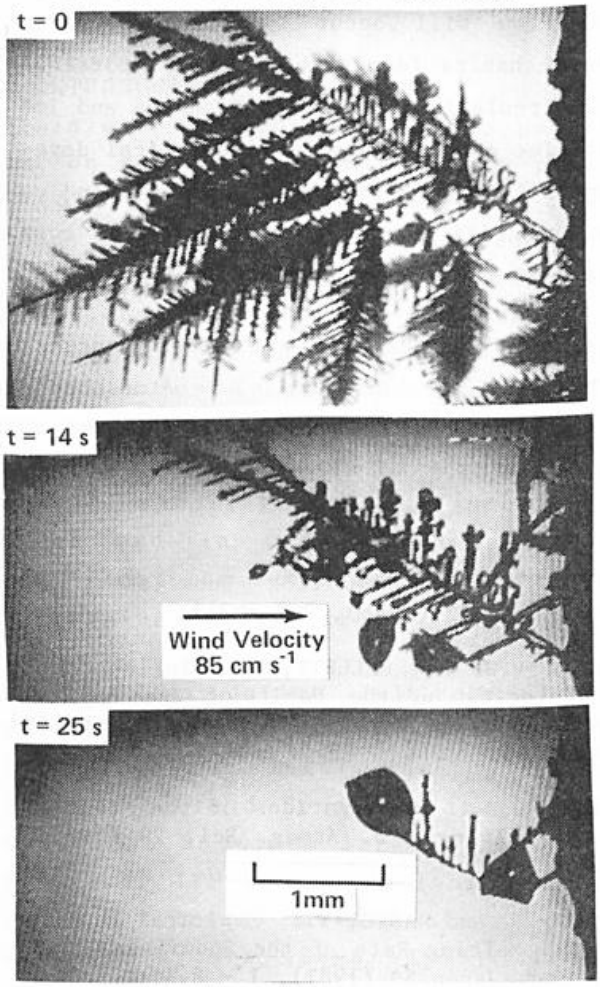


Fig. 2: Melting of dendritic crystals at T_a = +3°C, T_w = +2.1°C and 85% Relative Humidity.

3.2 MORPHOLOGY OF COLUMNS:

Melting of a cluster of columns is shown in Fig. 3. Melted water first filled the hollow inside of the columns, then accumulated at the forks. Usually one droplet formed in the middle of each crystal, and was shed when it reached a diameter of about 400μm. In most of the cases a second droplet of a smaller size (about 25μm) was formed and shed. Water droplets which were produced during the melting of columns did not contain ice pieces.

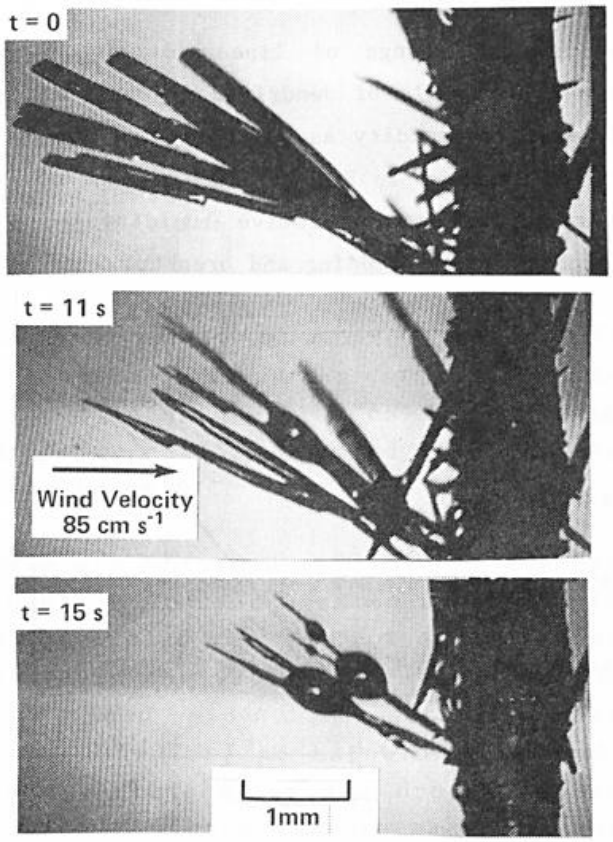


Fig. 3: Melting of columns at Ta = +1.5°C, Tw = +0.4°C and 80% Relative Humidity.

3.3 MORPHOLOGY OF PLATES:

Melting of plates was different from dendrites and columns, melted water spread over the surface and covered the crystals. Neither breakup nor shedding was observed (Fig. 4).

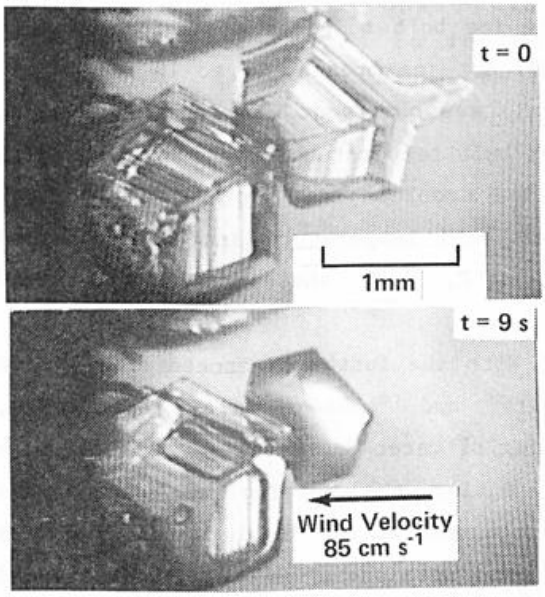


Fig. 4: Melting of a plate at T_a = +1.5°C, T_w = +0.4°C and 80% Relative Humidity.

3.4 MELTING RATES

The rate of change of linear dimensions along a or c axis of dendritic crystals at 90% Relative Humidity as a function of temperature is shown in Fig. 5. Measurement of the rates at lower relative humidity was difficult due to shedding and breakup.

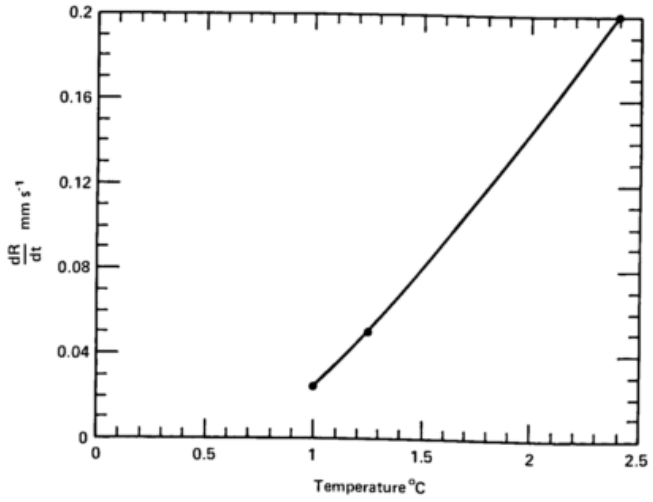


Fig. 5: Rate of change of linear dimensions along a or c axis at 90% Relative Humidity.

4. CONCLUSIONS

i. During the evaporation of columns and plates, no ice breakup was observed.

ii. Evaporation of dendritic ice crystals at low relative humidity and ice bulb temperature proceeded without any ice breakup. As the ice bulb temperature approached 0°C, significant ice breakup (7 to 10 pieces per crystal) was observed. For positive values of wet bulb temperature around 0°C, shedding of mixed droplets and ice pieces occurred. As wet bulb temperature increased, beyond about 2°C, only shedding of water was observed.

iii. With the further increase of relative humidity and ambient air temperature, shedding of water decreased.

iv. During the melting of columns, an average number of two droplets (about 400 µm and 25 µm) were shed. Melting of plates did not produce any secondary droplets.

It is inferred from our laboratory results that, the occurrence of breakup and shedding will be determined by the temperature and relative humidity of the ambient air and will result in quite different structures of the radar bright band. Secondary particle production will occur only for specific crystal habits (dendrites). The importance of recirculation of both large drops and ice particles on the overall microphysical development (TELFORD 1986, p.555) will depend on the probability of reincorporation of such particles into an appropriate updraft.

This work was carried out under Contract #ATM 8715636, Division of Atmospheric Science, National Science Foundation, Washington, D.C.

5. REFERENCES

FUJIYOSHI, Y.: Melting Snowflakes, J. Atmos. Sci. 43 (1986), 307 - 311.

KELLER, V.W. and HALLETT, J.: Influence of Air Velocity on the Habit of Ice crystal Growth from the Vapor. J. Cryst. Growth 60 (1982), 91 - 106.

KNIGHT, C.A.: Observations of the Morphology of Melting. J. Atmos. Sci. 29 (1971), 1123 - 1130.

MATSUO, T. and SASYO, Y.: Empirical Formula for the Melting Rate of the Snowflakes. J. Met. Soc. Japan 59 (1981), 1 - 8.

RASMUSSEN, R.M.; LEVIZZANI, and PRUPPACHER, H.: A Wind Tunnel and Theoretical Study on the Melting Behaviour of Atmospheric Ice Particles: III. J. Atmos. Sci. 41 (1983), 381 - 387.

TELFORD, J.W.: Comment on the paper "Microphysical Properties of Supercooled Cumulus Clouds in which an Ice Particle Multiplication Process Operated" by MOSSOP, S.C. Quart. J.R. Met. Soc. 112 (1986), 555-560.

A NEW MECHANISM FOR ICE INITIATION IN WARM-BASED MIDWESTERN CUMULI

Robert R. Czys

Illinois State Water Survey
Climate and Meteorology Section
Champaign, Illinois USA

1. INTRODUCTION

Collisions between supercooled precipitation drops are examined as a possible source for ice in the warm-based summer convective clouds of the central United States. Microphysical observations taken during the summer of 1986 as part of the Precipitation Augmentation for Crops Experiment (PACE) have shown, as was originally reported from Project Whitetop (Braham, 1964), that ice can originate at temperatures warmer and in concentrations higher than might be expected solely from ice-forming nuclei (IFN).

On two days during July 1986, PACE collected microphysical data at the -10°C level. Initial ice concentrations determined from 2-D images were as much as 35 times larger than typical summer IFN concentrations measured over the central United States using membrane filters (Czys, 1977). It was not unusual for PACE86 clouds to develop graupel concentrations between 10 to 20 ℓ^{-1} with mean diameters from 125 to 325 μm before cloud top temperature reached -11°C. All clouds developed ice in the presence of supercooled rain and this is one clue that has led to the consideration of freezing as a product of an active supercooled coalescence (cold-rain) process.

2. LABORATORY EVIDENCE

An exploratory investigation was conducted to determine if supercooled distilled deionized water could be made to freeze when subjected to mechanic shocks. In each of four experiments about two dozen millimeter-size drops (≈100 $\mu\ell$ per drop) were placed on a chrome stage smoothly coated with petroleum jelly. The stage was then placed in an open-top cold box and the drops were slowly cooled to a temperature below 0°C.

Data was obtained at constant temperature for drops cooled to -10°C and for drops cooled to -15°C. The air temperature in the vicinity of the drops was -13°C and -16°C, respectively. Here only data for the experiment at -10°C is reported. After the drops had been cooled to these temperatures a length of time elapsed and then mechanical shocks were transmitted to the cooling stage by repeated tapping with a plastic mallet.

Figure 1 shows drop freezing probability with time for drops cooled to -10°C for two different trials distinguished by the dashed and solid line. The time at which the drops began to receive mechanical shocks is indicated by the arrows. As can be seen in Fig. 1 undisturbed, most of the drops re-

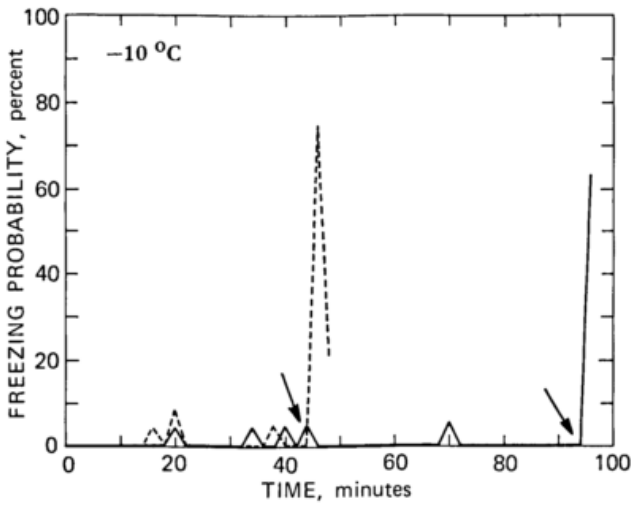


Figure 1. Freezing probability verses time for drops cooled to -10°C.

mained supercooled for lengths of time far in excess of the 3 minutes or so it takes for a cloudy air parcel to pass from 0 °C to -10°C at ≈8 m s^{-1}. At -10°C only 5 drops in 24 froze during the 90 minutes preceding mechanical disturbance and for the other run only 4 drops in 24 froze during 45 minutes. Nearly identical results were obtained in the experiment at -15°C.

Fig. 1 also shows that freezing probability jumps sharply precisely at the onset of mechanical disturbances. This result suggests that more than chance was involved in the freezing of the drops. However, further investigation is warranted since these results are prone to uncertainties introduced from the use of a supporting substrate.

3. PHYSICAL MECHANISM

Adiabatic cooling in the vicinity of mechanically induced bubble nucleation is proposed as the physical mechanism for ice nucleation. If a liquid is subjected to a sufficient pressure decrease (or a temperature increase or both), bubble growth occurs and the associated local temperature effects depend on growth rate relative to the rate at which dissolved air can come out of solution. Net adiabatic cooling is possible if the bubble expands faster than the dissolved air is drawn out of solution. Once a bubble forms its collapse is always limited by the slow rate at which the air dissolves back into the water.

A simple calculation suggests that adiabatic temperature decreases on the order of 100°C are possible assuming that a spherical cluster of gas molecules expands to 0.5 μm radius. Thus, ice nucleation may occur spontaneously. However, expansion may not be perfectly adiabatic since some addition of gas molecules to the bubble occurs. Thus in some cases, only enough cooling may be produced to activate a submerged IFN.

Estimates of the amount of pressure difference needed to cause a bubble vary from -500 mb for homogeneous nucleation to a lower limit of -5 mb for aerated tap water (Hueter and Bolt, 1955). Actual thresholds may be lower given the difficulty of bubble detection and the fact that cloud and rain drops may contain large amounts of impurities.

Admittedly, the physical mechanism presented here is based on conjecture, but since bubble formation should precede ice nucleation (Goyer *et al.*, 1965), the occurrence of a bubble may at least have predictive value.

4. DROP-FREEZING POSSIBILITY

In a numerical simulation of drop rebound, Foote (1975) has shown that an intricate pressure field evolves within a drop during the period of compression to eventually produce a negative pressure difference of 2.4 mb. Foote's calculation is for an initially spherical drop, 1.19 mm diameter impacting a wall at 30 cm s^{-1} and is characterized by a Weber Number of 1.42. The Weber Number gives a non-dimensional measure of drop deformation from the ratio of impact pressure to curvature pressure.

At impact, the pressure field takes the form of a sharp spike with maximum and minimum of 35 and 2.5 mb. Simultaneously, a circular surface wave propagates away from the impact point and associated with it an internal circulation evolves. When the wave reaches the top of the drop where the internal circulation reverses, the pressure field shows a maximum and minimum of 3.8 and -2.4 mb.

The pressure difference in Foote's calculation does not exceed the -5 mb criteria for heterogeneous bubble formation, but is close enough to suspect that pressure differences sufficient for bubble growth may occur for re-

bounds characterized by larger Weber Numbers.

Figure 2 shows lines of constant Weber Number (WE) and was calculated using the equation:

$$WE = (\rho_w r \Delta V^2)/\sigma \qquad (1)$$

where ρ_w is the density of water, ΔV^2 is the differential terminal velocity and σ is surface tension of water. This equation is slightly different from the one used by Foote (1975) since small drop radius is used to better represent deformation curvature in collisions between dissimilarly sized drops (Ochs *et al.*, 1986).

For Fig. 2 the linear relationship WE=0.60×ΔP was used to extrapolate from Foote's work. Thus negative pressure differences greater than 5 mb correspond to collisions with WE > 3 and ΔP < -500 mb for WE > 300. The stippled area in Fig. 2 delineates the region of WE > 3 and hence the drop sizes for which heterogeneous bubble formation may be suspected. The lack of stippling for drops with R > 1000 μm and drops with r > 300 μm, indicates collisions with sufficient energy for drop breakup (Whelpdale and List, 1971). Use of Eq. 1 produced a maximum Weber Number of ≈280, just smaller than defined for the homogeneous bubble nucleation.

Figure 2 suggests that bubble formation might be possible for drop rebound in clouds once precipitation-size collector drops are produced. Whether the large drop, small one, both or neither freezes in rebound is a matter for future investigation as are the freezing possibilities of temporary and permanent coalescence.

5. SUMMARY

Previous considerations of cloud microphysical processes leading to ice initiation have generally ignored the active, supercooled coalescence mechanism that occurs in the warm-based cumulus of the central United States. In this paper it has been suggested that some collisions between supercooled drops may result in freezing and thus be a strong source of ice having powerful influence over the spectral evolution of liquid and solid particles.

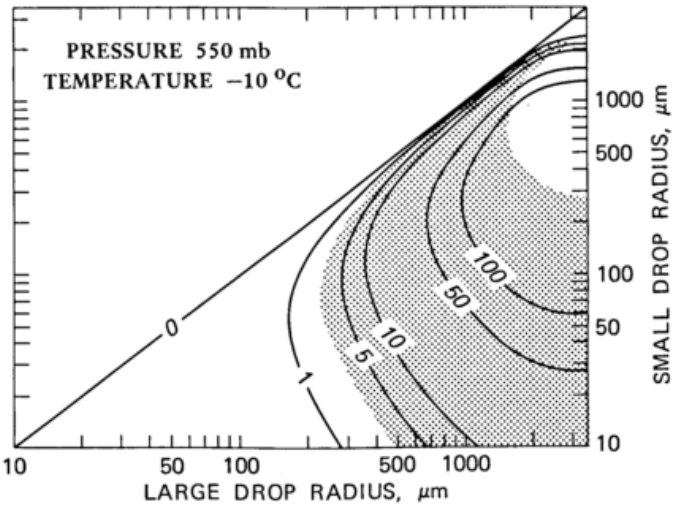


Figure 2. Lines of constant Weber Number. The stippled area delineates WE > 3.

Acknowledgement. This research has been conducted under cooperative agreement with the National Oceanic and Atmospheric Administration under contracts COMM NA86RAH06051 and COMM NA87RAH07077. The author wishes to thank Professor Roscoe R. Braham, Jr. for use of his drop freezing apparatus.

REFERENCES

Braham, R. R., 1964: *J.Atmos.Sci.*, 21, 640-645.

Czys, R. R., 1977: *Proc. Sixth Conf. on Inadvertent and Planned Weather Modification*, Champaign, Illinois, 29-32.

Goyer, G. G., T. C. Nhadra and S. Gitlin, 1965: *J.Appl.Met.*, 4, 156-160.

Foote, G. B., 1975: *J.Atmos.Sci.*, 32, 390-402.

Hueter, T. F. and R. H. Bolt, 1955: *Sonics*. John Wiley and Sons, p 230.

Ochs, H. T., R. R. Czys and K. V. Beard, 1986: *J.Atmos.Sci.*, 43, 225-232.

Whelpdale, D. M., and R. List, 1971: *J.Geophys.Res.*, 76, 2836-2856.

SPREADING OF SUPERCOOLED WATER DROPLETS ON AN ICE SURFACE

Ya Yi Dong and John Hallett
Desert Research Institute
Reno, Nevada 89506

1. INTRODUCTION

In spite of its importance in graupel formation, the spreading processes of water droplets are poorly understood. One of the difficulties is that the surface energy between ice and water, which is extremely important in the spreading process, cannot be measured directly because of the non-equilibrium state during freezing. On other hand, the effects of the so-called quasi-liquid layer on an ice surface on spreading have not been carefully considered. The present experiment was designed to investigate behaviour of supercooled water droplets spreading on different ice surfaces under various temperatures. It was found that the spreading ratio of water droplets slowly increases with temperature on a "dry" ice surface, but increases rapidly with temperature when a quasi-liquid layer exists on the ice surface above -4°C. It was also found that the curvature of the ice surface has a strong influence on the water spreading. The traditional concept of contact angle is not applicable in this case.

2. EXPERIMENT

A brass tower temperature conditioner is set up in a freezer to minimize the effects from the environment. The tower is about 80 cm in height, 18 cm in diameter and is cooled by circulating antifreeze. A thermo-electric plate is located on the bottom of the tower to obtain better temperature control. A microscope is set up in the same freezer, so that the samples can be examined as soon as possible after they are removed from the thermo-electric plate. Ice crystals are selected from a freezing water surface and the crystal axis orientation checked by crossed polaroids. Water droplets are fed from the tower top at least 10 minutes after the ice sample is put on the thermo-electric plate and temperature equilibrium is reached. The water droplets fall through the tower and accrete on the ice surface at terminal velocity. Only limited number of droplets are fed to minimize effects of latent heat and obtain clear pictures of individual events. The ice samples are then removed and examined under the microscope. The whole procedure is carried out in the freezer, and finished in 5-10 minutes so that effect of evaporation is neglegible.

3. RESULTS

The experiment was carried out for basal and high index surface at temperatures from -18°C to -1°C. Fig. 1 shows the spreading ratio, which is defined as a ratio of radius of a spread droplet base to its height, is different on basal and high index surfaces at -3°C. It is interesting to note that the spreading ratio increases relatively slowly with temperature under -2°C on basal surface, and increases dramatically above -2°C. The same behaviour was observed on high index surfaces but the transition point is about -4°C. This observation implies that the spreading ratio is influenced by the thickness of quasi-liquid layer (FURUKAWA, 1987, p.665). The spreading ratio as a function of temperature



a) Droplet spread on a basal surface

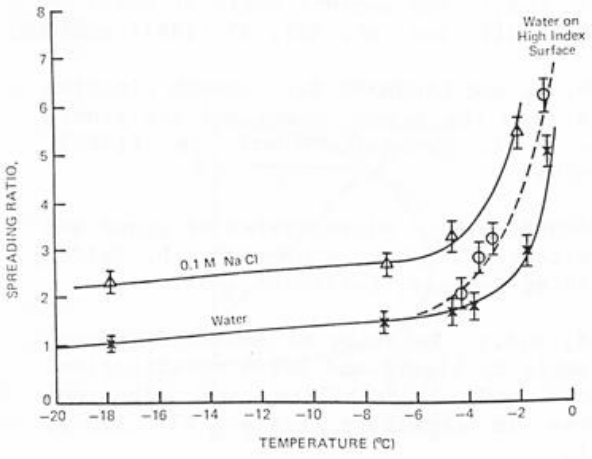


100 µm

b) Droplet spread on a high index surface

Fig. 1: Different spreading ratios of supercooled droplets on different ice crystal surfaces near melting point. Temperature -3°C.

is plotted in Fig. 2. Over the whole temperature region examined, the droplets spread and freeze as cones with a tip on top. The angle between the side of the cone and the ice substrate is strongly dependent on temperature (Fig. 3). This result agrees well with Hansman's experiment (1988). The observation also reveals an interesting phenomenon: at low temperature (<-10°C),



___ on basal surface.

--- on high index surface.

Fig. 2: Spreading ratio as a function of temperature.

the ice substrate is strongly dependent on temperature, which is plotted in Fig. 3.

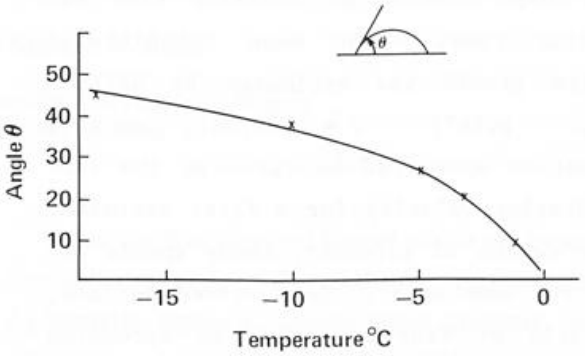
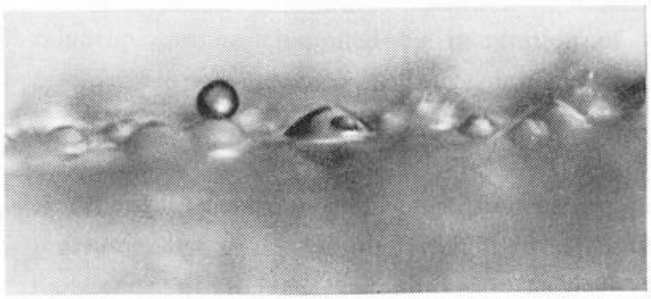


Fig. 3: Angle between cone side and flat ice surface as a function of temperature.

supercooled water droplets freeze as individual spheres when they land on a curved ice surface through they would spread as cones on flat surface under the same conditions. Fig. 4 shows an example.



100 µm

Fig. 4: An example of spherical frozen droplet on a curved surface.

4. DISCUSSION

The above observation demonstrates an important spreading behaviour related to the riming process. A number of previous studies showed some disagreements in shape of freezing droplets because the effects of quasi-liquid layer and curvature of the collector was not considered. When a water droplet reaches a flat ice surface, it is nucleated immediately at the contact point, the released latent heat warms up the substrate (near the landing point) to near 0°C. A quasi-liquid layer will form in this

area. The water droplet will continue to spread until it is completely frozen. The final shape depends on freezing time and spreading time. The mean velocity of dendrite growth was estimated by HALLETT (1964, p.667) $V = 0.08\ T^2$ cm s^{-1}. Deformation speed can be taken as the initial droplet velocity for a first estimate. In the region of interest, these speeds can be of the same order. On a curved surface, the ratio of freezing speed to spreading speed (the speed of the droplet to cover ice surface) is higher than that on a flat surface. Therefore, droplets are more likely to freeze as spheres instead of cones on a curved surface. The two processes are shown in the Fig. 5. The result implies that

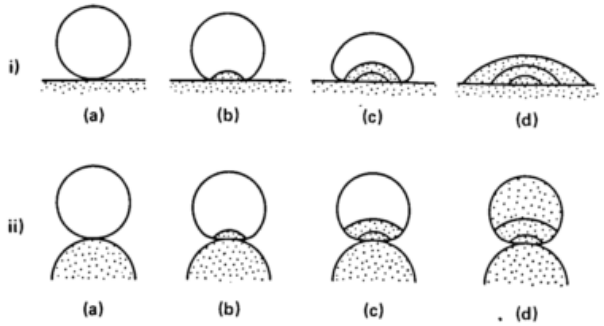


Fig. 5: A model of spreading on flat and curved surface.

riming behaviour is strongly dependent not only on temperature and kinetic energy, but also the size and curvature of ice particles and droplets. Small droplets retain their original shape when they are collected by small ice particles, but spread on relatively flat surfaces. Finally, it should be pointed out that the concept of contact angle is not applicable in this case. The final angle between the surface of frozen droplet and substrate can be as large as about 100° for collector surfaces with different curvature. From the view point of free energy, the wettability S of water on ice is: $S = \gamma_{sv}^{\circ} - (\gamma_{sl} + \gamma_{lv}^{\circ})$ (ZISMAN 1964, p.1) where γ_{sv}° is free energy of interface, and γ_{lv}° the term for the liquid-vapor interface. In the temperature region 0°C to -40°C, the value of the term $(\gamma_{sl} + \gamma_{lv}^{\circ})$ remains constant or increases slightly with temperature decrease (PRUPPACHER 1978, p. 104 and 129); γ_{sv}° increases with temperature decrease. Since $S > 0$ at 0°C, we can conclude that supercooled water droplets would spread over ice surface with contact angle of zero at any temperature, if freezing were not taking place; this can give an apparent constant angle (KNIGHT 1967, p.250). The dominant factor of spreading on ice is the ratio of spreading speed and freezing speed, but not surface free energy.

This work was carried out under NSF Contract #ATM-8715636, Division of Atmospheric Science, National Science Foundation, Washington, D.C.

5. REFERENCES

FURUKAWA, Y.; KURODA, I; and YAMAMOTO, M.: Study of the transition layer on the surface of an ice crystal. J. Crystal Growth. 29 (1986), 82, p.665-677.

HALLETT, J.: Experimental studies of the crystallization of supercooled water. J. Atmos. Sci. 21 (1964), p.677-682.

HANSMAN, R.J.; Jr. and TURNOCK, S.R.: Investigation of surface water behaviour during glace ice accretion. AIAA 26th Aerospace Sciences Meeting. AIAA (1988), paper 0015.

KNIGHT, C.A.: The contact angle of water on ice. J. Coll. and Int. Sci. 25 (1967) p.280.

KURODA, T. and LACHMANN R.: Growth kinetics of ice from the vapour phace and its growth forms. J. Crystal Growth 56 (1982), p.189-205.

PRUPPACHER, H.R.: Microphysics of cloud and precipitation. 1978, p.104-129. D. Reidel Publishing Company, Durdrecht, Holland.

ZISMAN, W.A.: Relation of equilibrium contact angle to liquid and solid constitution. Contact Angle wettability and adhesion. Advances in Chemistry series 43 (1964), p.1-51.

A MODEL OF THE ELECTROSTATIC-AERODYNAMIC SHAPE OF RAINDROPS

Catherine Chuang and Kenneth V. Beard

Department of Atmospheric Sciences, University of Illinois
105 S. Gregory Avenue, Urbana, Illinois 61801

1. INTRODUCTION

Early theoretical and semiempirical models to predict the shape of raindrops have been subject to varying restrictions either in physical realism or in applications. A new model based on the equilibrium equation across a curved surface was developed by incorporating an aerodynamic pressure and electrostatic effects. The method of applying an empirical pressure distribution around a sphere, originally proposed by Savic, has been refined to include variations in the pressure distribution with Reynolds number and drop distortion. A finite volume technique was used to calculate the shape dependent electric effect with a numerically generated boundary-fitted coordinate system.

2. EQUILIBRIUM EQUATION

The equilibrium shape of an interface was determined by Laplace's pressure balance at each point on the surface

$$\sigma(1/R_1 + 1/R_2) = \Delta P \qquad (1)$$

where σ is the surface tension, R_1 and R_2 are the principal curvature radii, and ΔP is the net pressure. The curvatures were evaluated using a tangent angle coordinate system in a vertical plane (Hartland and Hartley, 1976), where $1/R_1 = d\phi/ds$ and $1/R_2 = \sin\phi/x$ (see Fig. 1).

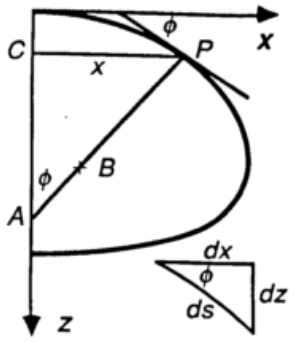


Fig. 1. Diagram for the drop surface with R_1 given by BP and R_2 by AP.

There are five physical factors which are expected to control the shape of raindrops: surface tension, hydrostatic pressure, aerodynamic pressure, internal circulation and electric stress. The initial step in developing the model was a force balance among the first three factors

$$\sigma(d\phi/ds + \sin\phi/x) = 2\sigma/R_t + \Delta\rho g z + (P_{top} - P)_a \qquad (2)$$

where R_t is the radius of curvature at the top, $\Delta\rho$ is the density difference between water and air, and $(P_{top} - P)_a$ is the aerodynamic pressure change from the upper pole.

The accumulated upward force due to airflow past the raindrop can be computed by integration of the aerodynamic pressure acting on the total drop surface A:

$$-\int_A P_a \cos\phi \, dA = mg \qquad (3)$$

Eq (3) implies that the supporting force from aerodynamic pressure must equal the total weight to satisfy the requirement of mechanical equilibrium. The shape was calculated by forward integration of $d\phi/ds$ for assumed values of the initial curvature at the top with a boundary condition $d\phi/ds = \sin\phi/x = 1/R_t$, where $x = z = \phi = 0$. An iterative scheme is applied to determine the initial curvature at the top ($1/R_t$) necessary to achieve the proper volume for a particular drop size.

3. MODIFYING THE PRESSURE DISTRIBUTION

Before each computation of drop shape, the aerodynamic pressure distribution was adjusted for the effects of drag beginning with an appropriate distribution for a sphere. Measurements of the surface pressure around rigid spheres at very large Reynolds number ($Re = 10^4 - 10^5$) and numerical results ($Re = 400$) are practically identical in the unseparated region. The distributions for high Reynolds number are rather flat behind the separation point and show only a few degrees variation in the location and breadth of the pressure dip. The distribution of Fage (1937) was used, but instead of applying the data directly to the calculation as in the

perturbation model of Savic (1953) and Pruppacher and Pitter (1971), an adjustment was made before each calculation to obtain the appropriate pressure drag for a particular Reynolds number.

In the range of Reynolds number applicable to larger raindrops (d = 2 - 9 mm) the pressure drag (C_{dp}) was approximated by an empirical formula as

$$C_{dp} = C_d [\, 1 - 13.4\, Re^{-0.58} \,] \qquad (4)$$

where C_d is the total drag. This interpolation formula was obtained by using end points from LeClair *et al.* (1970) at Re = 400 and Achenbach (1972) at Re = 75 000.

The adjustment of pressure drag was made by altering the pressure distribution of Fage in the wake region (88° to 180°) and the intermediate region (72° - 88°) using

$$\begin{aligned} \kappa'(\psi) &= 1 - \Gamma[1 - \kappa_{fage}(\psi)] \quad 88° \le \psi \le 180° \\ \kappa'(\psi) &= 1 - \Gamma'[1 - \kappa_{fage}(\psi)] \quad 72° < \psi < 88° \end{aligned} \qquad (5)$$

where Γ is a constant and $\Gamma' = 1 - (1 - \Gamma)(\psi - 72°)/16$ provides a linear transition between the unseparated region at 72° and the wake at 88°. The value of Γ was adjusted before the shape calculation so that the pressure drag, obtained by integration $\kappa'(\psi)$ over the surface of a sphere, was the appropriate fraction of the weight as given by (4).

4. AERODYNAMIC SHAPE OF RAINDROPS

As discussed in Beard and Chuang (1987) an excessive pressure amplitude is required to offset the entire weight, since the pressure drag can offset only the fraction C_{dp}/C_d. A mean weight was used by replacing the density difference in (2) by 0.5 $(1 + C_{dp}/C_d)\,\Delta\rho$. The amplitude of the pressure distribution κ' was readjusted before every calculation, by using $\kappa = \Lambda\,\kappa'$, where the constant Λ is determined by integration such that the pressure drag equals the mean weight. This step was needed to adjust for the effect of distortion.

Successive calculations were made using an updated pressure distribution based on the previous drop shape, with κ' obtained from a new value of Γ to satisfied (4), and with κ obtained from a new value of Λ. Iteration was stopped after the raindrop shapes were sufficiently converged (typically 4-8 cycles). The final pressure distributions are similar to those shown in Beard and Chuang where the pressure amplitudes increase with distortion, *i.e.*, the pressure dip lowers.

The computed aerodynamic shape of raindrops are shown in Fig. 2 for d = 1 to 6 mm. The drop shapes are placed with the center of mass at the origin with corresponding dashed circles having the radius of the equivalent volume sphere. The flatter base for larger raindrop results from the increasing influence of hydrostatic and aerodynamic effects. Because of the absence of a dimple in the base, the raindrop cross sections in Fig. 2 are also profiles.

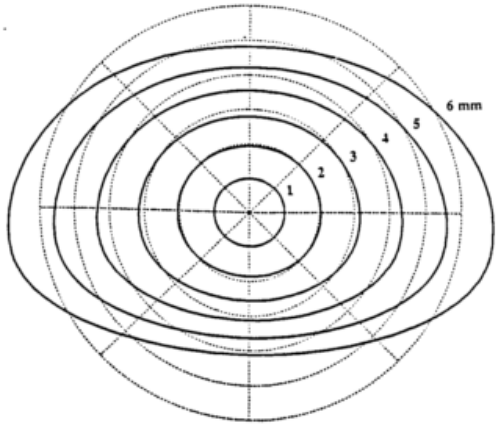


Fig. 2. Model results for aerodynamic drops.

5. ELECTROSTATIC EFFECT ON DROP SHAPE

In the absence of space charge, the static potential distribution for any conductor configuration can be determined from Laplace's equation. The electric stress from either an applied electric field or surface charges will decrease the pressure difference ΔP by an amount $E_s^2/8\pi$ which modifies the equilibrium equation to

$$\sigma(d\phi/ds + \sin\phi/x) - E_s^2/8\pi = 2\sigma/R_t + \Delta\rho g z + (P_{top} - P)_a \qquad (6)$$

where E_s is the magnitude of electric field in electrostatic units (e.s.u.) at the outside surface of drop. The main difficulty in solving for the electrostatic effect is that the drop shape must be known. A numerical iterative method was used to solve the unknown boundary shape. In order to avoid loss of accuracy, Laplace's equation for the electric potential was solved in a domain with boundaries that are coincident with the drop surface. The boundary-fitted coordinate systems was numerically generated by taking the transformed curvilinear coordinates to be solutions of a suitable elliptic partial differential equation in the physical plane (Thompson *et al.*, 1974). Laplace's equation was solved by a finite volume method to simplify the Neumann boundary condition on the polar axis.

The effect of a uniform vertical electric field on the drop shape is illustrated in Fig. 3 for d = 1 - 6 mm and E = 9 kV/cm. Stronger electric stress in the regions of the poles makes the shape more rounded than the aerodynamic shape. The axis ratio (α_e) under different magnitudes of vertical electric field are given in Table 1.

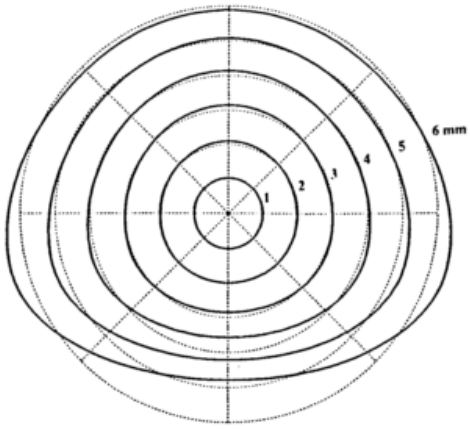


Fig. 3. Model results for aerodynamic-electrostatic drops.

TABLE 1. Axis ratios for drops in a vertical electric field.

E (kV/cm)	d =	Axis Ratio 2	3	4	5
1.0		0.847	0.768	0.703	0.649
2.0		0.851	0.773	0.708	0.654
3.0		0.858	0.781	0.716	0.661
4.0		0.869	0.792	0.727	0.672
5.0		0.884	0.809	0.743	0.688
6.0		0.903	0.830	0.765	0.708
7.0		0.928	0.859	0.794	0.737
8.0		0.961	0.897	0.835	0.776
9.0		1.005	0.950	0.895	0.836

6. DISCUSSION

Model results for aerodynamic shapes when compared with observations in wind tunnels follow the trend in measurements of the equilibrium axis ratios even for extremely large drops. The computed shapes for the pure electrostatic distortion are very close to the theoretical study by Taylor (1964). The results for aerodynamic-electrostatic drops are similar to the mean shapes and axis ratios obtained by Richards and Dawson (1973) from photographs of drops in a wind tunnel with a vertical electric field.

7. ACKNOWLEDGMENTS

This material is based upon work supported by the National Science Foundation under Grants ATM84-19490 and ATM86-01549. Any opinions, findings, and conclusions or recommendations expressed in this material are those of the authors and do not necessarily reflect the views of the National Science Foundation.

8. REFERENCES

Achenbach, E., 1972: Experiments on the flow past spheres at very high Reynolds numbers. *J. Fluid Mech., 54,* 565-575.

Beard, K. V., and C. Chuang, 1987: A new model for the equilibrium shape of raindrops. *J. Atmos. Sci., 44,* 1509-1524.

Fage, A, 1937: Experiments on a sphere at critical Reynolds Numbers. Aero. Res. Comm., England, Rep. and Memo. No. 1766, 20 pp.

Hartland, S., and R. W. Hartley, 1976: *Axisymmetric Fluid-Liquid Interfaces.* Elsevier, 782pp.

LeClair, B. P., A. E. Hamielec and H. R. Pruppacher, 1970: A numerical study of the drag on a sphere at low and intermediate Reynolds number. *J. Atmos. Sci., 27,* 308-315.

Pruppacher, H. R., and J. D. Klett, 1978: *Microphysics of Clouds and Precipitation.* Reidel, Boston, 714 pp.

Pruppacher, H. R., and R. L. Pitter, 1971: A semi-empirical determination of the shape of cloud and rain drops. *J. Atmos. Sci., 28,* 86-94.

Richards, C. N., and G. A. Dawson, 1973: Stress on a raindrop falling at terminal velocity in a vertical electric field - A numerical method. *Phys. Fluids, 16,* 796-800.

Savic, P, 1953: Circulation and distortion of liquid drops falling through a viscous medium. Natl. Res. Council, Canada, Rep. NRC-MT-22, 50 pp.

Taylor, G., 1964: Disintegration of water drops in an electric field.*Proc. Roy. Soc. London, A280,* 383-397.

Thompson, J. F., F. C. Thames, and C. W. Mastin, 1974: Automatic numerical generation of body-fitted curvilinear coordinate system for field containing any number of arbitrary two-dimensional bodies. *J. Comp. Phys., 15,* 299-319.

MEASUREMENTS OF THE PARTITIONING OF AEROSOL MASS AND NUMBER BETWEEN CLOUD DROPLETS AND INTERSTITIAL AIR

John Ogren, Jost Heintzenberg and Kevin Noone

Department of Meteorology, University of Stockholm,

S-106 91 Stockholm, Sweden

1 INTRODUCTION

The incorporation of aerosol particles into clouds is of central importance to both cloud chemistry and cloud physics. The number of cloud droplets is determined by the number of aerosol particles that act as cloud condensation nuclei, while the mass of aerosol particles scavenged by the droplets determines to a large extent the chemical composition of the droplets. In a recent study, TEN BRINK ET AL. (1987) reviewed the available measurements of the efficiency of nucleation scavenging of aerosol particles by clouds and reported that "there have been few measurements that have unambiguously and precisely determined the efficiency of this process in natural clouds.

Model calculations (JENSEN AND CHARLSON, 1984) suggest that the mass scavenging efficiency is a function of the mass of submicrometer particles and the updraft velocity, but little experimental evidence is available to confirm this functionality. Measurements by LEAITCH ET AL. (1986) are consistent with the model predictions, showing that lower number and mass scavenging efficiencies are associated with higher aerosol loadings, but the measurements of TEN BRINK ET AL. (1987) showed uniformly high mass scavenging efficiencies regardless of the aerosol mass loading.

Interpretation of the available measurements is hindered by one or both of the following limitations in the experimental methods: the total number and mass of aerosol particles (scavenged plus unscavenged) are unavailable, or the time resolution of the measurements is too low to resolve inhomogeneities in the cloud. Most of the works to date have relied on a comparison of in-cloud and out-of-cloud measurements to derive the scavenging efficiency, but have not measured the total mass and number of aerosol particles within the cloud. As a result, interpretation of the data requires assumptions about the relationship between total aerosol mass and number within and outside of the cloud. Interpretation of measurements obtained with low time resolution (e.g., those based on collected samples of interstitial air) may also require the assumption that the cloud was present during the entire sampling interval.

Both of the above limitations apply to the present work. However, these limitations are the result of the current implementation of the sampling technique, not of the technique itself. Accordingly, the focus of this paper is to describe our approach to measuring scavenging efficiencies and to present data demonstrating the feasibility of the method.

2 EXPERIMENTAL APPROACH

Measurements were performed in stratocumulus clouds on Mt. Åreskutan in central Sweden (63°26'N, 13°6'E, 1250 m asl) during the summer of 1986. Cloud droplets greater than 4 μm radius were sampled with a counterflow virtual

impactor operated in a vertical wind tunnel (OGREN et al., 1985; NOONE et al., 1988). The sampled droplets were evaporated and then counted with a condensation nucleus counter (TSI model 3020). The light scattering coefficient (σ_{sp}) of the residual aerosol particles, determined with an integrating nephelometer, was used as a surrogate for the mass of aerosol particles. The liquid water content (LWC) of the cloud was determined by measuring the water vapor concentration resulting from evaporation of the cloud droplets, using a Lyman-alpha hygrometer (ZUBER and WITT, 1987). An identical nephelometer and condensation nucleus counter sampled particles smaller than 1 µm radius following removal of larger particles and droplets with a cyclone. The nephelometers were of a design similar to that reported by HEINTZENBERG and BÄCKLIN (1983), with a detection limit of 10^{-7} m^{-1}. This sensitivity allowed even the very low aerosol light scattering coefficients in cloud interstitial air to be quantified.

The submicrometer aerosol measurements were obtained during field testing of a system for baseline measurements in Arctic air, and were recorded as five-minute medians of 1 Hz measurements. This time resolution was optimized for variations occurring over synoptic time scales, rather than cloud time scales. As a result, inhomogeneities in the clouds on time scales shorter than 5 minutes (of order 2 km) could not be resolved in the submicrometer aerosol measurements. The measurements obtained with the CVI system were recorded with time resolutions of 1-10 seconds, and frequently showed rapid variations in drop number concentration and LWC that were not apparent in the submicrometer aerosol data.

3 RESULTS

Submicrometer aerosol σ_{sp} typically dropped by at least a factor of ten when clouds were present, while the number concentration (N) of submicrometer particles rarely decreased by more than 50 percent. An example of the effect of cloud passage on σ_{sp} is illustrated in Fig. 1. During periods when a cloud was present, as indicated by LWC (inoperative prior to 11:50) and σ_{sp} of the cloud droplet residues, the sum of the light scattering coefficients of the submicrometer aerosol particles and residual cloud droplets was lower than the out-of-cloud submicrometer aerosol σ_{sp}. This is attributed to the presence of unsampled droplets between 1 and 4 µm radius. Assuming that the total aerosol light scattering coefficient was constant within the cloud, examination of Fig. 1 suggests that the mass of particles associated with droplets in the 1-4 µm range in the dense portion of the cloud

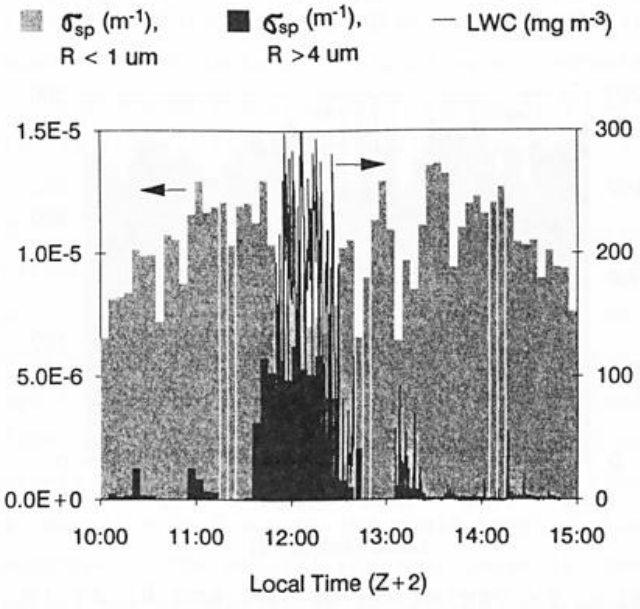


Fig. 1: Variation of LWC and σ_{sp} associated with submicrometer particles (light-shaded area) and cloud droplets (dark-shaded area) during passage of a cloud. Note that the height of the stacked bars corresponds to the sum.

(around 12:00, when the sampling site was about 300 m above cloud base) was comparable to the mass of particles associated with droplets greater than 4 µm.

The corresponding picture for the effect of clouds on N (Fig. 2) is quite different. Here, the number of cloud droplets larger than 4 µm radius was less than 2% of the number of particles outside of the cloud, while the total dropped by about 20% in the cloud (again, the "missing" particles are thought to be associated with 1-4 µm droplets). The low scavenging efficiency for particle number, combined with the high scavenging efficiency for particle mass, suggests that the unscavenged particles were quite small. This finding is consistent with simultaneous measurements of the size distribution of the interstitial particles, which typically showed a mode under 0.1 µm radius.

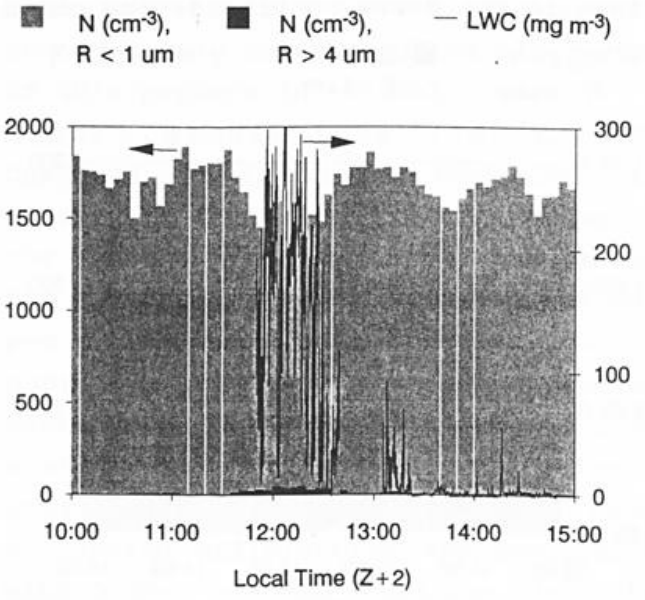


Fig. 2: Variation of LWC and N, as in Fig. 1.

4 CONCLUSION

In the relatively unpolluted, stratocumulus clouds frequently encountered at the site, well over half of the mass of submicrometer particles was typically found in the droplets. In contrast, fewer than half of the number of submicrometer particles was contained in the cloud droplets. In order to obtain more precise determinations of the scavenging efficiencies, the CVI is being redesigned to allow sampling of droplets down to 1 µm radius, and the time resolution of the submicrometer aerosol data is being improved.

5 REFERENCES

HEINTZENBERG, J.; BÄCKLIN, L.: A high sensitivity integrating nephelometer for airborne air pollution studies. *Atmos. Environ. 17* (1983), p. 433-436.

JENSEN, J.; CHARLSON, R.: On the efficiency of nucleation scavenging. *Tellus 36B* (1985), p. 367-375.

LEAITCH, W.; STRAPP, J.; ISAAC, G.; HUDSON, J.: Cloud droplet nucleation and cloud scavenging of aerosol sulphate in polluted atmospheres. *Tellus 38B* (1986), p.328-344.

NOONE, K.; CHARLSON, R.; COVERT, D.; OGREN, J.; HEINTZENBERG, J.: Cloud droplets: Solute concentration is size dependent. *J. Geophys. Res.* (1988), in press.

OGREN, J.; HEINTZENBERG, J.; CHARLSON, R.: In-situ sampling of clouds with a droplet to aerosol converter. *Geophys. Res. Lett. 12* (1985), p. 121-124.

TEN BRINK, H.; SCHWARTZ, S.; DAUM, P.: Efficient scavenging of aerosol sulfate by liquid-water clouds. *Atmos. Environ. 21* (1987), p. 2035-2052.

ZUBER, A.; WITT, G.: Optical hygrometer using differential absorption of hydrogen Lyman-α radiation. *Appl. Optics 26* (1987), p. 3083-3089.

THE CALCULATION OF SUPERSATURATIONS AND GROWTH OF DROPLETS IN CONTINENTAL CUMULUS CLOUDS

Keith Bower and Tom Choularton
Dept. of Pure and Applied Physics
University of Manchester Institute of Science and Technology
P O Box 88
Manchester M60 1QD, UK

There has been much recent debate concerning the mechanism by which drops in continental cumulus clouds are able to grow to radii in excess of 25 μm, to enable the initiation of further growth by coalescence to produce warm rain. In-cloud measurements have shown that enhanced growth of up to 5 μm beyond the largest radii predicted by adiabatic growth is often observed (HILL and CHOULARTON, 1985, BLYTH and LATHAM, 1985) and this is consistent with the work of other authors (eg. BAKER et al, 1980, TELFORD and CHAI, 1980) who envisage dry air entrainment as playing a major role in droplet growth in such clouds.

A model has been developed by HILL and CHOULARTON, 1986, to include the effects of dry tropospheric air entrainment on the growth of a droplet spectrum in cumulus clouds. Such entrainment is considered to occur on localised scales, and in the model discrete blobs of dry tropospheric air gradually mix with the surrounding cloud, evaporating totally those drops nearest to the blob but causing little or no evaporation of more remote drops. This leads to the evaporative cooling of the blob as it becomes saturated, but the region mixes with surrounding cloud and continues to rise if sufficient momentum can be entrained. This will cause a high supersaturation to develop which will then decline rapidly as cloud condensation nuclei (CCN) become activated. Hence the model predicts that such mixing will have the effect of reducing the number concentration of droplets of all sizes but with the spectra retaining the same overall shape. The effects of several such events will cause cloud supersaturations to be higher than corresponding adiabatic values, and they will not be closely tied to updraught speed. Increased supersaturations are expected to be responsible for the observed enhanced growth, and further results of mixing are expected to include an increase in the bimodality of spectra, and a reduction in mean droplet lifetime when compared to the ascent times of air parcels travelling from cloud base to cloud top.

Observations from several aircraft passes through continental cumulus clouds obtained during the CCOPE experiment on 12 July, 1981, have been analysed in an attempt to test these predicted results of dry air entrainment. The general properties of one such pass are shown in Figure 1. In general there exist broad regions (500-1500 m across) of similar droplet number concentrations N, liquid water contents L, and mixing history (eg. regions A, B, C). In addition, there are smaller regions 1, (<200 m wide) showing negative deviations of N, L, updraught W, and temperature T, which cannot be attributable to sampling error, and are considered to be regions of recent entrainment. A comparison of average droplet spectra from such regions with those obtained from neighbouring broader regions is shown in Figure 2 for four passes. It can be seen that a reduction in N across the whole spectrum has occurred. The general spectral shape is retained for droplet sizes above 5 μm, but below this there is evidence of the CCN reactivation expected to occur in the high supersaturations following a mixing event.

A method to calculate supersaturations present in the CCOPE passes was devised using the observed values of T, pressure p, W, and

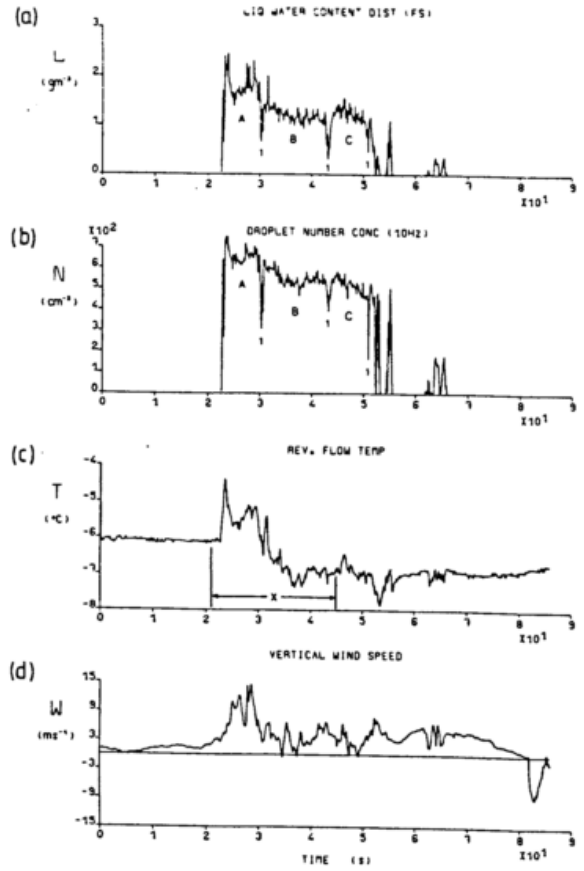


Figure 1. Distribution of (a) FSSP total liquid water content L, (b) number concentration N, (c) dry bulb temperature T, and (d) vertical wind velocity W, all measured at 10Hz for pass 13.

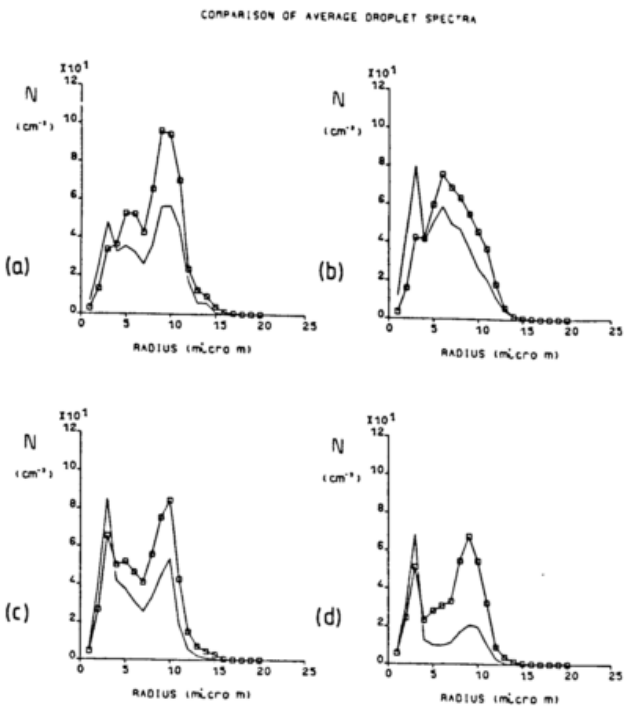


Figure 2. Comparison of average droplet spectra from regions (1) of recent entrainment (curve with no symbols), with average spectra from neighbouring cloud regions (curve with symbols) for (a) Pass 6, (b) Pass 13, (c) Pass 7 and (d) Pass 14.

droplet spectra. These were included in an adiabatic growth model, with a prescribed initial supersaturation of 0.1%. Integrating the model forward with a timestep of 0.01 s, the equlibrium supersaturations were calculated (usually within an altitude change of 7 m, and development time of 1.29 s). Figure 3 shows the supersaturations S, and updraughts, W, used in their calculation for one cloud pass. Figure 4 shows the corresponding S versus W plot, and as predicted illustrates that the two parameters are not related closely except in regions of similar mixing history.

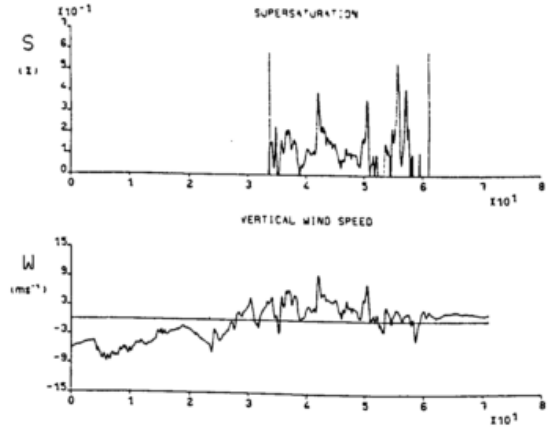


Figure 3. Distributions of calculated supersaturation and vertical velocity for Pass 5.

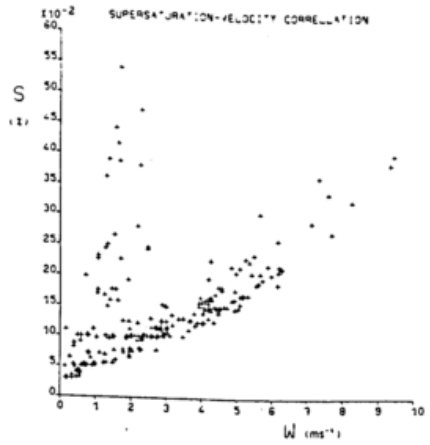


Figure 4. Calculated supersaturation versus vertical velocity for Pass 5.

For comparison purposes, a representative droplet spectrum developed from a measured CCN distribution was allowed to develop adiabatically, from the observed cloud base conditions in a constant updraught profile to the

observation level. Number concentrations of activated droplets were adjusted to reproduce the observed values of N. In total, eight sets of data were allowed to develop to the observation level and cloud top in this way, and the resultant adiabatic spectra were found to be much narrower than the observed with a very much higher liquid water content. A comparison of maximum droplet radii revealed that the adiabatic values were on average 19% smaller than the observed, corresponding to a difference of 3-4 μm, and that the corresponding adiabatic supersaturations were 26% lower.

The effect of the enhanced supersaturation on droplet growth was then modelled by reducing the number concentration of activated droplets in the adiabatic model so as to reproduce the observed supersaturations at the observation level. This resulted in the average maximum droplet size being increased by 16% but it was still 6% smaller than the average observed maximum. However, this process takes no account of the statistically favoured droplets which are envisaged to avoid evaporation following entrainment in the model, but which do experience the high S pulses. Hence number concentrations were reduced still further in the adiabatic model so as to reproduce the 'observed' potential supersaturations at the observation level. This increased maximum droplet sizes to within 1% on average of the observed values (although there was a large spread of $\pm$ 6% in results). It therefore seems reasonable to suggest that the enhanced growth can be accounted for taking into consideration the enhanced observed supersaturations which occur following several dry air entrainment events.

Finally, average droplet lifetimes were calculated by considering the time taken for embryo droplets to develop to an average size equal to the observed value in an adiabatic model. Starting at cloud base or from some higher level under observed conditions, estimates of mean lifetime of between 1.5 and 4.5 minutes were obtained depending on the updraught profiles prescribed. With a profile which increased linearly from the cloud base updraught to the observation level value, an average mean lifetime of 3 mins was obtained. As predicted this is considerably shorter (by a factor of about 0.2) than the parcel ascent time from cloud base to the observation level, and is similarly shorter than the average reported age of these clouds. In addition, a mean droplet lifetime of less than 5 mins, which is also a measure of the average interval between mixing events, has important consequences for the chemistry occuring within the droplets, especially so for the aqueous phase oxidation of sulphur dioxide by hydrogen peroxide and ozone. Only the former process will be important, the latter requiring a timescale of several tens of minutes. The entrainment process will also help to replenish the oxidant, thus enhancing sulphate production in the drops.

REFERENCES

BAKER, M.B.; CORBIN, R.G; LATHAM, J.: The Influence of Entrainment on the Evolution of Cloud Droplet Spectra: I. A Model of Inhomogeneous Mixing. Quart. J. Roy. Met Soc. 106 (1980) 581-598.

BLYTH, A.M.; LATHAM, J.: An Airborne Study of Vertical Structure and Microphysical Variability Within a Small Cumulus. Quart. J. R. Met. Soc. 111 1985) 773-792

HILL, T.A.; CHOULARTON, T.W.: An Airborne Study of the Microphysical Structure of Cumulus Clouds. Quart. J. R. Met. Soc. 111 (1985) 517-544.

HILL, T.A.; CHOULARTON, T.W.: A Model of the Development of the Droplet Spectrum in a Growing Cumulus Turret. Quart. J.R. Met. Soc. 112 (1986) 531-554.

TELFORD, J.W.; CHAI, S.K.: A New Aspect of Condensation Theory. Pageoph 118 (1980) 720-741.

ON THE OBSERVATIONS OF CLOUD TEMPERATURE AND LIQUID WATER CONTENT USING A LYMAN-α AND AN FSSP SENSOR

Jørgen B. Jensen, Darrel Baumgardner
National Center for Atmospheric Research[1] Boulder, CO 80307

Graciela Raga
Department of Atmospheric Sciences, University of Washington, Seattle, WA 98195

1. INTRODUCTION

The 1985 Joint Hawaiian Warm Rain Project was an aircraft experiment designed to explore the processes leading to warm rain in cumulus clouds off the coast of Hawaii. During the five weeks of the experiment a very large number of cumuli were sampled by the University of Wyoming King Air in a systematic manner.

For a detailed discussion of the aircraft instrumentation we refer to COOPER *et al.* (1984); here we will only discuss the reverse flow temperature sensor, the EG&G dew-point thermometer, a Lyman-α humidity sensor mounted with a reverse flow shielding inside the fuselage, and a PMS FSSP.

We have analyzed 134 penetrations from 22 clouds sampled on six days during July of 1985. A total of 3126 1-second samples were classified as in-cloud.

2. RAW TEMPERATURE MEASUREMENTS

Wetting of temperature sensor elements during certain circumstances have previously been described by e.g. LENSCHOW and PENNELL (1974). Wetting of heating of air passing by the sensor evaporates some of the water and cools the sensor element. The adiabatic heating depends on the aircraft true air speed and this effect is corrected for; there is no correction for the effect of evaporative cooling.

The evidence for sensor wetting is twofold: (i) A comparison between parcel buoyancy and vertical wind speed showed that most parcels were both negatively buoyant *and* ascending. (ii) A transient "cooling spike" was commonly found upon exit from cloud, when the wet sensor element suddenly is immersed in highly sub-saturated air. Therefore we have chosen to use the Lyman-α sensor on the aircraft to estimate the temperature of saturated, cloudy air.

3. CALIBRATION OF THE LYMAN-α SENSOR

Descriptions of Lyman-α sensors for measurements of atmospheric water vapor have been given by eg. TILLMAN (1965). Since the present calibration technique differs from previous methods, we will describe it in some detail. After calibration we can calculate a Lyman-α derived dew-point temperature, $T_{L\alpha}$. This is useful as a fast response dew-point temperature measurement outside cloud as well as an estimate of the temperature of saturated cloudy air.

In the following calculation we will assume that collimated light with wavelengths between $\lambda_{min} = 115$ nm and $\lambda_{max} = 132$ nm is emitted with intensity $I_0(\lambda)$ and that it is detected with intensity I. Given that water vapor and oxygen are the only significant absorbers for this wavelength range in the lower atmosphere, we can write the Beer law as:

$$I = \int_{\lambda_{min}}^{\lambda_{max}} I_0(\lambda) \exp\left\{ -\frac{k_v(\lambda)\rho_v \Delta s}{\rho_{vref}} - \frac{k_x(\lambda)\rho_x \Delta s}{\rho_{xref}} \right\} d\lambda \qquad (1)$$

Here $k_v(\lambda)$ and $k_x(\lambda)$ are the absorbtion coefficients for water vapor and oxygen respectively, ρ_v and ρ_x are the vapor and oxygen densities, ρ_{vref} and ρ_{xref} are the reference densities of vapor and oxygen at STP, and Δs is the pathlength. Since both $I_0(\lambda)$, $k_v(\lambda)$ and $k_x(\lambda)$ depend strongly on λ and since $I_0(\lambda)$ may change with time, it is next to impossible to evaluate

eq. (1) exactly. We will therefore simplify eq. (1) by using average values of $I_0(\lambda)$, $k_v(\lambda)$ and $k_x(\lambda)$, i.e.:

$$I = I_0 \exp\left\{-\frac{k_v \rho_v \Delta s}{\rho_{vref}} - \frac{k_x \rho_x \Delta s}{\rho_{xref}}\right\} \quad (2)$$

For the subsequent processing we have:

$$V_{out} = c_4 \ln\{c_1 c_2 I + c_3\} + c_5 \quad (3)$$

where V_{out} is the voltage which is stored on tape, c_1 and c_3 are unknown constants, and c_2, c_4 and c_5 are laboratory measured constants.

Combining eqs. (2) and (3) and reorganizing yields:

$$\frac{\rho_v}{\rho_{vref}} k_v \Delta s + \frac{\rho_x}{\rho_{xref}} k_x \Delta s - \ln\{c_1 c_3 I_0\} = -\ln\left[\exp\left\{\frac{1}{c_4}(V_{out} - c_5)\right\} - c_3\right] \quad (4)$$

From day to day the maximum value of V_{out} increased until an upper limit of about 3.2 Volts was reached. At this point we found that the current-to-voltage converter offset, c_3= 0.0028 Volt.

By taking three segments with constant dew-point temperature from an environmental sounding we can use the EG&G dew-point sensor in combination with the pressure and reverse flow sensors to "calibrate" the Lyman-α. For the three sounding segments we can calculate (ρ_{v1}, ρ_{v2}, ρ_{v3}), (ρ_{x1}, ρ_{x2}, ρ_{x3}), and (eq. (4): RHS_1, RHS_2, RHS_3). Using eq. (4) to form three equations with three unknowns, we can solve for $k_v \Delta s$, $k_x \Delta s$ and $\ln(c_1 c_3 I_0)$; i.e. the Lyman-α sensor is "calibrated". For 15 calibartions we find that the average $k_v/k_x \approx 10$.

After a calibration has been made, a double iteration is used to find the Lyman-α temperature. First step is to guess the water vapor density, ρ_v. Secondly we iterate $T_{L\alpha}$ until the equation of state for water vapor is satisfied to a sufficient degree, calculate oxygen density and test if the LHS and RHS of eq. (4) matches sufficiently.

One final adjustment to $T_{L\alpha}$ was made in the following way. At cloud base there will normally be a small difference between the Lyman-α and reverse flow temperature due to a slight offset between the sensors. This offset was added to the EG&G dewpoint temperature and the solution of the three equations with three unknowns repeated until the reverse flow temperature and the Lyman-α temperature were equal at cloud base.

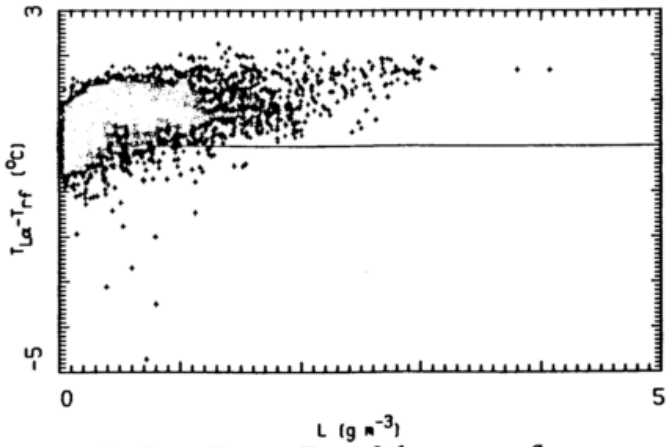


Fig. 1. Cooling, $T_{L\alpha} - T_{rf}$, of the reverse flow sensor with respect to the Lyman-α sensor due to wetting shown as function of the liquid water content, L.

4. CORRECTED TEMPERATURE MEASUREMENTS

Fig. 1 shows the difference, $T_{L\alpha} - T_{rf}$, for all cloudy 1-second samples. Most of the samples show less than 1.5 °C cooling from wetting; maximum values are close to 2 °C. This compares favorably with the theoretical predictions by LENSCHOW and PENNELL (1974).

Using the Lyman-α derived temperature we find that most ascending parcels indeed are positively buoyant.

The deviation of the cloudy air temperature from the adiabatic temperature, $T_{L\alpha} - T_a$, as function of height, z, is shown in Fig. 2. If we estimate an uncertainty in the cloud base temperature of ±0.5 °C, which translates into an uncertainty of T_a of ±0.5 °C, it seems reasonable to assign an uncertainty in $T_{L\alpha}$ of ±0.5 °C. Fig. 2 shows that a large number of the cloudy samples have temperatures which can not be discerned from the adiabatic values. 49 % of the samples have -1 °C $< (T_{L\alpha} - T_a) <$ 1 °C; these occur all the way from cloud base to cloud top.

5. CORRECTIONS TO LWC MEASUREMENTS

The liquid water content, LWC, was derived from droplet size distribution measured with a PMS FSSP

probe. The observed liquid water mixing ratios were compared to the values predicted from adiabatic ascent from cloud base. Fig. 3 shows that the observed values never exceed 0.4 of the adiabatic values. Entrainment and mixing is expected to dilute many of the samples; however, it is disturbing that none of the data approach adiabatic values.

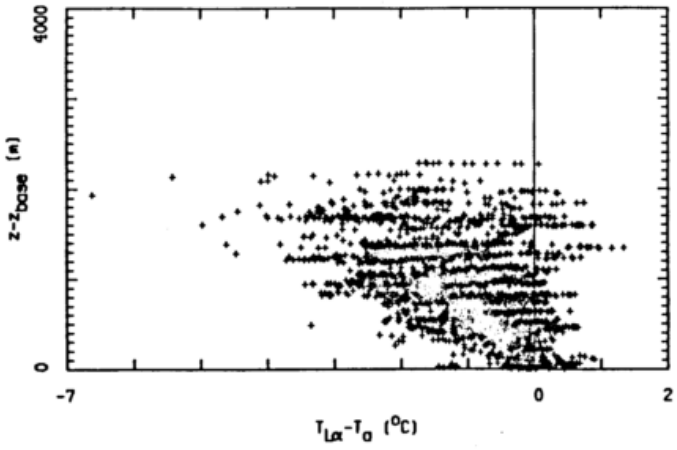


Fig. 2. Cooling of cloudy parcels due to entrainment, $T_{L\alpha} - T_a$, shown as function of flight level above cloud base, $p_{base} - p$.

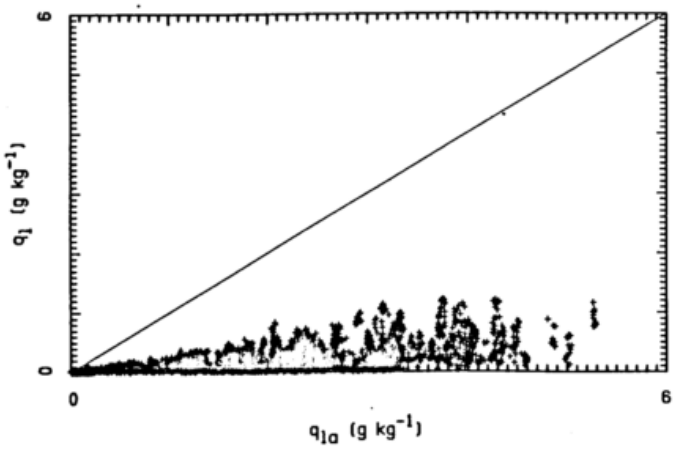


Fig. 3. Raw FSSP liquid water mixing ratio as function of adiabatic liquid water mixing ratio.

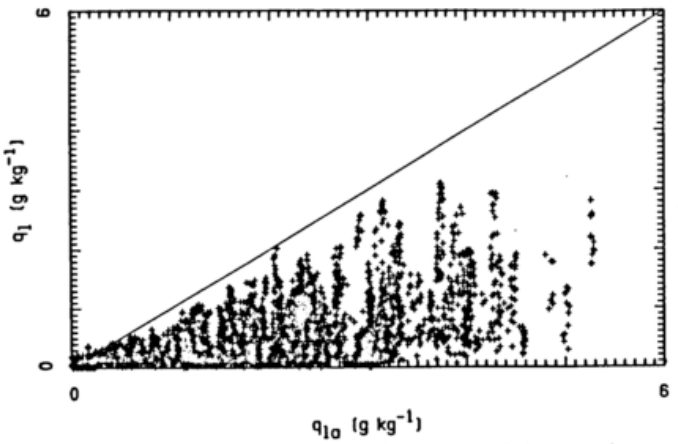


Fig. 4. Corrected FSSP liquid water mixing ratio as function of adiabatic liquid water mixing ratio.

An in-depth analysis of the FSSP (BAUMGARDNER, 1988) showed that significant corrections to the measurements were necessary to correct for sample volume variations, for undersizing that result from electronic response time limitations and for laser beam inhomogeneities. These effects are especially significant when droplet spectra are as broad as they were in the Hawaii trade clouds.

Correction algorithms were derived based on the operating characteristics of the FSSP and were applied to the measurements from this study. The results are shown in Fig. 4 where the comparison between observed and predicted values appear more sensible.

ACKNOWLEDGMENTS Thanks are due to Dr. W.A. Cooper of NCAR and Dr. A. Rodi from University of Wyoming for much help and many stimulating discussions. The present study was in part supported by National Science Foundation under grant ATM 8420816.

REFERENCE LIST

BAUMGARDNER, D. (1988): Cloud droplet growth in Hawaii orographic clouds. *Ph. D. Dissertation*, University of Wyoming, 311 pp.

COOPER, W.A. (1978): Cloud physics investigations by the University of Wyoming in HIPLEX 1977. Rept. #AS119, Dept. of Atmos. Sci., Univ. of Wyoming, Laramie, Wyoming, 321 pp.

LENSCHOW, D.H. and W.T. PENNELL (1974): On the measurement of in-cloud and wet-bulb temperature from an aircraft. *Mon. Wea. Rew.*, **102**, 447-454.

RAGA, G., J.B. JENSEN, J. WEWTLAUFER and M.B. BAKER (1988): Characteristics of cumulus band clouds off the coast of Hawaii. This volume.

TILLMAN, J.E. (1965): Water vapor measurements utilizing the absorbtion of vaccum ultraviolet and infrared radiation. *Humidity and moisture, measurements and control in science and industry*, **1**, *Principles and methods of measuring humidity in gasses.* R.E. Ruskin, Ed., New York, Reinhold, 428-433.

EVALUATION OF DROPLET GROWTH RATES IN HAWAIIAN OROGRAPHIC CLOUDS

Darrel Baumgardner
National Center for Atmospheric Research*
Boulder, Colorado

1. INTRODUCTION

The present study was designed to provide more accurate and higher rate measurements of evolving cloud droplet populations than previously possible. The orographic clouds formed by the island of Hawaii were selected for evaluation because of their temporal stability, relatively low levels of turbulence, and warmer than freezing cloud tops. The results of these measurements are compared with predictions from a droplet growth model.

2. DROPLET GROWTH MODEL

In the one dimensional model that was developed the identity of each droplet is maintained after it is activated and until it coalesces with another droplet or leaves the cloud. This technique was utilized so that stochastic fluctuations could be evaluated during the growth process. The cloud condensation nuclei concentration, N, was paramaterized as a function of the percent supersaturation, S, by using a power law relation, $N = CS^k$, where the values of C and k were measured (Hudson, private communication) as 34 and 0.55, respectively. The droplets initially grow by condensation during the parcel's adiabatic ascent and while coalescence is possible at any point during the growth process, it is insignificant until the median volume droplet diameter is greater than about 25 μm (about 500 seconds of growth). Coalescence was modeled using the method of Gillespie (1975) where a Monte Carlo technique is used to generate the next time of coalescence and to select which two droplets coalesce based upon a joint probability distribution established by the collection kernels of each droplet pair. This method was selected to examine the assumptions that are used when coalescence is modeled with the kinetic coagulation equation. The model was intialized with the measured cloud base temperature and pressure for each cloud study. The vertical motion of the air parcel was characterized by the measured profile of vertical velocity with altitude. The time period of the model was determined by the vertical velocity structure and depth of each of the three clouds that were evaluated.

3. MEASUREMENT METHODOLOGY

The primary variables measured were the cloud droplet size and number distributions. A forward scattering spectrometer probe (FSSP) and 260X one dimensional optical array probe, both manufactured by Particle Measuring Systems (PMS, INC., Boulder, Co.) provided measurements in the size range of 2 μm to 150 μm. An assessment of their operational and measurement limitations (Baumgardner, 1988) showed that differences could be resolved between droplet distributions that had grown for a minimum of 100 seconds. Figure 1 shows model results where droplet distributions were grown for 400 seconds (solid line) and 500 seconds (dashed line). The droplet spectra are displayed as if measured by the FSSP and 260X and have been adjusted to account for the inherent uncertainties and limitations imposed by the instruments. The measurement errors are estimated by using a Monte Carlo simulation of the instruments that accounts for the complex interactions among the factors that limit the instruments' operation. These errors are shown

*Sponsored by the National Science Foundation

as vertical bars in each size channel. This figure shows how the measurement uncertainties can mask the differences in the spectra grown for different times.

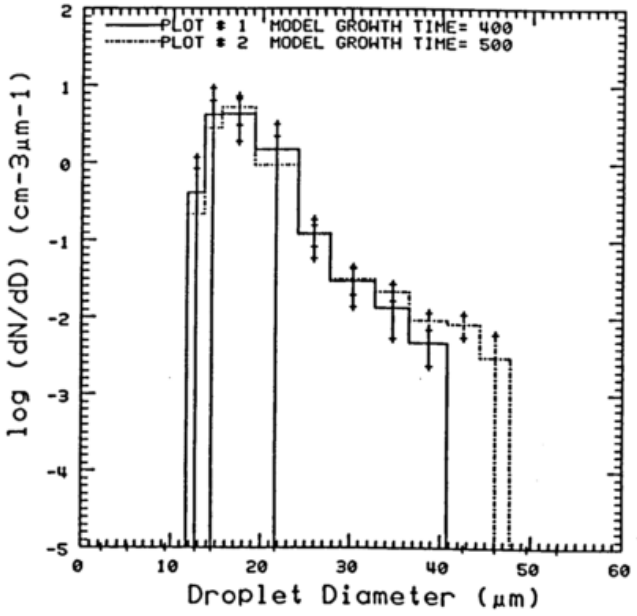


FIGURE 1

4. RESULTS

Seventeen research flights were conducted during the field project to evaluate droplet growth rates. Three separate clouds are evaluated in the present study to illustrate particular similarities and differences between predicted and observed distributions. Each of the clouds had well-defined edges and eddy dissipation rates less than 10 cm^3 s^{-3}. The clouds appeared laminar in structure and convective elements were neither observed visually or indicated by the measurements. The three clouds differed somewhat in general structure as summarized in the following table.

CASE	CLOUD BASE ALT. (m)	CLOUD BASE TEMP. (°C)	CLOUD BASE PRESS. (mb)	CLOUD DEPTH (m)	CLOUD LENGTH km	MAX GROWTH (s)
A	2900	7	705	≈300	≈ 7	300
B	2000	11	795	≈400	≈10	500
C	900	16	920	≈600	≈25	> 2000

The aircraft penetrated the clouds in successive upwind and downwind tracks that closely followed the ascending airflow.

Examples of predicted and observed measurements from each of the cloud studies are shown in Figures 2-4. The model results, adjusted for the measurement uncertainties, are shown as solid lines. The observed results, shown as dashed lines, are from measurements taken at altitudes where the estimated growth time from cloud base is within ±50 seconds of the growth time used by the model. The shape parameters listed on the figures help identify similarities and differences between the predicted and measured spectra. The droplet diameter within which 95% of the water is

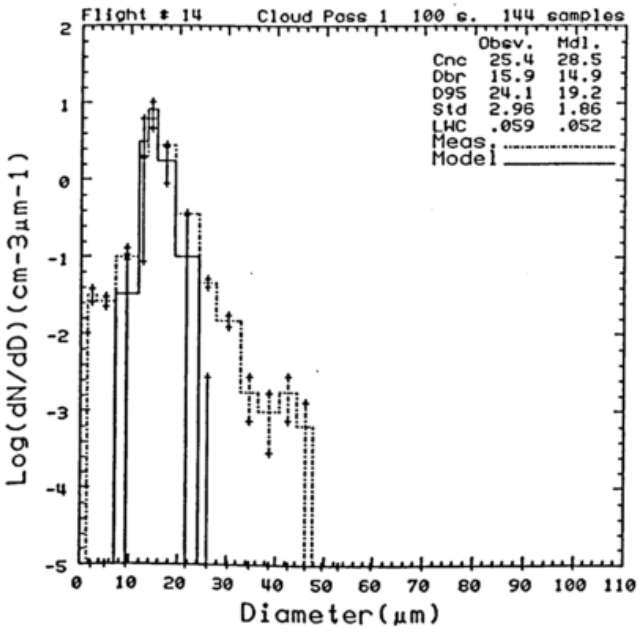


FIGURE 2

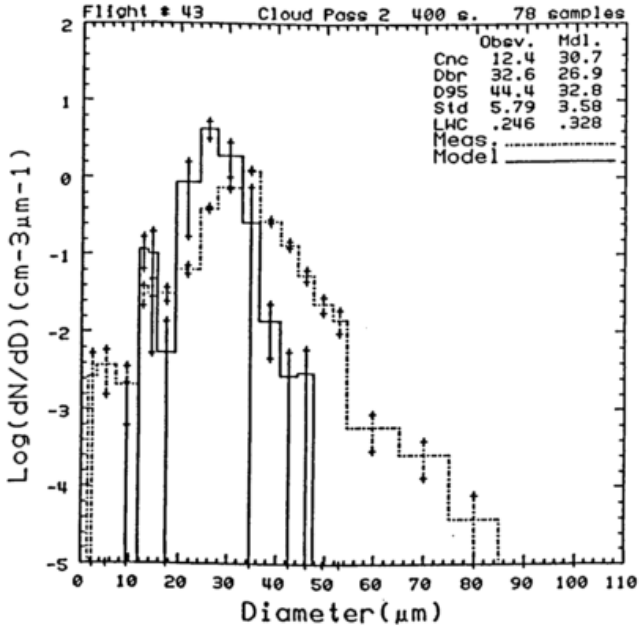


FIGURE 3

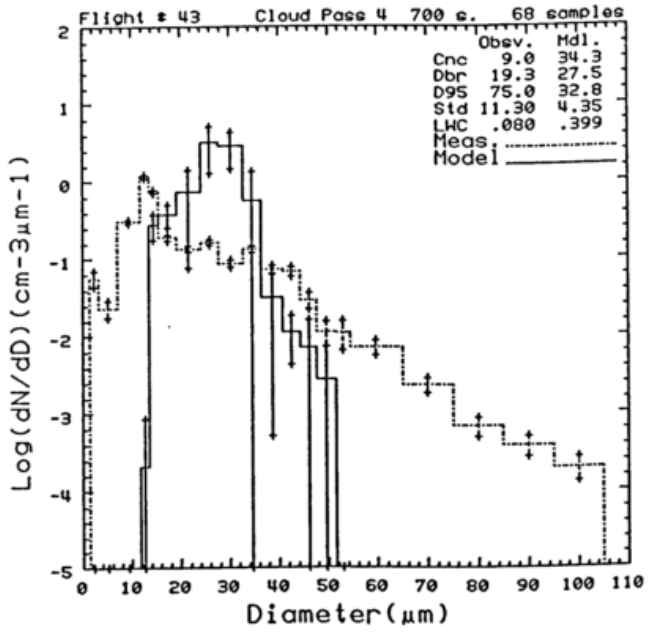


FIGURE 4

contained (D_{95}) helps identify differences in the large droplet tail of the spectra. In all three cases there were larger droplets observed than were predicted, regardless of the growth time. In the first cloud study, the measured and predicted concentrations, mean diameters, and LWCs were in excellent agreement after 100 seconds growth and yet droplets were observed twice as large as predicted by the model. In the somewhat deeper and wider cloud of the second case, the differences are even more pronounced at the large droplet end of the spectrum. In this case the LWCs were in reasonable agreement but the measured concentrations are a factor of two lower than predicted. The measurements of the third cloud study show little agreement in concentration, mean diameter or LWC with the predicted results. In all three of these cases there was no evidence that measurements were contaminated by droplets from higher levels and yet much larger than predicted droplets are observed regardless of growth time or cloud depth. It is unlikely that the larger droplets are the product of coalecence in the first two cases because of the short growth periods and small collection kernels.

Initializing the model with additional giant salt nuclei in concentrations equivalent to those measured outside the cloud had a negliglible effect on the resulting droplet distribution. In the third case study the model had begun producing larger droplets by the selected growth time; however, these larger droplets did not account for those that were observed. Enhanced growth could be produced if elevated collection kernels were used in the coalescence calculation; however, these effects were offset if realistic concentrations were used in the model such as seen in the measurements. The comparisons of predicted and measured droplet distributions in the relatively simple case of low turbulent, orographic, warm clouds indicate that larger droplets appear in quantities greater than predicted from conventional theories. After a thorough scrutiny of the droplet growth model there does not appear to be a of the fundamental physical processes that govern droplet growth. The problem that the model did not address is the characterization of a fluctuating environment within which droplets grow and interact. Recent studies by Cooper et al (1986) show that flucuations in the velocity and moisture fields surrounding cloud droplets will have major effects on their rates of growth. The focus of future research should be on the development of models that correctly characterize the structure of the environment.

5. REFERENCES

Baumgardner, D., 1988: Cloud droplet growth in Hawaiian orographic clouds. Phd. Thesis, University of Wyoming. 311 pp.

Cooper, W.A., D. Baumgardner, J.E. Dye, 1986: Evolution of the droplet spectra in Hawaiian orographic clouds. Prepints 23rd Conf. Cloud Physics. 52-55

Gillespie, D.T., 1975: An exact method for numerically simulating the stochastic coalescence process in a cloud. J. Atmos. Sci., 32, 1977-1989.

STUDIES OF WARM-RAIN DEVELOPMENT

William A. Cooper

National Center for Atmospheric Research*
Boulder, CO 80307, USA

1. INTRODUCTION

The development of rain in warm (>0°C) clouds must be due to the combined effects of condensation and coalescence following collisions, and the theoretical basis for each of these processes is well known. However, the detailed shape of the size distribution produced by condensation has a controlling influence on the rate of coalescence, and this shape is affected by entrainment of dry air, mixing of various cloud parcels, and radiative effects. In this paper, some aspects of these processes are examined in several cloud types where rain formed through warm-rain processes.

2. THEORETICAL DISCUSSION

The diffusional growth equation (and kinetic coefficients) of FUKUTA and WALTER (1970) were used in the following, and the integrations of the stochastic coalescence equation (SCE) were based on the techniques of BERRY and RINEHARDT (1974) and the collision efficiencies of KLETT and DAVIS (1973) or, at large size, those of BEARD and GROVER (1974).

The effects of fluctuations in the diffusional growth rates can be studied through use of the quasi-steady supersaturation, $S_{qs}=a_1W/(a_2I)$ where W is the updraft, I the integral radius (equal to N<r> where N is the droplet concentration and <r> the mean radius), and a_1 and a_2 are coefficients first determined by SQUIRES (1952). The growth of a droplet is determined by $\int S(t')dt'$ where S(t') is the time-dependent supersaturation in its environment, so its growth is determined by the integral

$$A_{qs}(t)=\int S_{qs}(t')dt' = \int_0^t \frac{a_1\, W(t')}{a_2\, I(t')}\, dt' \quad . \quad (1)$$

Let W and I be represented in terms of mean and fluctuating quantities: $W(t')=W_o+W'(t')$ and $I(t')=I_o+I'(t')$ where W_o and I_o are means for the period $0<t'<t$. Then, expansion of (1) and neglect of higher-order terms in I' leads to

$$A_{qs}(t) \simeq A_o\left[1 - \frac{W_o t}{Z}\left(\frac{\overline{I'}}{I_o} + \frac{\overline{I'W'}}{I_oW_o}\right)\right] \qquad (2)$$

where $A_o=(a_1Z)/(a_2I_o)$ and $Z=\int W(t')dt'$. In (2), an overbar indicates a time average so $\overline{I'}=(1/t)\int I'(t')dt'$. The effect discussed by BARTLETT and JONAS (1972) (whereby higher updrafts produce higher supersaturations accelerating droplet growth so as to cancel effects of fluctuations among droplets reaching a given altitude) is incorporated through the replacement $Z=\int W(t')dt'$ which constrains the droplet to a given ascent. This constraint must also be applied to the remaining terms when the meaning of the overbars is interpreted.

The two fluctuating terms in (2) provide mechanisms for enhancement of droplet growth, if for a particular droplet either $\overline{I'}$ or $\overline{I'W'}$ is less than the corresponding ensemble mean. In the first term, the competition with neighboring droplets is reduced, and in the latter term the growth is enhanced by cycling along favored trajectories so that some droplets experience ascent in regions with low I (favoring growth) and descent in regions with high I (minimizing evaporation). For significant enhancement of growth, the first term is probably negligible because the effects must occur for one average ascent and cannot accumulate as

*NCAR is sponsored by the National Science Foundation.

they can for the second term which can cause continued broadening and growth with time for appropriate trajectories.

The first term can represent the enhancement process suggested by BAKER and LATHAM (1979), while the process suggested by TELFORD and CHAI (1980) involves vertical cycling and so involves the second term as well. The approach taken in this paper will be to use the observed variability in I' or I'W' as a measure of the enhancement that might be possible through such processes.

GUZZI and RIZZI (1980) showed that the power radiated from a cloud droplet (Q) changes the growth rate as if the supersaturation changed by $C_I=L_vQ/(4\pi r\lambda R_wT)$ where L_v is the latent heat of vaporization, r the droplet radius, λ the conductivity (compensated for kinetic effects at the drop surface), R_W the gas constant for water vapor, and T the temperature. DAVIES and RIDGWAY (1984) found that Q varies approximately as $r^{2.5}$, and in that case C_I varies as $r^{1.5}$. Large droplets thus experience a larger effective supersaturation than small droplets, so this is a mechanism for broadening of a droplet spectrum near cloud tops or wherever there is a net power loss by the droplets. If values from ROACH (1976) are used for typical radiation losses by droplets, it can be shown (via a derivation too lengthy for this abstract) that the above process of broadening leads to doubling of the dispersion of the droplet size spectrum in about 15 min, and so can be an important factor broadening the droplet spectrum near the tops of clouds.

3. CLOUD TYPES CONSIDERED

3.1 Hawaiian Wave Clouds

Cloud passes flown along airflow trajectories in shallow wave clouds over the southern end of the island of Hawaii were used to document the evolution of the droplet size distribution. These passes, discussed by COOPER et al. (1986), showed that the initial formation of the droplet spectrum was as expected from calculations based on the observed updrafts and CCN spectra at cloud base. However, calculated coalescence rates in these clouds were negligible because liquid water contents were low (0.25 g/m^3) and mean droplet diameters were small (20-25 μm).

In contrast, the observations (Cooper et al., 1986; Baumgardner, 1988) showed that large droplets developed surprisingly fast. For diameters >80 μm, the concentration exceeded 10/L after about 400 s of travel through the cloud, and some droplets were >150 μm in diameter. Drops of 500 μm diameter also appeared below the downwind portions of some of these clouds. The development of these large droplets occurred after entrainment of dry air through the cloud top (at the trade inversion) partially evaporated portions of the cloud and produced a variable cloud structure.

COOPER et al. (1986) suggested that this mixing led to enhanced growth of some droplets. Two additional results can be added to support that contention. First, values of I'W' were highly variable, as shown in Table 1. Values of $I'W'/(I_oW_o)$ as low as -3 were found, and there was poor correlation between I' and W' so a range of possible correlations could apply to various droplet trajectories. Second, a Monte Carlo calculation was used to simulate motion through the turbulent region of the clouds. In this calculation, the updraft fluctuated over the observed range (constrained so that the droplet remained in the cloud) but the integral radius was chosen randomly from among the observed values while both fluctuations changed randomly at 6 s intervals. The result was pronounced spreading of the droplet size distribution and production of 80-100 μm droplets in concentrations comparable to those observed, even without any coalescence.

3.2 Marine Stratocumulus Clouds

A shallow Sc layer located about 100 km west of San Francisco was observed to produce drizzle-size precipitation although it was only 350 m

thick and the temperature was everywhere above 9°C. Maximum droplet concentrations were about 250 cm^{-3}, and mean diameters were <20 μm throughout the cloud. Again, calculations (with sizes and liquid water contents exceeding those observed) indicated that there would be little precipitation except after coalescence for >1.5 h with maximum liquid water content, and such times are unlikely for persistence of individual parcels or droplets in the Sc layer. There was less variability in available growth conditions than in the Hawaiian wave clouds, and the conditions seemed to be marginal or perhaps too weak to produce a significant enhancement of growth by condensation, as indicated in Table 1. Because of the long persistence times of these clouds, radiative cooling may contribute to the development of large droplets in a case such as this where conditions otherwise appear marginal for any development of drizzle or rain.

3.3 Cumulus Clouds

Similar enhancements of diffusional growth were sought in cumulus clouds, especially in the turbulent regions near cloud tops. Regions were often found having enough variability in I'W' to support some enhancement of droplet growth rates in the maritime (but, as yet, not the continental) cases. However, in these cases the sensitive dependence of the calculated coalescence rates on liquid water content makes the coalescence calculations unreliable guides to the expected rates of warm-rain formation. In Hawaiian cumulus clouds, the liquid water contents produced by adiabatic ascent would be 3-4 g/m^3 in the upper regions of the clouds, and if any parcels rose unmixed then the rates of coalescence would be so fast that the much slower potential enhancement of condensation rates by turbulent fluctuations (as in Table 1) would be insignificant. Enhancement of diffusional growth rates may be significant in cases where entrainment prevents adiabatic ascent of some parcels, but it appears more likely that the adiabatic ascent of a few parcels could initiate coalescence growth and then drizzle-size droplets could spread through the cloud.

4. CONCLUSIONS

These results suggest that diffusional growth may be enhanced in some highly mixed regions of maritime Cu in a manner similar to that in the wave clouds, but that this effect is minor in updraft cores or in the Sc layers examined.

TABLE 1: EXAMPLES OF TERMS IN EQ. (2)

(W_o estimated = Z/t for wave and Sc cases)

Cloud type	σ_I/I_o	$\sigma_{IW}/(I_oW_o)$
Hawaiian wave	0.5	0.6
Hawaiian Cu:		
updrafts	0.2	0.15
cloud top	0.5	0.6
Marine Sc	0.25	0.3

ACKNOWLEDGMENTS: The aircraft support was provided by the Research Aviation Facility, National Center for Atmospheric Research, which is sponsored by the National Science Foundation, and by NASA contract NAS5-27783 to the University of Wyoming.

REFERENCES

BAKER, M. B. and J. LATHAM, 1979: The evolution of droplet spectra and the rate of production of embryonic raindrops in small cumulus clouds. J. Atmos. Sci., 36, 1612-1615.

BARTLETT, J. T. and P. R. JONAS, 1972: On the dispersion of the sizes of droplets growing by condensation in turbulent clouds. Quart. J. Roy. Meteor. Soc., 98, 150-164.

BAUMGARDNER, D. B., 1988: Evaluation of droplet growth rates in Hawaiian orographic clouds. 10th International Cloud Physics Conference.

BEARD, K. V. and S. N. GROVER, 1974: Numerical collision efficiencies for small raindrops colliding with micron size particles. J. Atmos. Sci., 31, 543-550.

BERRY, E. X and R. L. RINEHARDT, 1974: An analysis of cloud drop dropth by collection. Part I: Double distributions. J. Atmos. Sci., 31, 1814-1824.

COOPER, W. A., D. BAUMGARDNER and J. E. DYE, 1986: Evolution of the droplet spectra in Hawaiian orographic clouds. Preprints, Conf. on Cloud Physics, Snowmass, Amer. Meteor. Soc., C52-55.

DAVIES, R. and W. RIDGWAY, 1984: Some effects of solar radiation on cloud microphysics. IRS 1984: Current Problems in Atmospheric Radiation, 171-173.

FUKUTA, N. and L. A. WALTER, 1970: Kinematics of hydrometeor growth in a vapor-spherical model. J. Atmos. Sci., 27, 1160-1172.

GUZZI, R. and R. RIZZI, 1980: The effect of radiative exchange on the growth by condensation of a population of droplets. Contributions to Atmos. Physics, 53, 351-365.

KLETT, J. D. and M. H. DAVIS, 1973: Theoretical collision efficiencies of cloud droplets at small Reynolds numbers. J. Atmos. Sci., 30, 107-119.

ROACH, W. T., 1976: On the effect of radiative exchange on the growth by condensation of a cloud or fog droplet. Quart. J. Roy. Meteor. Soc., 102, 361-372.

SQUIRES, P., 1952: The growth of cloud drops by condensation. Aust. J. Sci. Res., 5, 66-86

TELFORD, J. W. and S. K. CHAI, 1980: A new aspect of condensation theory. Pure Appl. Geophys., 19, 934-965.

RADAR OBSERVATIONS AND MODELLING OF WARM RAIN INITIATION

Anthony J Illingworth
Visiting Scientist
NCAR*, Boulder
Colorado 80307, USA

and

I Jeff Caylor
Dept. of Physics
UMIST
Manchester M60 1QD, UK

1. INTRODUCTION

Differential radar reflectivity observations of early echoes of rain in warm convective clouds in the UK and Alabama, USA, indicate that precipitation initially forms as raindrops greater than 4mm in size but present in concentrations of less than one per cubic meter. The differential reflectivity, ZDR, (10 log (ZH/ZV)), where ZH and ZV are the radar reflectivities measured with horizontal and vertical polarizations, respectively. ZDR provides a measure of the shape of the hydrometeors, and because raindrops are oblate to a degree which depends upon their size, the magnitude of ZDR is a unique function of raindrop size (Table 1). ZDR is a ratio and so is independent of concentrations, but once the mean size is known then the conventional reflectivity, ZH, can be used to derive an estimate of raindrop concentration (SELIGA and BRINGI, 1976).

2. RAINDROP SIZE AND CONCENTRATIONS

If we assume an exponential raindrop size distribution:

$$N(D) = No \exp(-3.67 D/Do)$$

where N is the concentration of drops of diameter D and Do is the eqivolumetric diameter, then by summing the contributions of the various sizes of raindrops present we may calculate the values of ZDR as a function of Do (Table 1, final columns, spectrum truncated at 8mm). The value of No is then linearly dependent upon the magnitude of ZH. In Figure 1 the solid lines are the values of Z and ZDR as Do varies but No is kept constant. The total drop concentration is given by NoDo/3.67. Many observations have shown the average raindrop size distribution to be that proposed by Marshall and Palmer with No=8000 $m^{-3} mm^{-1}$. A long series of radar observations of Z and ZDR (CAYLOR and ILLINGWORTH, 1987) has confirmed that the average value of ZDR of rain for a given Z does indeed lie upon the No=8000 curve in Figure 1.

We shall be discussing early echoes which have values of ZDR of 3 or 4dB, and would be expected to have Z values of 56 to 67dBZ for Marshall-Palmer rain. Instead the values are 30dBZ lower, implying values of No reduced by a factor of 1000. For example from Figure 1 we see that a value of Z of 15dBZ accompanied by a ZDR of 3dB implies a value of No of only $0.8 m^{-3} mm^{-1}$, or a drop concentration (Do=2.5mm) of $0.7 m^{-3}$.

3. CHILBOLTON RADAR (UK) OBSERVATIONS

A vertical section through a young convective cloud with anomalously high ZDR is displayed in Figure 2 (for other examples and details of the radar, see ILLINGWORTH et al, 1987). Values of Z of 30dBZ are accompanied by a ZDR above 4.5dB, which imply (Figure 1) large drops (6mm) in concentrations of only one per cubic meter. This cloud persisted for twenty minutes with no great change in character; the 2700 data points obtained during this period are displayed in Figure 3, where each star represents the average value of ZDR for every 2dBZ step in Z. The solid line in Figure 3 is the No=8000 curve from Figure 1; showing that the low concentration of large raindrops persisted throughout the twenty minute period.

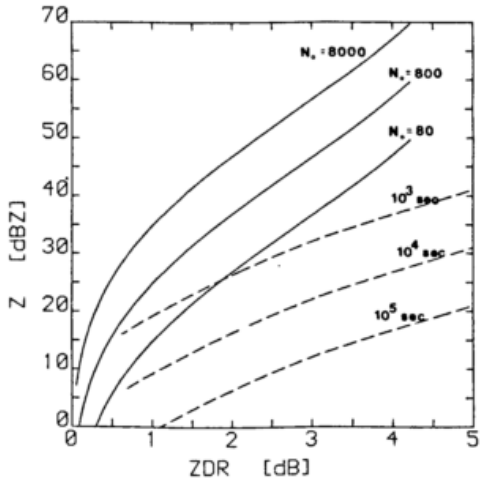


Figure 1. The variation of Z and ZDR as a function of 3 values of No (solid lines). The dashed lines show the expected lifetime for a 5mm diameter drop.

TABLE 1

Size (mm)	Axial Radial	ZDR(dB)	Do (mm)	ZDR(dB)
4	0.778	2.49	1	0.62
5	0.708	3.48	2	2.31
6	0.642	4.42	2.5	3.03
7	0.581	5.33	3	3.56
8	0.521	6.70	4	4.22

Values of axial ratio (from BEARD and CHUANG, 1987) and ZDR for various sizes of raindrop. The Mie-Gans calculations are supplied by Dr Holt, Department of Mathematics, University of Essex, and apply to raindrops at 0°C and 3.0765 GHz.

*The National Centre for Atmospheric Research is sponsored by the National Science Foundation.

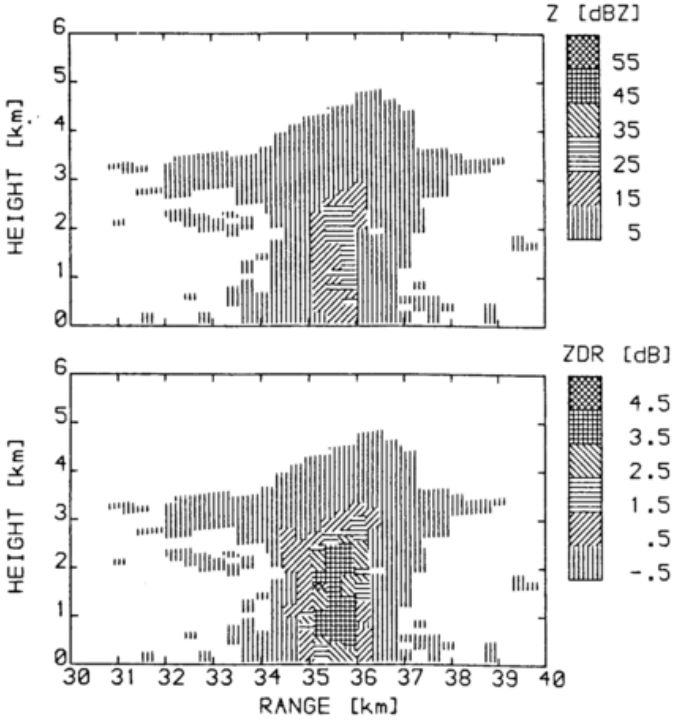


Figure 2. A vertical scan on 20 June 1980 displaying anomalously high ZDR.

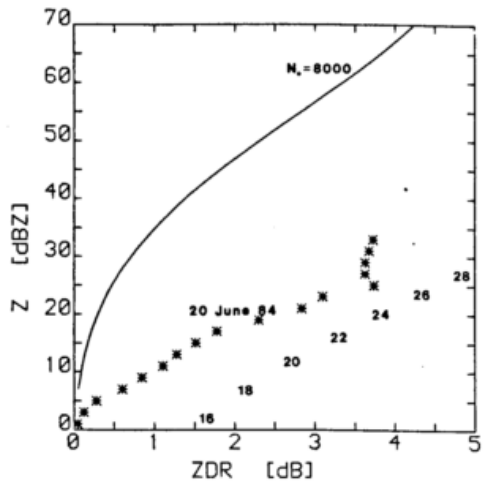


Figure 3. Averaged Z and ZDR over a 20 minute period for the cell in Figure 2. For comparison the model output as a function of time (minutes) and the Z and ZDR for a drop size distribution with No = 8000 are shown.

4. GIANT NUCLEI MODEL

To explain such low concentrations of large raindrops, CAYLOR and ILLINGWORTH (1987) extended a suggestion (JOHNSON, 1982) that each large raindrop formed on an ultra giant nuclei (>30um) , present in the background concentration at this low level (JUNGE, 1972). Figure 3 shows the prediction of the simple model in which Z and ZDR increase as the giant nuclei sweep out cloud water of LWC 2 g m-3, the numbers indicate time in minutes elapsed since initiation of the model with nuclei concentrations (in units of m^{-3} per unit log interval of radius)of 10^{3} for 10um radius to $3X10^{-2}$ for 100um.

Only a few large raindrops grow, and the depletion of the cloud water is negligible. The model is linear in that increasing the LWC merely changes the time scale but not the Z/ZDR dependence; in addition, increasing the nuclei concentration merely scales up the values of Z leaving ZDR unchanged. The Chilbolton cloud persisted 20 minutes and it is not possible to give a specific age to various parts of the cloud. In view of the uncertainty of the absolute concentration of giant nuclei, the observed general dependence of Z with ZDR is consistent with the model.

5. ALABAMA DATA, NCAR CP2 RADAR

First echoes formed at temperatures above zero on many days during the 1986 MIST (MIcroburst Severe Thunderstorm) project. These early echoes were also normally accompanied by anomalously high values of ZDR. A particularly clear example was on 10 July, when the evolution of a very weak echo less than 2km in diameter was observed in its entirety. In 20 minutes the echo grew from zero to 20dBZ and then collapsed; the top of the radar echo reached only 5km (slightly above the freezing level), but during this time values of ZDR in the cloud increased to 4dB, the ZDR core then descended as the rain fell to ground.

Figures 4 and 5 show the specific values of each Z/ZDR data point for two successive vertical sections through the maximum echo. The numbers plotted for each point represent the height of the data to the nearest kilometer. The evolution is consistent with the model in Figure 3, in that the concentration of drops is constant and less than one per cubic meter, 5 minutes after the appearance of the echo, the value of ZDR was 3dB, growing to 4dB in the subsequent three minutes. This is consistent with the maximum drop size increasing from 4.5 to 6mm (Table 1) by sweeping out cloud water of LWC 2 g m^{-3}.

6. CONCLUSIONS.

We have presented evidence that early echoes of warm clouds consist of a very few drops which grow to a large size by sweeping out cloud water. Because concentrations are so low this can happen without exhausting the supply of liquid water, and also with a negligible number of collisions causing the drops to break up. LOW and LIST (1982) found that for a collision to cause shattering, both raindrops must be larger than 1mm. For a given Do the lifetime of a large raindrop will be inversely proportional to No; in Figure 1 the dotted lines join the values of Z and ZDR for lifetimes of 1000, 10000, and 100000 seconds for a 5mm drop. The large raindrops in Figure 4 and 5 will survive for over an hour before collision-induced rupture. This situation should be contrasted to Figure 6 showing the Z/ZDR scatter plot for a normal mature cloud on 6 July 1986, the values are closer to the average No=8000 curve, and the lifetime of the larger drops is less than a minute.

Warm rain measurements in Texas (CARBONE and NELSON, 1978) and in Hawaii (BEARD et al, 1986) also indicate low values of No and high Do. Conventional airborne instruments do not generally have a large enough sample volume to obtain meaningful statistics of the very low concentrations inferred from the radar. In Hawaii one 8mm raindrop was sampled, supporting the idea that such raindrops are indeed stable in the atmosphere if they do not undergo collisons. Drops up to 9mm are stable in low turbulence wind tunnels (PRUPPACHER and BEARD, 1970).

We suggest that convective raindrops first form on embryos which are present in concentrations of about one per cubic meter. Such embryos could be giant nuclei, or alternatively could be ice crystals. The number of ice crystals seeding such a cloud might be expected to be more variable, and to be much greater if the cloud top was higher, yet the raindrop concentrations always seem to be very low. A raindrop distribution of a few large drops would appear to be very stable, but once break-up occurs, either due to the occasional collison or spontaneously if the drops become too large, then many small fragments are produced, and the distribution rapidly and irreversibly changes to the more normal Marshall-Palmer distribution.

ACKNOWLEDGEMENTS

This research was supported by the Meteorological Office, by NERC Grant GR3/5896 and by AFOSR-87-0046. Our co-workers S M Cherry and J W F Goddard pioneered the implementation and interpretation of the ZDR data at Chilbolton. We thank Profs Bringi, Forbes, Fujita and Wakimoto for allowing us access to the MIST data. IJC acknowledges the assistance of an ORS scholarship and AJI thanks members of the FOF at NCAR for many useful discussions.

REFERENCES

BEARD, K.V.; JOHNSON, D.B.; BAUMGARDNER, D.: Geophys. Res. Letters. 13 (1986) 991-994.

BEARD, K.V.; CHUANG, D.: J. Atmos. Sci. 44 (1987) 1509-1524.

CARBONE, R.E.; NELSON, L.D.: J. Atmos. Sci. 35 (1978) 2302-2314.

CAYLOR, I.J.; ILLINGWORTH, A.J.: Q. J. Roy. Meteorol. Soc. 113 (1987) 1171-1191.

ILLINGWORTH, A.J.; GODDARD, J.W.F.; CHERRY, S.M.: Q. J. Roy. Meteorol. Soc. 113 (1987) 469-489.

JOHNSON, D.B.: J. Atmos. Sci. 39 (1982) 448-460.

JUNGE, C.E.; J. Geophys. Res. 77 (1972) 5183-5200.

LOWE, T.B.; LIST, R.: J. Atmos. Sci. 39 (1982) 1591-1618.

PRUPPACHER, H.R.; BEARD, K.V.: Q. J. Roy. Meteorol. Soc. 96 (1970) 247-256.

SELIGA, T.A.; BRINGI, V.N.: J. App. Meteorol. 15 (1976) 69-76.

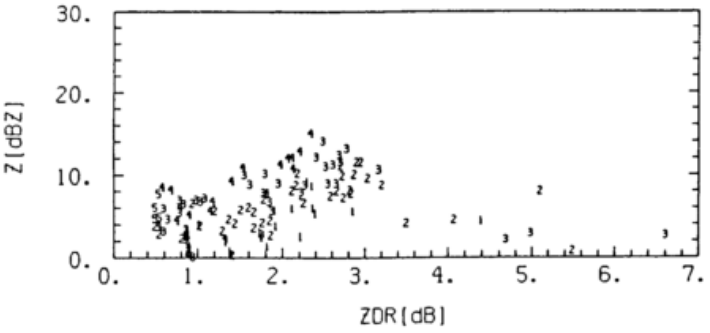


Figure 4. Scatter plot of Z and ZDR for each data point from a young echo on 10 July 1986 at 1301 CDT indicating low concentrations of large drops.

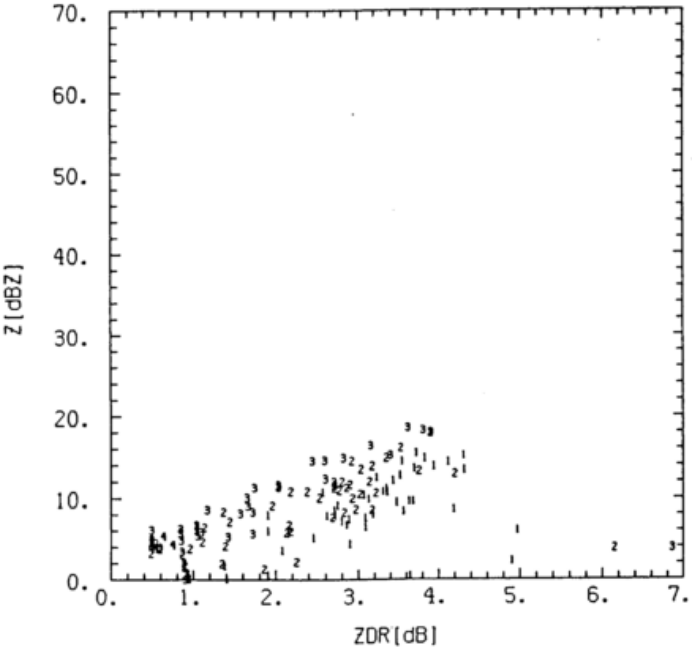


Figure 5. Values of Z and ZDR from the same cloud as Figure 4 observed 3 minutes later.

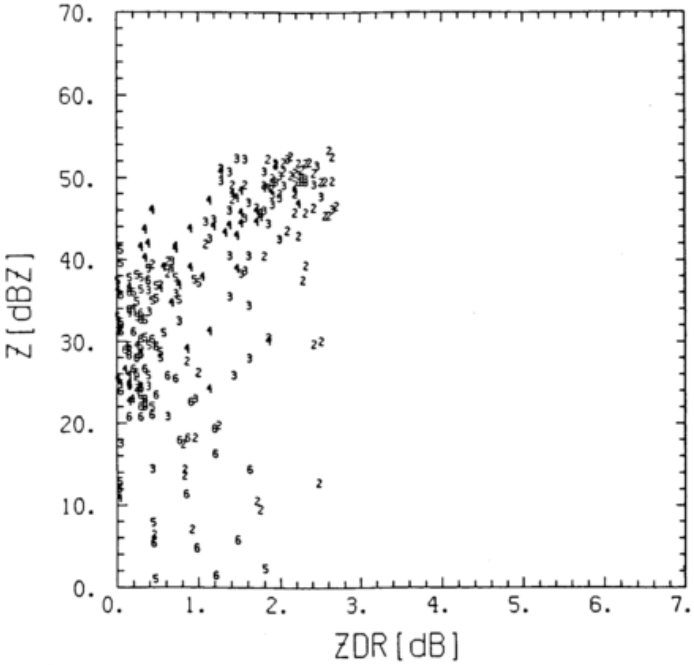


Figure 6. Z and ZDR data points from a mature convective cloud on 6 July 1986 at 1426 CDT indicating a Marshall-Palmer drop size distribution.

A TEST OF ICE CRYSTAL PRODUCTION BY AIRCRAFT

Gabor Vali, R. D. Kelly and F. Serrano

Department of Atmospheric Science, University of Wyoming
Laramie, WY 82071, U.S.A.

1. INTRODUCTION

In light of the importance of aircraft observations in the studies of cloud and precipitation processes, the possibility that the aircraft themselves may modify the clouds deserves serious consideration. Of the various microphysical and dynamical effects of aircraft on clouds, the generation of ice crystals (Aircraft Produced Ice Particles, APIP) has received most attention recently. The initial report of direct observations of this phenomenon (Rangno and Hobbs, 1983) was followed by further evidence (Rangno and Hobbs, 1984 - positive; Gordon and Marwitz, 1986 - negative), a discussion of possible implications (Mossop, 1984), and by a suggestion for the mechanism of APIP production (Vonnegut, 1986).

The experiments described here were undertaken in order to provide a broader data base on the conditions of APIP generation and on the controlling factors of the process. A tracer was used to ascertain proper sampling of the affected cloud volume so that both false positive and false negative conclusions could be avoided. This report is based on the first two attempts to carry out the experiment; the results must be considered preliminary.

2. TRACER TECHNIQUE

To clearly distinguish ice crystals produced by the passage of an aircraft through a cloud from ice crystals of other origins, it is necessary to intercept or re-trace the path of the aircraft as closely as possible. This requires navigation of the aircraft in an appropriate flight pattern with respect to the cloud (moving frame of reference). In order to provide independent confirmation of interception, a tracer was employed, consisting of a pair of pulses of high concentrations of ice crystals. The use of ice crystals as tracers provided the important advantage that detection of these crystals could affirm not only that the aircraft path was intercepted, but also that the cloud conditions were such that ice crytals could grow and would thus permit APIP to be detected, if generated. The tracer pulses were generated over a small fraction of the flight path; the remainder of the path served as the region to examine for the presence of APIPs.

3. EXPERIMENTAL METHOD

The experiments were carried out using the University of Wyoming King Air 200T twin-engine turboprop aircraft. Instrumentation included particle imaging probes, a cloud droplet counter, two devices for liquid water content measurement, inertial navigation system, and temperature and humidity sensors. Tracer crystals were generated by the release of a liquid spray of freon, i.e. by homogeneous nucleation. Navigation with reference to the cloud was directed by a computer-generated vector giving the sum of the airspeed vectors over the lapse of time from the point of reference.

Flights along straight lines, through regions of supercooled liquid water content, constituted the test regions. Two pulses of tracers were generated approximately 1 km apart, followed by turns leading to a reverse path through the tracer pulses about 3-5 minutes later. Detection of high ice crystal concentrations from the freon releases was taken as

an indication that the plume originating along the earlier flight path was intercepted. The magnitude of the plume spread was calculated from the observed rate of turbulent energy dissipation; flight segments falling within the plume of an earlier flight track were designated as "plume" regions. So far, only cases in which the plume interception is confirmed by one tracer pulse have been obtained, but even one anchor point and identical aircraft heading on the initial and repeat passes provides a fairly long region over which sampling of the plume is assured. Detection of both tracer pulses, to define the line of the plume, would provide even greater confidence in sampling the plume.

Ice crystal concentrations, sizes and shapes were monitored using an optical array probe of 12 μm/element resolution (1D-C probe), and two imaging probes of 25 μm/element (2D-C) and 200 μm/element resolution (2D-P). Concentrations to be presented here refer to those derived from the 1D-C probe, as it was the most sensitive to the small crystal sizes encountered in this work.

4. RESULTS

Results from experiments in two different clouds are available so far, with two separate experiments in one of the clouds. *Of the three tests, two have shown no evidence for the generation of APIPs; in one case there is evidence for APIPs.*

The May 21, 1987 experiment near Laramie, Wyoming, was carried out in tenuous altostratus at -9.5°C. The LWC was sporadic, with values <0.2 g m^{-3}. Ice crystal concentrations were around 0.1 per liter. Of the two releases of freon, each along a 400 m flight segment, separated by 1.3 km, only one fell in a region of liquid water content. This pulse, when sampled 4 minutes later, was seen to have resulted in an ice crystal plume of >10 lit^{-1} over 600 m. The rest of the 6.2 km long "plume" region was found to have remained essentially unchanged both with respect to LWC and ice concentrations.

Two experiments were carried out on Nov. 20, 1986 near Sacramento, California, in a layer cloud of moderate LWC, through which ice crystals were falling from higher clouds. The temperature at the test level was -12°C. LWC regions extended to 10-15 km regions with 0.2 to 0.5 g m^{-3}. The ice crystal precipitation falling though the cloud layer consisted of few tens of crytals per liter of up to 3 mm sizes.

One of the experiments on Nov. 20, 1986 produced essentially the same result as the May 21, 1987 test. The evidence is that no APIP were generated. The other experiment on Nov. 20, 1986 produced a different result. The procedure was similar to that already described, but only one tracer pulse was generated about midway along a 10-km flight leg. The relevant results are shown in Fig. 1. Portions C and D of the original flight track were re-traced about 3 min later, with a reverse heading. FR_D indicates the period of freon release, P_{D1} is the "plume" region corresponding to D, FI_{D1} shows where the tracer crystals are evident (highest concentrations), and P_C is the "plume" corresponding to segment C. The tracer plume was subsequently traversed at 90° with respect to the original heading; the detected plume is labelled FI_{D2}. The important observation in this test is that through P_{D1} there is a significant increase in ice concentration above the background values. The increase appears to be confined to a line along the flight track, as evidenced by the absence of similar increases on either side of FI_{D2}. In P_C, no increase above the background can be distinguished.

5. ANALYSIS

The evidence shown in the foregoing section points to the conclusion that aircraft *may produce ice crystals when passing through supercooled water clouds, but only when certain combinations of conditions exist.* With the limited number of cases so far available it is

risky to try to delineate what those conditions are. The last of the cases described was different from the other two in the higher engine torque utilized (1540 ft-lb, versus ~1300 ft-lb for the other cases); this is indicative of greater airframe icing and is accompanied by greater fuel consumption. If the critical factor is related to engine torque, the difference between P_C and P_D would have to be ascribed to having missed the plume in P_C, where there was no tracer pulse to confirm proper positioning. Flight segments C and D were very similar, but a possibly significant difference was present in the size-distributions of cloud droplets. The possibility also has to be admitted that the ice crystals detected in P_D were of natural origin and had fallen from the sample altitude in the time interval between sampling P_D and FI_{D2}.

Acknowledgement: We thank our colleagues for building and operating the aircraft system. The National Science Foundation supported this work through Grant ATM 8611185.

REFERENCES:

GORDON, G. L.; MARWITZ, J. D.: APIP testing using a tracer. Preprints Tenth Conf. Wea. Modif., A.M.S., Arlington, Virginia, (1986), pp. 61-63

MOSSOP, S.C.: Comments on "Production of ice particles in clouds due to aircraft penetration". J. Clim. Appl. Meteor. 23 (1984), 345.

RANGNO, A. L.; HOBBS, P. V.: Production of ice particles in clouds due to aircraft penetrations. J. Clim. Appl. Meteor. 22 (1983), 214-232.

RANGNO, A. L.; HOBBS, P. V.: Further observations of the production of ice particles in clouds by aircraft. J. Clim. Appl. Meteor. 23 (1984), 985-987.

VONNEGUT, B: Nucleation of ice crystals in supercooled clouds caused by passage of an airplane. J. Clim. Appl. Meteor. 25 (1986), 98.

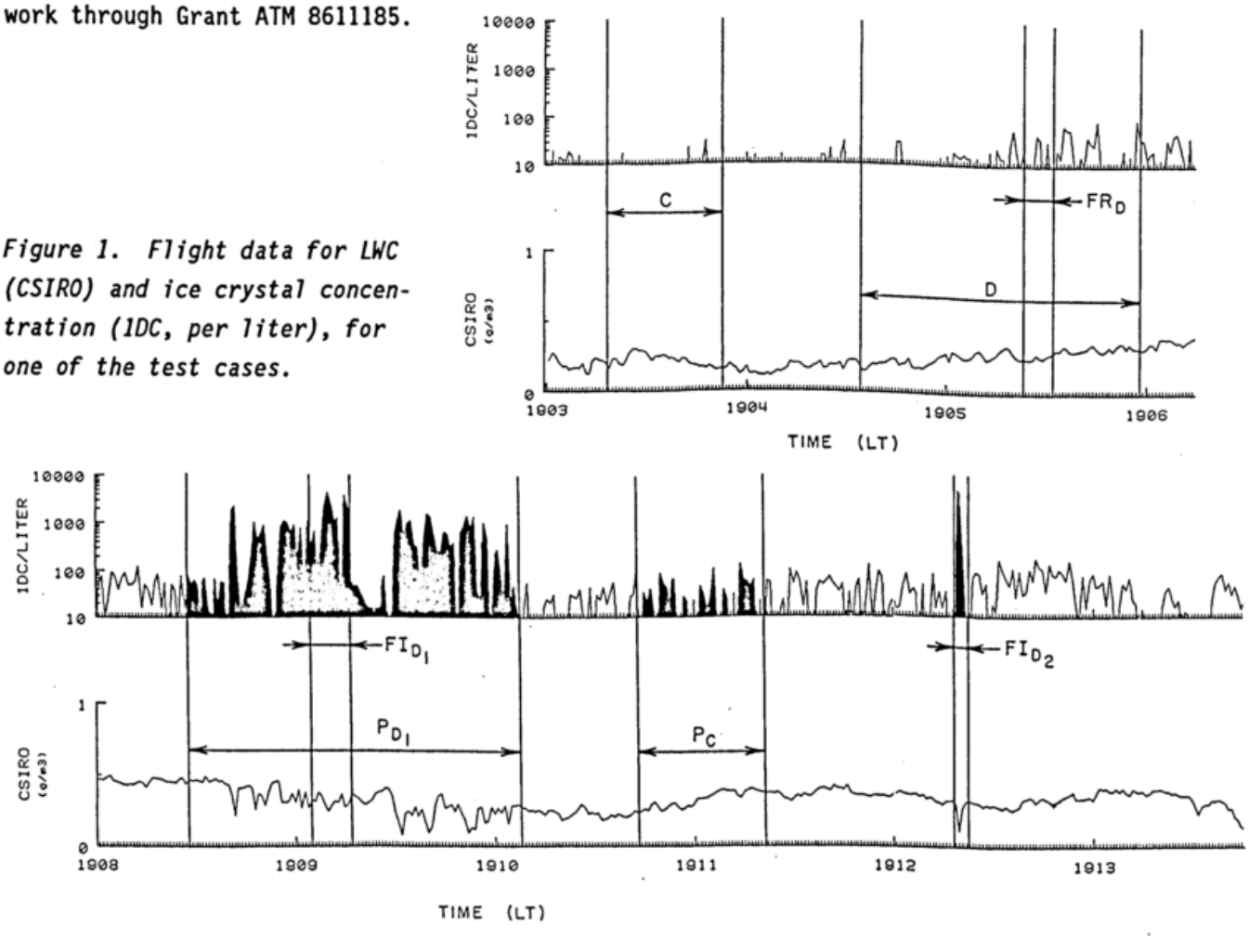


Figure 1. Flight data for LWC (CSIRO) and ice crystal concentration (1DC, per liter), for one of the test cases.

AIRBORNE STUDIES OF THE ICE PHASE IN MARITIME CLOUDS AROUND THE BRITISH ISLES

by

P.R.A. Brown[1] and T.W. Choularton[2]

[1] Meteorological Office, Bracknell, UK., [2] UMIST, Manchester, UK.

1. INTRODUCTION

Evidence that the the Hallett-Mossop process of secondary ice production is active in natural clouds has been obtained on a number of occasions (e.g. MOSSOP, 1985). Theoretical (MASON, 1975) and experimental (KELLER AND SAX, 1981) studies have suggested the importance of the cloud dynamics in distributing the products of secondary ice production through the cloud and its effects on such factors as precipitation formation. We have examined data obtained in maritime clouds around the British Isles to study the formation and distribution of the ice phase in clouds with top temperatures in the range of -8 to -15 °C.

2. INSTRUMENTATION AND DATA

Ice crystal concentrations were measured using both standard PMS 2-D optical array probes and an airborne holographic system, which was also used to obtain the concentrations of cloud droplets larger than about 10 μm in diameter. Holographic measurements of ice columns exceed those from the 2-D cloud probe by a factor of about 5, due to detection and sizing errors in the 2-D probe itself and errors in the 2-D processing software which cause an overestimate of the effective sample volume (BROWN AND DARLISON, 1988).

Individual cloud cells were penetrated at different levels and no evidence was found of ice crystals generated by previous penetrations (RANGNO AND HOBBS, 1983). 2-D Cloud probe images from case H750 are shown in Fig. 1, the separate sections

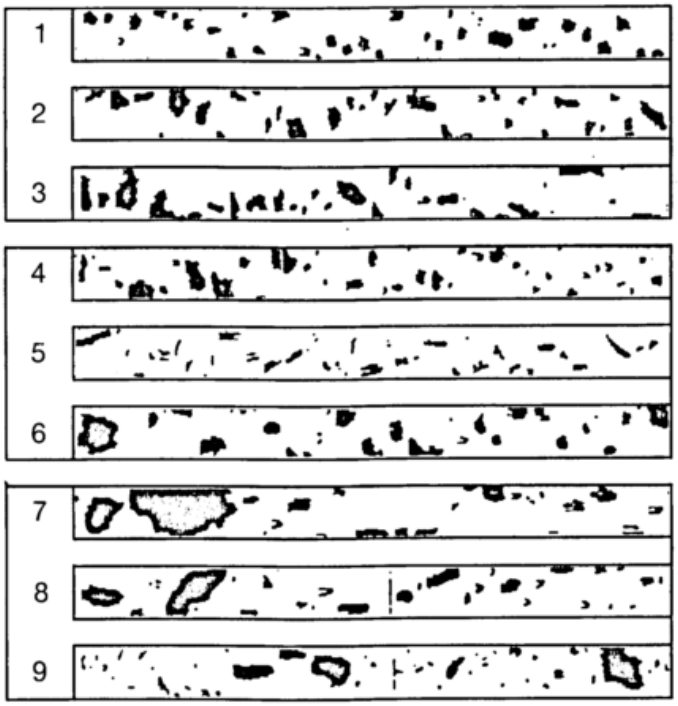


Fig. 1 2D Cloud probe images from Flight H750. The numbered sections correspond to those in Table 1.

corresponding to those of Table 1 which contains values of various parameters averaged over short periods during three penetrations of the cloud. This case illustrates several of the features which have been observed in clouds of a similar depth and which are described below.

3. SECONDARY ICE PRODUCTION AND THE EFFECTS OF CLOUD DYNAMICS.

A prominent feature is the increase in the concentration of ice columns in the main updraught between -4.6 and -8.3 °C. At the colder level, the column size spectrum has mode and maximum lengths of about 150 and 650 μm respectively. The latter corresponds to a fall velocity of about 0.8 ms^{-1}, hence the columns are being transported upwards from

Table 1. Flight H750 18/09/85

Cloud-top temperature = −11.0 °C
Cloud-base temperature = +5.1 °C

Temperature of flight level (°C)	Section	Vertical velocity ($m\ s^{-1}$)	Liquid water ($g\ m^{-3}$)	2D Cloud probe (a)	(b)	Holographic data (c)	(d)	(e)
	1	0.17	0.00	4.7	26.8			
−10.2	2	0.87	0.04	18.3	27.8			
	3	0.27	0.03	12.9	26.2			
	4	−0.60	0.02	14.6	24.9	24.3	60.7	
−8.3	5	1.79	0.24	46.6	19.4	118.6	296.6	7.0
	6	−0.13	0.00	5.4	21.3			
	7	−0.05	0.20	25.7	19.4	34.1	26.7	
−4.6	8	3.37	0.52	9.8	11.0	19.3	11.9	18.4
	9	0.44	0.18	31.6	13.9	63.8	54.9	

(a), (d) Columns, $L > 140\ \mu m$ (l^{-1})
(b) Irregular ice, $L > 140\ \mu m$ (l^{-1})
(c) Columns, $L < 140\ \mu m$ (l^{-1})
(e) Droplets (cm^{-3})

warmer regions below. The presence of large rimed particles in concentrations of 1-2 l^{-1} together with substantial liquid water contents in the updraught at -4.6 °C suggests that the columns were produced by the Hallett-Mossop process of ice splinter production during riming (HALLETT AND MOSSOP, 1974). The mode and maximum lengths are in agreement with values calculated assuming that the base of the secondary production zone is at -2.5 °C with peak production at -4.5 °C.

Large concentrations of columns are also detected in regions of weak updraught less than 1 ms^{-1}. Holographic data show that a substantial fraction of these are smaller than 140 µm in length. As water-saturated conditions still exist, the crystals will have a linear growth rate of about 1 µm s^{-1} (RYAN et al., 1972). The small updraught and fall velocities suggest that the small columns will be detected close to their original formation level. In support of this, peak column concentrations in weak updraught regions tend to be found close to the -4.5 °C level of peak splinter production.

Clouds with stronger updraughts than the H750 case tend to have low column concentrations at all levels within the updraught core, probably due to the reduced time available

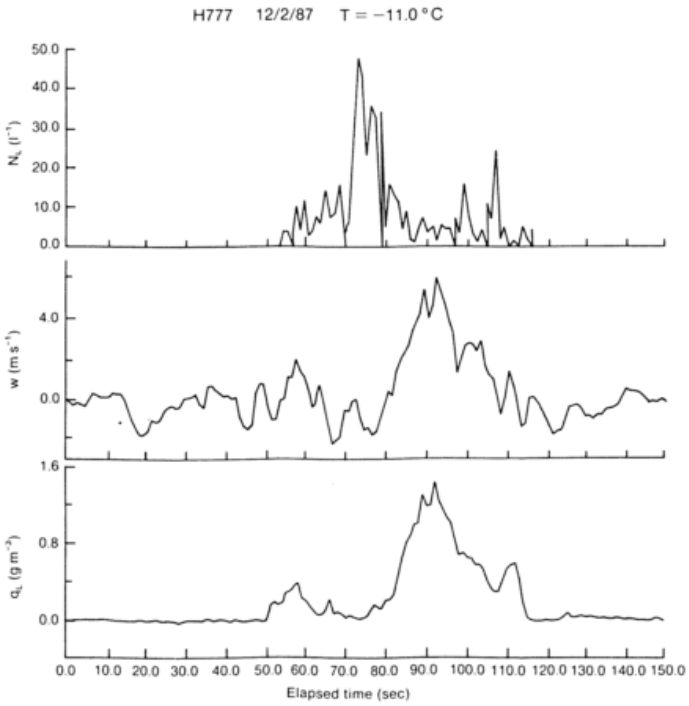


Fig. 2 Data from a single cloud penetration on Flight H777, when the cloud-top temperature was −15.0 °C. N_L is the concentration of crystals larger than 300 µm, w the vertical velocity, and q_L the liquid water content.

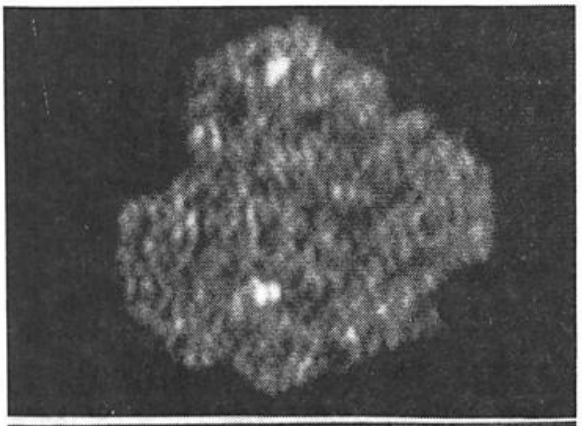
for splinter production in a parcel ascending through the splinter production zone. With top temperatures of nearer -15.0 °C found in these clouds, the ice distribution is dominated by rimed dendritic crystals presumed to have been generated at cloud-top and carried to lower levels in downdraughts (Fig. 2).

Since the cloud top is largely depleted of liquid water, the secondary columns will be unable to grow by riming unless they can be recirculated back into regions of ascent lower in the cloud. Data from another case shows evidence of this occurring at the -2.5 °C level of the base of the secondary ice generation zone.

4. THE ICE PHASE IN CLOUD-TOP REGIONS

Near the top of the H750 cloud, irregular ice particles of 150-300 µm in size are found in concentrations of 15-25 l^{-1} with a complete absence of liquid water (see Section 1, Fig. 1 and Table 1). They cannot therefore have acquired this shape by riming growth in-situ.

a)



b)



Fig. 3 Holographic images from near cloud top, Flight H708. Crystal dimensions are a) 220 µm, b) 213 µm.

It is also unlikely that they are the result of riming growth of secondary columns generated lower in the cloud, as holographic images of columns of about these dimensions show only very light riming. Crystals which have rimed sufficiently to have acquired a quasi-spherical appearance in 2-D images will thus be larger than the observed irregular particles.

Holographic images taken in these cloud-top regions show a number of examples of plate-like unrimed crystals of a size which could explain the appearance of the 2-D images (see Fig. 3). The plate-like habit suggests strongly that these crystals have formed and grown at temperatures close to cloud top. Other holographic images show frozen drops of 60-150 µm in diameter. 2-D images from unglaciated clouds of a similar depth sampled on the same day as the H750 case show the presence of liquid drops of up to 130 µm in diameter at levels just below cloud top. It is thus conceivable that the irregular particles have been generated by a mechanism involving drop freezing, as suggested by HOBBS AND RANGNO (1985). It is not yet known whether this cloud top glaciation evolves independently of the processes occurring lower in the cloud. Data from more vigorous clouds does however suggest that cloud-top ice formation and its downwards transport may become the more dominant process as cloud top temperatures approach -15 °C.

5. SUMMARY.

The Hallett-Mossop process has been shown to be active within maritime convective clouds around the British Isles. The distribution of the secondary ice columns depends in detail on the cloud dynamics. Ice crystals are also generated separately at cloud top by a mechanism which we speculate may involve the freezing of large drops as suggested by HOBBS AND RANGNO (1985). The relationship between this process and the secondary ice production lower in the cloud has not yet been determined.

REFERENCES

BROWN P.R.A and DARLISON A.G.: Preprints, 10th. Interntl. Cloud Physics Conf. 15-20 Aug. 1988.

HALLETT J. and MOSSOP S.C.: Nature 249 (1974) pp26-28.

HOBBS P.V. and RANGNO A.L.: J.Atmos.Sci. 42 (1985) pp2523-2549.

KELLER V.W. and SAX R.I.: Quart.J.R.Met.Soc. 107 (1981) pp679-697.

MASON B.J.: Quart.J.R.Met.Soc. 101 (1975) pp675-679.

MOSSOP S.C.: Quart.J.R.Met.Soc. 111 (1985) pp183-198.

RANGNO A.L. and HOBBS P.V.: J.Clim. and Appl.Meteor. 22 (1983) pp214-232

RYAN B.F., WISHART E.R, and SHAW D.E.: J.Atmos.Sci. 33 (1972) pp842-850

PRECIPITATION INITIATION MECHANISMS IN CLOUDS OVER NORTH INDIA

R.N. CHATTERJEE, P. PRAKASH, G. SINGH
AND
R.K. KAPOOR

INDIAN INSTITUTE OF TROPICAL METEOROLOGY
PUNE-411005, INDIA.

1 INTRODUCTION

Proper understanding of precipitation initiation mechanisms in clouds of any region is of fundamental importance. Occurrence of initial radar echo below or above freezing level, has been used by many investigaters to study whether the collision-coalescence process or the Bergeron-Findeisen process is responsible in the release of precipitation. Battan (1953) based on the study of formation and spread of precipitation in 123 convective clouds under the Thunderstorm Project in U.S.A. during 1947 found that the initial echo formation was at temperatures warmer than 0° C in 60 per cent cases and therefore concluded that the mechanism of precipitation initiation in these clouds were purely due to collision-coalescence process. BRAHAM (1964) in project Whitetop observed his findings similar to those of BATTAN. BRAHAM found that about 50 % of the first echoes were entirely warmer than 0° C, 10% colder than 0° C, and 40% straddled the freezing level. Similarly, BRAHAM and DUNGEY (1976) in the St. Louis area under the Project METROMEX found 40% of the first echoes warmer than 0° C, 7% completely colder than 0° C, and 53% straddled the freezing level.

In India, a limited study over two years period, 1958 to 1959, was carried out in and around Delhi and the heights considered were the maximum reached by echo tops during the periods of survey. In particular, height determinations were repeated in case of cells which were below 0° C level, to see if any of these later developed into cold type. The study showed that except during the winter when rain cells of warm type were of rare occurrence, about 30 to 40% of precipitating clouds during the monsoon season were of warm type (RAMANAMURTHY et al., 1960). Hereafter, we shall refer rain initiation mechanisms by Bergeron-Findeisen, coalescence-cum-ice and collission-coalescene processes respectively from a-,b-, and c-type rain cells. In a-type rain cells, widespread precipitation field giving echo with melting band appears. Rain on such occasions is usually of long duration and fairly steady in character. In b-type rain cells, observations reveal rain showers from tall convective clouds which do not exhibit any melting band feature, although the rain cell extends well above 0° C level. Rain on such occasions is of relatively short duration and high intensity, and is characterised by marked fluctuations in rates of precipitation. This is often called mixed process. In c-type rain cells, precipitation is mostly in the form of dizzle from warm convective clouds whose tops are limited to below 0° C level. DE and RAKSHIT (1961) found that precipitation echoes from convective clouds in the Calcutta region were more than in 90% cases due to c-type process.

In this paper, an attempt has been made to study the role of different precipitation initiation mechanisms in clouds over Delhi region in north India during different seasons using radar observations of precipitation echoes collected during an extensive 16-years period from 1960-1975. A year consisted of four seasons, namely, winter (December to February), pre-monsoon (March to June),

monsoon (July to September) and post-monsoon (October to November). Heights of the freezing levels during winter, pre-monsoon, monsoon and post-monsoon seasons have been taken as 3.5, 5.0, 4.5 Kms respectively. Details of investigations are presented.

2 EQUIPMENT USED

NMD-451A, a Japanese make radar operating on 3.2 cm wave length and having peak output 250 KW has been used for the study. Its radiating system consists of a feed-horn and a parabolic reflector two meters in diameter, which shapes the beam to 1° in both azimuth and elevation. The duration of transmitted pulse is one microsecond and its repetition frequency is 300 per second. Minimum detectable signal is -90 dBm.

The radar is equipped, in addition to the conventional Plan Position (PPI), Range Height (RHI) and Amplitude Modulated (A-Scope) indicators, with a special arrangement called Range Elevation Indicator (REI) on which depth and elevation of echoes are displayed in true proportions when scanned at elevational angles between -1° and 90°. The maximum range of the radar is 300 km on PPI, REI and A-Scope, and 100 km on RHI. Range markers 2.5, 5, 10, 20 and 60 km apart are provided in the 10, 20, 50, 100 and 360 km ranges respectively. The RHI is supplied with height markers at intervals of 2.5 and 5 km respectively in its 10 km and 20 km height ranges. The overall sensitivity of the radar set is such that it can just detect raindrops of diameter about 0,33 mm at a distance of 100 km, if they are presented in concentration of 100 per litre.

3 METHOD OF OBSERVATIONS

The 3.2 cm weather radar was used to survey precipitation occurrences within 100 km around Delhi (28° 35'N, 77° 12'E, 210 m MSL), and data collected on rain cells were grouped according to heights reached by their echo tops. For this purpose, an examination was firstly made, on the PPI scanning at near zero elevation, of the broad features of rain cells and their distribution. The cells are then randomly picked up and projected on RHI or REI to determine the heights of their tops. Generally, heigt measurements of individual echoes were repeated at intervals up to 5 minutes to determine their maximum vertical growth. To ensure correct height of the topmost part of the rain cell, the azimuth was fixed for scanning at each elevation that it passed through the brightest portion of echo at that level. This was necessary, as quite frequently it was seen that the azimuth corresponding to the highest point of echo from a rain cell was very different from that at which echo was strongest near ground. In this study hourly observations made from 1000 to 1700 hrs. IST have been used.

4 RESULTS AND DISCUSSIONS

4.1 FREQUENCY DISTRIBUTION OF PRECIPITATING CLOUDS

During winter, pre-monsoon, monsoon and post-monsoon seasons, a total of 7346 convective clouds were studied within 100 km around Delhin in 16-years period from 1960 to 1975. These were classified in the indicated class intervals and are shown in Table 1. The clouds which extended beyond 16 km were put under one category. It may be seen from Table 1 that during winter clouds had maximum echo top heights limited to 12 km. However, during pre-monsoon, monsoon and post-monsoon seasons, echo top heights extended beyond 16 km in 9,50 and 1 cloud cases respectively. During monsoon season in as much as 1.03% cases echo tops were above 16 km. The maximum echo top height encountered was 19 km.

4.2 DISTRIBUTION OF a-, b- AND c-TYPE RAIN CELLS.

Distribution of a-, b- and c-type rain cells of the above 7346 convective clouds studied is shown season-wise in Table 2. It may be noted from Table 2 that c-type rain cells were maximum during monsoon 2672 (54,9%) followed by winter, pre-monsoon and post-monsoon seasons; b-type rain cells were maximum in pre-monsoon or summer season 868 (57,0%) followed by winter, post-monsoon and winter seasons; a-type rain cells were found maximum during post-monsoon season 39 (30,5%). On annual basis a-, b- and c-type rain cells were 10.5, 41.2 and 48.3% respectively. The disparity noted compared to 1958 and 1959 observations especially in the case of c-type cells in winter is perhaps due to lesser data in that season.

REFERENCES:

BATTAN, L.J. (1953) J. Meteor., 10,311-323.

BRAHAM, R.R.JR (1964) J. Atmos. Sci., 20,563-568.

BBRAHAM R.R.JR and DUNGEY; M. (1976) Proc. Int. Conf. on Cloud Physics, July 26-30, 1976, Boulder Colo, U.S.A., 275-278.

DE, A.C. and RAKSHIT, D.K. (1961) Indian J. Met. Geophys., 12,2,289-298.

RAMANAMURTHY; BH. V., BISWAS; K.R. and B.K. GHOSH DASTIDAR (1960) Indian J. Met. Geophys., 11,4, 331-346.

Table 1: Frequency of occurrence of a-, b- and c-type rain cells among indicated height intervals in different seasons.

Season	Height (Km)					
	≤4.0	4.1-8.0	8.1-12.0	12.1-16.0	16.0	Total
Winter	249	543	36	-	-	828
Pre-monsoon	155	882	406	70	9	1522
Monsoon	939	2799	813	267	50	4868
Post-monsoon	17	90	14	6	1	128
Total	1360	4314	1269	343	60	7346

Table 2: Distribution of a-, b- and c-type rain cells in different seasons.

Season	a-type	b-type	c-type	Total
Winter	112	394	322	828
Pre-monsoon	133	868	521	1522
Monsoon	488	1708	2672	4868
Post-monsoon	39	57	32	128
Annual	772	3027	3547	7346

EVIDENCE OF PREFERENTIAL ZONES OF ICE MULTIPLICATION BY SPLINTERING IN CONVECTIVE CELLS

Jean-François Gayet, Christophe Duroure and R.G. Soulage
LAMP, University of Clermont II, B.P. 45, 63170 Aubière (France)

1. INTRODUCTION

A lot of field situations have conformed so closely to the requirements of the HALLETT-MOSSOP (1974) splintering, as established by laboratory experiments, that there can be little doubt that it was an active process producing ice multiplication (MOSSOP, 1985). The purpose of this paper is to show, from a small scale analysis of in situ microphysical and dynamical measurements, that the "splintering" process occurs on preferential zones in convective cells. These measurements were collected during the "Landes-Fronts 84" experiment (held in the South-West of France in summer 1984) from an instrumented Transall aircraft together with a ground meteorological radar system. The aircraft was equipped with a complete set of microphysical probes (FSSP, 1D and 2D) (LAROCHE et al., 1985).

2. DESCRIPTION OF THE CLOUD SYSTEM

This study concerns the measurements collected on June 6th 1984. The radar analysis performed from the Rabelais system (8 mm wavelength; SAUVAGEOT, 1982) shows that the cloud system was characterized by several convective cells (Fig. 1) having a mean reflectivity of about 35 dBZ (maximum value 45 dBZ) and a cloud base and top of 1000 m (+3°C) and 5000 m (-20°C) respectively. The radiosounding (performed 1 h before the experiment) indicates a negligible vertical wind shear in intensity and direction on the cloud extent and a wet layer (80% humidity) up to 4000 m. The radar analysis also reveals a low reflectivity zone (-5 dBZ, Fig. 1) located between the 5000 and 7000 m levels which corresponds to the cirrus cloud observed from the aircraft and the ground. The flight track segment is reported on the corresponding vertical reflectivity profile according to the tracking radar information (500 m accuracy on aircraft position). We shall discuss now the aircraft measurements obtained on this flight segment performed at 2700 m (-6°C) level.

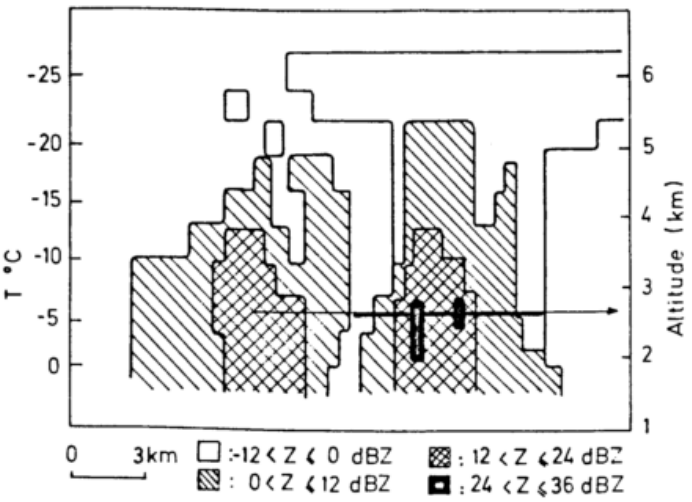


Fig.1 : Vertical profile of the reflectivity obtained from the Rabelais 8 mm radar.

3. EVIDENCE OF PREFERENTIAL ZONES OF SPLINTERING

3.1 EXAMPLE OF DATA OBTAINED AT -6°C

The example presented below is typical of the measurements obtained at this level in the cloud system of June 6th 1984. On Fig. 2 are reported time series (100 m space resolution) of microphysical parameters (LWC : liquid water content ; CI and DI : concentration and mean size of the ice particles greater than 60 µm ; CH and DH : concentration and mean size of precipitation particles greater than 250µm) and the vertical airspeed (WA). In the main updraft region (5 m s^{-1}) labelled A, the cell does not exhibit any ice particle on about 1000 m of horizontal extent and it is not mixed with the environmental air because of the liquid water

content which has a similar value as the adiabatic one (2 g m^{-3}). These characteristics contrast with those of regions labelled B in which high ice concentrations (100 to 600 l^{-1}) of small crystals (~40 µm) are measured. These small particles have been identified as columns from the 2D-C probe (Fig. 3). Large graupels (Fig. 3) having a mean size ranged from 1 to 2.5 mm are also found in the B regions. As for the cloud droplets, they are characterized by a broad spectrum centered on 21 µm and having concentations of droplets larger than 24 µm and smaller than 13 µm, of 25 cm^{-3} and 15 cm^{-3} respectively. All these characteristics are consistent with the HALLETT-MOSSOP (1974) ice multiplication criteria to explain the large ice crystal concentrations in the B regions.

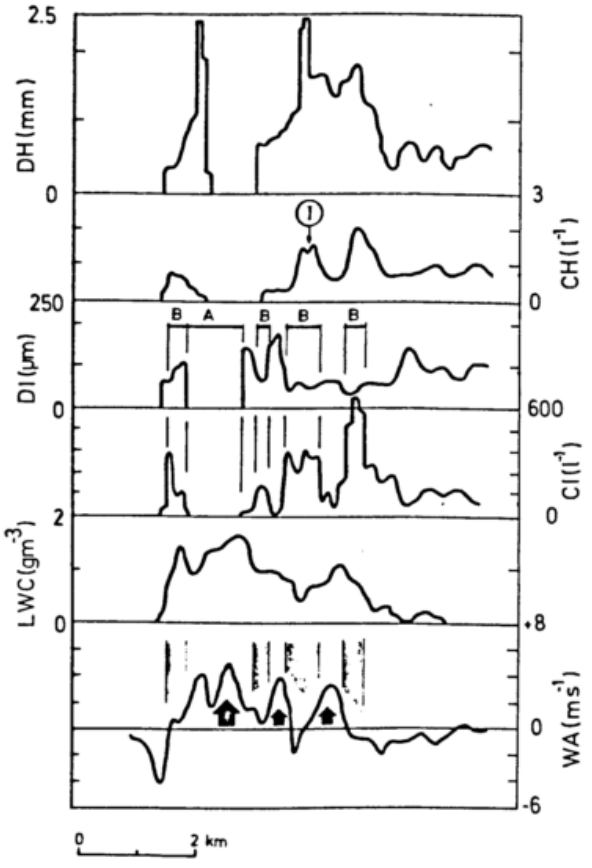


Fig. 2 : Time-series of microphysical parameters and vertical air velocity (2700m/ -6°C level). The corresponding aircraft segment is reported on Fig. 1 (thick line).

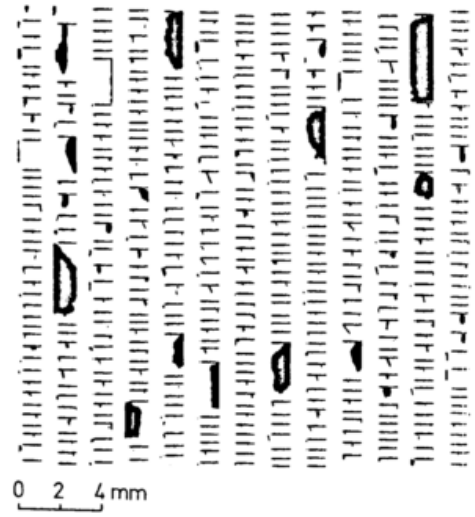


Fig.3 : Example of 2D-C images sampled at point I on Fig. 2.

3.2 DISCUSSION

A small scale analysis of the time series of Fig. 2 shows that the large ice concentrations of the B regions are firstly, extended on only a few hundred meters (200 to 400 m) and secondly, linked to the dynamical activity. As a matter of fact, these B regions are associated to the zones located on the edges both of the main and the secondary updrafts. On the contrary, the updraft regions (identified with dark arrows on Fig. 2) are characterized by zero or low values of ice crystal concentrations. It should be noted that the above characteristics were often evidenced in the Landes-Fronts 84 experiment, during the sampling of convective cells in which the splintering process was efficient. In order to exemplify more precisely this observation, we have reported (on Fig. 4) the mean values of the ice crystal concentration as a function of the mean vertical air velocity calculated in the cloud regions above-defined. The standard deviations of the vertical air velocity measurements are also reported on Fig. 4. Despite the fact that the limits of the cloud zones are arbitrarily defined, Fig. 4 clearly shows that the largest ice crystal concentrations are preferentially found outside (on the edges) of the updrafts. Furthermore, the correspondence between the ice crystal concentration (CI) and the mean size (DI) of these particles (Fig. 5) indicates that the largest concentrations (~ 400 l^{-1}) are

associated with the smallest crystal size ($\sim$40 µm). This suggests that the origin of the small crystals issued from the splintering process takes place near the points of measurement that is to say not in the updraft cores but preferentially on the edges of the updraft (B regions). On the contrary, the updraft regions (Fig. 4) are characterized by much lower concentrations ($< 50\ l^{-1}$) of large ice particles (rimed columns ranged from 80 to 200 µm). These observations indicate that these particles have a longer residence time in the cloud and may arise from the B regions by mixing or recycling. The low concentration of these recycled particles suggests that the mixing of the updrafts is not very efficient at this stage of cloud development. Our observations are consistent with the conceptual model of LAMB et al. (1978) which suggests, despite a rapid natural glaciation, that the heating that results tends to be ineffective in controlling the dynamic structure of the cell. This is due to the fact that this glaciation occurs in regions located outside the updraft cores where the buoyancy is considerably reduced or becomes negative and where the supply of supercooled water may be rapidly depleted or cut off.

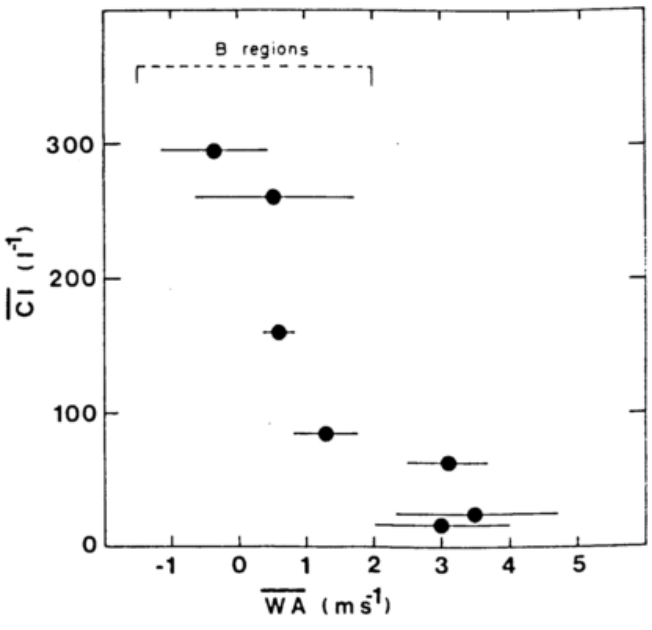


Fig. 4 : Mean ice crystal concentration versus the mean vertical air velocity.

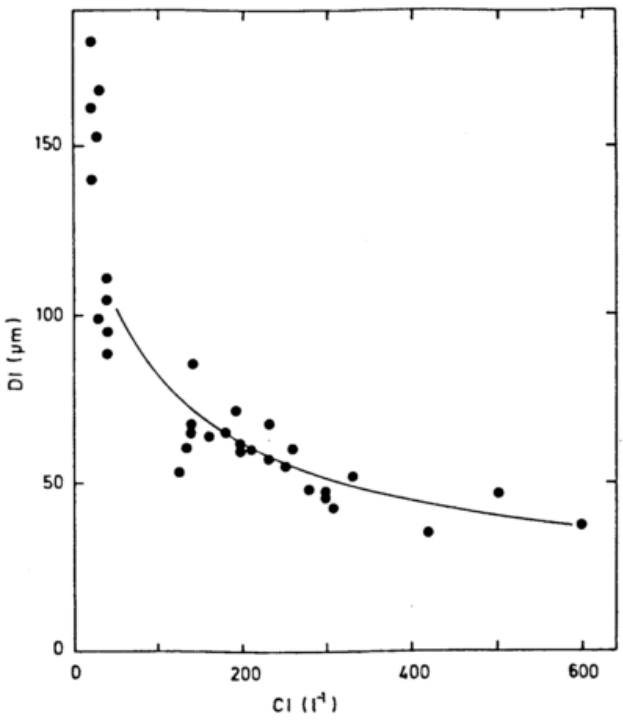


Fig. 5 : Correspondence between the concentration and the size of the ice crystals.

4. ACKNOWLEDGEMENTS

This research was supported by the grants DRET/INSU n° 8334308 and 8534016. We would like to thank B. Campistron for his help in the 8 mm radar interpretation. The manuscript correction and typing is due to O. Guillot.

5. REFERENCES

HALLET J. and S.C. MOSSOP, 1974 : Production of secondary particles during the riming process. Nature, 249, 26-28.

LAMB D., J. HALLET and R.I. SAX, 1978 : Microphysics of invigorated cumulus development. Proc. AMS Conf. on Cloud Physics and Atmos. Electricity, Issaquah, Wash.

LAROCHE P. et al., 1985 : In-flight thunderstorm environmental measurements during the Landes 84 campain. 10th Int. Aerospace and Ground Conf. on Lightning and Static Electricity, Paris.

MOSSOP, S.C., 1985 : The origin and concentration of ice crystals in clouds. Bull. American Meteor. Soc., 66, 264-272.

SAUVAGEOT H., 1982 : Radarmétéorologie. Télédétection active de l'atmosphère. Eyrolles. Paris.

MICROPHYSICAL CHARACTERISTICS OF WARM-BASED CUMULI: OBSERVATIONS AT -10°C

Robert R. Czys

Illinois State Water Survey
Climate and Meteorology Section
Champaign, Illinois USA

1. INTRODUCTION

As part of the Precipitation Augmentation for Crops Experiment (PACE), the microphysical properties of untreated and treated (with either AgI or placebo) cumulus clouds are being investigated. PACE is a research program to determine precipitation alterations attainable by dynamic seeding during the growing season of the central United States and to determine the benefits and liabilities of such alterations. The overall goals and objectives of PACE have been discussed by Changnon (1986).

The exploratory phase of PACE began in the summer of 1986 with field operations using airplanes and radar. This paper reports on data collected in 20 natural clouds from 3 days in July 1986.

2. DATA

Table 1 gives a summary of microphysical properties of natural clouds measured at -10°C on three different days. On July 8, clouds feeding into an air mass thunderstorm positioned over the southeastern corner of Indianapolis, IN, were sampled. On July 24, data was obtained in 5 clouds feeding an air mass thunderstorm located northwest of St. Louis, MO. And, on July 30, data near -10°C was gathered for a cloud feeding a warm front thunderstorm. Each cloud is identified by the month, day, cloud number and penetration number. Missing data for clouds 708c2p1 and 708c6p1 was caused by momentary failure of the data acquisition system.

The clouds represented in Table 1 were mostly youthful, individual cumulus associated with a larger storm cloud. These were clouds which met the PACE visual criteria for seeding. They showed a hard "blocky" appearance, and had tops which were easily passing through the -10°C level which is approximately 20 kft over the central USA during the summer. The representative sounding for each day showed no evidence of either a shallow temperature inversion or a dry layer in mid-levels to restrict vertical cloud development. They were mostly warm-based and had base temperatures and heights of: +16C and 6000', +15C and 6500'. and +8C and 11000', for July 8, 24, and 30, respectively. The airplane weather avoidance radar often displayed an echo during cloud approach.

Cloud maturities in Table 1 were approximated during cloud approach by the flight meteorologist and pilot from a visual estimation of the amount of cloud above flight level. Cloud top temperatures can be inferred from these maturities by assuming a moist adiabatic lapse rate of approximately -2°C/1000 ft at -10°C. Thus, estimated cloud top temperatures are approximately, -10 to -11°C for *, -11 to -12°C for **, -12 to -15°C for ***, -15 to -20°C for **** and colder than -20°C for *****.

2.1 SUPERCOOLED PRECIPITATION DROPS

Microphysical observations from 1986 confirm the existence of copious amounts of supercooled drizzle and rain drops at -10°C in moderately vig-

Table 1. Summary of Cloud Properties

Cloud ID	Penetraton Time (CDT)	Duration (sec)	Maturity*	Cloud Dia. (km)	Cloud Temp. (°C)	Thermal Buoy. (°C)	Peak Updraft (m/sec)	Mean/Max FWC (g/m^3)	Mean/Max JWC (g/m^3)	Mean Drop Dia. (μm)	Mean Conc. (cm^{-3})	S.P.D.**
708c1p1	151643	42	**	2.5	-8.6	0.4	12	0.4 0.5	0.4 0.7	13	190	Yes
708c2p1	157751	--	**	---	---	---	--	--- ---	--- ---	--	---	Yes
708c3p1	153237	94	****	5.5	-9.3	1.2	15	0.2 0.3	0.0 0.2	17	60	No
708c3p2	153933	43	*****	1.6	-8.0	---	10	0.3 0.5	0.4 0.8	13	140	Yes
708c4p1	153418	58	****	2.8	-9.5	---	7	0.2 0.3	0.2 0.4	14	80	No
708c4p2	153827	62	*****	3.9	-7.9	---	3	0.1 0.3	0.1 0.2	19	20	No
708c5p1	154417	89	**	4.5	-8.9	0.4	17	0.4 0.8	0.7 2.9	15	140	Yes
708c6p1	154552	--	****	---	---	---	--	--- ---	--- ---	--	---	No
708c7p1	155828	68	**	4.4	-10.6	0.3	14	0.2 0.4	0.1 0.3	15	70	Yes
708c8p1	155958	73	****	4.7	-10.1	0.6	15	0.0 0.1	0.0 0.0	22	10	No
708c9p1	161419	56	**	4.3	-9.7	-0.3	17	0.3 0.6	0.8 2.4	13	140	Yes
708c10p1	162623	41	**	3.2	-8.4	0.7	5	0.1 0.2	0.0 0.1	22	20	Yes
708c11p1	162718	26	**	2.1	-8.7	1.1	15	0.7 1.0	3.5 3.8	16	250	Yes
708c12p1	162920	62	**	3.2	-8.8	0.4	15	0.3 0.5	0.3 0.5	15	120	Yes
724c1p1	142420	110	****	8.6	-9.3	1.2	15	0.3 0.8	0.3 0.9	14	130	Yes
724c2p1	143016	133	**	10.9	-10.5	0.4	5	0.2 0.6	0.1 0.7	16	50	No
724c3p1	144550	54	**	4.0	-8.1	-1.0	3	0.4 0.8	0.5 1.5	13	170	Yes
724c4p1	144941	75	****	5.4	-7.7	2.8	8	0.4 0.7	0.8 2.3	14	200	Yes
724c5p1	145612	43	**	3.0	-8.1	-0.8	3	0.2 0.6	0.2 0.7	13	110	Yes
730c6p1	172639	67	****	2.2	-10.9	-0.6	12	0.4 0.5	0.5 1.2	13	220	No

* Maturity:

	*	**	***	****	*****
Estimated height of cloud top above flight level	100-500'	500-1000'	1000-2500'	2500-5000'	>5000'

** S.P.D. = Supercooled Precipitation Drops

orous midwestern clouds with warm bases. The yes in the column labeled S.P.D. of Table 1 indicates that at least centimeter size splashes were observed on the airplane windshield during periods of positive vertical acceleration. These observations were later verified using the recording of a forward looking video camera.

These observations suggest that loading of the updraft by the bulk of the condensate mass is more severe in young clouds than older ones. Of the 11 clouds estimated to have tops no higher than 1000 ft above flight level, 10 contained supercooled rain. Comparatively, only 3 of the 9 clouds with tops higher than 2500 ft above flight level had supercooled rain drops as part of their composition.

Supercooled precipitation drops represent a substantial fraction of the total amount of supercooled water in young clouds. Estimates of the liquid water content from the 2DC and 2DP records suggest that on average 60% of the total water content comes from drops larger than 50 μm diameter.

2.2 CLOUD BUOYANCY

Two physical effects must be taken into account when considering the net buoyancy of a cloudy parcel of air. The first effect is thermal and will produce a positive or negative component to the net buoyancy depending on the temperature difference between cloud and environment and the temperature must include an adjustment for water vapor content. The second component represents the negative effect of loading by the mass of the condensate contained in the parcel.

The buoyancies listed in Table 1 were calculated with respect to the temperature difference between the main cloud updraft and environment. They

do not include the effects of water vapor since we have little useful dew point data, nor do they reflect the mass of the cloud condensate. From representative thermodynamic soundings the relative humidity of the environment air was estimated to be 50% and if the cloudy parcel is assumed to be just saturated then buoyancy would be enhanced by 0.25°C due to the presence of water vapor. However, this enhancement is generally balanced by the mass of the cloud droplets ($D < 45$ μm) since about 0.5 g m^{-3} corresponds to about -0.25°C. Thus, to the extent larger hydrometeors are absent the buoyancies in Table 1 are a good first estimate.

If the negative effect of loading by large particles is taken into account using the 2DC and 2DP data, then most of the clouds in Table 1 are negatively buoyant. This suggests that the updrafts, typically peaking between 3 and 17 m s^{-1}, were in a state of deceleration. Hence, any buoyancy enhancements resulting from imposed glaciation may be expected to only reduce the rate of updraft deceleration.

The data also suggests that young clouds are less buoyant than older ones. This difference may be greater than indicated by the buoyancies in Table 1, since younger clouds tend to contain larger masses of liquid water than older and because older clouds may have received benefit from the release of latent heat as a product of natural glaciation.

2.3 ICE

Initial ice concentrations determined from the 2-D images of optical array probes (OAP) were as high as 35 times the ice nuclei concentration measured over the central United States using membrane filters (Czys, 1977). The ice appeared mostly as graupel in sizes between 25 and 1000 μm diameter. It was not unusual for clouds with tops no colder than -11°C to develop graupel concentrations of 10 to 20 ℓ^{-1} with mean diameters from 125 to 325 μm. Low concentrations of rectangular-solid and rectangular-hollow OAP images, perhaps the shadows of columns, are the only evidence we have for the existence of vapor grown ice crystals.

3. SUMMARY

The microphysical features of the clouds observed suggest that supercooled liquid water is present in quantities sufficient for buoyancy enhancement by imposed glaciation. However, the clouds in this sample exhibited negative buoyancy by the time cloud top reached the -10°C level. This suggests that the most attainable dynamic effect may be to only decrease the rate updraft deceleration.

REFERENCES

Changnon, 1986: Illinois weather modification program: PACE. Preprints Conf. on Weather Modification. Arlington, VA, 315-319.

Czys, R. R., 1977: University of Chicago measurements of ice-forming nuclei from METROMEX. Proc. Sixth Conf. on Inadvertent and Planned Weather Modification, Champaign, IL, 29-32.

ACKNOWLEDGEMENT

This research has been supported by the Precipitation Augmentation for Crops Experiment (PACE), conducted under cooperative agreement with the National Oceanic and Atmospheric Administration under contracts COMM NA86RAH06051 and COMM NA87RAH07077.

A Comparative Study of Laboratory Thermals and Atmospheric Clouds.

H. Johari*, G. Taylor**, M. Baker** and R. Breidenthal*

*Department of Aeronautics and Astronautics, ** Geophysics Program
University of Washington
Seattle, WA 98195

1. INTRODUCTION

Recent field observations of convective clouds have revealed features of cloud structure which had not been predicted on the basis of early models. These observations have given rise to new conceptual models of cloud evolution. It is the purpose of this paper to examine these models in the light of laboratory simulations of convective cloud development.

The cloud features to be explained by a new conceptual model can be summarised as follows.

(1) Thermodynamic analysis of in-cloud air at a fixed level often reveals a single mixing line structure, which has been interpreted to mean that the source of entrained air within the sampled part of the cloud was restricted to a narrow layer within the environment. BOATMAN and AUER (1983), LA MONTAGNE and TELFORD (1983), JENSEN (1985), and others have shown that the source region is usually within a kilometer of the observation level, and often is slightly above it.

(2) Fine scale structure in microphysical fields (JENSEN ET AL., 1985) is often quite uniform over several hundreds of meters, even in cloudy air which has been substantially diluted by entrainment.

(3) Regions of undiluted cloudbase air, often several hundred meters in lateral extent, have been found in many convective clouds at altitudes far above cloud base.

(4) Cloud edges are 'hard' during cloud growth, suggesting that lateral diffusion is not an important entrainment mechanism, although regions of maximum liquid water content are usually near the center of the rising stream.

(5) As pointed out by WARNER (1970) and confirmed extensively since, the average ratio of observed to adiabatic liquid water content is always less than about 0.5, and declines slightly with height above the first few hundred meters. Laterally entraining similarity plume models which reproduce this average profile cannot reproduce observed cloudtop heights.

(6) Droplet spectral shapes suggest that entrainment takes place in localised events (BAKER ET AL., 1984) and that each cloud parcel undergoes only one or very few of these events (JENSEN ET AL., 1985).

2. LABORATORY SIMULATION

Our experiments consist of the release of a mixture of alcohol and glycol into a water tank which is neutrally stratified. When the release is instantaneous, we refer to the buoyant fluid as a thermal and when the release is continuous over some time interval comparable with the time of rise of the buoyant fluid, the buoyant mass is said to form a plume. The parameters of the buoyant fluid at any point are described in terms of the density $\rho(p)$, where p is the fraction of the alcohol glycol mixture in the buoyant fluid. For certain compositions, the density of the mixed fluid is greater than that of the environment. The nonlinear relation only approximates the shape of the analogous atmospheric relation.

One measure of the effect of the buoyancy reversal on the 'cloud' dynamics is given by

$$D_* = \frac{1}{p_*} \frac{\rho(p_*)-\rho(0)}{\rho(1)-\rho(0)} \qquad (1)$$

This parameter varies between 0 (for 'neutral' thermals and plumes) and 7.0 in our experiments. We stratify all the experimental results by this parameter in the following discussion.

2.1 THERMALS

Thermals were generated by overturning an inverted hemispherical cup at the bottom of the tank. A small volume of buoyant fluid initially confined by the cup then rises. In the first two diameters of its ascent, there is negligible mixing of the buoyant fluid with its environment. Mixing (defined as the molecular scale chemical process through which the buoyancy can change) begins after approximately one vortex revolution.

In the absence of buoyancy reversal, $\rho(p)$ is a linear function of p. JOHARI (1988a) has measured the distance L which a thermal ascends before every parcel of released fluid mixes with at least ϕ parcels of environmental fluid. ϕ is termed the equivalence ratio, and is equal to $(1 - p)/p$. L is known as the flame length from the combustion literature.

Figure 1 shows L/d_0 for thermals which are still rising, for a range of values of D_*. To within experimental accuracy, L/d_0 is independent of D_*. Buoyancy reversal does not affect mixing rates in rising thermals.

The evolution of the thermals, however, is highly dependent on D_* . Whereas the neutral thermal leaves no wake, a wake is left behind in the buoyancy reversing case, and the amount of fluid left behind increases with D_*. For $0.7 < D_* < 1.0$ the thermal often splits in two, part ascending and part descending. The altitude of the bifurcation is always $4d_0$. There are two remarkable features of the bifurcation: the two components

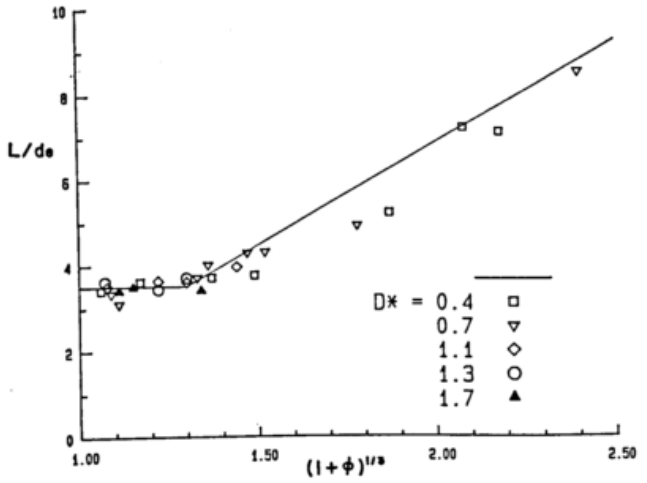


Fig. 1. Nondimensional flame length L/d_0 plotted against a function of the equivalence ratio ϕ (where $1+\phi = 1/p$) for five different values of D_*. The line represents the behavior of inert thermals.

have approximately the same density, and that density is greater than that of the environment. The upper portion rises in spite of its negative buoyancy, apparently assisted by an impulse from the bifurcation itself.

2.2 PLUMES

Buoyant fluid is emitted at a constant speed, u, from a nozzle of diameter d_0. JOHARI (1988b) has measured the molecular mixing rate inside the plumes as a function of the initial Richardson's number,

$$Ri_0 = \frac{\rho(1) - \rho(0)}{\rho} \frac{g d_0}{u^2} \qquad (2)$$

the ratio of buoyant to momentum forces at the nozzle. He shows that a dilution argument, following BROADWELL (1982), yields the following far field expression:

$$\frac{L}{d_0} = \text{const.} p^{-3/5} Ri_0^{-1/5} \qquad (3)$$

For $p \rightarrow 1$, the maximum height of adiabatic transport in plumes is $L/d_0 = 8$, which is more than twice the value found for thermals.

3. DISCUSSION

Since the generation of buoyancy by latent heat is not simulated in the laboratory, we choose for our comparisons cloud cases in which the virtual moist adiabat more or less parallels the sounding within much of the cloud layer. We have examined data from the CCOPE (1981) and JHWRP (1985) experiments which meet this criterion. The height dependent values of D_* vary within a range roughly equal to that in the laboratory. Buoyancy sorting seems to be absent for mean cloud layer values of D_* less than about 1.0, and downward mixing is strongest for D_* greater than about 4.0-5.0, in nonprecipitating clouds.

The definition of cloud aspect ratio Z/d_0, where Z is cloudtop height, poses a problem. Using reasonable estimates for d_0 yields aspect ratios of order 1-5. Thus we see that the finding of undiluted cloud base air near cloudtop is consistent with the laboratory results; in fact, in the absence of the topping inversion we might expect to see undiluted parcels at much higher levels.

The relevant Richardson number in the atmosphere is much larger than those in the laboratory. The dependence of the cloud properties on initial buoyancy and momentum is qualitatively similar to results of numerical model studies (TAYLOR, 1987; FERRIER, 1988) which show that excessive instability at low levels produces large entrainment rates there, and thus damps cloud growth.

4. CONCLUSIONS

According to recent models of convective clouds, developed to explain points (1)-(6) of our introduction, air rises adiabatically from cloud base in a thermal (RAYMOND and BLYTH, 1986) or plume (JENSEN, 1985). It mixes in a series of discrete gulps with the environment. After each gulp, the mixed fluid tends toward its position of hydrostatic equilibrium, as suggested earlier by TELFORD and WAGNER (1980). Most of the cloud mass is then this 'wake' of mixed fluid.

The crisp edges, small scale uniformity and extended adiabatic ascent of some parcels which characterize convective clouds are all found in the laboratory. The laboratory simulations suggest that evaporative cooling in buoyant flows can cause ejection of wake material, and that undiluted parcels can last through ascents of several diameters. It can be shown (RICHARDS, 1961) that passage of a thermal through a sharp inversion also causes ejection of fluid from the thermal; thus the effect of stratification in the environment may add to the wake produced by evaporative cooling. It appears from the laboratory simulations and atmospheric observations that the new models are physically realistic in this respect. However, the segregation of undiluted air in the early stages of ascent to cloudtop, as suggested by RAYMOND and BLYTH (1986), is not seen in the laboratory; we recall that even for high enough D_*, the laboratory thermals bifurcate, ascending and descending parcels have the same (dilute) mixture ratio.

While it appears necessary to invoke adiabatic ascent of some parcels to explain the observed heights of cloudtop, as well as the presence of undiluted cloudbase air aloft, it appears, for the reasons cited above, that the basic flow pattern inside convective clouds in some cases may be nearer that of starting plumes than that of thermals. Plumes have the same crisp edges and locally uniform interiors as thermals, but in plume parcels of different mixing ratio can coexist at the same level. The core of a starting plume can be almost undiluted while other regions at the same level within the plume are quite dilute. Recent numerical one-dimensional cloud models (FERRIER, 1988; TAYLOR, 1987), which are more plume-like than thermal-like, give satisfactory

agreement between cloud properties and observations in convective situations. We note that recent investigation of the in-cloud composition (TAYLOR and BAKER, unpublished) using such a model, shows that roughly half the air inside a convective cloud at any level has usually been entrained from the local environment. The starting plume model, moreover, is more consistent than the thermal model with observed time dependence of cloud properties.

It is, of course, clear that atmospheric clouds are more complex than the laboratory flows, that they probably consist of collections of convective elements, and that intermixing of fluid from different parts of the cloud produces effects quite unlike those which can be reproduced in these experiments. The examination of laboratory flows, however, is an enlightening method with which to investigate individually certain interesting aspects of the atmospheric phenomenon.

Acknowledgement: This research was partially supported by NSF grants ATM-8420816, 8609376 and 8611225.

REFERENCES:

AUSTIN, P.; JENSEN, J.; BLYTH, A.; BAKER, M.: Turbulent Mixing and Microphysical Variability in Two Warm Cumulus Studies. *J. Atmos. Sci. 42* (1985), 1123-1138.

BAKER, M.; BREIDENTHAL, R.; CHOULARTON, T.; LATHAM, J.: The Effects of Turbulent Mixing in Clouds. *J. Atmos. Sci., 41* (1984), 299-304.

BOATMAN, J.; AUER, A.: The Role of Cloud Top Entrainment in Cumulus Clouds. *J. Atmos Sci. 40* (1983), 1517-1534.

BROADWELL, J.: A Model of Turbulent Diffusion Flames and Nitric Oxide Production. *TRW Doc. 38515-6001-UT-00,* 1982.

FERRIER, B.: One Dimensional Time Dependent Modelling of Squal Line Convection. PhD Dissertation, U. Washington, 1988.

JENSEN, J.: Turbulent Mixing, Droplet Spectral Evolution and Dynamics of Warm Cumulus Clouds. PhD Dissertation, U. Washington, 1985.

JENSEN, J.; AUSTIN, P.; BAKER, M.; BLYTH, A.: Turbulent Mixing Droplet Spectral Evolution and Dynamics of Warm Cumulus Clouds. *J. Atmos Sci. 42* (1985), 173-192.

JOHARI, H.: A Laboratory Study of Thermals with Evaporative Cooling. Eighth Symposium on Turbulence and Diffusion, AMS, San Diego, (1988a).

JOHARI, H.: An Experimental Investigation of Mixing in Buoyant Flows. PhD dissertation, U. Washington, (1988b).

LA MONTAGNE, R.; TELFORD, J.: Cloud Top Mixing in Small Cumulus. *J. Atmos. Sci. 40,* (1983), 2148-2156.

PALUCH, I.: The Entrainment Mechanism in Colorado Cumuli. *J. Atmos. Sci. 36* (1979), 2467-2478.

RAYMOND, D.; BLYTH, A.: A Stochastic Mixing Model for Nonprecipitating Cumulus Clouds. *J. Atmos Sci. 43* (1986), 2708-2718.

RICHARDS, J.: Experiments on the Penetration of an Interface by Buoyant Thermals. *J. Fl. Mechanics 11* (1961), 369-385.

TAYLOR, G.: A Numerical Investigation of Sulfate Production and Deposition in Midlatitude Continental Cumulus Clouds. PhD dissertation, U. Washington, (1987).

TELFORD, J.; WAGNER, P.: The Dynamical and Liquid Water Structures of the Small Cumulus as Determined from Its Environment. *Pure and Appl. Geophys. 118* (1980), 935-952.

TURNER, J.: Jets and Plumes with Negative or Reversing Buoyancy. *J. Fluid Mech. 26* (1966), 779-792.

WARNER, J.: On Steady State One-Dimensional Models of Cumulus Convection. *J. Atmos Sci. 27* (1970), 1035-1040.

ENTRAINMENT AND FINE-SCALE (MOLECULAR) MIXING

Ilga R. Paluch and Darrel G. Baumgardner

National Center for Atmospheric Research*
Boulder, Colorado 80307, USA

1. INTRODUCTION

Recent fine-scale measurements of cloud-droplet concentrations indicate that entrainment in cumulus clouds can produce very nonuniform mixtures on the scale of meters. These data have been interpreted to imply that the larger turbulent eddies cause most of the bulk entrainment and coarse mixing, while fine-scale (molecular) mixing takes place within intermittent small eddies or vortex cores (Baker *et al.*, 1984). In the past it has been difficult to determine to what extent fine-scale mixing has taken place within a mixed cloud volume, because the sampling distances were too large to resolve its fine-scale structure.

2. LOCAL DROPLET CONCENTRATIONS

A new kind of measurement of the distribution of distances (or times) between droplet arrivals at the FSSP (Baumgardner, 1986) enables a "local droplet concentration" to be estimated regardless of the scale of the patchiness of the cloud. Droplets which have been well mixed in some particular volume will be randomly spaced within that volume. The distance, d, between one particle and the next is described by the exponential probability density function

$$P(d) = \alpha e^{-\alpha d}, \; d > 0 \qquad (1)$$

where $1/\alpha$ is the average distance between particles. The spacing between particles is measured from an aircraft as an elapsed time, t, $d = Vt$, where V is the airspeed, and $1/\alpha$ is the average elapsed time between particles which is determined by

$$\alpha = NAV \qquad (2)$$

where N and A are the average droplet concentration and the FSSP sample area.

With the new method of measuring elapsed time between particles, the measured time is categorized in one of thirteen channels, where the width of each channel is 20 μs, corresponding to a spacing interval of approximately 2 mm at a typical research speed of 100 m s^{-1}. Elapsed times are accumulated in these size channels every 0.1 seconds, or approximately every 10 m. If the droplets are positioned randomly in space, the measured frequency distribution will take the form of the function given in (1), and a value for α can be determined from the slope of the distribution. Then, using the known values for A and V, (2) is used to determine the local droplet concentration, N.

Figure 1 shows distance interval distributions of droplets measured upon entering cloud. When the calculated slope for randomly distributed droplets with the measured average concentration (light line) matches the slope of the histogram, then the droplets are randomly distributed throughout the sample volume. When the calculated slope is flatter than the observed, then the sample volume contains some empty or droplet-poor regions. The latter is typically observed within 20 or 30 m of clear-air samples. The data in the last four plots of Fig. 1 come from a high liquid water region where the droplet concentration is nearly constant. In this region the slopes of the interarrival distance distributions are constant and co-

*The National Center for Atmospheric Research is sponsored by the National Science Foundation.

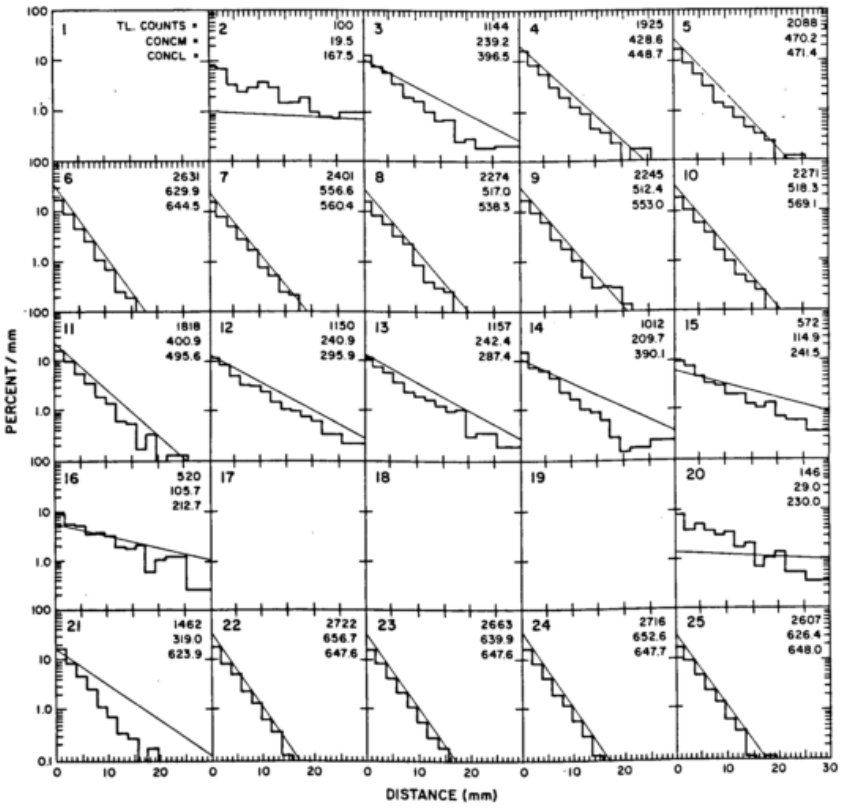


Fig. 1. Histograms of the distribution of distance between droplets arriving at the FSSP. The data are 10 m averages (10 Hz). CONCM is the average concentration, CONCL is the concentration derived from the droplet arrival time distribution slope. The latter ignores empty regions and represents the dominant *local* droplet concentration. The light line shows the expected slope for randomly distributed droplets corresponding to the measured average concentration.

incide with those computed from the measured average concentrations, indicating that the droplets are indeed randomly distributed throughout the sample volumes. Such uniformly random distributions were typically observed in adiabatic or nearly adiabatic cloud regions.

3. MIXING AT INTERFACES BETWEEN CLOUD AND CLEAR AIR

Comparisons between the average and local concentration can provide information about the structure of the interface. If an interface is diffuse, with a gradual increase in droplet concentration from cloud edge inward, then the average and local concentrations are approximately equal, and both increase gradually, as sketched in Fig. 2a. If the interface is irregular or patchy but there is no fine-scale mixing and thus the interface remains locally sharp, then the local concentration remains constant and it is always higher than the average concentration, as shown in Fig. 2b.

Examples of variation in the average and local concentration encountered near cloud and clear-air boundaries are shown in Fig. 3. As can be seen the local concentration is usually significantly higher than the average concentration, indicating the presence of clear or droplet-poor air within the sample volumes. Simple diffuse interfaces, as in Fig. 2a, extending over distances of several tens of meters were not observed. Adiabatic local concentrations and low average concentrations, as in the case of the irregular interface in Fig. 2b, were also not observed. In most cases the local concentration decreases toward the cloud edge, but to a lesser extent than the average concentration, indicating that the interface is both

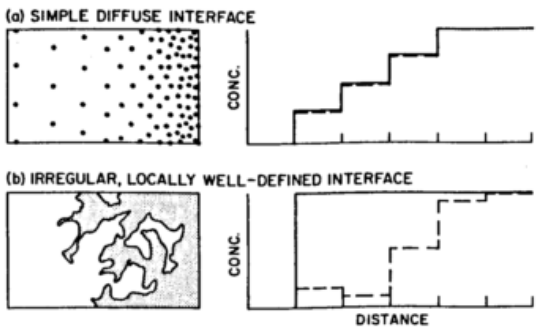


Fig. 2. Two kinds of interfaces and the expected changes in the dominant local concentration and the average concentrations with penetration distance (solid and dashed lines, respectively). a: simple diffuse interface; b: irregular but well-defined interface.

somewhat diffuse and irregular. This implies that coarse and fine-scale mixing take place concurrently within the same cloud volumes.

4. IMPLICATIONS FOR CLOUD DROPLET GROWTH AND AIRPARCEL RECYCLING

The present observations indicate that most of the mixing takes place in narrow regions within tens of meters of clear-air boundaries. Substantially diluted, more-or-less uniformly mixed cloud volumes extending several hundreds of meters across are not observed, though such volumes are often postulated in microphysical parcel models. If the mixed airparcel concept is applicable to the type of continental cumulus investigated here, then the mixed airparcels must be much smaller in size, perhaps only several meters or a few tens of meters across.

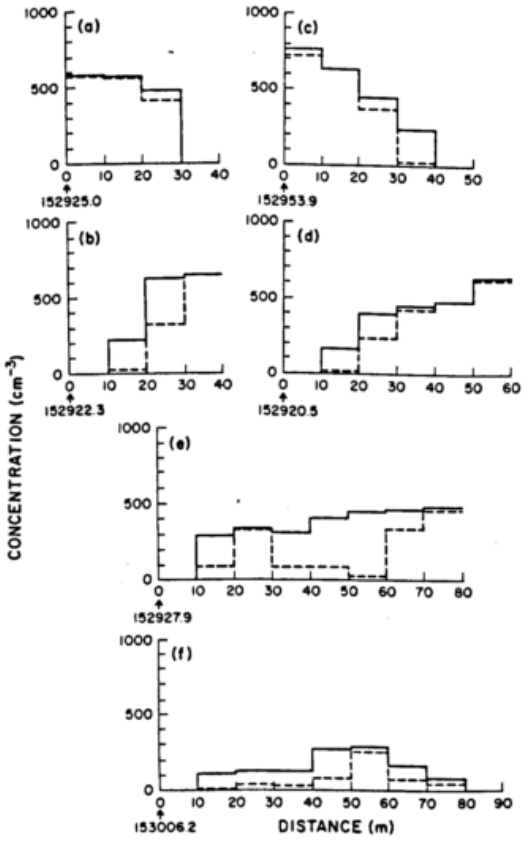


Fig. 3. Examples of interfaces encountered at cloud and clear-air boundaries. Solid line — dominant local concentration, dashed line — average concentration derived from the droplet arrival time distribution slope, both measured over 10 m penetration distances.

The fine-scale features of the mixing process together with the activation of new cloud droplets in ascending, diluted cloud volumes provide a plausible explanation of why mixing does not appear to promote cloud-droplet growth in continental cumulus clouds (Paluch and Baumgardner, 1988), contrary to what has been predicted in some microphysical parcel models (Baker and Latham, 1979; Telford and Chai, 1980). For continental clouds, estimates show that if activation of new droplets is taken into account, then to produce an increase in droplet size detectable with our present 1.5 μm radius resolution the distances a diluted cloud volume must ascend are of the order of hundreds of meters or more. These distances are one or two orders of magnitude larger than the typical dimensions of the diluted cloud volumes. In the presence of turbulence, these mixed cloud volumes might be expected to rise without being destroyed through further mixing over distances several times their characteristic dimensions, but not over distances that are one or two orders of magnitude larger.

5. REFERENCES

BAKER, M. B., and J. Latham, 1979: The evolution of droplet spectra and the rate of production of embryonic raindrops in small cumulus clouds. *J. Atmos. Sci.*, **36**, 1612–1615.

BAKER, M. B., R. E. Breidenthal, T. W. Choularton, and J. Latham, 1984: The effects of turbulent mixing in clouds. *J. Atmos. Sci.*, **41**, 299–304.

BAUMGARDNER, D., 1986: A new technique for the study of cloud microstructure. *J. Ocean and Atmos. Tech.*, **3**, 340–343.

PALUCH, I. R., and D. G. Baumgardner, 1988: Entrainment and fine-scale mixing in a continental cloud. To be published in *J. Atmos. Sci.*

TELFORD, J. W., and S. K. Chai, 1980: A new aspect of condensation theory. *Pure Appl. Geophys.*, **113**, 1067–1084.

AIRBORNE STUDIES OF THE INFLUENCE OF ENTRAINMENT ON THE VERTICAL AND HORIZONTAL MICROPHYSICAL STRUCTURE OF SMALL CUMULUS CLOUDS

John Latham* and Alan M Blyth+

*Physics Dept., University of Manchester Institute of Science and Technology
PO Box 88, Manchester M60 1QD, UK

+Physics Dept. and Geophysical Research Centre, N.M.I.M.T.
Socorro, New Mexico 87801, USA

Although recent major field experiments have yielded significant quantities of information on the fine-scale microphysical structure at essentially constant altitude within clouds, little data is available on the associated vertical structure. In an attempt to redress this deficiency we present and discuss measurements made using the University of Wyoming King Air research aeroplane, during the CCOPE experiment conducted in Montana, USA, in the summer of 1981. We restrict our attention to non-precipitating, essentially ice-free cumulus clouds which were studied either by making a series of horizontal penetrations at different altitudes encompassing almost all of the depth of the cloud (typically 2 to 3 km) over as short a period as possible. The principal microphysical measurements (obtained using a PMS Forward Scattering Spectrometer Probe, FSSP) were of liquid-water content (L, also measured with a Johnson-Williams device); cloud droplet size distribution (n(d)), where d is the droplet diameter within the range 2 to 32 μm; and the droplet number concentration (N). These parameters were recorded at 10 Hz, corresponding to a spatial discrimination of about 10 m; information on N was also available at 50 Hz (~ 2 m). Standard meteorological parameters and size distributions of larger hydrometeors were also measured, but it was necessary to sacrifice the quantity of the dynamical data in order to minimise the time over which the vertical structure was determined.

We concentrate attention herein on describing the microphysical structure (especially in the vertical), examining the role of entrainment of environmental air in producing it, and discussing the embryonic raindrops which the PMS 1-D probe revealed were often present in particular regions of the clouds studied.

Information was gathered in flights through 7 clouds. On some occasions we present diagrams which superimpose data from all 7 clouds. On other occasions - where we are particularly concerned to examine fine structure - we present comprehensive data from one particular case study (Cloud A, 23 June), in which the observed relationships were characteristic of those found in all cases. Over the 7 case studies the cloud base temperature (TB), the cloud top temperature (TT) and the cloud depth (CD) ranged roughly from 13°C to -3°C, -6°C to -15°C and 1.5 km to 3.5 km respectively; the corresponding values of these parameters for Cloud A were 5.5°C, -15°C and 2.5 km.

Microphysical structure, generally speaking, was found almost everywhere within the clouds studied, independent of the distances from their horizontal and vertical boundaries at all scales down to the lowest limit of measurement (~ 2 m). Characteristic examples of significant fluctuations in L, N and mean droplet diameter $\bar{d}$ measured at 10 Hz during horizontal penetrations through the upper and lower regions of Cloud A are shown in Figures 1 and 2 respectively. Consecutive droplet spectra, illustrating structure in n(d) on spatial scales down to 10 m in this cloud, are presented in Figure 3. Values of the coefficient of variability, K, are seen (Figure 4) to be usually in excess of unity at all 6 levels of penetration of Cloud A, indicating considerable structure in N, which is not simply due to random distributions of the droplets. On the other hand, on many occasions, K ~ 1 in adiabatic regions.

Figures 5, 6 and 7 present 10 Hz scatterplots of L/LA (LA is the adiabatic liquid-water content), N and d respectively for all altitudes, Z, above cloud base at which penetrations were made through Cloud A. The cloud is seen to be substantially sub-adiabatic at every level, with wide ranges in individual values of L/LA, and average values ranging from about 0.2 to 0.4. Individual values of N are seen to vary enormously at each level; the average values increasing slowly with Z. Less scatter is observed in the 10 Hz values of $\bar{d}$, the average values being substantially less than the calculated adiabatic ones, which always exceed the peak values of $\bar{d}$. Examination of Figures 5, 6 and 7 reveal that reductions in N and $\bar{d}$ below the maximum (adiabatic) values at each level contribute about equally to the sub-adiabaticity in L.

There can be little doubt that the microphysical structure found in the clouds is a consequence of entrainment. Paluch analyses, which were performed where possible indicate that entrainment occurs at all levels, the source of the entrained air at any level lying between that level and no more than about 1 km above it. The substantial levels of sub-adiabaticity resulting from entrainment will shorten droplet lifetimes significantly, which may have important chemical implications - as might also, the role of entrainment in replenishing depleted supplies of oxidants.

Figures 8 and 9 show the distribution with Z of L/LA and N respectively for all clouds

studied. The scatter in L/LA is appreciable, but the tendency reported by Warner (1970) - curve displayed - for it to diminish rapidly with Z is not confirmed in our studies. In each, L/LA is roughly independent of Z. Substantial variability is found in N, with a tendency for the average droplet concentration to increase with altitude above cloud base, possibly as a consequence of activation of condensation nuclei at higher levels where the updraught is stronger and/or L has been diminished by entrainment.

Analysis of 1-D probe data for three particular detailed multipenetration studies of ice-free clouds on 27 July, revealed the presence of substantial concentrations (~ 10 /l of water drops in the approximate size range 60 to 120 μm in the central and upper regions, but not near cloud base. Adiabatic spectra - determined from calculations based on measurements made in the lowest regions penetrated - indicate that the largest droplets grown by condensation are too small to produce the observed embryonic raindrops. The fact that they were not found in the lowest penetration through each cloud, and the observation (Figure 10) that their number concentrations at any level do not systematically increase with increasing L, militate against the idea that they were formed on giant nuclei. Whether or not their presence is attributable to the ingestion of the residue of a decaying thermal by a newer one, enhanced growth associated with entrainment or some other mechanism remains to be established.

REFERENCE

Warner, J.: 1970 On steady-state one-dimensional models of cumulus convection. J Atmos Sci, 27 (1970) 1035-1040.

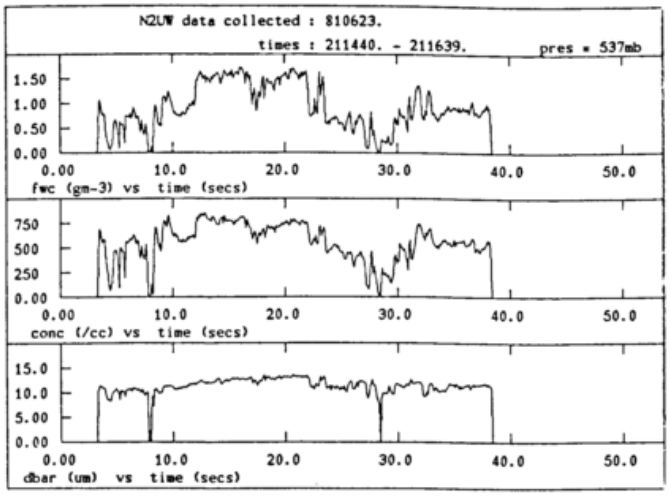


Figure 1. Cloud A. Variation of L, N and $\bar{d}$ with time t for one penetration.

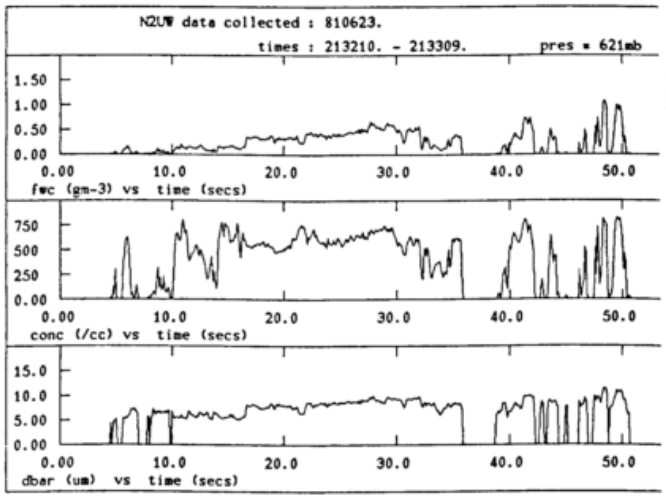


Figure 2. Cloud A. As Figure 1.

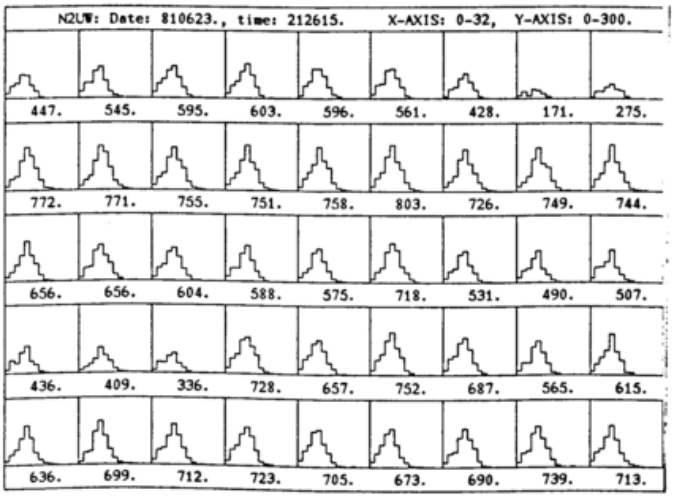


Figure 3. Cloud A. Consecutive 10 Hz droplet spectra. The number under each spectrum is N (cm^{-3}).

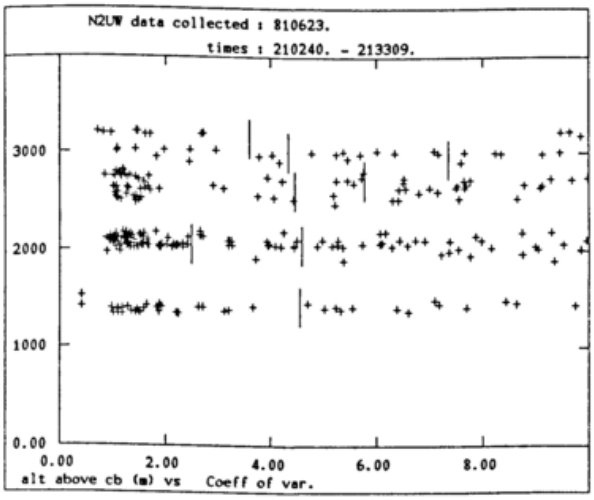


Figure 4. Cloud A. Values of K for each penetration.

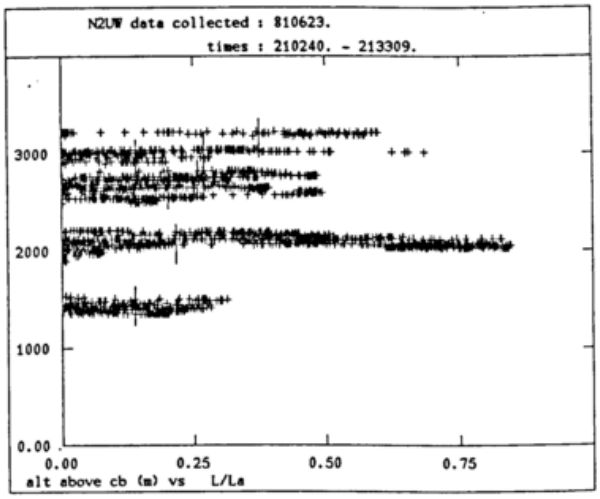


Figure 5. Cloud A. L/LA values for each penetration (10 Hz).

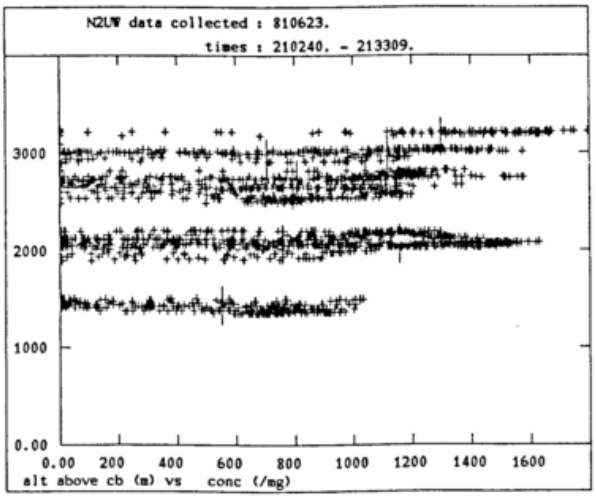


Figure 6. Cloud A. N values (/mg) for each penetration (10 Hz).

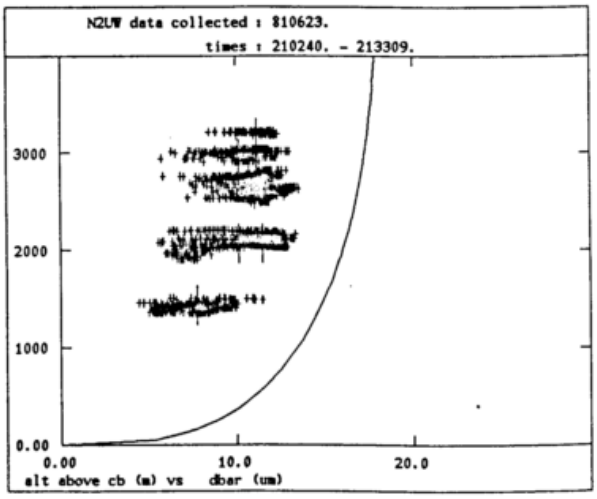


Figure 7. Cloud A. d values (μm) for each penetration (10 Hz). The solid line is for adiabatic growth.

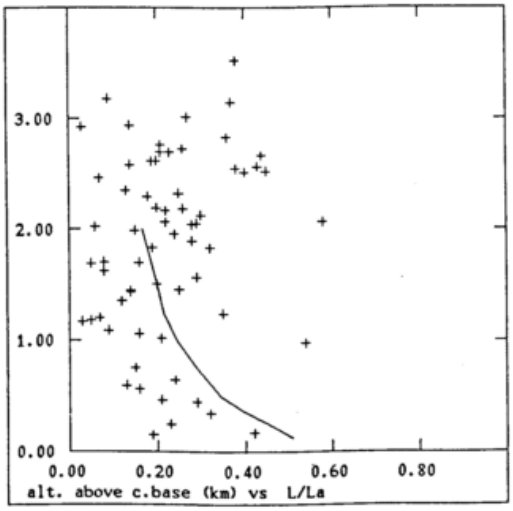


Figure 8. All 7 clouds. Variation of L/LA with height above cloud base. The solid line is from Warner (1970). Points are averages for each penetration.

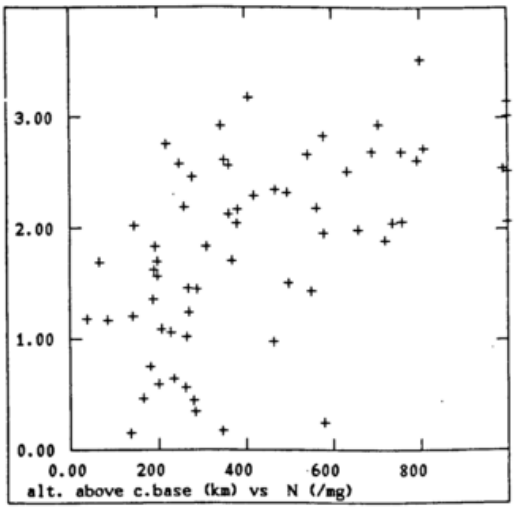


Figure 9. All 7 clouds. Variation of N (/mg) with height above cloud base. Points are averages for each penetration.

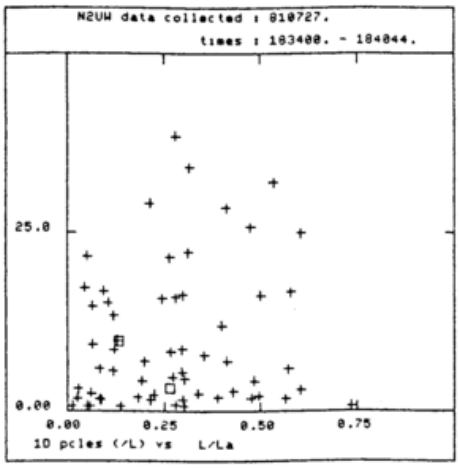


Figure 10. Variation of concentration of embryonic raindrops (/l) with L/LA. Cloud E (27 July)

ENTRAINMENT SITES, MIXING PROCESSES IN WARM CONVECTIVE CLOUDS. EFFECT ON DROPLET GROWTH

Elizabeth Hicks, Arlette Rigaud, Jacqueline Gagneux and Constantin Pontikis

Météorologie Nationale, EERM-CRPA
Magny-les -Hameaux (France)

1. INTRODUCTION

Entrainment and mixing of non cloudy air into cumulus clouds is currently proposed as a mechanism which broadens the droplet spectrum and creates larger droplets which are the first to start growing by coalescence and may initiate precipitation. In this paper we present the results of an analysis of data collected in September 1983 during a field experiment at Voves (France) which is focussed on the following questions: a) Do measurements made at different levels in a cloud indicate the same source of entrained air? b) Does the mixing process during an entrainment event support the droplet conserving or non conserving hypothesis? c) Does entrainment and mixing enhance cloud droplet growth in the condensation spectrum?

2. DATA

Three non precipitating shallow warm clouds , with depth ranging between 600 and 2300 meters, sampled on 9, 12 and 15 September have been selected for this analysis.

The environmental sounding and 1 Hz in-cloud measurements of pressure, temperature (Rosemount and Reverse-Flow sensors), dew-point temperature (G-E sensor), liquid water content (JW and FSSP) and droplet spectra (FSSP) were made by the instrumented EERM Piper Aztec aircraft. The FSSP value of the liquid water content Q_l and the Rosemount temperature were used in all thermodynamic analysis. The criteria used to ensure that samples were wholly in-cloud was $Q_l > 0.1\ gm^{-3}$.

The presence of precipitation-sized drops was detected by an 8mm Doppler radar and the study was limited to cloud regions with weak echo . An overview of this field experiment, instrumental accuracies is given in Pontikis et al.(1987).

3. ENTRAINMENT SOURCES

The source of entrained air is obtained by using Paluch's thermodynamic method where the total water mixing ratio Q is plotted against the wet equivalent potential temperature θq for in-cloud measurements, cloud base and the environmental sounding.

Table 1 summarizes the correlation coefficient of the linear regression through the in-cloud θq,Q values for every penetration in the 3 clouds as well as information about cloud base, cloud top and entrainment levels. In most cases the in-cloud θq, Q values form a fairly linear distribution (with more scatter towards cloud top) indicating a single source of entrainment. Every cloud undergoes cloud top entrainment.

date	N° cl.	Pmb base/top	Pmb obs. lev.	Pmb entr. lev.	Cor. Coef.
9/9	1	895/672	840	670	0.92
			805	670	0.91
			750	670	0.76
12/9	2	848/785	811	795	0.9
			793	795	0.57
15/9	3	844/660	810	810	0.85
			750	660	0.95
			695	680	0.78

Table 1 : Cloud characteristics, entrainment levels associated to each traverse and the correlation coefficient of the regression line in the θq - Q analysis.

Fig.1 (a,b,c) presents the Paluch diagrams for the 810mb, 750mb and 695mb levels of cloud 3. There are points with θq,Q values larger than the mean base point values due to natural variability. Lateral entrainment at the lower level of the cloud (810mb) and cloud top entrainment at the higher levels (750 and 695mb) is observed.

The strong linearity of the in-cloud θq,Q values at 750mb tend to indicate a single entrainment source at cloud top (660mb), although the cloud parcels have most probably already been diluted below. One would expect the in-cloud θq, Q values to be therefore distributed in the area delimited by: a) the best fit line passing through the in-cloud θq, Q values at 810 mb, b) the lines passing through the extreme θq, Q values of the 810mb level and the θq, Q value of the local environmental sounding which corresponds to the second source of entrained air (660mb). Such a pattern is observed and to a lesser extent for

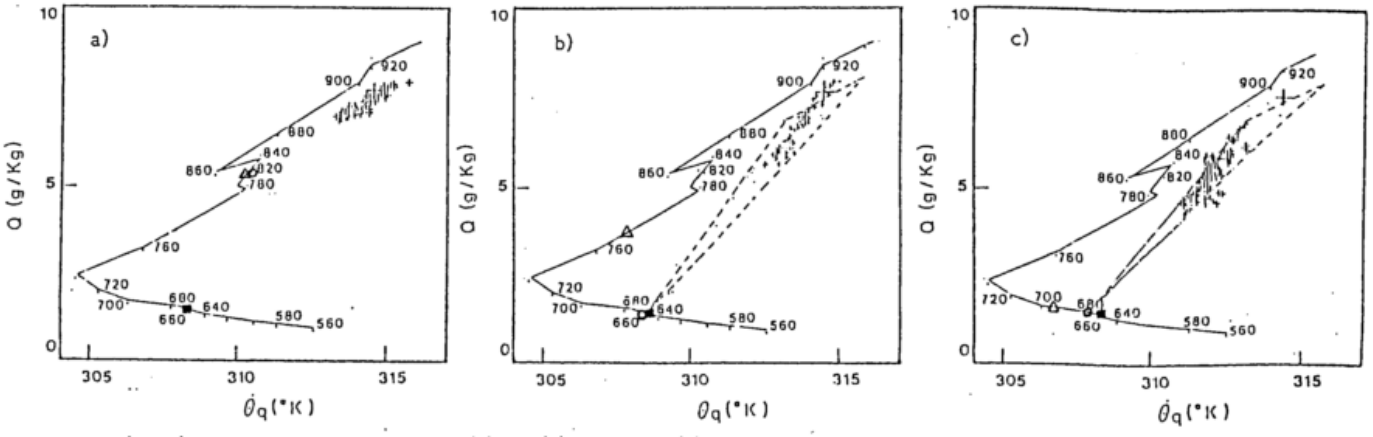


Fig. 1(a,b,c).Paluch diagrams for the 810(a), 750(b) and 695mb(c) levels of cloud 3. The symbols △,○,■ on the environmental sounding denote respectively the levels of observation, entrainment and cloud top.

the 695 mb level where the entrainment source is situated at 680mb.

This is a confirmation of the validity of the Q-vs-θ_q diagrams but emphasizes the importance of multi-level penetrations in a cloud before concluding to cloud top entrainment as the only source of cloud dilution.

In the presence of cloud top entrainment, the dilution of the cloud is due to penetrative downdraughts and mixing between cloud parcels of varying degrees of dilution. In our study, penetrative downdraughts may reach 170mb under the entrainment level (cloud 1) and have similar depth to those which are responsible for the dilution of the clouds studied by Blyth and Latham (1985) and Paluch (1979).

4. MIXING PROCESS

A similar analysis to Jensen's (1985) N-vs-F diagrams has been applied in order to determine the mixing process involved during entrainment events. When one source of entrained air is responsible for the dilution of the whole cloud, each cloudy parcel, independently of its life history and mixing state can be labelled by two quantities: F, the mass fraction of cloud base air it contains which is determined by the Paluch diagrams and R, the ratio between the measured and undiluted droplet number per unit mass. A parcel which is just saturated but droplet free is characterized by F=Fs and R=0. At a given level, the F, R values of each cloudy parcel may be plotted in a diagram and different hypothesis can be tested if the points lie within or beyond certain areas:

- homogeneous mixing (in the terminology of Baker and Latham (1979)): no droplets totally evaporate and the F,R points lie within the droplet conserving (D.C.) area delimited by $F.Rmin<R<F.Rmax$, up to F=Fs.
- inhomogeneous mixing: some droplets totally evaporate and F,R points are under the D.C. wedge. If a constant proportion K of droplets of all sizes totally evaporate during mixing to maintain saturation while the droplet size distribution does not change, the F,R points lie along the straight line R=F(1-K(F)) passing through points (1,1) and (Fs min,0) where Fs min is the value of Fs at the entrainment level. When the observation level is lower than the entrainment level, the local value of Fs is higher than Fs min and only parcels with F>Fs will contain droplets.

If F,R points are scattered above the D.C. wedge, there has been secondary activation of droplets in the corresponding cloudy samples.

Fig.2 (a, b) presents R-F diagrams for two traverses respectively in cloud 1 and 3. At the 810 mb level of cloud 3 (Fig. 2a), lateral entrainment dilutes the cloud parcels. The absence of F, R points in the droplet conserving wedge for F<0.93 as well as the scatter of points along the R = F(1-K(F)) line suggests an inhomogeneous mixing process between undiluted cloud parcels and environmental air. This is confirmed by the presence of similar spectral distributions in undiluted and diluted parcels with droplet number per unit mass differences larger than those due to natural variability.

Similar conclusions may be made for the 750 mb level of cloud 1 (Fig. 2b), but in this case, the entrainment event involves already mixed parcels, as most F, R points lie under the R = F(1-K(F)) line.

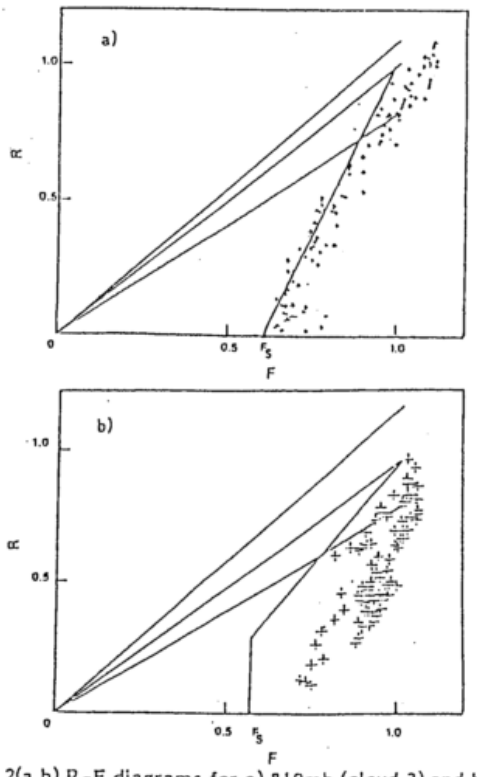


Fig. 2(a,b) R-F diagrams for a) 810mb (cloud 3) and b)750mb(cloud 1) levels which support the droplet non conserving hypothesis.

Table 2 summarizes the results of the observation made in the R-F diagrams corresponding to all cloud penetrations.

In the case of cloud 1, the larger number of points within the droplet conserving limits is not a consequence of the mixing process itself but reflects the fact that many parcels were not greatly diluted at the time of observation.

The absence of samples with F, R values above the droplet conserving wedge tends to attenuate any assumption of secondary droplet activation.

N°cl.	Pmb	% R, F points			
		in D.C. F > 0.95	in D.C.	under D.C.	above D.C.
1	840	62	62	38	0
	805	24	43	57	0
	750	16	17	83	0
2	811	0	25	75	0
	793	33	72	28	0
3	810	35	37	63	0

Table 2 : Pourcentage of droplet conserving and non conserving mixing events in each cloud (D.C. stands for droplet conserving wedge).

One may conclude that these data generally fail to support a droplet conserving hypothesis like in Jensen et al.'s studies (1985, 1986) but do agree with a mixing process where drop sizes do not change and a proportion of drops of all sizes are totally removed to reduce the liquid water content.

Similar observations were reported by Telford and Wagner (1981) from their measurements in the tops of marine stratus and were considered as a direct consequence of the ETEM process where "the thorough mixing inside the dry entity evaporates completely all the drops first entering it" (Telford et al. (1984)).

5. INFLUENCE OF DILUTION ON DROPLET GROWTH

Droplets in ascending diluted cloud samples could grow by condensation to larger sizes than in undiluted parcels as the condensed water is released on fewer droplets.

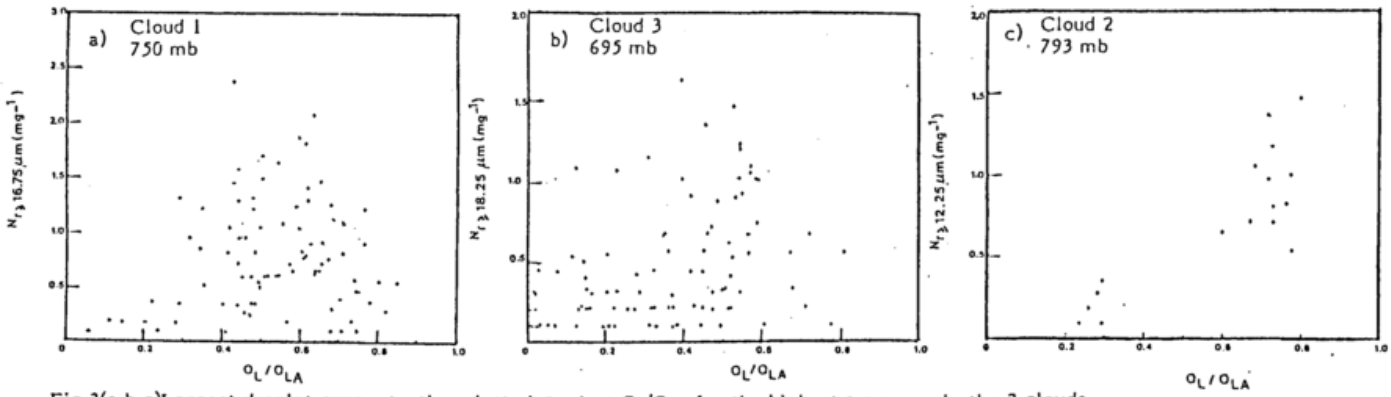


Fig.3(a,b,c)Largest droplet concentration plotted against Q_l/Q_{la} for the highest traverses in the 3 clouds.

The examination of droplet spectra collected during the CCOPE experiment on different days have led to contradictory results concerning enhanced droplet growth due to mixing with environmental air (Blyth and Latham (1985), Hill and Choularton (1985) , Paluch and Knight (1986)).

We have plotted the concentration of the largest droplets against the ratio between the measured and adiabatic liquid water content which represents the degree of dilution of cloudy parcels (as F may not be used in all cases).The diagrams corresponding to the highest traverses in the 3 clouds, where there is the most opportunity in finding large droplets ,are shown in Fig.3(a,b,c). For the deepest clouds, the data show great scatter and there is not a good correlation between the largest droplet concentration and Q_l/Q_{la}. The highest concentrations of large droplets are found in parcels with an intermediate dilution degree (Q_l/Q_{la}=0.4). The deep downdraughts in the clouds and recycling of cloudy parcels (Telford and Chai (1980)) are the predominant factor of enhanced droplet growth in the case of cloud top entrainment whereas the nature of the mixing process (droplet conserving or non conserving) is secondary. However for the lower levels of cloud 3, the droplet non conserving mixing process associated to lateral entrainment events may also play a significant role in the creation of bigger droplets Baker et al.(1980)).

In the most shallow cloud, at all levels, the largest droplet concentrations in undiluted parcels are higher than in the diluted ones. Recycling of parcels are limited to a very small depth and most probably when cloud top was sampled cloudy parcels had undergone insufficient cycling to create significant droplet growth.

Fig.4(a,b,c) presents histograms of the frequency of occurence of droplets in the highest occupied channel (shaded histogram) compared to the frequency of occurence of droplet concentrations at the highest traverse of each sampled cloud. The presence of large droplets is equally probable in parcels

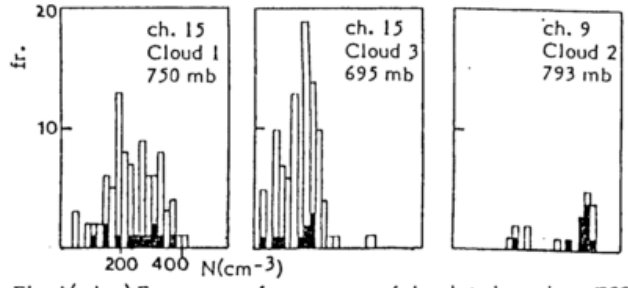


Fig. 4(a,b,c) Frequency of occurence of droplets in a given FSSP channel (denoted by ch. in each box)(shaded histograms) compared to the frequency of occurence of droplet concentrations.

with low or intermediate droplet concentrations, whereas they are absent in parcels with the highest concentrations, for cloud 1 and 3. However at the top of cloud 2, there is a higher probability of finding droplets with r≥13.75μm in the least diluted parcels.

6. CONCLUSIONS

The conclusions from the results may be summarized as follows:

a) The source of entrained air observed at a given level is generally the cloud top, but lateral entrainment may affect the lower levels in a cloud.

b) Mixing is a droplet non-conserving process.

c) Dilution and buoyancy-driven recycling of cloudy parcels enhances droplet growth in shallow warm cumuli.

REFERENCES

Baker, M. B. and J. Latham, 1979 : The evolution of droplet spectra and the rate of production of embryonic raindrops in small cumulus clouds. J. Atmos. Sci., 36, 1612-1615.

Baker, M. B., R. G. Corbin and J. Latham, 1980 : The influence of entrainment on the evolution of cloud droplet spectra. I : A model of inhomogeneous mixing. Quart. J. Roy. Meteor. Soc.,106,581-598.

Blyth, A. M. and J. Latham, 1985 : An airborne study of vertical structure and microphysical variability within a small cumulus. Quart. J. Roy. Meteor. Soc., 111, 773-792.

Hill, T. A. and T. W. Choularton, 1985 : An airborne study of the microphysical structure of cumulus clouds. Quart. J. Roy. Meteor. Soc., 111, 517-544.

Jensen, J. B., P. H. Austin, M. B. Baker, and A. M. Blyth, 1985 : Turbulent mixing, spectral evolution and dynamics in a warm cumulus cloud. J. Atmos. Sci., 42, 173-192.

Jensen, J. B. and M. B. Baker, 1986 : Preprints, AMS Conf. Cloud Physics, Snowmass, 145-148.

Paluch, I. R., 1979 : The entrainment mechanism in Colorado cumuli. J. Atmos. Sci., 36, 2467-2478.

Paluch, I. R. and C. R. Knight, 1986 : Does mixing promote cloud droplet growth? J. Atmos. Sci., 43, 1994-1998.

Pontikis, C., A. Rigaud and E. Hicks,1987 : Entrainment and mixing as related to the microphysical properties of shallow warm cumulus clouds. J. Atmos. Sci., 44, 2150-2165.

Telford, J. W. and S. K. Chai, 1980 : A new aspect of condensation theory. Pure and Appl. Geophys., 118, 720-742.

Telford, J. W. and P. B. Wagner, 1981 : Observations of condensation growth determined by entity type mixing. Pure Appl. Geophys., 119, 934-965.

Telford, J. W., T. S. Keck and S. K. Chai, 1984 : Entrainment at cloud tops and the droplet spectra. J. Atmos. Sci., 41, 3170-3179.

STRUCTURE OF UPPER CLOUDS BOUNDARY USING THE LIDAR DATA

V.E.Zuev, V.S.Shamanaev, I.E.Penner
I.V.Samokhvalov

Institute of Atmospheric Optics,SB USSR Acad.Sci., Tomsk, 634055, USSR

1. INTRODUCTION

In solving many of the climatological and aerometeorological problems one should have a good knowledge of sizes and fluctuation characteristics of inhomogeneities forming the upper clouds boundary (UCB). An airborne lidar is a useful tool for these measurements.

2. METHOD OF OBSERVATION

2.1 INSTRUMENTATION

The measurements were carried out using a polarization lidar "Svetozar-3" (SHAMANAEV 1985) mounted on an IL-18 aircraft for sounding the clouds through the aircraft optical-glass window in the direction to the Earth. The laser wavelength was 532 nm, the transmitted beam divergence was 1.0 mrad, the angle of the receiver field of view was 1 to 13 mrad. The received signals were digitized with 3.75 m spatial resolution of the computer. The return signals were recorded on magnetic disks at intervals of 20 to 23 m over the entire flight range. Also, the radiation temperature of clouds was measured.

2.2 CRITERIA

The distance to UCB was measured using five criteria at a time. Two of them were employed in the paper: the distance from the aircraft to the signal start r_o and the signal maximum r_m. Based on these quantities the mean gradient of scattering coefficient for UCB (that is, water content) was calculated as

$$\mu_G = \frac{1}{2(\Delta\tau)^2} \cdot \frac{\tau_0 - \Delta\tau}{\tau_0 + \Delta\tau} \qquad (1)$$

where $r = r_m - r_o$.

To monitor the UBC phase state one calculated the lidar return depolarization ratio profile using formula $D(H) = F_\perp(H)/F_\parallel(H)$, where $F_\perp$ and $F_\parallel$ are the return-signal depolarization and polarization components, respectively. In order for the UCB behavior along the horizontal path to be analyzed, the UCB structural functions were calculated by the formula

$$b(\tau) = \bar{S}^2 \frac{1}{n} \sum_{k=1}^{n} [H(\tau + \ell_k) - H(\ell_k)]^2, \qquad (2)$$

where S^2 is the UCB variance, l_k is the point on the flight path. In many of the situations UCB does not conform to the laws of stationary random processes. The correlation functions therefore are not always applicable.

2.3 THE FLIGHT SCHEME

The cloud field Sc was chosen for conducting the experiments. The flights were carried out during several days both along the perimeter and the diagonals of the square with the center in the Barents Sea and coordinates 74°45' N.L., 31° E.L. The observations with the cloud lidar instrument were also obtained during the flights in

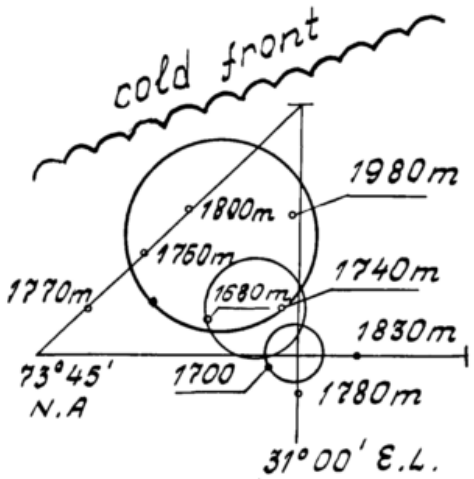


Fig. 1. Scheme of flight

this area along the circumferences 10 km, 20 km and 40 km in diameter. As a rule, the wind distorted the shape of circles and drifted their centers from the point chosen, see Fig.1. The numbers here denote the average UCB above sea level during the flight on 27 February 1987.

3. RESULTS

The cloud field presented in Fig.1 was studied during 2 hours. In this area the average UCB of the Sc field was 1660 to 1830 m. Only in one segment of the flight path a local cloudiness "dome" to the 1980 m UCB was observed. The UCB structural functions are presented in Fig.2. Curve 1 is for the small circle (Fig.1); curve 2 is for the Western part of the middle circle; and curve 3 is for the Eastern part of the large circle. For the areas 2 and 3 there is a zone of mutual overlapping. Function $b(\tau)$ was constructed with the interval τ =1300 m with averaging over 20 laser flashes. For the small circle, the mean UCB height H = 1720 m with the r.m.s. deviation H = 114 m. For the areas of the middle and large circles analyzed in Fig.2, H = (1680 $\pm$ 60) m and H = (178 $\pm$ 55) m, respectively. All the three circles have a common horizontal characteristic length of UCB inhomogeneities 5 to 8 km. In addition the middle circle has UCB fluctuations with 21 to 26 km characteristic length, and in the large circle, it is 13 and 28 km. It is interesting to note that the structural functions $b(\tau)$ constructed with a minimal interval along the flight line (20-50 m) never have a saturation area smaller than 1 km. That is the small-scale UCB fluctuations (tens of meters) cannot be considered as a stationary random process on the flight paths shorter than 1 km. The radiation temperature of clouds varied along the flight path by not more than 3°C and did not correlate with the UCB fluctuations.

For example, in the Northern part of the large circle, the scattering coefficient gradient $\mu_\sigma = (1.3 \pm 1) 10^3$ km^{-2}. The value of the scattering coefficient σ varies from 20 km^{-1} to 31 km^{-1} with 50% fluctuations for the upper 50-m cloud layer. The depolarization gradient μ_β was also measured in the upper 50-m cloud layer. For example, in the central part of the large circle μ_β has the values (4.6 $\pm$ 1.0) km^{-2} to (2.9 $\pm$ 0.9) km^{-2}. As shown in the papers (SAMOKHVALOV 1982, p.1050; ZUEV 1984, p.38), this is consistent with the UCB water droplet state.

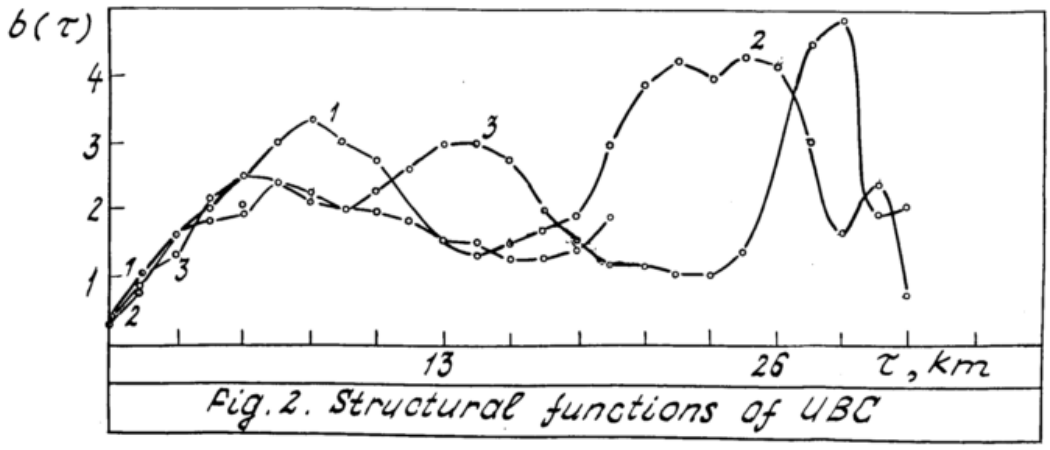


Fig. 2. Structural functions of UBC

SAMOKHVALOV, I.V.; SHAMANAEV, V.S.: Izv.Akad.Nauk SSSR Fiz.Atmos.Okeana 18 (1982) N. 10, p.1050-1055.

SHAMANAEV, V.S.; ABRAMOCHKIN, A.I.: Airborne polarization lidar "Svetozar-3". 1985.Rukopis' dep. VINITI N. 6225-85 Dep.

ZUEV, V.E.; KREKOV, G.M.; SAMOKHVALOV, I.V. et al. : Meteorologiya i gidrologiya, 1984, N.4, p.38-45.

TURBULENT TRANSPORT PROCESSES WITHIN AND BELOW SMALL CUMULUS CLOUDS

Anne M. Jochum

DFVLR, Institut für Physik der Atmosphäre
D-8031 Oberpfaffenhofen, Fed. Rep. of Germany

1. INTRODUCTION

In 1986 multiple aircraft measurements were conducted in the cloud-topped convective boundary layer (cbl) over complex terrain in South Germany to investigate the structure of turbulence and transport processes within and below clouds and to study the interaction between cloud- and sub-cloud-layer.

Three powered gliders and a jet aircraft all equipped for turbulence measurements were simultaneously flying along the same horizontal flight leg with fixed vertical spacing. The use of several research aircraft provides a very good spatial and temporal resolution. The gliders were scanning the subcloud boundary layer whereas the jet was collecting data (including microphysics) within and above the clouds. The data from the different aircraft are combined to yield vertical profiles of mean fluxes and spectral characteristics as well as information on the mean horizontal structure of thermal or cloud up- and downdrafts in various heights. Vertical profiles of mean meteorological parameters were obtained from rawinsondes and an additional aircraft. Airborne downward looking lidar gives information on the structure of the inversion zone and of the cloud layer.

Quadrant analysis and conditional sampling techniques are used to identify and investigate the main physical processes and scales contributing to vertical transport. First results from a case study with weak ambient winds are presented. There the observed clouds appear to be closely related to thermals in the mixed layer. Therefore the emphasis is laid on turbulence structure and transport rather than microphysical or radiative processes.

2. OBSERVATIONAL DATA

The measurements were conducted in the convective boundary layer over hilly terrain (maximum height variation 100m) in South Germany. Three instrumented powered gliders (Jochum et al., 1987) and the jet research aircraft Falcon-E (Fimpel, 1987) were simultaneously flying along the same horizontal flight leg with fixed vertical spacing to measure turbulence data. Wind profiles are derived from occasional ascents or descents of the Falcon. During selected runs above the inversion a downward scanning lidar onboard the Falcon (Mörl et al., 1981) delivered two-dimensional cross sections of the cbl structure as shown in Figure 1.

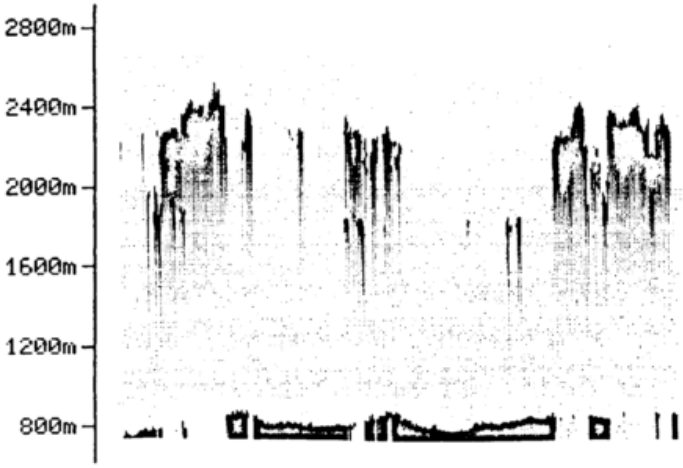


Figure 1. Lidar scan of cbl structure 14.07.1986.

The observational period covered four days in July 1986 characterized by high pressure, light to moderate winds, fair weather with varying light cloud cover. Results from a day (14.07.1986 noon) with weak ambient wind and 2-3/8 small cumulus cloud cover are presented. The data (11-13 local time) cover 26 individual measurement runs. The turbulence data are low-pass filtered to eliminate high frequency noise beyond sensor resolution, and high-pass filtered to remove scales larger than the convective scale. The resulting scale range is from 17m to 3.5km.

In order to understand the physical processes involved in turbulent heat transfer and its relation to the turbulence structure, two different methods of analysis have been pursued. For conditional sampling vertical velocity was chosen as the indicator series to distinguish a convective element (updraft) from its environment. The threshold defined to separate 'updraft' (larger than mean plus threshold) from 'environment' values is set to half the standard deviation of the indicator function. sensitive to the exact magnitude of the threshold). A minimum event length of 100m (except where otherwise mentioned) is specified in order to prevent very small bursts within larger events from splitting these coherent structures.
Another method of analysis consists of partitioning time series of temperature and vertical wind into the four quadrants of the $\theta' - w'$-plane and of computing fluxes and other quantities for each of

these quadrants which represent different physical processes (for details of the method see e.g. Grossman, 1984): Warm updrafts ($\theta' > 0$ and $w' > 0$) are thermal motions, cold updrafts penetrating thermals, warm downdrafts represent entrainment of warm air from aloft, cold downdrafts are compensating sinking motions. Contributions from each of these processes to total transport and area fractions covered by the corresponding motions are computed this way.

3. RESULTS

The data from the different aircraft are combined. All heights are normalized with the inversion height z_i . The composite vertical profiles in Figures 2-3 are derived by interpolating data from individual runs to normalized heights of multiples of $0.1z_i$ and averaging consecutive profiles over quasistationary periods of time. Figures 4-6 show the individual data points to illustrate the degree of scatter.

Three classes of length scales are introduced by appropriately filtering the data. Figure 2 shows the contributions of these scale ranges to sensible heat flux. The class covering eddies smaller than 170m represents turbulence of stochastic character. Its contribution of less than 10% is limited to the lowest third of the cbl. The class of intermediate size scales contains motions forming organized motions up length scales comparable to the cbl depth. They are most important in the lower half of the cloud-topped cbl, whereas in a cloudfree cbl they contribute significantly to the negative total flux in the upper third of the cbl (Jochum, 1988). The scales larger than cbl depth carry most of the flux in the upper half of the cbl.

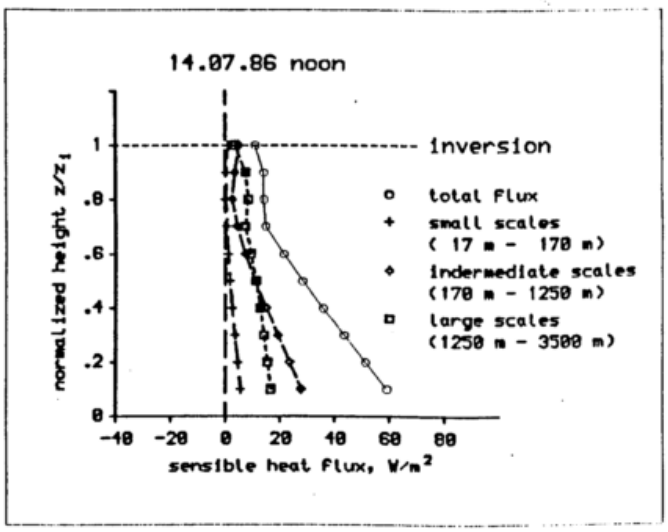


Figure 2. **Scale ranges contributing** to sensible heat flux. See text for details. Height is normalized by inversion height z_i.

The contributions of different physical processes to total sensible heat flux are identified using quadrant analysis. Figure 3 shows that everywhere in the cloud-topped cbl the vertical heat flux is dominated by warm updrafts (thermals). Cold downdrafts (compensating sinking motions) are also important, contribution to total flux about half as much as warm updrafts. In the upper half, two more types of motion (penetrative thermals and entrainment of warm air from aloft) contribute to total flux but they are much less significant than in cloudfree cases (Jochum, 1988).

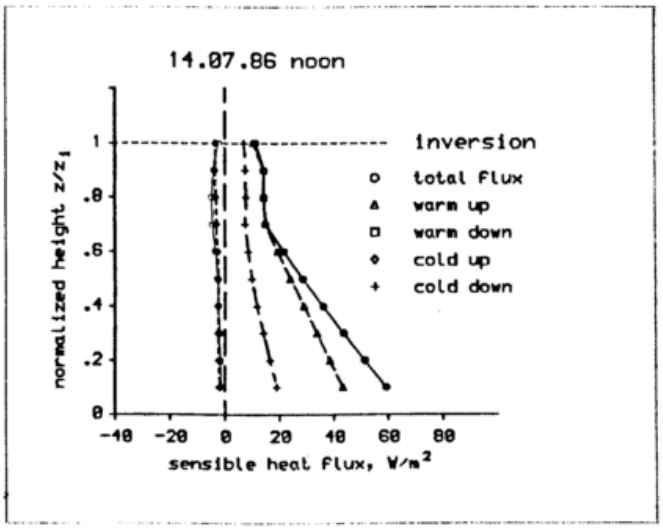


Figure 3. **Physical processes contributing** to sensible heat flux. See text for details.

Some statistics of updrafts are shown in Figure 4: the average thermal intersection length for events larger than 100m on the left, and the average number of updrafts per 10km on the right. In order to get information on smaller scale structure the minimum event length of 35m was evaluated additionally and is plotted in Figure 4 as crosses. Smaller events are most important in the lowest part of the boundary layer. Data from a cloudfree day which had otherwise comparable conditions are shown in the same figure as solid and dashed curves.

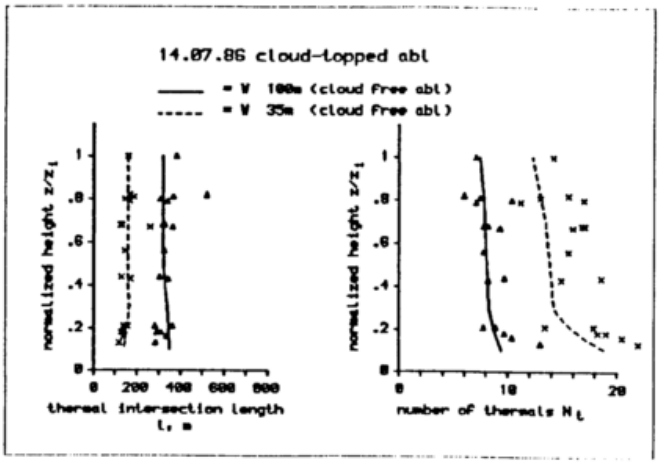


Figure 4. **Mean updraft intersection length** and average number of updraft intersections per 10km.

Physical properties of convective elements were also derived from the conditional sampling data. The average temperature excess of updrafts compared to their environment is shown in Figure 5. For the cloud-topped boundary layer investigated here there is no region of negative buoyancy below the inversion, whereas in cloudfree cases the level of neutral buoyancy is in the upper third of the cbl. The average vertical wind velocity excess as shown in Figure 6 increases upwards in contrast to the cloudfree case shown as solid line.

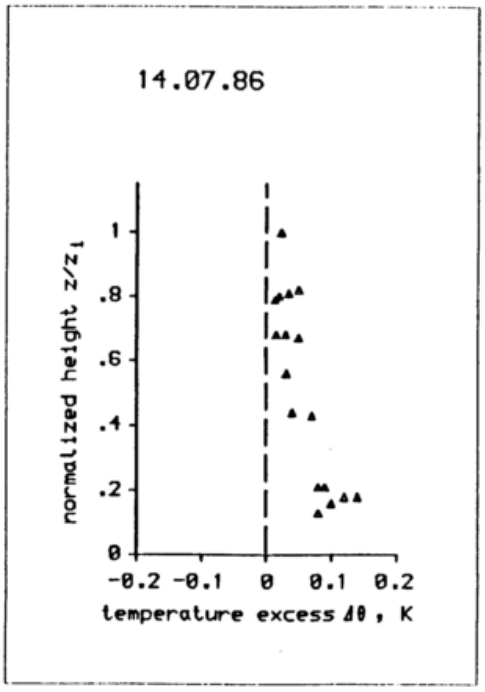


Figure 5. **Mean temperature excess** of updrafts over environment.

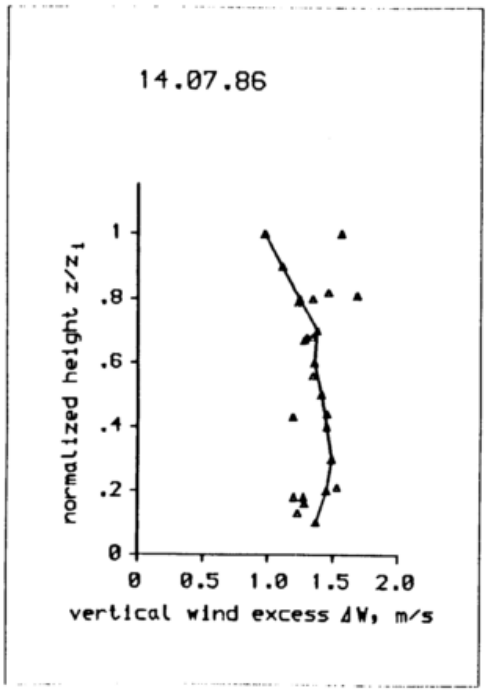


Figure 6. **Mean vertical wind velocity excess** of updrafts over environment. Solid line shows cloudfree case.

REFERENCES

Fimpel, H.P., 1987: The DFVLR meteorological research aircraft Falcon-E: Instrumentation and examples of measured data. *Proc. Sixth Sympos. on Meteorological Observations and Instrumentation, New Orleans, 10-16 Jan 1987, Amer. Meteor. Soc., 212-216.*

Grossman, R.L., 1984: Bivariate conditional sampling of moisture flux over a tropical ocean. *J. Atmos. Sci.*, **41**, 3238-3253.

Jochum, A.M., 1988: Turbulent transport in the convective boundary layer over complex terrain. *Proc. Eighth Sympos. on Turbulence and Diffusion, San Diego, 25-29 April 1988, Amer. Meteor. Soc..*

Jochum, A.M., M.E. Reinhardt and H. Willeke, 1987: Three DFVLR powered gliders - a meteorological measurement system for the investigation of the atmospheric boundary layer. *Proc. Sixth Sympos. on Meteorological Observations and Instrumentation, New Orleans, 10-16 Jan 1987, Amer. Meteor. Soc., 217-220.*

Mörl, P., M.E. Reinhardt, W. Renger and R. Schellhase, 1981: The use of the airborne LIDAR System 'ALEX F 1' for aerosol tracing in the lower troposphere. *Beitr. Phys. Atmosph.*, **54**, 403-410.

INSTABILITY THEORY IN CLOUDS AND THE PARAMETERIZATION OF EDDY VISCOSITY COEFFICIENTS

Yoshimasa Takaya

Meteorological Research Institute
Tsukuba, 305 JAPAN

1 INTRODUCTION

We propose a theory which describes the mechanism of the entrainment or mixing between cloudy air and the surrounding clear air which is a generalization of the conditional instability of the first kind. There, the tilted stratification of the thermodynamical and cloud-physical variables in the cloud plays an important role. This theory explains the fractal-like structure of the convective cloud and predicts the horizontal angle of the node or the hollow of the cloud. Further we take the effect of this instability into our numerical simulation of the convective cloud as the eddy terms and obtain the result that the history of the collective motion of the convective clouds sensitively depends on these eddy terms.

2. INSTABILITY THEORY IN CONVECTIVE CLOUDS

In order to exploit the instability theory in convective clouds, we think a system whose physical variables are velocity fields, potential temperature, water-vapour mixing-ratio and cloud-water mixing-ratio whose stratification is tilted nearly along the boundary of the cloud. We divide each variable into three parts; hydrostatic part, spatially meaned dynamical part and turbulent part. We obtain a set of equations for these turbulent variables with linear approximation. If we assume the normal mode solution to these variables

$$\exp(\sigma t - ip.r), \qquad (2.1)$$

where σ is interpreted to be a growth-rate of the turbulence if it is real and positive. p is a wave number vector and r is a coordinate vector. Eigenvalue equation becomes simply a following quadratic equation in σ if we assume the shape of the meaned cloud is either cylindrically symmetric or slub-symmetric;

$$\sigma^2 + \tau_{22}\sigma - g(i_2\cdot k)(i_2\cdot B) = 0, \quad (2.2)$$

where k is a unit vector which points to the vertical, i_2 is a unit vector which is defined by

$$i_2 = p\times(k\times p)/(|p||k\times p|)$$

and which parallels to the turbulent velocity v′. $\overline{V}$ is meaned velocity and τ_{22} is a component of meaned shear tensor defined along the unit vector i_2

$$\tau_{22} = (i_2\cdot\nabla)(i_2\cdot\overline{V}).$$

The vector B is defined by hydrostatic part and meaned part of thermodynamical and cloud-physical variables and their gradients. The physical meaning of B is as follows. If a parcel in a cloud experiences a virtual displacement along B, it acquires the maximum increase of buoyancy. The discrepancy between the direction of B and vertical comes from the tilted stratification in a cloud. Note that Eq.(2.2) does not depend on the length of the p but only on the direction of it. By changing the direction of i_2, the eigenvalue will be changed. Then the direction of i_2 which corresponds to the maximum growth-rate will be realized in nature. By calculating this direction at the peripheral part of the cloud, we can predict the direction of the node or the hollow of the convective cloud. The physical interpretation of this solution is as follows . The direction of buoyancy is vertical and simple parcel method can only say that the parcel must go up or down vertically. If we neglect the effect of the second part of Eq.(2.2), the most unstable mode selects the direction of i_2 just the middle of the

vertical and direction of B. It shows that the real motion of the cloudy air and the result of the parcel method are lead to different movements. The second term of Eq.(2.2) represents the effect of the advection of the meaned velocity by turbulent velocity. Therefore the most unstable mode is determined by a balance of the three effects; the vertically directed buoyancy itself, the maximum increase of buoyancy and the effect of advection of meaned velocity by turbulent velocity. The relative phases between the turbulent variables show that this mode transports heat, water-vapour and cloud water from inside of the cloud to the surrounding clear air and dilutes the cloud.

Instead of the observational data, we borrow thermodynamical and cloud-physical data from our numerical simulation. In Fig.1 we predict the distribution of the growth-rate and the direction of the most unstable mode at each grid point of the right half part of the simulated slub-symmetric cloud. These

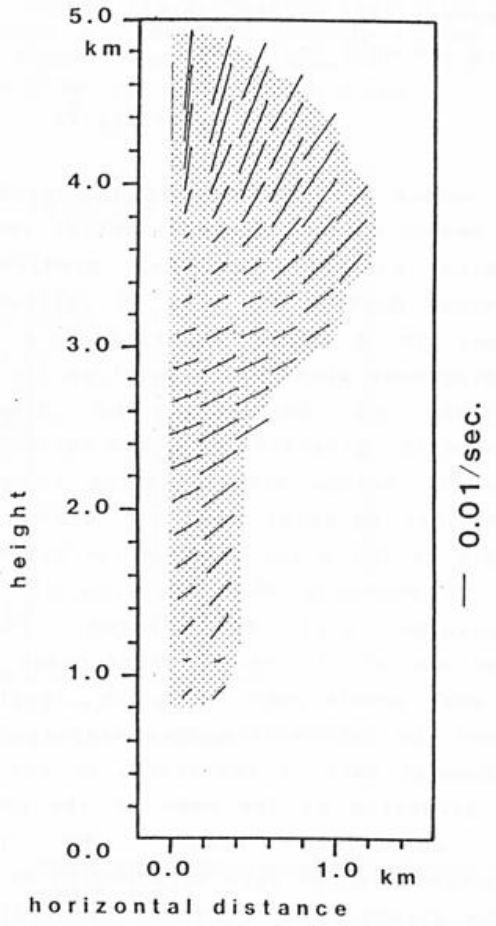


Fig.1 A right half part of the distribution of the most unstable direction of turbulent velocity. The length of the bar shows the magnitude of the growth-rate. Cloud region is indicated by the shaded region.

directions at the outer part of the cloud point to almost the middle of the vertical and the direction perpendicular to the surface of the cloud. The second point of our prediction is that the growth-rate is larger at the outer part of the cloud, especially at the cloud top, and smaller at the inner part. The third point is that our theory explains the fractal-like structure of the convective cloud. It tells that there exists the most unstable direction at each part of the cloud. Therefore a node at a moment, for example, is changed into the shape with nodes and hollows of smaller scale according to the instability at each point of that node and so on.

3. OBSERVATIONAL RESULTS

By using the time-lapse video recorder, we analyzed the progressive change of the shape of the convective cloud. In Fig.2, we show a frame of the videograph in which the direction of jetting out of the node is denoted by black arrow. The size of the arrow corresponds to the size of the node. Seeing this we recognize the fractal-like structure of the convective cloud. The direction of each arrow is generally steeper than that of the normal to the surface of the cloud, which agrees to our prediction. The second prediction in the former section is clearly seen in the observation by J. Warner(Ref.1).

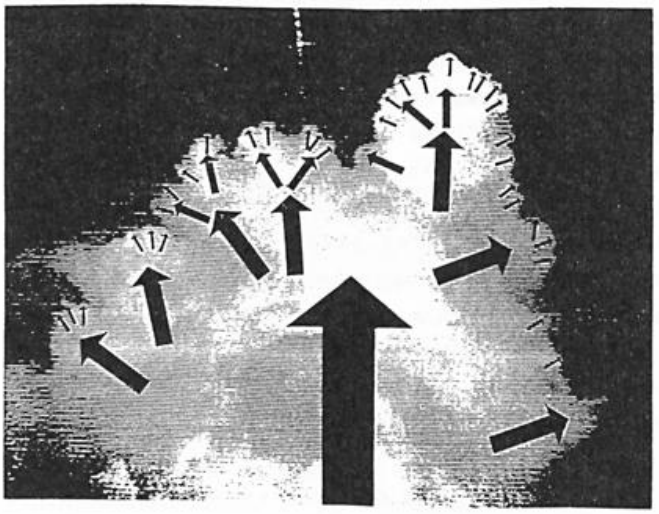


Fig.2 A frame of videograph which was taken on August 14, 1987 at Tsukuba. It shows the fractal-like structure of the convective cloud. Each black arrow shows the direction of the growing node and their size corresponds to the scale of the node.

4. PARAMETERIZATION OF EDDY TERMS IN CLOUDS

In order to parameterize the eddy viscosity terms in convective clouds, we assume that they are represented by the mode of the maximum growth-rate about which we studied in the former section. But our instablity theory is linear, so that the absolute value of the amplitudes cannot be determined. In order to complete the parameterization, we must fix the meaned-square of the turbulent velocity $\overline{v'^2}$. It should be determined by observational study. But at this stage our data is not enough to do it. Therefore we propose a following tentative parameterization to be

$$\overline{v'^2} = v_0^2(100\times\sigma)^2.$$

It means that the root-mean-square of the turbulent velocity may be proportional to the growth-rate itself. The value of v_0 is selected appropriately through the results of our numerical simulations which include this parameterization. In making our numerical model, we have no principles to fix the eddy terms at the outside of the cloud. Therefore we assume to add eddy viscosity terms with constant viscosity coefficients μ at each grid point. The results of the numerical simulation sensitively depend on the parameter μ and v_0. When we compare two cases in which μ is taken to be 25 m^2/sec. or 200 m^2/sec with other conditions being the same, the cloud easily rise in the former case. The reason is that in the former case the updraft and downdraft occur without difficulty because of the low viscosity at the outside of the clouds. Further we compare the two cases in which the parameter v_0 is 1 m/sec or 0 with other conditions to be the same. In the former case, the dilution of cloud occurs strongly at the outer part of the cloud in its growing stage. Therefore the conversion of the cloud-water to rain water is interrupted and the decrease of the total water-vapour in the domain is slower. In a simulation in which supply of the sensible heat is continued, the increase of the kinetic energy connected with the more of the water-vapour remained in the domain finally causes a formation of strong convective clouds.

5. CONCLUSIONS

The instability theory in convective cloud is proposed which is obtained by the combination of the observational study, theoretical study and numerical study. This theory predicts the fractal-like structure and the horizontal angle of the node or the hollow of the convective cloud. It also predicts that the entrainment or the mixing occurs most strongly at the cloud top and that the tubulence is rather weak at the inner part and stronger at the outer part of the convective cloud. These results agree qualitatively with the observations. Further this theory is applied to parameterize the eddy viscosity terms in numerical simulations of the convective clouds. There strong dilution of cloud occurs at the outer part of the cloud, especially at the cloud top. Then water-vapour is radiated around the cloud and the conversion of the cloud-water to rain-water is suppressed. Therefore the decrease of the water-vapour remained in the domain is delayed compared with the simulation in which the eddy terms are not included (v_0=0). If the supply of the water-vapour and sensible heat are continued, it is possible to rise finally a strong convective cloud. It shows that when we study the collective motion of the convective clouds, the eddy terms play a very important role.

REFERENCES

1. Warner, J.,1970: The microstructure of cumulus cloud. Part . The nature of the Updraft. J.Atmos. Sci.,27,682-688. (Fig.2)

THREE-DIMENSIONAL CUMULUS ENTRAINMENT STUDIES

by

Terry L. Clark , Piotr K. Smolarkiewicz and William D. Hall

National Center for Atmospheric Research [1]
Boulder, Colorado 80307

1. INTRODUCTION

KLAASSEN and CLARK (1985), KC, presented two–dimensional simulations of an inversion capped cumulus using 5 and 10 m spatial resolutions. The geometry of their no–shear, symmetrically forced calculations resulted in two specific realizations for the cloud. One was a shooting tower which was unstable to asymmetric perturbations resulting in a leaning tower and the second was a bubbling cloud top which remained symmetric and resulted in a downdraft near the cloud top which penetrated into the cloud interior. KC found by intercomparing benchmark calculations with those where *all* evaporation was eliminated that the nodal structure remained essentially identical up to the time when this assumption directly affected the large scale dynamics. These results cast strong doubt on the hypothesis of cloud top instability as possed by SQUIRES (1958) that entrainment is thermodynamically driven by the evaporation of droplets into entrained environmental air. As in the general Rayleigh–Taylor instability entrainment appears to be driven by the inviscid production of cloud boundary vorticity and the resulting dynamic instabilities. The present simulations extend the work of KC by considering a cumulocongestus cloud evolving in a no–shear environment. Questions involving the effect of excluding vortex tilting and stretching terms as well as questions involving the inherent differences in geometry between two– and three–dimensions can be addressed. The special bifurcation reported by KC is not likely to occur in three–dimensions. Also, the cumulocongestus case allows one to address questions on the effect of entraiment in limiting the depth to which a cloud can grow. The differences in the type of cloud considered limit any intercomparisons between KC and the present simulations to basic physical processes.

The dynamics and thermodynamics are analyzed using kinetic energy,KE, and enstrophy budget analysis. The kinetic energy tends to emphasize the larger scales of motion whereas, since the vorticity tends to reside towards smaller scales, it emphasizes the smaller scales. Intercomparison of these two scalars gives us some indication of the degree of convergence that has been attained for the various resolutions. PALUCH (1979) type, conservative variable analysis is used to investigate environmental source levels of air entrained into the cloud. The acutal mechanism and/or path of mixing must be determined by other means.

2. MODEL

The anelastic non–hydrostatic Clark model is used with three interacting domains. The outermost domain is 16.8 × 16.8 × 21.0 km using 300 m resolution in all dimensions. The second and third domains are centered in the horizontal with their lowest level at $z = 2.1$ km near the top of the heated boundary layer. The surface heating used is comprised of a uniform 100 W/m^2 plus a localized Gaussian component of 100 W/m^2 to insure a domain centered cloud. This framework allows us to perform experiments using 100, 75, 50, 37.5 and 25 m resolution in the active cumulus region. The environmental conditions were taken from 19 July 1981 CCOPE and the strong conditional instability for this case is shown

in Fig. 1. All mean winds were put to death for these experiments in order to minimize complicating physical effects.

3. Results

Figs. 2 and 3 show the KE and enstrophy profiles at various times for the 50 m resolution experiment which clearly indicate the clouds vertical development. The kinetic energy becomes nearly constant with height in the main cloud region whereas the enstrophy shows considerable vertical development with values increasing with height. These differences can be attributed to the different scale selection of kinetic energy and enstrophy where the latter emphasizes smaller scales and the upper levels of the cloud is becoming more chaotic. The KE profiles for all of the experiments are similar to Fig. 2 indicating that a better resolution of the entrainment physics has had little affect on the large scale dynamics for this particular vigorous cloud. The enstrophy shows a considerable response to spatial resolution and even at 25 m we have no indication of convergence of solution. As resolution increases the enstrophy increases. Fig. 4 shows profiles of enstrophy at t=38 min for the 50, 37.5 and 25 m resolution experiments. There is a noticeable increase in the upper level enstrophy as a result of increased baroclinic production of vorticity with increasing resolution. The entrainment physics is still possibly not well resolved even at 25 m resolution.

Fig. 5 shows a Paluch diagram for the 25 m case. This figure shows that air at the level analyzed is comprised of moist adiabatic air and environmental air from below to 400 m above that level. Model field data analysis indicates that the environmental air is brought down the outside and then into the cloud in distorted ring vorticies. The scale of the vortex rings accounts for the difference between parcel mixing levels.

Fig.6 shows a 3-D perspective view of the 25 m cloud at t=39 min.

4.Conclusions

Our preliminary analysis indicates that the large scale motions are well resolved using 100 m resolution. The smaller scale motions are very much affected by increased resolution as indicated by the enstrophy analysis. The entrainment was never active enough to limit the depth of growth of this cloud to below its equilibrium level. Two–dimensional Cartesian (x-z) calculations, however, do allow entrainment to limit the clouds depth. The over emphasis of entrainment due to 2–D Cartesian geometry should be recognized.

The source of entrained environmental air for this cumulocongestus cloud simulation was typically from below to ,in some cases, 400 m above the level analyzed. The mechanism which leads to entrainment appears to be the inviscid production of cloud boundary vorticity similar to found by KC. This simulated data will be used in further studies of the character of the small scale dynamics.

5.References

KLAASSEN G. and T.L. CLARK 1985:Dynamics of the cloud-environment interface and entrainment in small cumuli:Two-dimensional simulations in the absence of ambient shear. J. Atmos. Sci.,42,2621-2642.

PALUCH I., 1979:The entrainment mechanism in Colorado cumuli. J. Atmos. Sci.,36,2467-2478.

SQUIRES P., 1958:Penetrative downdraughts in cumuli. Tellus,10,381-389.

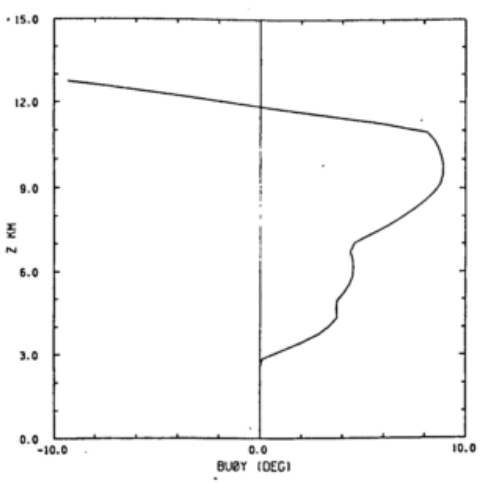


Fig.1 Parcel buoyancy versus height

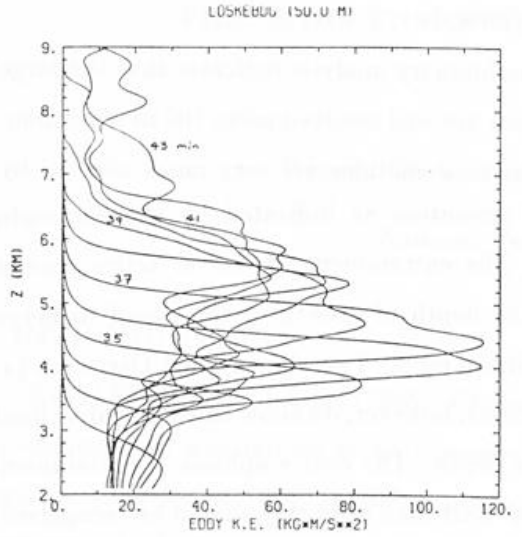


Fig.2 Kinetic energy vertical profiles from the 50 m experiment at various times.

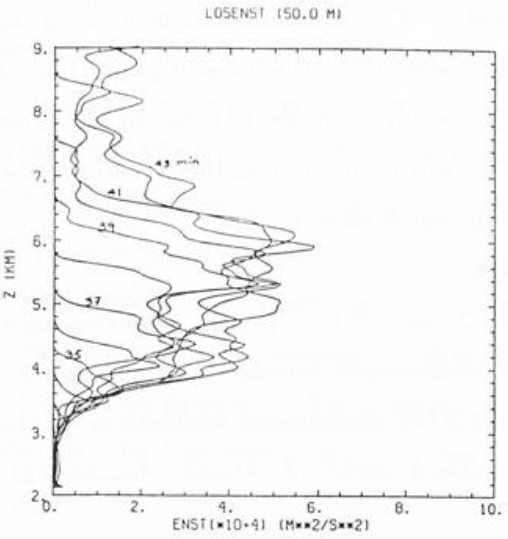


Fig.3 Enstrophy vertical profiles from the 50 m experiment at various times.

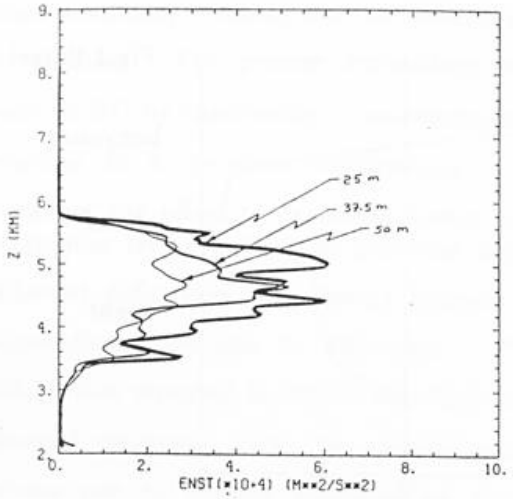


Fig.4 Vertical profiles of enstrophy at t= 38 min from the 50, 37.5 and 25 m cloud simulations.

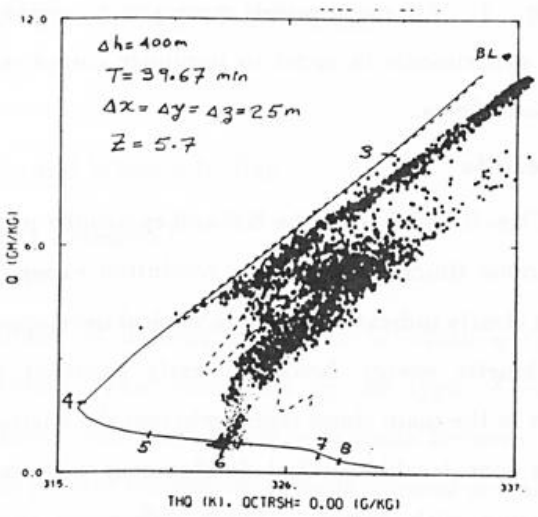


Fig.5 Paluch diagram at z=5.7 km from the 25 m simulation at t=39.67 min.

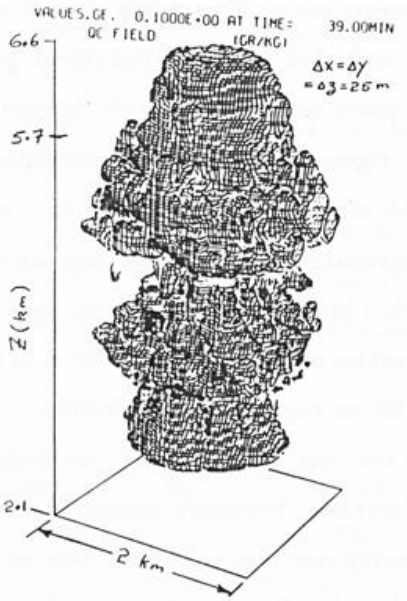


Fig.6 Cloud outline at t=39.0 min from the 25 m simulation.

[1] The National Center for Atmospheric Research is sponsored by the National Science Foundation

HETEROGENEOUS MIXING MEASUREMENTS IN SMALL NON-PRECIPITATING CUMULI

J.L. Brenguier

Direction de la Météorologie Nationale (EERM/CNRM)
31057 TOULOUSE Cedex FRANCE

1. INTRODUCTION

Experimental studies of the condensation process are based on measurements of the droplet spectra generally obtained with optical counters and particularly with the FSSP Knollenberg probe *. In such a counter, when two particles or more are simultaneously present in the beam, they are lost for the counting (coincidence losses). At the end of the droplet transit, a short delay is generated to allow for the processing. Particles crossing the beam during the delay, are also lost (dead-time losses). During a sampling period, two parameters are measured, the counted particle rate n_d and the activity A, the portion of time during wich the probe is active (transit times plus delays). Many empirical procedures have been proposed in the past to correct for coincidence and dead-time losses. They have been tested by laboratory simulations or computer simulations of the probe (Cerni, 1983; Baumgarder et al, 1985). By theoretical calculations of the relations between n_d, A and the actual particle rate n, it is possible to obtain a better estimate of the high droplet concentrations. A correction scheme is proposed, here, for the FSSP with a method for evaluating the homogeneity of the samples and the peak values of the droplet concentration in heterogeneous samples.

2. THEORETICAL ASPECTS

The statistical evaluation of the coincidence and dead-time losses in a retriggerable counter with delay is based on the hypothesis that the time interval between particle arrivals across the counter are exponentially distributed, i.e., that the droplets are randomly dispersed according to a Poisson distribution.

Droplets are coincident when their time interval is lower than their transit time τ across the laser beam of the probe. If τ is constant; the Laplace transform of the distributions of the coincident droplet series durations and of the time intervals between two successive series can be estimated. It is then possible to calculate the activity A and the counted particle rate n_d as functions of the actual particle rate n . For a retriggerable counter with delay, τ_d (Brenguier and Amodei, 1988):

$$\tau_d < \tau \begin{cases} n_d = nX \\ A = 1 - XX_d, \end{cases} \quad (1)$$

where $X = e^{-n\tau}$ and $X_d = e^{-n\tau_d}$,

$$\tau_d > \tau \begin{cases} n_d = nX/\big(1 + nX(\tau_d - \tau)\big), \\ A = 1 - X^2/\big(1 + nX(\tau_d - \tau)\big). \end{cases} \quad (2)$$

* FSSP: Forward Scattering Spectrometer Probe manufactured by PMS Inc. (Boulder, Colorado-USA)

In the FSSP, only droplets passing near the middle of the sampling tube (n_{d2}) are sized and they are followed by a long delay ($\tau_{d2} = 8.2\mu s$). The rest ($n_d - n_{d2} = n_{d1}$), about 80% is rapidly rejected and followed by a short delay ($\tau_{d1} = 2.2\mu s$). The proportion of accepted droplets n_{d2}/n_d is called the depth of field (DOF) fraction and is generally equal to 20%. Eq. 1 and 2 are, thus, combined to apply to the FSSP:

$$\frac{1}{n_d} = \frac{1-D}{n_{d1}} + \frac{D}{n_{d2}}, \qquad A = n_d\Big((1-D)\frac{A_1}{n_{d1}} + D\frac{A_2}{n_{d2}}\Big). \quad (3)$$

These relations are displayed on Fig.1 for $D = 20\%$. It appears that the activity, A, which is continuously increasing, is a better measured parameter to evaluate the actual particle rate, than the measured particle rate which reaches rapidly its maximum and gives ambiguous estimations at high droplet rates.

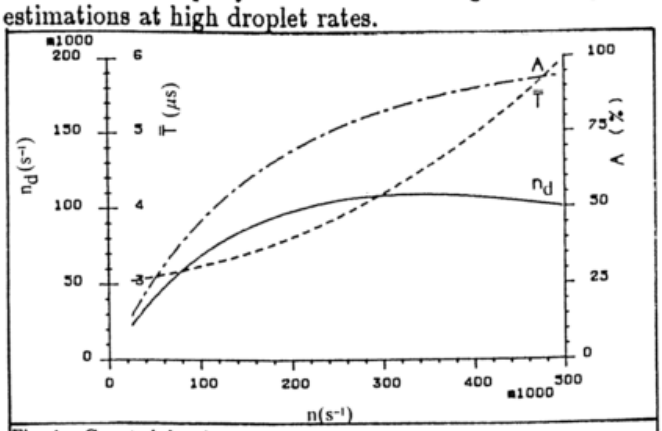


Fig. 1. Counted droplet rate, n_d, activity, A, and mean transit-time duration, $\overline{T} = A/n_d - \tau_d$, versus actual droplet rate, n.

3. CLOUD MEASUREMENTS

Measurements described here, have been performed with the Piper-Aztec of the Météorologie Nationale in 1984 (Chalon, 1987). Four levels where sampled in small non-precipitating cumuli with the FSSP set on range 0, with the velocity rejection. The size spectra where recorded at 5Hz while the activity A, the total strobe n_{d2} and the total reset $n_d = n_{d1} + n_{d2}$ where recorded at 1 Hz.

The measured activity A_m is slightly lower than the actual one. When a droplet enters the beam during the delay and leaves it during the reset duration ($\tau_r = 1.8\ \mu s$), the activity counter is not reactivated but the droplet is counted and followed by a short delay τ_{d1}. The measured activity A_m is expressed, then, as a function of the actual droplet rate n as (for details, see Brenguier, 1988):

$$A_m = A - n_d X \tau_r (1 - X_{d1}) \quad (4)$$

Fig. 2 shows the total reset n_d as a function of the measured activity A_m compared to the predicted values given by Eq. 3 and 4, for different values of τ. The observed values are in agreement with the theory for transit times τ fluctuating from $2\mu s$ to $3.5\mu s$.

The values of the actual droplet rate n and of the corresponding transit time τ are iteratively estimated by adjusting the measured parameters n_d and A_m to the predicted ones. To select the homogeneous samples, where the mean density is constant, an homogeneity factor, H_m, has been deduced from the 5 sub-countings of the droplet spectra, n_{mi}. The associated droplet rate (after D.O.F. and velocity rejection) is roughly proportional to n_d except for fluctuations of the rejection criteria which are studied in Brenguier (1988). The homogeneity is expressed as:

$$H_m = \frac{n_m}{5\ \max(n_{mi})} \quad \text{where} \quad n_m = \sum_{i=1}^{5} n_{mi}. \tag{5}$$

The estimated values of τ are inversely proportional to the aircraft velocity, v_a, in the range 58 $m\ s^{-1}$ to 80 $m\ s^{-1}$, with a slope $\pi\ d/4$ equal to 150 μm, i.e. $d = 190\ \mu m$. This is in agreement with the values measured on our FSSP, which are slowly increasing from $160\mu m$ in the middle of the DOF to $220\mu m$ at the limits of the sensible area. The difference between $\pi d/4\ v_a$ and the estimated value of τ is due to a lengthening of the transit-time in the amplifiers and depends on the droplet diameter. Laboratory tests of the probe give an estimate of this lengthening and the transit-time can, then, be calculated by:

$$\tau = \pi\ d/4\ v_a + (0.03\ \overline{\phi} + 0.035)\ 10^{-6} \tag{6}$$

where $\overline{\phi}$ is the mean diameter of the droplet spectrum.

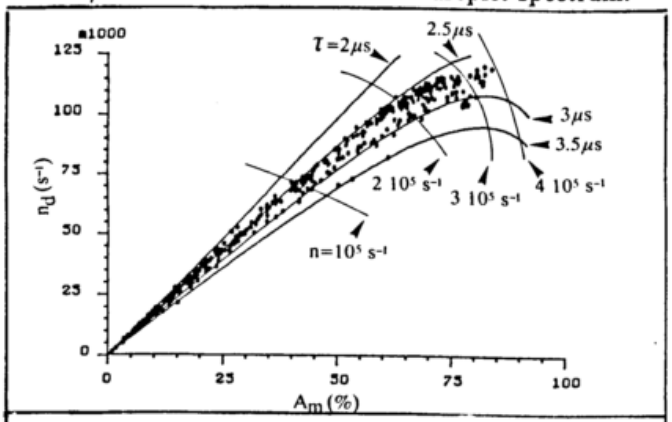


Fig. 2. n_d versus measured activity, A_m.

4. CORRECTION PROCEDURE

In 1981, Baumgardner proposed an empirical formula to estimate the actual droplet rate:

$$n = \frac{n_d}{1 - m\ A} \tag{7}$$

where m ranges between 0.5 and 0.8.

Eq. 3 and 4 give the limit of m at low droplet rates:

$$\lim_{n \to 0} m = \frac{(1-D)\tau + D\tau_{d2}}{\tau + \tau_d}, \quad \text{where } \tau_d = (1-D)\tau_{d1} + D\tau_{d2} \tag{8}$$

The correction factor m is estimated from the data points corresponding to the homogeneous samples:

$$m = 1/A_m(1 - n_d/n) \tag{9}$$

It is compared to the predicted values on Fig. 3. The lower m value in our FSSP is between 0.62 and 0.63, but it increases rapidly from 0.7 at $A_m \approx 0.50$ to 0.8 at $A_m \approx 0.80$.

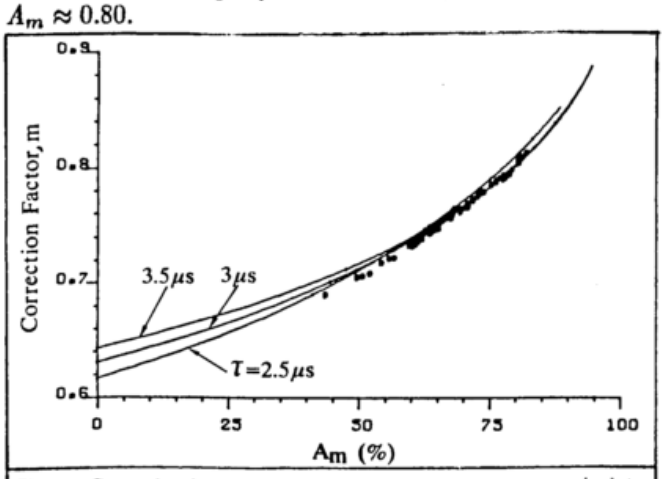


Fig. 3. Correction factor, m, versus A_m for homogeneous sample data.

The proposed correction scheme is based on the comparison of the measured and predicted values of the mean transit duration of the coincident droplet series:

$$\overline{T} = A_m/n_d - \tau_d \tag{10}$$

In an heterogeneous sample, this mean duration is the weighted average of the local values while n_d and A are the sum of the sub-values. This parameter is displayed on Fig. 4 as a function of the measured activity. Homogeneous sample values lie along the predicted curve while heterogeneous samples have values higher than the predicted one. This result is reasonable because the Poisson distribution is the random distribution which minimizes the probability of coincidence. The actual droplet rate is then estimated by calculating the individual droplet transit-time τ from the aircraft velocity and the measured mean droplet diameter (Eq. 6) and by iteratively comparing the measured values of $\overline{T}$ to the values deduced from Eq. 3 and 4, where D is the measured value of the DOF ratio.

At low activity, inaccurate estimations of $\overline{T}$ are lower than the minimum predicted value and n is estimated by comparing the measured to the predicted activity.

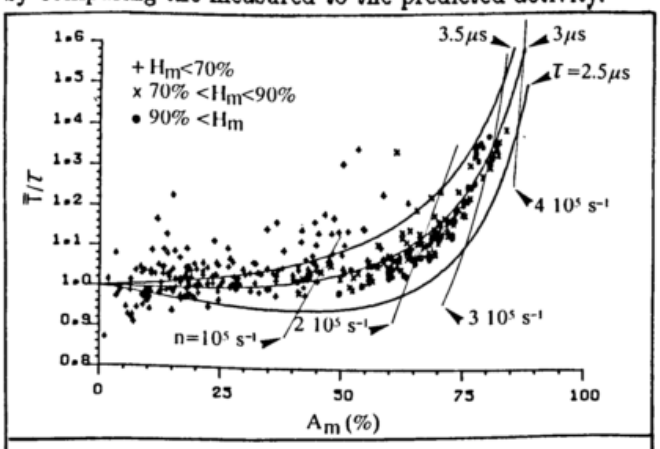


Fig. 4. Normalized mean transit-time duration, $\overline{T}/\tau$, versus A_m.

Fig. 5 shows the measured droplet rate (a) as a function of the static pressure compared to the droplet rate corrected with Eq. 9 (b) and with the results of the proposed correction scheme (c). The measured droplet rate is limited to 120 000 s^{-1}; values up to 250 000 s^{-1} are obtained from Eq. 9, while values as high as 4 10^5 s^{-1} are estimated with the proposed scheme. The total sensible lenght of the laser beam measured in the laboratory is approximately 14 mm. With a beam diameter $\approx$ 190 μm, the sampled volume at an aircraft velocity of 75 m s^{-1}, is then 200 cm^{-3}. With estimated droplet rates between 3 10^5 s^{-1} and 4 10^5 s^{-1} the droplet concentration ranges between 1500 cm^{-3} and 2000 cm^{-3}. These concentrations, covering a range of droplet diameters between 2 μm and 20 μm, are very high compared to the currently measured values. Relations (1) and (2) have been tested in our laboratory with a random pulse generator (Brenguier, 1988) and confirm the measured values of the characteristic times of our FSSP: τ, τ_{d1} and τ_{d2}. This agreement is reflected on Fig. 4, where data points follow the predicted behavior. For these reasons, we are confident on the high concentration estimations. However, by this procedure, we estimate the probability of coincidence and the related concentration for droplets randomly dispersed according to a Poisson distribution. The high values can be interpreted as cloud regions where the droplets are not randomly distributed but organized in clusters, where the local probability of coincidence is much higher.

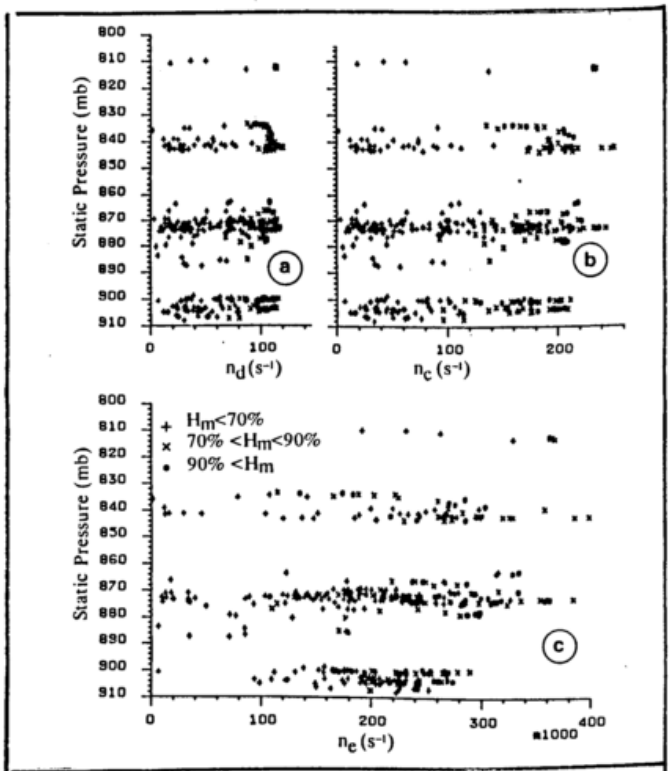


Fig. 5. Droplet rate vertical distribution, measured, n_d, corrected by Eq.9, n_c, and estimated by the proposed scheme, n_e.

5. HETEROGENEOUS SAMPLES

By using the mean transit duration to estimate the actual droplet rate, we have supposed that the heterogeneous samples are partly made of cloudy homogeneous regions, the rest being clear of droplet. The ratio of the measured activity to the predicted one is then equivalent to the evaluation of the homogeneity obtained with the 5 Hz sub-countings (Eq. 5), except that it applies at any scale. These parameters are compared on Fig. 6 which shows a good correlation between them. Estimated values equal to 1 correspond to values of $\overline{T}$ lower than the minimum predicted one (activity < 0.25). Both these parameters being completely independent, this result corroborates the proposed correction scheme.

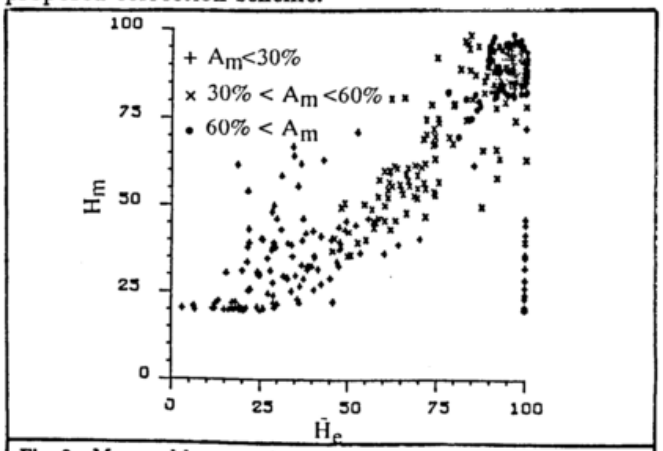


Fig. 6. Measured homogeneity, H_m, versus estimated homogeneity, H_e.

6. CONCLUSION

A new method has been proposed to correct the coincidence and dead-time losses in the FSSP. By adjusting the measured data to the predicted values of two independent parameters (n_d and A), it is possible to estimate high droplet rates for which the correction factor is important ($n_d/n \approx 3$).

The estimated values of the concentration are very high ($\approx$ 2000 cm^{-3}) compared to the values measured in the past. The method is also powerful to estimate the homogeneity of the samples. Thus it appears that 1 second samples, with a low concentration (low values of n_d and A) are in fact very heterogeneous (high value of the mean transit duration). These regions are better described as a succession of cloudy patches inserted in clear air. This observation is confirmed by the fluctuations of the droplet counts measured at an higher rate (5 Hz).

The method is based on the evaluation of the probability of coincidence refered to as a Poisson distribution. The very high values of the concentration shows that droplets are probably distributed in space less uniformly than provided by this ideal distribution.

REFERENCES

Baumgardner, D.,W. Strapp and J. Dye, 1985: Evaluation of the Forward Scattering Spectrometer Probe. Part II: Corrections for coincidence and dead-time losses. *J. Atmos. Oceanic. Technol.*, **2**, 626–632.

Brenguier, J.L. and L. Amodei, 1988: Coincidence and dead-time corrections for the particle counters. Submitted to *J. Atmos. Oceanic. Technol.*.

Brenguier, J.L.,1988: High concentration measurements with an FSSP. Submitted to *J. Atmos. Oceanic. Technol.*.

Chalon, J.P., 1987: Landes-Fronts 84, une expérience d étude des bandes convectives associées aux systemes frontaux. *La Météorologie* VII, 7-23.

Cerni, T.A., 1983: Determination of the size and concentration of cloud drops with an FSSP. *J. Climate Appl. Meteor.*,**22**, 1346–1355.

Dye, J.E. and D. Baumgardner, 1984: Evaluation of the Forward Scatterring Spectrometer Probe. Part I: Electronic and optical studies. *J. Atmos. Oceanic. Technol.*,**1**, 329–344.

THE CASE FOR SUBGRID-SCALE CONDENSATION IN NUMERICAL CLOUD MODELS

Frank B. Lipps and Richard S. Hemler

Geophysical Fluid Dynamics Laboratory/NOAA
Princeton, New Jersey, USA

1. INTRODUCTION

Recent calculations have been carried out simulating both mid-latitude and tropical convection using a three-dimensional numerical cloud model with a Kessler-type warm rain bulk cloud physics. Inside of clouds, where condensation is taking place, conservation of equivalent potential temperature θ_e is assumed for the subgrid-scale turbulence parameterization. In clear air, conservation of virtual potential temperature θ_v is assumed. Due to these different forms of turbulent mixing in clear and cloudy air, subgrid-scale condensation SGC occurs just below cloud base with resultant latent heat release. For both shallow and deep convection, this low level heating produces a more uniform vertical velocity maximum with time and maintains the cloud over a longer lifetime. For shallow convection, the rain reaching the ground is increased significantly.

2. THE SUBGRID-SCALE CONDENSATION

The formulation of the numerical model is similar to that given in Lipps and Hemler (1982, 1986a). In this section we describe the subgrid-scale turbulence parameterization which includes the subgrid-scale condensation SGC. The SGC was not present in earlier models due to an inconsistent treatment of the turbulent mixing of cloud water q_c. In the current model, prognostic equations are solved for the water vapor mixing ratio q_v and for the total q which is the sum of water vapor q_v and cloud water q_c. As in the earlier models, prognostic equations are solved for the rain water q_r and the potential temperature θ.

The role of the SGC can be seen by examining the vertical subgrid-scale fluxes $\rho_o\overline{w'q'}$ for the total q and $\rho_o\overline{w'q_v'}$ for the water vapor q_v. Following Lipps (1977), these fluxes are obtained from the subgrid-scale turbulence equations:

$$0 = -\frac{2}{3}E\frac{\partial q}{\partial z} - \frac{c_s}{\Delta}E^{1/2}\overline{w'q'} \qquad (1)$$

$$0 = -\frac{2}{3}E\frac{\partial q_v}{\partial z} - \overline{w'C_d'} - \frac{c_s}{\Delta}E^{1/2}\overline{w'q_v'} \qquad (2)$$

where c_s is a constant, $\Delta=(\Delta x\cdot\Delta y\cdot\Delta z)^{1/3}$, E is the subgrid-scale kinetic energy and $\overline{w'C_d'}$ is a subgrid-scale correlation associated with the condensation C_d. Compared with the treatment in Lipps (1977), gravitational buoyancy terms have been neglected in (1) and (2). The eddy diffusivity K_h is defined by

$$K_h = \frac{2}{3}\frac{\Delta}{c_s}E^{1/2} \qquad (3)$$

so that we may write

$$-\rho_o\overline{w'q'} = \rho_o K_h\frac{\partial q}{\partial z} \qquad (4)$$

$$-\rho_o\overline{w'q_v'} = \rho_o K_h\left(\frac{\partial q_v}{\partial z} + \left(\frac{2}{3}E\right)^{-1}\overline{w'C_d'}\right) \qquad (5)$$

where ρ_o is the base state density.

The equation for $\overline{w'C_d'}$ is obtained as in Lipps (1977):

$$\overline{w'C_d'} = \frac{2}{3}E\frac{f}{(1+\beta\gamma)}\left(\beta\frac{\partial\theta}{\partial z} - \frac{\partial q_{vs}}{\partial z}\right) \qquad (6)$$

where q_{vs} is the saturation water vapor mixing ratio and f is a parameter to indicate whether the particular grid point is in cloudy or clear air. Inside of clouds f=1, in clear air f=0, and near a cloud edge f is a fraction as described below. The parameters β and γ are specified as in Appendix A of Lipps and Hemler (1982):

$$\beta = \frac{L\,q_{vs}\,(1 + 1.608\,q_{vs})}{R_v\,T_o\,\theta_o}, \quad \gamma = \frac{L}{c_p\pi_o} \qquad (7)$$

Here L is the latent heat of vaporization, c_p is the specific heat of dry air, R_v is the gas constant for water vapor, and T_o, θ_o and π_o are the base state temperature, potential temperature and Exner pressure function.

The numerical grid is staggered in the vertical as shown in Fig. 1. Here we assume the cloud base is between the two grid points where θ, q_v, q and q_c are evaluated. The vertical velocity w and the correlation $\overline{w'C_d'}$ are evaluated at intermediate grid points. Note that in the cloud $q_v=q_{vs}$ and outside the cloud $q_{vs}-q_v > 0$ and $q_c=0$. The value of f near cloud base is given by

$$f = \frac{q_c}{(q_{vs} - q_v) + q_c} \qquad (8)$$

where q_c is evaluated at the upper grid point inside the cloud and $(q_{vs}-q_v)$ is given for the lower grid point below cloud base.

For the point below cloud base shown in Fig. 1, $q=q_v$ since $q_c=0$ there. The prognostic equations for q and q_v are different at this point, however, primarily because the forms of $-\rho_o\overline{w'q'}$ and $-\rho_o\overline{w'q_v'}$ are different as indicated by equations (4) and (5). In order to allow $q=q_v$ at this point, we must add the subgrid-scale condensation SGC term in the q_v-prognostic equation. The requirement $q=q_v$ gives for SGC:

$$\rho_o SGC = \frac{\rho_o\, w\, q_c}{\Delta z} - \frac{\rho_o\, K_h\, q_c}{(\Delta z)^2} + \frac{\rho_o\, K_h}{(\Delta z)} \cdot \left(\frac{2}{3} E\right)^{-1} \overline{w'C_d'} \qquad (9)$$

where Δz is the vertical grid interval. The first two terms on the right are small numerical truncation effects. The primary contribution to SGC is through the third term which involves $\overline{w'C_d'}$. Using (6) for $\overline{w'C_d'}$ we find approximately:

$$\rho_o\, SGC \cong \frac{\rho_o\, K_h}{(\Delta z)} \frac{f}{(1+\beta\gamma)} \left(\beta \frac{\partial \theta}{\partial z} - \frac{\partial q_{vs}}{\partial z}\right) \qquad (10)$$

where f is evaluated from (8).

Thus $\overline{w'C_d'}$ plays a key role in the turbulence parameterization of moist convection. Inside of cloud, where equivalent potential temperature θ_e is conserved, the vertical fluxes $\rho_o\overline{w'\theta'}$ and $\rho_o\overline{w'q_v'}$ are specified by (A14) and (A15) of Lipps and Hemler (1982). Both of these vertical fluxes involve $\overline{w'C_d'}$ as given by equation (6) above. In clear air, where $\overline{w'C_d'} = 0$, both fluxes are downgradient in θ and q_v respectively.

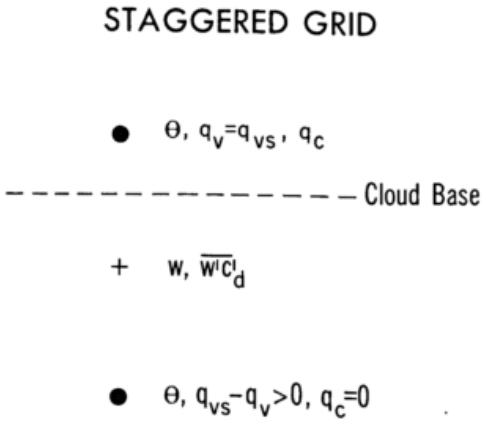


Fig. 1 The staggered grid in the vertical. Variables θ, q, q_v and q_c are evaluated at the dark points and w and $\overline{w'C_d'}$ are evaluated at the cross point. Dashed line is cloud base. See text.

3. MODEL CALCULATIONS

Three-dimensional numerical calculations have been carried out to simulate the deep moist convection observed in the central United States on 22 May 1976 (Ogura and Liou, 1980).

Four-hour simulations were performed for a model domain of 96 km in the east-west direction, 32 km in the north-south direction, and a vertical depth of 17 km. The horizontal and vertical grid lengths were 1 km and 0.5 km respectively. Open lateral boundary conditions were applied on the east and west boundaries and periodicity was assumed for the north and south boundaries. The convection was initiated with a warm bubble which resulted in a strong initial cell and secondary gust front outflows. These gust fronts initiated more realistic convection which had a squall line configuration in the north-south direction after 2.5 hours into the simulation.

In Fig. 2 is shown the maximum vertical velocity W with time for the calculation with the subgrid-scale condensation SGC (solid curve) and for the calculation without SGC (dashed curve). With SGC, it is seen that the vertical velocity of the first cell is maintained with time, and furthermore, a second major cell develops at 90 min which is stronger than any comparable cell in the calculation without SGC. After two hours, the two calculations are much more similar in appearance; however, the maximum vertical velocity remains somewhat larger for the simulation with SGC included.

In Fig. 3 is plotted the volume-mean, density-weighted condensation rates for the two calculations for the first hour of the simulation. The solid curve, for the calculation with SGC, indicates that the condensation did not decrease nearly as rapidly with time after the first cell developed. This result is consistent with

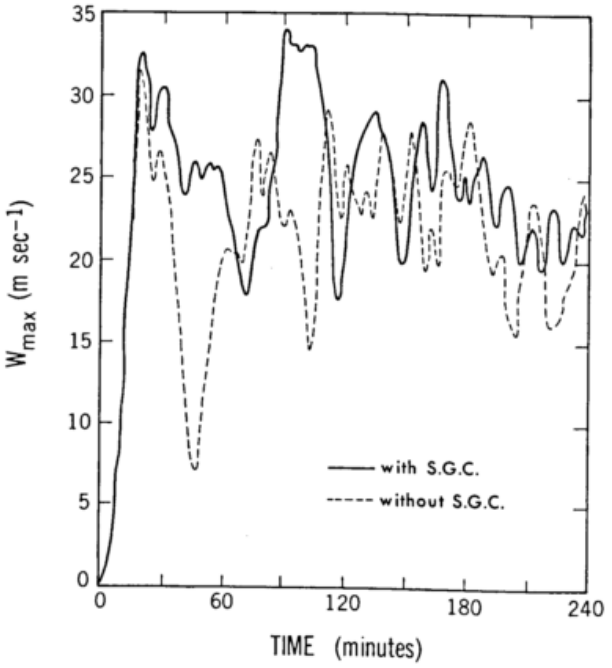


Fig. 2 Variation of maximum vertical velocity W with time for deep continental convection. Solid curve has SGC included. Dashed curve does not have SGC.

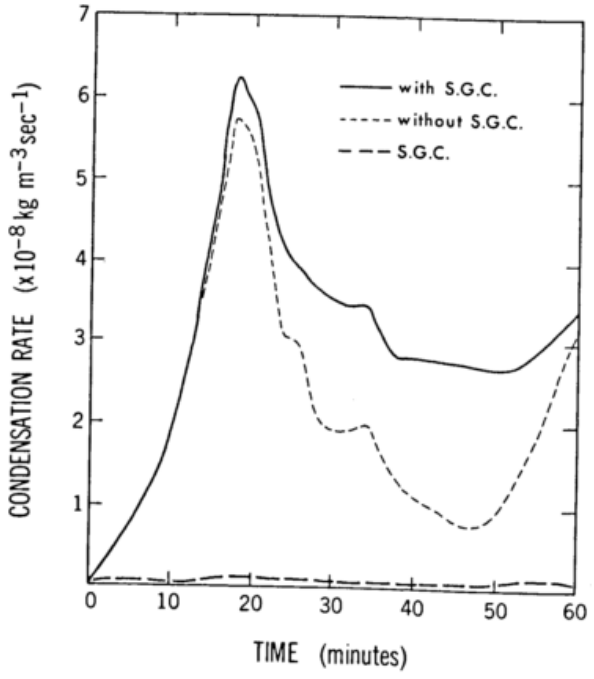


Fig. 3 Volume-mean, density-weighted condensation rate with time for deep continental convection. Solid curve has SGC included. Dashed curve does not have SGC. Long-dashed curve is that volume-mean ρ_0 SGC.

the maintenance of strong vertical velocity for the first cell as seen in Fig. 2. The long-dashed curve in Fig. 3 is for the volume-mean ρ_0 SGC. Although the SGC is at least an order of magnitude smaller than the total condensation, it is seen that its inclusion in the model has an important effect on the dynamics of the convection.

The SGC has been included in the shallow GATE simulations described by Lipps and Hemler (1986b). The increased values of maximum vertical velocity and of volume-mean condensation noted above were also found for the shallow GATE convection. In general, it appears that shallow convection is more sensitive to the inclusion of SGC. The rainfall reaching the ocean surface was slightly more than a factor of three larger for the simulation with SGC included. These values of precipitation are much closer to the observed rainfall rates.

REFERENCES

Lipps, F.B., 1977: A study of turbulence parameterization in a cloud model. J. Atmos. Sci., 34, 1751-1772.

Lipps, F.B., and R.S. Hemler, 1982: A scale analysis of deep moist convection and some related numerical calculations. J. Atmos. Sci., 39, 2192-2210.

_____, and _____, 1986a: Numerical simulation of deep tropical convection associated with large-scale convergence. J. Atmos. Sci., 43, 1796-1816.

_____, and _____, 1986b: Numerical modelling of a line of towering cumulus on Day 226 of GATE. WMO Weather Modification Research Programme. Report of the International Cloud modelling Workshop/Conference, WMO/TD-No. 139, pp. 187-191.

Ogura, Y., and M.-T. Liou, 1980: The structure of a midlatitude squall line: A case study. J. Atmos. Sci., 37, 553-567.

THE EFFECT OF TURBULENCE ON THE COLLECTION OF CLOUD DROPS: A STOCHASTIC MODEL

Gerhard Reuter

McGill University, Montreal

1. INTRODUCTION

Turbulent motions in convective clouds affect the collision-coalescence of water droplets via two different mechanisms. The first mechanism results from the fact that drops of different sizes respond with different inertia to a fluctuating turbulent velocity field. DE ALMEIDA (1979) modelled the effect of turbulent drag on the collection process. He found that the contribution of turbulent drag collection is dramatic for drops of sizes 10-30 μm.

A second mechanism affecting the coalescence of drops in turbulent air is active for drops having the same or different sizes. This mechanism is related to the eddy structure of a turbulent velocity field. At a given time, cloud drops can be contained in two spatially separated eddies. At a later stage, it might happen that these two eddies overlap and this might result in collision and merging of some of the drops in these eddies. This mechanism has been modelled by REUTER et al. (1988). The turbulent collection kernel can be computed with this stochastic model which is based on stochastic differential equations.

In this paper we will show the results of the growth of a cloud droplet population affected by gravitational collection and coalescence caused by overlapping eddies in turbulent air. The collection equation is solved by a very economical numerical scheme (EYRE et al., 1988) and the collection kernel is approximated with the stochastic model of REUTER et al. (1988).

2. MODEL DESCRIPTION

The classical kinetic (coagulation) equation is used to model the collision-coalescence among a population of cloud droplets. The dynamics of the collection process is contained in the collection kernel the form of which will be discussed later. The kinetic equation is solved using the numerical scheme of EYRE et al. (1988). This scheme is very economical as it makes use of adaptive mesh grading. The mass spectrum of droplets (ranging several orders of magnitude) is mapped to the interval (-1,1). The solution function is then approximated using a linear combination of cubic splines. The positions of the nodal points are allowed to move and are chosen optimally at regular time intervals. The optimization is performed by distributing the nodal points equally with respect to the arc lengths of the approximate solution function. Collocation reduces the problem to one of solving a system of ODE's for the expansion coefficients.

The collection kernel is computed using the stochastic model of REUTER et al. (1988). In addition to gravitational collection, the kernel is also affected by the probability of coalescence due to overlapping of turbulent eddies. The model is based on stochastic differential equations that govern the relative motion of two drops. The turbulence causes a random fluctuation to the relative droplet velocities. The magnitude of these random perturbations is related to the turbulent eddy diffusion coefficient. A detailed description of the model assumptions, the finite difference scheme and sample results are presented

in REUTER et al. (1988).

To solve the collection problem efficiently, we prefer to have an analytic formula for the collection kernel $K(r, R, \varepsilon)$ for a given pair of drops with radii r and R in a turbulent air characterized by an energy dissipation rate ε. The following formula approximates the values of K computed with the stochastic model.

$$K(r,R,\varepsilon) = \pi(r+R)^2 \, E(r,R) \cdot \{ \left| u(r) - u(R) \right| + 3{,}25 \, \varepsilon^{1/3} (r+R)^{1/3} \}$$

Here u(r) is the terminal fall speed of a drop with radius r and E(r,R) is the collection efficiency. The coalescence efficiencies are assumed to be unity. The collision efficiencies are specified with the formula of SCOTT and CHEN (1976) which provides a close fit for the Shafrir-Neiburger and Davis-Sartor collision efficiencies.

3. RESULTS

Numerical experiments are made with an exponential initial volume distribution. The liquid water content is 1 gm^{-3} and the mean initial radius is 25 μm. Figure 1 shows the evolution of the droplet population in turbulent air with ε = 1000 $cm^2 s^{-3}$. The results are given in terms of the droplet mass distribution $\tilde{N}(r)$ which is defined such that $\tilde{N}(r)dr$ equals the mass of droplets per unit volume of air with radii in the interval dr. (The mass distribution emphasizes the larger droplets more so than the usual size spectrum.) The curves show that the development of the coalescence is rather slow even for strong turbulence. If the turbulence is weaker, the growth is slower (Figure 2). Yet the results certainly show that overlapping of turbulent eddies contributes to the collection process.

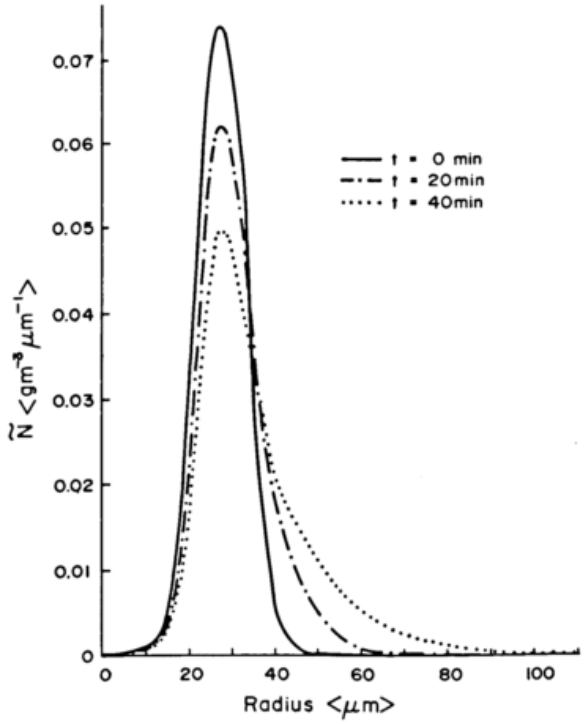


FIG. 1. Evolution of droplet mass distribution in turbulent air (ε = 1000 $cm^2 s^{-3}$).

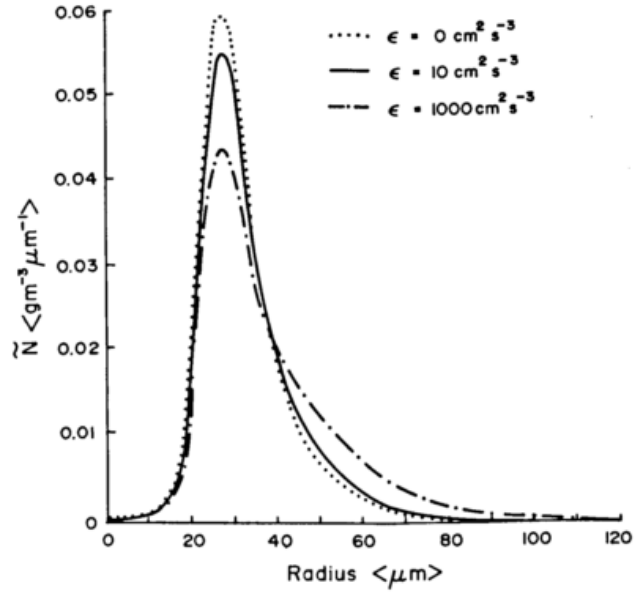


FIG. 2. Comparison of droplet mass distribution at 40 min for different values of turbulent energy dissipation rate ε.

4. REFERENCES

DE ALMEIDA, F.C.: The effects of small-scale turbulent motions on the growth of a cloud droplet spectrum. J. Atmos. Sci. 36 (1979), p. 1557-1563.

EYRE, D.; WRIGHT, C.J.; REUTER, G.W.: Spline--collocation with adaptive mesh grading for solving the stochastic collection equation. J. Comput. Physics (1988), in press.

REUTER, G.W.; DE VILLIERS, R.; YAVIN, Y.: The collection kernel for two falling cloud drops subjected to random perturbations in a turbulent air flow: A stochastic model. J. Atmos. Sci. (1988), in press.

SCOTT, W.T.; CHEN, C.-Y.: Approximate formulas fitted to the Davis-Sartor-Schafrir-Neiburger droplet collision efficiency calculations. J. Atmos. Sci. 27 (1970), p. 698-700.

THE EFFECT OF ICE PHYSICAL PROCESSES ON THE NUMERICAL SIMULATION OF WEST AFRICAN SQUALL LINES.

William D. Hall
National Center for Atmospheric Research[1]
Boulder, Colorado, U.S.A.

Jean Philippe Lafore
Etablissment d'Etudes et de Recherches Meteorologiques
CNRM/Toulouse, France

Tropical squall lines are a subject of great research interest since they provide a significant amount of precipitation to many areas in the tropics. An important question that is often asked is "What is the role of ice microphysical processes on tropical squall line mesoscale structures and precipitation characteristics?" The present study is inspired by the works of Dudhia, Moncrieff and So (1987), DMS, and Lafore and Moncrieff (1988), LM. These authors successfully quantified the observed dynamical structure of a fast moving (15 m/sec) tropical squall line using a two-dimensional model applied to a West African environment.

The present paper describes two-dimensional nested grid numerical experiments of Clark's 3–D cloud model. Calculations were performed to study the thermodynamic and dynamic response of tropical squall lines by ice phase microphysical processes. These simulations incorporate temperature and velocity profiles observed in the COPT 1981 field experiment. The numerical framework consists of three nested models with increasing resolution moving at a constant speed to insure that the squall line remains in the center of the highest resolution domain. Results of two numerical experiments with and without ice are presented. In the ice case the Koenig and Murray (1976) ice parameterization with a high seeding nucleation rate is applied; in the no ice or warm rain case the parameterization of Kessler described by Clark (1979). In both experiments the model is initialized as in DMS and LM with a cooling rate of $-0.01°C$ /sec maintained for ten minutes over a 12 km region above the ground with a depth of 3 km. The observed June 22, 1981 presquall sounding is used.

Figures 1 through 4 show the cloud water, rain water, buoyancy, and horizontal velocity perturbation fields for the warm rain case after 200 minutes of integration. Figures 5 through 10 show the cloud water, rain water, cloud ice, graupel, bouyancy, and horizontal velocity perturbation for the ice case at the same time. In both cases the propagation speed of the squall lines are similar (15 m/sec) and the convective region of the squall lines are characterized by a quasi-periodic sequence of convective cells moving at about one half the speed of the gust front. These convective cells first form on or near the gust front, move into the trailing region, and eventually dissipate. There are, however, marked differences between these two experiments. In the warm rain case, the density current is much stronger and concentrated near the ground. This resulted in larger vertical velocities near the gust front at this time. These differences were caused by the greater amount of rain in the warm rain case reaching ground and consequently more evaporative cooling resulted. The larger rain amount is a direct result of the Kessler parameterization. In both cases the autoconversion of cloud water to rain water occured when the cloud water exceeded 1 gram per cubic meter. When competing ice processes were present, less cloud water was available for autoconversion to occur. The second striking difference is the character of the rear inflow jet 75 to 120 km. behind the squall line. LM presented an hydrostatic argument which explained that the rear inflow jet is caused by horizontal gradients of buoyancy behind the squall line. In the ice case the combined differences of latent heat release into the upper levels, melting below 4.5 km., and precipitation loading resulted in a different the buoyancy field. This caused in the rear inflow jet position for the ice case to be at a higher level than in the warm rain case.

In these preliminary results it has been shown that the inclusion of simple ice phase microphysics can significantly alter the simulated results of a fast moving tropical squall line. Many other features such

[1]The National Center for Atmospheric Research is sponsored by the National Science Foundation

as the mesoscale accent within the stratiform anvil region, maintanance of the density current, and the resulting precipitation distribution of the simulated squall lines are currently being studied. Simulation results will be compared with the COPT field studies of Chong et. al. (1987).

REFERENCES:

CHONG, M., AMAYENC, P., SCIALOM, G., TESTUD, J.: A tropical squall line observed during the COPT 81 experiment in West Africa. Part 1: Kinematic structure inferred from dual-doppler radar data. *Mon. Wea. Rev.* **115** (1987) 670–694.

CLARK, T. L.: Numerical simulations with a three-dimensional cloud model: lateral boundary condition experiments and multicellular severe storm simulations. *J. Atmos. Sci.***36** (1977) 2191–2215.

DUDHIA, J., Moncrieff, M. W., and So, D. W. K.: The two-dimensional dynamics of West African squall lines. *Quart. J. Roy. Meteor. Soc.*, **113** (1987) 121–146.

KOENIG, L. R. and MURRAY, F. W.: Ice-Bering cumulus cloud evolution: numerical simulation and general comparison against obervations, *J. Appl. Meteor.*, **15** (1976) 747–762.

LAFORE, J. P. and MONCRIEFF, M. W.: A numerical investigation of the scale-interaction between a tropical squall line and its environment., submitted to *J. Atmos. Sci.* (1988)

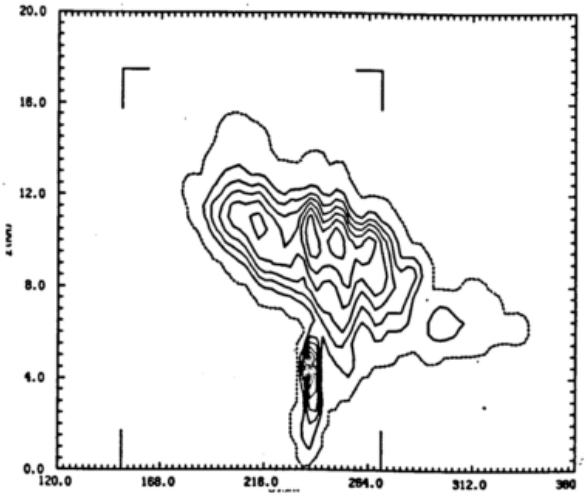


Figure 1. Cloud water field
Contour interval .5 g/kg

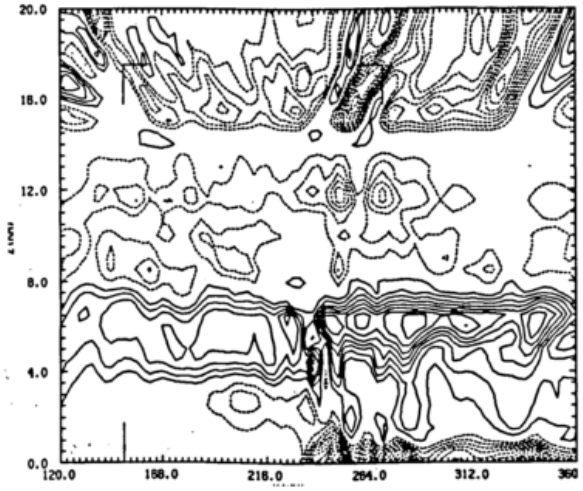


Figure 3. Bouyancy field
Contour interval .5° C

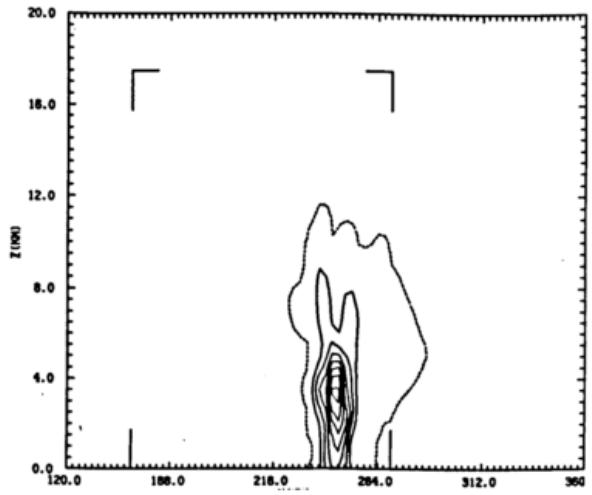


Figure 2. Rain water field
Contour interval .5 g/kg

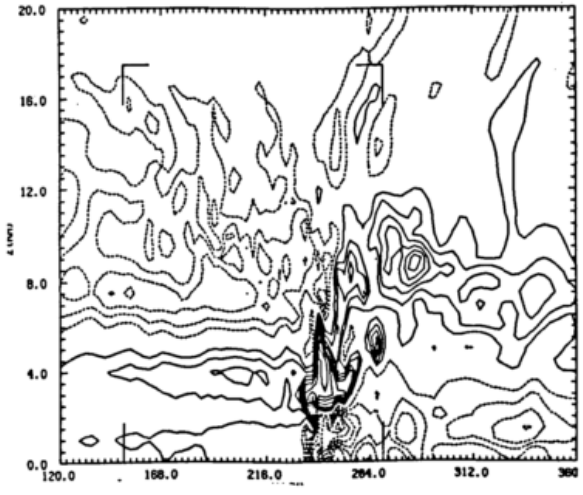


Figure 4. Horizontal velocity perturbation field
Contour interval 2 m/sec.

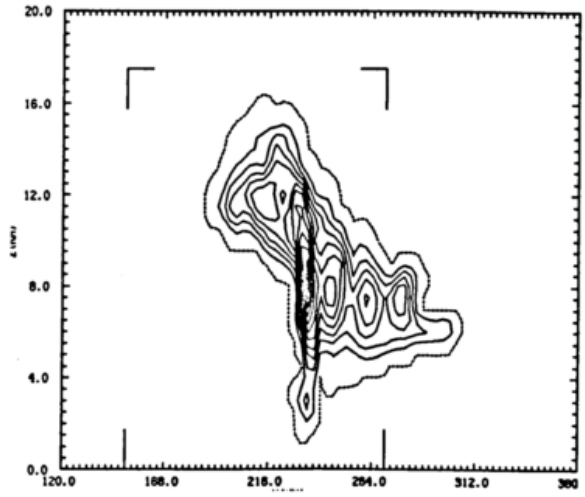


Figure 5. Cloud water field
Contour interval .5 g/kg

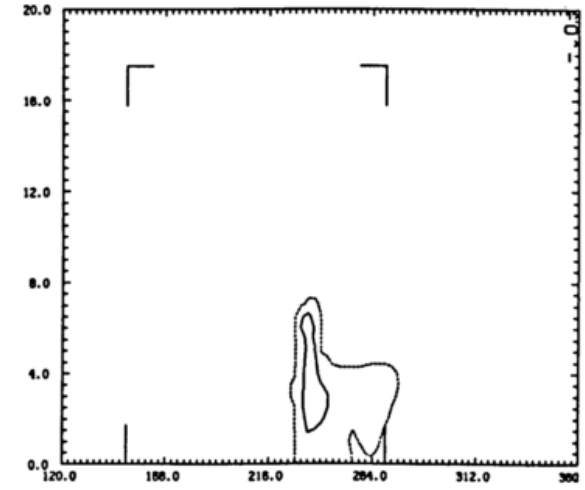


Figure 6. Rain water field
Contour interval .5 g/kg

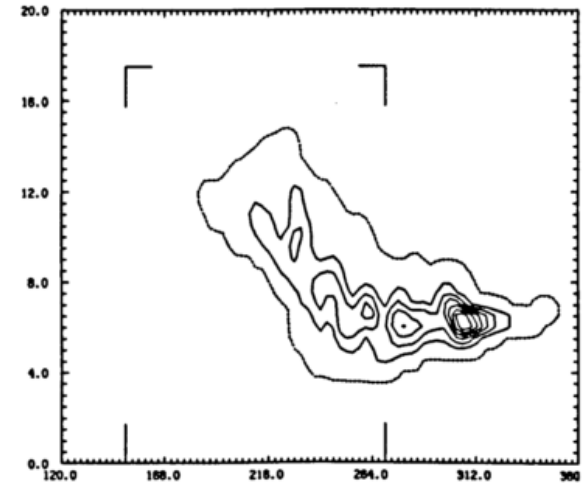


Figure 7. Cloud ice field
Contour interval .5 g/kg

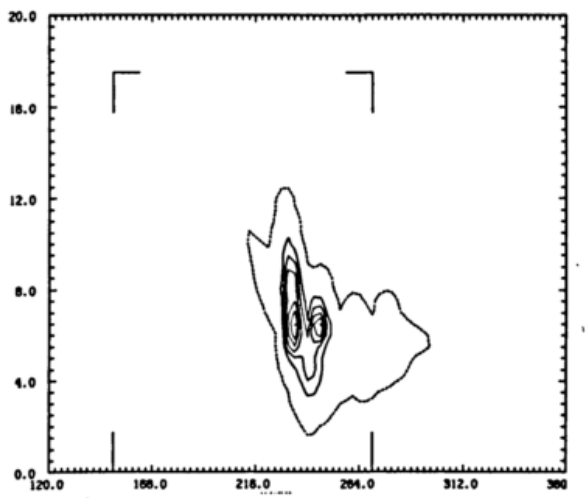


Figure 8. Graupel field
Contour interval .5 g/kg

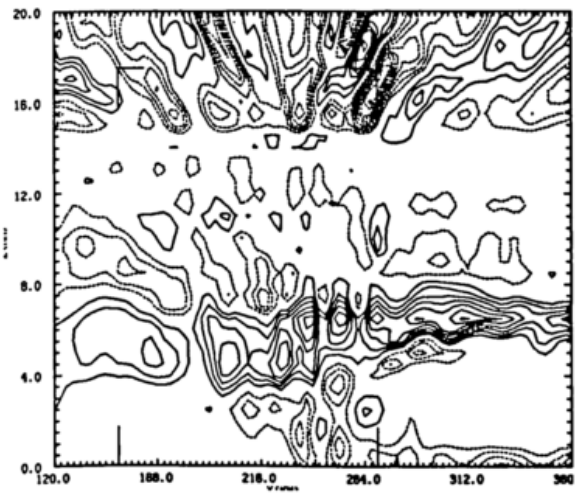


Figure 9. Bouyancy field
Contour interval .5° C

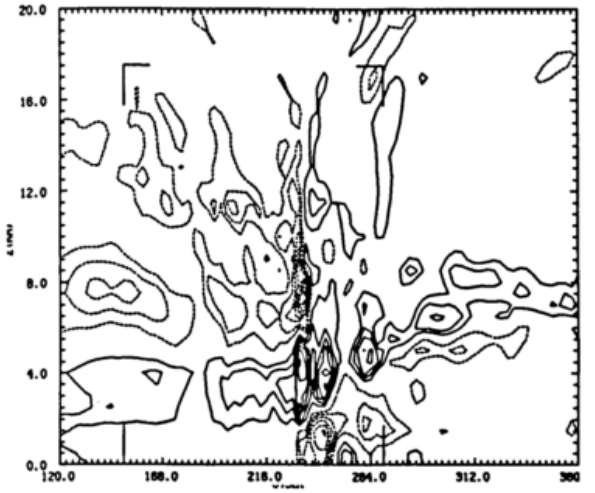


Figure10. Horizontal velocity perturbation field
Contour interval 2 m/sec

NUMERICAL SIMULATION OF MICROPHYSICAL PROCESSES IN CUMULONIMBUS

Hu Zhijin He Gaunfang

Academy of Meteorological Science,

State Meteorological Administration,Beijing,China

1. INTRODUCTION

Parameterized model is widely used for simulation of the microphysical processes in clouds. In its usual form the parameter N_0 for particle size distribution is assumed to be constant, then the number concentrations of particles (N) are diagnosed from their mass content(Q),This assumption does not agree with the observations and causes serious errors in simulation of some important microphysical processes, For example the ice nucleation and multiplication have small effect on Qi, but increace Ni significantly. According to Bergeron theory Ni have large effect on precipitation efficiency. It makes the basis of weather modification. A parameterized model prognosing both Q and N of various water particles(two-parameter model) had been established by Hu (1984) for stratiform clouds. Here a two-parameter model is presented for simulating the microphysical processes in cumulonimbus clouds. All the water substance is divided into 6 categories: vapor(V), clod drops (C), rain drops(r), ice crystals(i), graupels(g), and Hailstones(h). Hails have diameter larger than D*=0.5 cm.The partical size distrbutions are assumed to be the Gama functions. A truncated Gama function is assumed for hails: $N(D)=0$ for $D<D_*$: $N(D)=N_*\exp(-\lambda D)$, for $D\geqslant D_*$. Both parameters No and λ are variables and can be deduced from N and Q. For example, $N_h=N_{0h}\exp(-\lambda_h D_*)\lambda_h^{-1}$, $Q_h=6N_h\lambda_h^{-3}A_{mh}\left[1+\lambda_h D_*+\frac{1}{2}(\lambda_h D_*)^2+\frac{1}{6}(\lambda_h D_*)^3\right]$ where $A_{mh}=0.471\ \mathrm{gcm^{-3}}$.

2. MICROPHYSICAL EQUATIONS

Every microphysical variable, such as Qv,Qc,Qr,Qi,Qg,Qh,Nr,Ni,Ng,Nh, can be prognosed with consideration of advection, turburent, fall-out and sources:

$$\frac{\partial M}{\partial t}=-(W-V_m)\frac{\partial M}{\partial z}+k\frac{\partial^2 M}{\partial z^2}-E(M-M_*)+\frac{M}{\rho}\frac{\partial \rho V_m}{\partial z}+\frac{\delta M}{\delta t}$$

26 kinds of microprocesses are considered including condensation (deposition, evaporation) of cloud, ice, rain, graupel and hail (Svc, SVi, Svr, Svg, Svh); collection of cloud droplets by ice, rain, graupel and hail (Cci, Ccr, Ccg, Cch); collection of rain by ice, graupel and hail (Cri,Crg,Crh); collection of ice by rain, graupel and hail (Cir,Cig,Cih); ice nucleation and multiplication(Pvi,Pci); autoconversions

of cloud-rain, ice-graupel and graupel-hail (Acr, Aig, Agh); freezing of rain (Mrg); melting of ice, graupel and hail (Mir, Mgr, Mhr); ice-ice and rain-rain collection (Cii, Crr).

The source term for each variable are as following :

$$\frac{\delta Q_v}{\delta t} = -S_{vv} - S_{vr} - S_{vi} - S_{vg} - S_{vh} - NP_{vi}Q_{vo}$$

$$\frac{\delta Q_c}{\delta t} = S_{vv} - C_{ci} - C_{cr} - C_{cg} - C_{ch} - A_{cr} - NP_{ci}Q_{co}$$

$$\begin{cases} \dfrac{\delta Q_r}{\delta t} = S_{vr} + C_{cr} + A_{cr} + M_{gr} + M_{ir} + M_{hr} - M_{rg} \\ \text{If} \quad T \geqslant 273\ K, + C_{rh} + C_{ir} \\ \text{if} \quad T < 273\ K, - C_{rh} - C_{rg} - C_{ri} \quad (kk=0) \\ \qquad\qquad - C_{hr} + C_{gh} - C_{rg} - C_{ri} \quad (kk=1) \end{cases}$$

$$\begin{cases} \dfrac{\delta N_r}{\delta t} = NS_{vr} + A_{cr}/Q_{co} + NM_{gr} + NM_{ir} \\ \qquad\qquad - NM_{rg} + NC_{rr} \\ \text{If} \quad T \geqslant 273\ K, (M_{hr} + C_{rh})/Q_{ho} \\ \text{if} \quad T < 273\ K, - NC_{rh} - NC_{rg} - NC_{ri} \quad (kk=0) \\ \qquad - NC_{rh} - NC_{rg} - NC_{ri} - (C_{gh} + C_{rh} \\ \qquad\qquad - C_{wh})/Q_{ho} \quad (kk=1) \end{cases}$$

$$\frac{\delta Q_i}{\delta t} = S_{vi} + C_{ci} - C_{ir} - M_{ir} - C_{ig} - C_{ih} - A_{ig} + NP_{vi}Q_{vo} + NP_{ci}Q_{co}$$

$$\frac{\delta N_i}{\delta t} = NS_{vi} - NC_{ir} - NM_{ir} - NC_{ig} - NC_{ih} - NA_{ig} + NP_{vi} + NP_{ci} + NC_{ii}$$

$$\begin{cases} \dfrac{\delta Q_g}{\delta t} = S_{rg} + C_{cg} + C_{ig} - C_{gh} + A_{ig} + M_{rg} \\ \qquad\qquad - M_{gr} - A_{gh} \\ \text{If} \quad T < 273\ k, \quad + C_{rg} + C_{ir} + C_{ri} \end{cases}$$

$$\begin{cases} \dfrac{\delta N_g}{\delta t} = NS_{vg} + NA_{ig} - NA_{gh} + NM_{rg} - NM_{gr} \\ \qquad\qquad - NC_{gh} \\ \text{If} \quad T < 273\ k \quad + N_{oir} \end{cases}$$

$$\begin{cases} \dfrac{\delta \theta_h}{\delta t} = S_{rh} + C_{ih} + C_{gh} - M_{hr} + A_{gh} \\ \text{If} \quad T < 273\ K \quad + C_{gh} + C_{rh} \quad (kk=0) \\ \qquad\qquad + C_{wh} \quad (kk=1) \end{cases}$$

$$\frac{\delta N_h}{\delta t} = NA_{gh} - NM_{hr}$$

where Pvi, NPvi, Mgr, NMgr.etc. is the mass transformation rate and the number change rate due to ice nucleation, graupel melting, etc. respectively. Qvo, Qco, Qro, Qho is the initial mass of a nucleated ice, secondary ice, autoconverted raindrop and sheded water drop from hail respectively. Cwh is the threshold value of hail wet growth rate , which determines whether the hail is in dry growth regime (kk=0) or in wet growth regime (kk=1). Fc is a parameter describing the "width of cloud droplet spectrum" and prognosed:

$$\frac{\partial F_c}{\partial t} = -V\frac{\partial F_c}{\partial z} + k\frac{\partial^2 F_c}{\partial z^2} + \frac{\delta F_c}{\delta t}$$

$$\frac{\delta F_c}{\delta t} = \rho^2 Q_c^2 [120\,\rho Q_c + 1.6\,N_c/D_c]^{-1}$$

Equations for Svr, Svg, Cci, Ccr, Ccg, Cii, Crr, Pvi, Pci, Acr have little change from that of our stratiform cloud model (Hu 1984). The others cannot be presented here due to limitation of space.

3. CASE STUDIES

Some case studies had been done by this model combined with an one-dimensional time-dependent cumulus model after Hu (1985). Here are 3 typical examples.

3.1 SMALL CUMULONIMBUS CASE

The simulated convective cloud looked like a Cu cong. cloud, but transformed into Ci not. cloud after precipitation. The cloud top reached 7.7 km (-12^0C) . Calculated characteristics agreed with observations. It was shown that preci-

pitation formed through the warm-rain process (Acr, Ccr). Some of the raindrops freezed into graupel by collection of ice(Cri). Ice multiplicated by Hallett-Mossop process (Pci). Its rate increased with the accumulation of rain and graupel in the upper part of the cloud and reached 500 $(kg.s)^{-1}$, being 100 times as much as ice nucleation rate in this cloud.

3.2 HAILSTORM CASE

Simulated hailstorm was associated with a severe squall line. The height of radar echo was 9--12 km. Rainfall was weak, Max. accumulated hailstones on the ground was $436/m^2$ with mean diameter of 9 mm. Model output agreed with observation in many aspects. It showed that the updraft was strong (22 m/s). Raindrops formed through the warm-rain process in the upper part of cloud, where temperature was -24-- $-32^{o}C$. They freezed into graupel (Mrg) rapidly . The Bergeron process (Svi.Aig) was not effective. Graupel grew by riming (Ccg) and were suspended in the upper part of cloud. Only a few of them grew into hailstones and fell on the ground.Most of them evaporated with the dissipation of cloud, so the precipitation efficiency was very low.

3.3 TERRENTIAL RAIN CASE

Simulated "75.8" terrential rain brought very great loses. The max. rainfall of 7 Aug. 1975 was 1005 mm. Calculation showed that the updraft was not strong (about 4--5 m/s), and precipitation could fall out through the updraft. Rain was prolonged during the simulated time(144 min) and its total amount reached 186 mm. Precipitation formed mainly by the warm-rain process. Graupels formed by Cri and grew by Ccg,Crg. Ice formed mainly due to Pci . The Bergeron process (Svi, Aig) was not important. Water drops sheded from hailstones had some influence on precipitation development. The interactions of updraft, cloud and precipitation caused a periodic variation in their development with a period of 0.5--1 hour.

4. REFERENCES

Hu Zhiiin. Yan Caifan: A Numericai Model of Stratiform Clouds, Papers Presented at 9th International Cloud Physics Conference, Tallinn.USSR.1984.

Hu Zhiiin, Yan Caifan : The Effect of Salt-seeding in Warm Cumulus With Various Lifetimes. Papers Presented at 4th WMO Conference On Weather Modification, Honolulu, USA., WMO Report 2 . p 353, 1985.

A COMPARATIVE STUDY OF TWO MICROPHYSICAL SCHEMES IN A β MESOSCALE MODEL

Evelyne Richard and Nadine Chaumerliac

LAMP/OPGC, Clermont-Ferrand

1. INTRODUCTION

Two sets of microphysical parameterizations are compared under various orographic situations in a β mesoscale model (NICKERSON et al. 1986). One is the currently used Kessler parameterization (KESSLER, 1969) and the other is based upon Berry and Reinhardt's work (1973). These two parameterizations will be quoted as "K" and "BR" in the following. In both cases, cloud water mixing ratio is diagnosed from the predicted value of q (equal to the sum of the vapor mixing ratio , q_v and the cloud water mixing ratio, q_{cw}). In case of supersaturation, q_v is set equal to the saturated vapor mixing ratio and excess vapor is converted into cloud water.

There are two main differences in the K and BR parameterizations : the number of predictive variables and the assumed raindrop spectrum. For the K parameterization, the rainwater mixing ratio (q_{rw}) is predicted assuming a Marshall Palmer distribution function of the raindrops. For BR parameterization, both rainwater mixing ratio and total number concentration of raindrops (N_{rw}) are predictive variables, the raindrops being assumed lognormally distributed. In both cases, the processes taken into account are autoconversion, accretion, evaporation and sedimentation. Self collection of the raindrops is only considered in case of BR parameterization.

The autoconversion rates are expressed as

$$\left.\frac{d\rho_a q_{rw}}{dt}\right]_{aut.\ K} = \begin{cases} 10^{-3}\ (\rho_a q_{cw} - 0.5\ 10^{-3}) \\ 0 \end{cases}$$

if $\rho_a q_{cw} > 0.5$ g/m³

if not

$$\left.\frac{d\rho_a q_{rw}}{dt}\right]_{aut.\ BR} = \alpha(\rho_a q_{cw})^2$$

where ρ_a is the air density and α a function of the cloud spectrum parameters. Setting the dispersion parameter to 0.2775 (typical maritime value), α is equal to 0.66 for a mean cloud diameter of 35 μm (BR1) and to 0.15 for a diameter of 27.5 μm (BR2).

Note that in contrast to Kessler's rate, BR's rates allow for production of rainwater even for low cloud water contents. For cloud water content greater than 0.5 g/m³, Kessler's rate is in between the two Berry's rates.

2. MOUNTAIN WAVE SIMULATIONS

In order to compare the two parameterisations, the model is first run over an idealized two-dimensional bell-shaped mountain. A two layer atmosphere is considered with a lower layer of constant lapse rate up to 8 km and a isothermal layer aloft. The initial horizontal wind speed is uniformly 20 m/s and the relative humidity is 80 % below 3 km.

In Fig. 1 are plotted the vertical cross sections of the cloud water mixing ratios, rainwater mixing ratios and precipitations rates, computed after 6 hours of simulation for the Kessler parameterization and the BR1 and BR2 parameterizations. Cloud water fields are similar for K and BR2 while BR1 cloud is weaker due to more efficient conversion of cloud into rain. Precipitation intensities are also comparable between K and BR2 but the precipitation extends further downwind in case of BR2. It should be noticed that the corresponding rain water mixing ratios are quite different, BR2 rainwater mixing ratio being twice as

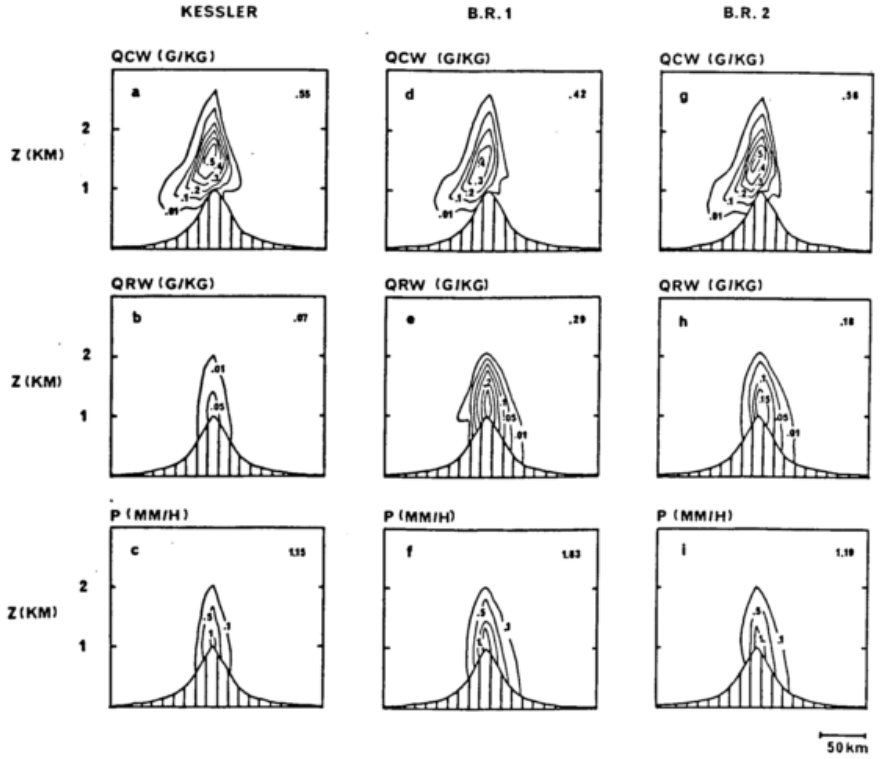


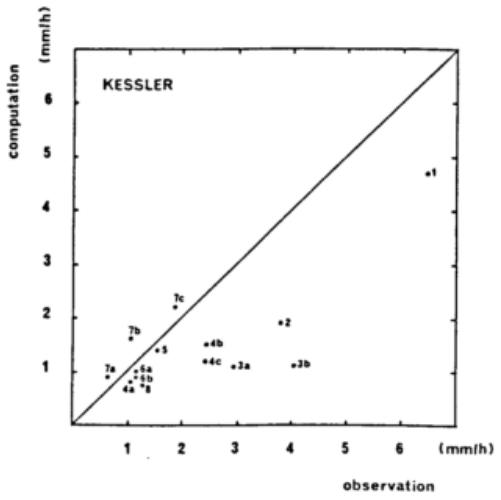
Fig. 1
Vertical cross sections of cloud water mixing ratio (q_{cw}), rain water mixing ratio (q_{rw}) and precipitation rate (P)

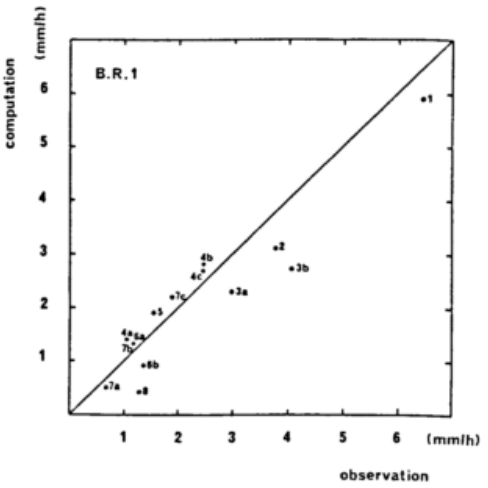
large as in the K case. This indicates that rainwater is carried by much larger drops in K than in BR2. As a consequence, the BR2 raindrops are more sensitive to the wind drift. This should be related to the differences already noticed in the spatial distribution of the precipitation.

3. FEEDER SEEDER CLOUD SIMULATIONS

The model is now applied to the problem of orographic enhancement of rain via the feeder seeder mechanism. This precipitation enhancement results from the washout of small cloud droplets orographically generated by raindrops originating in higher level large scale clouds. A detailed study of 14 seeding events observed in Southern Wales was presented by HILL et al, 1981. These observational data have been used to initialize the model (sounding, seeding precipitation rate) and to control the quality of the results (precipitation enhancement). Further details can be found in RICHARD et al, 1987. All the 14 cases have been run with the K, BR1, BR2 parameterizations. Fig. 2 shows for each parameterization a case by case comparison between observations and computations. BR1 and BR2 give much better agreement than K and BR1 is slightly better than BR2. Looking more closely at the results, cases 1 to 4, characterized by strong low level wind speed are systematically underestimated by the K parameterization. Fig. 3 gives the precipitation enhancements as a function of the low level wind speeds for the observations and the results from the three parameterizations. The four data sets have been fitted by a curve, $\Delta P = av^{k}$. All the parameterizations slightly underestimate the orographic enhancement in the range 10 to 20 m/s. For stronger wind values, there are larger discrepancies between the observations and the K results. Only the BR parameterizations are able to reproduce the observed dependency of the orographic enhancement on the low level wind speed.

This is mainly due to the fact that Kessler's parameterization produces fewer but larger raindrops than BR's parameterization. The K raindrops falling faster are then less advected and the residence time of the seeding raindrops within the cloud is shorter especially in case of strong low level winds.





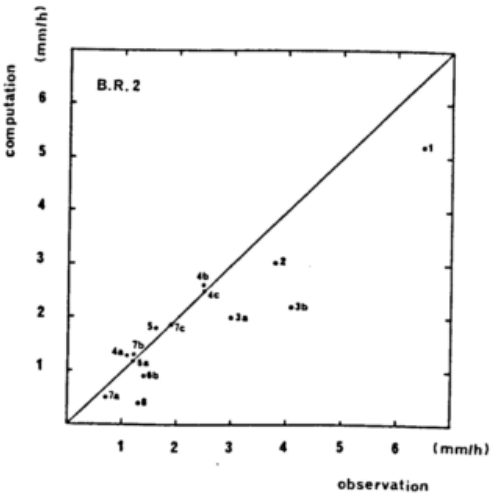


Fig. 2 : Computed orographic precipitation enhancement versus the observed one for 14 cases.

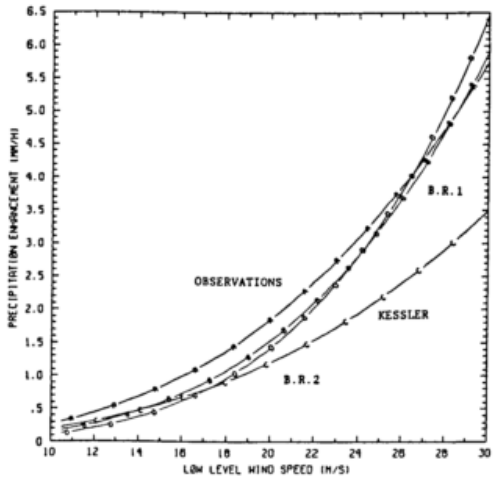


Fig. 3 : Variation of the orographic precipitation enhancement as a function of the mean low level wind speed

4. REFERENCES

BERRY E.X.; REINHARDT R.L. : Modeling of condensation and collection within clouds D.R.I. Phys. Sci. Pub.,Nr 16 (1973) Univ. of Nevada

HILL F.F.; BROWNING K.A.; BADER M.J. : Radar and raingage observations of orographic rain over South Wales. Quart. J. Roy. Meteor. Soc., Nr 107 (1981), P. 643-670

KESSLER E. : On the distribution and continuity of water substance in atmospheric circulations. Meteorological Monographs, 10-32 (1969) A.M.S., Boston

NICKERSON E.C.; RICHARD E.; ROSSET R.; SMITH D.R. : The numerical simulation of clouds, rain and airflow over the Vosges and Black Forest Mountains, a meso-β model with parameterized microphysics. Mon. Wea. Rev., Nr. 114 (1986), P 398-414.

RICHARD E.; CHAUMERLIAC N.; MAHFOUF J.F.; NICKERSON E.C. : Numerical simulation of orographic enhancement of rain with a mesoscale model. J. Clim. Appl. Meteor., Nr 26 (1987), P. 661-669.

GENERALIZED MICROPHYSICS SCHEME FOR USE IN MESOSCALE/CLOUD MODELS

Gregory J. Tripoli

University of Wisconsin, Dept. of Meteorology, Madison, WI 53715

Piotr J. Flatau and William R. Cotton

Dept. of Atmospheric Science, Colorado State University, Fort Collins, CO 80523

1 Introduction

Because of the diverse applications we envision for the Colorado State University RAMS (Regional Atmospheric Modeling System), we demand greater skill and flexibility in the formulation of our microphysics parameterization scheme than in previous models. Historically the number of categories of hydrometeors and the size-distribution of hydrometeors assumed in a model vary from investigator to investigator. It seems that there is an almost infinite set of combinations of particle size distributions, particles size-distribution parameters, and hydrometeor types that can be formulated in a cloud model. However, we have found that it is possible to express almost any microphysical parameterization in a common or universal format. We have therefore developed a *generalized* bulk microphysics parameterization capable of meeting our current and projected needs with a high degree of flexibility.

In spite of the apparent diversity of distributions used to define the sizes of particles in atmospheric polidisperse media (Feingold and Levin,1986) (clouds, fogs, aerosols), only a few basic types arise. These are: the generalized gamma distribution and its special cases, the normal distribution and its transformation (e.g., log-normal), the constant distribution, and the power law. The generalized or *modified gamma* function defines special cases: gamma, truncated gamma, Marshall-Palmer (or exponential), Khrgian-Mazin, doubly truncated Marshall-Palmer, and half-normal. Even the normal and log-normal size spectra can be linked to some of the mathematics arising in generalized gamma calculations.

In a bulk microphysical scheme, several water and(or) aerosol classes are usually considered, such as cloud droplets, rain, aggregates, graupel, pristine ice, aerosol, and hail. The cloud water may be taken as constant size, but rain drops are usually considered to be distributed according to Marshall-Palmer or log-normal functions. Assuming a constant size precludes coagulation (same terminal velocity), and it may be advantageous to consider cloud particles as distributed according to some other probability function, such as gamma.

The optimum distribution chosen for a given water class will depend on the application. For instance, a distribution which describes averaged terminal velocity well, may not be suitable to describe the radiative properties of the medium. In most cases, there is no universal physical principle behind the choice of the *hard-wired* distribution around which a given parameterization is usually built. Thus we would like to have the flexibility to switch fairly easily from one type of distribution to another.

The discretization of a continuous spectrum of liquid and frozen hydrometeors into arbitrary categories is another feature traditionally " hard wired" into bulk microphysics parameterizations. These categorizations are an attempt to include the gross characteristics of several identifiable ice and droplet habits into a cost-effective scheme. As with the choices of a distribution, the choice of discretization is not always universally applicable. We also would like to have the flexibility to easily redefine the properties and the number of hydrometeor categories.

The following paper summarizes methodology described more fully in Tripoli *et al.* (1988).

2 Size Spectra and Their Moments

2.1 Basic concepts

Several empirical formulas have been proposed for the spectra of various water categories. The spectral density $n(D)$ is defined such that $n(D)dD$ is the total number of particles, whose diameter is between D and $D+dD$, per unit volume of air. Hence

$$N_t = \int_0^D n(D)dD, \tag{1}$$

is the total concentration of particles of diameters smaller than D, per unit volume of air. To describe the particle size spectrum we choose the suitable probability density function (p.d.f) $f(D)$ defined on interval (D_{min}, D_{max}), with, most commonly, $D_{min} = 0$ and $D_{max} = \infty$. This p.d.f. is normalized to one, i.e.,

$$\int_0^\infty f(D)dD = 1. \tag{2}$$

In the development of a bulk parameterization scheme one is ultimately interested in the total mass or number density of the hydrometeors involved in a process, or in a numerical or mass weighted average of a quantity. For example, the total downward mass flux of water due to precipitation settling is obtained by integrating the mass flux of a single hydrometeor at each size over the whole distribution. Such an integration appears in the form:

$$\overline{g} = \int_{D_{min}}^{D_{max}} g(D)n(D)dD. \tag{3}$$

Normally, the function g exhibits the power law dependence,

$$g(D) = cD^p \tag{4}$$

where c and p are constants. In such case the problem reduces to finding generalized moment of the p.d.f. $f(D)$:

$$I(p) = \int_{D_{min}}^{D_{max}} D^p f(D)dD = D_n^p F(p). \tag{5}$$

Function F depends only on the distribution and the limits over which it is integrated. D_n is the *characteristic* diameter. In other words most of equations of the bulk parameterization schemes in use now (Cotton *et al.* , 1982; Lin *et al.*, 1983; Nickerson *et al.*, 1986) , can be written in one single and simple form:

$$\overline{g} = g(D_n)N_t F(p). \tag{6}$$

An implication of this result is that one can develop a universal scheme which can be applied to any one of several particle size-distribution functions.

One example of the moment is the water content, defined as

$$\rho_l = \int_{D_{min}}^{D_{max}} m(D)n(D)dD, \tag{7}$$

where ρ_l is the bulk water density and $m(D)$ the mass of a particle of diameter D. For spherical particles we have

$$m(D) = \frac{\pi}{6} D^3 \rho_w, \tag{8}$$

where ρ_w is density of the particle. From (8), (7) and (5):

$$\rho_l = \frac{\pi}{6} N_t I(3) = m(D_n) N_t F(3). \tag{9}$$

Now we have to specify functions $F(p)$ and characteristic diameter D_n.

2.2 Distributions

2.2.1 Generalized gamma distribution

A popular choice for a spectral density function to describe sizes of atmospheric particles is a generalized gamma function. Its definition is

$$f_{mg}(D) = \frac{c}{\Gamma(\nu)} \left(\frac{D}{D_n}\right)^{c\nu-1} \frac{1}{D_n} \exp\left[-\left(\frac{D}{D_n}\right)^c\right], \tag{10}$$

where D is diameter of particle. Constants ν and c define the *shape* of the distribution and with the *normalization* constant N_t the spectral density function is completely specified.

The p-moment of the generalized gamma distribution (10) is

$$I_{mg}(p) = \int_{D_{min}}^{D_{max}} D^p f_{mg}(D) dD = D_n^p F_{mg}(p), \tag{11}$$

where subscript mg stands for *modified gamma* and

$$F_{mg}(p) = \frac{\Gamma(\nu + p/c)}{\Gamma(\nu)}. \tag{12}$$

Thus the liquid water content for the modified gamma distribution is:

$$\rho_l = \frac{\pi}{6} N_t D_n^3 \rho_w \frac{\Gamma(\nu + 3/c)}{\Gamma(\nu)}. \tag{13}$$

The *gamma* distribution is obtained by setting $c = 1$ in all formulas in this section.

Table 1 summarizes the characteristics of seven specific distributions commonly used. The first five are special cases of the generalized gamma distribution. One of the the most commonly used distribution in atmospheric cloud physics is the Marshall-Palmer type wherein $c = 1$ and $\nu = 1$.

Distribution	Symbol	D_{min}	D_{max}	c	ν
Modified gamma	mg	0	∞	c	ν
Gamma	gam	0	∞	1	ν
Exponential (Marshall-Palmer)	MP	0	∞	1	1
Truncated Marshall-Palmer	tMP	D_{min}	D_{max}	1	1
Half-normal	hn	0	∞	2	1/2
Normal	nor	$-\infty$	∞	-	-
Log-normal	log	0	∞	-	-

Table 1: Summary of the size distributions and the shape parameters c and ν.

Name	Modified gamma	Log-normal
$F(p)$	$\Gamma(\nu + p/c)/\Gamma(\nu)$	$\exp(\sigma^2 p^2/2)$
D_{mean}	$\Gamma(\nu + 1/c)/\Gamma(\nu) D_n$	$\exp(\sigma^2/2) D_n$
D_{mode}	$(\nu - 1/c)^{1/c} D_n$	$\exp(-\sigma^2) D_n$
Water content q	$m(D_n) N_t \frac{\Gamma(\nu+3/c)}{\Gamma(\nu)}$	$m(D_n) N_t \exp(\frac{9\sigma^2}{2})$

Table 2: Special moments of size distributions

2.2.2 Normal distributions

The normal and log-normal distributions do not fit the family of gamma distributions. The general methodology for integration over the spectral density outlined above is entirely applicable however. The form of a normal distribution and log-normal distribution are respectively:

$$f_{nor}(D) = \frac{1}{\sqrt{2\pi}\sigma D} \exp\left[-\left(\frac{(D - D_n)}{\sqrt{2}\sigma}\right)^2\right], \quad D \in (-\infty, \infty), \tag{14}$$

and

$$f_{log}(D) = \frac{1}{\sqrt{2\pi}\sigma D} \exp\left[-\left(\frac{\ln(D/D_n)}{\sqrt{2}\sigma}\right)^2\right], \quad D \in (0, \infty). \tag{15}$$

The log-normal distribution is becoming widely used in bulk parameterizations. In the case of the log-normal distribution, $F(p)$ is simply defined:

$$F_{log}(p) = \exp\left(\frac{\sigma^2 p^2}{2}\right). \tag{16}$$

Characteristics of the family of normal distributions are also described in Table 1. Table 2 defines the function $F(p)$ for the modified gamma and log- normal distributions as functions of several common moments.

2.3 Example of bulk parameterization formula: Mass-weighted terminal velocity

We can not provide here details of the microphysics parameterization. A detailed technical report is being prepared Tripoli *et al.* (1988). As an example let us consider mass-weighted terminal velocity, given by

$$\overline{v}_i = \frac{1}{\overline{r}_i \rho_0} \int_{D_{min}}^{D_{max}} v_i(D_i) m_i(D_i) n(D_i) dD_i, \tag{17}$$

where i indicates one of several classes of hydrometeors in the model. After integration we obtain

$$\overline{v}_i = \frac{1}{\overline{r}_i \rho_0} v_i(D_{ni}) m_i(D_{ni}) N_{ti} F(p_{mi} + p_{vi}), \tag{18}$$

where p_{vi} and p_{mi} are powers of velocity- and mass-diameter dependence. Hence, we can change distributions by simply redefining F. The parameterization is written by forming a table of F(p) for each distribution function. Then the appropriate table is called, based on the desired form of the distribution.

All other processes such as: mass-diameter, density-diameter, vapor deposition, terminal velocities, coagulational growth (aggregation and collection) and nucleation are coded according to the same principle: determine power p, diagnose from the model characteristic diameter D_n and total concentration N_t, and find distribution-averaged quantities.

3 Hydrometeor classes and their interaction

Several different bulk microphysical parameterization schemes have been proposed in the literature, each dividing ice, water and aerosol into several assumed categories. In general, time dependent continuity equations are formed for the mass and in some cases there is a continuity equation for number concentration. In some log-normal-based predictive schemes, a third parameter is sometimes predicted. The water continuity equations are normally written in the form:

$$\frac{dr_i}{dt} = \sum_{j=1}^{N} CN_{j,i,i} - \sum_{j=1}^{N} CN_{i,j,i} + P_i \qquad (19)$$

and

$$\rho_o \frac{dN_i/\rho_o}{dt} = \sum_{j=1}^{N} NCN_{j,i,i} - \sum_{j=1}^{N} NCN_{i,j,i} + NP_i, \qquad (20)$$

where r_i and N_i are the mixing ratio and number concentration for category i, ρ_o is the air density, $CN_{l,m,n}$ designates the positive definite mixing ratio conversion tendency to category n resulting from the conversion of mass from hydrometeor category l to the category m, N is the number of categories, and P_i is the mixing ratio tendency of category i due to precipitation settling. NCN and NP are analogous tendencies for number concentrations. For mass continuity, it is required that $CN_{i,j,i} = CN_{i,j,j}$, although $NCN_{i,j,i} \neq NCN_{i,j,j}$.

The *art* of microphysical parameterization is found in the formulation of NCN and CN. Generally, a conversion tendency can be expressed in the form:

$$CN_{l,m,n} = H_{l,m,n}(CL_{l,m}, VD_{n,v}, ML_{n,k}, NU_{k,v}), \qquad (21)$$

where H is the arbitrary parameterization which is a function of several standard interaction terms. $CL_{l,m}$ is the collection of category l by category m, $VD_{n,v}$ is the vapor deposition (evaporation, or sublimation) of category n to the vapor category and $ML_{n,k}$ is the melting of category n into category k and $NU_{n,v}$ is nucleation of category n from vapor v.

Nucleation would be non-zero only when l is a vapor category and $m = k$ is a particular crystal category. The term may contain splintering, sorption/deposition, and phoretic effects. In some cases, nucleation tendency itself may depend on interaction terms. For instance, splintering will depend upon riming rate contained in $CL_{cloud,ice}$.

$VD_{n,v}$ and $ML_{n,k}$ are nonzero only if $m = v$ and $m = k$ respectively. The computed interaction term may or may not be used for the actual conversion tendency. For instance, the amount of rain collected by cloud water is not used as a tendency for the growth of cloud water, whereas the amount of cloud water collected by rain is used as loss to cloud water. On the other hand, both the amount of ice crystals collected by rain and the amount of rain collected by ice crystals may become a tendency for graupel. Hence the conversion term from category l to category m could be based on the interaction between l and a third category.

The conversion may also include such things as the arbitrary reclassification of a portion of the mass of one category to another. Auto-conversion of category l to another is typically expressed as a function of $CL_{l,l}$.

A similar form of the conversion tendency is give for NCN. The standard interaction terms can be formulated arbitrarily independent of the distribution using the methodology described in Section 2. Hence, given a complete set of $CL_{i,j}$, $VD_{i,v}$, $ML_{i,k}$ and $NU_{n,v}$, virtually any arbitrary parameterization is expressed by (21). Some additional *parameterization specific* features are found in the basic interaction equations themselves, most of which can be separated out. Such features include collision and coalescence efficiencies among others. Many *parameterization specific* features arise from simplifying approximations, which we attempt to eliminate.

4 Implementation

It is beyond the scope of this paper to specifically describe the implementation. Basically, we first diagnose all distribution parameters for each category based on either one or two predicted distribution parameters. We then compute all values of CL, VD, ML and NU among all categories. A set of conversions among categories is then computed based on these values. The conversion computation is modularized and can be changed easily. The collision and coalescence efficiencies are also modularized and easily varied.

The diagnosis of distributions and distribution parameters is defined either on input or in a modular form so it can be easily changed. The parameterization determines mixing ratio tendencies and, as an option, particle concentration tendencies for any hydrometeor category. Tendencies are based on an initially prescribed mixing ratio and second distribution parameter for each category. The second parameter may be a predicted concentration or a specified slope, intercept, or concentration. Depending on which second parameter is specified, the parameterization diagnostic routine will diagnose the others. In addition, the diagnostic routine (one for each category) prescribes which distribution is to be used and other pertinent things such as the terminal velocity-diameter and density-diameter relationships, habits and so on.

Acknowledgements

Research described here have been supported by the National Science Foundation Grant ATM-8512480.

References

Cotton, W. R., M. A. Stephens, T. Nehrkorn, and G. J. Tripoli, 1982: The Colorado State University three-dimensional cloud/mesoscale model - 1982. *J. Rech. Atmos.*, **16**, 295–320.

Feingold, G. and Z. Levin, 1986: The lognormal fit to raindrop spectra from frontal convective clouds in Israel. *J. Atmos. Sci.*, **25**, 1346–1363.

Lin, Y., R. D. Farley, and H. D. Orville, 1983: Bulk parameterization of the snow field in a cloud model. *J. Atmos. Sci.*, **22**, 1065–1089.

Nickerson, E. C., E. Richard, R. Rosset, and D. R. Smith, 1986: The numerical simulation of clouds, rain, and airflow over the Vosges and Black Forest Mountains: A meso-β model with parameterized microphysics. *Mon. Wea. Rev.*, **114**, 398–414.

Tripoli, G. J., P. J. Flatau, and W. R. Cotton, 1988: *Generalized microphysics scheme for use in mesoscale/cloud models.* Technical Report, Colo. State University, Fort Collins.

THE STUDY OF NUMERICAL SIMULATION ON THE FORMATION OF THE CLOUD DROPLET SPECTRA IN CUMULUS CLOUDS

Xiao Hui Xu Huaying Huang Meiyuan

Institute of Atmospheric Physics, Academia Sinica, Beijing, People's Republic of China

1. INTRODUCTION

As for the question about the relative roles of various collection processes in the formation of cloud-droplet spectra, there have been many studies, such as Gu Zhenchao(1980) and de Almeida (1979a), but most of them confined to analysing the microphysical processes. However, in a cloud the formation of cloud-droplet spectra is affected heavily by various macro variables of cloud as well. Precisely because of this, we will put the question into a dynamic model of cumulus cloud to discuss in this paper. In addition, we will still analyse the physical process of the formation of bimodal cloud-droplet spectrum in the cloud.

2. MODEL

The one-dimensional and time-dependent cylindrical cumulus cloud model adopted in this paper is similar to Xu Huaying *et al.*(1983) in basic structures (or confer Takahashi, 1976). But according to our researching questions, the model is improved in some aspects.

The values of gravitational collision efficiency used here are those given by de Almeida(1979b) in the case of turbulent energy dissipation rate $\varepsilon = 0$ cm^2s^{-3} (pure gravitation). In addition, we will use the two collision efficiencies under $\varepsilon = 1$ and 10 cm^2s^{-3} and the electric collision efficiency, to discuss the effects of various collection processes on the formation of cloud-droplet spectra.

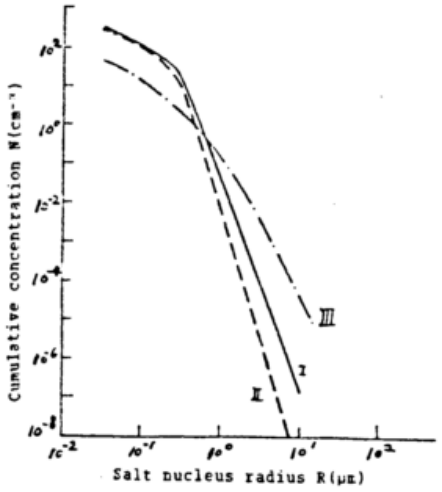


Fig.1. Initial dry salt nucleus spectra. Curves I and II represent the spectra of continental dry salt nuclei in the layers of from the ground to 200m height and from 200 to 4000m, respectively. Curve III represents the spectrum of maritime dry salt nuclei in the layer of the groud to 4000m height.

The environmental values are taken as the initial values of all variables in the cumulus air column. A cloud saturated initially from 400 to 1200m is stimulated by introducing a small disturbance updraft in the layer below 2000m. A typical, conditional,unstable stratification is used as environmental vertical distribution of temperature and humidity.

Here suppose that the cloud condensation nuclei are all taken as NaCl salt nuclei. Their radii are all greater than 0.03125μm and spectra are shown as Fig.1. The spectrum of maritime salt nuclei is that given by Woodcock (1972). The spectra of the continental salt nuclei with $R \geq 1\mu m$ are those given by Huang Meiyuan *et al.*(1982), and the spectra of $R < 1\mu m$ are given by extrapolating. The total concentrations of the nuclei are about 300 cm^{-3} for spectra I and II and about 55 cm^{-3} for spectrum III.

3. COMPUTATION RESULTS AND DISCUSSIONS

3.1 The Basic Characteristics of The Cloud-Droplet Spectra

It can be seen in Fig.2 that for both the droplet spectra of the continental cloud and those of the maritime cloud, they are all widening with height, their peak radii increasing and peak concentrations decreasing, only near the cloud top their widthes decreasing again. These characteristics agree with the vertical distribution characteristics of macro variables of the modeling clouds (the figure is omitted). So it can be used that the characteristics of the widest cloud-droplet spectrum in cumulus cloud represent some basic characteristics of micro-structures of the cloud.

According to our computation results, it was found that in the cloud the total concentration of cloud-droplets changes smaller with height, however, the concentration of big droplet of $R > 25$ μm first increases with height and attaines to its maximum in the middle-upper part of the cloud, and then decreases rapidly again.

3.2 The Bimodal Structure of The Cloud-Droplet Spectrum

Spectrum E in Fig.2a and that in Fig.2b show markedly bimodal structure. It is thus evident that the cloud-droplet spectra near the top of whether the continental or the maritime cumulus cloud appear this structure. The two peak radii in the continental case are about 4 μm and 10 μm at 15 min, while in the maritime case they are about 4μm and 15 μm.

According to the macro-features of the modeling cumulus cloud, it can be known that at the height appearing bimodal spectra, there is a stronger divergent air-flow. In the divergent region, for the salt nuclei and

relatively dry air of environment, only a few of them can be entered into the inside of the cloud by turbulence process. Such air-flow structure is advantageous to the condensation growth of small cloud drop-lets and salt-nuclei in the cloud. So larger concentration of the cloud-droplets appears at the radius of about 4 μm. Simultaneously, although a few of droplets with R > 10 μm are decreased because of being entrained into the outside cloud, the original shape and peak radius of the spectrum of large cloud-droplets are still remained. Therefore, a bimodal droplet spectrum appeares there. So it can be thought that the appearing of bimodal droplet spectrum has to do with the entrainment process of cloud.

3.3 *The Relative Roles of Various Collection Processes in The Formation of Cloud-Droplet Spectra*

It was found from our computations that the effects of following various collection processes on the spectrum distributions of droplets in the continental cloud are much the same as those in the maritime cloud. So we will only give the computation results of the former case, shown as Fig.3 and Table 1, and discuss them in detail. Following the symbol NC denotes no collection (pure condensation), C_1 the turbulent and gravitational collection in the case of $\varepsilon = 1\ cm^2s^{-3}$, Ce the electric collection. And C_1Ce denotes the turbulent and gravitational collection in the case of $\varepsilon = 1\ cm^2s^{-3}$ and the electric collection simultaneously. The rest is by analogy.

Firstly, Consider the case of the role of gravitational collection (C_0). As a comparison, the case of no collection (NC) is also calculated. It can be seen in Fig.3 and Table 1 that under the consideration of the gravitational collection, the cloud-droplet spectra are much wider than those under only considering the condensation, and to the concentration of large cloud droplets, such as R ≥ 40 μm, its growth rate is also increasing.

It can also be seen in Fig.3 and Table 1 that to the concentration of large cloud-droplets, its growth rate is increasing after considering small-scale turbulence. At 15 min the concentration of the droplets of R ≥ 40μm in Case C_1 attains to $2.91\times10^{-3}\ cm^{-3}$ and that of R ≥ 100μm comes up to 1.84 m^{-3}, which are 3.6 times and 8.7 times larger than corresponding one in Case C_0. As to Case C_{10}, there are the same results as well. The above results show that in the spreading of the cloud-droplet spectra in the earlier developing stage of cumulus cloud, the collection caused by small-scale turbulence plays a greatly promoted role, which can make the growth rate of the concentration of large cloud droplets to be over three times larger than that one corresponding to the case of the gravitational collection process without considering turbulence.

Analysing the collection efficiencies under the three ε values given by de Almeida(1979b), we can know that there is a direct influence of small-scale turbulence mainly on the collection growth of the big droplets with R < 40 μm. However, because of the quick increasing of these big droplets, it is of great advantage to much bigger droplets formed by other collection processes. So the small-scale turbulent collection can accelerate the growth of big droplets, thus playing an important promoted role in the spreading of cloud-droplet spectra.

Finally, consider the case that two arbitrary droplets taken separately unlike electric charges take place electrical collection in the gravitational field. The spectrum distributions of cloud-droplets in clouds are calculated under both the turbulent and gravitational collection and the electric collection (C_0Ce and C_1Ce), in which we have adopted a extrame advantageous collection efficiency to the collection growth of cloud droplets. It can be seen in Fig.3 and table 1 that the droplet spectra in the cloud of Case C_0Ce are a little wider than those in the cloud of Case C_0. At 15 min the concentration of

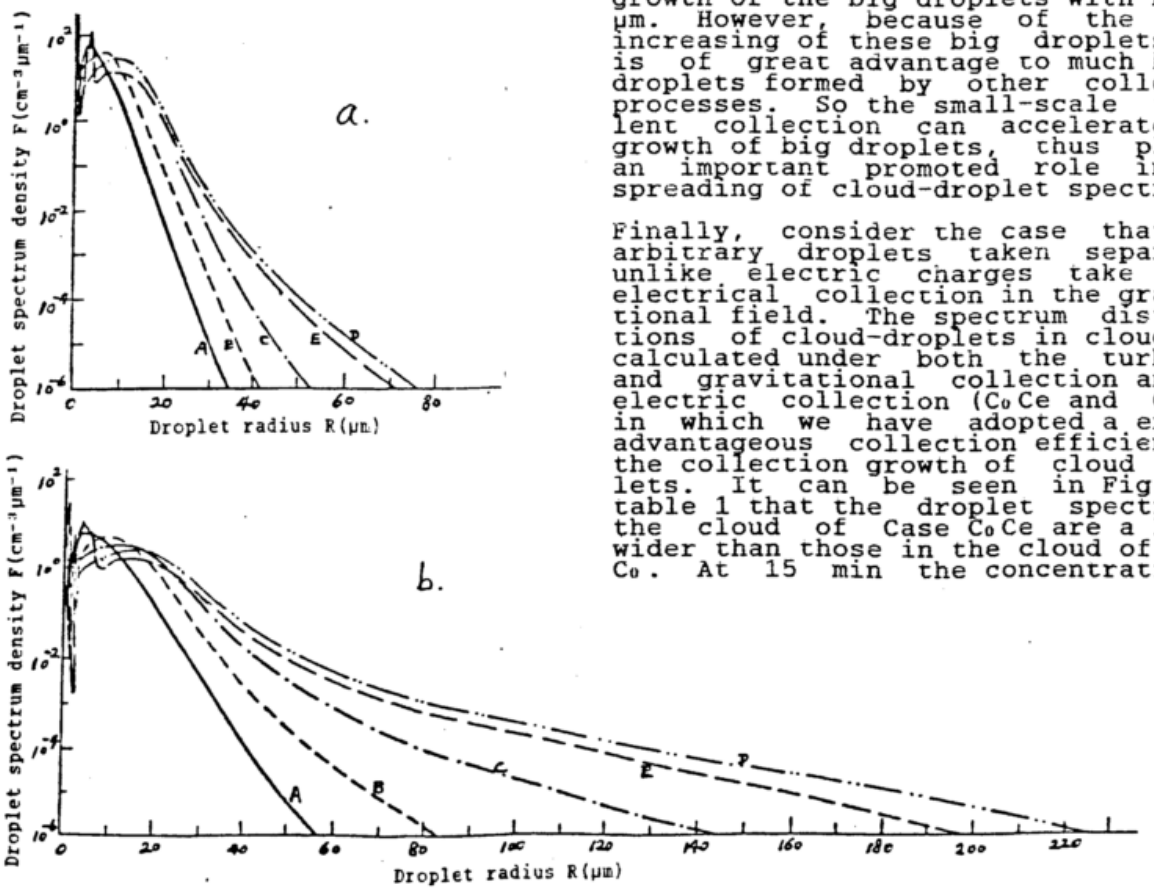


Fig.2. The distributions of cloud-droplet spectra in cumulus clouds at various heights (a. continental cloud; b. maritime cloud, both at 15 min). The symbols A, B, C, D and E represent the cloud-droplet spectra at 1000, 1400, 2000, 2600 and 2800 m height (the cloud base at 800m), respectively.

Table 1. The variables of the cloud-droplets at the heights of appearing the largest water contents (LWC) in continental cumulus clouds under the conditions of various collection processes. In this table, No.1, 2, 3, 4, 5 and 6 represent the collection processes of NC, C_0, C_1, C_0Ce, C_1Ce and C_{10}, respectively. R denotes the cloud-droplet radius in μm.

Time	5 min					10 min					15 min				
No.	Droplet concent. (cm^{-3})			LWC	Height	Droplet concent. (cm^{-3})			LWC	Height	Droplet concent. (cm^{-3})			LWC	Height
	20≤R<40	40≤R<100	100≤R	(g/kg)	(m)	20≤R<40	40≤R<100	100≤R	(g/kg)	(m)	20≤R<40	40≤R<100	100≤R	(g/kg)	(m)
1	0.577	*1.493E-7	7.578E-20	0.774	1400	2.460	1.113E-4	4.441E-17	1.245	2000	3.958	4.841E-4	7.616E-15	1.509	2600
2	0.582	4.420E-7	1.475E-15	0.774	1400	2.474	9.326E-4	4.203E-12	1.245	2000	3.984	6.388E-3	1.932E-7	1.509	2600
3	0.834	1.412E-6	2.137E-15	0.775	1400	3.213	4.413E-3	2.721E-11	1.246	2000	5.291	2.911E-2	1.839E-6	1.515	2600
4	0.760	7.526E-7	1.664E-15	0.772	1400	2.932	1.554E-3	1.060E-11	1.240	2000	4.878	9.972E-3	4.790E-7	1.504	2600
5	1.013	2.377E-6	2.263E-15	0.773	1400	3.663	6.625E-3	6.921E-11	1.241	2000	6.069	3.995E-2	4.053E-6	1.506	2600
6	0.697	1.714E-6	1.404E-17	0.767	1400	2.917	6.528E-3	3.676E-11	1.233	2000	4.715	4.289E-2	2.499E-6	1.496	2600

(* here 1.493E-7 = 1.493×10^{-7})

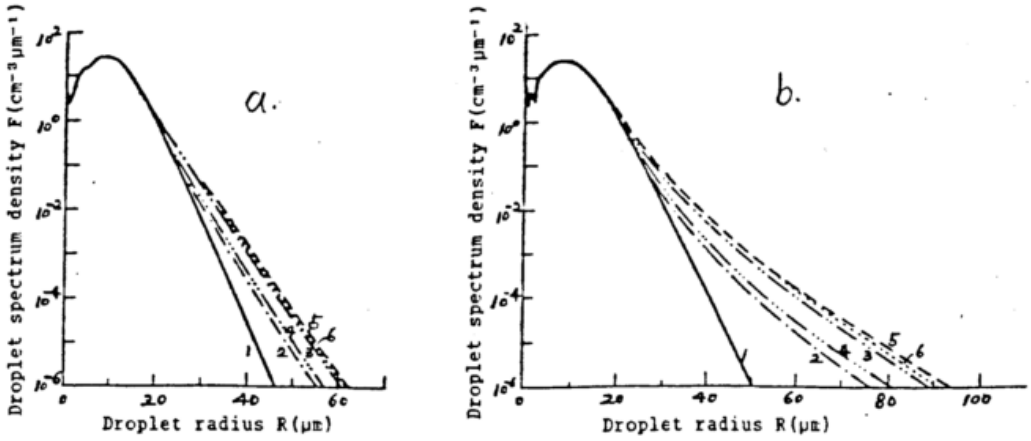


Fig.3. The cloud-droplet spectra in the continental cumulus clouds under the conditions of various collection processes (a. at 10 min and 2000m height; b. at 15 min and 2600m). Curves 1, 2, 3, 4, 5 and 6 in the Figure represent the collection processes of NC, C_0, C_1, C_0Ce, C_1Ce and C_{10}, respectively.

the droplets of R ≥ 40 μm and that of R ≥ 100 μm in Case C_0Ce are 0.56 times and 1.5 times larger than corresponding ones in Case C_0. Similarly, at the same time, the concentration of the droplets of R ≥ 40 μm and that of R ≥ 100 μm in the cloud of Case C_1Ce are 0.37 times and 1.2 times larger than corresponding ones in Case C_1. These computation results show that the role of electric collection is not large, even if such great advantageous condition of the cloud-droplet growth as above was used. Therefore, it can be thought that there is no large role of the electric collection mechanism in the growth process of small cloud-droplet in the earlier developing stage of cumulus cloud.

4. CONCLUSIONS

Based on the above analyses and discussions, we can obtain the several conclusions as follows.

1) The total concentration of cloud droplets in cumulus cloud has few changes with height, while the concentration of large cloud-droplets increases firstly with height in the middle-lower layer of cloud, and comes up to its maximum in the middle-upper part, and then decreases rapidly again.

2) The spectra of cloud-droplets near the cloud top have obvious bimodal structure, which has something to do with the entrainment characteristics between inside and outside of cloud at that height.

3) In the spreading of the cloud droplet spectra in the earlier developing stage of cumulus clouds, the gravitational collection process plays the most obvious role, the collection process caused by small-scale turbulence plays a greatly promoted role, which can accelerate the growth of big cloud-droplets, while the role of electric collection process is not significant.

REFERENCES

de Almeida, F.C., 1979a: The effects of small-scale turbulent motions on the growth of a cloud droplet spectrum, J. Atmos. Sci., 36: 1557-1563.

de Almeida, F.C., 1979b: The collisional problem of cloud droplets moving in a turbulent environment--Part II. Turbulent collision efficiencies. J. Atmos. Sci., 36: 1564-1576.

Gu Zhenchao, 1980: The Physics Fundaments of Clouds, Fogs and Precipitation. Science Press, Beijing, 1-29, 137-145 and 154-161.

Huang Meiyuan et al., 1982: Distributions of giant salt nuclei inside and outside cloud over the basin of Xin An Jiang, Scientia Atmospherica Sinica, 6:301-307. (in Chinese with English abstract)

Takahashi, T., 1976: Warm rain, giant nuclei and chemical balance--A numerical model. J. Atmos. Sci., 33: 269-286.

Woodcock, A.H., 1972: Smaller salt particles in oceanic air and bubble behavior in the sea. J. Geophys. Res., 77: 5316-5321.

Xu Huaying et al., 1983: A study on the growth of cloud droplets by condensation in cumulus clouds. Scientia Atmospherica Sinica, 7: 249-259. (in Chinese with English abstract)

Some Outstanding Problems on the Influence of Clouds on Radiation

Graeme L. Stephens

Department of Atmospheric Science, Colorado State University, Fort Collins, CO 80523

1. Introduction

The interaction of radiation with clouds is a topic of considerable interest to both the atmospheric radiation and cloud physics communities. It is also a topic germane to problems encountered in remote sensing and satellite meteorology and is of great importance in studies of climate and climate change. For many problems it is not only the manner in which clouds influence the radiative transfer processes that is important but also the way in which radiation might in turn change cloud is also crucial. The link between these two types of problems lies in the way that radiative transfer processes are related to the micro- and macro-properties of the cloud. This paper reviews some of the outstanding issues that impact on our ability to provide a meaningful description of the radiative processes in cloud both from the point of view of characterizing the radiative energy budgets of clouds and from the perspective of the remote sensing of cloud properties.

2. Relationship between radiative processes and microphysics

The two important parameters that influence the radiative transfer through clouds are cloud optical thickness τ, a product of the geometric depth (Δz) and extinction coefficient (α), and the single scatter albedo $\tilde{\omega}_o$. The bulk radiative properties of cloud, such as the albedo $\mathcal{R}$ and absorptance $\mathcal{A}$ depend on the combination of these parameters in the form (Ackerman and Stephens, 1987)

$$\mathcal{R},\ \mathcal{A} \rightarrow (1-\tilde{\omega}_o)\tau. \tag{1}$$

Thus parameterization of the cloud albedo, radiative heating and cooling and emission in terms of cloud properties requires some sort of relationship between α and $\tilde{\omega}_o$ and these cloud properties. The relation between α and $\tilde{\omega}_o$ and the cloud microphysics is now discussed.

2.1 Volume extinction

Volume extinction is related to the cloud microphysics through the formula

$$\alpha = \int_o^\infty n(\ell)a(\ell)Q_{ext}d\ell \tag{2}$$

where $n(\ell)$ is the cloud particle size distribution, ℓ is some characteristic size of the cloud particle, Q_{ext} is the extinction efficiency and $a(\ell)$ is the cross sectional area of the particle of size ℓ. Consider spherical cloud droplets for the present discussion. Under many circumstances $Q_{ext} \approx 2$ and (2) becomes

$$\alpha \approx 2A, \tag{3}$$

where A is the cross sectional area of the distribution $n(r)$ where r is now the droplet radius. Current radiation parameterizations relate the properly α to the cloud liquid water content w through the relationship

$$\alpha \sim \frac{3w}{2r_e}, \tag{4}$$

where r_e corresponds to the volume V to area A ratio of the size distribution. The extent to which α can be parameterized solely in terms of w alone depends on the degree that V and A are correlated, and thus the extent to which r_e is determined by w. To illustrate the relationships between V and A, consider $n(r)$ as given by

$$n(r) = const.r^{\beta-1}e^{-r/a}. \tag{5}$$

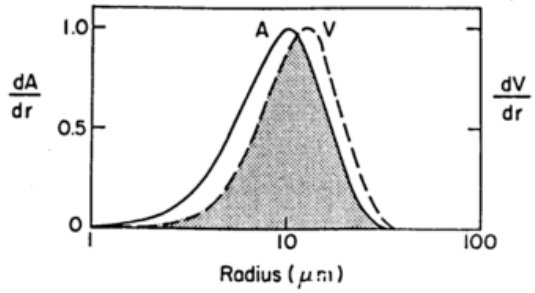


Fig. 1 Surface (S) and volume (V) distributions based on the size distribution expressed by (5) with $\beta = 3$ and $a = 10\mu m$. Note that the contributions to most of the total area and volume come from contributions by particles of the same size (shaded region).

Fig. 1 shows the cross sectional area and volume distributions calculated using (5) as a function droplet radius and demonstrate a high degree of correlation for the example given. However, the relationship between V and A varies considerably according to $n(r)$. Consider a distribution of the type

$$n(r) \approx C_1 r^{\beta-1}e^{-r/a_1} + C_2 e^{-r/a_2} \tag{6}$$

which has an elongated large particle tail. The extent to which A and V overlap for this case depends on the relative concentrations of small to large particles (Fig. 2).

The simple analysis given above emphasizes current problems encountered in radiation modeling and parameterization of cirrus cloud in particular. Among these are:

- the need to know the abundance of small ice particles and the ratio of small to large ice particle concentrations (Fig. 3). This information then provides some indication of whether the radiative properties of ice clouds can be expected to be functions of ice water path alone. The example given in Fig. 2a is one for which this relationship would not be expected to be unique.
- The extent to which scattering properties like Q_{ext} depend on crystal habit and if so what is the "characteristic" dimension of the crystal?

Another example that provides for ambiguous radiation - cloud water relationships is now illustrated. Twomey (1977) noted that the effects of pollution on radiation might be most notable through the influence of pollution on cloud microphysics rather than directly

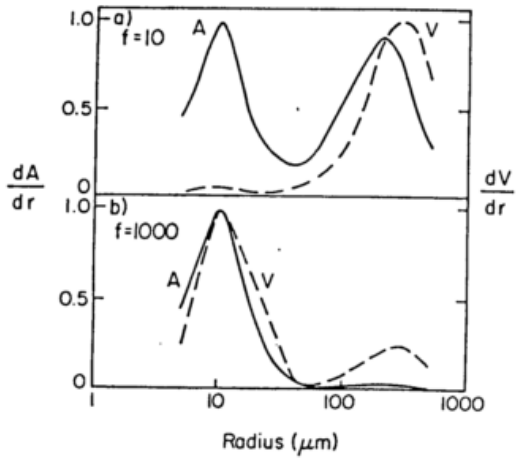


Fig. 2 Surface (S) and volume (V) distributions based on the size distribution expressed by (6) with $\beta = 3$, $a_1 = 10\mu m$ and $a_2 = 100\mu m$ and for different ratios of C_1 to C_2. These ratios are expressed by the factor f which is the ratio of small to large particles. For large values of f, A and V are highly correlated (b).

on radiation itself. Twomey argued that an increase in pollution generally implied an increase in cloud nucleus concentrations and thus to an increase of cloud droplets. A more colloidally stable cloud, according to (4), has associated with it a smaller r_e for the same liquid water content; this leads to an increase of optical thickness and hence an increase of cloud albedo - the latter depending to some extent on the absorption characteristics of the aerosol. This argument seems to be supported in AVHRR satellite images of $3.7\mu m$ radiation which clearly show the localized effects of ship tracks on cloud albedo (Coakley, *et al.*, 1987).

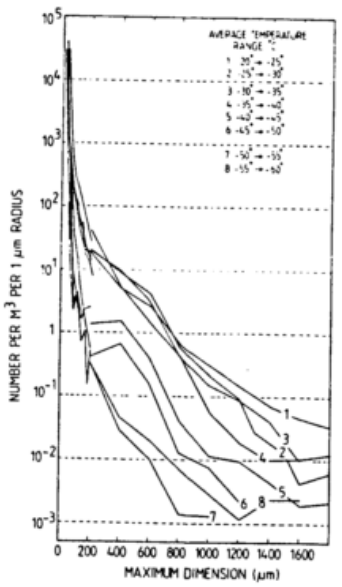


Fig. 3 The size distribution of ice crystals with a the maximum dimension range of $20 - 1800\mu m$ and for the eght temperature ranges indicated.

2.2 The single scattering albedo

The single scattering albedo $\tilde{\omega}_o$ is also an important parameter as it characterizes the absorption of a single cloud particle or a small volume of cloud containing a distribution of particles. Unfortunately the dependence of the single scatter albedo on the size distribution $n(r)$ is extremely complex. Ackerman and Stephens (1987) using a simplified scattering theory were able to demonstrate that

$$1 - \tilde{\omega}_o \sim 1 + c\kappa^{-1} r_e^p \qquad (7)$$

where κ is the absorption coefficient for water and c and p are constants. Those authors demonstrated that p in fact depends on the strength of absorption, i.e., on κ (Fig. 4) and therefore provided an illustration and understanding of how the bulk absorption and reflection properties of clouds depend on r_e and the vertically integrated liquid water path (Fig. 5). Understanding these kind of relationships are especially crucial in those studies that attempt to deduce various cloud properties using remote sensing techniques.

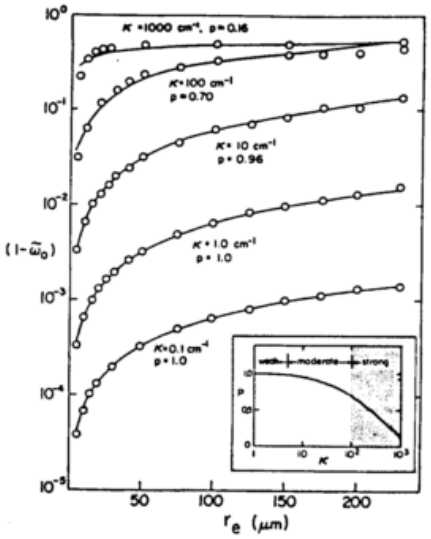


Fig. 4 Cosingle scattering albedo as a function of effective radius for selected values of κ. The solid curves represent the relationship described by (7) for the values of p indicated and the open circles apply to a scattering theory. The insert depicts the breakdown of the weak, moderate and strong absorption regimes (Ackerman and Stephens, 1987).

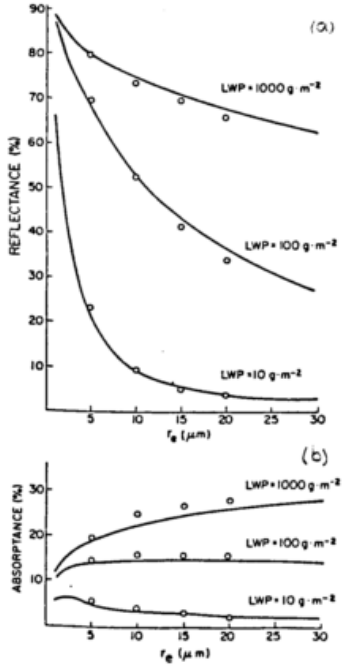


Fig. 5 Spectrally integrated $(0.7\mu m)$ values of (a) reflectance and (b) absorptance as a function of r_e for 3 values of integrated liquid water (LWP) (Ackerman and Stephens, 1987).

A number of issues thus emerge in our attempt to tie the radiative processes to cloud microphysical properties

- to what extent can $\tilde{\omega}_o$ be parameterized solely in terms of cloud liquid water content?
- Can simple $\tilde{\omega}_o$-size relations like (7) be derived for non spherical ice particles?
- If so, to what extent can the bulk radiative properties of ice cloud be characterized in terms of ice water path?

A particularly vexing problem that seems to have grown over the years is the so called shortwave absorption paradox and perhaps points to current problems in specifying $\tilde{\omega}_o$. The paradox can be simply stated: many measurements of cloud absorption considerably exceed the largest values obtained from theory (Fig. 6). There are several reasons to be concerned with this general lack of agreement:

- absorption of solar radiation by some clouds is not negligible and can be as large as the cloud top longwave cooling,
- it is a measure of the uncertainty in our understanding of either the radiative transfer within cloud, or the microphysical structure of the cloud or both,
- it creates major uncertainties in the development of cloud remote sensing methods which are based on spectral measurements (e.g., Stephens and Platt, 1987 (Fig. 7)).

The explanations of the paradox range from

- lack of fidelity in measurements,
- improper characterization of the cloud microphysics in the calculation - large droplets and absorbing aerosols can enhance absorption, and
- heterogeneity of the cloud and the inappropriateness of the assumption of horizontal homogeneity in the calculations.

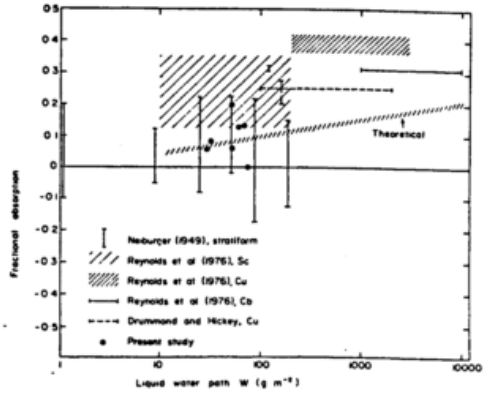


Fig. 6 Comparison of measured and calculated fractional shortwave absorption as a function of liquid water path. The shading about the line is the expected variability which may arise from differences in cloud type. The horizontal and vertical line, boxes and points are measured values (Stephens, 1978).

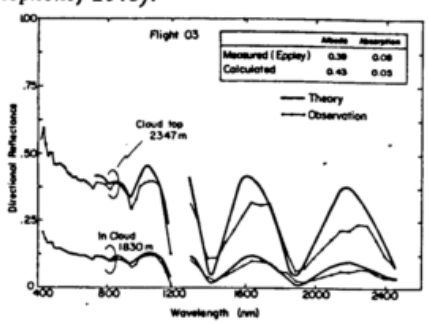


Fig.7 Comparison of theoretically calculated and observed spectral bidirectional reflectance from stratocumulus clouds (Stephens and Platt, 1987).

3. Impact of Cloud Morphology On Radiative Transfer

The motivation for much of this work has come from the climate community who desire to characterize the bulk radiative properties of the atmosphere on some scale (hundreds of kilometers) which is typically larger than that associated with cloud structure. However, the same issues arise in cloud modeling in which the averaged radiative budget of the cloud is required over some scale (the model resolution). The subgrid scale structure that must be treated is done so in terms of the areal cloud coverage parameter H using some type of *ad hoc* relationship

$$\mathcal{A} = \mathcal{A}_o(1 - H) + \mathcal{A}_c H \tag{8}$$

where $\mathcal{A}, \mathcal{A}_o$ and $\mathcal{A}_c$ are respectively the grid point radiative property, $\mathcal{A}_o$ the clear sky value and $\mathcal{A}_c$ the cloudy sky value. Yet (8) has no physical or theoretical basis. Even more significant, there is no unique relationship between $\mathcal{A}$ and H. Therefore, the issues that emerge are:

- What subgrid scale information do we need to characterize $\mathcal{A}$? H is not sufficient (and may not even be necessary).
- What is the form of the relationship between these new parameters and $\mathcal{A}$?
- How is this information connected to larger scale atmospheric variables?

Theoretical and observational studies have demonstrated that the radiative properties of cloud for most cases can be related to the vertically integrated cloud water in the more or less well defined way although it was noted above that exceptions to this relationship do exist. Other studies have also shown that the manner in which this water is distributed horizontally also significantly influences the characteristic radiative properties of the atmosphere. Results will be shown that demonstrate how cloud absorption, for instance, is organized in the horizontal according to the distribution of cloud liquid water content. It therefore seems that the radiation response in cloud is more intimately related to cloud structure including the organized scales of motion and turbulent scales of motion than previously thought.

4. Acknowledgement

This work was supported by the Atmospheric Sciences Section of the National Foundation under Contracts ATM-8519160 and ATM-8415127.

5. References

Ackerman, S. A. and G. L. Stephens, 1987: The Absorption of Solar Radiation by Cloud Droplets: An Application of Anomalous Diffraction Theory. *J. Atmos. Sci.*, **44**, 1574-1588.

Coakley, J., R. L. Bernstein, P. A. Durkee, 1987: Effect of ship-stack effluents on cloud reflectivity. *Science*, **37**, 1020-1022.

Heymsfield, A. and C.M.R. Platt, 1984: A Parameterization of the particle size spectrum of ice clouds in terms of the ambient temperature and the ice water content. *J. Atmos. Sci.*, **41**, 849-855.

Stephens, G. L. and C.M.R. Platt. 1987: Aircraft Observations of the Radiative and Microphysical Properties of Stratocumulus and Cumulus Cloud Fields. *J. Climate and Appl. Meteor.*, **26**, 1243-1269.

Twomey, S., 1977: The influence of pollution on the shortwave albedo of cloud. *J. Atmos. Sci.*, **34**, 1149-1152.

THEORY ON THE UNCERTAINTY IN CLOUD MIROPHYSICAL PROCESSES AND CLIMATE

Kuo-Nan Liou and Szu-cheng S. Ou

Department of Meteorology, University of Utah
Salt Lake City, Utah 84112, U.S.A.

1. INTRODUCTION

The objective of this paper is to investigate the interactive role of clouds and precipitation processes in a climate model. Section 2 presents the basic model structure and parameterizations for condensation, evaporation, and precipitation. Results simulated from the cloud-climate model are discussed in Section 3, where the potential link between microphysical cloud processes and climate is theorized. Finally, conclusions are given in Section 4.

2. THE CLOUDS AND CLIMATE MODEL

The present model for the investigation of the role of clouds and precipitation in climate is based on the 1-D climate model developed by Liou et al. (1985). However, we have modified the model by incorporating cloud liquid water and precipitation equations. In addition, we have also developed parameterization equations for condensation, precipitation, and evaporation terms, based on fundamental cloud microphysical processes in connection with the climate model. The basic 1-D, steady-state equations for the specific humidity q, cloud liquid water q_m, and precipitation flux $\tilde{P}$ may be written in the forms

$$\frac{\partial}{\partial z}(\rho\,\overline{w'q'}) = -\eta\,\rho\,Q_c + (1-\eta)\,\rho\,E_r \quad , \tag{1}$$

$$\frac{\partial}{\partial z}(\rho\,w_c\,q_m) = \eta\,\rho\,Q_c - \eta\,\rho\,P \quad , \tag{2}$$

$$\frac{\partial}{\partial z}(\eta\,\tilde{P}) = \eta\,\rho\,P - (1-\eta)\,\rho\,E_r \quad , \tag{3}$$

where ρ is the air density, η the cloud cover, Q_c, E_r, and P the rates of condensation, evaporation, and precipitation generation, w_c the vertical velocity in the cloudy region, and $\rho\,\overline{w'q'}$ the eddy flux of the specific humidity.

Let w_0 and q_0 denote the vertical velocity and specific humidity, respectively, in the clear region. It is assumed that there is a uniform distribution of large-scale parameters in clear and cloudy regions. This assumption has been widely used in the parameterization of cumulus convection. Thus, the eddy flux of the specific humidity $\rho\,\overline{w'q'} = \eta\,w_c\,q_c + (1-\eta)\,w_0\,q_0$, where the specific humidity in the cloudy region $q_c \cong q_s(T)$, the saturation specific humidity. The horizontal averages of temperature T, specific humidity q, and vertical velocity w, may be expressed by $\chi = \eta\,\chi_c + (1-\eta)\,\chi_0$, where χ can be T, q, or w. For large-scale cloud formation, we may safely assume that $T_c = T_0 = T$. Since there should be no vertical displacement in 1-D space, the vertical velocity $w = 0 = \eta\,w_c + (1-\eta)\,w_0$. Thus, $w_0 = -\eta\,w_c/(1-\eta)$. The vertical velocity in the cloudy region can be derived from Richardson's equation in a manner described in Liou et al. (1985). Finally, based on the horizontal averaging procedure, the cloud cover is related to the specific humidity in the form $\eta = (q/q_s - h_0)/(1 - h_0)$, where $h_0 = q_0/q_s$ denotes the threshold relative humidity. The threshold relative humidity is parameterized in terms of its surface value in the form, $h_0 = h_0(p*)\,[(p/p* - 0.02)/0.98$, where $p*$ denotes the surface pressure, and $h_0(p*)$ is set to be 0.8.

On the basis of the steady-state, 1-D diffusion theory for water vapor and latent heat transports, the rate of condensation for a given particle size distribution may be expressed by

$$Q_c = k_c\,(q/q_s - 1) \quad , \tag{4}$$

where k_c represents the rate coefficient for condensation, which is a function of the mean particle radius $\bar{r}$ and temperature. The rate of precipitation generation due to autoconversion and accretion, according to the collision theory, may be derived in the form

$$P = (k_1 + k_2\,\tilde{P}^{0.791})\,q_m \quad , \tag{5}$$

where the rate coefficient for autoconversion, $k_1 \cong 1.5\times10^{-7}\,\bar{r}^4$ (μm^{-4} sec^{-1}), and $k_2 \cong 0.931\,\rho^{-0.105}$, using the Marshall and Palmer raindrop size distribution. This parameterization equation is similar to that developed by Kessler (1969) and Ogura and Takahashi (1971) for thunderstorm clouds, except that k_1 in the present formulation is a function of the mean radius to the fourth power.

The time rate of change of mass for raindrops due to evaporation may be expressed in an equation analogous to the one for condensation. Including a ventilation factor (Beard and Pruppacher, 1971), we find

$$E_r = (k_{e1}\,\tilde{P}^{0.417} + k_{e2}\,\tilde{P}^{0.604})\,(1 - q/q_s) \quad , \tag{6}$$

where the evaporation rate coefficients k_{e1} and k_{e2} are functions of the air density and temperature.

The rates of condensation, evaporation,

and precipitation generation are now parameterized in terms of the specific humidity q, cloud liquid water content q_m, and precipitation flux $\tilde{P}$. The rate coefficients k_c, k_{e1}, and k_{e2} are functions of temperature and are therefore interactive with the perturbation due to radiative forcings through the thermodynamic equation containing temperature and solar and IR fluxes.

3. NUMERICAL RESULTS AND THEORY ON THE ROLE OF CLOUD MICROPHYSICAL PROCESSES IN CLIMATE

In order to simulate the present mean annual condition (control run), we have used the following input data: a solar constant of 1360 W m^{-2}, average cosine of the solar zenith angle of 0.5, duration of sunlight of 12 h, surface albedo of 0.13, and CO_2 concentration of 330 ppmv. The ozone and molecular profiles used correspond to the standard atmospheric condition. Parameterizations of the radiative properties of clouds and the scheme for the cloud cover follow those described in Liou et al. (1985). Moreover, based on the observed particle size distributions, we have assumed (climatological) mean particle radii $\bar{r}_c$, of 4, 5, and 25 μm for low, middle, and high clouds, respectively.

In the control run, the temperature and specific humidity profiles computed from the model compare closely with climatological data. The liquid water contents simulated from the model are 0.23, 0.14, and 0.006 g m^{-3} for low, middle, and high clouds, respectively. These values agree with the observed data presented by Matveev (1984). The total cloud cover and annual precipitation generated from the 1-D globally averaged model also agree well with climatological data.

In the perturbation experiments, we uniformly increase and decrease the climatological mean particle radii for all three cloud types by a value $\Delta\bar{r}$ (= $\bar{r}$-$\bar{r}_c$) ranging from 0 to 3 μm. We use a doubling of the CO_2 concentration as the initial radiative forcing to investigate the effects and feedbacks of the mean particle radius on the climatic temperature perturbation. The results are illustrated in Fig. 1. For the fixed cloud cover, liquid water content, and mean particle radius, a doubling of CO_2 produces a temperature increase ΔT of 2.3°C, which is referred to as the standard temperature change. In our previous studies, we illustrated that the introduction of an interactive cloud cover program (Liou et al., 1985) and/or an interactive cloud liquid water content program (Ou and Liou, 1987), in connection with the climate model, leads to negative feedbacks. Increased temperatures will cause the surface evaporation to increase. Subsequently, cloud cover and liquid water content also increase, and less solar radiation is absorbed by the atmosphere and surface. Thus, clouds appear to stabilize the temperature perturbation due to the anticipated increase in CO_2 concentration.

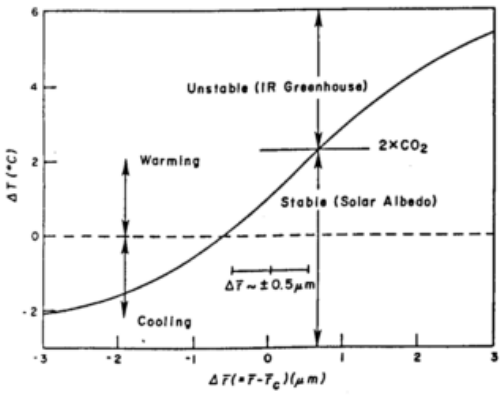


Fig. 1 Perturbation temperature change ΔT as a function of the deviation from the climatological mean cloud particle radius $\bar{r}_c$ resulting from a doubling of CO_2. The solid line ($2xCO_2$) denotes the standard temperature change when cloud cover, liquid water content, and mean particle radius are fixed in the experiment.

However, if we allow the cloud particle radius to vary in the interactive cloud and precipitation program, several temperature perturbations occur. If the perturbed cloud paricle radius is within about 0.5 μm, $0 < \Delta T < 2.3$°C, implying that the perturbation due to a doubling of CO_2 is stabilized because of an increase in cloud cover and liquid water content. In this case, the solar albedo effects predominate and the presence of clouds produces a negative feedback to the climate system. If, however, $\Delta\bar{r} > 0.5$ μm, there would be a possibility for a runaway greenhouse effect, that is, the radiative forcing produced by a doubling of CO_2 could produce a surface warming of 5.6°C (as opposed to 2.3°C when feedbacks from clouds were not considered) in the case when $\Delta\bar{r} = 3$ μm. On the other hand, if the perturbed particle radius $\bar{r}$ is less than $\bar{r}_c$ by 0.5 μm, cooling instead of warming occurs when CO_2 is doubled. The surface temperature could be cooled by as much as -2°C due to a significant increase in cloud cover and liquid water content. Thus, there would be a possibility for the occurrence of an ice age.

On the basis of the preceding results, simulated from a 1-D climate model with an interactive cloud formation and precipitation program, the statisical and stochastic nature of cloud microphysical processes and their potential link to climate are theorized. Our theory is derived from the fact that the initiation of precipitation is directly proportional to the fourth power of the mean cloud particle radius.

Theory 1: If the perturbed mean cloud particle radius $\bar{r}$ is less than the climatological mean cloud particle radius $\bar{r}_c$, precipitation decreases, leading to increases in cloud cover and liquid water content. Thus, the solar albedo effects outweigh the IR greenhouse effects. The perturbed temperature due to a positive radiative forcing is stabilized.

Theory 2: If the perturbed mean cloud particle radius $\bar{r}$ is larger than the climatological mean cloud particle radius $\bar{r}_c$, precipita-

tion increases, leading to decreases in cloud cover and liquid water content. Thus, the IR greenhouse effects outweigh the solar albedo effects. The perturbed temperature due to a positive radiative forcing is amplified.

4. CONCLUSIONS AND HYPOTHESES ON THE UNCERTAINTIES IN CLOUD MICROPHYSICAL PROCESSES

In Section 3, we theorized about the effects of clouds/radiation on climatic temperature perturbations based on the deviation of the perturbed cloud particle radius from the climatological mean value. We pointed out that cloud cover and liquid water content are directly related to precipitation processes, which are governed by the mean particle radius. In particular, we illustrated that the rate of precipitation generation is directly proportional to the fourth power of this radius. In the context of a 1-D cloud/radiation climate model, we further showed that uncertainties in the parameterized growth equations are largely attributable to uncertainties in the assumed particle size distribution. These uncertainties, in our view, are statistical and stochastic in nature and cannot be predicted entirely by the thermodynamic and dynamic laws governing the formation of clouds and precipitation.

In connection with our theories on the link between microphysical cloud processes and the stability of the climate and climatic perturbations, we propose the following two probabilities for perturbations of the climatological mean particle radius due to temperature feedbacks:

Hypothesis 1: The reaction rate involving the formation of embryonic sulfuric acid nuclei increases due to greenhouse warming. More nuclei are available to compete for water vapor, resulting in small cloud particles. The probability of the production of precipitation reduces and, at the same time, cloud cover and liquid water content increase in the atmosphere (stable climate).

Hypothesis 2: The condensation rate coefficient increases due to greenhouse warming. This leads to an increase in cloud liquid water content. There is a probability that large cloud particles could form and increase the production of precipitation. Subsequently, cloud cover and liquid water content decrease in the atmosphere (unstable climate).

In summary, the cloud mean particle radius is one of the critical elements that control the stability of the climate and climatic perturbations. Thus, we must develop a climatology of the mean particle radius for clouds over the globe in order to understand the role of clouds in climate.

5. ACKNOWLEDGMENTS

This research was supported by NASA Grant NAG-732 and Air Force Office of Scientific Research Grant AFOSR-87-0294. Sharon Bennett typed and edited the manuscript.

REFERENCES

Beard, K.V. and H.R. Pruppacher, 1971: A wind tunnel investigation of the rate of evaporation of small water drops falling at terminal velocity in the air. J. Atmos. Sci., 28, 1455-1464.

Kessler, E., 1969: On the Distribution and Continuity of Water Substance in Atmospheric Circulations. Meteor. Mongr., No. 32, American Meteorological Society, 84 pp.

Liou, K.N., S.C. Ou and P.J. Lu, 1985: Interactive cloud formation and climatic temperature perturbations. J. Atmos. Sci., 42, 1969-1981.

Matveev, L.T., 1984: Cloud Dynamics. D. Reidel, Dordrecht, Holland, 340 pp.

Ogura, Y. and T. Takahashi, 1971: Numerical simulation of the life cycle of a thunderstorm cell. Mon. Wea. Rev., 99, 895-911.

Ou, S.C. and K.N. Liou, 1987: Effects of interactive cloud cover and liquid water content programs on climatic temperature perturbations. Atmospheric Radiation: Progress and Prospects, Science Press, Beijing, China, 433-440.

IN SITU MEASUREMENTS OF "SHIP TRACKS"

Lawrence F. Radke, Jamie H. Lyons and Peter V. Hobbs
Atmospheric Sciences Department, University of Washington
Seattle, Washington 98195 USA
and
James E. Coakley
National Center for Atmospheric Research
Boulder, Colorado 80307 USA

1. INTRODUCTION

It has long been known that cloud droplet concentrations are strongly influenced by cloud condensation nuclei (CCN) (Twomey and Warner, 1967) and that anthropogenic sources of pollution can affect CCN concentrations (Radke and Hobbs, 1976). More recently it has been suggested that CCN may play an important role in climate through their effect on cloud albedo (Twomey et al., 1984; Charlson et al., 1987).

An interesting example of the effect of anthropogenic CCN on cloud albedo is the so-called "ship track" phenomenon. Ship tracks were first observed in satellite imagery when the ship's emissions were evidently needed for the formation of a visible cloud (Conover, 1966). However, they appear more frequently in satellite imagery as modifications to existing stratus and stratocumulus clouds. The tracks are seen most clearly in satellite imagery by comparing the radiance at 3.7 μm with that at 0.63 and 11 μm (Coakley et al., 1987). To account for the observed change in radiance, droplet concentrations must be high, and the mean size of the droplets small, in ship tracks.

In this note we describe what we believe to be the first *in situ* measurements in what appears to have been a ship track.

2. OBSERVATIONS

During the FIRE study of marine stratus off the coast of California in the summer of 1987, a number of ship-tracks were detected with 3.7 μm satellite radiance measurements. Interceptions of ship track-like features by the University of Washington's C-131A research aircraft were made on July 2, 7 and 10. The July 10 case is described here.

On July 10 a ship track-like feature (hereafter referred to as "the feature") was penetrated by the aircraft between 1557 and 1615 UTC in the vicinity of 32°N and 120°W. The surface synoptic situation was dominated by a subtropical high off the California Coast with the winds from the N-NW. The GOES satellite imagery showed rather uniform stratocumulus in the area. Several ship track-like features are visible in the GOES 2015 UTC imagery. The satellite image that is closest in time to our aircraft observations is the NOAA-10 satellite imagery for 1537 UTC. This shows a linear track near the feature that we intercepted, however, there is a possibility that the feature on the satellite imagery is a mesoscale cloud boundary.

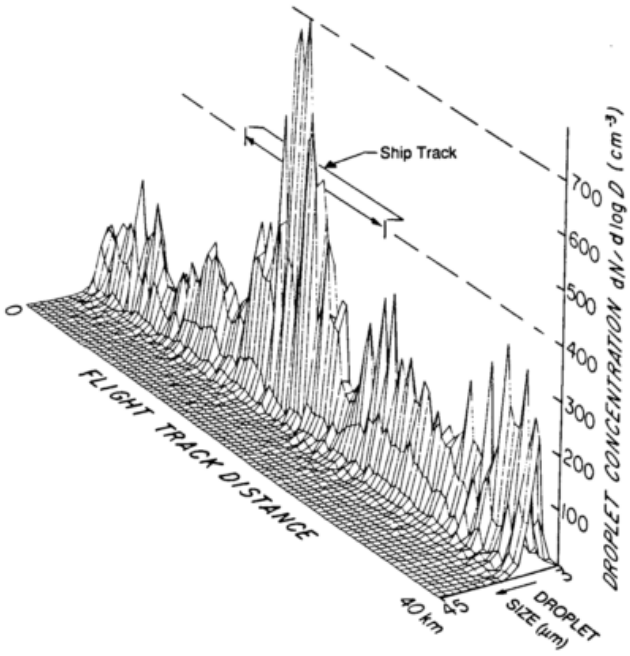


Figure 1: Cloud drop size distributions in 3-D perspective across the ship track-like feature on 10 July 1987.

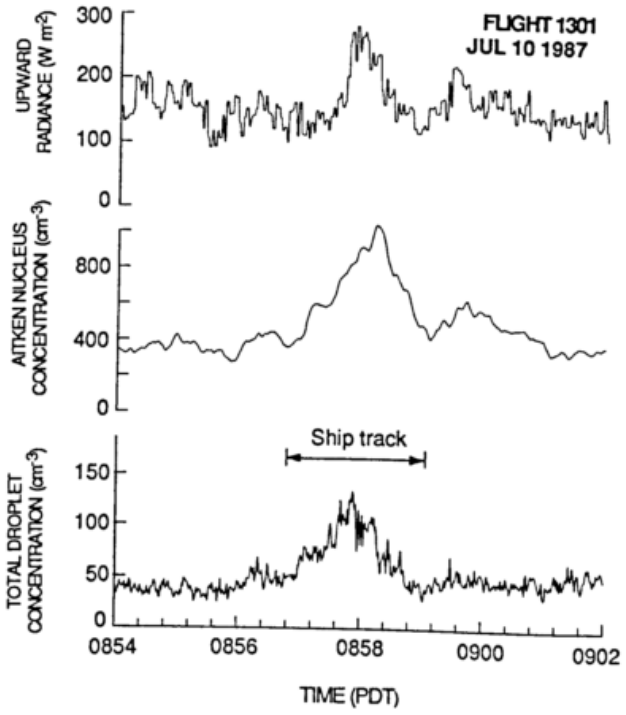


Figure. 2: Total cloud drop concentrations, Aitken nucleus concentrations and broadband upward radiance measurements across the ship track-like feature on 10 July 1987.

The first aircraft penetration of the ship track-like feature was made at 1557 UTC, when the aircraft was located about midway between the top and bottom of a stratocumulus layer about 500 m thick. The change in the drop size distribution across the feature is clearly revealed by the microphysical measurements shown in Fig. 1. The feature can also be seen in Fig. 2, where total drop concentrations are shown. The increase in liquid water content in the feature was about 30%.

Also shown in Fig. 2 are measurements of Aitken nucleus concentrations, which show a sharp increase across the feature. The Aitken nucleus measurements were made within the cloud and represent mainly the cloud interstitial aerosol (Radke, 1983). However, a fraction of these nuclei may be the evaporated residues of cloud drops. Hence, while in cloud, a modest correlation is to be expected between drop and Aitken nucleus concentrations. Nevertheless, the sharp increase in Aitken nuclei in the feature must have been due to a dramatic increase in interstitial particles, particles that did not serve as CCN in the cloud. Such particles could well have been combustion products from a ship's engine.

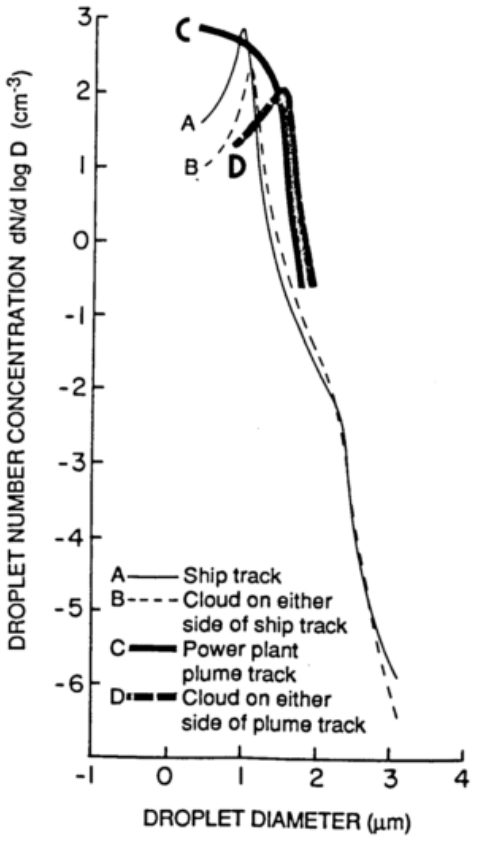


Figure 3: Cloud droplet size distributions averaged across (A) and on either side of (B) the ship track-like feature on 10 July 1987. Overprinted are corresponding data showing the effect on a cloud of the emissions from a coal-fired electric power plant (from Hobbs et al., 1980).

Coincident with the feature was an average increase of ~ 16% in upward radiance detected by the Eppley broad-band radiometer aboard the aircraft (Fig. 2). Coakley et al. (1988) show that the change in upward radiance, ΔR, is related to a change in cloud drop concentration ΔN by:

$$\Delta R \simeq \frac{1}{12}\frac{\Delta N}{N} \qquad (1)$$

Substituting the value of $\frac{\Delta N}{N}$ $(= \frac{100}{50})$ from our measurements into (1) yields $\Delta R \simeq 17\%$.

3. DISCUSSION

Is it feasible that the modifications to the cloud structure described above could have been produced by emissions from a ship? In Fig. 3 we show the drop size distributions measured in and on either side of the feature. Also shown in Fig. 3 for comparison, are

measurements of the effect on the cloud drop size distribution of the emissions from a 1000 MW coal-fired electric power plant on a cloud 13 km downwind of the plant (data from Hobbs et al., 1980). It can be seen that the two effects are similar. Hobbs et al. calculated that the flux of CCN active at 0.2% supersaturation from the coal power plant, including gas-to-particle conversion in the plume, was ~ 10^{16} - 10^{17} s^{-1}. This is a large source of CCN, comparable to the emissions from a large urban area or industrial complex (Radke and Hobbs, 1976).

Assuming a ship speed of 10 m s^{-1}, and using the measurements of 16 km and ~ 500 m for the width and depth, respectively, of the feature, and an increase in droplet concentration in the feature of 100 cm^{-3}, we calculate that in order for a ship to produce the observed changes in drop concentrations it would have had to produce ~ 10^{16} CCN s^{-1}. This requires the ship to be a very large (perhaps unreasonably large) source of CCN. However, in addition to fuel combustion, a ship can cause CCN to be lofted into the atmosphere by generating sea-salt particles through cavitation, splashing and bubble bursting. Particle production by these processes can produce substantial numbers of particles in the 0.1 - 1 μm size range (Radke, 1977). Since these particles serve as very efficient CCN, they could augment the combustion products from a ship and thereby play a role in the formation of ship tracks. Also, the dynamic effects suggested by the increase in liquid water content in the feature would increase the supersaturation in the cloud and thereby activate additional CCN. A ship might also loft additional water vapor through emissions and/or stirring of the boundary layer.

Despite these various means by which ships might modify clouds, we have to conclude that ship tracks are a surprising phenomenon that is not yet fully explained.

Acknowledgments. This work was supported by National Science Foundation Grant ATM-8615344.

4. REFERENCES

CHARLSON, R. J.; LOVELOCK, J. E.; ANDREAE, M. O.; WARREN, S. G.: Oceanic phytoplankton, atmospheric sulfur, cloud albedo and climate. *Nature*, 326 (1987), 655-661.

COAKLEY, J. A.; BERNSTEIN, R. L.; DURKEE, P. A.: Effect of ship-track effluents on cloud reflectivity. *Science*, 237 (1987), 1020-1022.

COAKLEY, J. A.; BERNSTEIN, R. L.; DURKEE, P. A.: Effect of ship-stack effluents on the radiative properties of marine stratocumulus: Implications for man's impact on climate. In *Aerosols and Climate* (Eds. P. V. Hobbs and M. P. McCormick). Hampton, VA: A. Deepak Publishing. 1988.

CONOVER, J. H.: Anomalous cloud lines. *J. Atmos. Sci.*, 23 (1966), 778-785.

HOBBS, P. V.; STITH, J. L.; RADKE, L. F.: Cloud active nuclei from coal-fired electric power plants and their interactions with clouds. *J. Appl. Meteor.*, 19 (1980), 439-451.

RADKE, L. F.; HOBBS, P. V.: Cloud condensation nuclei on the Atlantic seaboard of the United States. *Science*, 193 (1976), 999-1002.

RADKE, L. F.: Marine aerosol: simultaneous size distributions of the total aerosol and the sea-salt fraction from 0.1 to 10 μm diameter. In *Atmospheric Aerosols and Nuclei* (Eds. A. F. Roddy and T. C. O'Conner). Galway, Ireland: Galway University Press. 1977.

RADKE, L. F.: Preliminary measurements of the size distribution of cloud interstitial aerosol. In *Precipitation Scavenging, Dry Deposition and Resuspension* (Eds. H. R. Pruppacher, R. G. Semonin and W. G. N. Slinn). New York: Elsevier. 1983.

TWOMEY, S. A.; PIERGRASS, M.; WOLFE, T. L.: An assessment of the impact of pollution on global cloud albedo. *Tellus*, 36B (1984), 356-366.

TWOMEY, S. A.; WARNER, J.: Comparisons of measurements of cloud droplets and cloud nuclei. *J. Atmos. Sci.*, 24 (1967), 702-703.

RADIATION INDUCED GROWTH AND EVAPORATION OF DROPLETS IN BOUNDARY LAYER CLOUDS

Roger Davies

Department of Meteorology, McGill University, 805 Sherbrooke Street West,
Montreal, Que H3A 2K6, Canada

1. INTRODUCTION

Long-lived boundary layer clouds are a major component of the climate system and may offer the best opportunity for experimental measurement of the response of clouds to radiative processes. We have examined some possible responses using a high resolution radiative transfer model, theoretical considerations of supersaturation feedback, and models of diffusional growth and sedimentation of cloud droplets. These theoretical predictions are presently being examined against the experimental measurements made in marine stratocumulus during the First International Satellite Cloud Climatology Program Regional Experiment (FIRE).

2. THEORY

The radiative transfer model uses high spectral and vertical resolution to produce broadband flux divergences of shortwave and longwave radiation. It includes the effects of droplet scattering, absorption and emission by both droplets and gas, and vertical discontinuities in temperature and liquid water content. The radiation budgets of individual droplets are also obtained as functions of their radius and position within the cloud.

Droplet growth rates are determined as by Davies (1985) and Alves (1987), allowing for supersaturation feedback. In the absence of turbulence, droplet response to radiation is found to be significant, with droplets of all sizes growing under conditions of net longwave loss. The effect is greatest in the top few meters of the cloud where the longwave loss is a maximum. Inclusion of turbulence changes this result and reduces the overall growth rate. Smaller droplets now tend to evaporate, whereas the larger droplets maintain significant growth rates.

The theoretical result is illustrated in Figure 1, which shows the droplet growth rates predicted by our model for a typical boundary layer stratiform cloud under two limiting assumptions: (a) radiation alone with no turbulent heat exchange, and (b) radiation together with a fully efficient turbulent heat transfer. *In situ* measurements of cloud microphysics made by others during FIRE are currently being analyzed to see whether these limiting assumptions are consistent with observation.

3. REFERENCE

Adil R. Alves, "*On the Interactions of Longwave Radiation, Microphysics, and Turbulence in Boundary Layer Clouds.*", Ph. D. thesis, Purdue University, 184 pp, 1987.

R. Davies, "Response of Cloud Supersaturation to Radiative Forcing", *J. Atmos. Sci., 42,* 2820-2825, 1985.

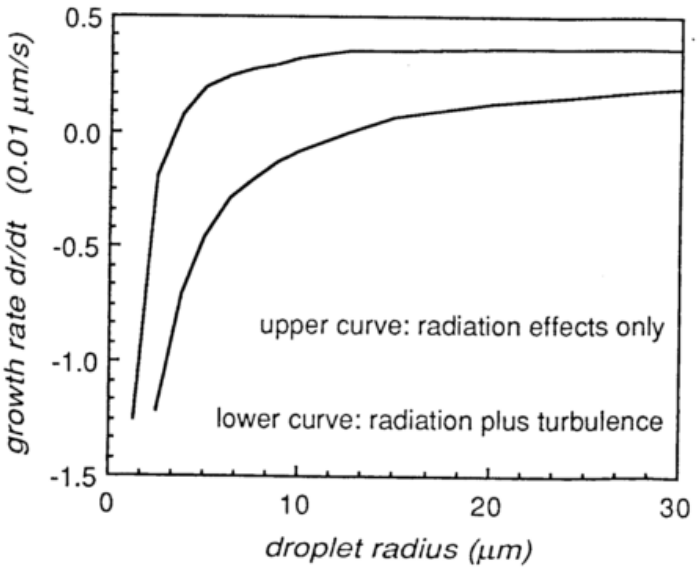


Fig. 1. Radiatively induced droplet growth at the top of a modeled stratiform cloud

CLOUD AND AEROSOL OPTICAL DEPTHS

R. F. Pueschel(1), P. B. Russell(1), T. P. Ackerman(2),
D. C. Colburn(1), R. C. Wrigley(1), M. A. Spanner(3), J. M. Livingston(4)

(1)NASA Ames Research Center, Moffett Field, CA 94035; (2)Pennsylvania State University, University Park, PA 16802; (3)TGS Technology, Moffett Field, CA 94035; (4)SRI International, Menlo Park, CA 94025

1. INTRODUCTION

Airborne sun photometry is essential to provide information on horizontal and vertical variations of optical depths in order to assess climatic feedback mechanisms of clouds. The Ames airborne sun photometer measures optical depths in six spectral intervals from 380 to 1020 nm simultaneously with a frequency of 0.5 Hz from outside an aircraft in a feedback-controlled active tracking mode. The instrument consists of a solar tracking system, a detector module, a temperature control system, a nitrogen purge system, a mechanical drive chain and a data acquisition system (MATSUMOTO 1987). In 1986/87, the instrument was operated in two large field programs. First, it was part of the instrument package aboard the NASA C-130 research aircraft that supported the First ISLSCP (International Satellite Land Surface Climatology Project) Field Experiment (FIFE) over the Konza Prairie in Kansas (38.9 - 39.1°N; 96.4 - 96.6°W). Second, it was flown on the Sandia National Laboratories Twin Otter research aircraft to measure the smoke optical depths of forest fires and a jet-fuel pool fire (PUESCHEL ET AL. 1988).

2. RESULTS AND DISCUSSION

2.1 BACKGROUND OPTICAL DEPTHS

The FIFE intensive field campaigns between May and October 1987, and the fire investigations in the fall of 1986 provided opportunities to measure, respectively, the optical depths in clear atmospheres between the appearances of broken stratus clouds, and the optical depths in the vicinity of smokes. Typical background optical depths were 0.06-0.07 at 380 nm, decreasing to 0.006-0.007 at 1020 nm. The wavelength dependence of optical depths in the vicinity of forest fire smokes is rather steep: the Angstrom exponent, α, of particulate optical depths (that is, total optical depths corrected for Rayleigh scattering, NO_2 and O_3 absorption) varied from a 2.4 ± 0.3 near a Los Angeles controlled burn to 3.3 ± 0.6 in the vicinity of a fire near Fresno, CA. The atmosphere near Albuquerque, NM outside the jet-fuel smoke had a more typical Angstrom exponent of 1.2 ± 0.2. The background particulate optical depths in rural Kansas showed still less wavelength dependence with $\alpha < 1.0$. We conclude that (human) activities can alter the chemical and optical properties of background atmospheres to affect their spectral optical depths. Effects of water vapor adsorption on aerosol optical depths are apparent, based on data of the water vapor absorption band centered around 940 nm.

2.2 SMOKE OPTICAL DEPTHS

Smoke optical depths show increases above the background atmosphere by up to two orders of magnitude. The Angstrom exponent of the undiscriminated data set shows a bimodal frequency distribution with modes $2.0 < \alpha < 2.3$ and $-0.3 < \alpha < 0$. The latter mode becomes more pronounced as we discriminate against smaller optical depths. We conclude that the smoke aerosol is composed of two components. One component is dominated by particles that are relatively small in size and, consequently, scatter/absorb in the blue; this aerosol affects the optical properties of smokes at small optical depths. A second component, which is associated predominantly with high optical depths, is characterized by neutral, or slightly anomalous, extinction. The effects of dilution on the magnitude of optical depth, and of coagulation on its wavelength dependence in aging smokes have been documented by the measurements. Aged forest fire smoke shows anomalous extinction in 20% of all cases; the Angstrom exponent spectrum has modes of $1.3 < \alpha < 1.5$ and $-1.0 < \alpha < -0.8$. The wavelength dependence of the optical depth of smoke from the jet-fuel fire showed a more neutral behavior than did that of the forest fire smokes. We conclude that the wavelength dependence of smoke optical depths depends critically on the fuels that

feed the fires, and on the residence time in the atmosphere of the smoke cloud. Under the assumption of similar opacity near 1000 nm it appears that, in the visible and near-ultraviolet, forest fire smokes would have greater opacity than jet fuel fire smokes. Beyond 1000 nm, however, forest fire smokes would have less opacity than fuel fire smokes.

2.3 CLOUD OPTICAL DEPTHS

On clear days, tenuous clouds of limited horizontal extent were observed. When the total optical depths measured through these clouds were corrected for molecular scattering and gaseous absorption by subtracting the total optical depths measured through the background atmosphere, the resultant values were lower than those of the background aerosol at short wavelengths. The spectral dependence of these cloud optical depths was neutral, however, in contrast to that of the background aerosol or the molecular atmosphere. This optical property of the atmosphere is attributed to high-altitude ice crystals at low concentrations. Similar to forest fire smokes, stratus clouds increase the optical depths by several orders of magnitude above that of background air. In contrast to forest fire smokes, however, their Angstrom exponent frequency spectra are unimodal. Separating out the effects of haze by discriminating against low optical depths, the Angstrom coefficient is $\alpha \equiv 1.0$. The cloud optical properties have been linked to their microphysical properties by inverting the spectral optical depth data to derive columnar particle size distributions (KING ET AL. 1978).

KING, M. D.; BYRNE, D. M.; HERMAN, B. M.; REAGAN, J. A.: Aerosol Size Distributions Obtained by Inversion of Spectral Optical Depth Measurements. J. Atmos. Sci. 35 (1978), pp. 2153-2167.

MATSUMOTO, T.; RUSSELL, P. B.; MINA, C.; VAN ARK, W.; BANTA, V.: Airborne Tracking Sunphotometer. J. Atmos. Ocean. Tech. 4 (1987), pp. 336-339.

PUESCHEL, R. F.; LIVINGSTON, J. M.; RUSSELL, P. B.; COLBURN, D. A.; ACKERMAN, T. P.; ALLEN, D. A.; ZAK, B. D.; EINFELD, W.: Smoke Optical Depths: Magnitude, Variability and Wavelength Dependence. J. Geophys. Res. (submitted).

AN OBSERVATIONAL STUDY OF RADIATIVELY DRIVEN CONVECTION

S Nicholls
Meteorological Office, Bracknell

1 INTRODUCTION

Interest in the cloud-topped boundary layer (CTBL) has increased considerably in recent years, acknowledging the importance of cloud-radiation feedback in climate simulations, the desire to interpret cloud structure from satellites and the requirement to provide more detailed local forecasts. Progress towards these goals demands a thorough understanding of the interaction of the physical processes active in CTBL's, including microphysics, radiation and turbulent transfer. One of the important differences of CTBL's compared to other types of boundary layer is that radiative effects can dominate the layer dynamics. For example, mixing may proceed entirely independently of surface processes in free, elevated cloud layers. This paper concentrates on aspects of the convective motion found such conditions and which are responsible for the cellular patterns commonly observed in stratocumulus. Understanding these motions is essential if the evolution of layer cloud is to be successfully modelled since they control both vertical transport and entrainment across layer boundaries. These results should also be useful in assessing the realism of large eddy simulations which are increasingly being employed to study entrainment.

Flight No	Cloud Depth (m)	h (m)	w_* (m/s)	T_{v*} (K)	q_{T*} (g/kg)	ΔE (K)	$\langle T_v' \rangle$ (K)
511	320	370	0.57	0.026	0.028	0.021	-0.052
526	450	480	0.57	0.020	0.044	0.054	-0.040
528	190	480	0.63	0.024	0.021	-0.002	-0.048
620	340	700	0.78	0.025	0.028	0.031	-0.050

Table 1. Details of cases analysed (see also Ref 1)

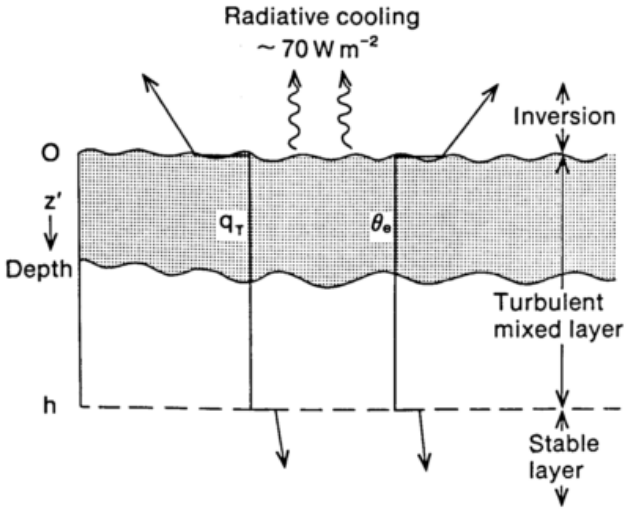


Fig 1 Schematic of conditions encountered. The cloud layer is shaded. The variation of equiv. potential temp. (θ_e) and total water mixing ratio (q_T) with height are also shown.

2. THE DATA

These were collected on four flights by the MRF C130 aircraft in horizontally uniform, unbroken sheets of stratocumulus over the sea around the UK. See Table 1 for details. In each case, the cloud layer occupied the upper part of a mixed layer within which vertical gradients of the conserved quantities θ_e and q_T were found to be small (Fig 1). Cloud top was marked by a strong inversion with a slightly stable region beneath the lower mixed layer boundary. The clouds were between 190m and 450m thick, while the mixed layer depth, h, varied from 370m to 700m. Mixed layer turbulence was being maintained by buoyant convection alone, with shear production negligible (Ref 2). Buoyancy production is largest just below cloud top (Ref 2) and is primarily due to radiative cooling. IR cooling from the top few tens of metres at cloud top is typically ~70 Wm^{-2}.

3. CONDITIONAL SAMPLING

The intense local cooling at cloud top sets up convective motion in the form of negatively buoyant downdraughts. These have been investigated using conditional sampling. Downdraughts (events) were defined by the nearest zero crossing points whenever the vertical velocity exceeded a threshold of $-0.5w_*$ (Fig 2). The minimum acceptable width, d, was h/20 (~25m) and events had to be separated by at least one data point (~6m). When scaled using the mixed layer quantities (w_*, T_{v*}, q_{T*}, defined in Ref 1 and see Table 1) a surprisingly consistent picture emerges.

Downdraughts occupy a maximium fractional area, ~0.37, just below cloud top (Fig 3). They are an efficient means of transport and are responsible for over half the heat, water vapour and liquid fluxes despite occupying well under half the area. The average intersected event width increases and the encounter frequency decreases with distance below cloud top (z'). The distribution of intersected widths near cloud top can also be shown to be consistent with observed cellular patterns if downdraughts are assumed to occupy relatively narrow regions (~0.1h-0.15h wide) around the periphery of larger area updraughts (diameter ~0.5h).

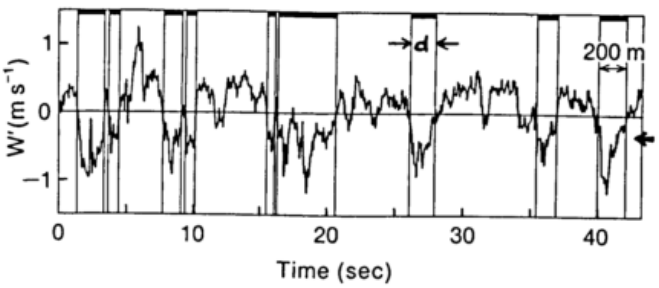


Fig 2. Vertical velocity data from part of a run near cloud top showing downdraughts chosen by the conditional sampling algorithm. The threshold ($-0.5w_*$) is arrowed.

Conditionally sampled statistics show that, on average, downdraughts are both cooler and drier than their surroundings in the upper part of the mixed layer (Fig 4). These contrasts are largest near cloud top, decreasing to around zero near z'=0.5h, as downdraughts mix with surrounding cloud. Thus, downdraughts near cloud top contain both air which has been radiatively cooled as well as dry air entrained from above cloud top which has been cooled and moistened by evaporation. Since q_T is conserved over short timescales during mixing, the fraction of air within the downdraught originating from above cloud can be estimated using $\langle q_T' \rangle$. This can then be used to calculate the expected mean buoyancy change of the downdraughts due solely to mixing and subsequent evaporation,

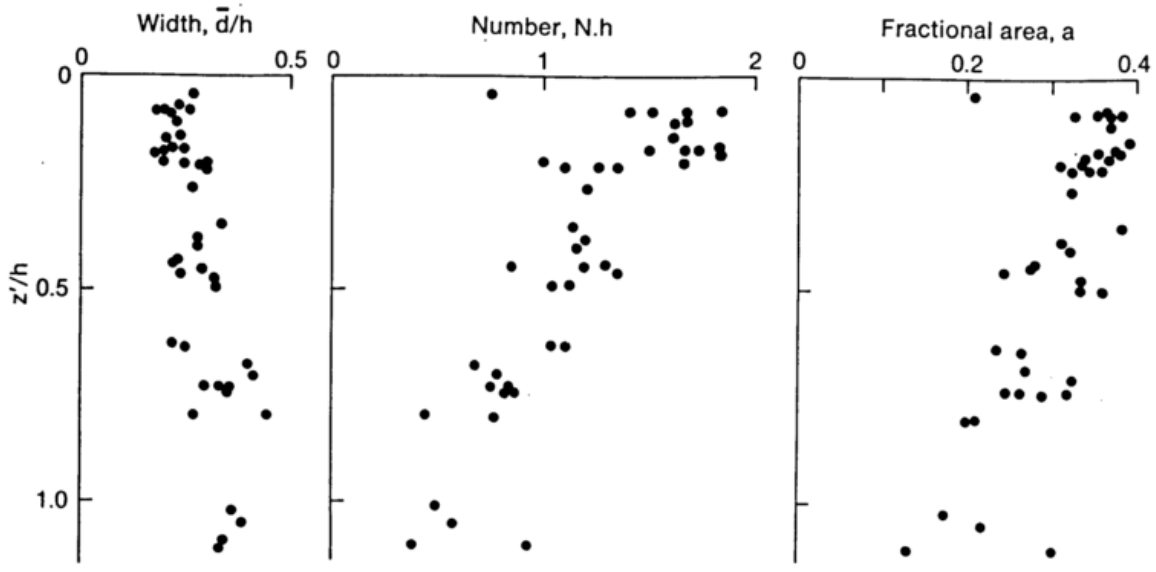


Fig 3. Run-averaged downdraught properties: mean event width ($\bar{d}$), number encountered (N) and area occupied.

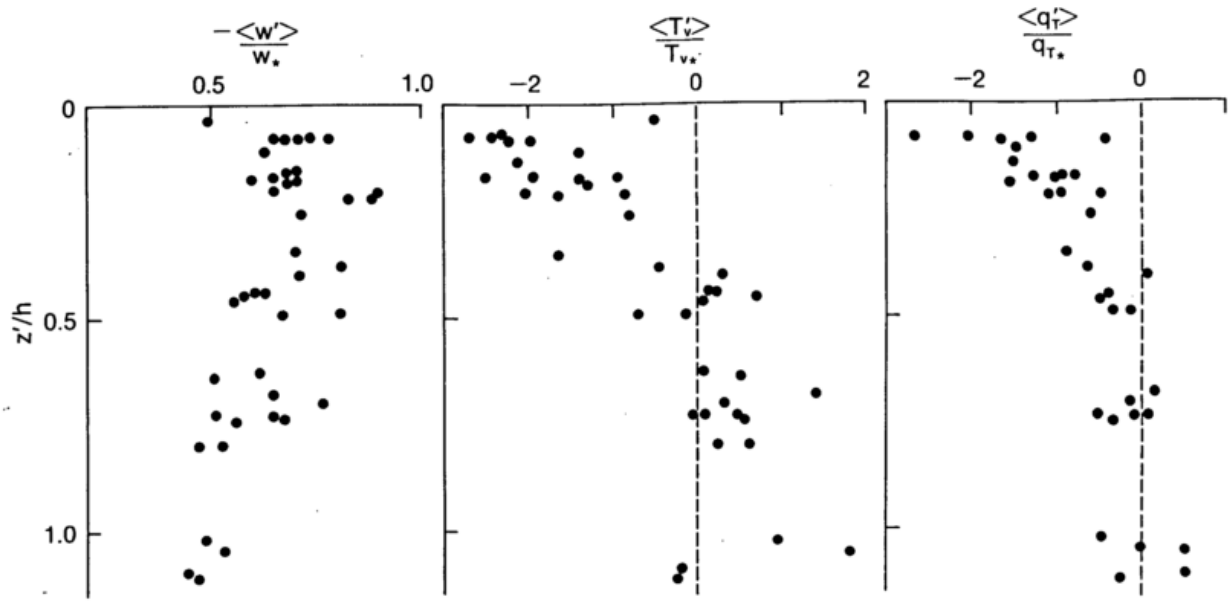


Fig 4. Event-mean vertical velocity $\langle w' \rangle$, virtual temperature $\langle T_v' \rangle$ and total humidity $\langle q_T' \rangle$ deviations from the run average. See Table 1 for scaling.

(ΔE in Table 1). These are small and have the wrong sign in all but one case to explain the observed values of $\langle T_v' \rangle$ listed alongside. Only radiative cooling can produce the observed negative buoyancy. A few minutes exposure to the cooling rates of several degrees per hour calculated to exist at cloud top would be sufficient.

These temperature and moisture differences between events and their surroundings are smaller than those found in corresponding convective layers over heated land or sea surfaces (Refs 3,4), but this is compensated by the greater fractional area occupied by the downdraughts. The cloud top interface is thus ventilated more effectively than an aerodynamically rougher land or sea surface.

Although events near cloud top are relatively cool and dry on average, the conditional mean values are still quite small. Fluctuation levels within events are large compared to the mean deviation for all quantities except w. Downdraughts therefore also contain pockets which are both relatively moist and positively buoyant. The mean buoyancy deficit of the downdraughts is more than sufficient to explain their downward acceleration, but the poor correlation between w' and T_v' within events suggests that the well defined event vertical velocity signature (near cloud top) results from the horizontal convergence of circulations constrained by the overlying inversion rather than direct buoyant instability at cloud top. In this interpretation, horizontal circulations formed by updraughts spreading out under the inversion scour the cloud top interface, incorporating air which has been radiatively cooled and/or partially mixed with inversion air before being forced down in narrow convergence zones. These downdraughts subsequently accelerate because of their net negative buoyancy,mixing internally and with the surrounding cloud. Updraughts compensating for this downward mass flux rise until they near the inversion where they are forced to spread out. This interpretation is also consistent with the measured turbulent kinetic energy balance (Ref 2).

4 REFERENCES

1. Nicholls S & Leighton J R 1986 Quart J R Met Soc, **112**, 431-460
2. McVean M & Nicholls S 1988 Proc Xth Intl Cloud Phys Conf, Bad Homburg
3. Lenschow D H & Stephens P L 1980 Boundary Layer Met, **19**, 509-532
4. Greenhut G & Khalsa S 1985 J Atmos Sci, **42**, 2550-2562

RADIATIVE INFLUENCES ON PRECIPITATING MESOSCALE SYSTEMS

W.R. Cotton and S. Chen

Dept. of Atmospheric Science, Colorado State University, Fort Collins, CO 80523

G. Tripoli

University of Wisconsin, Dept. of Meteorology, Madison, WI 53715

1 Introduction

A number of researchers have speculated that radiative effects are important to the lifecycle of both tropical and extra-tropical mesoscale convective systems. Gray and Jacobson (1977), for example, noted that oceanic, tropical deep convection exhibits an early morning maximum and early evening minimum in heavy rainfall. It is also commonly observed that certain types of extratropical mesoscale convective systems (MCS), especially mesoscale convective complexes (MCCs), occur preferentially at night (Maddox, 1981; 1983). Wetzel *et al.* (1983) speculated that the destabilization caused by radiative cooling may be one factor contributing to the propensity for MCCs to form at night. It therefore seems worthwhile to examine the affects of longwave and shortwave radiation on simulated mesoscale convective systems.

In this paper we describe the results of model sensitivity experiments to long-and short-wave radiation using the Colorado State University Regional Atmospheric Modeling System (RAMS). The model response to radiation is investigated for three different MCSs: an isolated MCS over the High Plains of the United States, a pre-frontal squall line observed during the Australian Cold Fronts Research Program, and an orogenic MCS to the east of the Colorado mountains.

2 Summary of model

The model used in this study is the CSU RAMS which is derived from the cloud model described by Tripoli and Cotton (1982) and Cotton *et al.* (1982; 1986), and the mesoscale model described Mahrer and Pielke (1977). The model contains physical parameterizations for cloud microphysics (Cotton *et al.*, 1982; 1986) which include liquid and ice phase precipitation processes. Longwave and shortwave radiative tendencies on θ_{il} (Chen and Cotton, 1983) are computed in cloudy regions by assuming all condensed water is in the liquid phase. No consideration is given to the unique radiative properties of the ice phase. Only longwave radiative effects are considered in the High Plains MCS whereas both short-and long-wave radiative effects are in the Australian squall line and the orogenic MCS. In the High Plains MCS and the Australian squall line, surface temperatures are specified and held fixed throughout the simulations. In the orogenic MCS simulation, soil temperature and soil moisture are predicted with an underlying soil model described by McCumber and Pielke (1981) and a surface energy balance model described by Tremback and Kessler (1985). Vertical and horizontal turbulent mixing is modeled using an eddy viscosity approach similar to that described by Tripoli and Cotton (1982).

The model equations are integrated by finite difference techniques described by Tripoli and Cotton (1982) for a non-hydrostatic, compressible system using a time-splitting procedure. Vertical grid resolution is 0.5 km in the High Plains MCS and the Australian squall line, whereas it is 0.25 km at low-levels and 0.75 km in the free atmosphere in the orogenic MCS. Horizontal grid resolution is 1.5 km (High Plains MCS), 1.0 km (Australian squall line) and 1.08 km (orogenic MCS).

3 Sensitivity to Radiation

3.1 High Plains MCS

In this case a two-dimensional version of RAMS was applied to the simulation of a U.S. High Plains MCS that was observed on July 14-15, 1984 during the AIMCS experiment. A detailed description of the experiment is given in Chen and Cotton (1988). A control simulation was established that exhibited many features in common with observed MCSs. The storm is dominated by a single persistent convective cell that contained a multi-branched updraft two of which fed the leading and trailing stratiform anvil cloud. A third updraft branch returned to the surface in what Knupp (1987) referred to as an "up-down" downdraft. This convective-scale downdraft mixed with mid-level air entering from the rear of the system. The contribution of longwave radiative flux divergence to the cloud heating rates is shown in Figure 1. A maximum of 35-40°C/day cooling near cloud top and a maximum of 20-25°C warming near the cloud base can be seen. The horizontal average of the longwave heating profile over the model domain yields approximately 16°C/day cooling at cloud top and 11°C/day warming at cloud base similar to results inferred by Cox and Griffith (1979) and Webster and Stephens (1980) in tropical clusters.

Turning off radiation reduced the warming within the stratiform cloud layer by 2°C, the magnitude of the surface cold pool was 1 C warmer, and the cloud top was 2°C warmer. The precipitation rate in the stratiform region with and without radiation is nearly identical. Likewise, differences in total surface precipitation after 4 h of simulation is small. It is possible that the slowly-settling ice crystals formed near the stratiform cloud top did not have enough time to reach the surface or seed the water-rich regions in the 4 h of simulation time. Also the ice crystal model tends to develop too many small ice crystals thus further reducing a surface precipitation response.

Although the microphysical structure failed to show significant changes due to the absence of longwave radiation, the internal cloud circulation increased noticeably when longwave radiation was activated. Figure 2a and 2b show the simulated circulation fields at 4 h for the radiation and no-radiation cases. The mesoscale updraft and downdraft strengths were similar in the leading stratiform regions while they were in general 0.5 to 1.0 m/s stronger when radiation was included. Likewise, peak convective-scale updraft strengths were in general stronger in the radiation experiment with the maximum value over 4 h being 28 m/s with radiation and 18 m/s without radiation. In the case with radiation, a nearly 80 km long, continuous band of jet-like

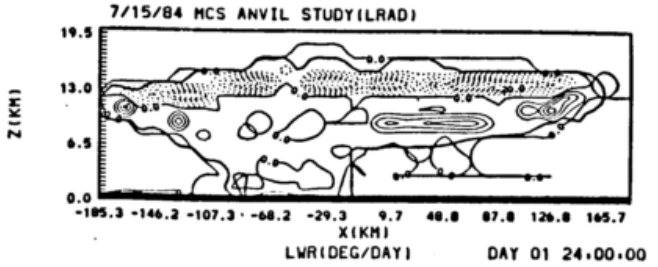


Figure 1: Longwave radiation cooling/heating rate. The contour interval is every 5°C.

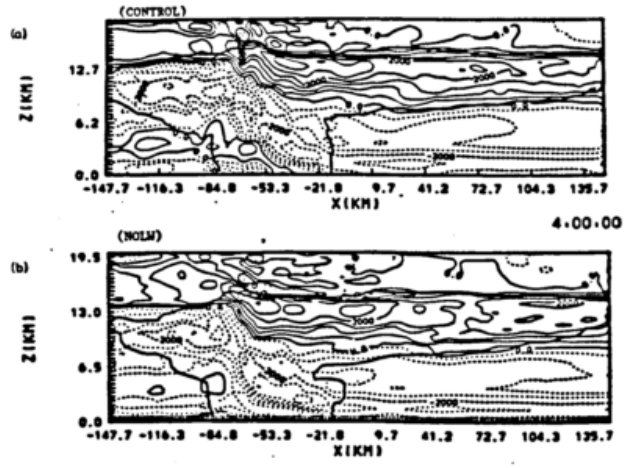


Figure 2: The horizontal velocity field for (a) control experiment and (b) no longwave radiation run. Dashed lines represent wind from the southwest and the solid lines represent wind from the northeast. The contour interval is 5 $m\ s^{-1}$.

rear-to-front, inflow at middle levels is evident with speeds of 3 to 5 m/s whereas it is only 2 to 4 m/s and not as continuous with radiation turned off.

3.2 The Australian squall line

In this case CSU RAMS was applied to the simulation of a squall line that was observed during the Australian Cold Fronts Research Program (CFRP) (Garrett *et al.*, 1985). The squall line occurred in a situation in which cold marine post-cool-frontal air from the south intermixes with hot and relatively dry air from the north. The cool marine air advancing from the south is relatively dry and stable, and produces some cloud near 1.5-2 km elevation. In advance of a frontal zone, a rising "conveyor belt" of relatively dry continental air advances southward from the north Australian interior. Because the relative humidity is low, saturation within this overrunning layer is not reached until it approaches 5 km MSL. This results in the formation of a shallow stratiform cloud in which all the potential convective instability is between the air residing at 500-700 mb and the air at 200-300 mb.

The simulations supported the hypothesis that unstable convection might be initiated by virga settling from the stratiform region of the conveyor belt into the post-frontal airmass. Initial evaporative cooling induced by virgae, generated vertical motions both upstream and downstream of the evaporatively cooled region. The sub-cloud circulations induced convergence in the subcloud layer which results in moderate intensity convection due to the conditional instability in the layer. Liquid water produced in the weak, conditionally unstable layer results in the formation of precipitation which further strengthens the sub-cloud convergence and the squall line circulation.

As in the High Plains MCS, longwave radiative flux divergences were turned off to examine the importance of radiation to the simulated squall line. Figure 3a and 3b show the simulated circulation fields and vertical velocity for the case with and without radiative effects, respectively, after 3 h of simulation. Turning off radiative effects weakened the system as a whole. Ice crystal mixing ratios diminished by over 0.5 g/kg and no precipitation reached the surface. Peak updraft and downdraft velocities weakened from the control by more than 50%. Downdraft velocities were actually stronger in the no radiation experiment early in the system lifecycle, but did not subsequently increase. The overall organization of the bands is strikingly different at 3 h with the no-radiation simulation exhibiting a stronger left band than the control.

The sensitivity to radiative effects in this case is not too surprising since the conditional instability in the upper parts of the cloud layer is relatively weak. Thus the destabilization caused by cloud top radiative cooling enhances the updrafts which, in turn,

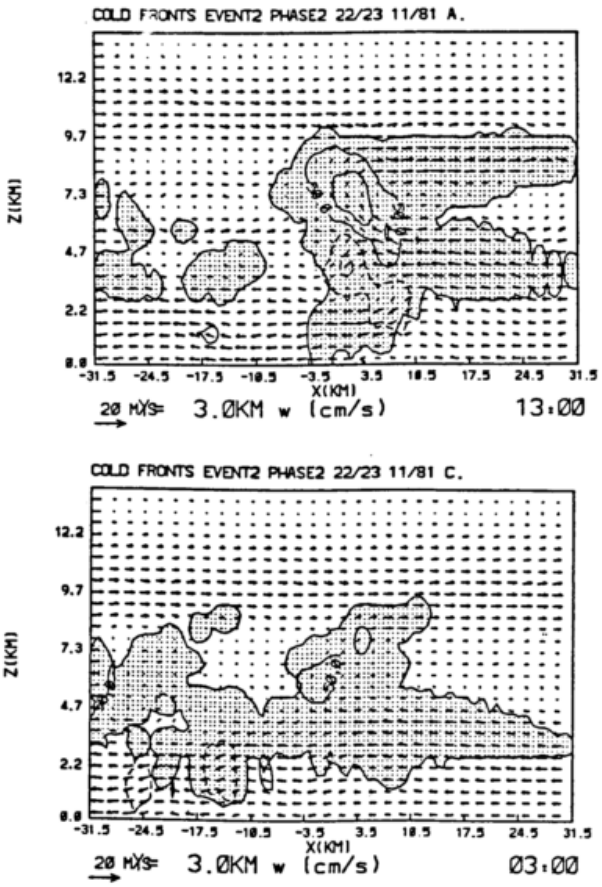


Figure 3: Predicted fields at 3 h of integration. In (a) radiation is included, thus integration corresponds to a time of day. Integration began at 10:00 CST and this time is therefore 13:00 CST. Vertical coordinate is height and horizontal coordinate is distance. Shading represents region where condensate exists, contoured fields are of w at intervals of 1 m/s beginning at 0.5 $m\ s^{-1}$. Radiation is turned off in (b). Because radiation is turned off, time begins at zero h.

produces more condensate and precipitation. The greater precipitation results in more sub-cloud evaporative cooling thus invigorating the downdraft circulation which perturbs the cloud layer divergence and so on. For further details see Ryan et al.(1988).

3.3 An Orogenic MCS

The objective of this simulation was to examine the interactions between topographically-induced mesoscale circulations and deep convection as observed on a particular case study (Cotton *et al.*, 1983; Wetzel *et al.*, 1983). Shortwave and longwave radiation effected the surface energy budget as well as the thermodynamic structure of the cloudy and cloud-free atmosphere. The simulations described in detail by Tripoli (1986) and Tripoli and Cotton (1988a,b) were run for over 24 h on a two-dimensional domain that extended from the Colorado/Utah border eastward to central Kansas with 1.08 km horizontal resolution. As in the above experiments a control simulation was established and then the sensitivity of the model to radiative effects examined. In the sensitivity run longwave radiative flux divergences caused by clouds were neglected while daytime solar heating and radiative flux divergences in a cloud-free atmosphere were considered. In the control simulation deep convection first developed in the mountains and then organized into a mesoscale system which propagated over the plains to the east in the early afternoon. The MCS continued to propagate eastward on the plains undergoing cycles of intensification and decay. At sunset, longwave radiative cloud top cooling uninhibited by solar heating, destabilized the upper troposphere. The initial destabilization of the anvil leads to momentary explosive growth of the mesoscale circulation. Figure 4 illustrates the smoothed circulation field, at

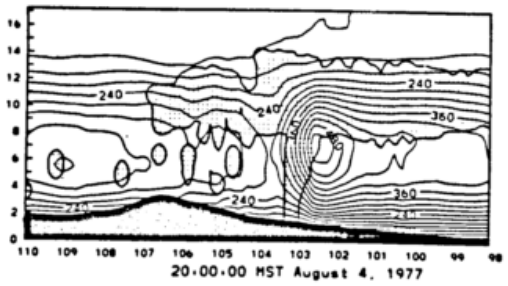


Figure 4: Predicted meso-β-scale fields at 2000 MST for control case. Variables are as labeled. The fields represent 80 grid point (86 km) running averages of actual predicted variables. Streamfunction fields are calculated relative to the $10\,m\,s^{-1}$ storm motion. Contour interval is 500 $g\,cm^{-1}s^{-1}$. The boundary for condensate in excess of 0.01 $g\,kg^{-1}$ (cloud boundary) is drawn by a heavy dark line and the region within is lightly shaded. The surface topography is depicted by the black shading. The vertical axis is height in km above mean sea level (MSL) and the horizontal axis is west longitude.

2000 MST at the time of sunset. Gravity waves which had previously been emitted into the stratosphere now became trapped after sunset by the unstable cloud top layer. As a result the previously singular meso-β-scale upward circulation cell dispersed over several competing regions of meso-β-scale upward motion.

Turning off longwave radiation cloud top cooling did not effect the simulation appreciably prior to sunset. At sunset, however, the explosive growth simulated in the control case was considerably weaker. Whereas the control convection dispersed into meso-β-scale competing circulations after sunset, the no-longwave radiative cooling case remained concentrated in a single meso-β-scale cell. The differences being largely due to the differences in the propagation of gravity waves due to lower stability in the cloud top radiation experiment. The impact of radiation on surface precipitation can be seen in Figure 5. The major difference occurs at a longitude of 103 (degree) where the control experienced pronounced intensification at sunset.

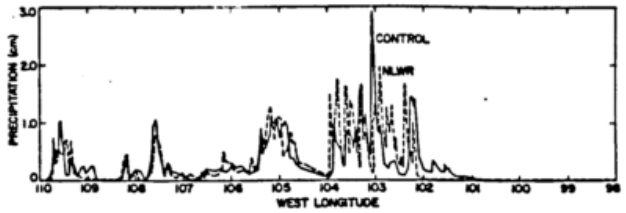


Figure 5: Accumulated precipitation in cm (vertical axis) versus horizontal location W longitude (horizontal axis). Curves for control case and NLWR case drawn.

4 Summary

These three cases illustrate that longwave radiation can have a significant influence on the behavior of mesoscale convective systems. The simulated interactions between radiation and the dynamics of MCSs is strong enough to merit further refinement in both the radiation and microphysical parameterizations. The impact of longwave radiation can involve some very complex interactions that in some cases is directly related to the destabilization of the cloud layer while in other cases the link is more indirect through the trapping of gravity wave energy in the troposphere.

Acknowledgements

We acknowledge Brian Ryan's contribution to the Australian squall line simulations. Brenda Thompson processed the manuscript. The research was supported under National Science Foundation Grant #ATM 8512480. Computations were performed at the National Center for Atmospheric Research (NCAR). NCAR is sponsored by the National Science Foundation.

References

Chen, C., and W.R. Cotton, 1983: A one-dimensional simulation of the stratocumulus-capped mixed layer. *Boundary-Layer Meteorol.*, **25**, 289-321.

Cotton, W.R., M.A. Stephens, T. Nehrkorn, and G.J. Tripoli, 1982: The Colorado State University three-dimensional cloud/mesoscale model - 1982. Part II: An ice phase parameterization. *J. de Rech. Atmos.*, **16**, 295-320.

Cotton, W.R., G.J. Tripoli, R.M. Rauber, and E.A. Mulvihill, 1986: Numerical simulation of the effects of varying ice crystal nucleation rates and aggregation processes on orographic snowfall. *J. Clim. Appl. Met.*, **25**, 1658-1680.

Cotton, W.R., R.L. George, P.J. Wetzel and R.L. McAnelly, 1983: A long- lived mesoscale convective complex. Part I: The mountain-generated component. *Mon. Wea. Rev.*, **111**, 1893-1918.

Cox, S.K., and K.T. Griffith, 1979: Estimates of radiative divergence during Phase III of the GARP Atlantic Tropical Experiment: Part II. Analysis of Phase III results. *J. Atmos. Sci.*, **36**, 586- 601.

Garrett, J.R., W.L. Physick, R.K. Smith, and A.J. Troup, 1985: The Australian summertime cool change. Part II: Mesoscale aspects. *Mon. Wea. Rev.*, **113**, 202-223.

Gray, W.M., and R.W. Jacobson, Jr., 1977: Diurnal variation of deep cumulus convection. *Mon. Wea. Rev.*, **105**, 1171-1188.

Knupp, K.R., 1987: Downdrafts within High Plains cumulonimbi. Part I: General kinematic structure. *J. Atmos. Sci.*, **44**, 987-1008.

Maddox, R.A., 1981: The structure and life-cycle of midlatitude mesoscale convective complexes. Atmospheric Science Paper No. 336, Dept. of Atmospheric Science, Colorado State University, Fort Collins, Colorado, 80523, 311 pp.

Maddox, R.A., 1983: Large-scale meteorological conditions associated with midlatitude, mesoscale convective complexes. *Mon. Wea. Rev.*, **111**, 1475-1493.

Mahrer, Y. and R.A. Pielke, 1977: A numerical study of the airflow over irregular terrain. *Beitrage zur Physik der Atmosphare*, **50**, 98-113.

McCumber, M.C. and R.A. Pielke, 1981: Simulation of the effects of surface fluxes of heat and moisture in a mesoscale numerical model. Part I: Soil layer. *J. Geophys. Res.*, **86**, 9929-9938.

Tremback, C.J. and R. Kessler, 1985: A surface temperature and moisture parameterization for use in mesoscale numerical models. Preprints, 7th Conference on Numerical Weather Prediction, 17-20 June 1985, Montreal, Canada, AMS.

Tripoli, G.J., 1986: A numerical investigation of an orogenic mesoscale convective system. Ph.D. dissertation, Colorado State University, Dept. of Atmospheric Science, Fort Collins, Colorado 80523. (Atmospheric Science Paper No. 401).

Tripoli, G.J., and W.R. Cotton, 1982: The Colorado State University three-dimensional cloud/mesoscale model - 1982. Part I: General theoretical framework and sensitivity experiments. *J. de Rech. Atmos.*, **16**, 185-220.

Tripoli, G., and W.R. Cotton, 1988: A numerical study of an observed orogenic mesoscale convective system. Part 1. Simulated genesis and comparison with observations. Submitted for publication to *Mon. Wea. Rev.*

Tripoli, G., and W.R. Cotton, 1988: A numerical study of an observed orogenic mesoscale convective system. Part 2. Analysis of governing dynamics. Submitted for publication to *Mon. Wea. Rev.*

Webster, P.J. and G.L. Stephens, 1980: Tropical upper-tropospheric extended clouds: Inferences from Winter MONEX. *J. Atmos. Sci.*, **37**, 1521-1541.

Wetzel, P.J., W.R. Cotton and R.L. McAnelly, 1983: A long-lived mesoscale convective complex. Part II: Evolution and structure of the mature complex . *Mon. Wea. Rev.*, **111**, 1919-1937.

CIRRUS MICROPHYSICS AND INFRARED RADIATIVE TRANSFER: A CASE STUDY

Thomas P. Ackerman[1], Andrew J. Heymsfield[2], Francisco P. J. Valero[3], Stefan Kinne[3]

[1]Department of Meteorology, Pennsylvania State University, University Park, PA
[2]NCAR, Boulder, CO
[3]NASA Ames Research Center, Moffett Field, CA

1. INTRODUCTION

The First ISCCP Regional Experiment (FIRE) consists of several research activities designed to study the role of clouds in global climate in support of the International Satellite Cloud Climatology Program (ISCCP). The first cirrus intensive field observation period was conducted from 13 October, 1986 to 2 November, 1986 in central Wisconsin, USA. The details of FIRE and the cirrus observation period can be found in Cox et al. (1987) and Starr (1987).

One of the primary objectives of FIRE was to aquire co-incident measurements of cirrus cloud microphysical properties such as particle size distribution and particle shape and morphology and measurements of infrared intensity and flux. On a variety of occasions during the observation period, data was acquired nearly simultaneously in space and time by the NCAR KingAir in cloud and by the NASA ER-2 at an altitude of about 19 km. In this paper, we have chosen to present data obtained on 28 October. The particular aircraft data of relevance to this case study consist of upwelling infrared intensities and fluxes measured from the ER-2 and observations of cloud particle size distributions and particle phase and morphology made from the KingAir. In addition, broad-band flux measurements were available both in and below the cirrus layer from the KingAir.

2. DATA

The synoptic situation on 28 October was characterized by a warm front passing through the observing network. Associated with the warm front passage was the development of various types of convective cirrus. Ground-based and airborne lidar showed numerous cirrus generating cells producing a cirrus layer with a variable optical thickness. For a period of approximately an hour (16:30 to 17:30 GMT), the two aircraft flew stacked, timed "racetracks" (a pattern of two longer parallel sides and shorter curved ends) in an area of developing cirrus. Due to the factor of 2-3 times greater speed of the ER-2 and the much shorter turning radius of the KingAir, the racetrack of the latter was completely enclosed by that of the ER-2, as well as being much shorter in length. Thus, only twice during each racetrack pattern were the two planes briefly observing the same general column of air. Furthermore, since the each aircraft's navigation has some error in position, the exact point of coincidence is difficult to define. Consequently, we have taken the approach of developing a composite cirrus layer from the KingAir observations taken during this time period and comparing it with average radiation fields observed by the ER-2.

The KingAir flew its racetrack legs at 7 altitudes ascending from 6 to 8 km. During each leg, several size distributions were acquired using PMS 2-D shadow probes. Glass slides were used to collect ice crystals by exposing the slide to the airstream and allowing crystals to impact on it. The slides were kept cold in CO_2 ice and returned to the ground for analysis of particle shape and size.

Observations of the upwelling 10.5 μm and 6.5 μm radiances and broad-band infrared flux were made from the ER-2. The radiance measurements were made with a 2-channel, nadir-viewing instrument continuously calibrated by a reference cell filled with liquid nitrogen. The instrument field of view is a 15° cone. The IR flux were measured by a flat plate radiometer that has a specially designed aperture with a cosine response.

3. DATA ANALYSIS

From the ice crystal slides and the 2-D shadow probe, it was observed that the majority of crystals were bullets and bullet rosettes, the latter typically consisting of 3 to 5 bullets. Using this information and the number of crystals per size bin, we are able to develop two different types of size distributions for model calculations. In the first, we simply compute the amount of ice water in a given size interval based on the average aspect ratio of the bullets. From the ice water amount, we can then compute the number of spheres for either equivalent volume or cross-section. The extinction coefficient for the spheres can then be computed from MIe theory. Average distributions and coefficients are computed for each aircraft leg, allowing us to develop a vertical profile of the composite cloud. Alternatively, we separate the rosettes into their individual bullets and bin the bullets into the appropriate size interval. We assume that the bullets can be approximated as cylinders and then compute the extinction and scattering coefficients. Again, average values are computed for each leg, allowing the development of vertical profiles.

The radiances are also analyzed statistically over the flight period. Histograms of the radiances are plotted

and means and variances calculated. Since the cloud temperature is know from radiosonde and KingAir measurements and the surface radiation temperature from below cloud measurements from the KingAir and clear-sky measurements from the ER-2, it is possible to convert the 10 μm radiances to distributions of cirrus optical depth.

An infrared multiple-scattering model is then applied to the composite cloud and atmosphere. The calculated radiances and fluxes for the various assumed size distributions are compared to the observed radiances and fluxes. The mean and variances of the calculated radiation field, based on the observed variability in the size distributions, is compared with the observed mean and variances. On the basis of these calculations, we can assess the validity of various particle size and shape approximations. Given reasonable agreement, we can also assess the infrared radiative exchange within the cirrus layer and the average heating rates.

4.REFERENCES

Cox, S. K.; McDougal, D. S.; Randall, D. A.; Schiffer, R. A.: FIRE – The First ISCCP Experiment. *Bull. Amer. Meteor. Soc.* 68 (1987) 114-118.

Starr, D. O'C.: A cirrus-cloud experiment: Intensive field observations planned for FIRE. *Bull. Amer. Meteor. Soc.* 68 (1987) 119-124.

THE COLLECTION EFFICIENCY OF A MASSIVE FOG COLLECTOR

Robert S. Schemenauer and Paul I. Joe
Atmospheric Environment Service
4905 Dufferin St., Downsview, Ontario, Canada M3H 5T4

1. INTRODUCTION

The Camanchaca Project is designed to determine if fog water can serve as a new type of arid zones water supply. The background of the 2 year project is described in SCHEMENAUER et al. (1988). Estimates of the amounts of water that can be deposited by fogs are given in SCHEMENAUER (1986,p.303). Coastal stratocumulus cloud decks are blown onshore by the prevailing low level winds on the coast of Chile. The clouds are intercepted by the coastal mountains and extensive periods of high elevation fog (camanchaca) result. The fog is collected by large meshes called atrapanieblas. The choice of optimum sampling location is done by conducting preliminary experiments on relative fog water collection using small collectors (SCHEMENAUER et al. 1987, p.1285). This paper will describe the results of measurements designed to determine the collection efficiency of the atrapanieblas.

2. THE NOVEMBER 1987 FIELD PROJECT

2.1 FIELD SITE

The site is 60 km north of the city of La Serena in north central Chile. The main experimental location is on a ridge at 780 m (29° 26'S, 71° 15'W). It is 6 km from the village of Chungungo on the Pacific coast. Water from 60 large collectors on El Tofo will be delivered to Chungungo by the end of 1988.

2.2 INSTRUMENTATION

The 40 m^2 atrapanieblas are 10 m long and 4 m high. The top of each collector is 6 m above ground. The collecting material is a double layer of black nylon mesh that is made in Chile. The mesh is a triangular weave of a flat fiber about 1 mm wide. The fiber is woven into a mesh with a pore size of about 1 cm. The atrapanielas are being installed at several locations from 710 m to 780 m on El Tofo. Measurements of the characteristics of the fog droplet sizes and concentrations were made with two Particle Measuring Systems Forward Scattering Spectrometer Probes (FSSPs). One FSSP was mounted immediately in front of an atrapaniebla but moved 0.5 m off centre, Figure 1. The second FSSP was mounted behind the atranpaniebla 0.5 m off centre in the other direction. The calibrations of the FSSPs were checked before and after the two week field project using glass beads. Both FSSPs were equipped with aspirators to pull the droplets through

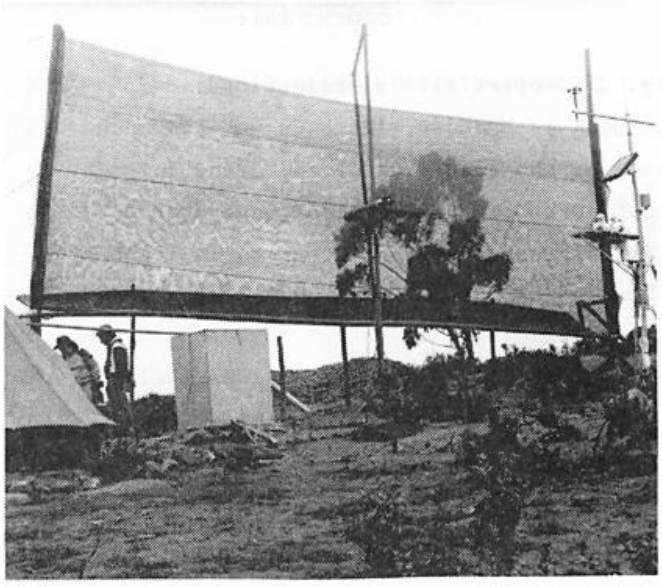


Fig. 1: Atrapaniebla with the forward FSSP.

the measuring section at a constant 25 m s^{-1}. A complete set of meteorological measurements was made 6 m in front of the forward FSSP and at the same height.

3. DROPLET SIZE DISTRIBUTIONS

The drop size distributions usually had a single peak with a mode near 10 µm. Maximum sizes ranged from 15 to 30 µm with larger droplets seen only rarely. Due to a data acquisition failure in the field, large amounts of data were not collected. However, some results from the FSSPs are available. Figure 2 shows the average number of droplets counted by the two FSSPs during four 5 s periods between 1735 and 1745 local time on 12 Nov1987. The peak in the size distribution is at 12 µm as the fog approaches the mesh.

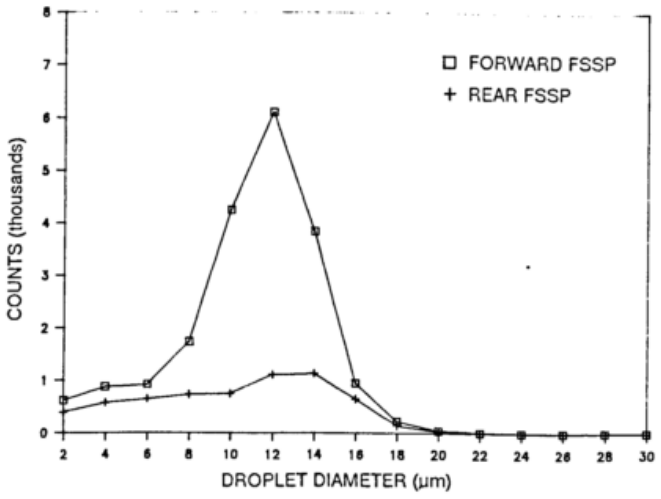


Fig. 2: Droplet size distributions.

The peak is broader, 12 to 14 µm, and much lower on the rear side of the mesh. In each location there was the occasional drop to 28 µm. The average concentration in front of the mesh was 231 cm^{-3} and behind the mesh 73 cm^{-3}.

4. FOG LIQUID WATER CONTENT

The fog liquid water content (LWC) calculated from the distributions in Figure 2 was 0.20 g m^{-3} in front of the mesh and 0.063 g m^{-3} behind the mesh. On average, 69% of the fog water was removed by the mesh. Figure 3 shows how the fog LWC was distributed as a function of the droplet

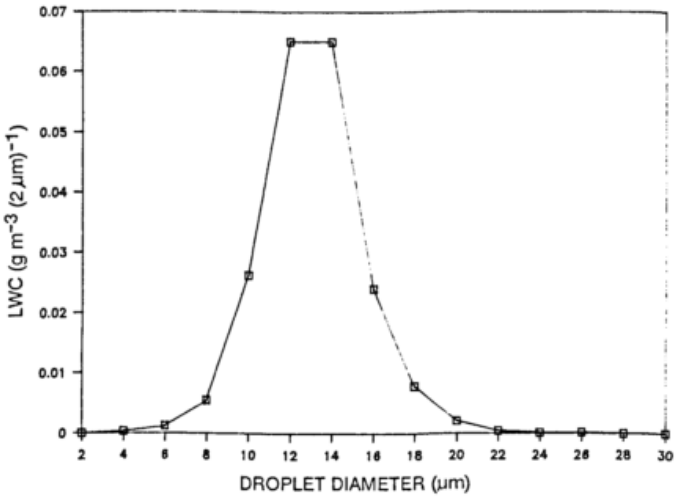


Fig. 3: LWC distribution (forward FSSP).

diameter in front of the mesh. Figure 4 shows the ratio of the LWC behind the mesh to that in front as a function of droplet diameter. The double layer of mesh appears

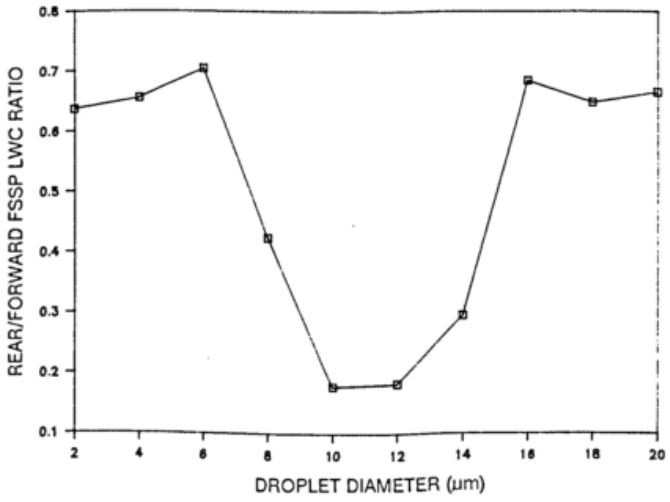


Fig. 4: LWC ratio as a function of size.

to be efficient in removing fog water in the part of the spectrum where most of the water is found. The ratios for droplets larger than 20 µm are not shown since fewer than 10 droplets were counted in 5 s in these channels. In the 10 and 12 µm size channels where the mode of the distribution is, only 18% of the fog water is passing through the mesh. At the time of these measurements, the wind was 6.5 m s^{-1} and the temperature 10.8 °C.

5. MEASURED MESH EFFICIENCY

The double layer of mesh removed 69% of the fog water in the centre of the mesh. If we assume the fog LWC and wind speed were evenly distributed across the atrapaniebla,

then the 40 m^2 collector should have had an output of 36 cm^3 s^{-1}. The actual output as measured by a flowmeter averaged 18.5 cm^3 s^{-1} for the 10 min period from 1735 to 1745. Some water, perhaps 15%, was being lost due to a poor design for the trough at the bottom of the atrapaniebla. But this cannot explain the fact that the ouput was only 52% of the estimated water available. This suggests there may be some unevenness in the water distribution or collection efficiency over the collector surface.

6. THEORETICAL COLLECTION EFFICIENCY

A single layer of the Rashell mesh covers ≈ 50% of the surface area defined by a 40 m^2 atrapaniebla. The double layer of material covers only ≈ 75% of the area since fibers can overlap. Figure 5 gives the collection

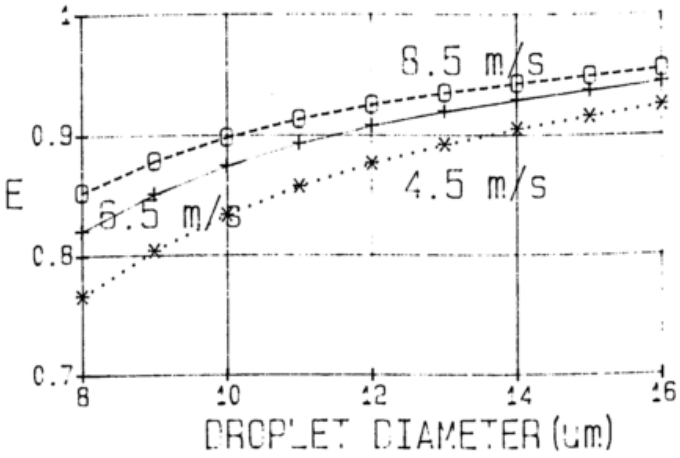


Fig. 5: Collection efficiency calculations. efficiencies of a 1 mm ribbon as a function of air speed and droplet size according to the computations of Langmuir and Blodgett (1946). The ribbon will collect droplets of 13 µm diameter (mid-point of LWC distribution) travelling at 6.5 m s^{-1} with an efficiency of 92%. The LWC passing through an unobstructed 40 m^2 area is 40 m^2 x 6.5 m s^{-1} x 0.2 g m^{-3} = 52 g s^{-1}. Introducing a mesh covering 75% of the area yields 52 g s^{-1} x 0.75 x 0.92 = 36 cm^3 s^{-1}. This is the same as the expected yield calculated from the FSSP data at the center of the collector. Both values are higher than the measured output of 18.5 cm^3 s^{-1} even when increased by 15% to 21 cm^3 s^{-1} to allow for trough losses.

Assuming a lower average wind speed of 4.5 m s^{-1} over the collector only reduces the collection efficiency to 0.89, resulting in an expected output of 35 cm^3 s^{-1}. It appears that about 40% of the water in the swept out volume is not reaching the surface of the collector as a result of the air being forced around the collector and carrying the droplets with it.The wind flow around the collector will be examined in detail during the next field period.

7. CONCLUSIONS

The measured output from a 40 m^2 fog water collector is ≈ 58% of the expected output based on measured and calculated collection efficiencies at the center of the collector. Reduced collection efficiencies due to a lower average wind over the mesh cannot explain the discrepancy. It is postulated that blockage of the wind by the large collector results in flow around the edges of the collector and thus a lower water droplet availability for collection.

8. REFERENCES

LANGMUIR, I., BLODGETT, K.B.: A mathematical investigation of water droplet trajectories. Army Air Force Technical Report No. 5418, Washington, D.C., (1946) 68 pp.

SCHEMENAUER, R.S.: Acidic Deposition to Forests: the 1985 Chemistry of High Elevation Fog (CHEF) Project. Atmosphere-Ocean, 24 (1986) #4, pp. 303-328.

SCHEMENAUER, R.S., CERECEDA, P., CARVAJAL, N.: Measurements of Fog Water Deposition and Their Relationships to Terrain Features. J. Clim. Appl. Meteor., 26, (1987) #9, pp. 1285-1291.

SCHEMENAUER, R.S., FUENZALIDA, H., CERECEDA, P.: A neglected Water Resource: the Camanchaca of South America. Bull. Amer. Meteor. Soc., 69 (1988) #2, pp. xx-xx.

THE USE OF AUTOMATIC PARTICLE RECOGNITION TO IMPROVE THE DETERMINATION OF BULK QUANTITIES FROM PMS 2-D PROBE DATA IN CIRRUS

A.G Darlison and P.R Brown

U.K Meteoroligical Office.

1. INTRODUCTION

Extracting results for bulk parameters from PMS 2d probe data requires us to determine the crystal habits present beceause crystals of different geometry have different average density and fall speed.

Although algorithms for classifying images have been developed their performance on cirrus data has not been tested. Here we investigate the behaviour of our classification software on typical cirrus images.

Furthermore the physical properties of some cirrus crystals are not well-known. We asess likely errors from this source by comparing alternative sets of density and fall speed formulae. We also test the validity of assuming a single dominant particle type.

2.PARTICLE CLASSIFICATION

The image classification scheme is based on the Fourier transform method of Duroure(1983), which detects symmetric images. The sum of the harmonics measures the edge 'roughness' which, together with the 'area ratio' (the product of the major and minor axes divided by image area) distinguishes non-symmetric particles. Images smaller than 6 diodes (150 microns) are not classified.

In the cirrus data we have examined bullet-rosettes and columns are common. Many images however have an irregular but roundish outline and are thought to be mainly irregular spatial crystals, presumably of thick plates and columns. They are frequently the dominant particle type.

Figure 1 shows the effect of this scheme on some cloud probe data. Columns and bullet rosettes are correctly selected. This is verified by time-series plots of the concentrations of rosettes and irregular spatials, which confirm subjective impressions of the variation of dominant particle through the layer.

Out-of focus irregular spatials of size 150 to 200 microns are sometimes classified as bullet-rosettes (Figure 1(d)). The effects of this mis-classification are exacerbated beceause it results in incorrect depth-of field estimate and hence overcounting.

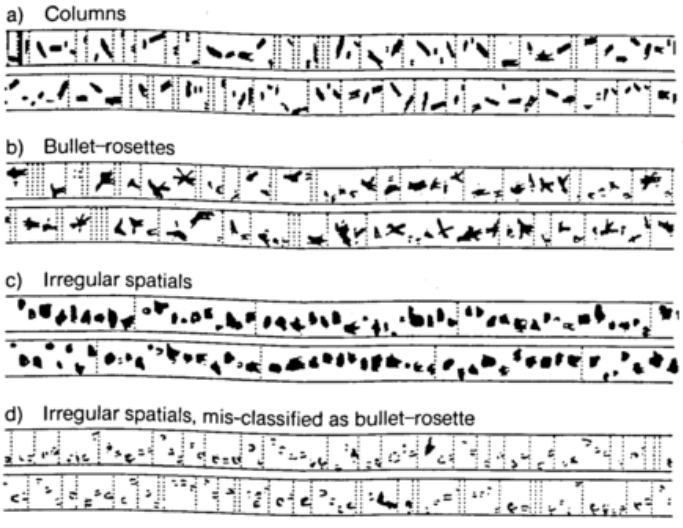


Figure 1. Sample results from the image classification scheme. Flight H786, ascent in frontal cirrus from 5 km altitude to 9 km.

3. MASS AND FALL SPEED FORMULAE

A summary of the various formulae for mass and fall speed appears in Table 1. They are based on the datasets of Heymsfield(1972), taken in

cirrus; Cunningham(1978), taken in U.S East Coast deep cyclonic systems; and Locatelli and Hobbs(1974). Note that in the 'equivalent sphere approximaton' for fall velocity, the particle is placed in an impermeable but massless circumscribed sphere and Stokes formula is used.

Suite 3 was not designed with cirrus in mind and has the following drawbacks i) no altitude correction is applied to fall velocities; and ii) the depth of field for bullet-rosettes is calculated using the maximum dimension rather than an estimate of the width of a branch.

	SUITE 1	SUITE 2	SUITE 3
COLUMNS	$D = 0.82\,A^{0.48}$; $A \leqslant 0.02$ $D = 0.61\,A^{0.41}$; $A \geqslant 0.02$ (HEYMSFIELD)	$D = 0.42\,A^{0.35}$; $A \leqslant 0.16$ $D = 0.52\,A^{0.46}$; $A \geqslant 0.16$ (CUNNINGHAM)	AS SUITE 1
	$U = (-0.528 + 157.33\,D_{MAX} - 85.27\,D_{MAX}^2) \times 10^{-2}$ (HEYMSFIELD)	AS SUITE 1	$U = 0.7\,D_{MAX}^{0.41}$
BULLET-ROSETTE	$D = 0.72\,A^{0.47}$; $A \leqslant 0.088$ $D = 0.67\,A^{0.44}$; $A \geqslant 0.088$ (TETRAHEDRON OF COLUMNS)	$D = 0.50\,A^{0.39}$; $A \leqslant 0.21$ $D = 0.61\,A^{0.51}$; $A \geqslant 0.21$ (CUNNINGHAM)	AS SUITE 2
	$U = (-1.2 + 97.86\,D_{MAX} - 28.17\,D_{MAX}^2) \times 10^{-2}$ (HEYMSFIELD)	$U = 0.69\,D_{MAX}^{0.41}$ (LOCATELLI AND HOBBS)	$U = 0.7\,D_{MAX}^{0.41}$
IRREGULAR SPATIAL	$D = 0.56\,A^{0.32}$ (LOCATELLI AND HOBBS)	$D = 0.52\,A^{0.40}$ (CUNNINGHAM)	—
	$U = 0.897\,D_{MAX}^{0.90}$ (EQUIVALENT SPHERE)	$U = 0.69\,D_{MAX}^{0.41}$ (LOCATELLI AND HOBBS)	—
SMALL (≤ 0.15 mm)	$D = 0.935\,A^{0.5}$ (SPHERE, DENSITY 0.57)	$D = 0.82\,A^{0.48}$ (HEYMSFIELD)	DEPENDS ON BLANKET CLASSIFICATION
	$U = 7.24\,D_{MAX}^2$ (STOKES' FORMULA)	AS SUITE 1 FOR COLUMNS	
DEPTH OF FIELD	MIN AXIS FOR COLUMNS WIDTH OF BRANCH FOR BULLET-ROSETTE MAJ AXIS FOR OTHERS	MIN AXIS FOR COLUMNS AND SMALL PARTICLES WIDTH OF BRANCH FOR BULLET-ROSETTE MAJ AXIS FOR OTHERS	MIN AXIS FOR COLUMNS MAJ AXIS FOR OTHERS

Table 1. Formulae for the melted diameter D (mm) and fall velocity, U, ($m\,s^{-1}$) in terms of maximum particle dimension, D_{MAX} (mm), and projected area A (mm^2).

4. RESULTS AND DISCUSSION.

Generally we find that suite 1 produces larger values for bulk quantities than suite 2. For columns the factor is about 2 for both IWC and precipitation rate; for rosettes about 1.5; and for aggregates 3 to 4 for IWC and 2 for precipitation rate. However for small particles we find that suite 1 gives lower values; a factor of 0.5 for IWC and 0.3 for precipation rate.

Number concentrations are of course identical for particles larger than 150 microns but for small particles suite 1 undercounts by a factor of about 3 relative to suite 2. This accounts for the lower values of other bulk quantities.

Figure 2 shows the final result (summed over particle types for suites 1 and 2) together with the results from a run assuming blanket classification of bullet rosette (suite 3).

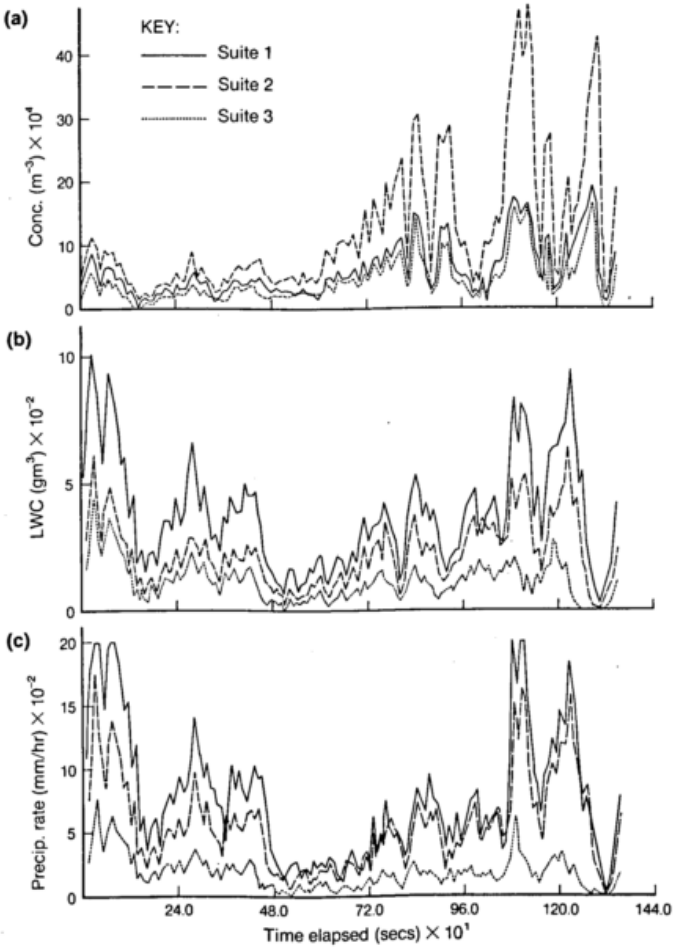


Figure 2. Bulk parameters derived from the same dataset used in Figure 1, using alternative mass and fall speed formulae.

First note that the general structure in the cloud does not depend on which suite is used. This is thought to arise from the negative correlation between average particle size and

concentration which is observed in this set of data.

The plot of particle concentration shows that suites 1 and 3 are in close agreement because the largest contribution comes from small particles which are treated in the same way. However (2) gives results up to three times higher due to the different depth of field calculation for small particles. When analysing 2d data some independant means of establishing the habit of small crystals, such as holography or replication, is clearly needed.

The plot of IWC shows (2) yielding higher values than (1), reflecting the higher estimates for the mass of most particle types in (1). Although (2) gives higher concentrations these do not contribute much to the IWC which resides mostly in larger particles. Suite 3 gives even lower values for IWC than (2) despite using similar mass formulae, highlighting the effects of naive depth of field calculation for bullet rosettes. Note however that (2) and (3) are similar at the start of the run where most particles are irregular spatials. Had the effects of mis-classification, mentioned above, been important this would not have been observed. Those particles which are mis-classified do not make a dominant contribution to the IWC. We conclude that providing particles are correctly classified and the depth of field calculated suitably, IWC estimates could be accurate to a factor of 2.

The trace for precipitation rate shows fairly close agreement for (1) and (2) because differences in fall velocity calculation tend to compensate for differences in mass calculation. This is fortuitous and the real uncertainty in precip. rate is probably a factor of 3 or 4. Note the much lower results from (3). These are still an underestimate even when corrected for altitude (x1.7), again reflecting the effects of naive depth of field calculation.

SUMMARY

1) An automatic particle recognition scheme based on both Fourier transforms and geometry is found to successfully distinguish cirrus particles.

2) Some poorly imaged crystals are mis-classified as bullet rosettes. Such images are over-counted because of depth-of-field effects, but this does not seriously affect bulk quantities.

3) Uncertainties in mass and fall speed relations introduce errors in the corresponding bulk quantities: a factor of 2 for IWC and 3 to 4 for precipitation rate.

4) Number concentrations inferred for small particles depend on what is assumed about their shape in the depth of field calculation. However this source of error is unlikely to affect other bulk parameters.

REFERENCES

Cunningham,R.M 1978 Am. Met. Soc. Boston. iv Symp. Met. Obs & Instr, Denver. 345-9

Duroure,C 1978 J Rech Atmos 16 pp71-84

Heymsfield 1972 J. Atmos. Sci 29 1348

Locatelli,J.D and Hobbs,P.V J. Gephys. Rs. 79 2185

THE COMPARISON OF HOLOGRAPHIC AND 2-D PROBE MEASUREMENTS OF ICE CRYSTALS.

by

P.R.A. Brown and A.G. Darlison

Meteorological Office, Bracknell, UK

1. INTRODUCTION

Measurements of ice crystal concentrations have been made in glaciating maritime cumulus clouds using both PMS 2-D Optical Array Probes and an airborne holographic system (CONWAY et al, 1982; BROWN 1988). For columnar crystals of length greater than 140 µm, the holographic values are a factor of about 5 larger than those from the 2-D probes. Similar factors are also found for irregular ice particles larger than 140 µm and for all ice particles smaller than this limit. We examine various sources of error in both instruments in an attempt to explain the causes of this discrepancy.

2. DATA

The data were obtained during penetrations of two glaciating maritime cumulus clouds (BROWN et al., 1988). The concentration comparison is shown for columnar crystals in Fig. 1, in which the holographic data are averages from a single hologram and the 2-D values are 1 s averages which span the hologram exposure time. Fig. 2 shows size spectra of columnar crystals for data taken from part of a single cloud penetration, the holographic data being an average of four individual exposures and the 2-D data being a 5 s average covering this period. The average concentration difference factor for the whole data set is about 5, whilst for the data in Fig. 2 it is closer to 10. In the latter case the factor appears to be roughly constant over the size range 200-350 µm.

3. ERRORS IN HOLOGRAPHIC DATA

The sample volume of the holographic device

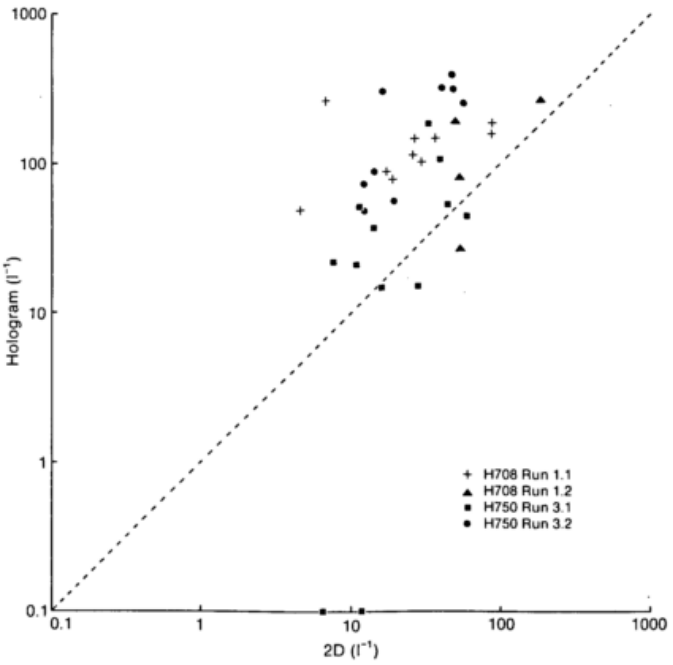


Fig. 1 Comparison of measurements of the concentration of columns with L > 140 µm.

is well-defined by the optical layout of the system (BROWN, 1988). Errors are therefore thought to be derived from two main sources. Firstly, the images themselves are of rather variable quality and it is possible, where the quality is very poor, to fail to identify some of them. This is however most significant for small sizes (less than 50 µm) and will in any case result in undercounting. Second is the effect of the airflow around the pod which houses the holographic camera. This has been examined using the simple model of KING (1984,1985), from which some generalized results may be obtained.

The shadow zone, bounded by a particle trajectory which grazes the pod nose (Fig. 3), has a maximum depth of about 3 cm, for

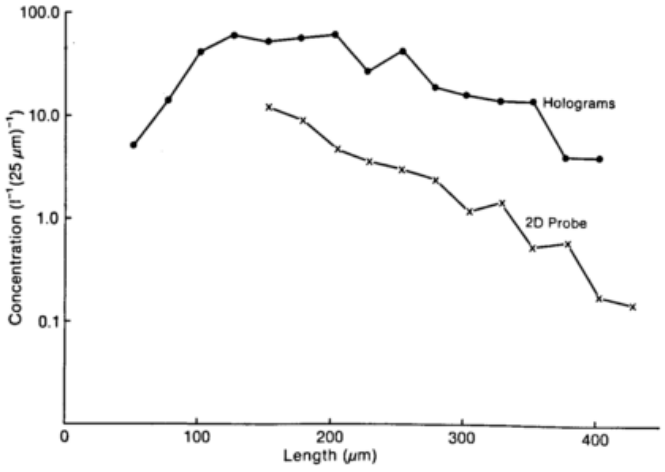


Fig.2 Size spectra of columns from holographic and 2-D data, flight H750. Temperature = -8.5 °C.

liquid droplets of about 30 µm in diameter or columns of about 170 µm in length. The former figure has been confirmed by measurements. Outside the shadow zone, the compression of particle trajectories increases the apparent concentration above the free-stream value by a factor which is a function of the particle size. This enhancement factor does however decrease rapidly away from the pod surface, and when averaged over the whole 25 cm depth of the holographic sample volume amounts to no more than about 30% for most sizes of columnar crystal. Those particles which strike the nose of the camera pod upstream of the sample aperture may fragment and give rise to spurious small ice particles. These however are generally easily identified by their concentration in the region close to the pod surface, and it is normal practice to exclude this from the hologram analysis.

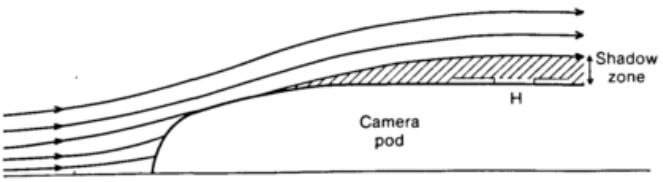


Fig. 3 Schemetic view of particle trajectories around holography camera pod. H shows position of sampling aperture.

4. ERRORS IN 2-D PROBE DATA

In the processing of 2-D data, individual images are automatically type-classified by a procedure described by DARLISON AND BROWN (1988). The comparison of this scheme with manual classification of some of the data from this study is shown in Table 1. The possible mis-classification of images may interact with other sources of error in 2-D data described below.

The depth of field for an individual image is given according to KNOLLENBERG (1970) by:

$$D_f = 3/2 * D_{eff}^2 / l \qquad (1)$$

where D_{eff} is the effective dimension of an image which determines its diffraction properties and l is the illumination wavelength. For droplets and near-spherical ice particles, D_{eff} is taken to be the width of the widest slice, whereas for columnar crystals it is taken as the column width. The latter is significant as it means that the depth of field will be smaller than the probe sample gap for all columns shorter than 650 µm (assuming a 4:1 axis ratio).
Quasi-spherical irregular ice particles will generally have a minor axis larger by a factor of about 2 than that of a column of the same major axis length. Any such image mis-classified as a column will have its depth of field overestimated by a factor of 4. If 20% of irregulars are mis-classified as columns and vice-versa then the measured concentration of columns may be about 85% of the true value, whilst that of irregulars may be around 150%.

TABLE 1 Comparison of manual and automatic image type classification.

		Automatic	
		Columns	Irregular
Manual	Columns	160	20
	Irregular	36	128

TABLE 2 Software overestimate of 2-D sample volume for columns (4:1 axis ratio).

Length * width of shadow (μm)	Measured width	Sample Vol. overestimate
100 * 25	32.3	1.66
200 * 50	64.8	1.68
300 * 75	94.3	1.58

We have subsequently found that the algorithm used by the processing software to determine the column width gives a systematic overestimate, which will in turn cause an overestimate of the depth of field and hence the sample volume of the 2-D probe. The effect of this error for columns of different dimensions is shown in Table 2. These figures assume random orientation of crystals relative to the diode array. The sample volume overestimate may be larger for certain preferred orientations, and are also larger for larger axis ratios.

We have measured the time response of our 2-D cloud probe by monitoring the output from the photodetector amplifiers with the beam being chopped rapidly, and found a minimum rise/fall time of about 0.9 μs, corresponding to 3-4 clock cycles at the normal aircraft true airspeed of 100 ms^{-1}. The effects of this are twofold. Firstly, images with a dimension of less than about 100 μm will not cause the probe to trigger. Secondly, images larger than this will be undersized in the direction perpendicular to the diode array by a factor of 2 for 100 μm images, approaching unity at about 200 μm. This undersizing can cause underestimates of the depth of field and sample volume in a similar manner to that described above. It will also act to shift the entire 2-D measured size spectrum towards smaller sizes.

5. SUMMARY AND CONCLUSIONS.

The holographic sample volume is unambiguous in its definition and predictions about airflow-induced distortions of holographic data have been at least partially tested by measurement. We therefore consider that the main causes of the concentration discrepancies lie with the 2-D system. No single source of error can account for the whole of the factor of 5-10 difference, although most act in the correct sense. We hope to model the operation of the 2-D probe, incorporating photodiode response and an improved calculation of the width of columns, with a view to developing more accurate sample volume estimates than those currently employed by our software.

The effects of probe response time will be of extra significance in cirrus cloud for two reasons, firstly because many of the particles are expected to be bullet-rosettes with a number of columnar arms, and secondly because the true airspeed at cirrus altitudes is in the range 120-140 ms^{-1}. The diode response time is then of the order of 5 clock cycles and the possible non-detection and undersizing therefore extend to larger sizes.

REFERENCES

BROWN P.R.A.: submitted to J.Atmos.Oceanic Technol (1988).

BROWN P.R.A., CHOULARTON T.W., and GRIGGS, D.J.: submitted to Quart.J.R.Met.Soc (1988).

CONWAY B.J., CAUGHEY S.J., BENTLEY A.N., and TURTON J.D.: Atmospheric Environment 16 (1982) pp1193-1207.

DARLISON A.G. and BROWN P.R.A.: Proceedings 10th Interntl. Cloud Physics Conf., 15-20 Aug. 1988.

KING W.D.: J.Atmos.Oceanic Technol. 1 (1984) pp5-13

KING W.D.: J.Atmos.Oceanic Technol. 2 (1985) pp539-547

KNOLLENBERG R.G.: J.Appl.Met. 9 (1970) pp86-103

DEVELOPMENT OF HYDROMETEOR VIDEO SONDE

Masataka Murakami and Takayo Matsuo

Meteorological Research Institute,
Tsukuba, Ibaraki 305, Japan

1. INTRODUCTION

In studies of cloud and precipitation formation, it is important to know the microphysical structure of clouds as well as the dynamical structure. Measurements of microphysical properties of precipitation clouds have been often made by airplanes equipped with a J-W hot wire device, a FSSP, and 2-D Optical Array Probes. Despite the convenience of these measuring instruments, they still have some problems. The instruments do not have sufficient ability to discriminate between cloud droplets and ice crystals nor the ability to reproduce a detailed shape of cloud and precipitation particles. Furthermore, from the viewpoint of airplane safety, research airplanes are sometimes restricted from operating in shallow orographic clouds and wintertime severe convective clouds.

To overcome these difficulties, we developed a special sonde called a Cloud Particle Video Sonde (CPVS) (Murakami *et al.*,1987). It provided high quality images of cloud and precipitation particles up to 1 mm in size. However, for better understanding of precipitation formation processes, it is necessary to measure the precipitation particles larger than 1 mm. To meet this requirement, we have improved the CPVS in many respects, and made a Hydrometeor Video Sonde (HYVIS).

In this paper, we describe the HYVIS and expose its capabilities through a report of some observations.

2. OUTLINE OF HYDROMETEOR VIDEO SONDE SYSTEM

To obtain particle images together with meteorological data, the HYVIS and a standard rawinsonde are attached to the same balloon and are launched into clouds at ascent velocity of about 5 m/sec. The HYVIS transmits images of hydrometeors taken by two TV cameras over a 1,687 MHz microwave link to a ground station in real time so that it does not need to be retrieved later unlike a snow crystal sonde developed by Magono and Tazawa (1966). At the same time , meteorological elements such as temperature, humidity, and pressure are also transmitted at a frequency of 1,680 MHz (see Fig.1). These two microwaves of different frequencies are received by one antenna assembly with a 1.2 m parabolic dish. The received signals are fed through a Power Splitter to two receivers (RD65A and SAR-4; Meisei Electric Co.). The video signal from the HYVIS is detected at the SAR-4 receiver with FM Demodulator and then fed to a Video Mixer. The video signal mixed with the time data from a Time Code Generator is recorded on a video cassette tape and is simultaneously displayed on a CRT.

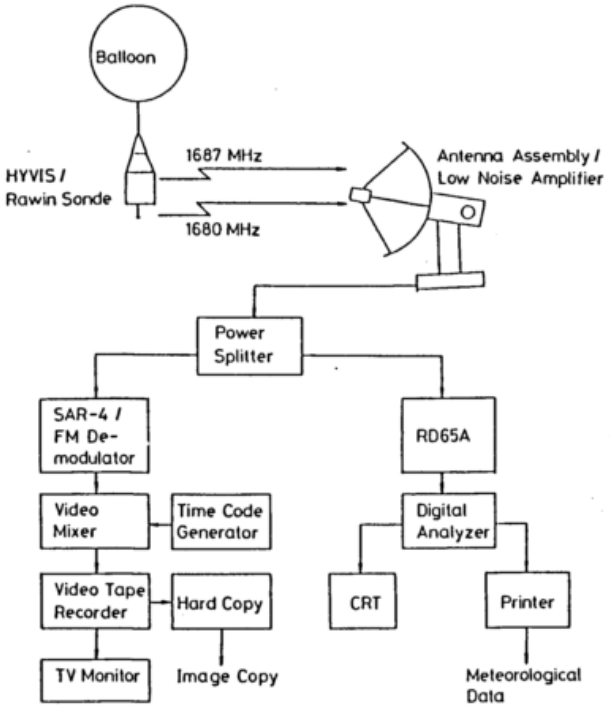


Fig.1. System diagram.

The meteorological signal is detected at RD65A receiver and processed through a Digital Analyzer to be displayed on a CRT and to be printed out in the form of temperature, relative humidity, pressure, height, windspeed, and wind direction in real time.

3. DESCRIPTION OF HYDROMETEOR VIDEO SONDE

As shown in Fig.2, the HYVIS has two small TV cameras with different magnifications to take pictures of hydrometeors from 7 μm to 2 cm in size. Hydrometeors fall through the particle inlet (25 mm X 50 mm) and collect on a transparent particle dish. For first 4 seconds, TV camera A takes pictures of the cloud particles on the dish. Then TV camera B takes pictures of the precipitation particles for another 6 seconds. During the latter half of the shooting of TV camera B, a new part of the particle dish is pulled out.

TV cameras A and B have optical systems with magnifications of 7X and 0.33X, and takes pictures of 0.8 mm X 1.1 mm and 15 mm

X 20 mm areas on the particle dish, respectively. The particle dish is a roll of 35 mm leader film for procession. A special water-repellent coating is given to the surface of the film. The film is pulled out of a film magazine by a winding mechanism with a small DC motor and driving chains. Total length of the film is 15 m, and this capacity is long enough to continue an observation for 50 minutes and up to a height of 15 km.

The video signal from the TV cameras is transmitted to a ground receiving station through a Band-pass Filter (cut-off frequency=1 MHz), a Video Amplifier, and a FM Transmitter. The nominal transmission power is 0.6 W.

Two TV cameras, electronics circuits, and lithium batteries are stored in a heat insulating box to protect them from cold temperatures in the upper air. Dimensions of the HYVIS are 225 mm X 152 mm X 410 mm, and its weight is approximately 1.3 kg.

4. DETERMINATION OF COLLECTION EFFICIENCY

In order to deduce the concentration of cloud and precipitation particles from the number collected on the particle dish, it is necessary to know the collection efficiency of the HYVIS for hydrometeors. To determine the collection efficiency of the HYVIS for water droplets, the collision experiment was carried out at various air speeds in a wind tunnel. The HYVIS and a reference ribbon of 3 mm width were simultaneously exposed to an air stream containing sprayed water droplets, and the number of collected droplets was compared between the HYVIS and the ribbon. The collection efficiency showed no significant air speed dependency so that the mean value of the collection efficiency E expressed by the

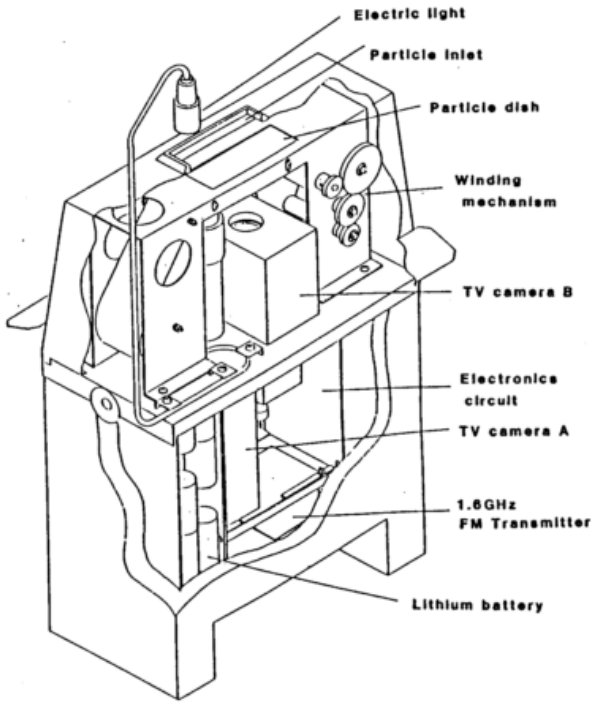


Fig.2.Cutout view of the HYVIS.

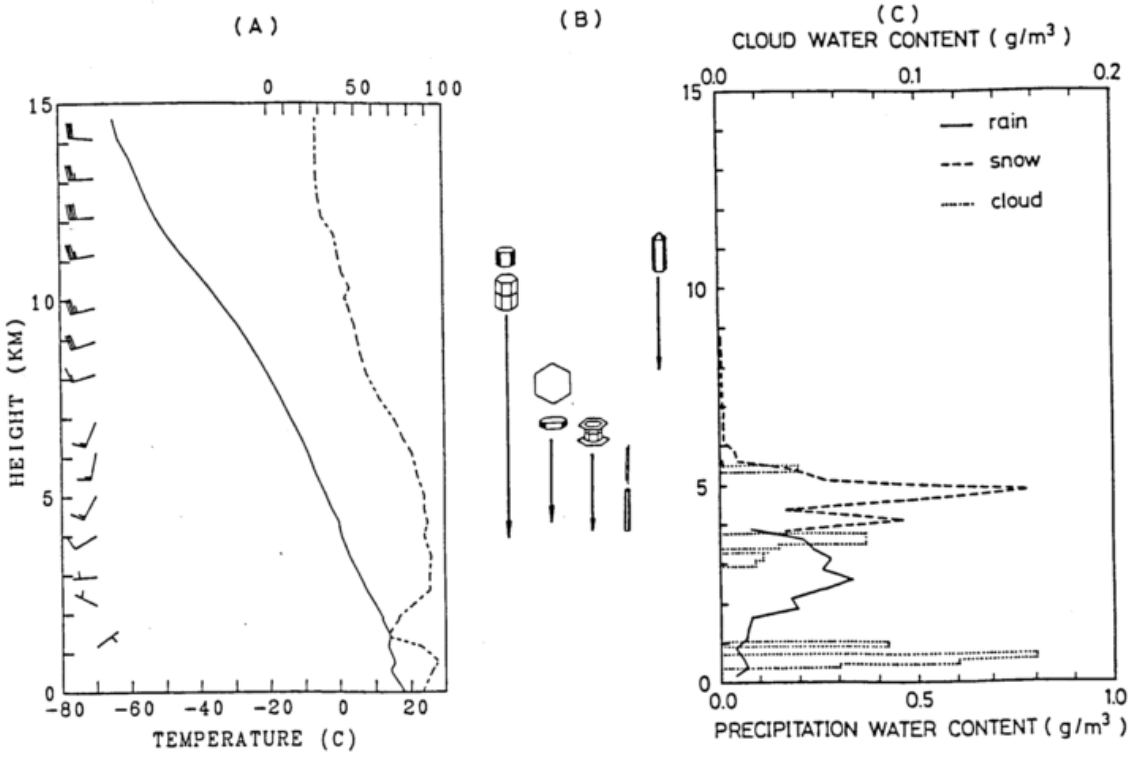


Fig.3. Microphysical structure of clouds along the ascent of the HYVIS: (A) temperature (solid line),relative humidity (broken line), and wind; (B) snow crystal types observed aloft; (C) rain water content (solid line), snow water content (broken line), and cloud liquid water content (dotted line).

following equation will be used regardless of air speed to calculate the number concentration of cloud droplets ($D \leq 130$ μm) in the next section.

$$E = 0.0067D + 0.14 \quad . \qquad (1)$$

The collection efficiency for droplets larger than 130 μm is assumed to be unity.

As for wet snowflakes from 1.5 mm to 3.5 mm, the collection efficiency was determined to be 0.77 from field experiments although the data were scattered to a great extent. For dry snow crystals, it is difficult at the present time to determine a reliable collection efficiency because of a large scatter in collection efficiency data and bounce-off effect. Therefore, in calculating the number concentration of snow crystals, we corrected the raw data on the number concentration by a certain factor assuming the continuity of mass flux of precipitation particles across the melting layer.

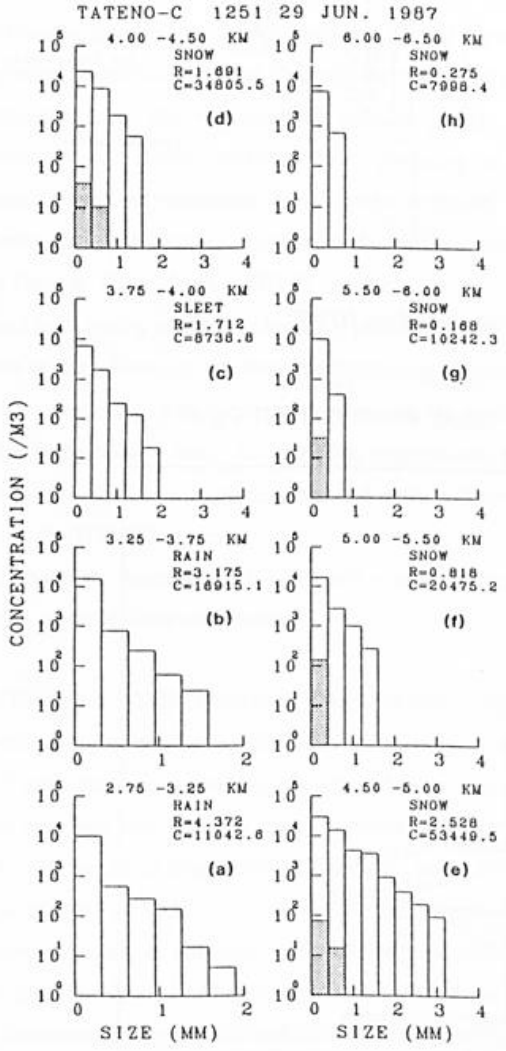


Fig.4. Change in size distributions of precipitation particles along the ascent of the HYVIS. Shaded bars represent supercooled drops. At the upper right of each figure shown are precipitation rate (R; mm/hr) and total concentration of precipitation particles (C; particles/m^3).

5. AN EXAMPLE OF HYVIS OBSERVATION

By using the HYVIS along with a rawinsonde, the microphysical structure of stratiform precipitation clouds was observed over the Tsukuba Area of Kanto Plain, Japan, on 29 June1987. The balloon equipped with the HYVIS and a rawinsonde was launched at 12:51 JST and required thirty minutes to make observations up to 11 km which was the cloud top height. At that time, this study area was located about 300 km north of a stationary front (Baiu front). Temperature, relative humidity, and wind profiles obtained from the balloon observation are shown together with snow crystal types observed aloft, cloud liquid water content, rain water content, and snow water content in Fig.3. Snow water content was computed from the size distribution of snow crystals using mass vs. maximum dimension relationships derived by Davis (1974).

A vertical change in size distributions of precipitation particles from 2.75 to 6.5 km MSL are shown in Fig.4. The HYVIS ascended in stratiform clouds except for the layer between heights of 4.5 and 6.0 km where it was under the influence of a convective region embedded in stratiform clouds. Broadening in size distributions in Figs.4e-4g indicated the rapid growth of needle type crystals in this region through a seeder-feeder mechanism. The upper part of the convective region consisted of supercooled cloud droplets. Also existed a sparse drizzle layer of 1.5 km depth just above the 0°C level. Rain drops grew through a collection of cloud droplets during their fall from 3.75 to 2.75 km MSL. Size distributions of clouds droplets in this layer and the convective region are shown together with those in lower cumulus clouds in Fig.5.

Examples of hydrometeor images taken by the HYVIS are shown in Fig.6. As seen from Fig.6b, most of elementary sheathes and

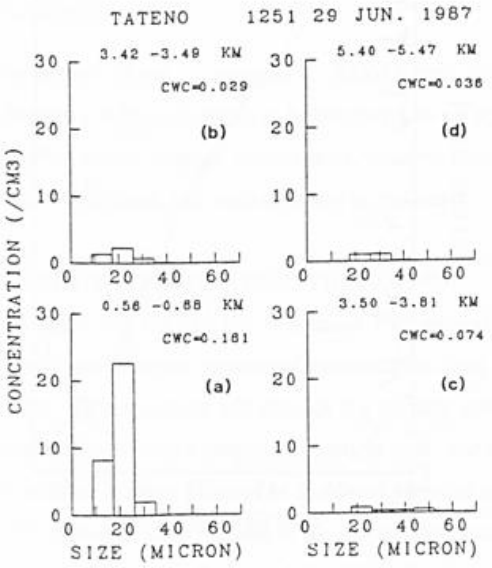


Fig.5. Size distributions of cloud droplets measured at different heights. At the upper right shown is cloud liquid water content (g/m^3).

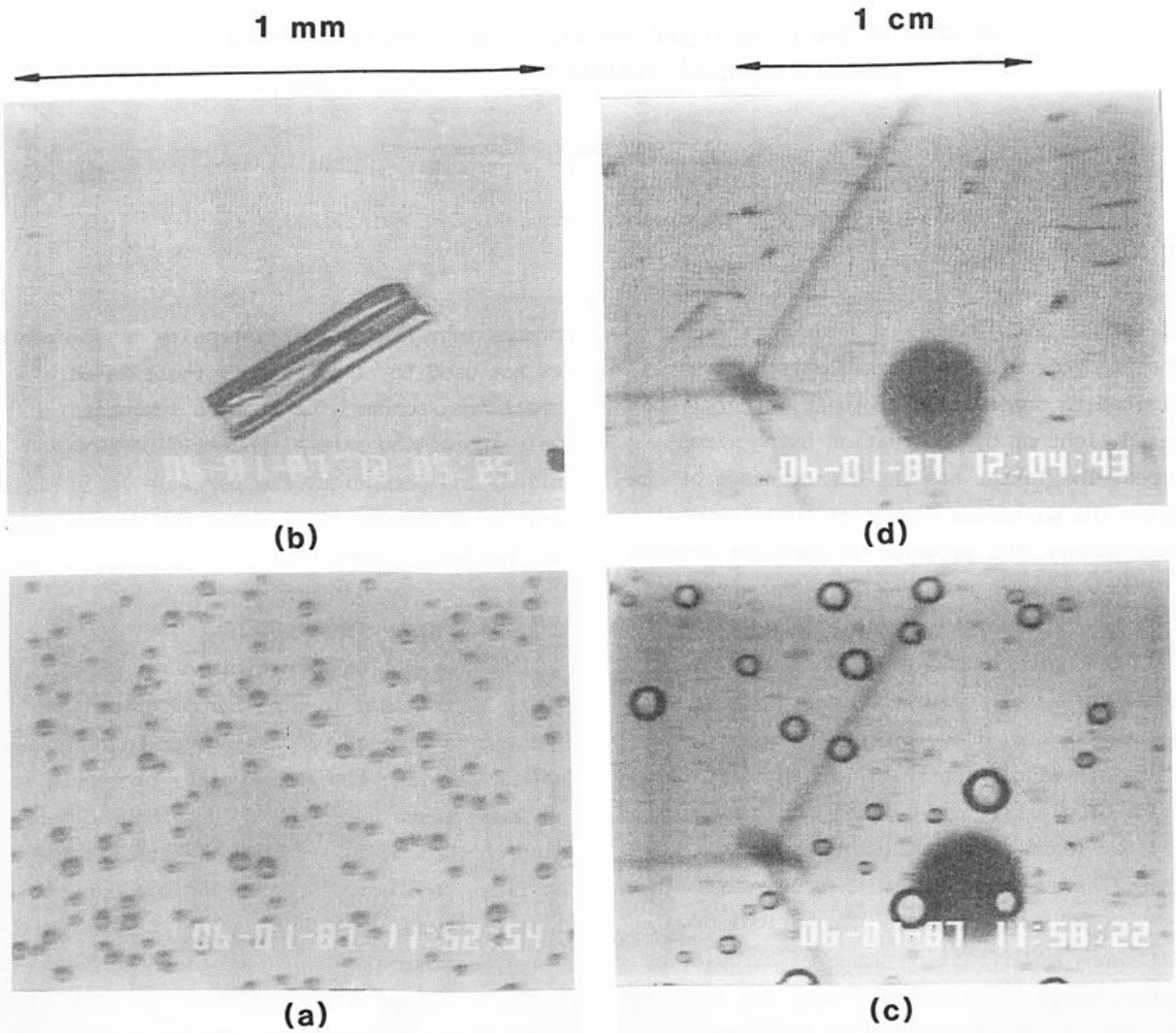


Fig.6. Examples of hydrometeor images: (a) cloud droplets observed at 0.6 km MSL (14.3℃); (b) sheath at 4.9 km MSL (-3.4℃); (c) rain drops at 2.5 km MSL (8.4℃); (d) needle type crystals at 4.7 km MSL (-2.2℃).

needles which rapidly grew in the convective region had no rime coverage on them although lightly rimed hexagonal plates were rarely observed there. This means that dominant mechanism of crystal growth in the feeder cloud was vapor deposition.

6. CONCLUSIONS

A special sonde (HYVIS) for measuring cloud and precipitation particles has been briefly described.

The HYVIS provides high quality images of hydrometeors from 7 μm to 2 cm in size and a fine vertical resolution (~50 m) of microphysical structure in clouds. Advantages of the HYVIS have been demonstrated by briefly highlighting the observational results of stratiform clouds associated with a stationary front.

The capabilities of the HYVIS makes critical measurements possible in otherwise inaccessible clouds such as wintertime severe convective clouds and shallow orographic clouds. The HYVIS measurements should lead to an improved understanding of clouds and precipitation formation processes and their modification potential.

REFERENCES

Davis, C. I. , 1974: *Ph.D. Thesis*, Dept. Environ. Sci., Univ. of Wyoming, Laramie, Wyoming.

Magono, C. and S. Tazawa, 1966: Design of " snow crystal sonde". *J. Atmos. Sci.*, **23**, 618-625.

Murakami, M., T. Matsuo, T. Nakayama and T. Tanaka, 1987: Development of Cloud Particle Video Sonde. *J. Meteor. Soc. Japan*, **65**, 803-809.

THE STUDY OF THE INTERSTITIAL AEROSOL PARTICLES AND CLOUD DROPLETS WITH DIGITAL IMAGE ANALYSIS OF DIFFRACTION IMAGES

R. Jaenicke and R. Sörensen

Institute for Meteorology, University of Mainz, FRG

1. INTRODUCTION

The study of airborne particles is currently limited to observation of their integral scattered light or by observation using miroscopes. The latter has the disadvantage of studying the particles depart of their natural surrounding. The progress in computer science and manufacturing now makes it possible to look at the discrete particle in a different way. An approach to a new technique will be presented here. The method used can be described as "digital image processing".

There are significant hints in the diffraction image of a particle for defining it as a droplet, at least as a particle of spherical shape, or as a particle with rough surface (STRAUBEL, VAN DE HULST). A spherical droplet will show a diffraction image of circular geometry, while a dry one will not. The individual particle is illuminated by laser beam and the diffraction image is directly recorded by a video camera connected to either a recorder or a personal computer (Fig.1).

2. METHOD

2.1 PARTICLE DETECTION

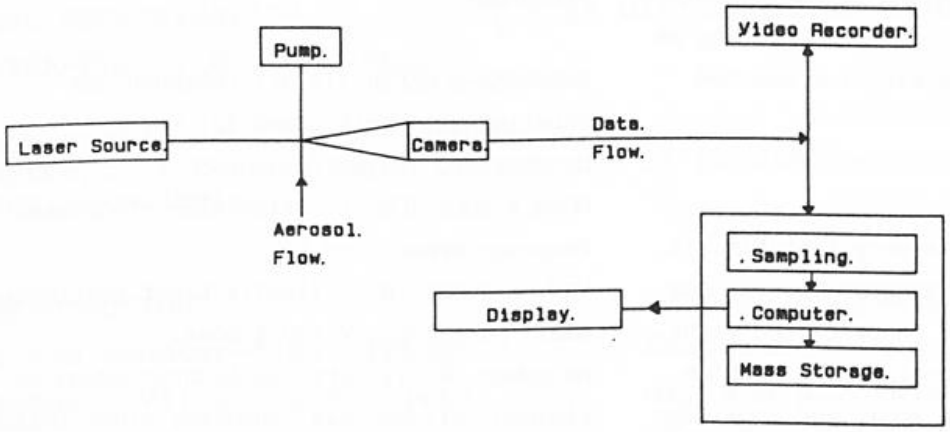
The particles are sent through the laser beam using clean air sheet technique so that single particles can be isolated. With no particle present in the beam, the intensity maximum of the laser light is masked out so that the camera will not detect any scattered light except for some noise which is virtually always present. A particle crossing the beam will scatter the light and so the camera will see an increase in integral measured intensity. The computer is able to detect this increase and takes a snapshot of the camera image for processing. As integral intensity measurement is not used for this method, there is only a small area scanned for changes in intensity. Only increasing intensities will be recognized. The detection of a particle lasts about 1/25 of a second. Fig.1 shows the system and its hardware components.

2.2 PROCESSING

When a snapshot of a particle has been made, there is no limit in time for processing its image. The time of processing can be regarded as non-sampling time. Currently, processing of an image lasts about 10 to 30 seconds depending on the complexity of the scattered image. At first, the computer will check a horizontal line for symmetry in intensity. If symmetry is given, another process takes place to detect circular symmetry, otherwise the particle is classified as non-spheric. The algorithm used is looking for areas of identical intensity, so constructing a polygone, framed by an inner and an outer circle. The construction of these circles may be seen in Fig.2. Fig.3 shows the scattering image of a large, irregular shaped particle. Fig.4 is a pseudo-three-dimensional view at the intensity distribution of a spherical shaped particle (droplet).

2.3 LIMITATIONS

As can be noted from above, the processing itself is relatively slow, depending on the used algorithms and the number of digitized images per second. So real time processing is not yet possible. If the time for computation can be reduced significantly, it might be possible to advance to about 30 images per second which will be classified. Another improve will be to



SYSTEM OVERVIEW Digital Image Processing.

Fig. 1
Required Hardware

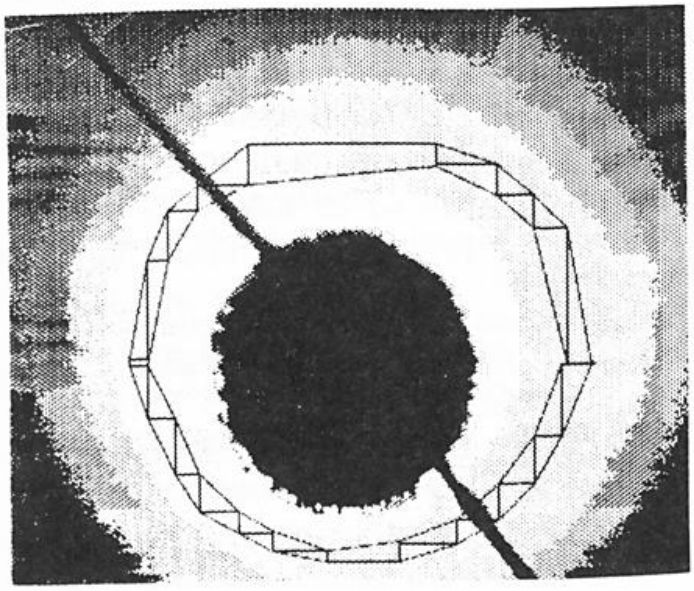


Fig.2: The process of detecting a circular shaped diffraction pattern

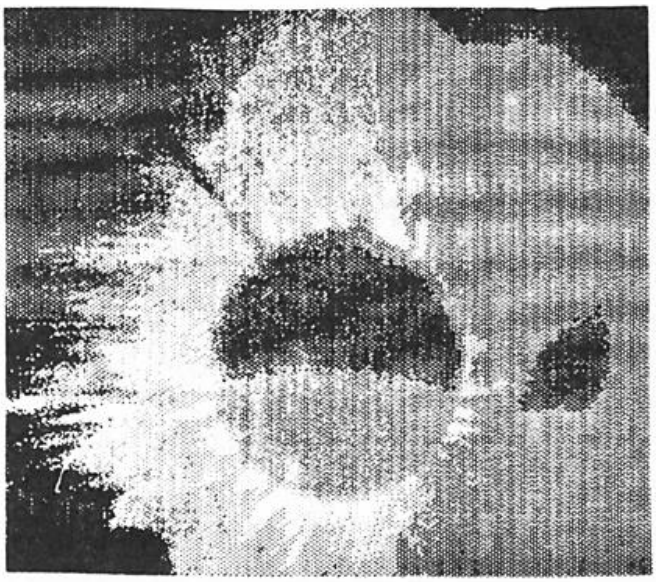


Fig.3: Printout of an irregularly shaped diffraction image

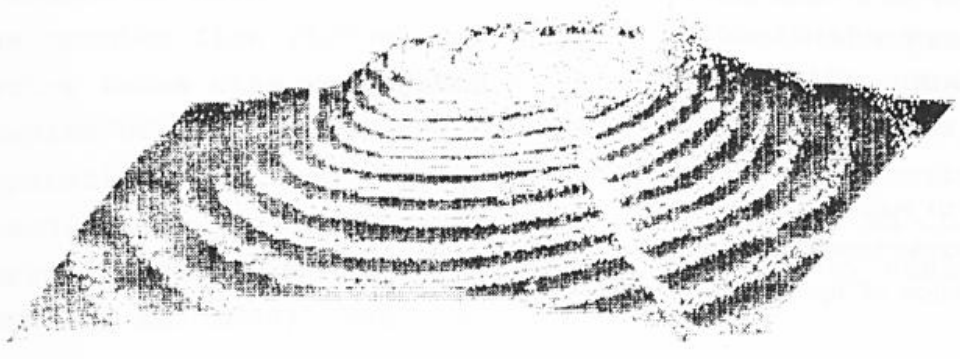


Fig.4
Pseudo-three-dimensional intensity distribution produced by a spherical particle

abandon digital processing and reduce computation to the calculation of data, sampled by an analogous device like some circular mounted light detectors.

2.4 ADVANTAGES

Digital image processing is very flexible. It is possible to develop strategies for various samling problems depending on scattered light. When the structure and solution of a problem is evident, one is able to apply the knowledge to somewhat more specific machines. Another advantage is that one can observe the process of sampling and processing data on a monitor. The decision criteria may be manually corrected or interrupted. Any method of interpreting sampled data may be used, as integral intensity, intensity scattered into a specific sector or angle or pattern recognizing, i.e. contrast measurement. A large number of algorithms are available in helping with pattern matching, spectral analysis or noise reduction. Figs. 2 to 4 are matrix printouts of image data, the quality of the images is much better than on these printouts.

3. USAGES

Currently a method is developed to use the shown apparatus in fog so that it is possible to obtain distributions of inactive particles and droplets. A real-time application is in progress to sample dry (inactive) particles for further analysis. For the present, the system is limited to laboratory usage. In field applications, one would sample images with a video recorder and analyze them in the laboratory; with the recorder as a "mass storage system", there is no need for real time processing of the sampled data.

4. ACKNOWLEDGEMENT

The study is carried out with support of the German Science Foundation Sonderforschungsbereich "Chemistry and Dynamics of Hydrometeors".

REFERENCES

BERGMANN-SCHÄFER (1978): Lehrbuch der Experimentalphysik, Band III Optik. de Gruyter, 7th Ed.

BORN & WOLF (1965): Principles of Optics. Pergamon Press, 3rd Ed.

VAN DE HULST, H.C. (1957): Light scattering by small particles. Wiley & Sons.

BROSSMAN, R. (1966): Die Lichtstreuung an kleinen Teilchen als Grundlage einer Teilchengrößenbestimmung. Dissertation an der TH Karlsruhe, Fakultät für Maschinenbau und Verfahrenstechnik.

GIESE/DE BARY/BULLRICH/VINNEMANN (1962): Tabellen Miefunktionen. Akademie-Verlag Berlin.

ROSENBERGER, D. (1975): Technische Anwendungen des Lasers. Springer-Verlag.

STRAUBEL, H. (1981): Elektro-optische Messung von Aerosolen. Technisches Messen 48, Heft 6, p.199.

STROKE, GEORGE W. (1969): An Introduction to Coherent Optics and Holography. Academic Press, 2nd Ed.

VAN DE HULST, H.C. (1957): Light Scattering by small Particles. Wiley & Sons.

ON THE DETERMINATION OF DROPLET SIZE DISTRIBUTIONS WITH THE COUNTER-FLOW VIRTUAL IMPACTOR

B. Johansson and J. Heintzenberg
Department of Meteorology, University of Stockholm
S-10691 Stockholm

1 INTRODUCTION

With the counter-flow virtual impactor (CVI) cloud droplets within an adjustable size range can be sampled for subsequent physical and chemical analyses without interference from gases and unactivated particles.

For a full understanding of the sampled cloud the analyses in the CVI need to be related to the cloud droplet size distribution.

Below, we present a new way of obtaining this size distribution through an inversion of parameters which are measured in the CVI. This method of retrieving the cloud drop size distribution has the advantage of yielding an internal consistency with the chemical properties measured in the same probe.

2 SOURCE OF DATA

The counter-flow virtual impactor takes size segregated samples of cloud droplets, separating them from the surrounding air and unactivated particles (OGREN ET AL. 1985; NOONE ET AL. 1988). The sampled droplets are evaporated in a flow of warm, dry and particle free air. Then their liquid water content (LWC) is measured in the gas phase with a Lyman-α hygrometer (ZUBER and WITT, 1987). The non-volatile residues of the droplets are counted with a particle counter (CNC). By adjusting the cut-size, (r_{50}), of the CVI, the lower size limit of the sampled droplets can be varied in a range from ca 2 to ca 20 µm radius; r_{50} corresponds to a 50 % droplet collection efficiency. According to the CVI-calibration (NOONE ET AL., 1988), the collection efficiency for the droplet number concentration (CNC-efficiency) can be approximated by an incomplete ß-function. Figure 1 shows an example for an r_{50} = 9 µm. The average absolute deviation, that is the square root of the sum of the squared deviations between the calibration curve and the approximating ß-function, is .02 units on our efficiency scale.

3 INVERSION ALGORITHM

The measured property S, (droplet mass or number) is related to the droplet size distribution dN/dr through a Fredholm-integral equation where the kernel K(r) is the size dependent collection efficiency of the CVI in terms of either droplet number or liquid water content.

$$S = \int_0^\infty K(r) * dN(r)/dr)\ dr \qquad (1)$$

By multiplying number-counting efficiencies with $4\pi r^3/3$ the counting efficiencies are converted to mass collecting efficiencies, (using a density of 1 g/cm^3 for water). Now, information from both CNC and LWC data can be used jointly to retrieve the drop size distribution.

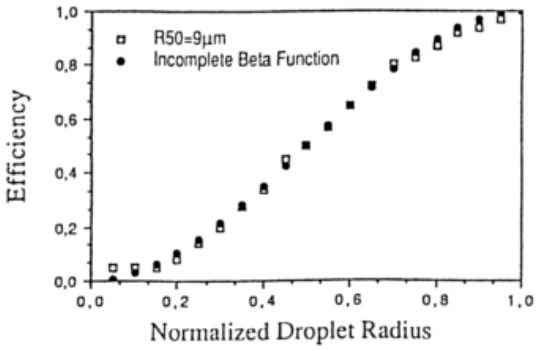


Fig. 1: Incomplete ß-function, approximating the CVI collection efficiency at a cut radius r_{50} = 9 µm. This function is shifted left and right with varying r_{50}-value.

Equation (1) has no general analytical solution. However, by writing it as a finite sum (as in equation 2) we can find a numerical solution to the equation assuming a histogram representation of the size distribution instead of the continuous function in equation (1).

$$S = \sum_{l=1}^{L} K_l * (dN/dr)_l\ dr \qquad (2)$$

L is the total number of columns, $(dN/dr)_l$ is the value of the drop size distribution in the histogram column, l, K_l is the kernel averaged over the interval δr, of the column. The numerical method for solving equation (2) is based on the algorithm of HEINTZENBERG (1978). It is a randomized minimization search technique where the basic idea is to find a histogram-type size distribution whose properties (here CNC and LWC) have a minimum deviation from the measured (synthetic) properties. The minimization is done by an iterative least square fit.

4 RESULTS

Inverting synthetic data allows us to see how well the CVI has to perform to retrieve a good approximation of the drop size distribution. How many different size segregated

samples need to be taken to be able to yield an acceptable picture of the true size distribution? Is it necessary to increase the range in which size segregated samples can be taken (at present this range goes from ca 2 to ca 20 µm)? How do realistic measurement errors affect the inversion result?
As an example, figure 2 shows an inversion result using 12 different cut radius settings in the hypothetic range from 2 to 40 µm.

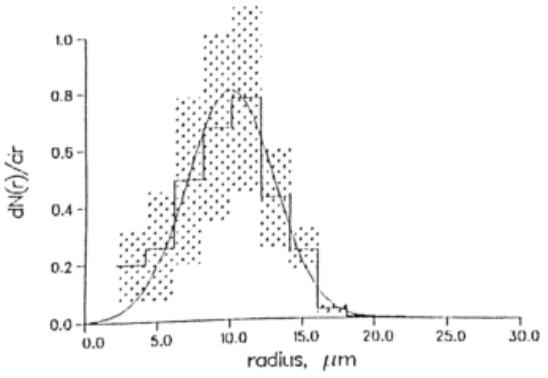


Fig. 2: Inversion results using r_{50} = 2, 4, 6, 8, 10, 12, 15, 20, 25, 30, 35, and 40 µm and a 5% measuring error, (details, see text).

The synthetic data were calculated for the Gaussian distribution (shown by the full smooth line in figure 2). The histogram distribution is the mean of 80 separate inversions. The scatter of the inversion results is shown by the shaded bars. The measurement error in the synthetic data of CNC and LWC was set to 5 % . The average absolute deviation between the inverted size distribution and the initial size distribution was .06 units on our concentration scale. This deviation depends both on the measurement error and the error induced by the inversion.

REFERENCES

HEINTZENBERG, J.: Particle size distributions from scattering measurements of non-spherical particles via Mie-theory. Contr. Atmos. Phys. 51 (1978), p. 91-99.

NOONE, K.J.; CHARLSON, R.J.; COVERT, D.S.; OGREN, J.A.; HEINTZENBERG, J.: Design and calibration of a counterflow virtual impactor for sampling of atmospheric fog and cloud droplets. Aerosol Sci. Technol., in press, 1988.

NOONE, K.J.; CHARLSON, R.J.; COVERT, D.S.; OGREN, J.A.; HEINTZENBERG, J.: Cloud droplets: Solute concentration is size dependent. J. Geophys. Res., in press, 1988.

OGREN, J.A.; HEINTZENBERG, J.; CHARLSON, R.J.: In-situ sampling of clouds with a droplet to aerosol converter. Geophys. Res. Lett. 12 (1985), p. 121-124.

ZUBER, A.; WITT, G.: Optical hygrometer using Differential Absorption of the Hydrogen Lyman-alpha Radiation. Appl. Optics 26 (1987), p. 3083-3089.

MULTIPARAMETER CHARACTERIZATION OF RAINDROP SIZE DISTRIBUTION BY THE POLARIMETRIC DFVLR RADAR: FIRST RESULTS

M. Chandra *A. Schroth* *E. Lueneburg*

DFVLR, Institut fuer HF-Technik, 8031 Wessling, West Germany

1. INTRODUCTION

The application of radar for obtaining the precipitation rate is important not only in the field of operational radar meteorology but also in microwave propagation research. Since the coherent polarimetric DFVLR radar, ref.(1), has become operational, efforts to obtain radar estimates of rainrates have been in progress. In this connection the radar determination of the raindropsize distribution via a two parameter description, ref.(2), and a three parameter description, ref.(3) are being investigated. In this paper we report demonstrative calculations involving the two parameter description of the radar determined, raindropsize distribution, N(D). The results of the implementation of the mentioned three parameter technique in the sense of its applicability and limitations would be presented at the conference subject to the availibility of appropriate radar data.

2. THEORY AND METHODOLOGY

The rainrate, R (mm/hr), is given by

$$R = 0.6\pi 10^{-3} \int V(D)\, N(D)\, dD \qquad (1)$$

where V(D), in m/s, is the fall-velocity of the raindrop of equivolume drop diameter, D(mm). The key to the radar determination of rainrate lies in its capability to characterize N(D), from radar observables.

In the radar determination of N(D), the microphysical interpretation of the polarimetric radar observables was obtained using the concept, ref.(3,4 & 5), entailed in the quantity χ_{ij}^{pq}, which arises from the mean value of the product of polarimetric echoes S_{ij} and S_{pq}^{*} corresponding to the instantaneous scattering amplitudes of the scatter volume. The practical implementation of this quantity is, however, cumbersome for its formulation retains the sensor characteristics explicitly. A far more 'application friendly' use of this quantity is possible by defining an equivalent reflectivity Z_{ij}^{pq} related to χ_{ij}^{pq}. This concept, invoked in ref.(3), may be seen as a polarimetric generalisation of the conventional single polarization equivalent reflectivity. This generalization may be formally described as:

$$Z_{ij}^{pq} = F \left(\frac{\lambda^4}{|K|^2 \pi^5} \right) \int_{D_{min}}^{D_{max}} s_{ij}(D)\, s_{pq}^{*}(D)\, N(D)\, dD \qquad (2)$$

Here s_{ij} and s_{pq} are the polarimetric scattering amplitudes of the raindrop of equivolume drop diameter D appropriately averaged for the canting and or the shape oscillation effects, and the rest of the terminology conforms to the one in refs.(4, 5) excepting the factor F. This term is simply unity if the "user" chose to exclude in the above definition (i.e. by having corrected for) the influences of internal and external propagation effects and the Doppler phase term . Details of these infuences may be found in refs.(3,5). Using this formalism, computer programmes were written for interpreting polarimetric quantities using an interpolation based inversion method (courtesy Dr. H. Schuster) for achieving a two and or three parameter radar description of the Gamma type N(D):

$$N(D) = N_0 D^{\mu} e^{(-(3.67+\mu) D/D_0)} \qquad (3).$$

employing the techniques suggested in refs.(2,3). Here, we report sample calculations of the N_0 and D_0 parameters for certain pre-chosen values of the μ parameter. The lack of necessary radar data (at the time of text formulation) prevent the reporting of the trials with the mentioned three parameter technique.

3. RADAR DATA AND ANALYSIS

Shown in figs. 1 are the RHI scans depicting the horizontal reflectivity (Z_{HH}^{HH} or simply Z_{HH}), the Z_{DR}($= Z_{HH}^{HH} / Z_{VV}^{VV}$), and the LDR (included for additional information only) signatures of the event considered. The choice of this event was influenced by the presence of the intense convective kernel accompanied by unusually large Z_{DR} values typically 6.0 db or greater. The results to be now described, being demonstrative in nature, are restricted to the range bins located along the "ray" marked as a dark solid line in fig.1a. The Z_{HH}, Z_{DR}, and LDR profiles along this "ray" are summarized in figs. 2. Shown in figs. 3 and 4 are the corresponding radar predicted values of the D_0 and N_0 parameters for the μ values of -2,0 and 2. Also, shown in fig. 3 are the results obtained via the following empirical relationships ref.(6), $Z = \alpha R^{\beta}$ and $D_0 = \varepsilon R^{\delta}$, where for Joss- thunderstorm conditions $\alpha = 500$, $\beta = 1.5$, $\varepsilon = 1.2$ and $\delta = 0.21$

Firstly, we note that the D_0 determination from Z_{DR} measurement is limited to Z_{DR} values not exceeding 5.1, 5.2 and 5.3 for μ values -2, 0, and 2, respectively. This limit is the natural consequence of the predefined axial ratios stemming from the Pruppacher - Pitter raindrop deformation rule, ref.(7). The calculations in the present case were done using a D_{max} of 8.0 mm and the scatter crossections were obtained for Pruppacher- Pitter spheroidal raindrops for $T = 15°C$ and f = 5.54 GHz using the Waterman T-matrix algorithm.

The investigations presented here cover the unusually wide range of Z_{DR} values (0.5 to about 7.1 dB) in a single event. To facilitate at least tentative arguments, the radar predictions of N(D), rainrate, etc, are presented along with the corresponding empirical results stemming from the reflectivity measurements alone. Bearing in mind that neither of the two results are more conclusive than the other and the severely limited size of the data base examined here, the "analysis" to be presented is meant to identify further investigations which would serve to clarify the detailed aspects of the use of the Z_{DR} and allied techniques. In this spirit, as a forward to this analysis, listed below are some investigations in progress, that would be, shortly, shown to be of importance in interpreting Z_{DR} values > 2 dB :

1. The Z_{DR} due to water coated oblate hailstones, based on simple trial model of such particles in convective cells.
2. A reassessment of the influence of the integration limits of eqn.(2) and the raindrop axial ratios based on experimental and or theoretical sources different from the Pruppacher-Pitter deformation law. The resonance backscattering effects ($D \approx 5.5mm$) only add to the importance of these effects.
3. The significance of nearly monodisperse raindropsize distributions

Progress and appraisal of results arising from these investigations would be relegated to the conference meeting. Returning to the specific results an inspection of fig. 3 reveals that D_0 predictions from Z_{DR} measurements and the corresponding empirical results for D_0 show close agreement with the $\mu = 0$ case for Z_{DR} values $<$ about 1.5 dB. Furthermore, the remaining D_0 values stemming from Z_{DR} larger than about 2 dB reveal greater and progressively increasing with Z_{DR} magnitudes, systematic departures from the empirical case. This suggests the need for a reexamination of the radar technique in light of the above listed items, particularly the latter two. In the results presented here, the untreated portions of the curves arising from the Z_{DR} values greater than the maximum interpretable values of Z_{DR} in rain, are left as broken-line horizontal flats. The results for N_0 in fig. 4 show wide variations about the fixed Marshall-Palmer value of 8000, and thereby emphasising the usefulness of the radar technique. The rainrate profiles due to radar measurements are shown in fig. 5. These results reveal in comparison with the empirical law, large systematic departures (overestimates) for values of Z_{DR} greater than about 2.5 dB, tying up with the systematic departures observed in the D_0 predictions (not fully illustrated due to large excursions with oscillatory behaviour). Similar inferences may be derived from the radar predictions of specific attenuation (for 20 GHz and horizontal polarization), shown in fig. 6 along with the corresponding empirical results due to the CCIR relationships using the empirical rainrate. These observations, yet again, are found in the corresponding results for the accumulated attenuation summarized in figure 7. These results in part emphasize the useful application of radar in obtaining attenuation estimates relevant to the propagation community and to the radar meteorologist from the point of correction of propagation contaminated radar echoes. The vertical line marked in the figure indicates the onset of the region of extra large values of Z_{DR} not analysible due to the reason mentioned earlier and therefore implying caution in the significance of the results beyond.

In fig. 8 we include, ad hoc, the results for radar predicted rainrates against the empirical values, as in figure 5, but this time for μ values of 5,10 and 15. These results somewhat surprisingly reveal a more correlated and a closer agreement between the empirical and the radar generated results for $Z_{DR} < 2.5$db , in contrast to the results for $\mu = -2$, 0 and 2 (not apparent in the illustrations). Also, the corresponding systematic departures observed in results of fig. 8, for $Z_{DR} > 2.5$ but smaller than the critical Z_{DR} values, are less pronounced than the results of fig. 5. These observations, far from being conclusive, however, do point to the significance of the μ parameter thus stressing the need of the radar determination of this parameter by methods such as of ref.(3).

4. CONCLUSIONS

Using Z_{DR} and Z_{HH} radar measurements, firstly radar estimates of D_0, N_0 were obtained, which were then used for obtaining estimates of rainrate, specific attenuation, and the accumulated attenuation along a selected "ray". Comparison with corresponding empirical results, where appropriate, revealed three key observations linked to the magnitudes of Z_{DR} values:

1. In the region of $Z_{DR} \leq 2.5$dB or so, the radar predicted parameters (with the exception of N_0) showed satisfactory and well correlated agreements with the empirical cases for predefined μ values in the range -2 to 2, though systematic departures were noticeable for Z_{DR} values $>$ about 1.5 dB. Interestingly, for larger μ values (5 to 15) not only was the agreement, in the considered cases of rainrate, improved but also observed for Z_{DR} values up to 2.5 dB, thereby indicating the possible usefulness of the μ parameter.
2. The, $2.5\text{dB} < Z_{DR} < 5.5\text{dB}$ values, interpreted as rain volumes, presented large systematic departures against the empirical results and in the same sense as observed in 1). This feature prompts the reexamination of the axial ratios of the larger raindrops $>$ D=5mm, bearing the suggestion that these drops may be more deformed than the description due to Pruppacher - Pitter equilibrium rule, and or the simultaneous presence of melting oblate hydrometeors.
3. $Z_{DR} > 6.5$dB or so cannot be simply interpreted in terms of raindrop size distributions. For $\mu = 15$ (a very monodispersive N(D))the largest Z_{DR} value interpretable, under the assumptions described in section 3 is about 5.5 dB and 6.5 dB for D_{max} of 8 and 6 mm, respectively. Hence, to be able to account for even larger Z_{DR} values observed , the need for considering mixed - phase hydrometeors in the convective shafts becomes important.

Finally, it may be added that any modelling of the hydrometeor volumes of the type suggested here should at some stage be qualified by additional ground based measurements (i.e. a distrometer, radio link, radiometer, etc.) or in situ aircraft measurements.

ACKNOWLEDGEMENTS

The authors gratefully acknowledge the help and contribution of several colleagues in the culmination of this work. In particular thanks are due to Dr. H. Hoeller for making available for this work the radar data collected by him. The help and generosity of Dr. H. Schuster is likewise acknowledged for allowing free access to his software (IP2PR and IP3PR) which enables a 2/3 parameter inversion of N(D) and a structured handling of radar data.

5. REFERENCES

1. Schroth, A., et al, Jan 1988, " A C-Band Coherent polarimetric Radar for Propagation and Cloud Physics Reasearch", to appear in J. Atm. & Oce. Tech.
2. Seliga, T. A. and Bringi, V. N., 1976, J. Appl. Met., 15, 69-76.
3. Chandra, M., et al, 1985, ICAP-85, Warwick, U. K., IEE Publ. Nr. 248, 11-17.
4. Chandra, M., et al, 1986, the 23-rd Rad. Met. Conf., Snowmass, Co., Paper Jp 19.38, Publ. by AMS.
5. Chandra, M., et al, 1987, ICAP-87, York, U. K., IEE Publ. Nr. 274, 328-333.
6. Joos, J, et al, 1968, Toronto, Int. Conf. Cloud Phy., 369-373.
7. Pruppacher, H. R. and Pitter, R. L., 1971, J. Atm. Sci, 28, 86-94
8. CCIR Doc.: Propagation in non-ionised media, vol. 5, Rep. 721-1, Geneva, 1982, 170-171.

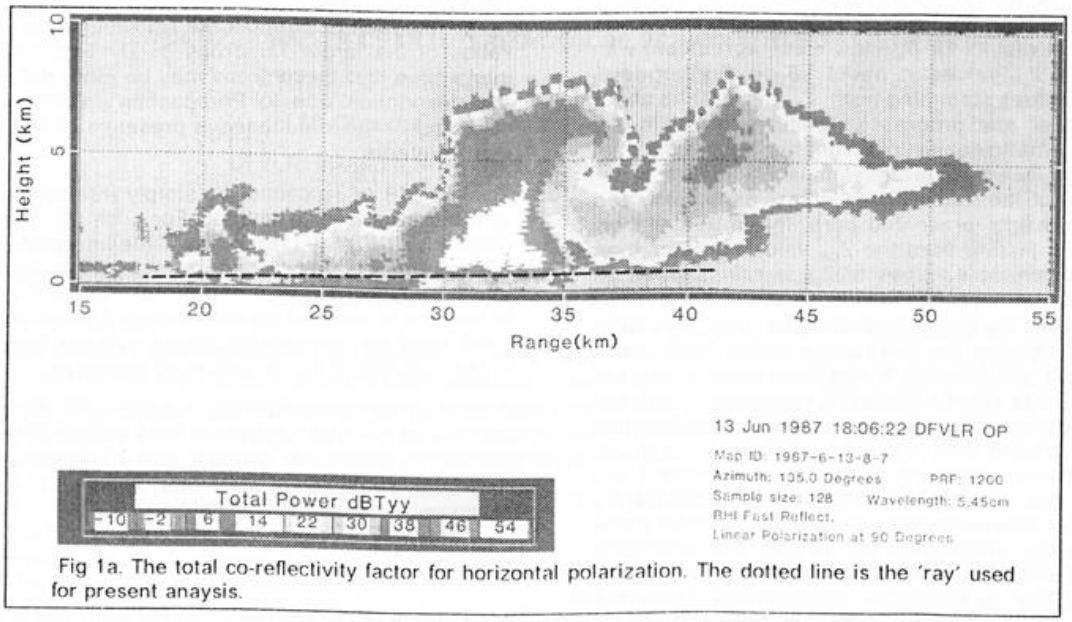


Fig 1a. The total co-reflectivity factor for horizontal polarization. The dotted line is the 'ray' used for present anaysis.

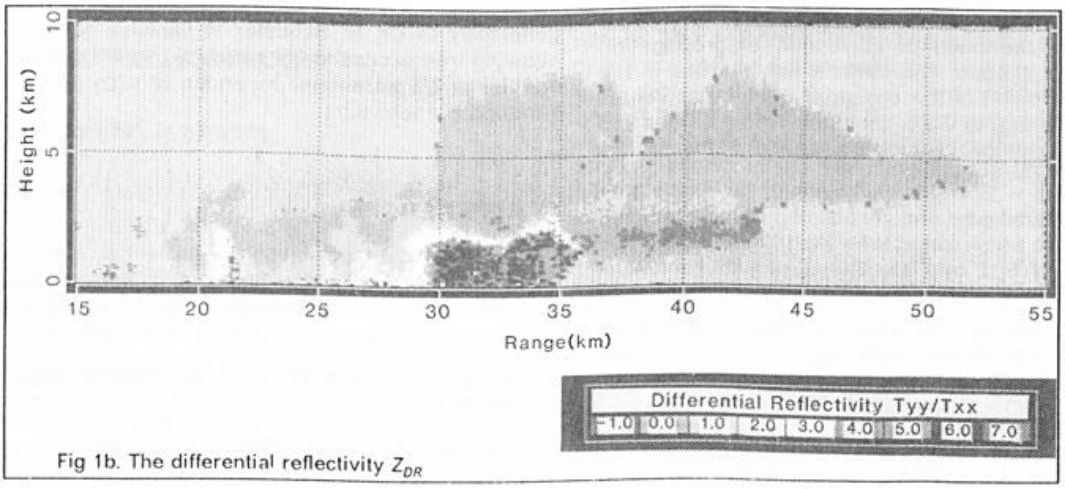


Fig 1b. The differential reflectivity Z_{DR}

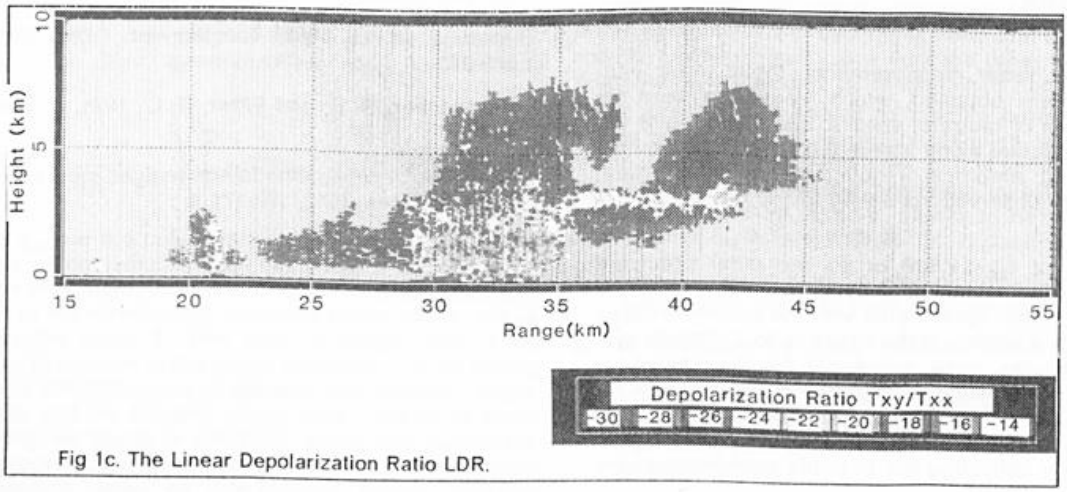


Fig 1c. The Linear Depolarization Ratio LDR.

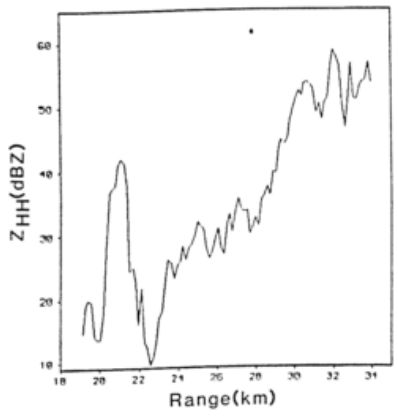


Fig 2a. The reflectivity (horizontal polarization) along the data ray.

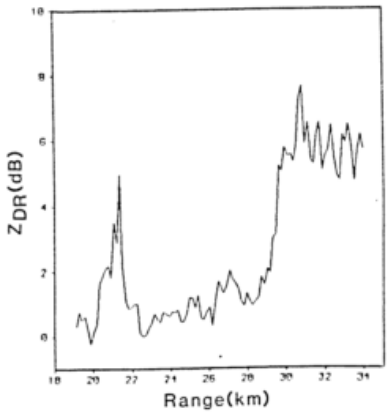


Fig 2b. The differential reflectivity along the data ray.

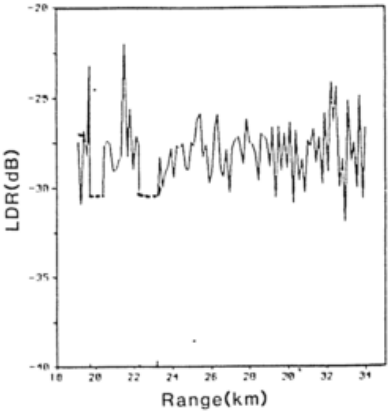


Fig 2c. The Linear Depolarization Ratio along the data ray.

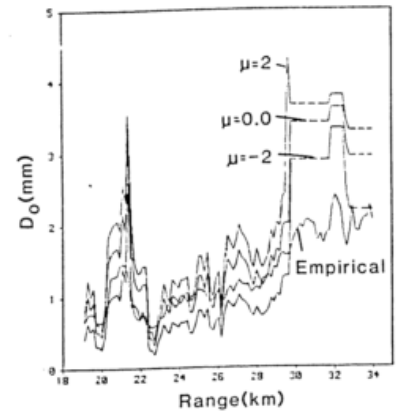


Fig 3. D_0 against range for μ =-2, 0, 2 and the empirical law.

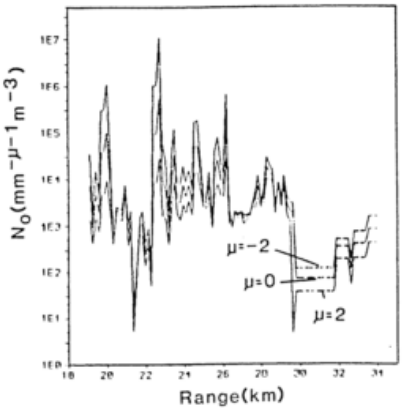


Fig 4. N_0 against range for μ =-2, 0, and 2.

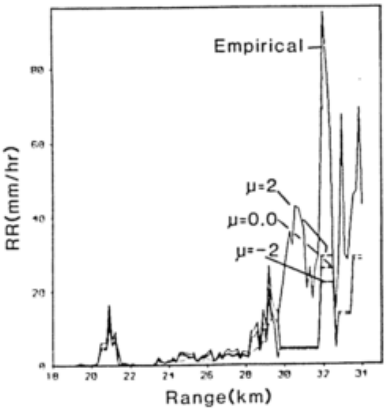


Fig 5. Rainrate against range for μ =-2, 0, 2 and the empirical law.

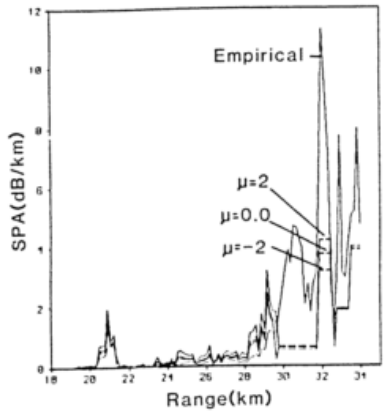


Fig 6. specific attenuation against range for μ =-2, 0, 2 and the CCIR empirical law for 20 GHz and horizontal polarization.

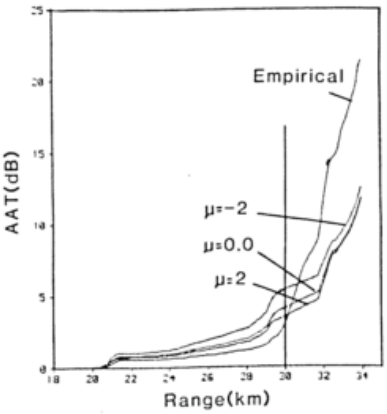


Fig 7. Accumulated (total) attenuation against range for μ =-2, 0, 2 and the CCIR empirical law for 20 GHz and horizontal polarization.

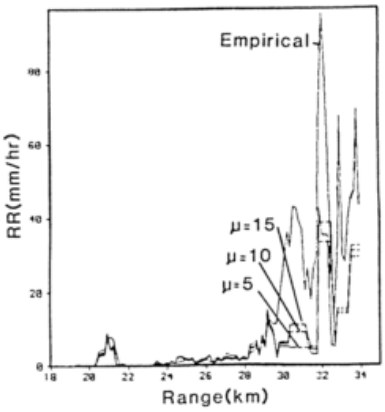


Fig 8. Rainrate against range for μ =5, 10, 15 and the empirical law.

AN INVESTIGATION OF THE EFFECT OF ELECTRICAL CHARGES ON THE COLLISION EFFICIENCY OF CLOUD DROPS

V.M.Kim

The Institute of Experimental Meteorology
Obninsk USSR

1. INTRODUCTION

The paper deals with theoretical investigations of the effects of drop electric charges on the gravitational coagulation process of drops of significantly various sizes with increasing their charge to the limiting values. The intermediate Reynolds numbers N_{Re} ranging from 10 to 60, which correspond to the falling velocities of the collector drops with radii R ranging from 100μm to 250μm are studied because of the lack of data on the strongly charged drop growth velocity due to coagulation with neutral and charged droplets of radii r from 1μm to 20μm. The drop size and charge range mentioned above is of practical importance because this is the range in which particle growth occurs in clouds including thunderstorm clouds (BARKER 1983, p. 631). The modification methods of warm clouds intended for precipitation growth enhancement are developed also in this range.

2. NUMERICAL MODEL

As far as in this work the size ratios of interacting drops $r/R \leq 0.1$ were considered the approximation of purely inertial deposition with allowance for external force was used in the model to describe the process of drop collision. The effect of droplet hydrodynamical field on the collector drop hydrodynamical field was not considered in this approximation. A numerical solution (RIVKIND 1976, p. 8) of the Navier-Stokes equations for flow-around a liquid sphere rather than a rigid one was taken as the field of velocities around a collector drop since the drag force coefficients of the collector drops available in the cited paper showed a more agreement with our experimental results for the drops (KIM 1986, p. 193). It was expected that the droplets are goverened by the Stokes law. To determine coulomb and induction forces of interacting drops we used the expression obtained in (DAVIS 1964, p. 499) for two conducting electrically charged spheres. The collision efficiency of the drops was obtained from the formula $E(R,r,Q,q) = y_c^2 \ (1 + r/R)^2$, where Q and q are the electric charges on the collector drop and on the droplet, respectively and y_c is the dimensionless critical horizontal offset of the center of the droplet from the center of the collector drop, when the droplet is 30 collector drop radii upstream.

3. DISCUSSION OF RESULTS

We obtained the numerical results on the effect of the induction forces on E when the collector drop charge Q changed to the limiting Rayleigh charge and q = 0 for N_{Re} = 10,15,30,50, 60. E versus droplet sizes or their Stokes numbers K for N_{Re} = 10 (R=103 μm) and 50 (R=216μm) are presented in Fig.1 and the curves for the neutral collector drops are also given for

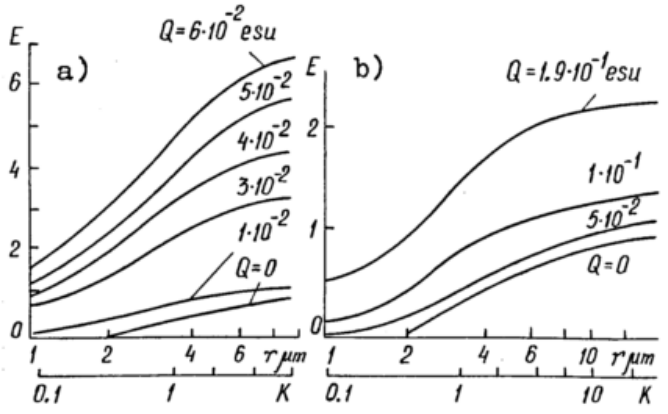


Fig.1: E versus r and K for various Q under the induction force: a) N_{Re}= 10; b) N_{Re}= 50

comparison. From these Figs one can see that for all droplet sizes studied E increases with increasing the collector drop charge, and the less r or the Stokes number of the droplet is the more E increases as compared to E for neutral droplets. For instance, for the limiting charge on the collector drop with radius 103μm the collision efficiency of the droplet with r = 2μm is 200 times higher and the droplet with r = 10μm is only four times higher than the collision efficiency for neutral droplets. The induction force effect on the increase in collision efficiency enhances with decreasing N_{Re}, and the increase within the drop size and charge range considered reaches two orders of magnitude.

The analyses of droplet trajectories and different relations of the forces effecting on the droplet allow to draw the following conclusions. The collision efficiency does not practically depend on N_{Re} at $N_{Re} \gg 30$ and at droplet Stokes numbers ranging from 0.1 to 40, if the parameter β is constant and more than 0.1 (β is the ratio of the induction force to the aerodynamic force affecting the droplet; $\beta = Q^2 r^2 C_{sc} / 3\pi\eta R^5 U_\infty$, where η is the dynamic viscosity of air, U_∞ -terminal falling velocity of a collector drop and C_{sc} is the Stokes-Cunningham slip correction). E increases with increasing K at $\beta < 1$ and decreases at $\beta > 1$. This derives from the fact that the increase of E at $\beta > 1$ occurs only due to the increase of droplet deposition on the back of the sphere (Fig.2) hence the particle inertia

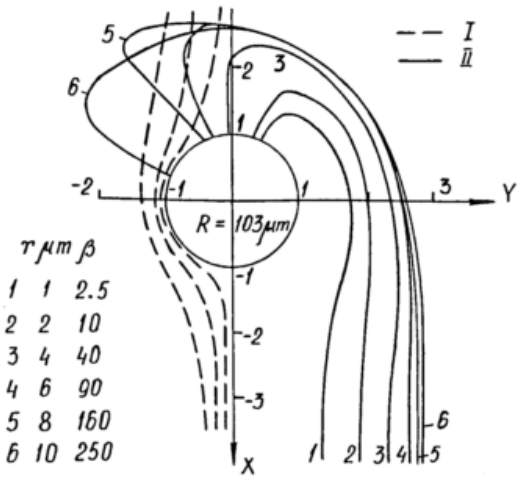


Fig.2: The critical trajectories of droplets with various sizes at the limiting charge on the collector drop with R = 103μm (N_{Re} = 10): I-streamline; II-critical trajectories

retards their deposition. The numerical results obtained for E at the induction interaction are in 10% agreement with our previous experimental results (BELYAEV 1984, p. 127). This indicates that the model is suitable for describing the coagulation process of electrically charged drops of significantly various sizes.

When considering simultaneous action of the coulomb and induction forces, the charge of the collector drop Q varied from 0 to its limiting value and the charge of droplets q was taken to be equal to the charge characteristic for thunderclouds, q = - 20 r^2esu. Fig.3 shows the value of E at

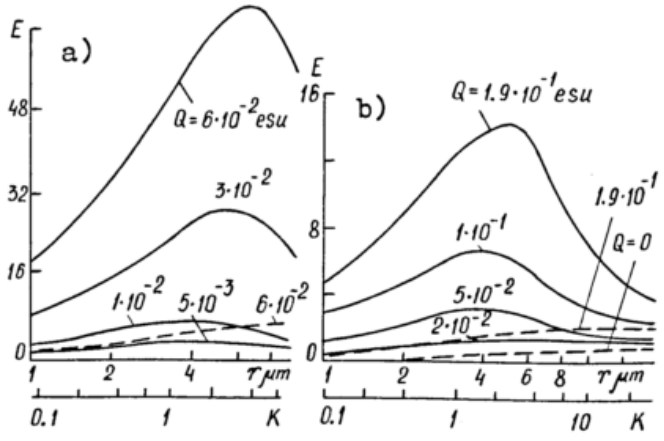


Fig.3: E versus r and K for various Q under the induction and coulomb forces: a) N_{Re} = 10; b) N_{Re} = 50; 1 - q = - 20 r^2 esu; 2 - q = 0

N_{Re} = 10 and 50 for various charged on the collector drop and q = - 20 r^2 esu versus r or K. For comparison E are also shown for the induction interaction (q = 0) at the limiting charge on a collector drop and E for neutral droplets. Under the simultaneous action of the coulomb and induction forces E at N_{Re} = 10 can reach 3 orders of magnitude for r < 2μm and one or two orders of magnitude for the other r compared to E for the neutral drops. The cylinder radius from which the droplets are scavenged reaches 8.5 collector drop radii. The action of the electrostatic forces decreases with increasing N_{Re}: the maximum value of E at N_{Re} = 10 is 64 and at N_{Re} = 50 is only 14. From Fig.3 and computation results for other N_{Re} it follows, that at all considered N_{Re} beginning from the particular collector drop charge Q the dependence of E on r or K becomes nonmonotonous, the maximum appeares at r ≈ (4 + 6)μm or K ≈ (1.5 - 3). The appearance of the maximum is accounted for by the dependence change of forces affecting the droplet.

4. REFERENCES

BARKER, E.; BICKNELL, J.A.; GRIFFITS, R.E.; LATHAM, J.; VERMA, T.S.: The scavanging of particles by electrified drops: radar echo intensification following lightning. Quart. J. Roy. Met. Soc. 109 (1983), p.631-644.

BELYAEV, S.P.; KIM, V.M.; MATVEEV, V.N.: On coagulation of charged and neutral cloud drops. Proc. of the 9th Intern. Physics Conf. Tallin. 1(1984), p.127-130.

DAVIS, M.H.: Two charged spherical conductors in a uniform electric fields: Forces and field strength. Quart. J. Mech. Appl. Math. 17 (1964b), p.499-511.

KIM, V.M.: Coagulation of neutral and charged water drops of significantly various sizes at intermediate Reynolds numbers. Phys. & Math. Cand. Degree Thesis. Obninsk. 1986, 193p.

RIVKIND, V.J.; RYSKIN, G.M.: Structure of the flow about a spherical drop moving in a liquid medium at intermediate Roynolds numbers. Fluid and Gas Mechanics. (1976) No 1, p.8-15.

MICROPHYSICAL AND ELECTRICAL PHENOMENA DURING FREEZING OF WATER DROPS

Adzhiev A.Kh., Tomazov S.T.

High Mountain Geophysical Institute, Nalchik.

Process of charging of hydrometeors during cloud water freezing play an essential role in the formation of an electrical structure of thunder clouds. The study of this phenomenon has not begun until recently. The research is based on the occurence of a considerable potential difference between the melt and solid phase, referred to as the effect of Workman-Reynolds-Ribeira (1954), and on the separation of considerable electric charges during an explosive splitting of freezing droplets. The analysis of work on charge separation during water freezing ADZHIEV (1986,42p.) shows that measurement of an inherent droplet charge involves great difficulties and the data obtained by various authors contradict in many aspects,

The majority of studies of the above phenomenon dealt with a residual charge of a frozen droplet. Such approach does not allow an accurate estimation of the total quantity of the electric charge, separated during the freezing of a droplet. It is well-known, that contact charging, associated with mass fragmentation during freezing, is responsible for the charge. So, the charge value and sign are changing depending on the phase (solid, liquid or gase) and the fraction separated from the droplet. A residual charge, stored after multiple mass splitting from the freezing droplet, does not characterize the above process to the right degree. Some results of experimental studies of the influence of various factors on the electric charge separation during water droplet freezing are presented. Evaluation of the charge is based on a continuous recording of the electric current from the freezing droplet. The source of the recorded electric current is the charge which originates on the freezing droplet due to mass fragmentation if there is a potential difference at the interface "vapor-water-ice". Voltmeter-electrometer "B7-30" with current sensitivity 10^{-15}a at an input impedance $5 \cdot 10^{11}$ ohms and capacity 20pF was used for studying charge separation during water droplet crystallization. Measuring error for the electric current from the freezing droplet was 1.8%, and the charge computation error was 2.6%. Besides, in order to study the electromagnetic radioemission during crystallization, we used amplitude- and frequency-response analyser XI-42, pulse analyser YP5-2 and spectrum analyser CK4-59.

A drop under study was put onto an electrode, connected to the electrometer. The electrode was placed into the cold chamber, cooled to -30°C at a given rate. The drop was observed continuously with a microscope. The beginning and the end of crystallization were determined visually. The electric current variation with time was recorded by potentiometer OH-804/I. A more detailed information on the transient processes was obtained by a storage oscilloscope C8-17. In the process of crystallization we recorded temperatu-

re for the beginning (covering of a supercooled droplet with an ice shell) and the end (complete freezing of a droplet) of crystallization, ejection of microparticles, changes of the drop's shape, appearance of the surface cracks, projections and branches sometimes amounting to 3-5 mm. Water droplets were put into the cold chamber at 0°C and cooled till complete crystallization at a rate of 1-1.5 deg/min. As a rule, crystallization began from the surface of the drop, by the formation of an ice coating. Then, during crystallization the solid coating became partially distorted, and the interface moved over from the drop's surface to its center, creating excessive pressure inside the drop, which resulted in cracks producing airbubles, microparticles of water and ice (section BC in Fig.1). The number

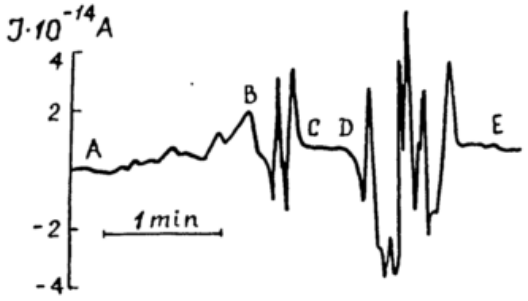


Fig.1. Current variation during droplet freezing (AC) and hail growth (DE).

of individual events of charge separation in some experiments reached 30, and the most intensive charge separation occured in the temperature range from -5 to -15°C. Normally, small pulses were observed when the droplet became ice-coated (A in Fig.1). In the experiments these pulses were positive in 99% of cases and negative in about 1%. Very often the droplets exploded into instantly freezing fragments. Maximum separation of electric charges is observed here. Explosive splitting of supercooled water droplets during crystallization is generally observed in the temperature range from -8 to -16°C. Probability of explosion here is 10-12% for water droplets with an electrical conduction $2.4 \cdot 10^{6}$ ohm/cm and pH=5.3.

Results of our studies indicate that a maximum charge, separated during an explosive splitting of droplets, could reach a value of 10^{-11}coul. If crystallization of the remainder continues after splitting, then the remainder of the droplet acquires a positive charge. If the explosive splitting occurs at the end of crystallization, then the charge of the remainder can be of any sign. The average value of the electric charge, separated in this process, is $3 \cdot 10^{-10}$coul. per 1g of frozen water.

Oscillography shows that the electric charge separation time for the explosive splitting is from 0.001 to 0.1s. The rate of current bulid-up is from $10^{-11}$to 10^{-10}a/s with an average value of $8 \cdot 10^{-11}$a/s. When there is no visual explosion, the droplet charging is observed from the moment of ice-coating formation till the complete freezing of the droplet.

The average size of ejected microparticles and their number were found to increase with the droplet diameter during the droplet crystallization at the interface of two unmixing, optically transparent liquids. A millimeter size freezing droplet ejects on the average 30 particles, 10 of them are qualified as solid ones by their shape and cclour. The size of the ejecting particles varied from 10 to 100μm, at an average value of 35μm. Chemical analysis of atmospheric precipitation revealed the presence of some ions: K^+, Ca^+, Na^+, SO_4^-, NO_3^-, NO_2^-, Cl^-, CO_3^-. The following chemical substances were selected, which dissociate into the

same ions in the aqueous solution: K_2SO_4, KNO_3, KCl, $CaCl_2$, NaCl, Na_2CO_3, $NaNO_3$, $NaNO_2$. Concentrations of the prepared solutions were of a wide range, i.e. 10^{-6} - 10^{-2}N. Studies of the crystallizing droplets of these solutions show that a concentration increase in excess of 10^{-4} N results in a sharp decrease of the separating charge. Analysis of the obtained results allows us to conclude that added ions play an important role in the process of charging of crystallizing droplets of the solutions.

In the atmosphere the process of droplet charging continues even after their complete freezing due to the impaction of a frozen nucleus with a supercooled droplet. The latter freezes, while spreading over the nucleus surface,and increases the size of a growing hailstone and its charge. Charge separation was studied in the laboratory experiments with crystallization and hail growth in an air flow, containing water aerosol. The flow velocity varied between 5 and 10 m s^{-1}. Temperature for the beginning of crystallization increased by 5-8°C and the charge increased up to 10^{-10} - 10^{-9}coul.· min^{-1} per one gramme of water. Hail growth was accompained by intensive charge separation (section DE in Fig.1).

Results of our studies show that dynamic structural changes at interfaces are accompained by electromagnetic emission in the wide range of frequences. Intensity of an acoustic signal was recorded by a piezoelectric sensor simultaneous to the recording of the electromagnetic spectrum. Spectrum analyzer and amplitude- and frequency-response analyser helped to follow the nature of the electromagnetic spectrum variation in the process of water crystallization. As a rule, this process begins from recording the maxima at 45 and 65 MHz, the spectrum is continuous with boundaries at 40-50 and 65-71 MHz. Further on, these maxima fade and new ones appear at 10-20 and 30-45 MHz, the spectrum nature here does not change. After that the process is accompained by a considerable widening of the upper frequency band up to 50 MHz and by an increase of pulses in the region of the upper limit of the band. Later on a continuous spectrum with maxima at 42, 54, 64 MHz is observed in this frequency range, and small intensity maxima emerge in the range 8-25 MHz. Termination of the process is characterized by a transition from a continuous spectrum to separate lines at frequences 52-56 MHz, 8-18 MHz and 24 MHz. Thus, the most typical frequences can be singled out, i.e., 8-20 and 32-50 MHz. Analysis of pulses of electromagnetic emission indicates that they are a sequence of series, consisting of individual pulses of 10^{-2} - 0.5μ s duration. The electromagnetic emission strength grows considerably when the acoustic signals emerge. This growth is associated with the appearance of cracks and ejection of microparticles from the freezing surface. Electromagnetic emission intensifies with an increase of the freezing rate.

ADZHIEV, A.: Generation and Separation of Electric Charges in Clouds During Hailstone Formation and Melting.Review Meteorologia. Obninsk. 1986, 42 p.

WORKMAN, E.; REYNOLDS, S.: Electrical Phenomena Occuring During the Freezing of Dilute Aqueous Solution and Their Possible Relationship to Thunderstorm Electricity. Phys. Rev. 94 (1954), Nr. 4, p. 1073-1075.

A DESCRIPTION OF CONDENSATION PROCESSES IN A TURBULENT THREE-PHASE CLOUD

Novosyolov L.N., Stepanov A.S.

Research & Scientific Amalgamation "Typhoon", USSR

A closed system of second-order differential equations has been obtained under the diffusion approach for a description of cloud thermal, hydrodynamic and microphysical characteristics evolution at all the stages of its spatial and temporal development. Droplet and ice particles spectra f in the processes of condensation and turbulent mixing change according to kinetic equations like

$$\left(\frac{d}{dt}+\hat{K}_1+\hat{K}_2\right)\frac{f}{\rho}=Q$$

$$\frac{d}{dt}=\frac{\partial}{\partial t}+W_i\frac{\partial}{\partial x_i},\quad \hat{K}_1=\frac{\partial}{\partial S}\dot{S}-\left(\frac{\partial}{\partial x_i}+\frac{\partial}{\partial S}A_i\right)K_{ij}\left(\frac{\partial}{\partial x_j}+\frac{\partial}{\partial S}A_j\right) \qquad (1)$$

$$\hat{K}_2=-K_{ij}\frac{\partial}{\partial S}\left(a_i\frac{\partial}{\partial x_j}+\frac{\partial}{\partial S}b_{ij}\right)$$

where S is the particles surface area, K_{ij} is the eddy diffusivity tensor, Q are the sources of particles, of melting and of crystallization, ρ is the density of air, A_i, a_i, b_{ij} are the functions of cloud medium parameters, $\vec{W}$ is the air flow velocity. Repetitive indices indicate summation. With the accuracy to a dimensional factor the component A_i are the mixing lengths in the size dimension domain controlling the contribution from turbulent mixing into the particles size dispersion growth rate σ :

$$\frac{d}{dt}\sigma \propto \frac{1}{2}K_{ij}A_i\left(A_j-4\frac{\partial\bar{S}}{\partial x_j}\right) \qquad (2)$$

where $\bar{S}$ is the mean surface area of the phase considered. The value of A_i varies within wide limits. In a three-phase medium it is determined primarily with the mean geometrical time of phase relaxation and with the heterogeneity of potential and pseudopotential temperature fields. In a mixed supercooled cloud fluctuations of $\frac{d}{dt}\sigma$ are possible at different stages of ice phase formation becoming both positive and negative. Therefore stochastic condensation does not obligatorily lead to the dispersion growth rate.

Universal expressions are obtained for turbulent heat and moisture fluxes in the inner and outer regions of a cloud. As it follows from the result obtained, heat- and mass-transfer take place somewhat differently from the phenomenological theory.

The latter complex operator $\hat{K}_2$ in (1) has its origin in the effect of nonadiabaticity of air parcels, that is significant at cloud formation and for the processes occurring at cloud boundaries.

In view of a water-drop stratiform cloud comparative numerical calculations have been performed for drop spectrum evolution with the use of (1) and of equations of the turbulence semiempiric theory ($A_i=a_i=b_{ij}=0$). The tendencies of spectra evolution appeared to be different. According to (1) the spectrum attained with time an extremely pronounced maximum, in the second variant mechanical mixing caused a considerable broadening of the spectrum. Such tendencies are not universal: depending on certain profiles of thermal, hydrodynamic and microphysical parameters other situati-

ons are possible.

The mathematical tool obtained describes the whole set of condensation processes in a three-phase cloud medium. When necessary this technique can be generalized for the case of sedimentation and coagulation processes.

EFFECT OF THE ELECTRIC FIELD ON THE RAINDROP SHAPE

Georgi Magradze

Geophysics Institute of the Georgian SSR Academy of Sciences, Z. Rukhadze Str. 1, Tbilisi 380093, USSR

Let us consider a raindrop of equivalent radius a_o falling with the terminal velocity $\vec{v}$ under the action of aerodynamic and gravitational forces. The velocity vector $\vec{v}$ is parallel to the electric field strength $\vec{E}_o$ and to the oz-axis directed downwards. It is well-known that the equilibrium state of a liquid drop corresponds to the minimum value of free energy. Neglecting the internal water circulation and assuming that the temperature in the reference system connected with the drop centre is constant, we write an expression for free energy in the form

$$F = \alpha \int_{S_o} dS - \frac{E_o}{2} \int_{S_o} \sigma z \, dS - mgz_o - \int_{V_o} p \, dV \qquad (1)$$

where the first term is the surface energy, the second is the conductor energy in the external electric field, the third is the potential energy of a raindrop and the fourth is the action of external force; α is the surface tension coefficient, σ is the surface charge distribution, z_o is the gravity centre position in the chosen reference system, p is aerodynamic pressure, s_o and v_o are respectively the surface and the volume of a drop.

We write expression (1) in terms of a spherical coordinate system; by virtue of symmetry considerations the drop must be symmetrical with respect to the oz-axis; therefore the surface radius-vector $r(\theta, \varphi)$ depends only on the angle θ. Since the expression for F depends only on the radius-vector of the drop surface, is a functional of r and the drop equilibrium corresponds to the minimum value of the functional F(r) on possible drop surface variations. The drop volume remains constant. Therefore an additional condition

$$\int_0^{\pi} r^3 \sin\theta \, d\theta = 2 a_o^3 \qquad (2)$$

is imposed on $r(\theta)$. Condition (2) can be excluded by the substitution $r(\theta) = C \cdot u(\theta)$, where C is a constant determined from (2). After the substitution the finding of the drop equilibrium reduces to the finding of the absolute minimum value of functional (1) by successive approximations. For this the initial drop shape is given, for which the function $\sigma(\theta)$ and the aerodynamic pressure distribution $k(\theta)$ are calculated, while the surface is varied so as to obtain the minimum value for F(u). Next, $\sigma(\theta)$ and $k(\theta)$ are calculated for a new value of $r(\theta)$ and the variation process is repeated until the surface points converge with a given accuracy. If under the given conditions F(u) has no minimum value, then the minimization process diverges and in that case the drop instability is observed. In this approximation the minimization process is accomplished numerically by the method of local variations (CHERNOUS'KO and BANICHUK, 1973). In calculations for $k(\theta)$ use was made of the function obtained experimental-

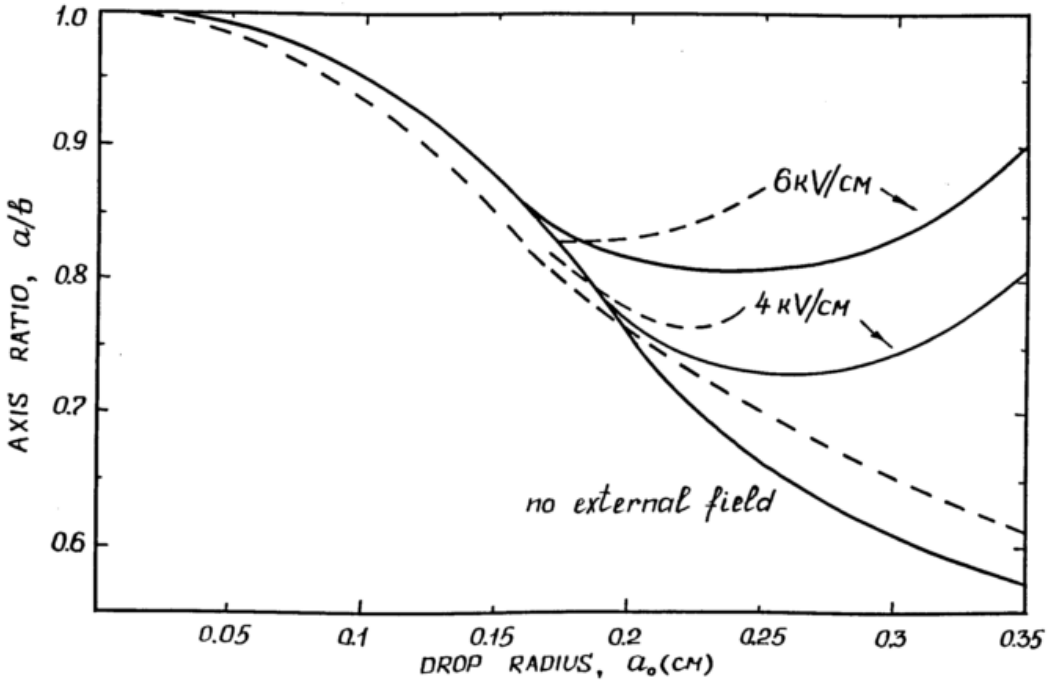


Fig. 1: Variation of the drop axis ratio a/b with the drop radius a_o for various values of E_o. The dotted line shows results from (RASMUSSEN et al. 1985) and (PRUPPACHER and PITTER 1971)

ly (FAGE 1937) with the correction for ellipsoidality suggested in (BEARD and CHUANG 1987). The correction for ellipsoidality was used with some modifications. The distribution of charge surface density was calculated by the numerical method based on the solution of a singular integral equation (MAGRADZE 1986).

When $E_o = 0$, for drops of radius $a_o \gtrsim 0.25$ cm a concavity develops in the drop bottom due to a strong aerodynamic pressure at the lower drop surface. The greater the radius, the larges the concavity. Similar results were obtained in (PRUPPACHER and PITTER 1971) for drops of $a_o \gtrsim 0.2$ cm. Fig. 1 shows the variation of the drop axis ratio a/b, where a is the vertical and b the horizontal drop size, with the radius a_o for various values of E_o.

The electric field strength $E_o \lesssim 6$ kV/cm practically has no effect on drops of radii less than 0.15 cm.

The electric field strength $E_o \lesssim 3$ kV/cm produces a weak effect on drops of radius $0.15 \lesssim a_o \lesssim 0.35$ cm. For $E_o \gtrsim 3$ kV/cm large drops become elongated along the strength vector; the greater the radius, the stronger the elongation. Thus for a drop of a_o = = 0.3 cm, the axis ratio a/b is equal to 0.62 when $E_o = 0$ but increases to 0.84 when $E_o = 6$ kV/cm.

The results obtained agree with experimental data from (RASMUSSEN et al. 1985). Our lower values of a/b as compared with experimental data can most probably be explained by using an inaccurate function in calculations of $k(\Theta)$.

REFERENCES

BEARD, K.V., and C. CHUANG: A new model for the equilibrium shape of raindrops. J. Atmos. Sci. 44 (1987), No.11, p. 1509-1524.

CHERNOUS'KO, F.L., and N.V. BANICHUK: Variation problems of mechanics and control (in Russian). Moscow: Nauka 1973, 238 p.

FAGE, A. Experiments on a sphere at critical Reynolds numbers. Aero. Res. Comm. England, Rep. and Memo (1937), No. 1766, 20 p.

MAGRADZE, G.D.: Numerical method of calculating the electric field of water hydrometeors (in Russian). Abstracts All-Union Symp. on Atmospheric Electricity (1986), p. 127.

PRUPPACHER, H.R., and R.L. PITTER: A semi-empirical determination of the shape of cloud and rain drops. J. Atmos. Sci. (1971), v. 28, p. 86-94.

RASMUSSEN, R., C. WALCEK, H.R. PRUPPACHER, S.K. MITRA; J. LEW, V. LOVIZZANI, P.K. WANG, and V. BARTH: A wind tunnel investigation of the effect of an external electric field on the shape of electrically uncharged rain drops. J. Atmos. Sci. 42 (1985), No. 15, p. 1647-1052.

DAMPED-OSCILLATION REPRESENTATION OF DROP-SPECTRUM EVOLUTION DUE TO COALESCENCE AND BREAKUP

Philip S. Brown, Jr.

Trinity College
Hartford, CT 06106, USA

1. INTRODUCTION

The research involves analysis and parameterization of model-generated raindrop spectra. In the model it is assumed that transient behavior of the drop spectrum is determined only by the effects of collisional breakup and coalescence. These binary drop-interaction processes are described by means of the fragment distribution function and coalescence efficiency of LOW AND LIST (1982a,b). The model-generated drop spectra are found to approach an equilibrium drop distribution that is unique in shape but that is proportional in size to the liquid water content of the system. When the initial drop spectra are assumed to have Marshall-Palmer form, the approach to equilibrium is not monotonic. Often the small-raindrop portion of the spectrum rapidly climbs to high concentration levels before settling back toward equilibrium. The phenomenon is evident in Fig. 1 which shows the log of number density n as a function of drop diameter D at various stages in the approach to equilibrium. (Also see LIST ET AL. 1987, p. 368.) It is the aim of this work to develop a simple parameterization that describes well the characteristic behavior of drop spectra evolving from Marshall-Palmer form. Such a parameterization could provide improved microphysics representation in moist convection models whose heavy demands on computer resources preclude detailed solution of the coalescence/breakup equation.

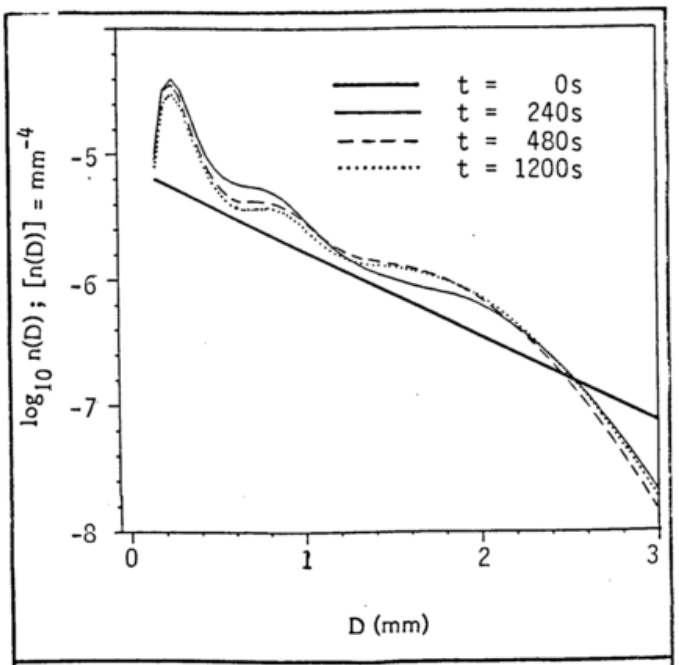


Fig. 1. Evolution of drop spectrum through coalescence and breakup. Initial distribution has Marshall-Palmer form $n(D) = N_0 e^{-\Lambda D}$ where $N_0 = 8 \times 10^{-6}$ mm^{-4} and $\Lambda = 1.559$ mm^{-1}. A non-monotonic approach to equilibrium is evident.

2. PARAMETERIZATION TECHNIQUE

The idea behind the parameterization is to represent $n(D)$ by a discrete drop-size distribution n_i, $i=1, \ldots, I$, and to express the set of values n_i in terms of exponential functions superimposed on the equilibrium distribution. The n_i's are governed by a dynamical system that results from discretization of the coalescence/breakup equation (e.g., LIST AND GILLESPIE 1976, p. 2008). The local behavior of the system near equilibrium is represented by the equation

$$\frac{d\underline{\varepsilon}}{dt} = \underline{A}\,\underline{\varepsilon} \qquad (1)$$

where $\underline{\varepsilon} = \{\varepsilon_i\}$ denotes the departure of $\{n_i\}$ from the equilibrium state $\{(n_{eq})_i\}$ and where $\underline{A}$ is the Jacobian matrix evaluated using equilibrium values of n_i. It follows from (1) that each component $\varepsilon_i = n_i - (n_{eq})_i$ is a linear combination of the functions $e^{\lambda_j t}$, $j=1,\ldots,I$, where the λ_j's are the (complex) eigenvalues of $\underline{A}$. It happens that combinations involving only a small number of exponential functions describe well the behavior of the components $n_i - (n_{eq})_i$ and thereby provide a simple parameterization of the evolving drop-size distribution. $\{(n_{eq})_i\}$ is determined once and for all

by numerical solution of the coalescence/breakup equation; the solution is advanced in time until numerical equilibrium is reached.

3. ADJUSTMENT FOR LIQUID WATER CONTENT

For the parameterization to be useful, the approximating functions $e^{\lambda_j t}$ and the equilibrium values $(n_{eq})_i$ must be readily adjustable to accommodate systems with arbitrary liquid water content. It is an inherent property of the coalescence/breakup equation that both the "rate constants" (i.e. the λ_j's) and the equilibrium drop size distribution are proportional to the liquid water content (SRIVASTAVA 1982, p. 1320). Once the λ_j's and $(n_{eq})_i$'s are determined for a system with liquid water content L^*, multiplication by the scaling factor L/L^*, immediately determines the corresponding quantities for a system with liquid water content L. The generality of the parameterization depends upon these proportionality relations.

4. CASE STUDY

Calculation of the eigenvalues for the case treated in Fig. 1 shows (i) that $Re(\lambda_j) < 0$ for each j so that the equilibrium is asymptotically stable, and (ii) that there are eigenvalues with $Im(\lambda_j) \neq 0$ so that the drop spectrum will oscillate on its approach to equilibrium. Analysis of model-generated solutions shows that one particular damped oscillation describes rather well the nonmonotonic behavior of $n_i - (n_{eq})_i$ for drop categories in the small raindrop portion of the spectrum. For these categories,

$$n_i(t) - (n_{eq})_i = c_i e^{-\mu t} \cos[\nu(t - t_i)] \qquad (2)$$

where $\lambda = \mu \pm i\nu$ are complex conjugate eigenvalues determined from the eigenanalysis and c_i, t_i are found by fitting the form (2) to the model-generated drop spectrum. The solid curve in Fig. 2 shows the model-generated solution $n_i - (n_{eq})_i$ for index i corresponding to a drop diameter of .27 mm. (This component is contained in the overall spectrum shown in Fig. 1.) The dashed curve in Fig. 2 represents the damped oscillation (2). The particular function given in (2) provides a reasonable approximation to the transient behavior of the spectrum not only at $D = .27$ mm but over the entire small-drop range, $D < .75$ mm. Other exponential functions can be used to model the mid-size and large-size portions of the spectrum. A composite of these submodels provides a parameterization that can represent the evolution of the overall spectrum shown in Fig. 1.

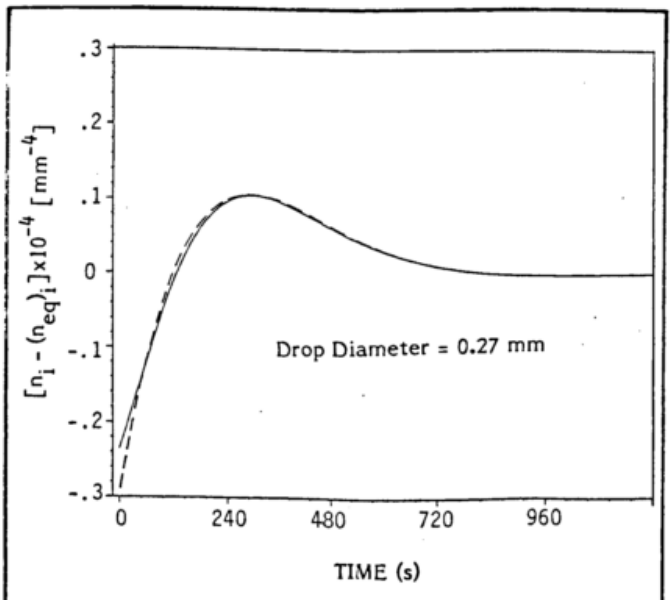


Fig. 2. Evolution of component $\varepsilon_i = n_i - (n_{eq})_i$, where ε_i is the departure of the drop spectrum from equilibrium for drop category i corresponding to mean drop diameter $D = .27$ mm. Solid curve represents values obtained by numerical solution of the coalescence/breakup equation; dashed curve represents the parameterization established in (2).

5. CONCLUSION

The analysis is directed toward finding a simple mathematical form to describe the transient behavior of $\{\varepsilon_i(t)\}$ which represents the departure of the drop spectrum from equilibrium. The functions $e^{\lambda_j t}$ provide such a description. The exponential functions damp in time, while some oscillate as they decay. One particular damped oscillation represents extremely well the departure of the drop spectrum from equilibrium in the small-drop range. The damped oscillation explains the non-monotonic behavior of a significant portion of the spectrum, and provides a convenient parameterization. Other representative functions of the form $e^{\lambda_j t}$ can be found to describe the temporal behavior of the mid-size and large-drop portions of the drop-size distribution.

ACKNOWLEDGMENTS

This work was supported by the Division of Atmospheric Sciences, National Science Foundation, under Grant ATM-8521417.

REFERENCES

LIST, R.; DONALDSON, N.; STEWART, R.E.: Temporal evolution of drop spectra to collisional equilibrium in steady and pulsating rain. J. Atmos. Sci. 44 (1987), pp. 362-372.

LIST, R.; GILLESPIE, J.R.: Evolution of raindrop spectra with collision induced breakup. J. Atmos. Sci. 33 (1976), pp. 2007-2013.

LOW, T.B.; LIST, R.: Collision, coalescence and breakup of raindrops. Part I: Experimentally established coalescence efficiencies and fragment size distributions in breakup. J. Atmos. Sci. 39 (1982a), pp. 1591-1606.

LOW, T.B.; LIST, R.: Collision, coalescence and breakup of raindrops. Part II: Parameterization of fragment size distributions. J. Atmos. Sci. 39 (1982b), pp. 1607-1618.

SRIVASTAVA, R.C.: A simple model of particle coalescence and breakup. J. Atmos. Sci. 39 (1982), pp. 1317-1322.

KINETIC EQUATION FOR POLLUTED CLOUD DROPLETS SPECTRUM

Isaac M. Enukashvily

Depart. for Research and Development. Israel Meteorological Service.
P.O.Box 25, Bet-Dagan, Israel.

1. INTRODUCTION

Investigation of pollutants distribution in polluted cloud droplets (PCD) spectrum is very important in many applications of PCD microphysics such as cloud seeding simulation, scavenging of aerosol (including radio-active) particles or pollutant gas molecules, generation of cloud droplets electric charge.
To study the microphysical processes in PCD population the number density function $n(x,y,t)$ depending on two characteristics of PCD has to be introduced (BEHENG, HERBERT, 1984 ;SMIRNOV ,NADEIKINA ,1984).
The value of $n(x,y,t)dxdy$ represents the number of PCD which contain liquid water phase with mass in the range $(x,x+dx)$ and pollutant with mass (or with charge for ions) in the range $(y,y+dy)$. t denotes time. In this study Kinetic equation for $n(x,y,t)$ is derived taking into account the microphysical processes of coalescence and diffusional growth of PCD. Analytic solutions of the coalescence kinetic equation (CKE) for PCD with constant coalescence kernel are obtained and the numerical method of moments (ENUKASHVILY,1980) is developed for numerical integrating CKE with an arbitrary coalescence kernel.

2. ANALYTIC SOLUTION OF CKE

To derive kinetic equation for $n(x,y,t)$ time evolution taking into account the above mentioned microphysical processes the balance of the value $n(x,y,t)dxdy$ in phase volume element $dxdy$ has to be considered. Using the known method (PRUPPACHER, KLETT,1978; SMIRNOV, NADEIKINA,1984) we have

$$\partial n(x,y,t)/\partial t+\partial((dx/dt)*n(x,y,t))/\partial x+\partial((dy/dt)*n(x,y,t))/\partial y=GCI-LCI \qquad ,(1)$$

where GCI and LCI are the gain and loss coalescence integrals respectively. CKE is obtained from (1) as:

$$\partial n(x,y,t)/\partial t=-n(x,y,t)*\int_0^\infty\int_0^\infty \sigma(x,y;u,v)\,n(u,v,t)dudv+$$
$$+(1/2)\int_0^x du\int_0^y \sigma(x-u,y-v;u,v)*n(x-u,y-v,t)n(u,v,t)dv \qquad ,(2)$$

where $\sigma(x,y;u,v)$ represents the coalescence karnel. Now we introduce the number density function moments

$$M_{k1}(t)=\int_0^\infty\int_0^\infty x^k y^1 n(x,y,t)dxdy \qquad ,(3)$$

so we have
$N(t)=M_{oo}(t)$; $L=M_{1o}$; $S=M_{o1}$; $M=L+S$,
where $N(t)$ is the total number concentration of PCD; L and S are the total masses of liquid water phase and of pollutant respectivly. M represents the total mass of PCD. The values

$$n(x,t)=\int_0^\infty n(x,y,t)dy \qquad ,(4)$$

$$n(y,t)=\int_0^\infty n(x,y,t)dx \qquad ,(4)$$

are the number density distribution functions of liquid water phase and of pollutant respectively in the PCD spectrum. From eq.(2) we obtain

$$\partial M_{k1}(t)/\partial t=\int_0^\infty\int_0^\infty n(u,v,t)dudv*\int_0^\infty\int_0^\infty \sigma(x,y;u,v)\,((1/2)(x+u)^k*(y+v)^1-x^k y^1)n(x,y,t)dxdy \qquad ,(5)$$

The abbreviated set of coupled differential equations (5) may be used for approximative numerical integrating the CKE (2) for an arbitrary coalescence kernel (ENUKASHVILY,1964;PRUPPACHER, KLETT,1978)

Now we take the PCD initial spectrum in the form :

$$n(x,y,0)=A\exp(-\beta x-\tau y) \qquad ,(6)$$

where A,β,τ parameters are determined by normalization conditions with given N(0),L and S. Setting $\sigma(x,y;u,v)$=constant in (2) and using the double Laplace transform to the CKE (2) as well we obtain

$$n(x,y,t)=\exp\{-(xN(0)/L)-$$

$$-(yN(0)/S)\}\{N(0)N(t)^2/LS\}*$$

$$*\sum_{m=0}^{\infty}\{(N(0)(N(0)-N(t)))/LS\}^m *$$

$$*(x^m y^m/(m!)^2) \qquad ,(7)$$

where $N(t)=N(0)/(1+(1/2)\,N(0)t)$.

For the PCD monodisperse initial spectrum

$$n(x,y,0)=N(0)\delta(x-x_o)\delta(y-y_o)$$

where δ is the Dirac delta function using again the double Laplace transform, we have

$$n(x,y,t)=(N(t)^2/N(0))\sum_{m=0}^{\infty}\{(N(0)-$$

$$-N(t))/N(0)\}^m * \delta\{x-(m+1)x_o\} *$$

$$*\delta\{y-(m+1)y_o\} \qquad ,(8)$$

By substituting (7)-(8) in (4) the number density functions n(x,t) and n(y,t) are obtained. Analytic solutions (7)-(8) of the CKE (2) with σ=constant may be used as a test problem for numerical methods for integrating the CKE (2) with an arbitrary coalescence kernel.

3.NUMERICAL METHOD OF MOMENTS

The CKE (2) may be written also in the form

$$\partial n(x,y,t)/\partial t=-n(x,y,t)*$$

$$*\int_0^{\infty}\int_0^{\infty}\sigma(x,y;u,v)n(n,v,t)\,du\,dv +$$

$$+\int_0^{x/2}du\int_0^{y/2}\sigma(x-u,y-v;u,v) *$$

$$*\,n(x-u,y-v,t)n(u,v,t)\,dv +$$

$$+\int_0^{x/2}du\int_0^{y/2}\sigma(x-u,v;u,y-v)n(x-u,v,t)*$$

$$*n(u,y-v,t)\,dv \qquad ,(9)$$

Method of moments for numerical integrating the CKE (9) is to seek a solution of the form (ENUKASHVILY, 1980)

$$n_{ij}(x,y,t)=W_{ij}(x,y,t)\sum_{K=0}^{\infty}\sum_{\ell=0}^{\infty}A_{ijK\ell}(t)*$$

$$*L_{iK}(x)L_{j\ell}(y) \qquad ,(10)$$

where $n_{ij}(x,y,t)$ is the number density function in PCD packet $(x_i,2x_i;y_j,2y_j)$ having liquid water mass in the range $(x_i,2x_i)$ and having pollutant mass in the range $(y_j,2y_j)$; $W_{ij}(x,y,t)$ is the weighting function; $A_{ijK\ell}(t)$ are expansion coefficients. $L_{iK}(x)$ and $L_{j\ell}(y)$ are polynomials orthogonal in the ranges $(x_i,2x_i)$ and $(y_j,2y_j)$ respectively with $W_{ij}(x,y,t)$. The expansion coefficients in (10) are expressed as a linear combinations of the $n_{ij}(x,y,t)$ moments.

Myltiplying the CKE (9) by $x^K y^\ell dxdy$ and integrating from x_i to $2x_i$ and from y_j to $2y_j$ respectively, and using the Bleck's known idea of sectional computations of double integrals (BLECK, 1970) as well as replacing number density functions $n_{ij}(x,y,t)$ in coalescence integrals by expansion (10) we obtain for $n_{ij}(x,y,t)$ moments an infinite set of coupled differential equations. However by abbreviating (10) a finite set of coupled differential equations may be obtained to compute finite number of $n_{ij}(x,y,t)$ moments in each seperate PCD packets and to compute approximate $n_{ij}(x,y,t)$ as well. The expressions

of the coalescence integrals in

$n_{i,j}(x,y,t)$ moments equations are

derived as well.

4.CONCLUDING REMARKS

4.1 Kinetic equation for the time evolution of PCD number density function $n(x,y,t)$ is derived; $n(x,y,t)$ evolves with time as a result of microphysical processes of coalescence, of condensation / evaporation and as a result of diffusion of pollutant gas molecules (or ions) from ambient air.
4.2 Analytic solutions of the CKE with constant coalescence kernel are obtained for exponential and monodisperse initial spectra of PCD using the double Laplace transform.
4.3 Numerical method of moments is developed for numerical integrating CKE with an arbitrary coalescence kernel.
4.4 To test the numerical method of moments a preliminary numerical computations are performed using as a test problem the above mentioned analytic solutions.

Acknowledgements. The author thanks A.Ianetz and H.Rosenthal for discussions.

5.REFERENCES

5.1 BEHENG,K.D; HERBERT,F.: Modelling the variation of aerosol concentration in drops as a result of scavenging and redistribution by coagulation. Proceedings of the 9th ICPC, 1(1984),Tallin, USSR,207-208.

5.2 BLECK,R.:A fast approximative method for integrating the stochastic coalescence equation. J.Geophys.Res. 75(1970), 5165-5171

5.3 ENUKASHVILY,I.M.:On the solution of the kinetic coagulation equation. Izv.Acad.Nauk SSSR, ser.Geofiz. (1964),N10, 944-948.

5.4 ENUKASHVILY,I.M.:A numerical method for integrating the kinetic equation of coalescence and breakup of cloud droplets. J.Atmos.Sci.37(1980), 2521-2534.

5.5 PRUPPACHER,H.R; KLETT,I.D.: Microphysics of clouds and precipitation. D.Reidel, 1978.

5.6 SMIRNOV,V.I.; NADEIKINA,L.A.: Analytical solutions to a kinetic equation for the cloud drop size spectrum formed by condensation in a turbulent medium. Proceedings of the 9th ICPC, 1(1984), Tallin, USSR,233-235.

LIQUID WATER CONTENT, MEDIAN VOLUME DIAMETER, AND TEMPERATURE IN DEPENDENCE ON THE HEIGHT ABOVE THE CLOUD BASE FOR DIFFERENT TYPES OF CLOUDS

H.-E. Hoffmann and R. Roth

Institut für Physik der Atmosphäre, DFVLR, 8031 Oberpfaffenhofen, F.R.G.

1 Introduction

The 'Icing of Aircraft' is investigated since about five years in the DFVLR-Institute for Atmospheric Physics. For this purpose, an aircraft has been equipped as an icing research aircraft (Hoffmann et al., 1986). By the results of icing flights which were conducted with this aircraft, it was tried first to answer the question in which manner the normalized icing degree is depending on cloudphysical parameters (Hoffmann et al., 1987). For improving the forecast of normalized icing degrees (Weather Service, 1980) we tried also during these icing flights to get information about the dependence of the icing relevant cloudphysical parameters on cloud parameters. Here cloud parameters mean the cloud species and the height above the cloud base. We have always got these informations when we could fly through the whole cloud from its top to its base respectively vice versa. The data which we have collected during such vertical soundings of clouds, shall serve as input data for the extension of a climatology of icing relevant cloudphysical parameters (Roach et al., 1984).
After describing our test procedure in section 2, the figures of section 3 show the dependence of the cloudphysical parameters liquid water content LWC, temperature T, and median volume diameter MVD on the height above the cloudbase for different types of clouds. To learn something about the reliability of our measurements concerning the LWC, in the figures of section 4 the liquid water content values measured with the Johnson-Williams hot wire instrument and the Knollenberg instruments have been plotted.

2 Measuring instruments employed and performance of measurements

For the plottings of the following figures only the measured values of a part of the whole instrumentation of the icing research aircraft were used. In section 3 the values for the LWC were measured by a Johnson-Williams hot wire instrument, the values for the temperature by a Rosemount platinum-wire instrument Rosemount, and the values for the MVD by the Knollenberg instruments FSSP and OAP. In section 4, besides the LWC-values which were measured by means of the Johnson-Williams instrument, also those LWC-values were used which were derived from the Knollenberg instruments FSSP and OAP.
The Johnson-Williams hot wire instrument and the Rosemount platinum-wire instrument are mounted on the nose cap, and the Knollenberg instruments FSSP and OAP at the lower side of the wings of the icing research aircraft. Their distance from the fuselage is about 4 m.
The measurements were carried out in the course of icing flights which were conducted in a region between the north edge of the Alps and a distance of about 100 km north of it. Each value of the points in the figures is the mean value formed on a flight time of 20 sec. That means a flight distance of about 1.2 km. Because of the greater reliability of the Knollenberg measuring values, for the figures of the sections 3 and 4 only flight sections have been taken when the cloud particles were fluid.

3 The dependence of cloudphysical parameters on the height above the cloud base

The following three figures are a selection of about 20 vertical structures of cloudphysical parameters which could be measured during our icing flights so far. In Fig. 1 LWC, T and MVD are depicted in dependence on the height above the cloud base in a St-cloud and in Fig. 2 the same parameters, but measured here in an Ac, As-cloud. During both these events there was no precipitation on the ground. The measurements for Fig. 3 have also taken place in an Ac, As-cloud but in this event, about 3 hours before, we had precipitations.

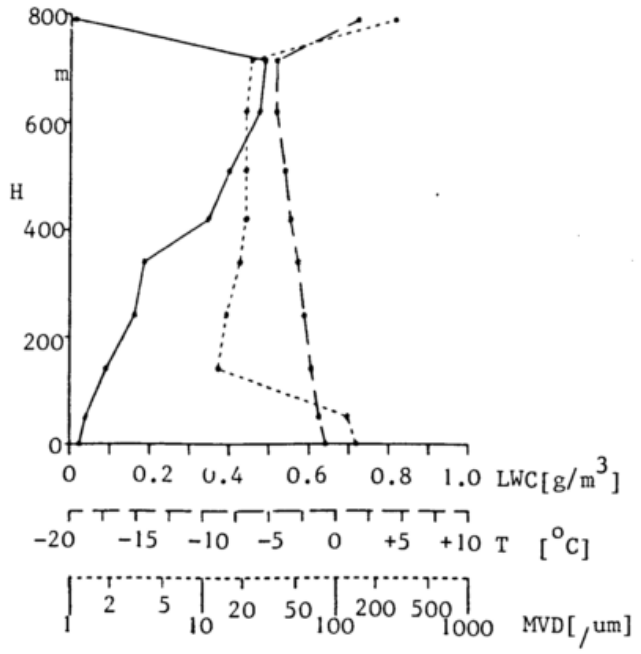


Fig. 1: The cloudphysical values liquid water content LWC, temperature T, median volume diameter MVD in dependence on the height above the cloud base H (St-Cloud).

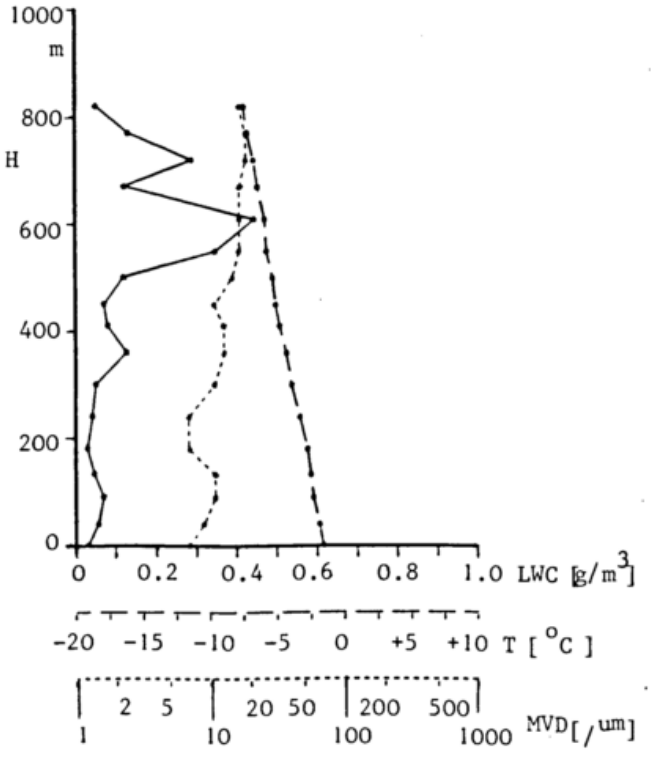


Fig.2: The cloudphysical values liquid water content LWC, temperature T, median volume diameter MVD in dependence on the height above the cloud base H (Ac, As-Cloud).

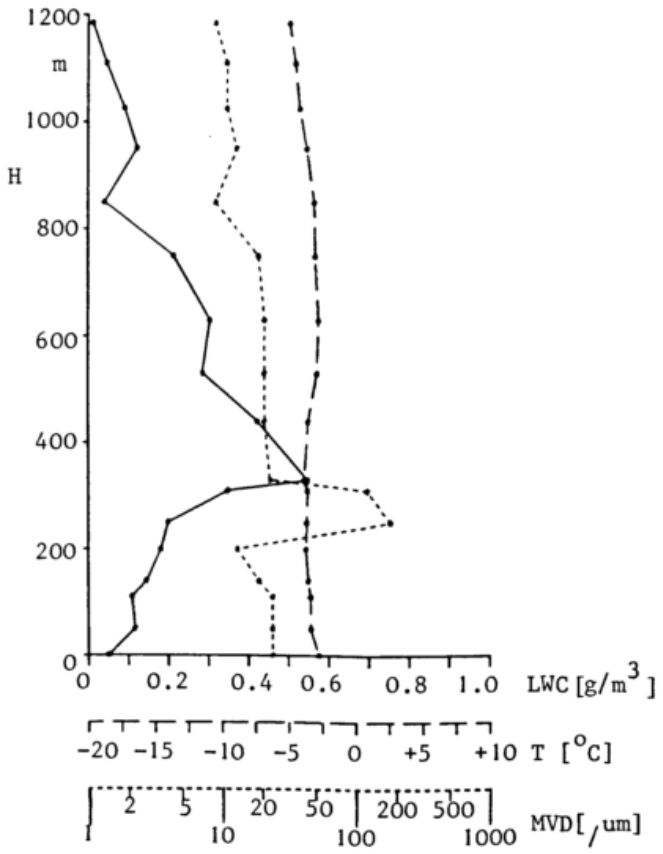


Fig. 3: The cloudphysical values liquid water content LWC, temperature T, median volume diameter MVD in dependence on the height above the cloud base H (Ac, As-Cloud).

Some remarks to the results of the Fig. 1-3

1. In the St-cloud (see Fig. 1) the LWC was growing continuously from the base up to the top and had there its maximum value of about 0.50 g/m^3.
   In the interior of this St-cloud the MVD had nearly constant values of about 20 μm. On the other hand, in the base and in the top the MVD had maximum values of about 200 and 300 μm.
2. In the Ac, As-cloud without precipitation on the ground (see Fig. 2) in the upper third of the cloud the LWC had a significant maximum.
   In the whole cloud the MVD had nearly constant values between 8 and 15 μm.
3. In the Ac, As-cloud, in which measuring was performed about 3h after precipitation on the ground, the maximum LWC value of about 0.5 g/m^3 was located in the lower third of the cloud. In the lower third the MVD, too, had a significant maximum of about 200 μm.

4 The LWC values, measured by Johnson-Williams and by Knollenberg instruments

For the comparison of LWC measurements, carried out by the Johnson-Williams instrument and by the Knollenberg instruments, the same flight sections as in the figures 1 to 3 were used. In the following figures 4 to 6, besides the LWC values of the Johnson-Williams instrument, also the LWC values derived from measurements by the Knollenberg instruments FSSP and OAP were plotted. In this case the measuring values of the FSSP were taken for the particle diameter 2 to 32 μm and for the particle diameters 34 to 600 μm those of the OAP instrument.

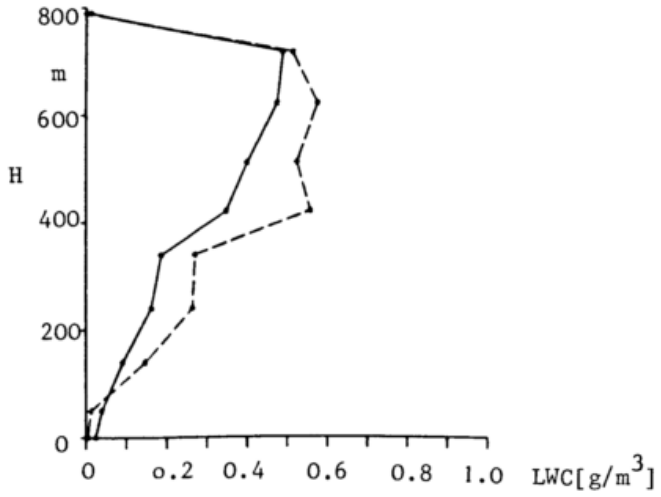


Fig. 4: Liquid water content LWC, measured by Johnson-Williams —— and by Knollenberg instruments--- in dependence on the height above the cloud base H (s. also Fig. 1).

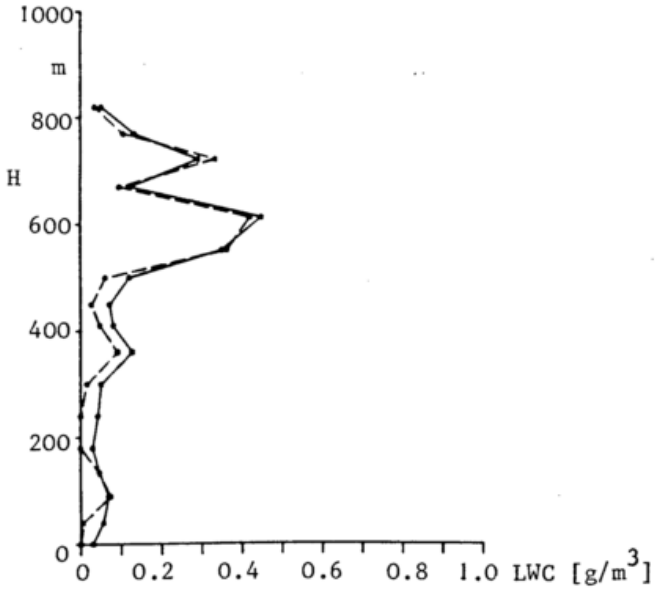


Fig. 5: Liquid water content LWC measured by Johnson-Williams —— and by Knollenberg instruments --- in dependence on the height above the cloud base H (s. also Fig. 2).

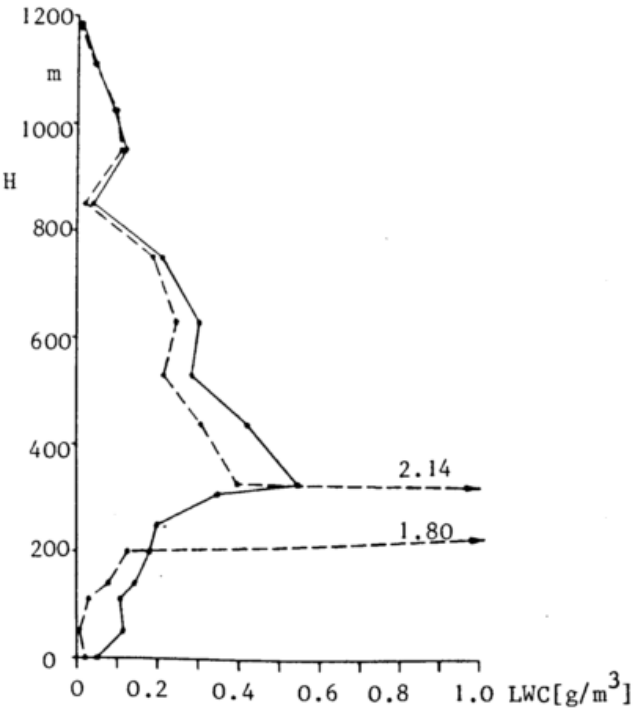


Fig. 6: Liquid water content LWC measured by Johnson-Williams —— and by Knollenberg instruments --- in dependence on the height above the cloud base H (s. also Fig. 3).

Some remarks to the results of the Fig. 4-6

1. The type of dependence of the LWC values from the height above cloud base is reproduced in the same way by both the measurements.
2. The LWC values, determined by the Johnson-Williams instrument were smaller (see Fig. 4) or greater (see Fig. 6) than those determined by the Knollenberg instruments.
3. Nearly always the differences between the measuring values of the two instruments were smaller than 35%. Only on two measuring points (see Fig. 6), the measuring values showed extreme differences.

5 References

HOFFMANN, H.-E., DEMMEL, J.: DFVLR's Icing Research Aircraft Do 28, D-IFMP, and its Measuring Equipment. ESA-TT-972 (1986)

HOFFMANN, H.-E., ROTH, R., DEMMEL, J.: Standardized Ice Accretion Thickness as a Function of Cloud Physics Parameters. ESA-TT-1080 (1987)

Weather Service: Forecaster's Guide on Aircraft Icing. AWS/TR-80/001, Air Weather Service, Scott AFB (1980)

ROACH, W.T., FORRESTER, D.A., CREWE, M.E., WATT, K.F.: An Icing Climatology for Helicopters. Special Investigations Memorandum 12, Meteorological Office Bracknell (1984).

A DETAILED EXAMINATION OF DISCONTINUITIES IN NATURAL RAIN SPECTRA

Harry C. Vaughan
Department of Meteorology
Iowa State University
Ames, Iowa 50011

I. INTRODUCTION

A natural distribution of free falling rain drops can be approximated by the Marshall-Palmer (M-P), 1948, relationship. However, close examination of short intervals of observed drop spectra show the slope ( ) and intercept (N_o) vary considerably from the M-P distribution (Waldvogel, 1974). In addition, systematic perturbations are frequently observed in the minute-by-minute observations of drop spectra. It can be shown that these perturbations, first thought to be random noise in the data, are, in fact, well defined and generally fixed local peaks in the mass distribution of tropical warm rains. Niederdorfer (1932) reported orderly perturbations in the form of an arithmetic progression in the drop spectra which he expressed as its corresponding mass. His work was not verified and interest in the phenomenon was dropped (Mason, 1972). A plausible explanation for lack of verification will be discussed in Section III.

II. DATA AND ANALYSIS

In this study all samples were collected on 24 cm diameter Whatman I filter paper treated with a water soluble dye applied with a specially designed air brush (Wiesner, 1895). Samples were made singly or in pairs every minute through the duration of 16 rain episodes at El Verde, Puerto Rico. Additional data were collected at St. Thomas, USVI. These data were all supported by local 00 and 12Z upper air soundings. Cloud base computations from psychrometric readings, at the time of the episode, put the cloud base between 130 and 180 meters above the sampling point. Stain impressions were read to the nearest 0.1 mm; in the case of non-symmetrical impressions, the observer made a judgment regarding the mean diameter. The double samples were each read by two observers; differences between their readings were insignificant, with a resulting correlation of better than +0.9. Data was computed and displayed as follows: actual exposure time (raw spectra) histograms, normalized semi-log plots of each sample drop spectra and a mathematical transformation to mass per drop size, with an increment of 0.1 mm, was also plotted (Fig. 1).

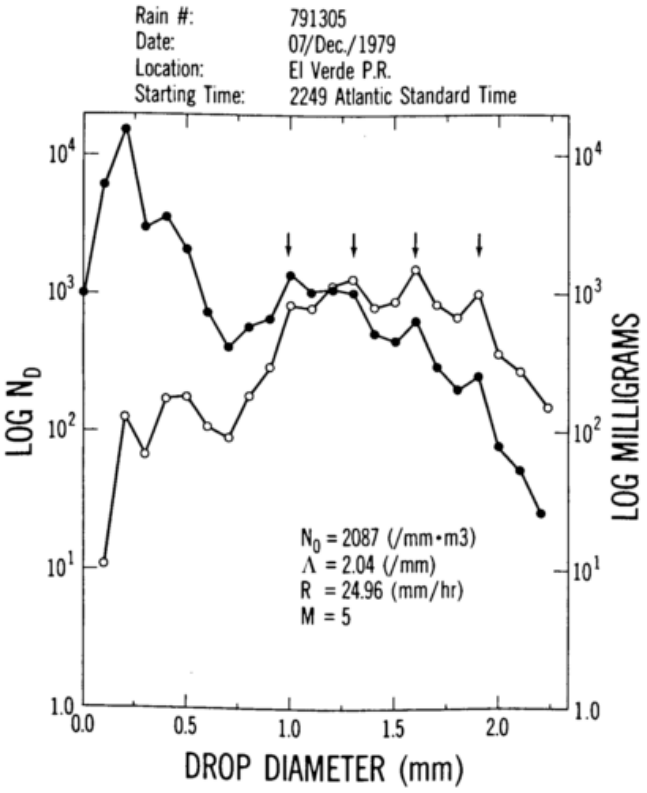


Fig. 1. The left-hand ordinate denotes the log of $N_D/M^3/0.1$ mm diameter (closed circles), the right-hand ordinate denotes the log of drop mass in milligrams/0.1 mm increment (open circles). The four arrows point to the four open circle peaks each with a null width of 0.2 mm.

One hundred and twenty-three dye paper samples containing approximately fifty thousand individual stain impressions show discernible depressions, or in some cases gaps to be present in the spectra for almost every sample. Monodispersed drop spectra were observed in the final minute of a few episodes. In these cases the number of drops per second was increased two or three fold and the resulting semi-log plot shows no perturbations. The term perturbation as used here is intended to describe the series of peaks, nulls, and null widths which make up the total drop distribution in each spectral sample. The null width is defined as the number of 0.1 mm increments between, but not including, two adjacent peaks. Within this null width is the null minim, which like

perturbation peaks has an apparent physical significance. Obviously, if each of the null widths are equal, the series of perturbations comprises an arithmetic progression (Fig. 1). In general, the peak and null minim represent indices which are mutually exclusive. Further, irrespective of the sample rain rate there seems to be specific peak and null minim positions, drop spectra, which reoccur more frequently than others, with 1.3 mm as the mode value. In an attempt to illustrate the relocation and relative magnitude of the numerous perturbations an entire episode is plotted as a continuous three-dimensional surface (Fig. 2).

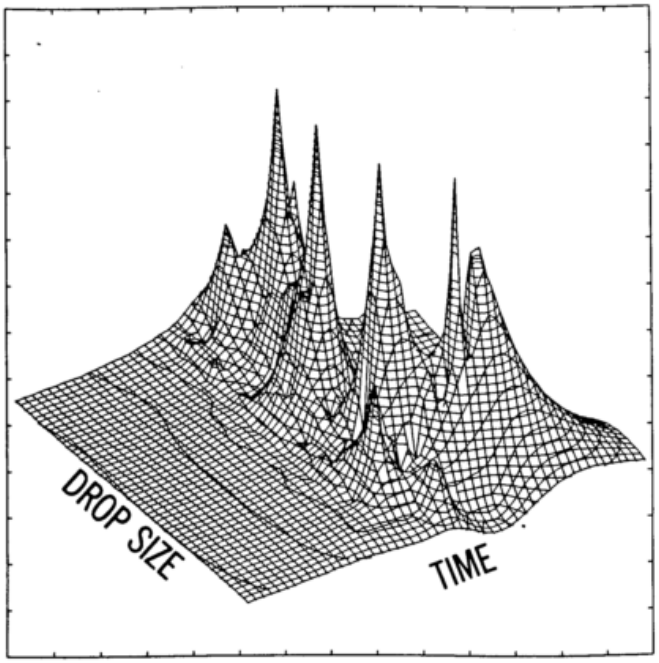


Fig. 2. The ordinate represents increasing drop size, the abscissa represents increasing time, and the Z axis, milligrams of water per drop size.

III. MODEL

To aid in understanding the development of both transient and seemingly stationary perturbations, a primitive cloud droplet growth model was developed where only the accretion growth mechanism was considered. Using a single composite calibration curve (Hall, 1972), in conjunction with several published cloud droplet data sets which provided the environmental background, a number of cloud model drop spectra were generated (Vaughan, et al., 1988). Starting with a cloud droplet environment with a near normal distribution, the model was able to generate a series of transient and semi-permanent perturbations within its simulated drop spectra, which extended to drizzle size drops. A number of test droplet environments were used, each resulting in a different positioning of the computer-generated perturbations. The perturbations observed in natural samples are supported by the model results and strongly suggest an ordered growth in a simple, warm rain process.

IV. CONCLUSIONS

As the model output suggests, if in nature there is a tightly regimented mechanical growth process, the product would be perturbations resulting from discrete jumps where only select drop size ratios make lasting coalescence. Further, it is hard to reconcile the systematic distribution of these perturbations from the largest drop size down through the rain spectra by a breakup mechanism. It is clear the perturbations are real with differences as great as an order of magnitude, in mg, observed between adjacent null minim and peaks. It was found when three point smoothing was applied to raw data the perturbations were lost, particularly in low rain rate samples. This suggests that a finely-balanced accretion process occurs in the development of the drop spectra. Clearly, at least a portion of these data supports results previously reported by Niederdorfer. Since few rain drop data sets have been read to 0.1 mm, the possibility of seeing these perturbations may have been lost. A detailed account of this study has been submitted for publication.

V. ACKNOWLEDGEMENTS

The author wishes to express sincere thanks to Gary R. White who assisted in collecting and testing much of the data and in writing portions of the data reduction program, and to Eric Quee for his work on the computer model and graphics.

VI. REFERENCES

Marshall, J. S. and W. Palmer, 1948. The distribution of rain-drops with size. J. Meteor., 5:4, pp. 165-166.

Mason, B. J., 1971. The physics of clouds. Oxford University Press, U.K.

Niederdorfer, E., 1932. Messimgem der Grosse der Regentropfen. Meteor. Z. 49:1, pp. 1-14.

Vaughan, H. C., E. L. Quee, and S. Terronez, 1988. A primitive cloud droplet growth model to study perturbations in the natural rain spectra. WMO Second International Cloud Modeling Workshop, Toulouse, France.

Waldvogel, A., 1974. The N_0 jump of rain-drop spectra. J. Atmos. Sci. 31:5, pp. 1067-1078.

Wiesner, J., 1985. Beitrage zur Kenntnis des Tropischen Regens. Sitzber. K. Akad. Wiss. Wien, Math.-naturw. Kl., 104, pp. 1397-1434.

CRYSTALLIZATION OF SUPERCOOLED SOLUTIONS

K. Harrison and J. Hallett
Desert Research Institute
Reno, Nevada 89506

1. INTRODUCTION

Solution drops exist in the atmosphere in supercooled states down to temperatures approximately equal to the sum of the possible supercooling of water itself and the equilibrium freezing point depression of the solution. Initial nucleation of these drops can take place by particulate impurities in suspension or by contact with aerosol particles. Drops can also be nucleated by insoluble mineral particles or bacteria on the surface of vegetation. Crystals growing from these solution drops lead to changes in solution concentration, and possibly convection which enhances local supersaturation; both effects change the growth rate and shape of the crystals.

The aim of this research is to study crystallization of uniformly supercooled solutions (Na_2SO_4, NaCl, H_2SO_4, HNO_3, HCl) and show how crystal growth velocity and habit depend on solution and concentration. The segregation coefficient for the solute in ice is measured by analysis of ice and solution, separated immediately after initial freezing, at different supercoolings. Subsequent solidification gives ion rejection at a varying rate depending on the geometry of the freezing, and may result in separation of hydrates, particularly when the initial concentration is high, as in haze (inactivated) droplets and low temperatures found in the Antarctic stratosphere. Electrical effects associated with rapid freezing are also investigated.

2. EXPERIMENTAL

A Schlieren optical system was used to investigate crystal growth and the presence of convection from the growing crystal. This system detects density gradients resulting from crystal growth and buoyant convection which could enhance growth and change ion segregation. Convection from a growing crystal could only be viewed if density and refractive index gradients were sufficient. In practice this requires concentrations > 0.2M.

Solutions were contained in cells with optical quality windows, volume 10 to 1000 ml, and located in a thermostated outer cell. Temperatures were uniform to $\pm$ 0.2°C, as judged by exploring the solution with a thermocouple. Nucleation was achieved by inserting a single crystal into the upper surface, or by inserting a seed crystal or a LN_2 cooled wire into a narrow plastic tube ending in the middle of the solution. Crystals grew from the seeding site into the solution as flat dendrites or needles, where shape and velocity depended on solute, its concentration and the supercooling.

The segregation coefficient for ice was measured by analysis of the ice and solution immediately after freezing by separation of liquid and solid. After separation, the pH and temperatures of the liquid and solid phase (after melting) were measured using a SelectroMark Analyzer. In order to obtain more information about segregation, preliminary experiments were made to measure the potential difference between a growing ice crystal and the solution it grew in.

An electrometer was used to measure the potential difference between a thin wire attached to the nucleating crystal and another wire placed in the solution.

3. RESULTS

Fig. 1 shows crystal growth in different aqueous solutions. The Schlieren optical system is sensitive to gradients of refractive index integrated along the line of sight and shows convecting plumes as solute rejection occurs. Convection visualized in this system shows plumes ascending (solute incorporated preferentially) or descending (solute rejected) depending on the solute and illustrates how the convective plume interacts with the growing crystal tip.

Convection influence on crystal growth only occurs within a limited range of supercooling, where convective velocity is greater than the growth velocity of the individual crystal. Dendrite growth velocity is approximately proportional to the square of the supercooling, ΔT.

Estimates of the segregation coefficient (±10%) were obtained from measurement of the composition of the ice and the rejected solution, which were separated after the initial freezing process was complete and the temperature of the ice/solution mixture had approached its new equilibrium temperature to within 0.2°C. Preliminary experiments measuring ice and rejected

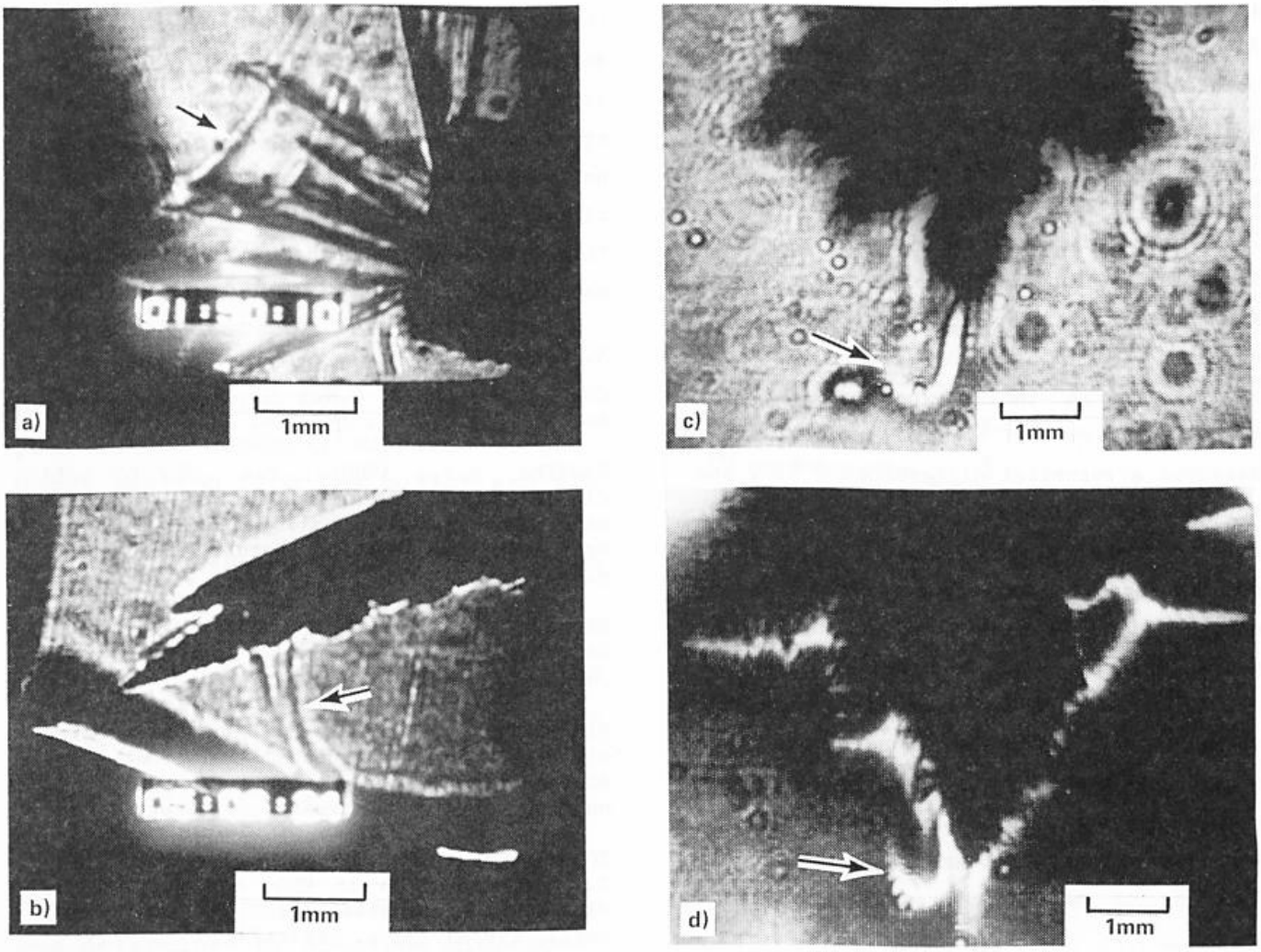


Fig. 1: Schlieren photographs of convection around growing crystals of: a) sodium sulfate decahydrate (2M, ΔT = 3.7°C), b) ice in sodium chloride solution (0.8M, ΔT = 0.4°C), c) ice in nitric acid solution (1M, ΔT = 1.0°C), and d) ice in sulfuric acid solution (1M, ΔT = 1.0°C).

solution indicate a pH decrease of 0.2 for H_2SO_4 and 0.02 for HNO_3. Further insight into the segregation was obtained by measurement of the potential developed between the crystal and the solution, although this technique was of limited use because of the complicated geometry of the crystal solution. For laboratory distilled water a maximum potential of +0.4V was reached; +4.8 V for 1M HNO_3.

4. DISCUSSION AND CONCLUSION

In the case of the decahydrate, it appears that stoichiometry is preserved and the convecting fluid results from solute loss at a fixed, but moving, boundary. In the case of ice, other possibilities exist. For H_2SO_4 it appears that the sulfate ion can replace five water molecules, and become incorporated in molecular ratio 1:30 (DE MICHELI and IRIBARNE 1963, p.767). Whether this is important in the other substances is yet to be determined. Workman and Reynolds (1949, p. 254) measured electrical effects between ice-solution interfaces based on a linear growth front at a growth rate of $\sim .01$ cm s^{-1}, compared with growth velocities of $\sim .1$ cm s^{-1} in these experiments. For dilute solutions (10^{-3} - 10^{-6}N) of NaCl they measured a potential difference of +30V and for dilute solutions of HNO_3 and H_2SO_4 effects were negligible. Our present results suggest that more extensive measurements need to be made in solutions at different supercoolings, and that substantial electrical effects may be present for higher concentrations under these conditions. Thus in hydrometeors, effects could occur at slow growth in weak solution, from selective shedding under wet growth, and also during freezing of highly supercooled individual drops.

From a different viewpoint substantial damage to vegetation could occur under specific conditions as concentrated solutions (possibly H_2SO_4) are rejected in the freezing of rime or dew. These concentrated solutions could dehydrate vegetation by osmosis, or lead to other damage. Solutions other than H_2SO_4 could have similar effects. This damage would occur under quite specific meteorological conditions, when high concentration solutions are accreted and frozen. This suggests that accretion of supercooled polluted fog and dew formation under high levels of pollution, followed by freezing, appears more likely than "acid" rain to cause damage to vegetation.

The importance of such studies in ice crystal growth is also illustrated by our lack of knowledge of surface absorption and solute incorporation of ice crystals growing from the vapor in the Antarctic atmosphere (CRUTZEN 1986, p.651 and TOON 1986, p.1284). Here high concentrations of HNO_3/HCl exist at temperatures below -80°C, where hydrate crystals may nucleate and give rise to quite unexpected structures and chemical reactions.

This research was funded by NASA Contract No. NAS7-918.

5. REFERENCES

COBB, A.W.; GROSS, G.W.: J. Electrochemical Soc. (1969) 116, p. 796-804.

CRUTZEN, P.J.; ARNOLD, F.: Nitric Acid Cloud Formation in the Cold Antarctic Stratosphere: a major cause for the springtime 'ozone hole'. Nature (1986), 324, p.651-655.

DE MICHELI, S.M.; IRIBARNE, J.: La Solubilité des Électrolytes Dans La Glace., J. Chem. Phys. (1962) 60, p. 767-774.

HARRISON, K.; HALLETT, J.: On the Freezing of Supercooled Aqueous Solutions and Atmospheric Chemical Reactions. Conference on Cloud Physics, Snowmass, CO, Sept., 1986.

TOON, O. B.; HAMILL, P.; TURCO, R.P.; PINTO, J.: Condensation of HNO_3 and HCl in the winter polar stratospheres., Geophys. Res. Lett., (1986) 13, p. 1284-1287.

WORKMAN, E.J.; REYNOLDS, S.E.: Electrical Phenomena Occurring during the Freezing of Dilute Aqueous Solutions and their Possible Relationship to Thunderstorm Electricity. Physical Review (1949) 78, p.254-257.

KINETICS OF ICE CRYSTAL FORMATION ON AEROSOL PARTICLES IN SUPERCOOLED FOG

Boris Gorbunov, Aleksandr Paschenko, Hatal'ya Kakutkina

Institute of Chemical Kinetics and Combustion

The experimental evidence on time characteristics of ice crystal formation is just scanty although their great importance for physics of clouds and governing the evolution of atmospheric processes cannot be denied. The present paper is concerned with the study of ice nucleation kinetics in a cloud chamber under the action of silver iodide, copper acetyl acetonate, phloroglucine and some metal oxides at 268, 263 and 253 K. To obtain the kinetic dependences, a two-section cloud chamber with automatic registration was constructed (Gorbunov et al. 1987, p.261). It is composed of a two-section cylinder with inside diameters of 0.2 and 0.4 m, respectively, divided by a fluoroplastic partition with openings. Vapour is continuously supplied to the upper section from the boiler and after cooling it passes through the openings to the lower one. Herein, on reagent aerosol particles, the ice crystals are formed which fall out from supercooled fog and are detected by a photoelectric counter. The kinetic dependences were also determined in the isothermal cloud chamber of 0.25 m^3 (Paschenko, Gorbunov 1987, p.269).

A mass-mean size of aerosol particles was determined by electron microscopy.

Experimental kinetic curves exhibit three peculiarities: the presence of some time lag in crystal formation, and the value of curve slopes at short and long times (Fig.1,2).

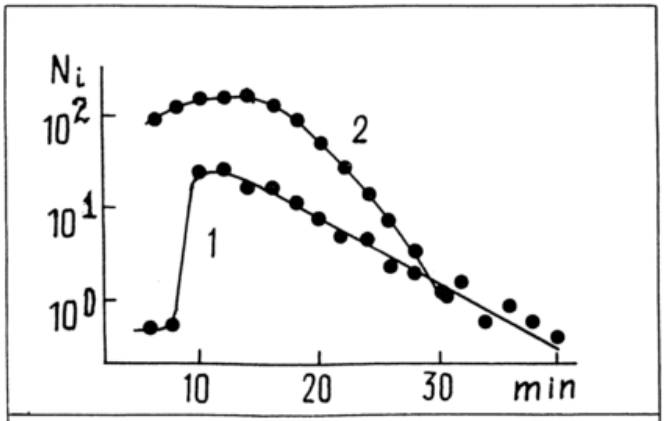


Fig.1: The kinetics of falling out of ice crystals formed on silver iodide aerosol particles in a 0.018 m^3 chamber at 263 K. Ni - the number of crystals per 1 mm^3 of chamber floor in 2 min. A mass-mean particle radius: 1 - 27 nm; 2 - 4 nm.

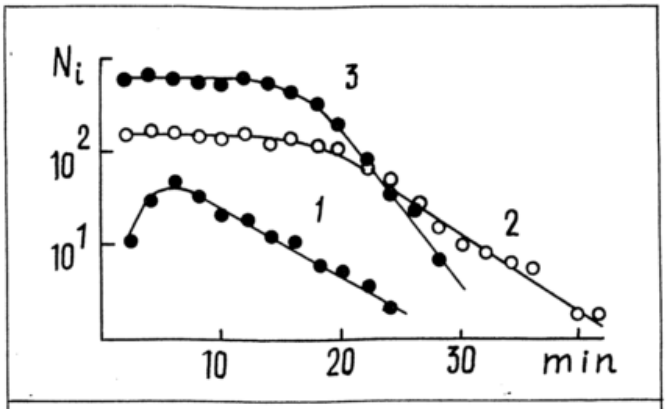


Fig.2: The same as in Fig.1 but for aerosol particles of copper acetyl acetonate in a 0.25 m^3 chamber at 263 K. A mass-mean particle radius: 1 - 120 nm; 2 - 85 nm; 3 - 110 nm (the curve if shifted by 0.5 along the ordinate).

It is shown that the time lag of ice crystal formation in the cloud cham-

ber is caused by the process of metastable medium relaxation after introduction of aerosols. An analysis of the slope of kinetic curves at long times showed that the ice crystal formation rate (K) is practically independent of fog temperature, the size of aerosol particles, the concentration of aerosol particles introduced into the chamber, the concentration of ice crystals formed herein (Fig.3).

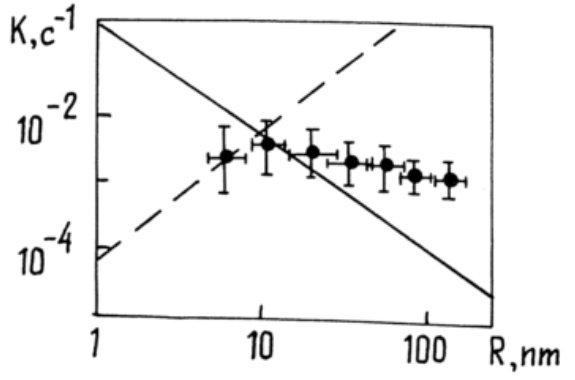


Fig.3: The dependence of ice crystal formation rate K=dlgNi/dt in cloud chamber at T=263 K on mean particle radius R for silver iodide. A solid line corresponds to a typical phenomenological dependence K on R calculated by a phenomenological theory. A dashed line corresponds to a collision mechanism of ice crystal formation.

At short times the dependence of the slope value on the ice crystal concentration in the chamber is revealed (Fig.4). This is observed at any temperature in both chambers and for all reagents. This dependence testifies to the interaction between the crystals during nucleation. Such a phenomenon, named the effects of vapour depletion, was observed earlier in diffusion chambers (Gorbunov et al. 1980, p.720). The interaction occurs at fairly large distances ~3 mm (Fig.4). Such a considerable influence may be accounted for by a high sensitivity of one of the stages of ice crystal formation (nucleation, growth or falling out) to the supersaturation in the chamber.

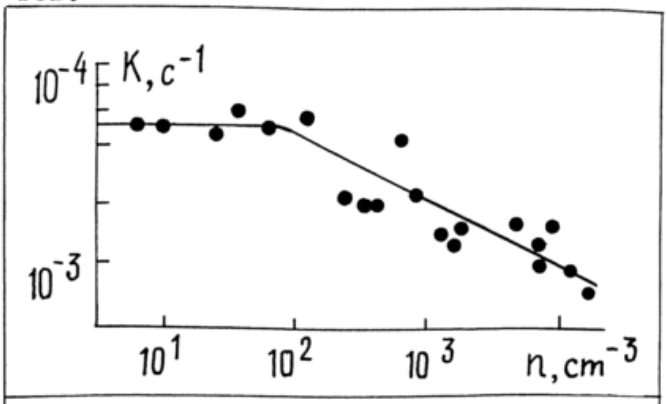


Fig.4: The dependence of ice crystal formation rate at the initial moment on the ice crystal concentration in a chamber (n) for aerosol particles of silver iodide.

It is theoretically shown that the slope of kinetic curves at long times must strongly depend on particle radii (Fig.3). In practice it is not so which is difficult to fit to classical concepts about the process of heterogeneous nucleation.

GORBUNOV, B.; KAKUTKINA, N.; KOUTZENOGII, A.; PASCHENKO, A.; SAFATOV, A.: J. Aerosol Sci. 18 (1987) Nr. 3, S. 261-267.

GORBUNOV, B.; KAKUTKINA, N.; KOUTZENOGII, K.; PSHENICHNIKOV, N.: Izv. AN SSSR, 16 (1980) Ser. FAO, S. 720.

PASCHENKO, A.; GORBUNOV, B.: J. Aerosol Sci. 18 (1987) Nr. 3, S. 269-275.

ABOUT SECONDARY ICE CRYSTAL PRODUCTION

T.Gzirishvili, V. Khorguani

Institute of geophysics, Acad. Sci., GSSR, Tbilisi, USSR

It has been shown earlier that in case of contact mechanism of nucleation on a free face of an aerosol particle placed at the surface of freezing drop, (Gzirishvili, 1967, p.58) the deposition of ice crystals can be observed. In the light of results received later (for example, GAGIN,NOZYCE, 1984, p.56) the abovementioned effect can be explained by the origin of local supersaturations over the water, round a freezing "warm" drop and, as a result of this, by stimulation of nucleation and growth of ice on aerosol particles.

The present paper deals with the peculiarities of collision of supercooled water drops with the ice surface, kinetics of the process of their solidification and origin of secondary ice crystal in the presence or absence of the external electric field.

The experiments were carried out in a minor cloud camera in the central part of which with the aid of electrodes vertically oriented electric field was established. Electrodes presented round brass plates with the diameter 2 cm and thickness about 2 mm. On the lower electrode a layer of ice was freezed with the same thickness about 3,5 mm.A drop of twice distilled water was suspended by a metal hair covered with a thin vaseline layer. It was placed between the electrodes and was thrown off at a necessary moment.

The experiments were conducted at the same temperature of -16°C while the drops were thrown off from the height of 10 cm.

In the absence of electric field, when colliding, the drop flattened and the extent of its spread about the ice surface turned to be the maximum, as a rule,-the freezing drop took the shapes from a spherical segment to cylindrical one with a conical top (Fig.1.)

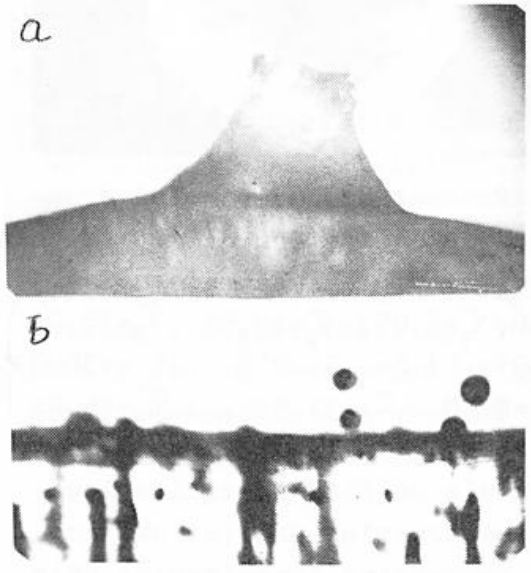


Fig.I- Crystallization of a droplet entraped by an artificial hailstone b) generation of ice particles

In the presence of electric field the extent of spreading of the drop diminished. The drop took the shapes from spherical one to stretched ellipsoid (Fig.2). Calculations were made of relative change of the crystallized water mass $w=1-\frac{m}{m_0}$ (m-the ice mass, m_0- the complete mass of a settled drop) and Fourie numbers $F_0=\frac{\alpha\tau}{L^2}$ (α-

the coefficient of ice thermal diffusivity, ℓ-characteristic length, τ-the time of drop crystallization from the moment of its collision with the backing).

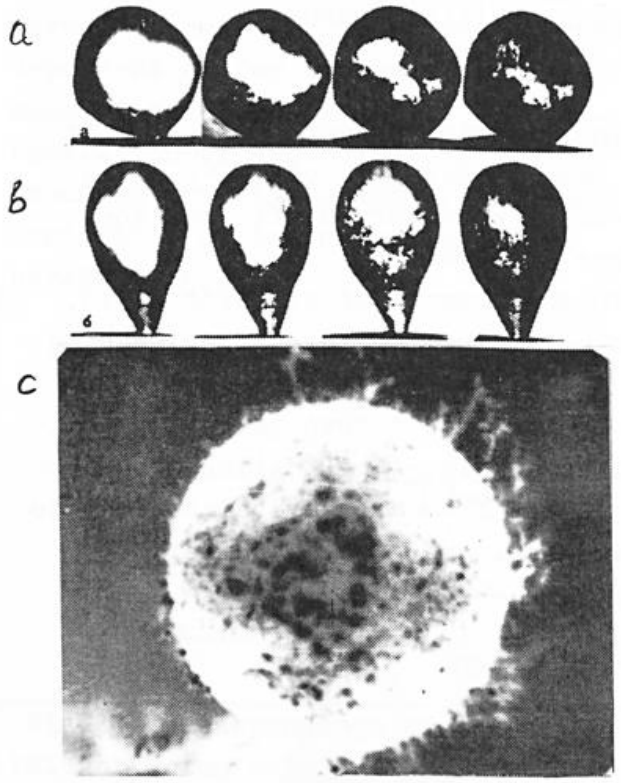


Fig. 2. Process of supercooled droplet crystallization after its collision with an ice substrate:a)S=4,1. 10^{-3},$\mathcal{V}$=0, τ_1=5,05s τ_2=48,5s , τ_3=75,0s τ_4=87,0s b) S=8,9.10^{-3}, $\mathcal{V}$ =+3000$\mathcal{V}$ τ_1 =6,0s τ_2=31,5s , τ_3=95,0s τ_4=87,0s c) Origin and growth of ice crystals on SiO_2 particles located on the freezing droplet surface.

When processing experimental data parameter S was introduced equal to the ratio of the area of joint base of the freezing drop to the area of its external surface. The curves of F_0 dependence on w for the values $S \geq 10^{-1}$ irrespective of the sign and of the potential magnitude, have the appearance given at Fig.3-a. One can see that their up-shift relative to each other is accompanied by the decrease of the value S. In case $S \leq 10^{-2}$ (Fig.3-b) the nature of F_0 dependence on w is determined by the sign and value of the potential applied to the backing.

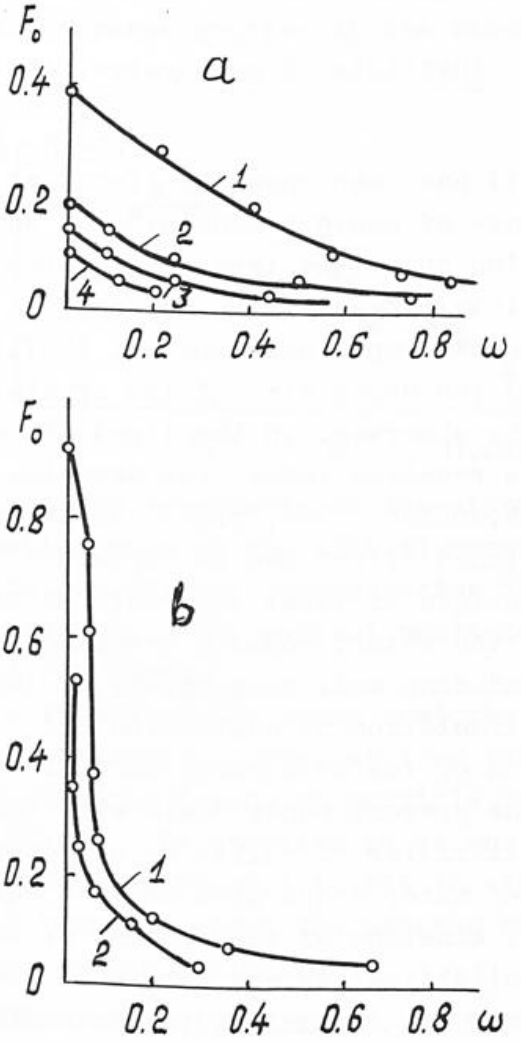


Fig 3. Dependence of F_0-Fourier number on W-parameter: a) 1- S=1,3. 10^{-1}, $\mathcal{V}$ =-6000$\mathcal{V}$; 2- S=2,9.10^{-1}, $\mathcal{V}$=+3000$\mathcal{V}$; 3- S=2,6.10^{-1}, $\mathcal{V}$=0; 4- S=8,4.10^{-1}, $\mathcal{V}$=0; b) 1-S=8,9. 10^{-3}, $\mathcal{V}$=+3000$\mathcal{V}$; 2- S=4,1.10^{-3}, $\mathcal{V}$=0.

Unlike of $S \geq 10^{-1}$, in the present case, as S increases, the curves have a tendency to shift upwards relative to each other. Figs.1 and 2 give photos of overcooled drops in the process of freezing for $S \approx 10^{-1}$ and $S \leq 10^{-2}$. For $S \leq 10^{-2}$, a counter advance of the crystallization front is observed from all the sides (Fig.2-a). The shape of the drop's ice cover does not change,

the process of crystallization is relatively protracted and the throw of ice splinters from the surface of a freezing drop is not observed. However in the presence of SiO_2 aerosol particles on the drop surface, in the process of its crystallization, the nucleation of ice crystals can be observed as well as their intensive growth Fig.2-b).

In the case of $S \geq 10^{-1}$, irrespective of the presence or absence of the electric field, when $10^{-1} \leq S < 10^{-2}$, at the negative values of the potential of the ice backing, the drop's crystallization front moves from its base to the summit causing the squeezing out of liquid masses of water and ice particles throw-off (Fig.1-b). The number of splinters is equal to 5 particles averagely. The activation of aerosol particles was not observed, as a rule $S > 10^{-1}$

Thus, the above-mentioned results permit to mark out processes favouring the formation of ice crystals: in one case - as a result of mechanic action, in another - as a result of activation of heterogeneous nucleation of ice. A qualitative evaluation shows that the generation of ice crystals is much more in the latter case. The explanation of this phenomenon logically lies in the origin of comparatively significant oversaturation. Indeed, when $S \leq 10^{-2}$, because of a worse heat removal through the ice backing much greater over heat of freezing drop surface should been expected (to this indicates prolonged process of drop crystallization) and as a consequence of this the rize of local oversaturation at its surface.

In the real atmosphere, in the presence of air flows, the picture apparently could not be changed qualitatively, as the thickness of temperature and dynamic boundary layers are roughly the same. This means that the heat transfer owing to thermal conductivity will be of the same order with the heat transfer owing to convection (Khorguani, 1984,p.95).

The above discussed phenomenon may one of the causes if ice crystal generation in the hail clouds. On the other hand, in the case of capture by a hail stone of large overcooled drops in the regime $S \leq 10^{-2}$ ice crystals will be formed. This, in its turn, would favour the growth of hail-stones in the medium with a mixed microstructure and promote the formation of spongly hail-stones.

References:

Gzirishvili T.G. Bulletin Academy Sci. Georgian SSR. Tbilisi,1967, Vol.15 No.2, pp. 56-61.

Gagin A.Nozyce H. Proc.11-th Int. Conf. Atm. Aeros. Cond. and Ice Nuclei. Budapest, vol.2, 1984, pp. 56-65.

Khorguani V.G. Microphysics of hail-stone generation and growth. Gidrometizdat, Moscow, 1984, p.183.

EXPERIMENTAL STUDIES ON SECONDARY ICE PARTICLE PRODUCTION

Akira Yamashita, Hiroyuki Konishi, Wataru Shimada,
Masayoshi Miyatake and Keisuke Tani

Osaka Kyoiku University, Tennoji-ku, Osaka

Mechanisms of secondary ice particle production were investigated by two series of experiments.

EXPERIMENT I

Artificially grown ice needles were evaporated in a subsaturation chamber placed under a stereoscopic microscope (Fig.1)

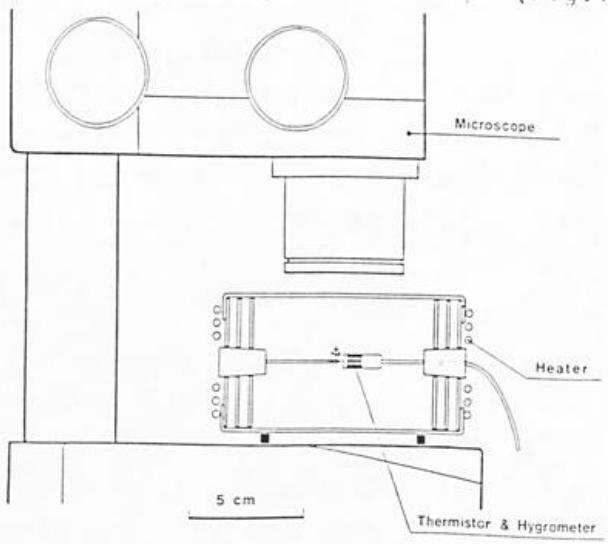


Fig.1 Section of apparatus

and the whole evaporating process of a needle was observed in situ by a video camera. By a series of experiments it was found that the length of an ice needle decreased not only by evaporation but also by fragmentation, fracture or deformation of a tip. An example of fracture is shown in Fig.2. Fractured tip was folded or moved intermittently, and gradually evaporated. Fractured tips were also ejected from the mother crystal frequently as shown in Fig.3. The deformation of an evaporating needle occurred when its tip became very thin; the thin tip was curved like a whisker. Experiments were carried out at temperatures between -0.5C and -12C and at relative humidities between 40% and 97%.

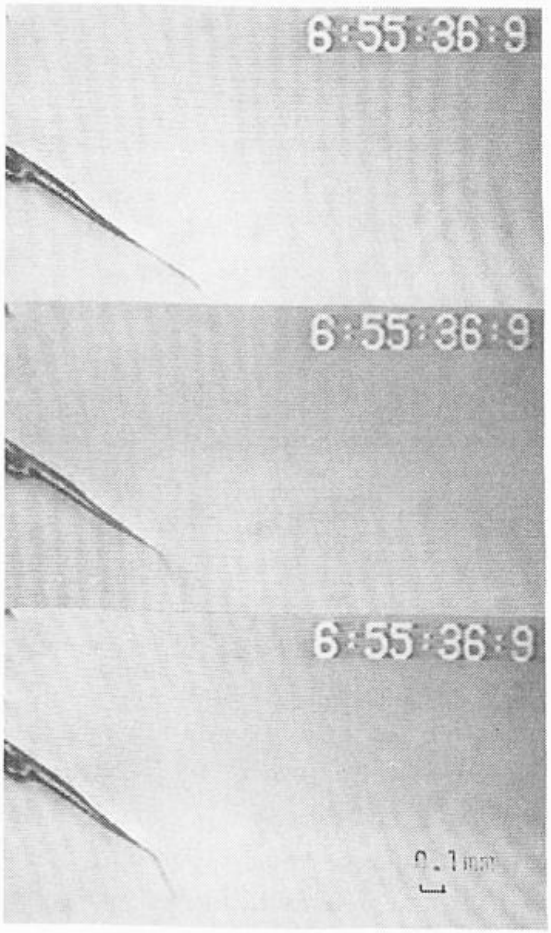


Fig.2 Fracture of needle. Three pictures show the change of the pointed tip in 0.1 second.

Experimental results are summarized in Fig.4. Fragmentations and fractures were observed at temperatures between -2.5C and -10C and at humidities lower than 85%, although they occurred rarely at humidities higher than 86% and at lower than 56%. As shown by double circles in this figure they occurred especially frequently at about -6C and at about 80%.

These results suggest the possibility of secondary ice crystals produced by evapolating ice crystals might play



Fig.3 Fragmentation of needle. Three pictures show the change of the pointed tip in 0.1 second.

important roles in nature.

EXPERIMENT II

Ice crystals including many gas enclosures were broken in a supercooled cloud for the purpose of clarifying the effect of expanding enclosed gas, and it was found that remarkable ice crystal enhancement occurred by the expansion of enclosed gas as large as 0.5-2.0mm in diameter. This type of secondary ice particle production also may be possible to occur in natural clouds because ice

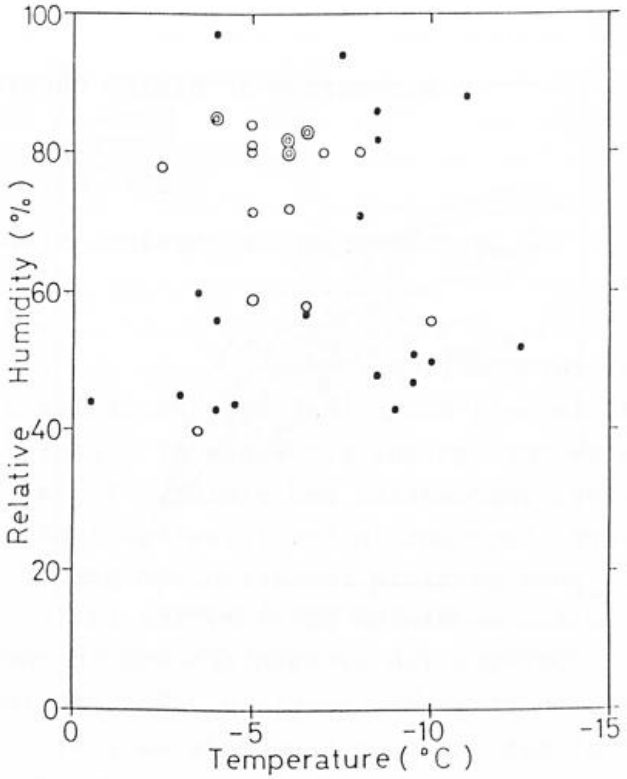


Fig.4 Conditions of experiments and occurrence of fragmentations and fractures

●: no fragmentation and fracture

o: fragmentations and/or fractures observed

◎: the occurrence especially frequent

pellets observed in Osaka on 7 March 1987 were found to contain gas enclosures of about 0.5mm in diameter at the maximum.

PROPORTION OF RIMING GROWTH PROCESS IN SNOWFALL PHENOMENA

Toshio Harimaya and Misao Sato

Department of Geophysics, Hokkaido University, Sapporo 060, Japan

1. INTRODUCTION

It is well known that snow particles grow through the processes of deposition, aggregation and riming. It is very important in the investigations of snow particle formation and precipitation mechanism to study the ratio of contribution by each process in the growth of a snow particle. But, no investigations have been made as yet. As snow particles fall to the ground maintaining the degree of aggregation growth as the number of snow crystals constituting an aggregated snow particle and the degree of riming growth as the riming amount, there is a possibility of measuring the ratio of contribution by each process. So we will concentrate on the riming growth process as the theme. The purposes of the present study are to establish the measuring method of riming amount on a snowflake and to study the difference of riming proportion in the growth of snow particles due to the difference of meteorological conditions and stages in the life cycle of snow clouds.

2. MEASURING METHOD OF RIMING AMOUNT ON A SNOWFLAKE

There are many studies on the riming properties of snow crystals (e.g. Harimaya 1975, p. 384). On the other hand, qualitative observations concerning riming amount on a snow particle were made by Hobbs et al. (1971, p. 152), Reinking (1975, p.745), and Fujiyoshi and Wakahama(1985, p. 1667). In this study we will make quantitative measurements improving on their methods. The measurement was made as follows. Snowflakes were caught on a piece of velvet cloth and a snowflake was selected as their representative. It was disassembled into each snow crystal by a bamboo skewer on a glass plate as carefully as possible so that it would not fracture. Then, all snow crystals constituting a snowflake were photographed. Fig. 1 shows an example of a disassembled snowflake. Each snow crystal was classified into three types, Type I, Type II and Type III as seen in Fig. 1 according to degree of riming and graupel particles were referred to as Type IV. Meanwhile relations as seen

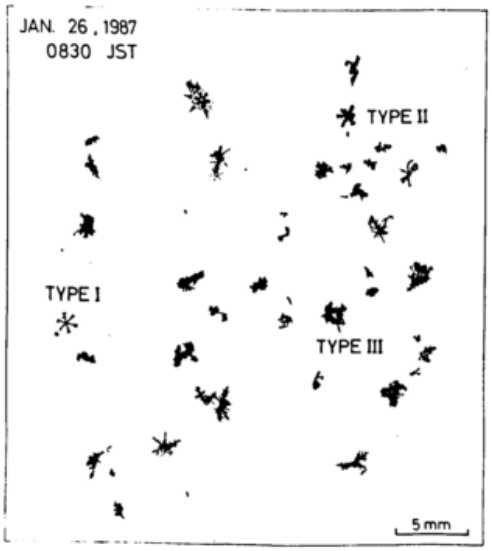


Fig. 1 All snow crystals constituting a snowflake. Examples in each type are shown by name.

in Fig. 2 were obtained from the measurements of the diameter and mass of snow crystals. The mass and riming mass of each snow crystal were obtained using these relations as follows. If we select a snow crystal of Type III and with a diameter of 3 mm by way of example, the mass is obtained from the equation of Type III as seen in Fig. 2 and the riming mass is estimated from the mass difference between a snow crystal (Type III) and unrimed snow crystals (Type I) with a diameter of 3 mm. Then, each mass and each riming mass were summed up and the riming proportion is presented by the ratio of total riming mass to total mass constituting a snowflake. The riming proportion of a graupel particle was assumed to be 100 %.

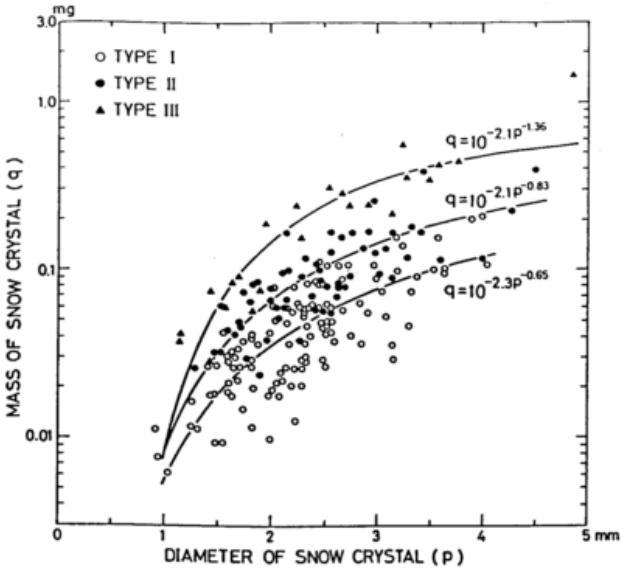


Fig. 2 Relation between the diameter and mass of snow crystals in each type.

3. RESULTS

3.1 DIFFERENCE OF RIMING PROPORTION DUE TO METEOROLOGICAL CONDITION

An example of radar reflectivity factor over the observation site, snowfall intensity, frequency of snow crystals in each type and riming proportion at the observation site is shown in Fig. 3. When a strong snow cloud passed over the observation site at about 0930 JST, the snowfall intensity increased, graupel particles fell and riming proportion increased. Then, the snowfall intensity continued to increase gradually and by contrast, the riming proportion decreased gradually. In the later stage, both the snowfall intensity and riming proportion became small. This time change is general during the passage of snow clouds. As it was inferred in Fig. 3 that the riming proportion is related to the snowfall intensity, the relation between the snowfall intensity

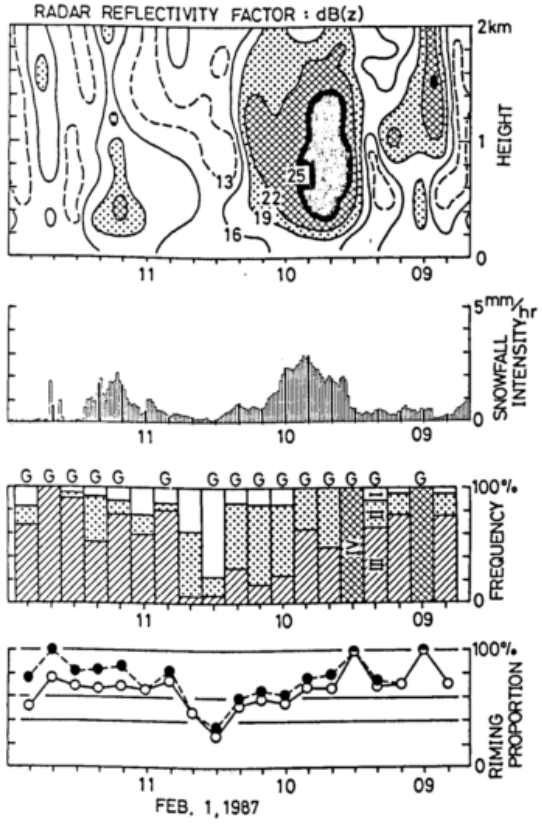


Fig. 3 Radar reflectivity factor over the observation site, snowfall intensity, frequency of snow crystals in each type and riming proportion at the observation site. Solid circles in the lower part indicate the riming proportion incorporating the effect of graupel particles.

and riming proportion was examined as shown in Fig. 4. The lower limit of riming proportion tends to increase with the increase of the snowfall intensity. Explained in detail, only the snowflakes with a large riming proportion fall when the snowfall intensity is strong and the snowflakes with a various value of riming proportion fall when the snowfall intensity is weak. But, in this part, the riming proportion is large when snow cloud is more active as represented by the radar echo pattern.

3.2 DIFFERENCE OF RIMING PROPORTION DUE TO THE STAGE IN LIFE CYCLE OF SNOW CLOUDS

In order to study how the riming proportion changes with the growth stage of snow clouds, snow clouds were classified into three stages, i.e., developing, mature and dissipating, based on the growth stage of snow clouds passing over the observation site. The relation between the growth stage and riming proportion are shown in Fig. 5 under the conditions with an equal radar reflectivity factor. In a wide range of radar reflectivity factor, the riming proportion is large at the developing and mature stages and small at the dissipating stage.

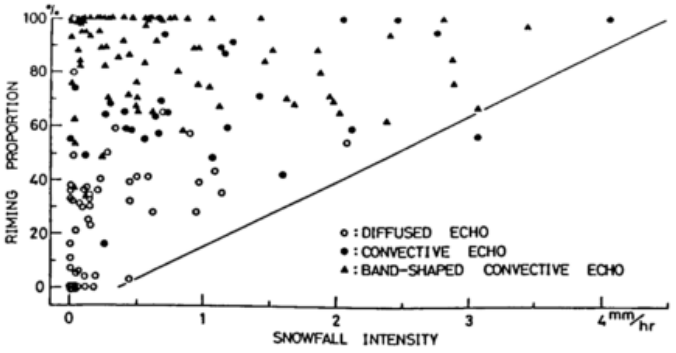


Fig. 4 Relation between snowfall intensity and riming proportion.

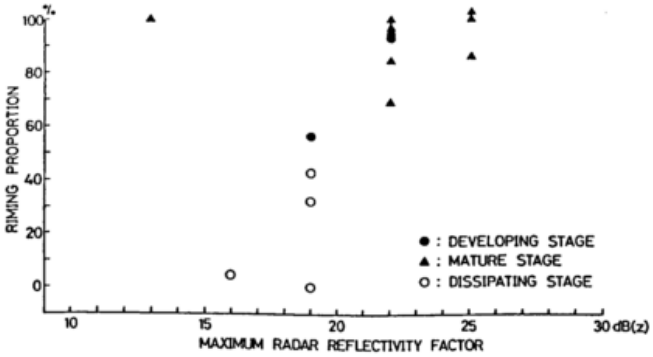


Fig. 5 Relation between the growth stage of snow clouds and riming proportion.

4. DISCUSSION AND CONCLUSION

The lower limit of riming proportion tends to increase with the increase of snowfall intensity. Snowflakes with various values of riming proportion fall when the snowfall intensity is weak. This is considered to be explained by the sorting of snow particles and the difference of meteorological conditions. The riming proportion is large at the developing and mature stage of snow clouds and small at the dissipating stage. This may probably be explained by the formation of cloud droplets and the riming process by snow particles.

5. REFERENCES

Fujiyoshi, Y.; Wakahama, G.: On snow particles comprising an aggregate. J. Atmos. Sci. 42 (1985) No. 15, p. 1667-1674.

Harimaya, T.: The riming properties of snow crystals. J. Meteor. Soc. Japan 53 (1975) No.6, p. 384-392.

Hobbs, P. V.; Collaborators: Studies of winter cyclonic storms over the Cascade Mountains (1970-71). Res. Rept. 6 (1971), Dept. Atmos. Sci., University of Washington 306 pp.

Reinking, R. F.: Formation of graupel. J. Appl. Meteor. 14 (1975) No. 5, p. 745-754.

THREE-DIMENSIONAL STRUCTURES OF SNOW CRYSTALS SHOWN BY STEREO-PHOTOMICROGRAPHS

Kunimoto Iwai
Faculty of Education, Shinshu University, Nagano
Japan

1. Introduction

Photomicrographs of natural snow crystals have been taken with the microscope of low magnification by many investigators(Bentley and Humphreys, 1931, Nakaya,1954, Magono and Lee, 1966).

Photomicrographs of plate-like snow crystals by Bentleys and Humphreys pariculary have given the impression on a person that they are represented as two-dimensional nature. Few investigation about their three-dimensional structures has been done, even though Nakaya(1954) showed a few side view photomicrographs of them. Therefore, stereo-photomicrographs of snow crystals are desirable to clarify their three-dimensional nature.Iwai(1981), (1983) showed a simple method how to take their stereo-photomicrographs.

However, the author is anxious of that most personae cannot observe them stereo-scopically by naked eyes.

Therefore, at the poster session in the present conference, stereo-photomicrographs of snow crystals will be shown with the simple stereo-scopes.

2. Examples of stereo-photomicrographs of snow crystals.

Photo. 1 shows a pair of stereo-photomicrograph of snow crystal classified as malformed type. Its side view photographs is also shown. We cannot understand the surface structures of this crystal from only one plane photograph,because of its complexity.

However, we can immediately understand that this crystal consists of two plates with different height, when we observe it stereo-scopically. we can see from the side view photomicrograph that these two plates are linked by a small and thin hexagonal plate. Two plates grow asymmetrically from the upper and lower parts of the small hexagonal plate and it becomes malformed crystal.

Photo. 2 shows stereo-photomicrograph of two resemble dendritic crystals. Both are the double plates which grow from the upper and lower pars of thin (crystal A, A' in side view) and thick (crystal B, B' in side view) hexagonal plates.

Photo. 3 shows a stereo-photomicrograph of a singl bullet type crystal taken along the c-axis.From stereoscopic view, we understand that apparent pyramidal faces are not crystallographic pyramidal faces but are mere skeleton structures.This finding will be important for explaning the halo with an angular radius of about 8° ,which is rarely observed. Because, this halo is attributed to the ray path from the crystallographic pyramidal face to the prism face(Wallace and Hobbs,1977).

3. Concluding Remarks

In this extended abstract, only 3 stereo-photomicrographs are shown. However, we have observed many natural snow crystals from the view point of three-dimensional structures for these 7 years.

The following are concluded:

1) Most of plate-like snow crystals (about 70 %)consist of 2 or more plate-like crystals having different forms and sizes.

2) A simple dendritic plate is rarely observed.

3) Apparent pyramidal faces of bullet crystal are not crystallographic faces but mere skeleton structures.

The author believes that stereo-scopic view of snow crystals are very useful to clarify their three-dimensional nature.

References

Bentley,W.A. and W.J. Humphreys,1931: Snow crystals,McGraw-Hill,New York.

Iwai, K.,1981: A simple method for taking stereo-photomicrographs of snow crystals.Tenki,28, 377-380.

Iwai, K.,1983: Three-dimensional Structure of plate-like snow crystals. J. Met. Soc. Japan,61,746-756.

Magono,C. and C.W. Lee,1966:Meteorological classification of natural snow crystals. J. Fac. Sci. Hokkaido Univ. Ser.7,2,321-335.

Nakaya, U., 1954: Snow crystals, Harvard Univ. Press.

Wallace,J.M. and P.V. Hobbs:Atmospheric Science.,Academic Press.

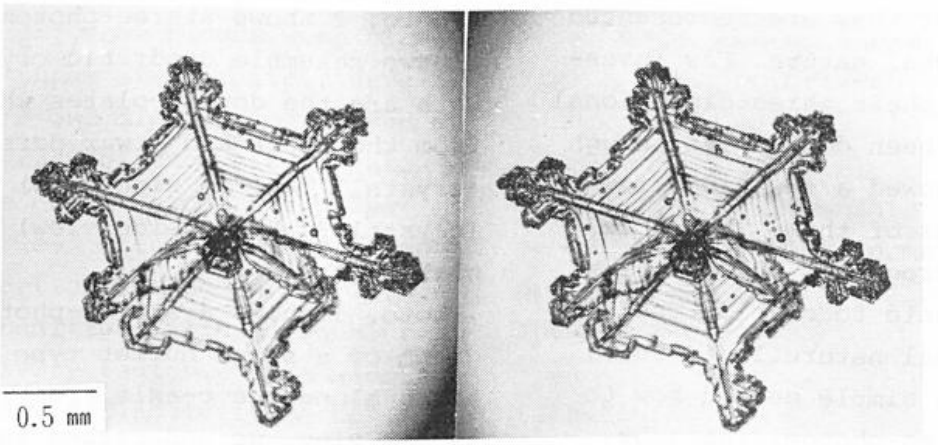


Photo. 1



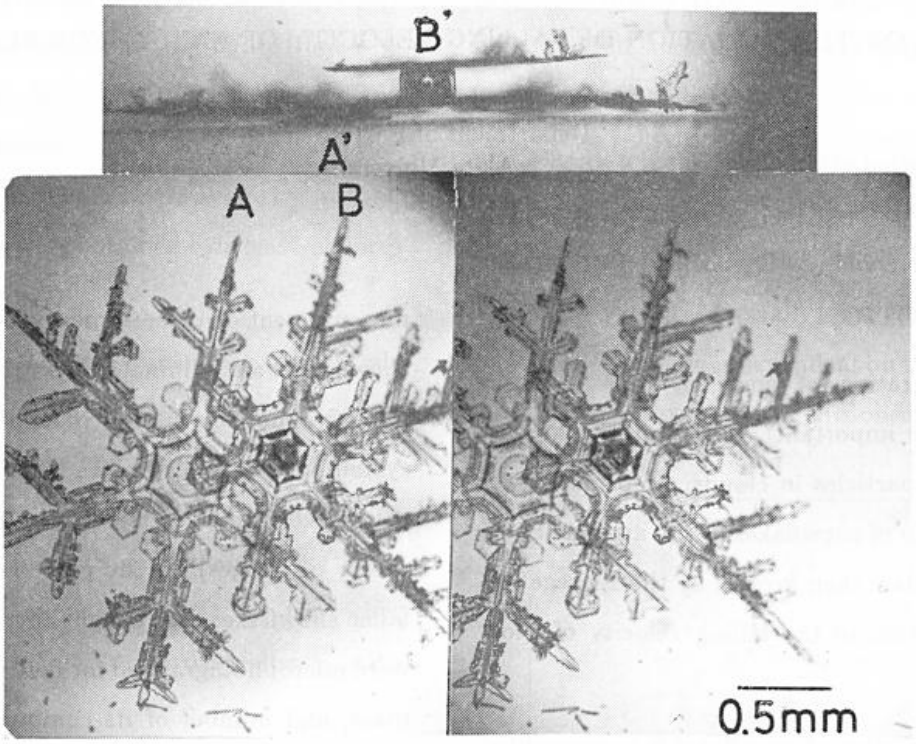


Photo. 2

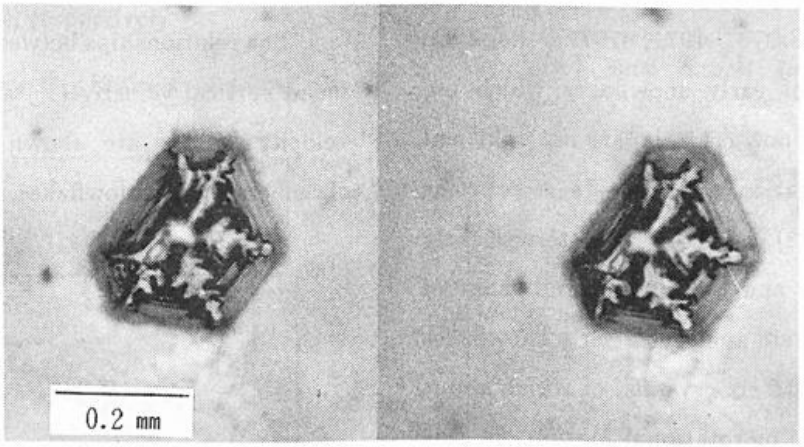


Photo. 3

ON THE VARIATION OF FALLING VELOCITY OF EARLY SNOWFLAKES

Masahiro Kajikawa [1]
Department of Earth Science
Akita University
Akita 010, Japan

1. INTRODUCTION

The aggregration of snow cyrstals to form snowflakes is an important process in the growth of precipitation particles in clouds. Information on the falling motion of snowflakes in the atmosphere is required to calculate their growth by the aggregation process, in addition to the falling velocity of snow crystals.

The falling motion of snowflakes is accompanied by the horizontal motion and both vertical and horizontal velocity variations (e.g., Sasyo, 1971, 1977; Zikmunda and Vali, 1972). Those velocity variations and horizontal motion are responsible for an increase in the collision efficiency of snowflakes. In the former observations (e.g., Sasyo, 1971, 1977), however, the available data of early snowflakes which are composed of several snow crystals, are not sufficient to study the aggregation process. In a previous paper (Kajikawa, 1982), the free-fall pattern of early snowflakes in still air and the number and shape of component crystals were analyzed. Early snowflakes are composed of two to six crystals, of which about 80% fall with a spiral or rotational motion. In this paper the correlations between velocity variations and features of unrimed early snowflakes will be analyzed and discussed.

2. METHOD OF OBSERVATION

Since the method of measurement of falling motion is the same as in the previous paper, the procedure will be described briefly. For the measurement of three-dimensional motion, a falling snowflake was illuminated by stroboscopic light and photographed by means of a stereoscopic camera system. The coordinates of the snowflake were calculated from successive corresponding points (the center of images) on the pair of photographs. The fallen snowflakes were caught on a sampling plate and were microphotographed for determining shape, size, mass, and number of its component snow crystals. In this paper, data obtained from the analysis of fall pattern of spiral type involving rotational type were used to reveal the variations of vertical and horizontal velocities.

3. RESULTS

The relationships between the mass (M) and the mean vertical velocity ($\overline{V}$) and the mean horizontal velocity ($\overline{V}_H$), are shown in Fig. 1. For the classification of snowflakes, the type describes the

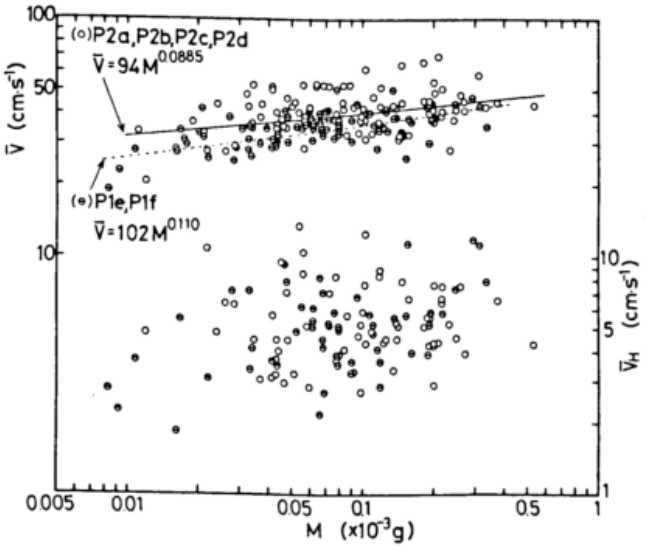


Figure 1. Relationships between the mass (M) of early snowflakes and the mean vertical ($\overline{V}$) and horizontal ($\overline{V}_H$) velocity.

[1] Present Affiliation: Scientific Visitor, National Center for Atmospheric Research, Boulder, Colorado, U.S.A.

largest component crystals (Magano and Lee, 1966) was used. It is evident from this figure that $\overline{V}_H$ has no relation to M. On the other hand, $\overline{V}$ has reasonable correlation to M, although the large amount of scatter appear in the velocity values. Empirical equations were obtained by a least-squares technique.

Figure 2 shows the nondimensional amplitude ($a' = a/d$) of the spiral motion, where a and d are the amplitude of the spiral motion and the size of snowflakes, respectively. It is clear that $\overline{V}_H$ is proportional to a' and is independent of the main type of component snow crystals. On the other hand, there is some trend toward smaller $\overline{V}$ with increasing a'.

The nondimensional frequency ($n' = nd/\overline{V}$) of spiral motion increases as Reynolds number ($Re = \overline{V}d/\nu$) increases and is independent of the shape of the component crystals, as seen in Fig. 3. Here n and ν are the frequency of spiral motion and the kinematic viscosity of air, respectively.

Figure 4 is the relationship between a' and n'. It is evident that a' is inversely proportion to n' and is dependent in some degree of the shape of component snow crystals.

Figure 5 is the relationship between $\overline{V}_H$ and the standard deviation (σ_v) of the variation in vertical velocity (V). Although σ_v increases slightly with $\overline{V}_H$, these values are usually smaller than 2 cm/sec (3 to 5% of $\overline{V}$) and are independent on the main shape of component crystals. σ_v in this observtion is smaller

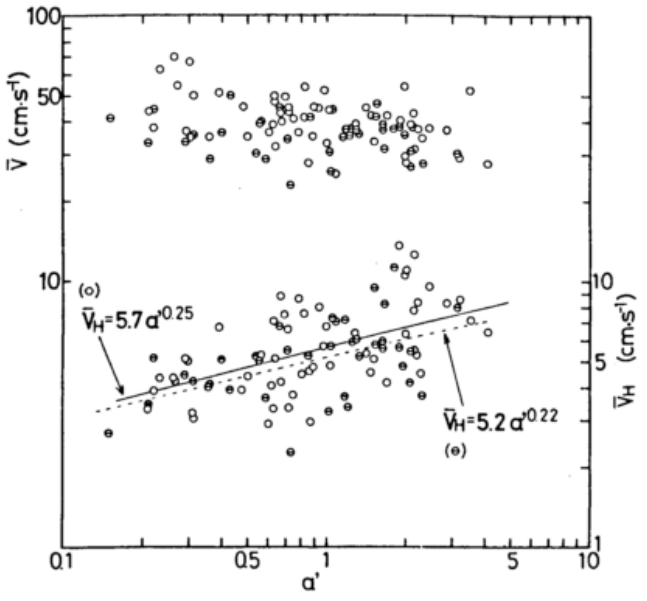


Figure 2. Relationships between the nondimensional amplitude (a') of the spiral or rotational motion and the mean vertical ($\overline{V}$) and the horizontal ($\overline{V}_H$) velocity. Symbols as in Fig. 1.

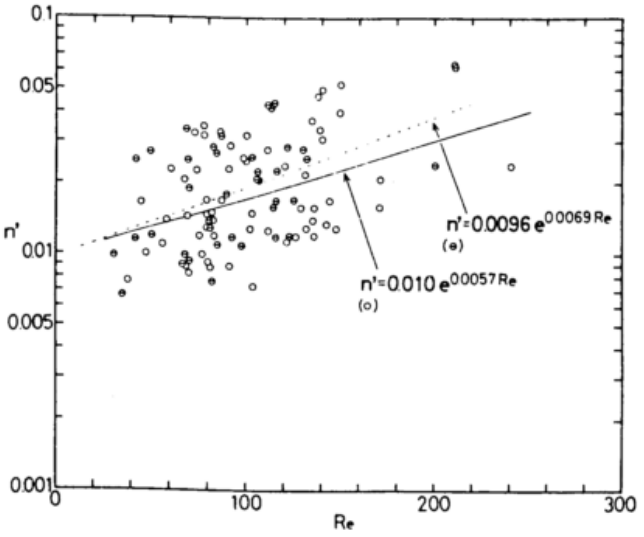


Figure 3. Relationship between the Reynolds number (Re) with respect to the mean vertical velocity and the nondimensional frequency (n') of the spiral or rotational motion.

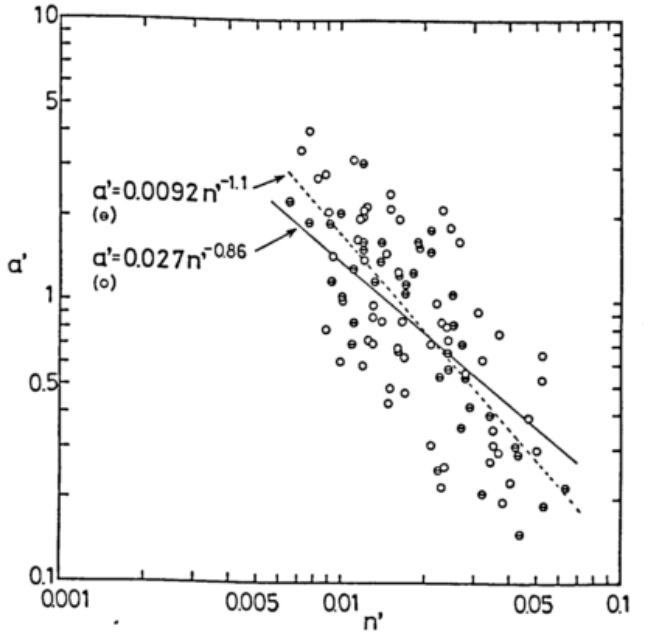


Figure 4. Relationship between the nondimensional frequency (n') and the nondimensional amplitude (a').

than the mean value (2.83 cm/sec) observed by Sasyo (1971). It seems that this difference is primarily due to the difference in the mean vertical velocity of the snowflakes in the two studies.

The relationship between $\overline{V}_H$ and the standard deviation (σ_H) of the variation in horizontal velocity (V_H) is shown in Fig. 6. It can be seen that σ_H increases with $\overline{V}_H$ and is independent of the shape of the component snow crystals. σ_H amounts to about 50% of $\overline{V}_H$ and is larger than σ_v. These values of σ_H are comparable to the mean value (3.0 cm/sec) observed by Sasyo (1971). From the results described above, it seems likely that in particular the variation of the horizontal velocity plays an important role in the aggregation process of snowflakes.

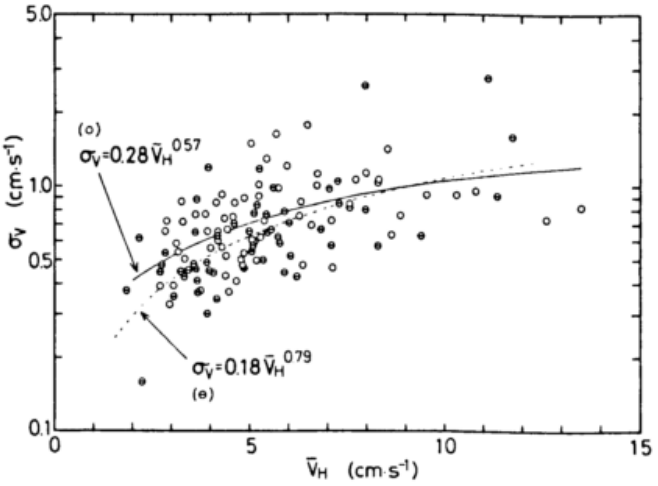


Figure 5. Relationship between the mean horizonal velocity ($\overline{V}_H$) and the standard deviation (σ_V) of variation in vertical velocity.

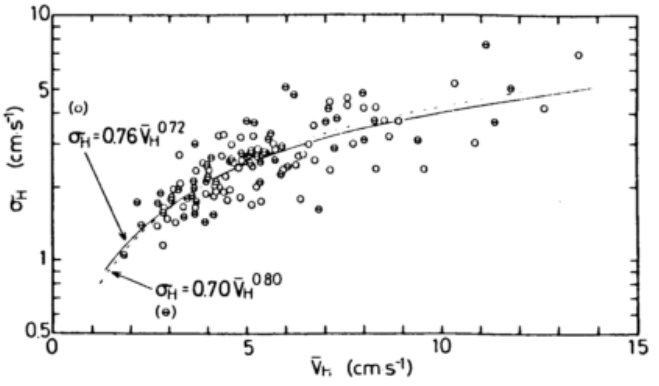


Figure 6. Relationship between the mean horizontal velocity ($\overline{V}_H$) and the standard deviation (σ_H) of variation in horizontal velocity.

4. CONCLUDING REMARKS

The falling motion in still air of early snowflakes, which are composed of two to six crystals, was analyzed by means of a stereo-photogrammetry.

The variations of vertical and horizontal velocity in the spiral or rotational falling motion were empirically obtained, as shown in Figs. 5 and 6. The standard deviation of variation in vertical velocity is small. On the other hand, the standard deviation of variation in horizontal velocity is considerbly larger and increases with mean horizontal velocity. Accordingly, it seems reasonable to conclude that in particular the variation of horizontal velocity plays an important role in the aggregation process of snowflakes.

The mean horizontal velocity can be estimated from the nondimensional amplitude of the spiral or rotational falling motion. The nondimensional amplitude is inversely related to the nondimensional frequency of spiral or rotational motion. And the nondimensional frequency can be estimated from the Reynolds number with respect to the mean vertical velocity of snowflakes.

5. REFERENCES

KAJIKAWA, M.: Observation of the falling motion of early snow flakes. Part I. Relationship between the free-fall pattern and the number and shape of component snow crystals. *J. Meteor. Soc. Japan.* **60** (1982) 797–803.

MAGONO, C.; LEE, C. W.: Meteorological classification of natural snow crystals. *J. Fac. Sci.* Hokkaido Univ. Serv. VII, **2** (1966) 321–335.

SASYO, Y.: Study of the formation of precipitation by the aggregation of snow particles and the accretion of cloud droplets on snowflakes. *Pap. Meteor. Geophys.* **22** (1971) 69–142.

SASYO, Y.: The collection efficiency of simulated snow particles for water droplets (II), On the oscillatory angular motion of the snowflake. *Pap. Meteor. Geophys.* **28** (1977) 159–168.

ZIKMUNDA, J.; VALI, G.: Fall patterns and fall velocities of rimed ice crystals. *J. Atmos. Sci.* **29** (1972) 1334–1347.

A PARAMETRIZATION SCHEME FOR THE COALESCENCE OF WATER DROPS USING THE STOCHASTIC COLLECTION EQUATION

C. Lüpkes[+], K. D. Beheng[++], G. Doms[+++]

+ Institut für Meteorologie u. Geophysik der Universität Frankfurt/Main, FRG
++ Institut für Meteorologie u. Klimaforschung, Kernforschungszentrum Karlsruhe/Universität Karlsruhe, FRG
+++Deutscher Wetterdienst Offenbach, FRG

1. Introduction

In numerical simulation models the formation of precipitation due to the collision/coalescence process is usually treated by two methods: on the one hand, by numerically solving the stochastic collection equation (SCE) governing the time evolution of a drop size spectrum or, on the other hand, by using a parametrization scheme dealing with bulk quantities such as liquid water contents. With respect to the latter, the most prominent scheme is that of Kessler (1969). His concept is based on the partition of the total liquid water content into a cloudwater and a rainwater portion. The conversion of cloudwater into rainwater is thought to be the result of two basic conversion mechanisms: (i) autoconversion, which means the transformation of cloud water to rainwater and (ii) accretion, which means an increase of rainwater mass. The corresponding conversion rates as given by Kessler have been derived partly by intuition and partly by crude approximations.
In this paper we describe how the partitioning concept of Kessler can be applied to SCE and how rate equations analogous to those presented by Kessler can be formulated. Then we compare results obtained by this method with those obtained by Kessler's scheme. Starting from this basis finally a new parametrization scheme is outlined.

2. The concept

Applying Kessler's partitioning concept analogously to SCE the important question arises: Which drop radius separating cloud droplets from raindrops should be chosen? This question may be answered by the numerical-empirical result that, nearly independent of an initial drop spectrum, the evolving drop size distribution function (in a specific ally transformed form) exhibits at about $r^* = 40$ µm radius a minimum value which is fairly stationary at longer simulation times. Thus, a drop radius of 40 µm seems to be appropriate to distinguish cloud droplets from raindrops. Accordingly we split the size distribution function $f(x)$, x: drop mass, into a cloud droplet part $f_c(x)$ with $x<x^* \sim (r^*)^3$ and into a raindrop part $f_r(x)$ with $x \geq x^*$ so that the total spectrum is given by $f(x) = f_c(x)+f_r(x)$. In the scope of this definition autoconversion and accretion denote the formation of raindrops with mass $x = x_1+x_2 \geq x^*$, as shown in Fig.1, where $x_1, x_2 < x^*$ as well as $x_1 < x^*$ and $x_2 \geq x^*$, respectively.

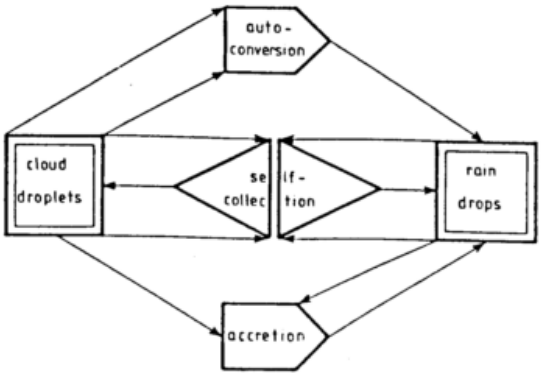


Fig.1 Scheme of the collection mechanisms

Additionally, selfcollection appears, which means the production of cloud droplets (raindrops) with mass $x<x^*$ ($x \geq x^*$) where $x_1, x_2 < x^*$ ($x_1, x_2 \geq x^*$). Obeying these mass relations and the separation of the drop size distribution function as indicated, the total rates of change of the cloud droplet and the raindrop part of the spectrum are then derivable as the sum of mode-specific 'differential' rates. From these rates mode-specific integral rates for arbitrary moments of both parts of the spectrum can be deduced. For the explicit formulation of both types of rates see Beheng & Doms (1986), Doms & Beheng (1986) and Beheng (1987).

The main results obtained from these investigations are as follows:

- Provided that the liquid water contents are the same, the shape of the initial drop spectrum strongly influences the magnitude and the time dependence of the conversion rates.
- Selfcollection of cloud droplets gradually leads to the formation of drops with mass $x \lesssim x^*$. Thus selfcollection is of special importance since drops in this size range are converted most effectively to raindrops by auto-

conversion.
- Concerning the cloud droplet range, autoconversion and selfcollection cause a narrowing and a broadening of that partial spectrum, respectively, resulting as a whole in a slight broadening; accretion has only a negligible effect on the spectrum's spread.
- Concerning the raindrop part of the spectrum, a strong broadening occurs due to the combined action of all collection modes.
- The autoconversion rate calculated by Kessler's formula is in principle unable to predict rates as have been computed by use of SCE.

All in all it can be stated that the major shortcomings of Kessler's scheme are that (i) cloud water is only represented by the liquid water content instead of a size spectrum and that (ii) raindrops are always described by an exponential function(Marshall-Palmer type) with constant number density for the hypothetical radius r=0. It has therefore been concluded that besides the cloud and rainwater content additional parameters have to be included to yield a more reliable parametrization scheme.

3. The new scheme

As a starting point the integral conversion rates derived by Beheng & Doms for the distinct modes of collection autoconversion, accretion and selfcollection have been used to predict, in addition to the rates of change of the liquid water contents, those of the number densities in each size range. In order to formulate these rates it was necessary to parametrize appropriately the collection kernel function K occuring in each integral expression. This was mostly done by assuming $K \sim x^2$ (cf. Long, 1974). Unfortunately the parametrization developed in that way did not reproduce the results obtained by solving SCE. This deficiency was due to the fact that the structure of the distribution function near r^*, which turned out to be of great importance, was not grasped with necessary accuracy. Therefore, the cloud droplet range (see fig.2) was repartitioned into two subranges (at a drop radius r^+ of about 20 µm) and consequently the integral

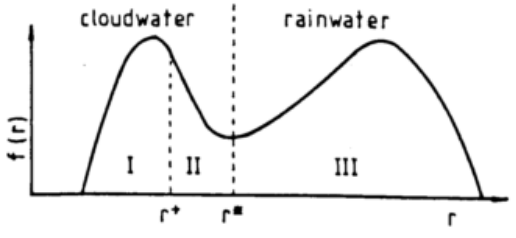


Fig.2 Scheme of the 3 drops ranges under consideration

conversion rates of Beheng & Doms were reformulated in correspondence with the new partitioning. A crucial point in this concept was that by applying the kernel approach mentioned above some integral rates could only be expressed as a function of the number densities at both separation radii r^+ and r^* as well as the radar reflectivities in both cloud droplet ranges. To determine these open variables specific distribution functions in each drop range are assumed as a closure condition: in region I and II a Gamma and an inverse Gamma function, respectively, governed by three parameters, where in each function one parameter is set constant and the remaining two parameters α_I, α_{II}, β_I and β_{II}, resp., are chosen to be variable in time; in region III an exponential function containing two variable parameters. The time rates of change of the parameters of these distribution functions can be formulated in terms of time rates of change of certain moments of the spectra. In summary this results finally in a set of ten coupled prognostic equations: six for the number densities and liquid water contents in the three drop regions and four for the parameters α_I, α_{II}, β_I and β_{II}.

The procedure of the numerical solution of these equations is as follows: (i) any given intial size distribution function is approximated by the specific functions prescribed in each size range. This consists in the determination of the four distribution parameters mentioned from the given number densities and liquid water contents in region I and II. In region III no drops are allowed to appear initially in order to exclude a contribution by accretion at the very beginning of the simulation. (ii) The prognostic equations for the three number densities and liquid water contents are solved by simple forward time integration. The open variables mentioned are calculated by iteration from the tendency equations for the four parameters.

4. Numerical results

In Figs.3 and 4 the results of the numerical simulation of the parameter scheme are compared to those obtained by solution of SCE, i.e. for the conversion rates due to accretion and autoconversion as well as for the time evolution of the rainwater content L_{III}. Two initial spectra s_1 and s_2 with liquid water contents $L = 10^{-6}$ gcm^{-3} and initial number densities $N_o = N(t=0) = 100$ cm^{-3} have been used which only differ by the specification of the initial radius dispersion coefficient ν (ν_1=.25 (s_1), ν_2=.40 (s_2)). The agreement between the two calculation

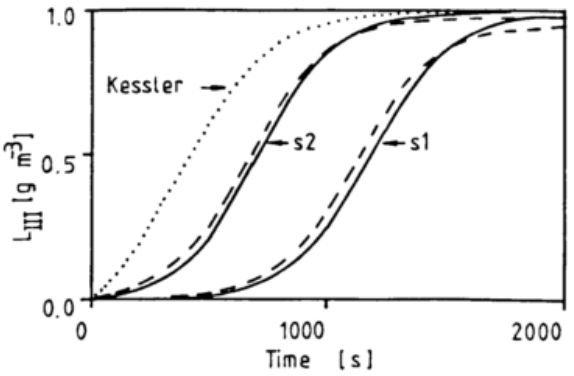


Fig.3 Rainwater content L_{III} as function of model time for Spectrum s1 and s2 obtained by the solution of SCE (dashed lines), the new parameter model (solid lines) and Kessler's scheme.

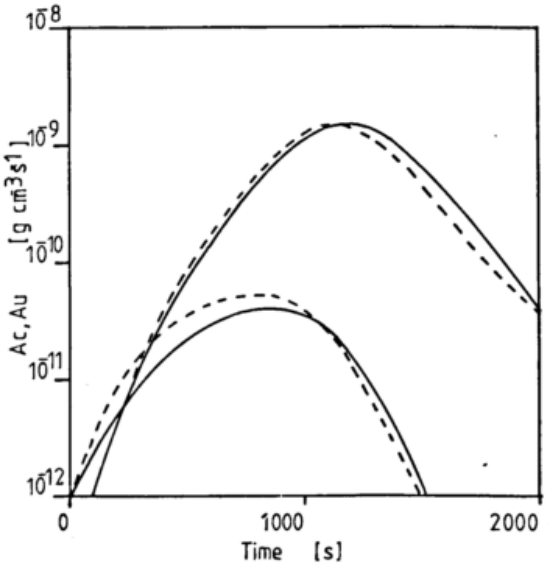


Fig.4 Mass density conversion rates as function ot model time for cloud water due to autoconversion (lower curves) and accretion (upper curves) obtained by the solution of SCE (dashed line) and the parameter model (solid line) for spectrum s_1.

methods is obviously good. Moreover, as already mentioned above, the structure of the initial size distribution function has a strong influence on the time evolution of the conversion rates and on that of the rain water content. Note that, when applying Kessler's scheme, only one curve occurs since for both initial spectra the same total liquid water content has been assumed.

5. References

BEHENG,K.D.: Zur mikrophysikalischen Modelltheorie des Auswaschens von Aerosolteilchen sowie der Bildung von flüssigem und eisförmigem Niederschlag, Berichte des Instituts für Meteorolgie u. Geophysik der Univ. Frankfurt a.M. 69 (1987), 78 p.

BEHENG,K.D.; DOMS,G.: A general formulation of collection rates of cloud- and raindrops using the kinetic equation and comparison with parametrizations, Beitr. Phys. Atmos. 59 (1986), p. 66-84

DOMS,G.; BEHENG,K.D.: Mathematical formulation of selfcollection, autoconversion and accretion rates of cloud- and raindrops, Meteorol. Rdsch. 39 (1986), p. 98-102

KESSLER,E: On the distribution and continuity of water substance in atmospheric circulations, Meteorol. Monogr. 32 (1969), 84 p.

LONG,A.B.: Solutions to the droplet collection equation for polynomial kernels, J. Atmos. Sci. 31 (1974), p. 1040-1052

ON THE DYNAMICS OF THE FALLING ICE CRYSTAL ZONE

Josef Podzimek
Department of Mechanical and Aerospace Engineering, and
Graduate Center for Cloud Physics Research
University of Missouri-Rolla, MO 65401

1. INTRODUCTION

This contribution focuses on aerodynamics of ice crystals or snowflakes in reference to evolution of falling ice crystal zone. The results of the investigation of particulate deposition on scavengers such as disks, plates, on thin oblate spheroids and long cylinders were published elsewhere (e.g., Podzimek and Martin, 1984).

2. MODELING OF THE ICE CRYSTAL ZONE

The numerical model is based on the previous work by Clark and List (1971) and Girard and List (1975) who assumed that body forces and aerodynamic drag of falling precipitation elements induce an air motion which affects the element dispersion and settling. In our two-dimensional model were neglected the thermodynamic terms related to water phase transition and to the thermal stratification of the atmosphere. To the standard equations for air mass conservation and linear momentum (with an isotropic turbulent exchange coefficient, K_t, and terms for the force acting on scavengers in gravitation field, - gq) was added the continuity equation for scavenger mixing ratio, q, and the energy equation in the form

$$\frac{\partial q}{\partial t} + \frac{\partial (qu)}{\partial x} + \frac{\partial}{\partial z}\,[q(w-V_S)] = 0 \ ,$$

$$\frac{\partial}{\partial t}\iint [\tfrac{1}{2}(u^2+w^2)+gqz]\,dxdz = -\iint gqV_S\,dxdz -$$

$$-K_t \iint [(\frac{\partial u}{\partial x})^2+(\frac{\partial u}{\partial z})^2+(\frac{\partial w}{\partial x})^2+(\frac{\partial w}{\partial z})^2]\,dxdz \ .$$

A simple relationship between the uniform size of scavengers and the settling velocity, V_S, was assumed. The effect of relaxation time for scavengers was neglected. Otherwise, the air velocity components, u, w, were calculated from the stream function and related to the vorticity which was used in the transport equation.

3. RESULTS OF MODELING

The calculation has been done for calm, homogeneous atmosphere and for the atmosphere with uniform horizontal wind velocity. The initial and boundary conditions for calm atmosphere are similar to those in quoted articles. Following parameters were considered to affect the evolution of scavenger (precipitation) zone: mixing ratio q [in the range from 0.01 g_s (scavengers)/g_a (air) to 0.04 g_s/g_a] scavenger settling rate, V_S, and turbulent exchange coefficient, K_t. Turbulent exchange coefficient was varying between 1.0 and 2.500 m^2/s.

The most important factor affecting the dispersion of precipitation elements and the induced downdrafts in the precipitation zone is the mixing ratio. This is documented well in Fig. 1 which shows the evolution of the downdraft velocities for q = 0.01 q_s/g_a and q = 0.04 g_s/g_a. The induced velocities have considerable impact on the mean height of the front center of the falling precipitation zone, z, in

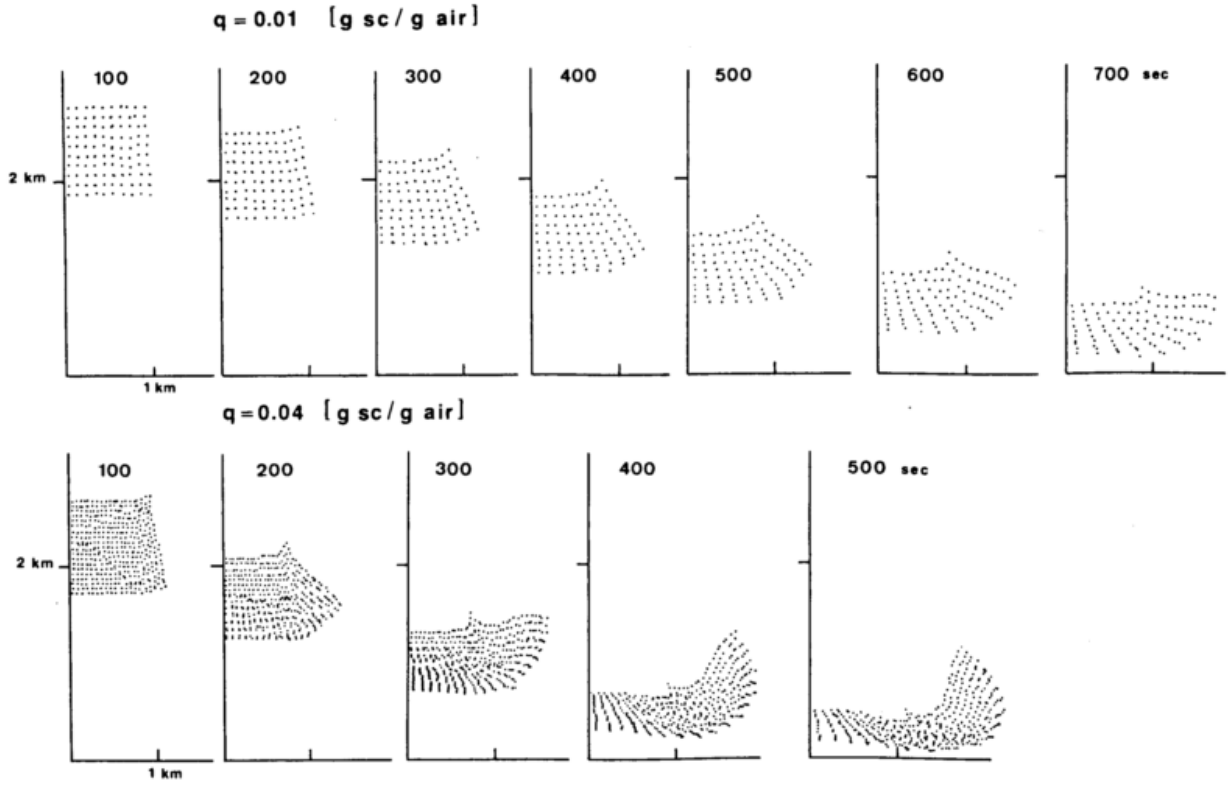


Fig. 1: Evolution of scavenger zone for q=0.01 and 0.04, V_S=1.5 m/s, K_t=1000 m^2/s.

Fig. 2 and on the maximum width of the dispersing zone, b_{max}. Less significant is the effect of turbulent exchange coefficient, K_t, on the induced velocities, u,w, and on the maximal width of the settling zone. Greater impact on the zone's evolution has the original shape of the initial scavenger zone. Thicker zones (e.g., 400 m x 400 m or 320 m x 500 m cross sections) induced downdrafts of around 0.2 m/s for scavenger settling velocity, V_S = 1.73 m/s, mixing ratio, q = 0.01 g_s/g_a and K_t = 1000 m^2/s. For comparison the downdrafts induced

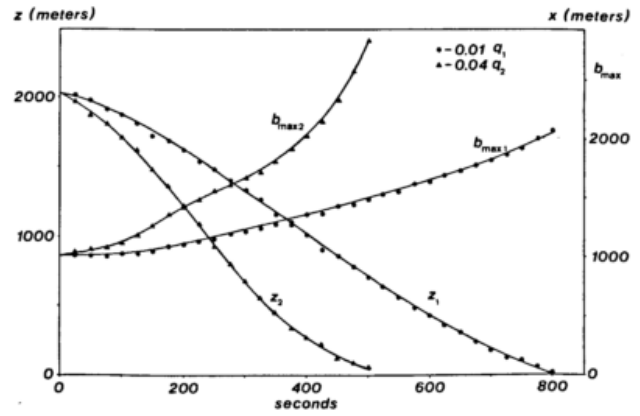
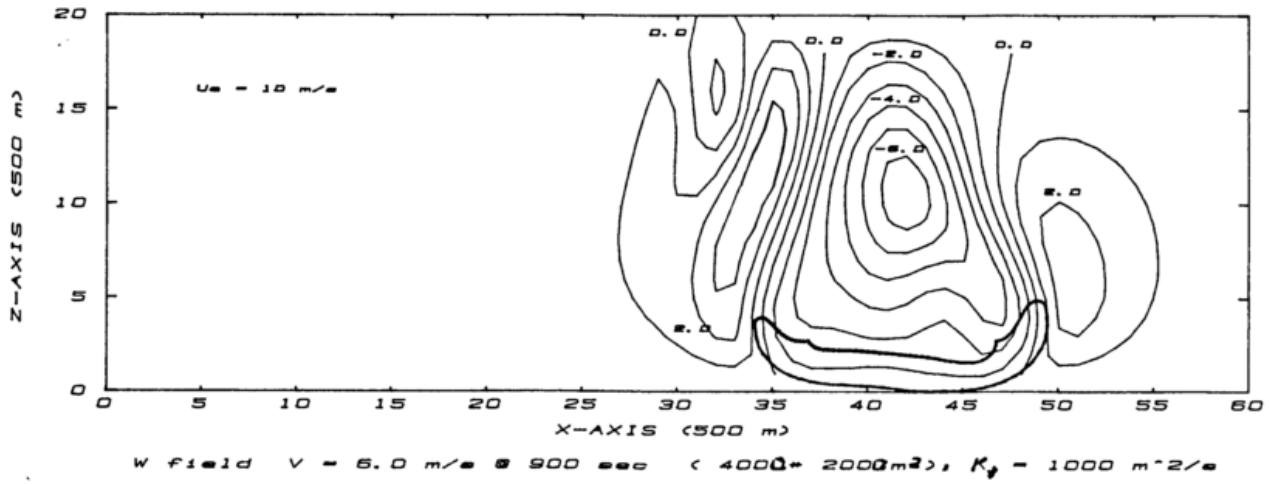


Fig. 2: Mean height, z, and the maximun width, b_{max}, of the scavenger zone.

by the scavenger zone of initial cross section of 800 m x 200 m after 400 seconds, amounted only to one half of those induced by thick scavenger zones. Usually several hundreds of seconds were necessary at a mixing ratio of 0.01 g_s/g_a for fully developed downdrafts.

The study of the impact of a uniform horizontal wind on the scavenger zone formation has been performed under the following assumptions: the component of the uniform horizontal wind velocity (in Fig. 3) was U = 1.0 m/s affecting the deformation of the scavenger zone with cross section of 4000 m x 2000 m. Scavengers--of mixing ratio of 0.01 g_s/g_a--were released at a height H_R = 7 km and constant turbulent exchange coefficient K_t = 1000 m^2/s. In this specific case the precipitation (scavenger) settling velocity was high, V_S = 6 m/s, and the main field dimensions were 30 km x 10 km. With the boundary conditions u = U, ζ (vorticity) = 0, $\frac{\partial \psi}{\partial x}$ = 0 at the control



W field V = 6.0 m/s @ 900 sec (4000 - 2000m²), K_y = 1000 m²/s

Fig. 3. Vertical components of velocities induced by falling scavenger zone.

volume (CV) entrance; w = 0, $\zeta_W = \zeta_{W+1}$, ψ = 0 at the ground; ζ = 0, $\frac{\partial \psi}{\partial x}$ = 0 at the CV exit and w = 0, ζ = 0, ψ = UH at the top of CV the induced velocities surpassed 10% of the scavenger free velocity.For very small individual ice crystals (with Re < 10) one can modify the drag coefficients for drops in order to obtain the coefficients for ice crystals of different shape, however, of the same volume like drops. This equivalent radii enable us to determine the "effective mixing ratio", q, and the crystal settling velocity, V_S, in the equations of our numerical model. The author found a simple relationship between drag coefficient, C_D and the Reynolds number in the form $C_D = A\ Re^{-0.466}$, where A is changing its value from 16.5 (for disks and hexagonal plates) to 38.0 for dendrites in the domain of 1 < Re < 200. The symmetrical plate type crystals start to oscillate around Re = 120 and the stellar or dendritic type crystals in the domain of Re between 300 and 500. The columnar type crystals start to oscillate and perform the trochoidal motion at Re ≅ 70. For small aggregates the application of the formula for the drag on porous bodies is possible.

5. CONCLUSION

Our study showed clearly that the most important parameter determining the evolution of a falling ice crystal zone is the "effective" mixing ratio of the crystals. The horizontal wind affects strongly the circulation inside and around the precipitation zone. Most of the crystals falling in nature do not perform an intense oscillatory motion except at side wind. Therefore the introduction of an "effective" mixing ratio in our falling precipitation zone equations is feasible.

ACKNOWLEDGEMENT

The work was supported by the U.S. Army Research Office under grant DAAK-11-83-K-0007. Mr. Tom Smith and Vladimir Wojnar who ably performed numerical calculations and laboratory experiments. Mrs. Vickie Maples' help while preparing the article for publication is highly appreciated.

REFERENCES

Podzimek, J. and Martin, J.J.: Deposition of particulates on charged planar scavengers, Preprint Vol.: VII Int. Conf. on tmospheric Electricity, Albany, AMS, Boston, 1984, p. 57-62.

Clark, T.L. and List, R.: Dynamics of falling particle zone, J. Atmos. Sci. 28 (1971) P. 718-727.

Girard, C. and List, R.: Thermodynamics of falling precipitation zones, Pageoph 113 (1975) p. 1035-1053.

A NEW DATABASE OF ICE PARTICLE SIZE SPECTRA FOR ALTITUDES UP TO 10 KM (30,000 FT)

Richard Jeck
Naval Research Laboratory
Washington, DC 20375 USA

1. INTRODUCTION

About 7600 nautical miles (14,000 km) of select ice particle measurements over the United States have been compiled into a single, computerized database for use in characterizing ice/snow particle size distributions and mass concentrations at flight altitudes. Data are from 50 research flights by six groups in eight projects with PMS 1-D and 2-D probes. Primary variables are average particle size spectra in the range 0.1 to 10mm from each of 1625 microphysically uniform cloud intervals or other convenient distances in wintertime clouds, snowstorms, cirrus and other high altitude clouds. This database provides an unusual, composite view of a large number of diverse ice particle measurements. Both the differences and similarities in ice particle characteristics among a wide variety of cloud and weather systems are evident. The database is illustrated here by plots of particle size, number density, and total mass as a function of temperature.

2. SOURCES OF DATA

Data were selected from published reports or archived computer tapes from flights in the following recent research projects (JECK, 1986): SCPP:1979-84 (REYNOLDS et al, 1986); NEWS:1982-83 (SELTZER et al, 1985); AFGL Cirrus:1977-79 (COHEN, 1981); AFGL LSCS (VARLEY, 1980); CCOPE:1981 (HEYMSFIELD, 1986); COSE-II:1979 (RAUBER, 1981); MIT Snow Growth:1980 (LO et al, 1982); OK-PRESTORM:1985 (CUNNING, 1986; HEYMSFIELD, 1987).

3. RESULTS

3.1 PARTICLE MASS

The ice particle mass that may be present at different flight altitudes is one of the primary interests in this newly assembled database. The mass, m, of individual particles is computed here using published (LOCATELLI and HOBBS, 1974) size-to-mass relationships of the form

$$m = A\ (d_{max})^B,$$

where the nominal particle sizes associated with the PMS probe bins are used for d_{max}, the largest dimension of the particle. The values of the parameters A and B depend on the type of particle (i.e., graupel, plates, unrimed dendrites, etc.). Particle types are often mixed or unknown, however, so for present purposes a "universal" equation with A=0.037 and B=1.9 is used for all particles. These two values represent most of the particles commonly observed in the database. The total ice particle mass (TIPM), or "ice water content" is obtained by summing the contributions from all the particle sizes represented by the available PMS probes. The greatest TIPM computed for any of the flights is about 2.8 g/m^3, in reasonable agreement with expectations.

The range and distribution of the computed TIPM's is seen in the scatterplot in figure 1. It appears that except for the relatively large mass concentrations possible in thunderstorm anvils (plotting symbol A in fig. 1) (HEYMSFIELD, 1986), TIPM's are likely to be less than 0.2 g/m^3 at temperatures below about -30^oC. The data at these temperatures are mostly from cirrus,

with a few samples from the upper reaches of deep winter storms. The maximum TIPM's increase steadily as the temperature increases from -25°C, probably indicating the onset of dendritic growth, riming, and aggregation. The largest mass concentrations occur over the temperature range of 0° to -15°C. These extreme masses are associated with the trailing stratiform region of a mesoscale convective system (MCS) over Kansas (symbol M in fig. 1) (HEYMSFIELD, 1987), and from frontal rainbands windward of the Sierra Nevada mountains in east-central California.

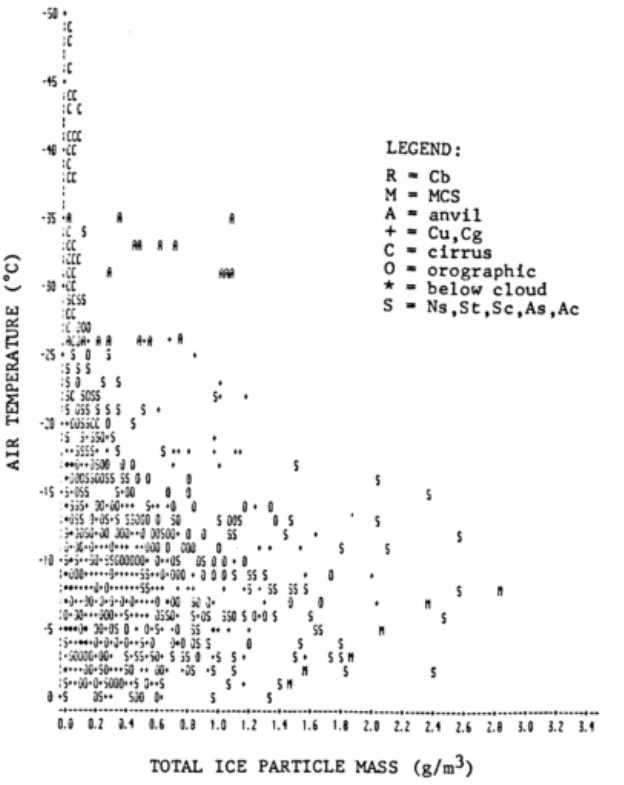


Fig.1: Total Mass vs. Temperature

3.2 PARTICLE CONCENTRATIONS

The numbers of ice particles (d_{max} > 100μm) that have been recorded per liter of air as a function of temperature are shown in figure 2. There is a gradual increase in maximum concentrations as temperatures increase from -50° to -10°C and then a decline as temperatures approach 0°C. The increase is probably due to the growth of extremely small particles into the size range d_{max} > 100μm under consideration here. The decline between -10° and 0°C is presumably due to aggregation and the fallout of precipitation sized particles in this temperature range. Peak concentrations are found between -5° and -10°C and appear to be no more than about 220/liter, except for MCS clouds where up to about 400/liter have been observed. At temperatures below about -30°C, maximum concentrations appear to be less than about 50/liter, except in thunderstorm anvils where nearly double those concentrations have been recorded. As with particle mass, extremes in particle concentration appear to reside in MCS and anvil clouds. Both are warm season phenomena and both are layer-type clouds associated with strongly convective systems.

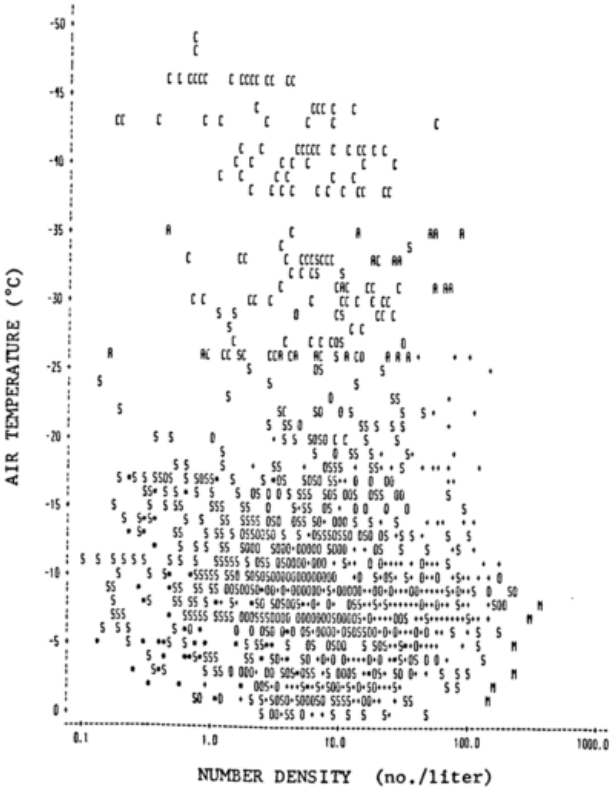


Fig. 2: Concentration vs. Temperature

3.3 PARTICLE SIZE

The non-conforming nature of anvil clouds stands out most clearly in a plot of maximum particle size vs. temperature (figure 3.) The maximum particle dimension (MPD) is determined from the highest PMS probe bin to contain at least one particle per cubic meter as an average over the uniform cloud

interval. Figure 3 shows the anvil data (symbol A) standing alone at temperatures between -25° and -35°C. Except for the large particles available in the anvil, there is otherwise a decrease in MPD with decreasing temperature below -15°C. Looked at another way, (excepting the anvil data), there is a trend to larger MPD's as temperatures increase from -50° up to about -12°C. The steady increase is probably due to the appearance of stellars and dendrites at temperatures greater than about -20°C, as well as to aggregation at the higher temperatures.

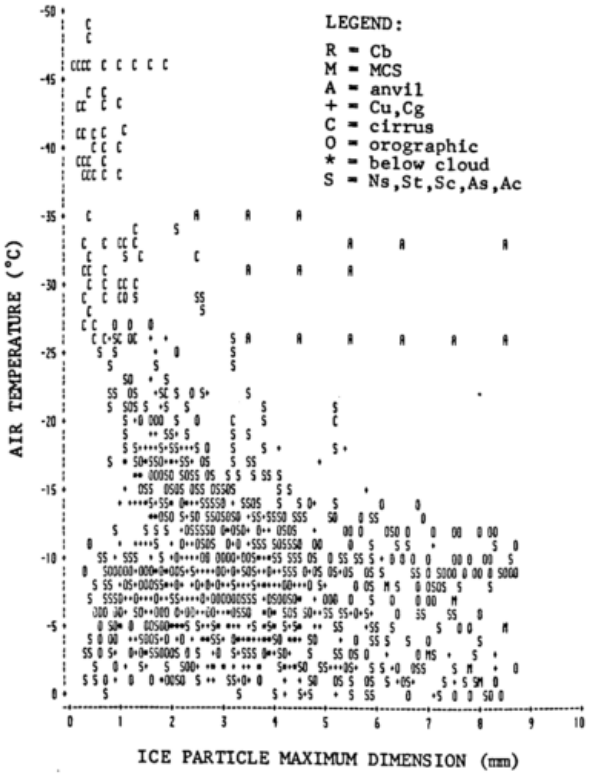


Fig. 3: Maximum Size vs. Temperature

4. ACKNOWLEDGEMENT

This research was sponsored by the United States Department of Transportation, Federal Aviation Administration.

5. REFERENCES

COHEN, I: Cirrus Particle Distribution Study, Part 8. Report No. AFGL-TR-81-0316(1981), Air Force Geophysics Laboratory, Hanscom AFB, Massachusetts 10731 U.S.A.

CUNNING, J: The Oklahoma-Kansas Preliminary Regional Experiment for STORM-Central. Bull. Amer. Met. Soc. 67 (1986) p. 1478ff.

HEYMSFIELD, A: Ice Particle Evolution in the Anvil of a Severe Thunderstorm during CCOPE. J. Atm. Sci. 43 (1986) p. 2463ff.

HEYMSFIELD, A: (1987) Private communication.

JECK, R: Airborne Cloud Physics Projects from 1974 through 1984. Bull. Amer. Met. Soc. 67 (1986) p. 1473-1477.

LO, K; PASSARELLI, R: The Growth of Snow in Winter Storms: An Airborne Observational Study. J. Atm. Sci. 39 (1982) p. 697-706.

LOCATELLI, J; HOBBS, P: Fall Speeds and Masses of Solid Precipitation Particles. J. Geophys. Research 79 (1974) p. 2185-2197.

RAUBER, R: Microphysical Processes in Two Stably Stratified Orographic Cloud Systems. Atm. Sci. paper No. 337 (1981). Colorado State Univ., Fort Collins, Colorado 80523.

REYNOLDS, D; DENNIS, A: A Review of the Sierra Cooperative Pilot Project. Bull. Amer. Met. Soc. 67 (1986) p. 513ff.

SELTZER, M; PASSARELLI, R; EMANUEL, K: The Possible Role of Symmetric Instability in the Formation of Precipitation Bands. J. Atm. Sci. 42 (1985) p. 2207-2219.

VARLEY, D: Microphysical Properties of a Large Scale Cloud System, 1-3 March 1978. Report No. AFGL-TR-80-0002 (1980). Air Force Geophysics Laboratory, Hanscom AFB, Massachusetts 01731 U.S.A.

A VERTICAL WIND TUNNEL FOR THE STUDY OF SNOWFLAKES AND EFFECTS OF ACCUUMLATED SNOW ON MATERIALS

Kenji Isono (Nagoya University),
Jutaro Kobayashi (Japan Weather Association),
Takehiko Gonda (Science University of Tokyo),
Yoshio Sasyo and Taro Mori (Suga Test Instruments Co., Ltd.)

1. INTRODUCTION

Most of vertical wind-tunnels for the study of snow have been designed and used for the study on the growth mode and other physical properties of snow crystals (for instance, Furukawa et al. 1980, P.29). Snow is often composed of snowflakes. The rates of snowfall and snow accumulation on ground and materials are affected by the features of aggregation of snow crystals and the size and other physical properties of snowflakes. A novel vertical wind-tunnel was constructed for the purpose of studying the process of snowflakes formation and effects of accumulated snow on materials for industrial use.

2. CONSTRUCTION AND PERFORMANCE

Fig. 1 shows a schematic diagram of the vertical wind-tunnel. Its main part, the snowfall tunnel ①, in which snowflakes are formed and fall against upward air current, is a cylindrical pipe made of stainless steel, 12 m in length and 55 cm in diameter. It stands vertically, penetrating four floors of a building. Its top end is connected to the return air duct ②, the lower end of which is connected to the air inlet on the wall of the tunnel near its lower end. This lower end is open to the test room in which observation, collection, examination of snow crystals and flakes, and tests of materials are made. The temperature of airstream in the snowfall tunnel and the return air duct is regulated by controlling the temperature of airstream surrounding them. The air temperature in the test room is maintained at temperatures not higher than that of airstream in which snow crystals and snowflakes grow, in order to prevent disturbances caused by convection of air in the tunnel. Cooled water is injected through an ultrasonic atomizers ⑥ for the formation of supercooled clouds in which snow crystals and flakes grow at humidities of water saturation. Seeding of clouds is intermittently made by expanding

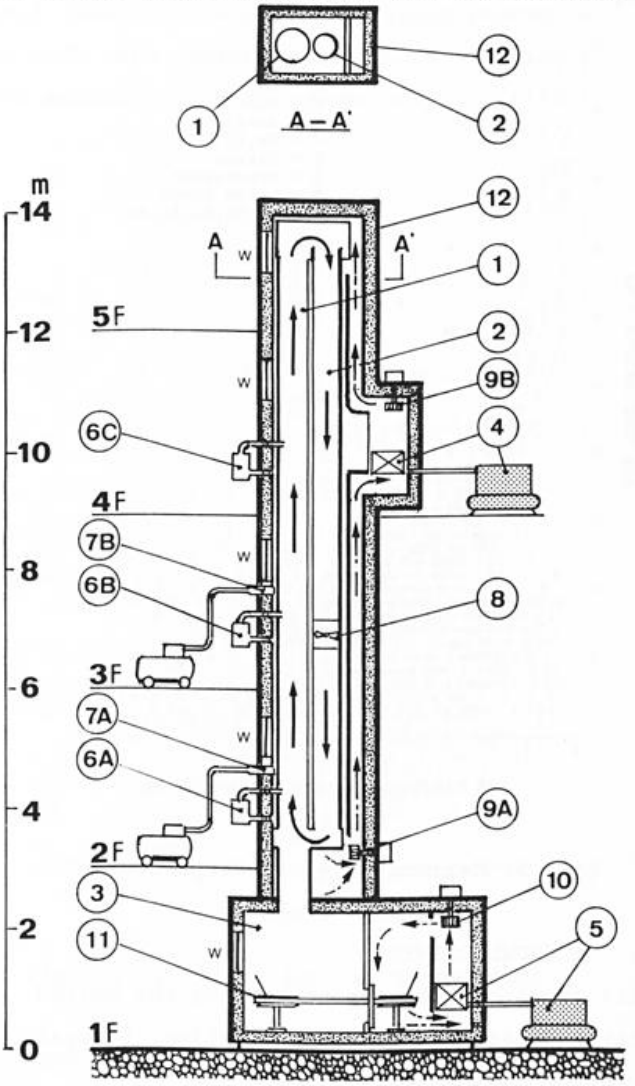


Fig. 1: The vertical wind-tunnel
1. Snowfall tunnel, 2. Return air duct, 3. Test room, 4 and 5. Temperature regulators, 6. Ultrasonic atomizers A, B, C, 7. Seeding devices, 8,9 and 10. Fans, 11. Table, W. Window.

compressed air through one of the injection nozzles (for instance, 1 sec every 3 min). The speed of airstream is controlled in the range from 4 to 120 cm/s by regulating rotational speed of the fan ⑧. Air stream is warmed in the top part of the tunnel to prevent ice crystals and snowflakes from circulating through the return air duct and growing again in the snowfall tunnel.

3. EXPERIMENTAL

The result of a preliminary experiment showed that features of snowfall varied markedly with the change of environmental parameters such as cloud temperature, upward airstream speed, seeding rate, the rate of supply of water etc. For instance, when the speed of upward air current was changed properly in accordance with the growth of snow particles, keeping other parameters constant, snow crystals and snowflakes of sizes larger than those formed when air speed was kept constant were formed. In the present paper, the result of experiments on snowfall from supercooled clouds of different significant temperatures, -4, -7, -15, and -20 C will be described. The values of environmental parameters other than cloud temperature were kept constant as follows,
The speed of upward airstream: 10 cm/s,
The rate of water supply: 0.3 cc/s,
The seeding rate: 600 ml of compressed ($8\ Kg/cm^2$) air in 1 sec every 3 min.
The mass of snowflakes fallen onto a plate of the size 25.5 x 20.1 ($512.55\ cm^2$) was measuered with an electronic balance on which the plate mounted horizontally. Measured values were printed out every 1 min by a printer. Snowfall process was watched through the windows on the wall of the tunnel and recorded continuously.
Fig. 2 shows a sample of snowflakes from clouds of -15 C. Fig. 3 shows photomicrographs of snowflakes formed in clouds of temperatures described above. These microphotographs shows the three-dimentional structures and constituent single crystals and frozen cloud droplets.

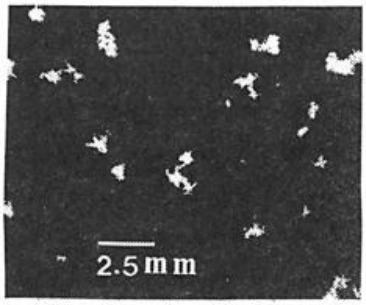


Fig. 2: Snowflakes
Cloud temperature: -15 C

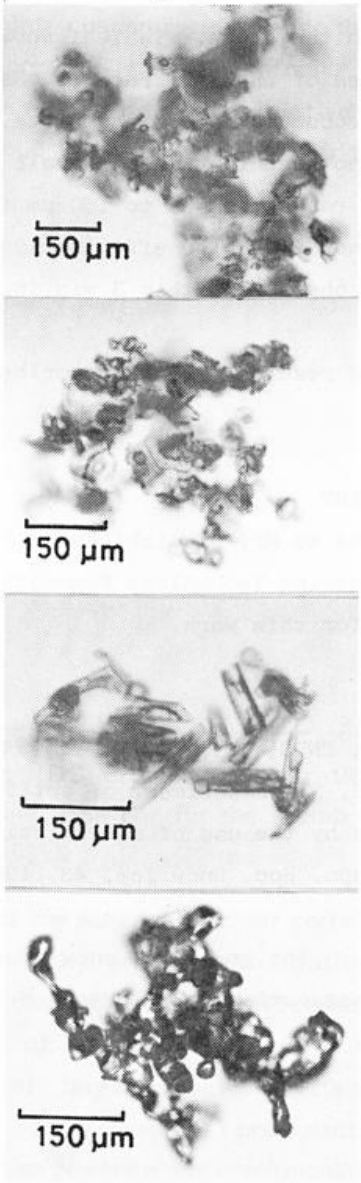


Fig. 3: Photomicrographs of snowflakes
Upward air speed: 10 cm/s
Cloud temperaturue: (a) -20, (b) -15, (c) -7 and (d) -4 C.
Predominant shapes of constituent single ice crystals; (a)Hexagonal plate, (b) Sector and star, (c) Sheath, (d) Hexagonal plate.

The temperature dependence of the shapes of the constituent crystals in snowflakes examined almostly coinsides with that expected from Kobayashi' diagram (Kobayashi 1961, P. 1363).
Fig. 4 shows the increase of mass of snowflakes accumulated on the plate with the elapse of time. The maximum rate of snowfall occured at about -15 C.
Fig. 5 shows the increase of depth of accumulated snow on the plate. Table 1 shows the average values of snowfall rate in mass and the rate of accumulation on the plate.
It is to be noticed that ice crystals of the sizes in the range from 50 to 150 μm aggregated and formed snow flakes so efficiently that snowfall was observed within 3 min in the test room.
More detailed results will be described elsewhere.

ACKNOWLEDGEMENT

Thanks are due to Mr. Nagaichi Suga, President of Suga Weathering Technology Foundation for his support for this work.

REFERENCES

FURUKAWA, Y., ENDO, T., MIZUNO, Y., NARUSE, K. and TAKAHASHI, T: Experiment of artificial snow crystals by the use of a vertical wind tunnel, J. Japn. Soc. Snow Ice, 43 (1980), 147-150.

KOBAYASHI, T.: The growth of snow crystals at low supersaturation, phil. Mag., 6 (1961), 1363-1370.

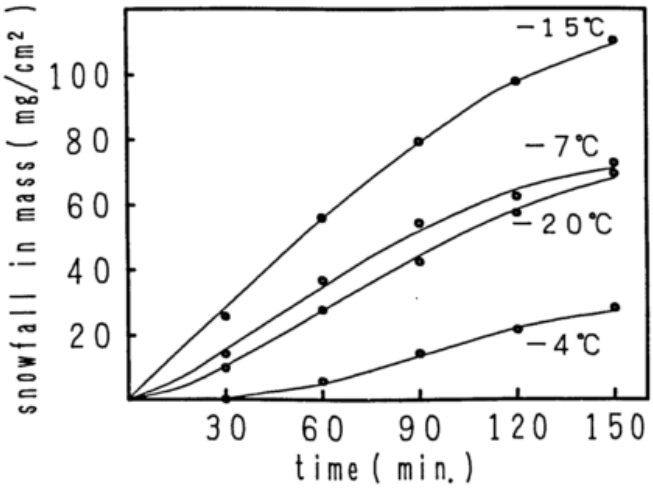


Fig. 4: Rate of snowfall
Ordinate: Accumulated mass (mg/cm^2)
Abcissa: Time after seeding

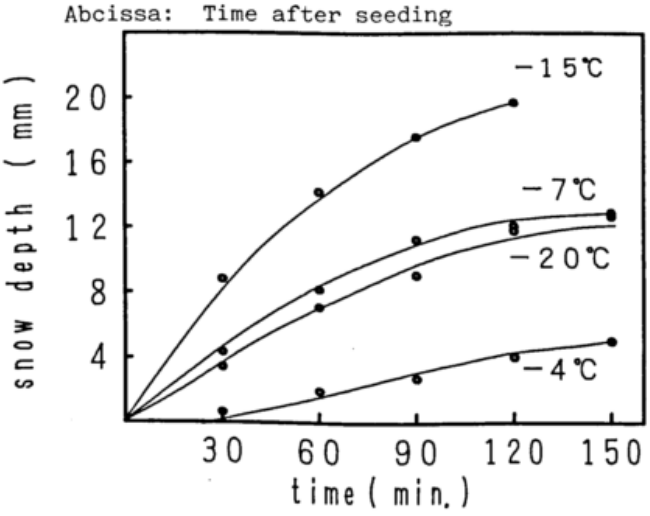


Fig. 5: Depth of accumulated snow

Cloud temperature (C)	Snowfall rate (mg/cm^2hr)	Accumulation (mm/hr)
-4	11	2
-7	29	5
-15	44	10
-20	28	5

Table 1: Average values of snowfall and snow accumulation

PROPERTIES OF THE PRECIPITATION EMBRYOS EVOLUTION IN CHARACTERISTIC HAWAIAN BANDCLOUDS

Arlette RIGAUD, Elizabeth HICKS, Jacqueline GAGNEUX, Constantin PONTIKIS

Météorologie Nationale EERM/CRPA
78470 Magny les Hameaux (FRANCE)

1- INTRODUCTION

The formation of precipitation-sized drops in warm convective clouds depends upon the existence of droplets in the radii range between 20μm and 50μm. Although the growth of droplets with radii <20μm through water vapor diffusion, collision and coalescence is negligible, they seem to be present in concentrations high enough to enhance precipitation even in non precipitating clouds. This fact is particularly observed in tropical and subtropical warm convective clouds.

In this work the formation and evolution of droplets in the radii range 20-75μm (1DC probe range) are studied for clouds observed during the Joint Hawaiian Warm Rain Project (JHWRP 1985). During this experiment, cloud bands generated by the low level convergence between the trade wind flow and the nocturnal land breeze have been sampled at different levels. That allows the analysis of the 1DC probe 10HZ measurements according to the cloud depth.

2- MICROPHYSICAL DATA

The measurements were made by using the FSSP device for droplets with radii between 0 and 22μm, and the 1DC probe for those with radii between 5 and 75μm. As the 1DC probe spectral bins partially overlap the FSSP ones, the analysis presented here concerns the 1DC classes 4 to 13. The comparison between liquid water contents observed by the Johnson-Williams device and those calculated by the FSSP shows that the FSSP underestimated the observed droplet radii. This is probably due to excessive corrections in order to take into account the FSSP artificial broadening. For this analysis we suppose that the observed spectral distributions in the FSSP and 1DC are correct.

3- GENERAL AND MEAN CHARACTERISTICS

Most of the clouds observed during this experiment were precipitating. They contained significant concentrations of droplets in the 1DC range above the 850mb level. There is no correlation between the FSSP droplet concentrations and the 1DC ones. Figure 1 presents the 1DC droplet concentration plotted against the FSSP one relative to the 765mb level of cloud 9 (10 july 1985). The data show great

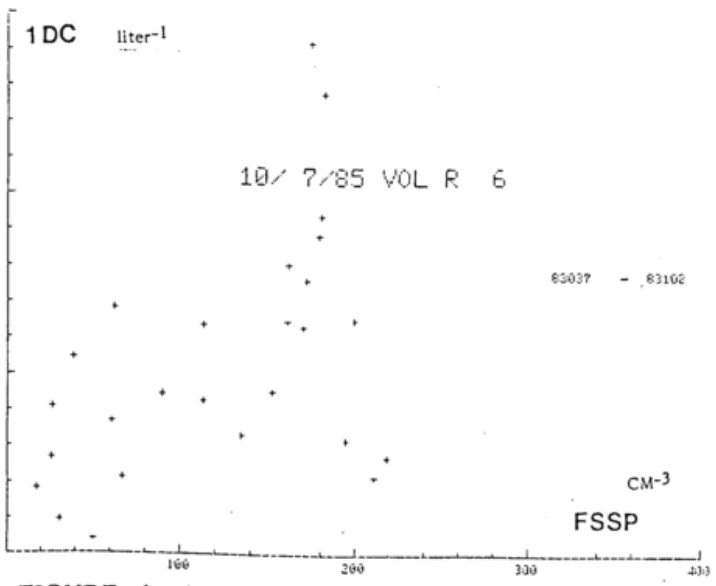


FIGURE 1: 1DC droplet concentration versus the corresponding FSSP one for the 765mb level of cloud 9 (10 July 1985).

scatter and the absence of clear correlation between the FSSP and 1DC droplet concentrations could result from the excessive FSSP corrections or from the production of droplets in the 1DC range through break-up of larger drops (R>120μm). Figure 2 presents the mean precipitation embryo concentration $\bar{N}$ versus the corresponding level height from cloud base ΔZ for all clouds observed during 10 instrumented flights. The behavior of the $\bar{N}$-ΔZ points can be represented by using an empirical formula : $\bar{N} = A.\ \Delta Z^B$. For the observations reported in figure 2 the values of A and B coefficients were respectively .26 and 5.

4- PRECIPITATION EMBRYO FORMATION

The precipitation embryo formation (1DC range) has been investigated by using the data series concerning

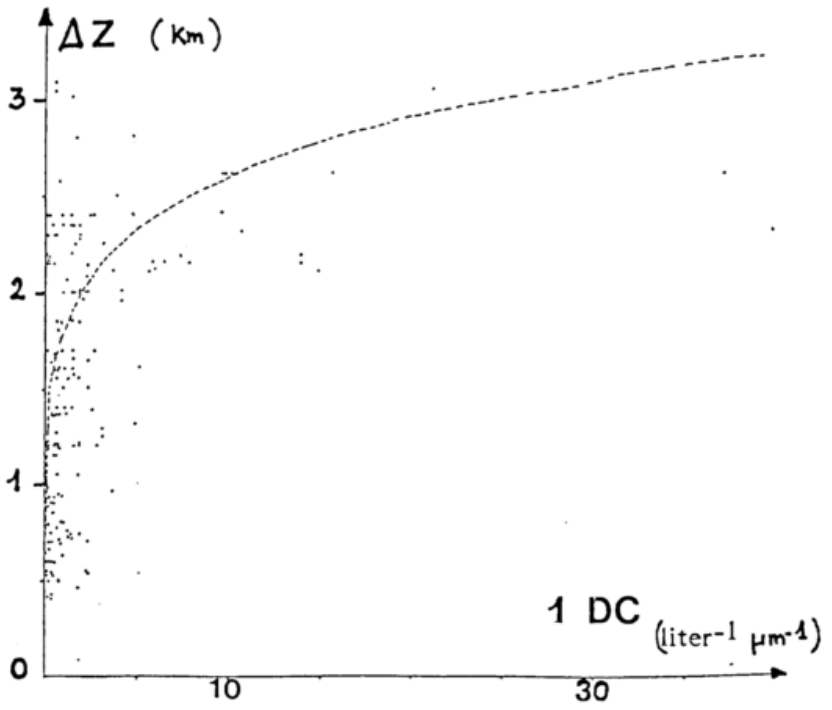


FIGURE 2: Mean 1DC droplet concentration as a function of height above cloud base for all sampled levels during 10 instrumented flights.

respectively cloud 8 sampled on 10 July 1985 and clouds 10 and 11 sampled on 19 July 1985. Clouds 10 and 11 were non precipitating with low 1DC droplet concentrations ($N_{1DC} < 0.05$ liter^{-1}). In order to exclude partially the possible 1DC range droplet production through breaak-up of larger drops (R>120um) in cloud 8, in which precipitating elements were present at upper levels, only data concerning the lower levels have been taken into account. Table 1 presents the observed mean microphysical level characteristics for these clouds. The cloud top altitude for the non precipitating ones was at 800mb while the precipitating cloud grew up to 700mb. The cloud base characteristics were :

P=937mb, t=17.9°C, Q=14g/Kg for clouds 10 and 11 (19 July 1985)

P=957mb, t=20.3°C, Q=15.8g/Kg for cloud 8 (10 July 1985).

The observed 1DC spectral distributions were non continuous for most of the observed samples. For exemple figures 3a and 3b present characteristic distributions with 3 populated classes. For all distributions the number of simultaneously populated classes varied between 1 and 5. No relation between spectral concentrations corresponding to different 1DC spectral bins was observed. The frequency of a non zero concentration in a given 1DC class is plotted versus the corresponding class number in figures 4a and 4b. The random character of spectral concentrations in the 1DC radii range in both cloud types (precipitating and non precipitating) seems to be in agreement with the stochastic evolution of

TABLE 1

P (mb)	FSSP (cm^{-3})	1DC (l^{-1})	P (mb)	FSSP (cm^{-3})	1DC (l^{-1})	P (mb)	FSSP (cm^{-3})	1DC (l^{-1})
698	71424	213	825	118692	1	805	73767	2
737	82605	97	857	47007	1	836	71295	1
741	74166	102	892	121788	1	866	39387	2
781	110943	59	901	87243	1	901	68265	0.6
827	112866	7	916	111168	0	926	87402	0
877	116220	4	922	67926	0	934	143805	0
928	31551	3	934	64770	0.6			
954	15759	1	936	91059	0			
	Cloud 8			Cloud 10			Cloud 11	

droplet growth through collision and coalescence. In these clouds during the first stage of the precipitation embryo formation, some droplets with large radii in the FSSP range could have grown stochastically through collision and coalescence beyond the 20μm growth limit up to the 1DC large radii classes.The observed 1DC droplet concentrations in the non precipitating clouds and in the non precipitating lower levels of the precipitating clouds are similar. They are larger than the 10^{-3} l^{-1} limit necessary to models to develop precipitation. (Jonas and Mason, 1974, Pruppacher and Klett, 1980). Probably all oceanic warm convective clouds in tropical and subtropical latitudes develop 1DC range precipitation embryos. However only those for which the vertical extend exceeds a lower limit (in this case approximately equal to 1000m) are capable of producing precipitation sized drops leading to warm rain. This fact is in good agreement with observations made in Guadeloupe (French West Indies) which lead to a linear dependance between precipitation and cloud thickness (Pontikis and al.,1983).

5- CONCLUSION

The 1DC data analysis shows that the mean vertical concentration of the corresponding droplets can be represented using an empirical relation $\bar{N} = N(\Delta Z)$ where ΔZ is the height above cloud base for some Hawaiian warm convective clouds observed during JHWRP 1985. Further the analysis leads to the conclusion that the 1DC droplet concentrations even in non precipitating clouds are larger than the lower limit necessary to produce precipitation in models. Therefore the vertical extend may play the main role in the warm rain production process in these clouds.

BIBLIOGRAPHY

JONAS P.R., MASON B.J. (1974) The evolution of droplets spectra by condenstion and coalescence in cumulus clouds. Quart.J.R.Met.Soc. 100, 286-295

PONTIKIS C., RIGAUD A., ASSELIN C., PESIN E. (1983) A 1D warm convective cloud model and precipitation measurements in Guadeloupe. A.M.S. 5th Conf. Hydromet. Tulsa, October 17-19

PRUPPACHER H.R., KLETT J.D. (1980) Microphysics of clouds and precipitation.

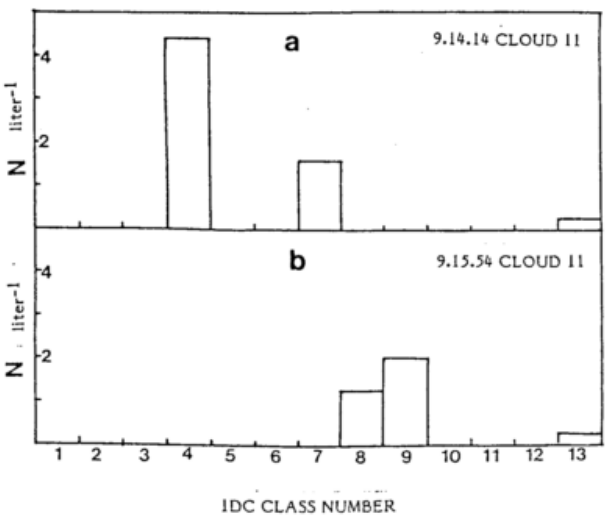


FIGURE 3(a,b): Characteristic discontinuous 1DC droplet spectral distributions observed in the percipitating cloud 11 (19 July 1985).

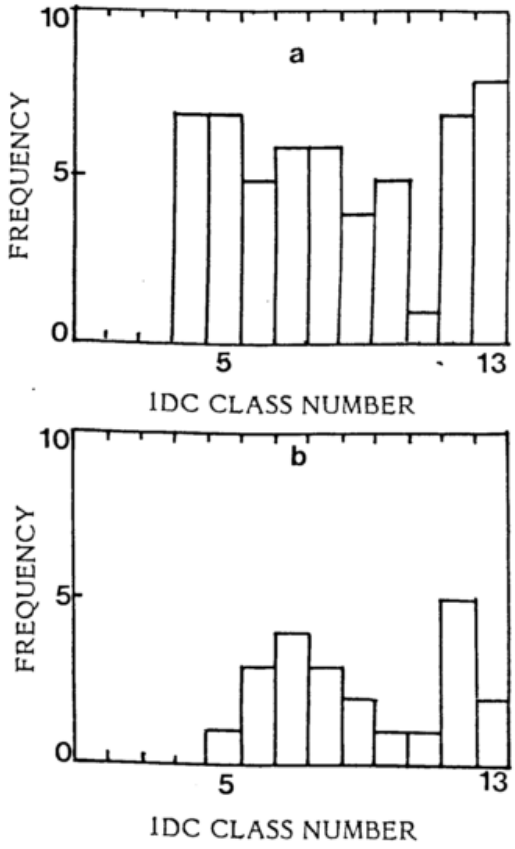


FIGURE 4(a,b): Frequency of non zero concentrations in the 1DC classes versus the corresponding class number.a)non precipitating clouds 10 and 11, b)precipitating cloud 8.

PATTERN OF AIR BUBBLE INCLUSIONS IN ATMOSPHERIC ICE FORMED DURING ACCRETION GROWTH

Pascal GRIBELIN, Pascal PERSONNE, Harumi ISAKA
L.A.M.P., U.A. CNRS n° 267, Université de Clermont II, B.P. 45, 63170 Aubière (France)

I. INTRODUCTION

Examination of thin sections of accreted ice deposits formed on fixed cylinders often shows the existence of well-organized channels of air bubble inclusions (KIDDER and CARTE, 1964 ; LAFORTE et al., 1984). By understanding how this pattern of air inclusions is formed, we may gain some physical insight into the growth process and physical structure of accreted ice.

For this purpose, riming experiments were carried out in an open wind tunnel located at the top of the Puy de Dôme mountain (1500 MSL). Fixed cylindrical rods of different diameters (from 0.3 to 5.0 cm) were used as rime collector for different environmental conditions and for different airflow speeds (from 20 to 60 m/s).

Experimental analysis of air inclusion channels has been supplemented by simulating the formation of the channels by means of a simple ballistic model of aggregation growth. These simulations show that statistical fluctuations and shadowing of droplet impingement are one of the important processes conditioning physical structure of rime deposits.

2. CHARACTERISTICS OF AIR INCLUSION CHANNELS IN ACCRETED ICE

Figure 1 represents an example of thin section of an ice deposit showing channels of air inclusions. These channels are distributed almost symetrically on both sides of a central zone without organized air inclusions. Detailed examination shows that these channels are formed by large elongated air bubbles almost linearly arranged. Characteristics of these channels, for example their convex or concave curvature with respect to the direction of airflow at infinite upstream, may depend on a number of physical factors such as cylinder diameter, airflow speed, cloud conditions, etc ...

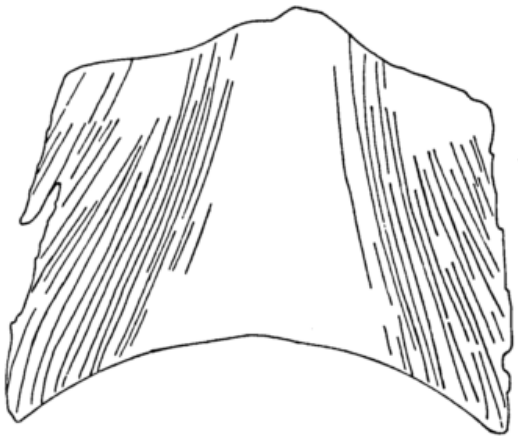


Figure 1 : Schematic representation of the thin section of an ice deposit formed on a fixed cylinder of 2.25 cm diameter (Ta = -8.9°C, liquid water content of 0.35 g m^{-3}, Va= 39 $m s^{-1}$, after 35 min. exposure time).

The surface temperature (Ts) of the rime deposits was estimated by resolving the local heat balance equation with experimental data (droplet spectrum, airflow speed, ...). This showed that the zones with air inclusions generally have a negative surface temperature corresponding to a dry growth regime. However, no organized air inclusion has been observed in the central zone of the rime deposits even if the calculated surface temperature remained negative over the whole cylinder surface. Consequently, some dynamical mechanisms of aggregation must be taken into account to explain the formation of these organized air inclusions.

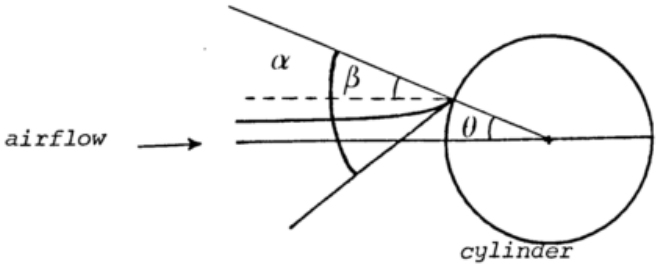


Figure 2 : Definition of the different angles :
- θ angular position on the cylinder surface ;
- β orientation of air inclusion channel ;
- α angle of droplet impingement.

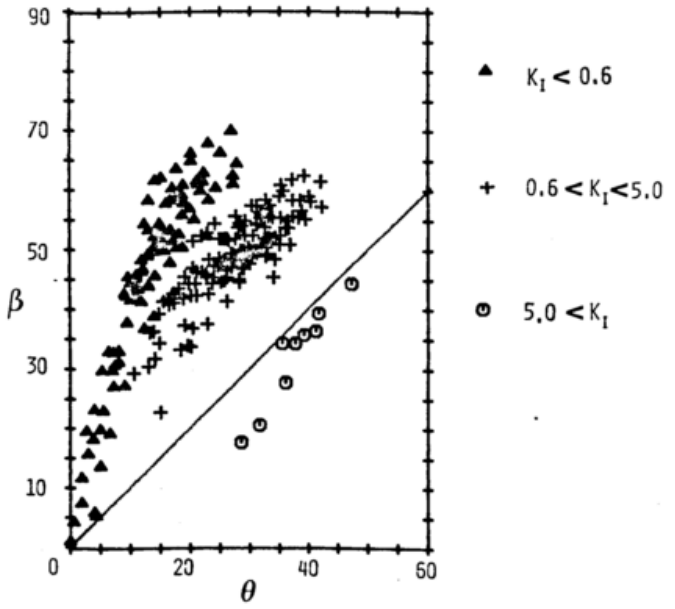


Figure 3 : Orientation β as a function of the angle θ on the cylinder for different ranges of the inertial parameter Ki.

3. ORIENTATION OF AIR INCLUSION CHANNELS

The orientation of air inclusion channels with respect to the ice surface is analysed. Since we could not always determine the form of the rime deposits during accretion growth, we have estimated the orientation β of the channels, defined as shown in Figure 2, at the interface ice-cylinder. Figure 3 shows the orientation of channels as function of the angular position θ on the cylinder surface. All experimental points can be classified in three categories according to the range of values of the inertial parameter defined by LANGMUIR and BLODGETT (1946).

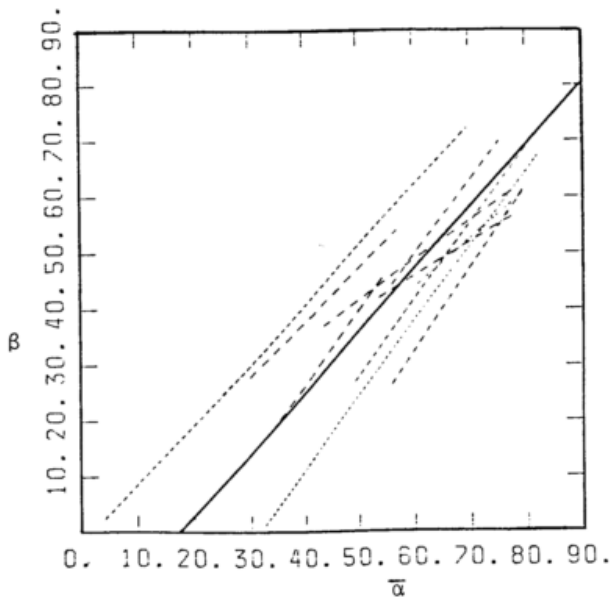


Figure 4 : Orientation β as a function of weighted mean impinging angle $\bar{\alpha}$ (the straight line represents the linear regression for all tests).

This dependence upon the inertial parameter suggests an influence of the direction of droplet impinging on the orientation of air inclusion channels. So, we have represented this orientation as a function of the mean impinging angle estimated for each droplet spectrum (Fig. 4). On this figure, the different dotted lines represent each test in its corresponding range of angles of droplet impingement and channel orientation, and the full line represents the mean regression relation corresponding to :

$$\beta = 1.1\alpha - 18°9 \qquad (1)$$

4. SIMULATION OF THE FORMATION OF AIR INCLUSION CHANNELS WITH A BALLISTIC MODEL

Working on the problems of vapor deposition of thin films of both metals and insulators, RAMANLAL and SANDER (1985) have simulated columnar microstructure of metal deposits with a ballistic model. Hence, the formation of air inclusion channels has been simulated by applying a similar ballistic model. Figures 5a and 5b represent examples of aggregates obtained by the ballistic model, on a plane, for two different angles of droplet impingement 0° (5a) and 80° (5b). On Figure 5a, no well-developed air inclusion organization can be

found, while a very definite channel organization appears on Figure 5b ; this seems to correspond to the absence of air inclusion channels in the central zone of rime deposits, mentioned above as one of the experimental findings. The orientation of channels as a function of the angle of impingement which is found can be given by :

$$\beta = \alpha - 13° \qquad (2)$$

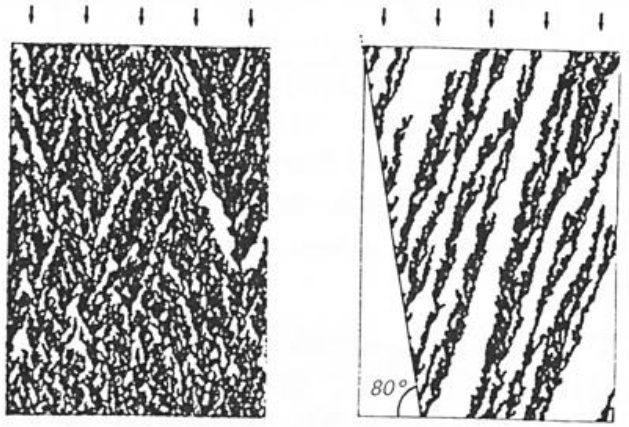


Figure 5 : Simulation of aggregates, on a plane, with ballistic model. The droplets come from the top to the bottom for :
a) an impinging angle of 0°
b) an impinging angle of 80°.

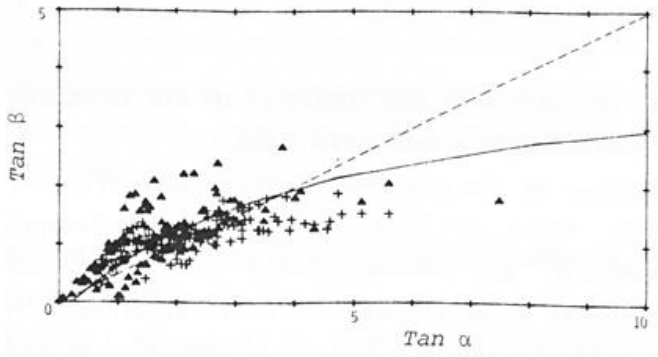


Figure 6 : Orientation β of channels as a function of the impinging angle α (— ballistic relation, --- Ramanlal-Sander relation). Different symbols represent experimental points corresponding to the 3 ranges of the inertial parameter.

This relation differs significantly from that proposed by RAMANLAL and SANDER :

$$\tan \beta = 1/2 \tan \alpha \qquad (3)$$

The comparison of these relations with the experimental results (see Fig. 6) shows that, in spite of the dispersion, relation (2) fits better experimental points than the RAMANLAL and SANDER's relation (3).

5. CONCLUSION

The pattern formed by air bubble inclusions, in accreted ice deposits, obtained under dry growth conditions, shows a quasi-linear arrangement, like channels. The orientation of channels of air inclusions is strongly dependent upon the experimental conditions and can be classified according to the value of the inertial parameter.

An analysis of simulation with a ballistic model shows that the columnar growth of aggregates occurs as results of a statistical fluctuation and a shadowing of droplet impingement. The angle of channel orientation is found experimentally to vary linearly as a function of the angle of droplet impingement ; this experimental result agrees well with the result of simulation study.

6. REFERENCES

KIDDER, R.E. and A.E. CARTE, 1964 : Structures of artificial hailstones. J. de Rech. Atmos., 4, 169-181.

LAFORTE, J.L., L.C. PHAN and N.D. DU, 1984 : Preliminary investigation on effect of wind speed fluctuations on ice accretion grown on fixed and rotating aluminium conductor. Second International Workshop on Atmospheric Icing of Structures, Trondheim, Norvège.

LANGMUIR, I. and K.B. BLODGETT, 1946 : Mathematical investigation of water droplet trajectories. G.E. Report, R.L. 244, Reprinted in Collected works of I. Langmuir, Pergamon Press, 335-393.

RAMANLAL, P. and L.M. SANDER, 1985 : Theory of ballistic aggregation. Phys. Rev. Lett., 54, 1828-1931.

ANALYSIS OF HAILSTONES FROM A SEVERE STORM AND THEIR SIMULATED EVOLUTION

Laura Levi* and Luisa Lubart

Servicio Meteorológico Nacional-Buenos Aires-Argentina

*Comisión Nacional de Energía Atómica-Consejo Nacional de Investigaciones Científicas y Técnicas

1 INTRODUCTION

Numerical models of hail growth have been applied in previuos works,in order to investigate the favourable conditions to the development of hailstones or to follow hail trajectories inside storms about which there was wide information obtained by aircraft penetrations, radar observations,etc.(Orville and Kopp,1977; Heymsfield,1983).

In this work,an attempt is made to obtain the possible trajectories and environmental conditions for hailstones with a structure derived from the crystallographic analysis of a stone sample.With this purpose,a growth model is applied in a simulated updraft,the parameters of which are adjusted so to obtain the expected trajectories.

2 THE MODEL

INPUT DATA:Initial particle radius Ro,density ρo and altitude Ho;cloud drop radius r=10μm; assumed time dependent functions for LWC and for either the vertical particle speed ΔV or the updraft speed W.

CALCULATED PARAMETERS:Drag coefficient C_d and terminal speed V;altitude H and ambient temperature Ta;surface temperature Ts;droplet impact speed Vi and rime density ρr;particle radius R;derived value for either W or ΔV.

Well known equations have been used to calculate most parameters.We only point out that: a) The rime density has been calculated from Heymsfield and Pflaum(1985) or from Prodi and Levi(1986),according to the range of the impact parameter rVi/Ts. b) The drag coefficient has been calculated from Heymsfield and Kajikawa(1987)for graupels and from Beard's equation for spherical particles,such as liquid drops and frozen drop embryos.The limit value C_d=0.55 has been used. c) The relation between H and Ta has been derived from the application of the Hirsch Model to the radiosounding data.

3 THE HAILSTONE SAMPLE

The sample of 163 large stones,3-5cm in size, was collected in Córdoba on 17 November 1981. The stone typically consisted of an embryo,a few millimeters in size,and of two successive main layers,respectively formed by transparent ice and large or medium size crystals(mean dimension range 2-0.5mm) and by opaque ice and small crystals 0.3 - 0.1mm in size.In a few cases opaque ice and small crystals prevailed in the whole structure.Most of the embryos were graupels but about 30% consisted of frozen drops 3 to 5mm in diameter.All frozen drops were surrounded by a thin opaque ice layer formed by small crystals.The graupel embryos had different shapes,conical or rounded. They usually consisted of opaque ice and small or medium size crystals.The structure of two typical stones,is shown in Fig.1.

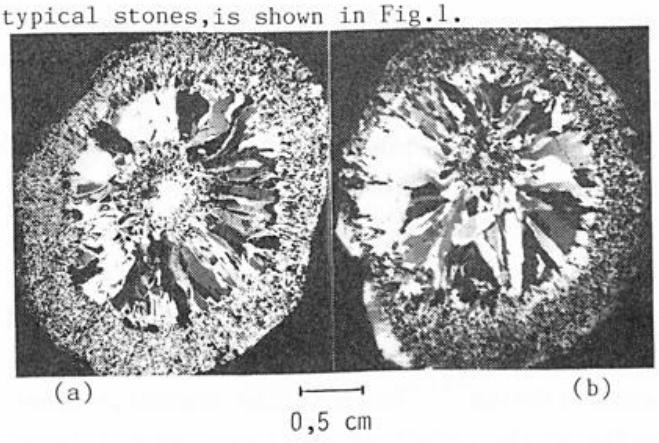


Fig.1. Typical hailstones of the studied storm
(a) FD embryo (b) Graupel embryo

4 MODEL APPLICATION

4.1 HAILSTONES GROWN ON FROZEN DROP EMBRYOS

The model was first applied to simulate the growth of hailstones showing a frozen drop embryo (FD), because this was considered convenient to obtain useful information from its crystalline structure. An example of the parameter evolution for a hailstone of this type is given in Fig.2.

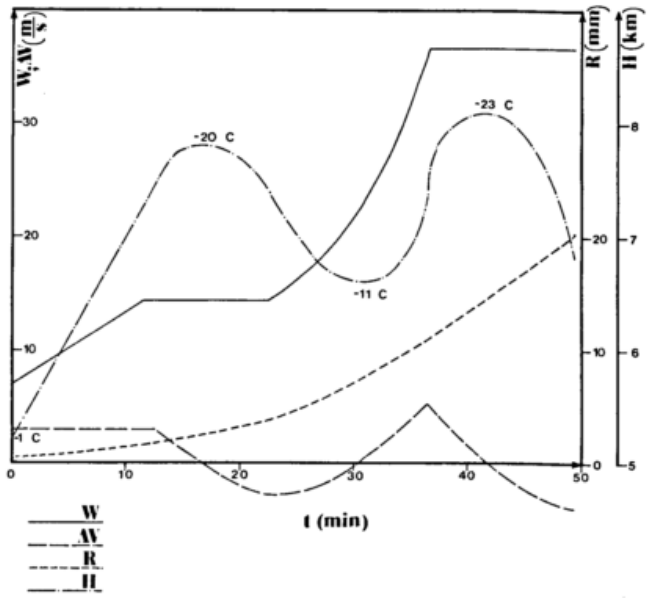


Fig.2. Parameter evolution for a FD embryo hailstone, initialized from a drop of Ro=0.4mm

The curves have been obtained for an initial raindrop of Ro=0.4mm, attaining a radius R=1.5mm at the level were it freezes. The upward motion of the drop was regulated so that this radius was reached at a temperature where the freezing probability for drops of this size is high (Vali and Stansbury, 1966) and where subsequent rime could consist of opaque ice and small crystals (Levi and Prodi, 1978). This conditions were satisfied by letting the drop freeze at Ta≅-15ºC and then continue its ascent up to Ta≅-20ºC. In order to satisfy the condition of dry growth at low Ts, it was assumed LWC=1gm^{-3}. The particle descent, responsible of the growth of the large crystal layer was simulated by keeping W at the value reached during the initial ascent, in the present case W=14ms^{-1}. Finally, ΔV was made to increase again to simulate the last ascent of the particle, during which the structure changed to small crystals. Since the main growth layers showed some evidence of wet growth, during this period LWC was augmented to 2gm^{3}, so that the enhanced growth rate of the particle, together with the larger values of ΔV, caused a rapid increase of W to about 35ms^{-1}.

4.2 HAILSTONES GROWN ON GRAUPEL EMBRYOS

The information that could be derived from the structure of graupels was more vague than that derived from frozen drop embryos. However, it could be noted that most of these embryos consisted of ice accreted about a small growth center with dimensions d $\lesssim$ 1mm. In the model, graupels were made to grow about particles of different densities, injected in the updraft at different altitudes. In all cases, the value of ΔV was regulated so that the level where Ta≅-20ºC was attained during the first minutes of the simulation, thus justifying the small crystal structure of most embryos. The growth of the succesive main layers formed by large and by small crystals was subsequently simulated, as in the case of the FD example. The evolution of W or ΔV were, however, different due to the different evolution of V. For instance, for a process beginning on an ice particle of radius Ro=0.5mm and density ρo=0.6gcm^{-3}, it was found that, to initiate the particle descent determining the transition from the embryo to the large crystal layer, the increase of the updraft had to be stopped when W=11ms^{-1}. This value is about 3ms^{-1} lower than that found for growth on a FD embryo. However, this relatively small difference is large enough to show that, if the assumed graupel would have been made to grow in the updraft calculated for the case of the FD embryo, the particle would have continued its ascent in the cloud growing as a small crystal structure all through. At this respect, it must be noted that the different evolution of V obtained for graupels is mainly determined by the different

X-Re relationship used to evaluate C_D. According to Heymsfield and Kajikawa (1978),this relationship gives an increase of C_D in the range $Re \sim 10^3$-10^4, which dependens on the shape and fall mode of the graupel. The free fall speed could consequently vary in this range for particles growing on different embryos,so that particles introduced in the same updraft could follow trajectories more or less different from that of those growing on FD embryos.

5 DISCUSSION AND CONCLUSIONS

The simulated hailstone trajectories indicate that the growth process, initialized at the stage where the embryos are formed,should have lasted about 50 minutes. This time could have been reduced if a larger LWC were assumed.However,the value LWC=$1gm^3$, used for the first part of the trajectories,was imposed by the structural characteristics of the initial rime layers.

According to the results,the stone would have grown during the first 30 minutes in a cloud zone where it was $W \leq 15ms^{-1}$,that is possibly in a feeder cell. During the last growth period, W had to be rapidly increased up to about $35ms^{-1}$, what shows that the hailstones attained the edge of the main updraft. Since,according to the Hirsch Model applied to the radiosounding (Saluzzi,1984),the updraft reached a maximum value $W=42ms^{-1}$, this fact agrees whith the assumption that the hailstones arrived at the edge of the main updraft,surrounding without crossing its center.

The stone analysis and the model application indicate that,during the growth period preceding the arrival at the main updraft,trajectories could have been located at quite different altitudes. This is shown by the structure variety of the main layers following the embryo and is supported by the observation that the C_D values can vary with the embryo shape and fall mode,determining important changes in the free fall speed of the particle.

In the present case the typical stucture shown in Fig.1 indicates that, out of the main updraft, the hailstones trajectories were more densely distributed at low levels where it was $-10 \geq Ta \geq -18$ºC. However,a cloud thickness of about 2km could have been interested in the phenomenon.

AKNOWLEDGMENTS. The authors are indebted to J.Moin for technical help and to the National Reseaech Council of Argentina for financial support.

REFERENCES

HEYMSFIELD,A.J.: Case Study of a Hailstorm in Colorado. Part IV: Graupel and Hail Growth Mechanisms Deduced through Particle Trajectory Calculations.J.Atmos.Sci.(1983),40,1482-1505.

HEYMSFIELD,A.J.;PFLAUM,J.C.: A Quantitative Assessment of the Accuracy of Thechniques for Calculating Graupel Growth.J.Atmos.Sci.(1985), 42,2264-2274.

HEYMSFIELD,A.J.;KAJIKAWA,M.: An Improved Approach to Calculating Terminal Velocities of Plate-like Crystals and Graupel.J.Atmos.Sci. (1987),44,1088-1099.

LEVI,L.;PRODI,F.: Crystal Size in Ice Grown by Droplet Accretion. J.Atmos.Sci.(1978),35, 2181-2189.

ORVILLE,H.D.;KOPP,F.J.: Numerical Simulation of the Life Story of a Hailstorm.J.Atmos.Sci. (1977),33,1596-1618.

PRODI,F.;LEVI,L.:Density and Surface Structure of Ice Accretions. J.de Physique (1987),48, C1-383.

VALI,G.;STANSBURY,E.J.: Time-Dependent Characteristics of the Heterogeneous Nucleation of Ice. Canadian J.Phys.(1966),44,477-502.

THE COLLECTION EFFICIENCIES OF SOFT-HAILSTONES FOR SUPER-COOLED WATER DROPLETS AND ICE CRYSTALS

W D Keith and C P R Saunders

Physics Dept., UMIST, Manchester, UK

1. INTRODUCTION

Theoretical studies of the collection efficiencies of hailstones for super-cooled water droplets and ice crystals have been limited by the difficulties arising from the rough nature of the surface of a riming soft-hailstone, by the non-spherical symmetry of ice crystals and, in the ice crystal case, by a lack of knowledge of the adhesion efficiency.

Laboratory studies have been performed to measure the increase, above the theoretical value, in the number of droplets collected by the rime surface under various conditions. The collision efficiency of a target for ice crystals was measured directly by comparing the number of ice crystals on the target with that number on a slide whose collision and adhesion efficiency was 100%.

2. EXPERIMENTAL PROCEDURE

The equations of motion of spherical particles around a smooth cylinder has been modelled by Ranz and Wong (1952) and Loffler and Muhr (1972) and others. However, these equations cannot be accurately applied to a riming hailstone due to the rough nature of the surface. A cloud of salt solution droplets of known size and concentration was drawn past a 5mm diameter target which had previously been rimed with pure water droplets. The volume of salt droplets in the pure rime was determined by measuring the conductivity of the rime. This volume was then compared with the theoretical volume predicted by the Loffler and Muhr equations. These experiments were repeated at various temperatures for impact speeds of 3 and 5 m/s.

The collision efficiency of a cylindrical target for ice crystals was measured directly with a modified formvar technique, (Keith 1987). An ice crystal cloud was drawn past a dry formvar target of diameter 5 mm at velocities ranging from 3 to 5 m/s. The number of crystals on the target was compared with the number on a wet microscope slide, taken at the same time, which had a collision and adhesion efficiency of 100%. The dry target simulated a soft-hailstone whose adhesion efficiency is less than unity. These experiments were performed at -6 and -10^{o}C with column and plate type crystals respectively. Further experiments were performed to determine the separation probability. Two identical targets, one dry- and one wet-formvar covered, were exposed to the crystal cloud and the separation probability was determined from the number of crystals on the targets.

3. RESULTS AND DISCUSSION

The salt water droplet experiments have shown that the collection efficiency of a target is enhanced by

the presence of rime on the surface. Macklin (1962) detailed extensively the nature of the riming surface under various conditions and showed that at warm temperatures (-5°C) the target was covered in clear ice whereas at colder temperatures, rime feathers could be seen protruding out from the surface. The nature of the rime is also dependent on the droplet impact velocity; at higher speeds the droplets spread on impact and the feather growth was inhibited. In these experiments, the volume collected at -5°C (3 m/s) and -8°C (5 m/s) was close to the theoretical value. Thus, this value is taken as zero and the relative increase in volume collected due to the presence of the rime feathers is shown as a function of temperature in Figure 1. It can be seen that at low speeds where feather growth is enhanced, the volume collected increases substantially at low temperatures. At higher speeds the feather growth is inhibited and the target surface remains effectively smooth with little increase in the volume collected at colder temperatures. The equivalent collector is defined as that smooth collector diameter which would theoretically collect the same volume as in the experiment. At 3 m/s this diameter is 3.2 mm whereas at 5 m/s the diameter is 4.8 mm compared with the actual diameter of 5 mm.

The collision efficiency of a target for ice crystals was found to increase from 0 to 100% at 3 m/s as the crystal size increased from 0 to about 80 μm. The target had a slightly higher collision efficiency for a plate crystal than for a column crystal of the same size. The collision

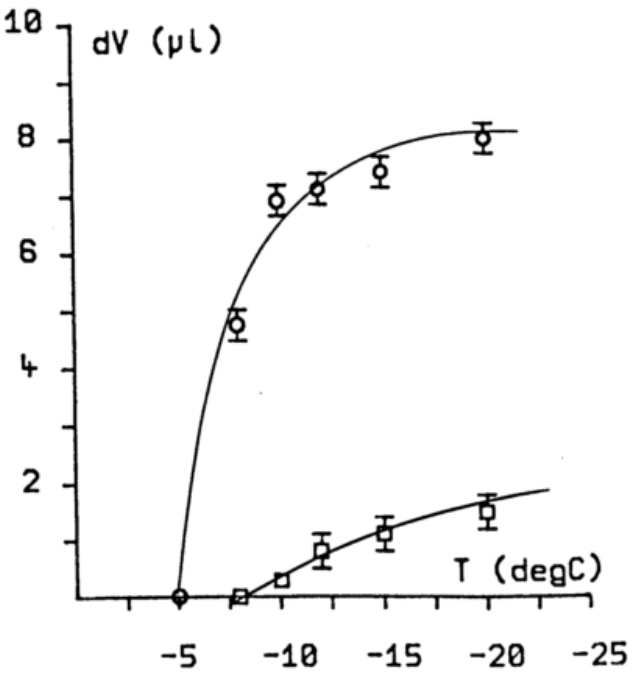


Fig.1: Volume of salt droplets collected as a function of temperature.

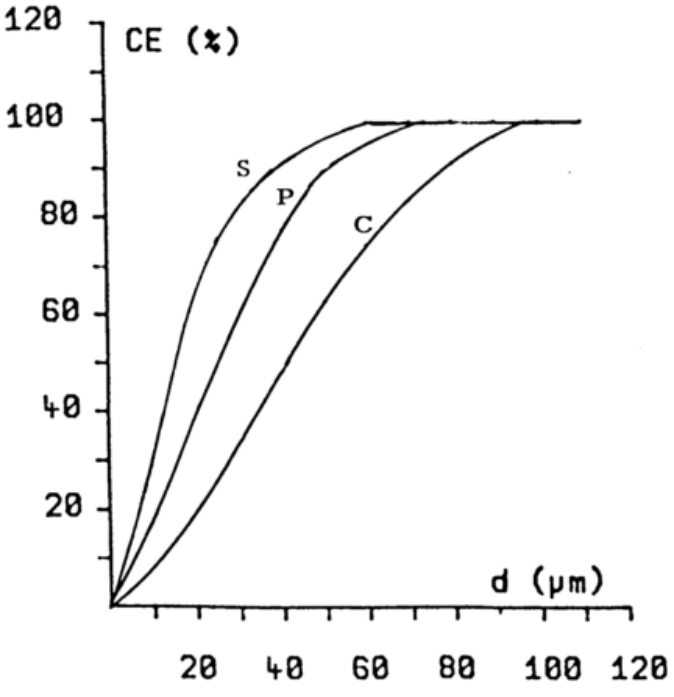


Fig.2: Collision efficiency as a function of particle diameter for spheres (S) plates (P) and columns (C).

iency increased with an increase in impact velocity and a decrease in target diameter. Figure 2 shows the collision efficiency for a 5 mm target as a function of particle size at 3 m/s for spheres (calculated from the Loffler and Muhr equations), plate and column ice crystals. The Loffler and Muhr equations would tend to overestimate the collision efficiency if the ice crystals were idealised to spheres. The separation probability was found to increase with crystal diameter and ranged from 0.1 to 0.5 for crystal sizes in the range 40 to 500 μm at 3 m/s. The collection efficiency, which is a function of the collision efficiency and the separation probability, was a maximum for crystals of diameter 100 μm at 3 m/s. This is due to the collision efficiency being 100% for larger sizes whereas the separation probability increases with crystal diameter.

4. CONCLUSION

These studies have shown that the theoretical collision efficiency equations cannot be accurately applied to a target with a rough surface as the equations will tend to underestimate the efficiency of capture. Calculations show, however, that the growth rate of a hailstone by riming is only increased by 6-18% in the temperature range -5 to -20°C at an impact speed of 3 m/s. At 5 m/s, the increase is around 2%. The collision efficiency of a target for ice crystals has been determined for the first time . The efficiency is less than 100% for small ice crystals and the efficiency is lower for column ice crystals than for plate ice crystals.

KEITH, W.D.: Thunderstorm Electrification. Ph.D. Thesis. UMIST, Manchester. (1987)

LOFFLER, F.; MUHR,W.: Die Abscheidung von Feststoffteilchen und Tropfen an Kreiszylindern infolge von Tragheitskreften. Chemie Ing-Techn 44 (1972), 510-514.

MACKLIN, W.C.: Density and Structure of Ice formed by Accretion. Q.J.R.M.S. 87 (1962) 30-50.

RANZ ,W.E.:WONG,J.B.: Impaction of Dust and Smoke Particles on Surface and Body Collectors. Indus. Eng. Chem. 44 (1952) 1371-1381.

SIMULATION OF CONICAL GRAUPEL BY USING A BALLISTIC MODEL

Pascal PERSONNE, Christophe DUROURE and Harumi ISAKA

L.A.M.P., U.A. CNRS n° 267, B.P. 45, 63170 Aubière (France)

1. INTRODUCTION

A number of ground-level and aircraft observations has been reported, for almost a hundred years, the existence of graupel of conical form among natural precipitation particles (BARKOW, 1908 ; NAKAYA and TERADA, 1935 ; MAGONO, 1953 ; ZIKMUNDA and VALI, 1972 ; BRINGI et al., 1984). Because of their particular form, cloud physicists have long been interested in understanding how and in what conditions riming process can lead to the formation of graupel of such a specific form. However, there is still no well established theory of conical graupel formation.

The purpose of this study is to try to gain some insight into the growth mechanism of rime deposits, i.e. to clarify to what extent the aggregation process determines by itself the form of rime deposits. The aggregate growth was simulated by means of simple 2D and 3D ballistic models, some characteristics of the form of simulated aggregates were compared with those of the rime deposits obtained in icing wind tunnel.

2. CHARACTERISTICS OF SIMULATED AND EXPERIMENTAL OBSERVED FAN-LIKE RIME DEPOSITS

Ballistic models have been developed recently to analyse physical properties of aggregates (FAMILY and VICSEK, 1985 ; LIMAYE and AMRITKAR, 1986 ; RAMANLAL and SANDER , 1985). In these models, impinging particles follow rectilinear trajectories from their randomly selected initial positions towards the growing aggregate ; as soon as a particle touches a point of the growing aggregate, the particle is integrated into the aggregate at the very point of contact. Impinging particles may or may not be deformed as they are integrated into the aggregate ; the present model supposes no deformation. When compared with the growth mechanism of real rime, the ballistic models might appear too simplified to simulate the actual rime growth, because they do not take into account, for example, the effects of the freezing process, the airflow deformation around the aggregate, etc. In spite of this, the application of ballistic models to the rime growth seems to be interesting, since it provides a very useful tool to separate characteristics from others depending upon aggregation process. Figures 1-a and 1-b represent a rime deposit grown from an initial

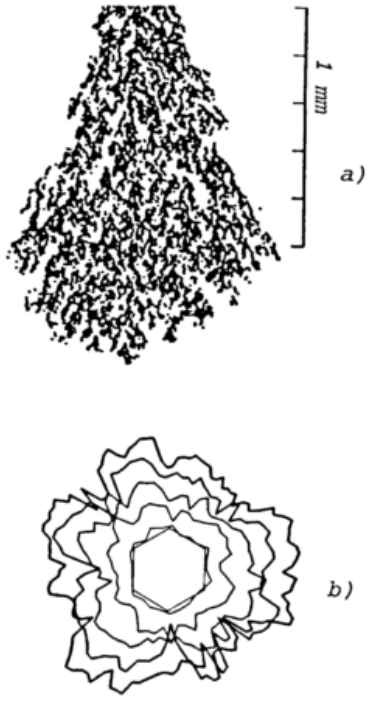


Fig.1: Conical aggregate simulated with a 3D ballistic model starting with an hexagonal plate of 300 µm diameter (after collection of 168500 droplets of 10 µm diameter)
a) Cross-section parallel to particle trajectories (20 µm thick)
b) Surface contours at 5 different heights (indicated on the scale in a)).

hexagonal plate by using a 3D ballistic model ; particle trajectories are rectilinear from bottom to top. The cross section of the deposit parallel to the droplet trajectories (Fig. 1-a) shows fanning out growth with fine open internal structure. The surface contours of the deposit at 5 different heights, shown in Fig. 1-b, are highly irregular. These characteristics are quite similar to those observed on real conical graupel.

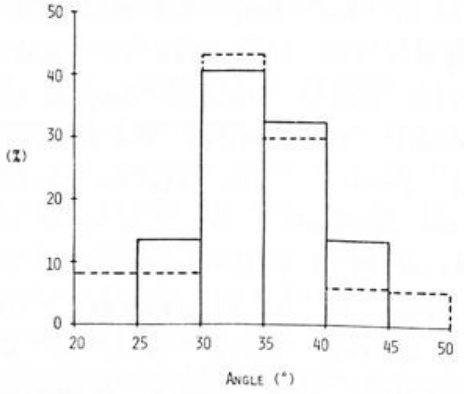


Fig.2 : Histograms of the apex angle of simulated and experimentally observed fan-like rime.
Solid line : experimentally observed,
Broken line : simulated.

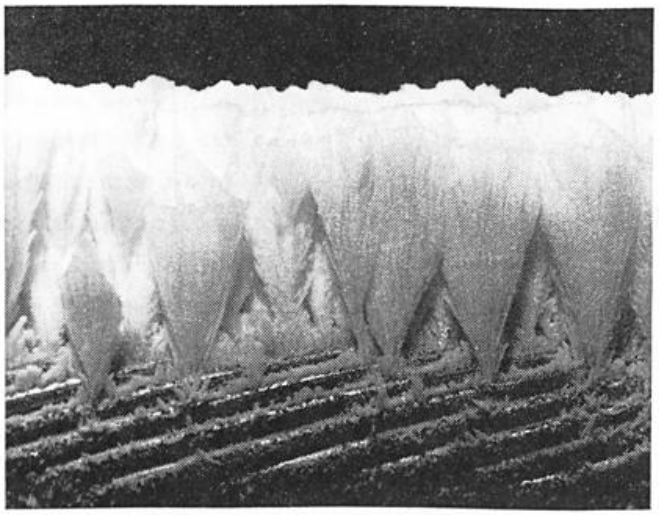


Fig.3 : Fan-like rime deposits obtained in icing wind tunnel.

The angle of fanning out may be considered as one of the basic characteristics of the aggregate growth. Figure 2 represents two histograms of this angle, the one determined from fan-like rimes obtained from icing wind tunnel experiments (Fig.3) and the other determined from fan-like deposits grown from an initial point with a 2D ballistic model. Since no noticeable difference of the apex angle was found between the 2D and 3D models, we used for these statistics the 2D model which is less computer-time consuming that the 3D one. These histograms show a good agreement of the apex angle between observed and simulated fan-like deposits ; most frequent values of the angle are around 35° for both cases. These simulations suggest that the basic form of the aggregation growth is fan-like (2D) or conical (3D) deposits with their base faced towards impinging particles. Hence, any deviation from this form should be considered as effects of other processes such as the non-instantaneous freezing or the flow deformation, which are not taken into account in the ballistic model. Any definite conclusion cannot be actually drawn on these subjects. Nevertheless, any significant variation of the apex angle was not found for a temperature range from -4 to -15°C of our icing experiment ; this seems to indicate that the freezing process does not affect very much this angle as far as the characteristic time of freezing is short enough. The flow deformation should have important effect on the form of the rime deposit. One of the present authors, P. PERSONNE, analysed the form of the deposit as a function of the inertial parameter defined by LANGMUIR and BLODGETT (1946) ; according to preliminary results of this analysis, the fanning out configuration of the rime growth seems to be more probable than the pointing into wind growth for normal conditions of conical graupel formation.

3. EFFECTS OF THE PARTICLE OSCILLATION ON THE APEX ANGLE

Wind tunnel experiments indicate that a conical particle starts an oscillating motion beyond a critical Reynolds number. Some cloud physicists, for example DONG and HALLETT (1986), suggested that such motion favours fanning out growth of conical graupel. In order to investigate effect of such a motion on the growth of fan-like or conical deposits, we simulated the aggregate growth with the 2D ballistic model, in which

the direction of impinging particles varies according to a normal distribution with the average angle of 0° and a fixed standard deviation. Figures 4-a, 4-b and 4-c represent the aggregates obtained for 3 different standard deviations, respectively of 10, 25 and 40°. The aggregates, simulated for standard deviations of 10 and 25°, grow into fan-like deposits with apex angle of 40 and 70°, which the aggregate for standard deviation of 40° loses completely its fan-like feature. These results imply that the amplitude of oscillating motion should be relatively small so that conical graupel might maintain its conical feature. The standard deviation of the orientation of conical graupel we estimated from 2D images published by BRINGI et al. (1984) is of the order of 12°, which seems to confirm relatively small amplitude of actual oscillating motion of conical graupel for their very existence. As for the apex angle, observed values vary in the range from 30 to 90°, which is quite similar to that from 30 to 70° obtained by the 2D ballistic model.

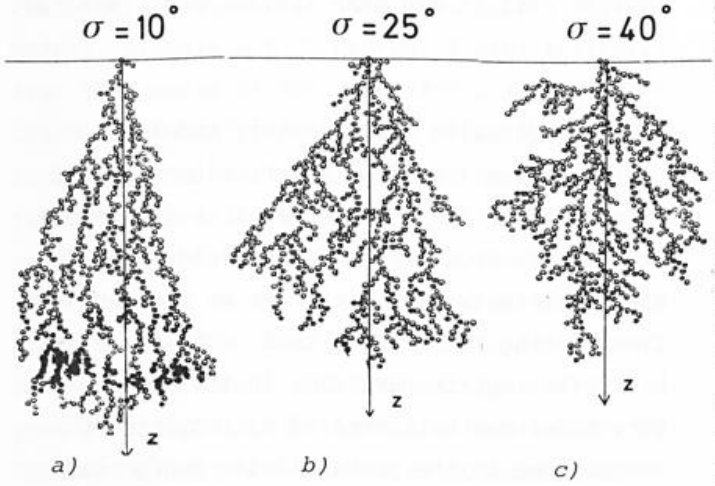


Fig.4 : Effects of oscillating motion of aggregates on their form.
a) : Standard deviation = 10°
b) : Standard deviation = 25°
c) : Standard deviation = 40°.

4. CONCLUSION

This study shows that, in spite of their much simplified physics, 2D and 3D ballistic models of aggregation can reproduce some basic characteristics of fan-like and conical rime growth. Further comparison of simulated and observed rime growth, under various growth conditions, may provide a way to appreciate influences of other physical processes on the growth mechanism of rime. In this way, the ballistic models of aggregation can be considered as a useful analytical tool in the study of rime growth.

5. REFERENCES

BARKOW, E., 1908 : Zur Entstehung der Graupeln. Meteror. Zeit. Vol. 25, 456.

BRINGI, V.N., T.A. SELIGA and W.A. COOPER, 1984 : Analysis of aircraft hydrometeor spectra and differential reflectivity radar measurements during cooperative convective precipitation experiment. Radio Sci., Vol. 19, 157-167.

DONG, Y.Y. and J. HALLETT, 1986 : Structure, fall orientation, and secondary ice formation by graupel, Proc. 23rd Conference on Radar Meteorology/Cloud Physics, Snowmass, Colorado, sept. 121-124.

FAMILY, F. and T. VICSEK, 1985 : Scaling of the active zone in the Eden process on percolation networks and the ballistic deposition model. J. Math. Gen., vol. 18, 175-181.

LANGMUIR, I. and K.B. BLODGETT, 1946 : Mathematical investigation of water droplet trajectories. Collected work of I. LANGMUIR, Pergamon Press, 335-393.

LIMAYE, A.V. and R.E. AMRITKAR, 1986 : Theory of growth of ballistic aggregates, Phys. Rev. A, Vol. 34, 5085-5090.

MAGONO, C., 1953 : On the growth of snow flake and graupel. Sci. Report of the Yokohama National University. Sec. I, n° 2, 18-40. Reprinted in Selected Papers of C. MAGONO in 1980.

NAKAYA, U. and T. TERADA, 1935 : Simultaneous observations of the mass, falling velocity and form of individual snow crystals. J. Fac. Sci. Hokkaido University. Ser. II, Vol. 1, n° 7, 191-200.

RAMANLAL, P. and L.M. SANDER, 1985 : Theory of ballistic aggregation. Phys. Rev. Lett., 54, 1828-1831.

ZIKMUNDA, J. and G. VALI, 1972 : Fall patterns and fall velocities of rimed ice crystals. J. Atmos. Sci., Vol. 29, 1334-1347.

COMPARISON OF MODEL RESULTS FOR MODELS OF DIFFERING MICROPHYSICAL DETAIL

R. D. Farley and H. D. Orville

Institute of Atmospheric Sciences
South Dakota School of Mines and Technology
Rapid City, South Dakota 57701-3995

1. INTRODUCTION

The Institute of Atmospheric Sciences has a longstanding interest in the hail problem dating back to the mid 1960's. Numerical modeling of hailstorms and hailstone growth has been a major facet of the research work. The models have evolved over the years to address different problem areas related to hailstorm research. One primary concern of our group has been to use cloud models to test hail suppression concepts. Towards that end, we have employed two versions of the same basic model -- a relatively simple model employing bulk water parameterization techniques which is used mainly for diagnostic purposes, and a hybrid form of the parameterized model which treats the precipitating ice field as twenty discrete size categories allowing for more in depth studies of hail growth processes and possible responses to seeding strategies. In this study we examine the similarities and differences in the results of these models applied to various storm types.

2. DESCRIPTION OF THE MODELS

The two models used in this study are identical except for their microphysical detail. Both models are two-dimensional, time-dependent cloud scale models with slab symmetry. The models are anelastic and use a vorticity (stream function) approach to obtain the velocity field, rather than using the primitive equations. ORVILLE and KOPP (1977) and CHEN and ORVILLE (1980) provide additional information on the dynamic framework of the models.

The simpler of these models is the bulk water model which is based on concepts suggested by KESSLER (1969). This model divides water and ice hydrometeors into five classes: cloud water, cloud ice, rain, snow and high density precipitating ice (graupel/hail). Rain, snow and graupel/hail, which are assumed to follow inverse exponential size distributions, possess appreciable terminal fall velocities. Cloud water and cloud ice have zero terminal velocities and thus travel with the air parcels. These five classes of hydrometeors interact with each other and water vapor through a variety of crude parameterizations of the physical processes of condensation/evaporation, collision/coalescence and collision/aggregation, accretion, freezing, melting and deposition/sublimation. The microphysical processes and parameterizations employed in the bulk water model are discussed in detail WISNER et al. (1972), ORVILLE and KOPP (1977), and LIN et al. (1983).

The more detailed hail category model also parameterizes the cloud water, cloud ice and rain fields. The difference is in the treatment of the precipitating ice field which is divided into twenty categories of ice particles ranging from 100 μm to 5 cm in diameter. Precipitating ice particles in the hail category model may be generated as frozen drop embryos due to the probabilistic and/or contact freezing of rain, and by the creation of embryos of ice origin via the Bergeron-Findeisen process and the aggregation of cloud ice crystals. Subsequent growth of the existing ice particle population is based on wet and dry growth concepts applied to the continuous accretion process. Sublimation and melting of the ice particles may also occur. Shedding of excess water during wet growth and melting are also allowed in both models. For more infor-

mation on the hail category model the reader is referred to FARLEY and ORVILLE (1986) and FARLEY (1987).

3. EXPERIMENTAL CASES

Both models have been exercised on four different storm cases, aspects of which have been reported elsewhere. Two of the cases are severe hailstorms from the CCOPE project in eastern Montana -- the severe supercellular hailstorm of 2 August 1981 which was reported earlier by FARLEY (1986) and the storm of 1 August 1981 which displayed characteristics of both multicellular and supercell type storms and is discussed in greater detail in KUBESH et al. (1988). A different class of hailstorm, but also from the High Plains region, is a moderate multicellular hailstorm from the Alberta Hail Project. This is the storm of 26 July 1983 discussed in FARLEY (1987). The final case is a maritime storm from Wallops Island, Virginia on 13 September 1983.

4. RESULTS

In terms of large scale structure, dynamic features and evolution, the results of the two models maintain a high degree of similarity over the course of the simulations for all four cases. Downdrafts tend to be slightly stronger in the hybrid model simulations, particularly for the severe storms which produce heavy precipitation. Temporal differences become more apparent in the later stages of the simulations due to the cumulative effects of differences in the growth and sedimentation of the precipitating ice field and the interaction of the precipitation shaft and associated downdraft with the boundary layer. These differences are most evident for the weaker Alberta case, especially regarding the character and evolution of the feeder cell.

For all three continental cases, maximum and domain totals of cloud water and cloud ice tend to be higher in the hybrid model whereas the tendencies for the precipitating particles show greater variability. The two CCOPE hailstorms generally show less rain and more precipitating ice in the hybrid model. The Alberta case consistently indicates greater precipitating ice in the hybrid model with no clear tendency for the rain. Results of both models for the maritime case display a greater degree of consistency.

Some of the aspects discussed above are indicated in Table 1 which presents the maximum values of the water contents and draft speeds. Also listed in Table 1 are the maximum radar reflectivity factors predicted by the models; these are consistently lower for the hybrid model due to differences in the treatment of ice physics. For the moderate Alberta hailstorm, the bulk model overestimates the reflectivity compared to observations whereas the hybrid model tends to underestimate the reflectivity for the storms which produce significant amounts of giant hail.

The production of precipitation, both precipitating ice and rain, is more efficient in the bulk model for the continental cases. Comparable domain totals in the earlier stages occur about 2 min later in the hybrid model. As the storm evolves this time lag increases to 4 to 5 min. After precipitation development has matured (after about 30 min) this time lag may be eliminated. The maritime case, which originates as a liquid process, does not display this time lag. For the continental cases the dominant precipitation mechanism is accretional growth of ice. Subsequent melting of the ice is the major source of rain in these cases. Accretional growth of rain is generally of secondary importance accounting for from 10 to 40% of the rain produced. The percentage is generally higher in the hybrid model because contact freezing of rain is less efficient. The maritime case is considerably different, with accretional growth of rain accounting for nearly 60% of the rain. Evaporative losses range from 15 to 30%.

The high degree of consistency in model results

TABLE 1: COMPARISON OF MODEL RESULTS

QUANTITY		ALBERTA BULK	ALBERTA DTLD	CCOPE 2 AUG BULK	CCOPE 2 AUG DTLD	CCOPE 1 AUG BULK	CCOPE 1 AUG DTLD	WALLOPS ISLAND BULK	WALLOPS ISLAND DTLD
EXTREME VALUES									
Maximum Cloud Water	(g/kg)	4.6	5.0	8.9	9.3	8.5	9.0	5.1	5.2
Maximum Cloud Ice	(g/kg)	1.5	1.5	5.2	6.0	6.8	8.5	1.6	1.4
Maximum Rain	(g/kg)	5.6	5.9	6.9	6.6	7.1	4.4	11.2	11.1
Maximum Precipitating Ice	(g/kg)	7.0	10.8	10.9	12.5	10.9	9.4	14.1	13.5
Maximum Updraft	(m/s)	25.2	31.5	54.3	56.6	50.0	49.9	30.6	31.3
Maximum Downdraft	(m/s)	13.9	13.5	28.6	28.8	25.9	25.1	17.3	21.0
Maximum Reflectivity Factor	(dBz)	70.5	60.1	70.9	63.4	69.4	60.1	75.0	65.4
SURFACE PRECIPITATION CHARACTERISTICS									
Peak Rainfall	(mm)	25.6	29.8	35.7	27.1	13.4	6.7	47.0	50.2
Integrated Rain	(kT/km)	158.8	127.8	198.5	152.5	90.9	41.2	246.7	248.3
Peak Hailfall	(mm)	11.7	3.6	26.7	8.8	0.8	1.6	3.4	3.0
Integrated Hail	(kT/km)	47.9	15.7	66.0	32.1	2.4	5.4	6.5	7.1
Integrated Vapor Flux	(kT/km)	955.0	971.4	1998.0	2002.3	1547.4	1381.5	1761.6	1615.6
Precipitation Efficiency	(%)	21.6	14.8	13.2	9.2	6.0	3.4	14.4	15.8

for the maritime case is a result of the dominant role of rain (which is parameterized in both models) in the initiation and development of precipitation with precipitating ice mainly in the role of a temporary storage medium. The greater variability in the continental cases, on the other hand, is due to the more pronounced effect of differences in the treatment of ice physics since the dominant precipitation mechanism is via the ice phase.

Table 1 also summarizes the character of the surface precipitation at the end of the simulations. The surface accumulations of precipitation display considerable variability depending on the model used and the particular case. Rain accumulations are generally greater for the bulk model in the continental cases although the Alberta case indicates a greater maximum rainfall depth. Hail accumulations are greater in the bulk model for the Alberta case and the 2 August CCOPE storm whereas the hybrid model is more effective at putting hail on the ground for the 1 August CCOPE case. The maritime case is markedly different in that the hybrid model is slightly more effective in putting precipitation on the ground. The precipitation efficiency is higher in the bulk model except for the maritime case.

Acknowledgments. We would like to thank Ms. Carol Vande Bossche for her invaluable assistance in the preparation of the manuscript. This research was sponsored by the National Science Foundation, Division of Atmospheric Sciences, under Grants ATM-8516940 and ATM-8603308. The calculations were performed using the facilities of the Scientific Computing Division of the National Center for Atmospheric Research, which is sponsored by the National Science Foundation.

REFERENCES

CHEN, C-H.; ORVILLE, H. D.: Effects of mesoscale convergence on cloud convection. J. Appl. Meteor., 19, (1980) 256-274.

FARLEY, R. D.: Simulation of the 2 August 1981 CCOPE hailstorm. Proc. 1st Intn'l Cloud Modeling Workshop/Conference, Irsee, F.R.G., July 1985, (1986) 99-110.

FARLEY, R. D.: Numerical modeling of hailstorms and hailstone growth. Part III: Simulation of an Alberta hailstorm-natural and seeded cases. J. Climate Appl. Meteor., 26, (1987) 789-812.

FARLEY, R. D.; ORVILLE, H. D.: Numerical modeling of hailstorms and hailstone growth. Part I: Preliminary model verification and sensitivity test. J. Climate Appl. Meteor., 25, (1986) 2014-2035.

KESSLER, E.: On the distribution and continuity of water substance in atmospheric circulations. Meteor. Monogr., 10, (1969) No. 32, 84 pp.

KUBESH, R. J.; MUSIL, D. J.; FARLEY, R. D.; ORVILLE, H. D.: The 1 August 1981 CCOPE storm: observations and modeling results. [Accepted by J. Climate Appl. Meteor., 1988]

LIN, Y-L.; FARLEY, R. D.; ORVILLE, H. D.: Bulk parameterization of the snow field in a cloud model. J. Climate Appl. Meteor., 22, (1983) 1065-1092.

ORVILLE, H.D.; KOPP, F. J.: Numerical simulation of the life history of a hailstorm. J. Atmos. Sci., 34, (1977) 1569-1618.

WISNER, C. E.; ORVILLE, H. D.; MYERS, C. G.: A numerical model of a hail-bearing cloud. J. Atmos. Sci., 29, (1972) 1160-1181.

AIRBORNE "CLOUD SIEVING"

Edward E. Hindman*

Physics and Atmospheric Science Department
Drexel University
Philadelphia, PA 19143, USA

1. MOTIVATION

Preliminary measurements of pH as a function of cloud droplet size by Hindman and Borys (1987) revealed that large droplets were more acidic than expected. The larger droplets were expected to be more dilute due to greater water vapor condenstation. These results were based on data collected in supercooled clouds during March, 1985 at Mount Washington Observatory (MWO), NH and during December, 1986 at Storm Peak Laboratory (SPL) in the northern Colorado Rockies. The cloud water collections at MWO were made using the Langmuir multicylinder device described by Howe (1981). The results were recently confirmed by Rancourt and Howe (1987) from measurements also with the multicylinder at MWO.

Cloud water collections as a function of droplet size were made at SPL using cloud sieves. The sieves are essentially "scientific tennis racquets" as described by Hindman and Borys (1987). For example, the sieves collect about 2 g of cloud droplets with diameters greater than or equal to 3, 7, 11 and 16 μm in a period of five minutes from a cloud moving at 10 m/s and containing 0.1 g/ m^3 liquid water.

One unknown with the cloud water measurements reported by Borys, et al. (1987) and Hindman and Borys (1987) is how representative the SPL measurements are of free-stream conditions in the cloud above SPL. While it is not possible to collect cloud water a few hundred meters above SPL due to aircraft safety restrictions, it is possible to make airborne measurements further up in the cloud as well as in other superccooled clouds. Consequently, there is a need for an airborne cloud sieve.

Langmuir multicylinders have been used for airborne icing studies by Brun, et al. (1955). The device is essentially a stack of five cylinders which are rapidly rotated to produce an even coating of ice. In this note an airborne cloud sieve is designed which improves the multicylinder in that the sieves can collect nearly equal amounts of cloud water independent of droplet size thus enabling a thorough chemical analysis.

2. PROCEDURES

2.1 Analysis of the multicylinder

The amount of cloud water collected by the airborne multicylinder of Brun, et al. was determined from the dimensions of the cylinders, a cloud liquid water distribution and an air speed value. The dimensions of the multicylinders were: 0.3175, 1.27, 3.175, 7.62 and 10.795 cm in diameter and all five cylinders were 5.18 cm in length. The liquid water distribution for a typical SPL cloud is shown in Fig. 1. The droplet cut-off sizes for a given cylinder diameter and airspeed are given in Fig. 2. The data in Fig. 2 were developed by Hindman and Borys from the Brun, et al. collection efficiencies.

Brun, et al. illustrate their multicylinder mounted on a DC-3 which flys at about 60 m/s IAS. Thus, using Fig. 2 extrapolated lineraly to 60 m/s (134 mph), the droplet cut-off diameters for the cylinders would be 4, 8, 13, 23 and 27 μm, respectively. Using these diameters and liquid water values from Fig. 1, the magnitude of the liquid water impacting the cylinders would be 0.18, 0.14, 0.056, 0.002 and less than 0.001 g m^{-3}, respectively. The volume swept out by each cylinder, assuming a 50% collection efficiency and a 10 km wide cloud (estimated from airborne measurements above SPL by Rauber and Grant (1986)), would be 0.82, 3.29, 8.2, 19.8 and 28 m^3. Multiplying the values of water impacting the cylinders by the volume swept out by the cylinders produces the mass of cloud water expected to be collected by each cylinder; respectively, 0.15, 0.46, 0.46, 0.040 and less than 0.028 g.

It can be seen from these results that the multicylinder device will be unable to collect the minimum required 2 g of cloud water on each cylinder during a single pass through a cloud at SPL. Thus, the cylinder areas need to be adjusted so each cylinder collects about the same amount of water. The simplest way to accomplish this requirement is to increase the length of the cylinders. This procedure transforms the multicylinder device into a cloud sieve.

2.2 Development of the cloud sieves

To collect 2 g of cloud water with each cylinder of the multicylinder, the length of the cylinders need to increase by a factor of, respectively, 13.3, 4.3, 4.3, 50 and 71.4. This means the 5.18 cm long cylinders would have to increase from 0.0518 m to, respectively, 0.68, 0.22, 0.22, 2.59 and 3.70 m in length. Thus, the stack of cylinders for the airborne multicylinder would increase in height from 0.259 m to 7.41 m. Such a height is impractical for airborne use. Thus, each cylinder can be broken into a number of cylinders of the same diameter so that the stack of cylinders is manageable. Essentially, the long, single cylinder is broken into a series of cylinders which forms a square, or a "scientific jail window", if you will.

*On loan from the Atmospheric Science Department,
Colorado State University, Ft. Collins, CO 80523 USA

This modification transforms the multicylinder into a cloud sieve. The transformation will make spinning the cylinders unfeasible. Rather, the increased area of the "jail window" cylinders will permit short exposures and, hence, an even ice deposit at the stagnation point of each cylinder. Consequently, rotation of the cylinders will be unecessary.

As a result of transforming the multicylinder into a cloud sieve, the largest two cylinders were modified. It was found that the original 7.62 cm diameter cylinder had to be reduced to 5 cm to collect 2 g of water from a SPL cloud. Further, to collect 2 g of water using the 10.795 cm cylinder, the cross-section area had to be increased to 3000 cm^3, resulting in a cylinder 375 cm in length. This would require a 0.75 m square "jail window". Thus, this sieve was eliminated because the stack of five "jail window" sieves was judged to be impractical, at this time, for airborne use. The design of the airborne cloud sieve is depicted in Fig. 3.

3. SIEVE SIMULATIONS

The airborne cloud sieve in Fig. 3 was simulated to fly at 60 m/s IAS through a winter-mountain cloud of the type reported by Rauber and Grant (1986). The water content distribution for this cloud, which was derived from their 16 January 1982 size distribution data, is shown in Fig. 1. The mass (m) of ice collected by the sieves is given by the following relationship:

$$m\ (g) = l \cdot a \cdot E \cdot LWC \qquad (1)$$

where l (m) is the length of the liquid water region traversed, a (m^2) is the cross-sectional area of the sieve, E is the collection effficiency of the sieve (0.50) and LWC (g/m^3) is the liquid water intercepted by the sieve. The LWC value is determined knowing the droplet cut-size (Fig. 2) and the liquid water distribution of the cloud (Fig. 1). The value for l was 10 km based on the Rauber-Grant measurements. The values of a are given in Fig. 3 . The values of LWC were 0.26, 0.26, 0.23 and 0.08 g/m^3, respectively, intercepted by the smallest to the largest sieve. The resulting values of m for the sieves were as follows: 2.1, 3.9, 6.9 and 9.2 g.

The airborne cloud sieve also was simulated to fly through a summer cumulus congestus cloud of the type reported by Cerni (1983) for 19 June 1980. The water content distribution for this cloud is shown in Fig. 1. Using (1), assuming l = 2 km and the values of LWC intercepted by the smallest to the largest sieve were, respectively, 1.0, 0.99, 0.89,and 0.36 g/m^3, the resulting values of m for the sieves are: 1.6, 2.9, 5.4 and 8.3 g.

4. DISCUSSION

It can be seen form the sieve simulations that the airborne cloud sieve is expected to collect greater than about 2 g of cloud water with diameters greater than or equal to 4, 8, 13 and 18 μm. It was found that to collect 2 g of drops greater than or equal to 24 μm, the designed sieve was too large for practical airborne use.

The operation of the airborne cloud sieve is expected to be as follows. A sieve will be kept in a freezer in the aircraft at a temperature equal to the ambient temperature. When the cloud is entered, the sieve will be rapidly mounted and deployed from the aircraft on a track. As soon as the cloud is exited, the sieve will be quickly retrieved and placed back into the freezer. The sieve probably will not work at air temperatures warmer than -5C due to aerodynamic heating of the sieve to greater than 0C. A number of identical sieves will be stored in the freezer. The whole deployment-retrieval process will be repeated with another sieve for a subsequent cloud pass. Upon landing, the ice deposits on the sieves should be kept frozen until chemical analyses are performed (eg. pH, conductivity, cation, anion, etc.).

5. CONCLUSIONS

The Langmuir rotationg-multicylinder was simulated to "fly" through the low liquid water content, wintertime clouds which occur over the northern Colorado Rockies. It was calculated that the multicylinder would collect insufficient cloud water for thorough chemical analyses. Consequently, an airborne cloud sieve was designed consisting of a series of sets of non-rotating cylinders to collect drops greater than or equal to 4, 8, 13 and 18 μm in diameter. It was found that collecting droplets greater than about 24 μm with the sieve may be impractical. The series of cylinders was designed so each set collects larger droplets than the previous set, but each set collects a similar amount of cloud water.

The behavior of the airborne cloud sieve was simulated in winter mountain clouds and summer cumulus clouds. It was found the device should collect sufficient cloud water (~2 to 9 g) over a droplet diameter range of 4 to 18 μm to perform thorough chemical characterizations. Such chemical information is expected to be valuable for improving understanding of the "acidification" of cloud droplets and the optical properties of cloud droplets.

6. ACKNOWLEDGEMENTS

This work was a portion of the research supported by NSF grants ATM-87-15060 (Atmospheric Chemistry) Dr. R. Borys, PI and ATM-87-04776 (Experimental Meteorology) Prof. L. Grant, PI and ONR contract N00014-84-C-0591 (Appl. Res. & Tech. Dir.) Prof. W. Schubert, PI.

7. REFERENCES

BORYS, R.D.; HINDMAN, E.E.; DeMOTT, P.J.: *J. Atmos. Chem.* Submitted (1987).

BRUN, R.J.; et al.: National Advisory Committtee for Aeronautics, Report 1215. (1955) 43 pp.

CERNI, T.A.: *J. Clim. Appl. Meteor. 22* (1983) 1346-1355.

HOWE, J.B.: *Ppts. 2nd Conf. Mt. Meteor.*, Am. Meteor. Soc., Boston (1981).

HINDMAN, E.E.; BORYS, R.D.: *Ppts. 4th Conf. Mt. Meteor.*, Am. Meteor. Soc., Boston (1987) 241-245.

RANCOURT, K.L.; HOWE, J.B.: *Mt. Washington Observatory News Bulletin. 28* (1987) 48-52.

RAUBER, R.M.; GRANT, L.O.: *J. Clim. Appl. Meteor. 25* (1986) 489-504.

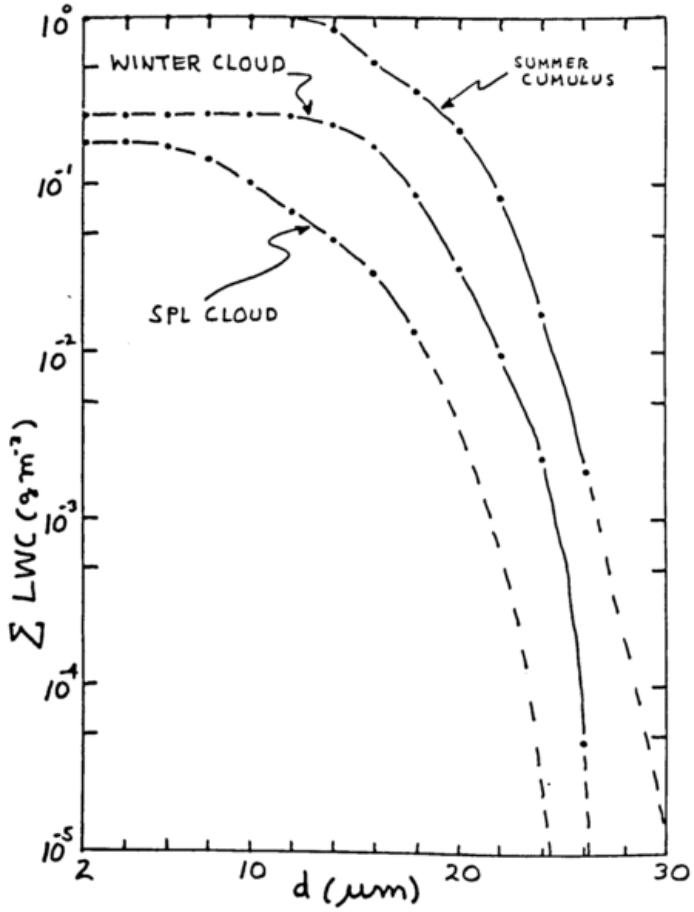


Fig. 1. Liquid water distributions from SPL clouds (from Hindman & Borys, 7-8 Jan 1985), a winter cloud (from Rauber and Grant, 16 Jan 1982) and a summer cumulus (from Cerni, 19 June 1980)

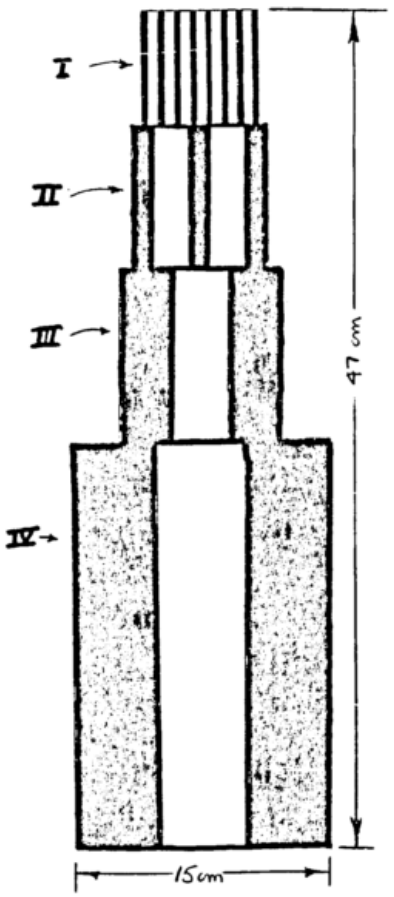


Fig. 3. Design of the airborne cloud sieve. The cylinder diameters (cm), cross-section areas (cm^2) and droplet cut-diameters (μm) at 60 m/s air speed are as follows: I-0.3, 16.1, 4; II-1.27, 29.72, 8; III-3.18, 60.33, 13 and IV-5.00, 230, 18.

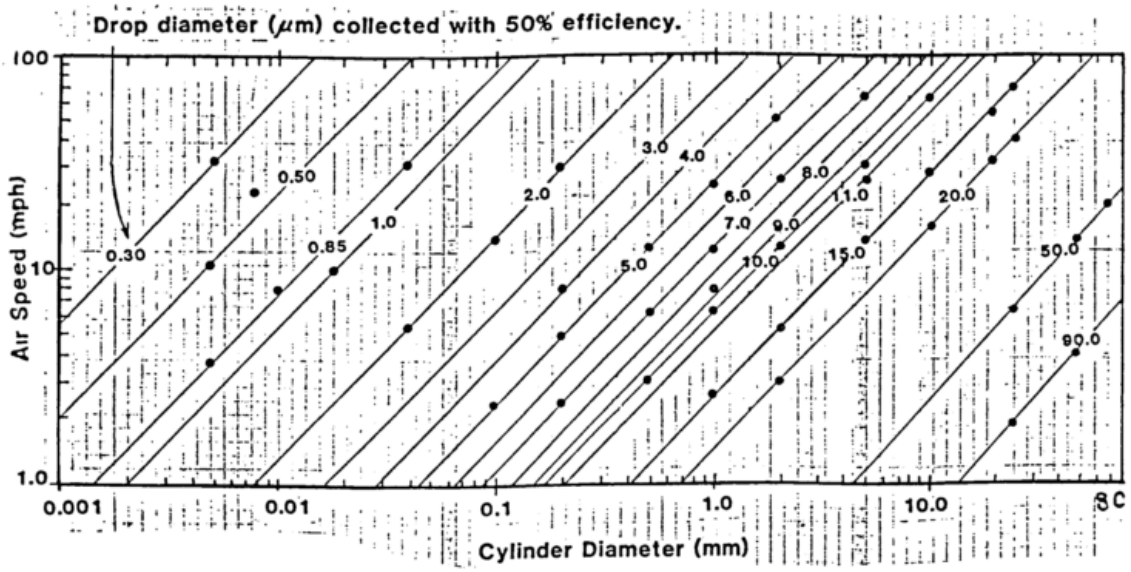


Fig. 2. The relationship between air speed, sieve cylinder diameter and the minimum droplet diameter collected with 50% efficiency.

CLOUD CAPTURE BY A MOUNTAIN TOP FOREST PT. I: ACIDITY AND DOSAGE DURATION

V. K. Saxena and N. -H. Lin
Department of Marine, Earth and Atmospheric Sciences
North Carolina State University, Raleigh, NC 27695-8208, U.S.A.

1. INTRODUCTION

Although Blank (1985, p. 312) has recently brought to attention a new type of forest decline in West Germany, only eight cases of apparent forest decline in the United States have been noticed (NAPAP, 1987, p. I-25) over past several years, causes for which may stem from air pollution. The extent of this decline and a classification of natural and anthropogenic causes are indeed debatable (Moses et al., 1987, p. 1141). Multiple natural and pollutant-induced stresses seem to be involved in such declines. Two unambiguous cases of pollutant-induced decline have, however, been identified (NAPAP, 1987, p. I-25) namely, the San Bernardino Mountain Regional Forest of the Los Angeles air basin and the Southern Sierra Nevada Forest. In both cases, the primary pollutant is believed to be ozone which could possibly act together with one or more pollutants. The mountain top forests in the Appalachians have been demonstrated (Saxena, 1987, p. 270; Saxena et al., 1986, p. 91, 1988a, 1988b; Saxena and Stogner, 1987, p. 190; Saxena and Lin, 1988) to be immersed in clouds and fogs for considerable periods of time. For example, Mount Mitchell, North Carolina (35 44'05"N, 82°17'15"W) forests are subjected to cloud and fog episodes during 71% of days per year, on the average. Noticeably, Mt. Mitchell is the highest peak (2,038 m MSL) in the eastern United States. These above cloud-base forests are also subjected to greater ozone stress than low-elevation forests. Causes of decline in such forests could be complex. One or more pollutants either acting individually or together could initiate decline process either through the tree roots or at the canopy. McLaughlin (1985, p. 512) has excellently belabored these points in discussing the impact of air pollutants on forests. In this paper, we analyze the data base for Mt. Mitchell for the summers of 1986 and 1987 regarding the acidity of cloud water and exposure of the mountain top forest to acidic substances in clouds.

2. DATABASE DESCRIPTION

Cloud-intensive observations at Mt. Mitchell were initiated in May 1986 under a U.S. E.P.A. project entitled, "Mountain Cloud Chemistry/Forest Explosure Study (MCCP)". A 16.5 m tall walk-up tower was fully instrumented. All meteorological parameters were sequentially monitored with auto sensors and were recorded with a data logger. The hourly cloud water collection manually commenced at the tower top upon occurrence of cloud events, using a teflon-string passive cloud water collector designed and fabricated by the Atmospheric Sciences Research Center (ASRC), State University of New York at Albany. The pH and total collected volume of sample were immediately measured within 15 min after collection. Cloud events were categorized into two classes, long cloud events with a duration exceeding 8 hr and short cloud events lasting no more than 8 hr. In general, the former are attributed to the frontal passages, and the latter to orographic lifting mechanisms. In addition to these two cloud event types, cloud events with precipitation are categorized as mixed events. A summary of the observed cloud events and the collected samples is given in Table 1. The corresponding accumulative and average duration of events are listed in events are listed in Table 2. Both tables show that total samples collected in 1986 were 70% in excess of 1987, and the frequency of long cloud events is half as that of short cloud events in 1986, but very few long cloud events were observed in 1987. However, the total number of cloud events for both years are not distinctly different. On the average, cloud episodes in 1986 were significantly longer than in 1987.

3. RESULTS AND DISCUSSION

Table 3 gives the summary of cloud chemistry on the basis of category of event types. The calculated pH values were highly correlated with field measured pH

Table-1 Summary of events and samples collected at Mt. Mitchell during the summer of 1986 and 1987.

Event Type	1986 events / samples		1987 events/ samples	
Long	13	101	5	46
Short	26	55	32	40
Mixed (with precipitation)	10	53	7	40
Total	49	209	4	126

Table-2 Accumulated duration and average duration.

Event Type	1986 accu. /	ave.	1987 accu. /	ave.
Long	170.50	13.12	53.00	10.60
Short	92.92	3.57	80.40	2.52
Mixed (with precipitation)	85.82	9.54	47.83	6.83
Total	349.24	7.23	181.23	4.12

values on the 97% level. The pH in both long and short cloud events were much lower than in mixed events. It is suggested that acidic contents are diluted by precipitation in mixed events. Sulfate, nitrate, ammonia and hydrogen ions were the dominant ions. On the average, sulfates alone can account for 78% and 63% of acidity for 1986 and 1987, respectively. The equivalent concentration of sulfate was about 2.5 and 3.5 times more than that of nitrate for 1986 and 1987, respectively. However, nitrate can approximately account for ammonia which is only attributed to bacterial production in forest area and is thought to be involved in neutralizing the acidity. More chlorine was measured than sodium in 1986, but these were meaasured on the same level in 1987.

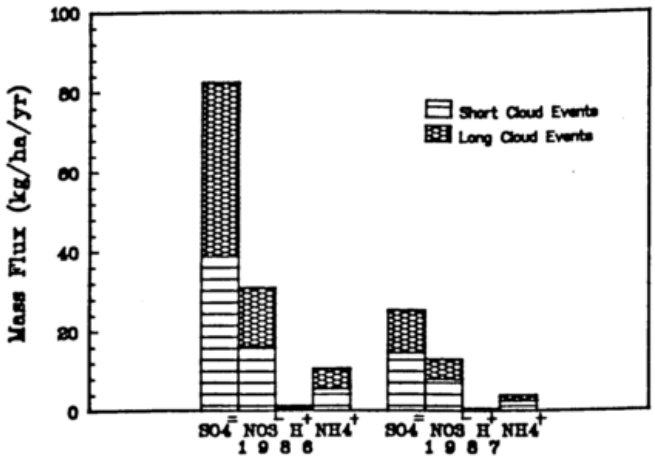


Fig-1 : Estimates of depositional flux due to direct cloud interception by the forest canopy at Mt. Mitchell, NC.

Table-3 Statistical summary of cloud chemistry at Mt. Mitchell for 1986 and 1987. (unit: ueq./L)

EventType	mea._pH	Cond.	Cl^-	NO_3^-	SO_4^{-2}	H^+	NH_4^+	Na^+	K^+	Ca^{+2}	Mg^{+2}	Σ anion	Σ cation	Σ ion	cal.* H^+	Cal.** pH
1986																
Long	3.47	-	24.54	153.60	575.58	477.95	184.20	16.29	3.25	30.59	9.95	753.72	722.24	1475.96	509.43	3.50
Short	3.41	-	31.49	285.14	844.08	630.29	313.97	18.86	6.77	84.24	23.67	1160.72	1077.79	2238.51	727.25	3.42
Mixed (with precipitation)	4.20	-	7.06	67.51	229.96	197.71	73.46	9.96	13.22	9.67	3.01	304.53	307.02	611.56	245.77	4.17
Total	3.63	-	22.07	165.66	553.76	444.00	189.59	15.06	6.09	39.18	11.82	741.50	705.74	1447.23	501.09	3.62
1987																
Long	3.57	174	16.28	144.41	350.70	390.44	133.23	4.42	2.35	19.64	5.68	511.39	555.77	1076.16	346.07	3.63
Short	3.43	244	45.29	220.91	564.02	462.58	276.34	36.57	5.06	30.42	11.15	830.21	811.59	1641.80	481.19	3.44
Mixed (with precipitation)	4.06	85	13.51	62.13	157.30	130.99	81.35	25.98	26.64	9.15	5.12	232.95	278.20	511.14	128.61	4.17
Total	3.72	165	24.55	144.06	353.47	320.86	160.20	24.23	11.73	33.01	9.01	522.08	555.04	1077.12	316.83	3.75

* The $[H^+]$ is derived directly from field pH value.
** Theoretical $[H^+]$, defined by the difference of cation and anion excluding hydrogen ion.
*** The pH value is derived from theoretical $[H^+]$.

In Fig. 1 are shown the results of our computations based on a micrometeorological model (Lovett, 1984, p. 362) that has been discussed by Saxena and Stogner (1987, p. 91) and Saxena et al. (1988a, p. 263). Evidently, due to direct cloud interception, deposition of sulfate ion is 82 and 26 kg ha^{-1} yr^{-1} for 1986 and 1987, respectively.

Acknowledgements. The research has been funded through a cooperative agreement with the United States Environmental Protection Agency (813934-01-2 and 812444-3-0). The contents of this paper do not necessarily reflect the views and policies of the EPA, nor the views of all members of the Mountain Cloud Chemistry (MCC) consortia, nor does mention of trade names or commercial or non-commercial products constitute endorsement or recommendation for use. Prof. Volker Mohnen is the Principal Investigator on MCC Project.

REFERENCES

BLANK, L. W.: A New Type of Forest Decline in Germany. Nature 314 (1985), 311-314.

LOVETT, G. M.: Rates and Mechanisms of Cloud Water Deposition to a Subalpine Balsam Fir Forest. Atmos. Environ. 18 (1984), 361-371.

MCLAUGHLIN, S. B. : Effects of Air Pollution on Forest: A Critical Review. J. Air Pollut. Control Assoc. 35 (1985), 512-540.

MOSES, H.; MOHNEN, V. A.; REIFSNYDER, W. E.; SLADE, D. H.: Summary Report on the Forest-Atmospheric Interaction Workshop, 1-4 October, 1985, Lake Placid, New York. Bull. Amer. Meteo. Soc. 68 (1987), 1141-1145.

NAPAP (National Acid Precipitation Assessment Program): Interim Assessment: The Causes and Effects of Acidic Deposition. Edited by Herrick, C. N. and Kulp, J. L., Washington D. C.: U. S. Government Printing Office, Vol. 1 (1987), 1-53.

SAXENA, V. K.; Mountain Cloud Chemistry Project at Mt. Mitchell, North Carolina: Strategies and Highlights. Trans. Amer. Geophys. Union (EOS) 68 (1987), 270.

SAXENA, V. K.; AGARWAAL, P.; RAMAN, S.: Wet and Dry Deposition of Air Pollution on the Forest Canopy as a Cause of Forest Decline. Conference on Tropical Micrometeorology and Air Pollution, New Delhi, India, February 15-19, (1988a), 260-265.

SAXENA, V. K.; COWLING, E. B.; STOGNER, R. E.; CRUME, R. V.: Cloud Chemistry Measurements at Mt. Mitchell, North Carolina. Preprints Conference on Cloud Physics. Boston: Amer. Meteor. Soc., 1986, 91-94.

SAXENA, V. K.; LIN, N. -H.: Relative Importance of Dry, Wet and Cloud Capture Mechanisms for Acidic Deposition. In: Measurements of Toxic and Related Air Pollutants, Pittsburgh: Air Pollution Control Association, 1988. (submitted).

SAXENA, V. K.; Stogner, R. E.: Wet Deposition on Forest Canopy at Mt. Mitchell, North Carolina. In: Measurements of Toxic and Related Air Pollutants, Pittsburgh: Air Pollution Control Association, 1987, 189-194.

SAXENA, V. K.; STOGNER, R. E. HENDLER, A. H.; DEFELICE, T. P.; YEH, J. -Y.; LIN, N. -H.: Monitoring the Chemical Climate of the Mt. Mitchell State Park for Evaluating Its Impact on Forest Decline. Tellus, 41B, 1988b, in press.

DETERMINATION OF CHEMICAL REACTION RATES IN FOG

Ralph Dlugi, Winfried Seidl

Meteorologisches Institut der Universität München
Theresienstraße 37
8000 München 2
F. R. G.

1 INTRODUCTION

A number of field experiments are described to study the oxidation and absorption of trace gases in radiation and advection fog. Most experiments were performed near ground in polluted areas (e.g. Fuzzi et al., 1984, Jacob, 1985). Only few data are available from vertically resolved measurements of microphysical and micrometeorological parameters and chemical compounds. Results from this kind of studies are presented and are discussed with respect to the oxidation of trace gases like SO_2 and NO_x and the formation of H_2O_2.

2 CONCEPT

A study of the chemical removal of trace gases by aerosol particles in the atmosphere requires that volume mass balances of each compound and species are determined. Therefore a set of coupled semi-empirical diffusion equations will be used as a theoretical framework to get some insight into this problem. Such equations (1) are also a means to decide which quantities have to be measured (e.g. Seinfeld, 1975).

$$\frac{\Delta[c_i]}{\Delta t} - v_j \frac{\Delta[c_i]}{\Delta x_j} - \frac{\Delta[c_i]\cdot v_s}{\Delta z} - \frac{\Delta}{\Delta x_j}\left(K_{jj}\frac{\Delta[c_i]}{\Delta x_j}\right) = R_i + S_i \quad (1)$$

The terms on the left hand side are the time dependent concentration c_i of the compound i, the advection of c_i, the sedimentation of c_i in the droplet phase (sedimentation velocity v_s), the turbulent transport of c_i, and - on the right hand side - the chemical transformation R_i and the source term S_i. From the chemical analysis of different compounds and the measurements of physical and meteorological quantities the left hand side of eq. (1) can be computed (Dlugi, 1988). If S_i is known, the set of coupled equations can be used to determine R_i in the atmosphere from the knowledge of the other terms and to compare these empirical reaction rates with calculated data from the numerical solutions of eq. (1) based on the rate laws from laboratory studies (e.g. Hoffmann and Calvert, 1985). In this way also the vertical transports - or simplified 'the deposition fluxes' - of different compounds can be determined.

3 EXPERIMENTS

Following the theoretical framework given by equation (1) the experimental concept at least must allow vertically resolved and time-dependent concentration measurements of the quantities being of interest. The horizontal advection can be approximated by the transport along a trajectory. Here the oxidation of SO_2 and NO_x by catalysts, soot, O_3, and H_2O_2 is considered. The sampling concept and the analytical methods are described by Dlugi (1986, 1988). These measurements were performed at the 200 m tower of the Nuclear Research Center, Karlsruhe, F.R.G., from 1984 to 1986 during October to April of each year. This site is located in a spruce forest with mean tree heights of about 12 m. For wind directions S - SW the plumes of the town of Karlsruhe, some power plants, and refineries cross the measuring site. Between the industrial areas and the tower a station of the Regional Environmental Protection Agency allows measurements of some compounds near the ground. Fig. 1 shows the tower with measuring heights, layers 1 - 5 of which the measuring points should be representative and the heights where fog was observed. The measured quantities are given in Table 1. The calculation of the turbulent exchange coefficients K_{jj} are performed according to Dlugi (1988). A mean advection velocity is used for each layer and each time step $\Delta t = 1 - 1.5$ h.

The reaction rates for a single layer and the whole layer can be calculated according to eq. (2) and (3) if the influence of horizontal gradients is small:

$$R_{i\,l}(\Delta z_l) = \frac{1}{\Delta z_l} \int_{z'_{l-1}}^{z'_l} \left| (\Delta[c_i]_{aq}/\Delta[H_2O])/\Delta t \right| dz \qquad (2)$$

(single layer reaction rate for fog and particles)

$$\overline{R_i} = \frac{1}{T} \sum_m \frac{1}{l_{max}} \sum_l R_{i\,l} \cdot \Delta t_m \; ; \quad T = \Sigma t_m ; \; l = 1,\ldots,5 \qquad (3)$$

(whole layer reaction rate for fog and particles).

Table 1: Measured Quantities at the Tower of the Nuclear Research Center

Measured Quantity	Height, m	Time Cycle
Pressure	1	10 min
incoming-, reflected-, outgoing-, global-radiation	2 in 100 m distance from the tower	4 s
dew point	2, 30, 100, 200, (20, 80)*	4 s
temperature	2, (20)*, 30, 60, (80)*, 100, 130, 160, 200	4 s
horizontal wind-velocity	2, (10)*, 20, 30, 40, 50, 60, 80, 100, 130, 160, 200	4 s
wind direction	(20)*, 40, 60, 80, 100, 160, 200	4 s
vertical wind direction, standard deviation of vert. wind direct., standard dev. of horiz. wind direct.	40, 100, 160	1 s
filter samples: H_2SO_4, NH_3, HNO_3, NO_3^-, $SO_4^{=}$, NH_4^+, K^+, Na^+, Ca^{2+}	2,10,30,60 or 80 100, (130)+, (160)+ (a - g)	45-90 min
impactor samples: single part. anions, cations, H_2SO_4	2,10,(30,80),100 (a,b,e)	(< 5 min) = 60 min

* Additional instrumentation for these measurements
\+ Not for all measuring days.
(Samples from surrogate surfaces were taken at 2 m and 10 m).

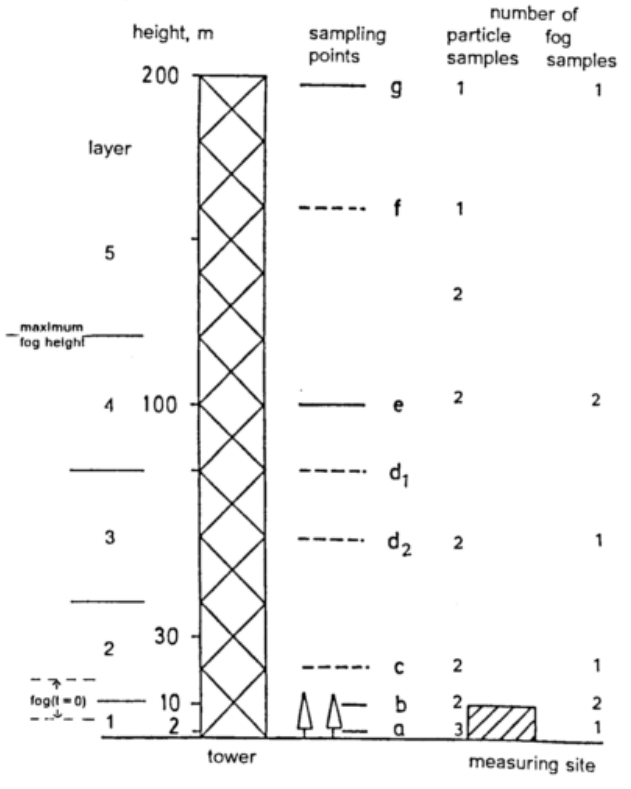


Fig. 1:
The tower of the Nuclear Research Center Karlsruhe with measuring heights, fog height for t = 0 and maximum height and 5 layers of which the measuring points are representative. At (g-a) also gas phase measurements were performed (SO_2, NH_3, HNO_3).

4 RESULTS

Some results of these experiments are summarized in Fig. 2 and Fig. 3. During night time, the mean SO_2-reaction rate according to eq. (3) in the whole, strongly polluted fog layer (Fig. 2), shows a behaviour like the rate for the oxidation by ozone or by the Fe-Mn-synergism (Fig.2). The O_3-concentration was below 30 ppb, while the SO_2-concentration reaches 780 ppb above the ground (100 m). Therefore the mean reaction rate should be caused during these situations by catalyzed reactions. During some fog events - when the wind direction was NW - N - the concentration of all pollutants were smaller by about a factor of three. In the morning during sunrise the rate of production of H_2O_2 in the fog water was determined. The largest rate was evaluated near the top of the fog while in deeper layers the production decrease remarkably. This can be caused only partly by entrainment of gaseous H_2O_2 if an upper limit of the entrainment velocity of 1 $cm \cdot s^{-1}$ is taken. So up to 70% of the H_2O_2 should be formed inside the fog layer.

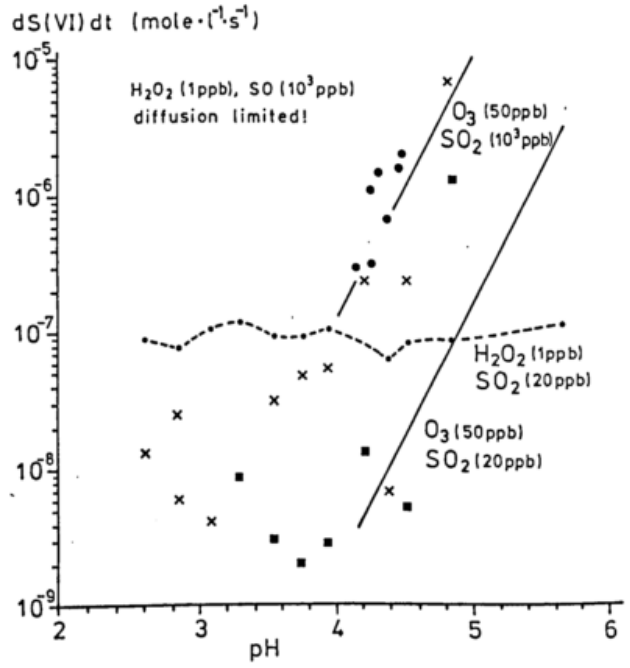


Fig. 2:
Comparison of field data for SO_2-oxidation:
●: own results
Rates calculated on the basis of data from Jacob et al. (1985):
$[Fe]_a = 10^{-5} - 10^{-6}$ mole/l
$[Mn]_a = 10^{-6} - 10^{-8}$ mole/l
$p_{SO_2} = 20$ ppb
x: Fe-Mn-synergism (Rate law from Ibusuki and Takeuchi, 1987)
■: Mn
•: H_2O_2 (Rate laws from Hoffmann and Calvert (1985)

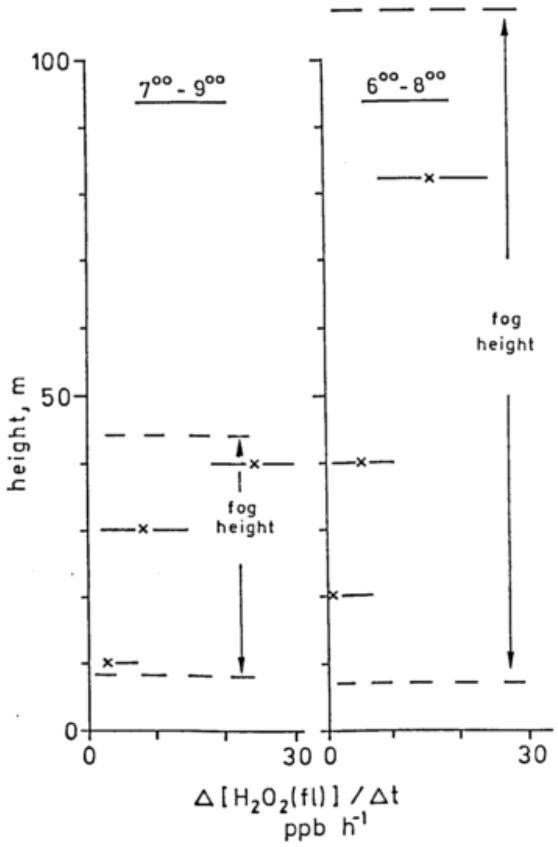


Fig. 3:
The production rate of H_2O_2 in the fog water as a function of the height.

5 LITERATURE:

DLUGI, R.: Aerosols. Formation and Reactivity. Proceedings of the Second International Aerosol Conference, West Berlin, 22-26 September 1986. Pergamon Press, New York 1986. p. 100-103

DLUGI, R.: Proceedings 16th Int. Techn. Meeting 'Air Pollution Modeling and its Application', Plenum Press, New York 1988. (in press).

FUZZI, S.; CASTILLO, R.A.; JUISTO, J.F.; LALA, G.G.: Chemical composition of Radiation Fog Water at Albany, New York, and its Relationship to Fog Microphysics. J. Geophys. Res. D89 (1984), p. 7159-7164

HOFFMANN, M.R.; CALVERT, J.G.: Chemical Transformation Modules for Eulerian Acid Deposition Modeling Project. National Center for Atmospheric Research. P.O.Box 3000, Boulder, CO 80307, 1985

IBUSUKI, T.; TAKEUCHI, K.: Sulfur Dioxide Oxidation Catalyzed by Mixtures of Manganese(II) and Iron(III) in Aqueous Solutions at Environmental Reaction Conditions. Atmos. Environm. 21 (1987), p. 1555-1560

JACOB, D.J.: Thesis, CALTECH-Report No. AC-2-85, Pasadena, CA. 1985

JACOB, D.J.; WALDMAN, J.M.; MUNGER, J.W.; HOFFMANN, M.R.: Chemical Composition of Fogwater Collected along the California Coast. Environ. Sci. Technol. 19 (1985), p.730-736

INSOLUBLE PARTICLES IN HYDROMETEORS

M. Krämer and L. Schütz

Institute of Meteorology, University of Mainz, Saarstr. 21, D-6500 Mainz, FRG

1. INTRODUCTION

The consequences of the anthropogenic environmental pollution on animal, plant and human life have caused among other things a variety of basic investigations on the composition of atmospheric wet deposition and the scavenging processes of atmospheric aerosol particles and gases.

The aim of our investigations are detailed studies of insoluble particles and dissolved material in cloud-, fog- and rainwater. We put special emphasis on the study of number size and volume distributions, total mass and elemental composition of the insoluble constituents about which we will present first results in this paper.

2. INSOLUBLE PARTICLES IN RAINWATER

2.1 SAMPLING AND ANALYSIS

Insoluble particles in rainwater have been investigated for several rain events. The samples have been collected near Mainz, FRG, one part in an agricultural area close to the university campus and the other part on the roof platform of the Institute of Meteorology.

All rainwater samples were collected with carefully cleaned wet-only collection devices.

The insoluble particles of the samples from the agricultural area were separated from the rain water by means of pressure filtration. Two types of filters were used for the analysis of submicron and and giant particles. The number size and volume distributions of this set of samples were determined in the range from 0.1µm up to 100µm radius by sizing and counting of the individual particles using one filter type for optical microscopy (for particles with $r > 2\mu m$) and the other one for scanning electron microscopy (SEM for $r<3\mu m$). The latter type of filter also served for determining the elemental compostion of single particles with the SEM by using energy dispersive X-ray analysis (EDX). The samples from the roof platform of the Institute of Meteorology were freezed immediately after collection. Number size and volume distributions of that set of samples were analysed with the aid of a Coulter Counter. This is a multichannel particle size analyser which provides a size distributions with the Coulter method of electrical conductivity. With the used orifice tube size one obtains distributions which cover a size range between 0.4µm and 8.0 µm.

2.2 RESULTS

The general shape of the microscopicy determined (MIC) distributions was much the same for all samples of this set as well as those obtained with the Coulter Counter (CC). Therefore a mean number size and a mean volume distribution were calculated for both the MIC-and the CC-distributions.

Comparison between the mean CC- and MIC-distributions (Figure 1) shows that the strong decrease of particle concentration density between 2µm and 3µm at the mean MIC-distribution is caused by the split in two subranges by using two different filters and microscopes. The number of the small giant particles was clearly underestimated. No explanation of this underestimation was found so far. In this size range the mean CC-distributions will be accepted as valid because of careful calibration of the instrument.

The mean distributions of insoluble particles

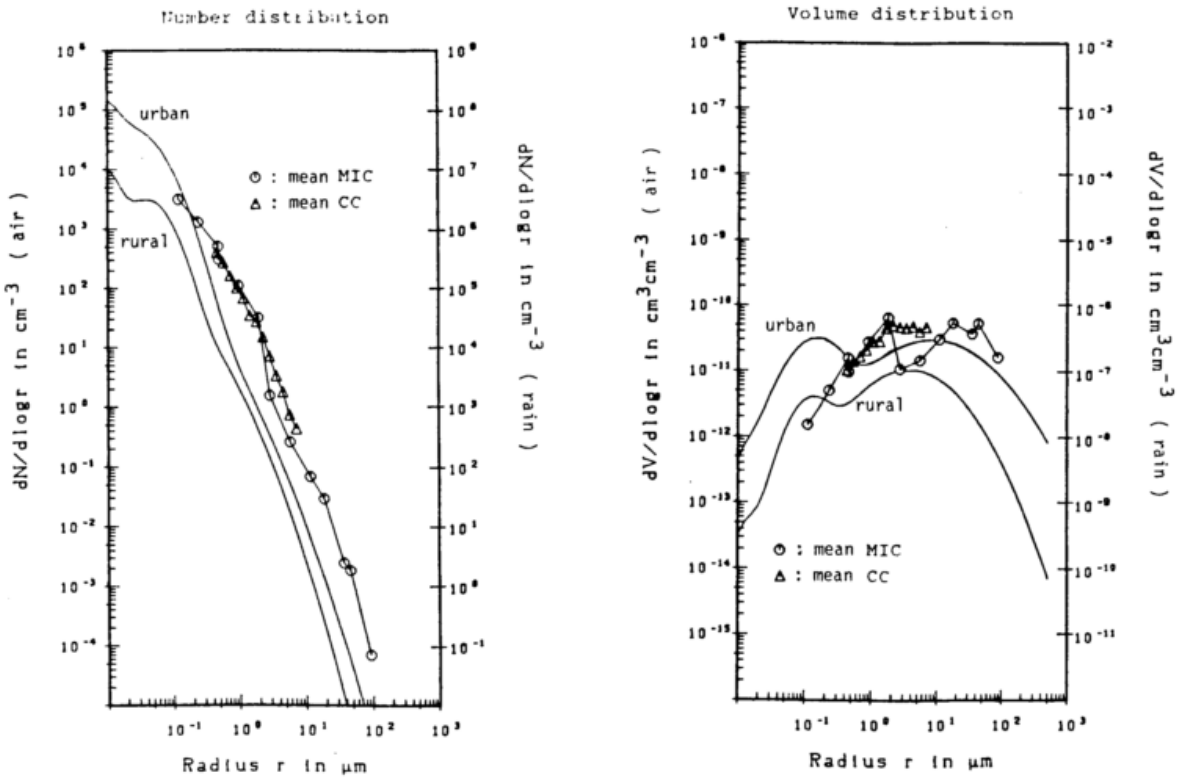


Figure 1

in rainwater were now compared with an average number size and volume distribution of urban and rural aerosol particles in air (JAENICKE 1987). For particles with $r > 0.5\mu m$ radius the shape of the number size distribution of insoluble particles in rain follows the shape of the average distribution of aerosol particles. In this size range no major size selective removal processes could be seen. For $r < 0.5\mu m$ radius the number size and and in particular volume distribution tends to flatten compared with the average distribution of aerosol particles. This effect is not caused by the increase of the fraction of soluble material in the atmospheric aerosol particles in this size range (KRÄMER 1987), but rather might be an indication of a size selective removal process. In the scavenging of aerosol particles a minimum between 0.1µm and 1.0µm particle radius is seen. This is called the 'Greenfield' or 'Scavenging gap' (PRUPPACHER et al. 1978) and the flattening of the distribution of insoluble particles may reflect this gap.

The total insoluble mass in rainwater was calculated by the integral over the volume distribution multiplied with the assumed particle density of 1.5 gcm^{-3}. It ranges between 1 and 4 mg per liter rainwater.

The elemental composition of approximately 60 single particles was determined for one sample.

Fly ash, biogenic and mineral particles could be identified by comparison with investigations of MAMANE et al. (1985), WEBBER et al. (1985), PARUNGO et al. (1978) and DELMONTE et al. (1984), who have characterized the elemental composition of large particles at a rural site and coal-fly ash particles. No correlation was found between the size of particles and their elemental composition or their appearance. The main elements contained in all investigated insoluble particles were Al, Si, Fe, followed by S and K. Na, Mg, Cl, Ca, Ti, Zn, Cu and Au were present as trace substances (Figure 2). PARUNGO et al. (1978) came to similar results when analysing particles emitted by a coal-fired power plant. This implies that the particles of this sample mainly consist of combustion residues.

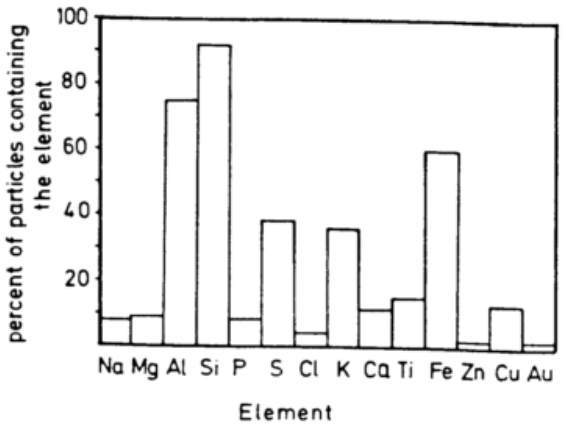


Figure 2

3. ACKNOWLEDGEMENTS

The authors would like to express their thanks to Dipl. Ing. M. Weidenauer of the Institute of Anorganic and Nuclear Chemistry from the Technical University of Darmstadt who carried out the EDX and to K. Geis of the Institute of Environmental Physics from the University of Heidelberg for determining the number size distributions with the Coulter Counter.
This work was supported by the German Science Foundation (DFG).

REFERENCES

DELMONTE, M.; BRAGA MARCAZZAN, G.M.; SABBIONI, C.; VENTURA , A.: Morphological, physical and chemical characterization of particles emitted by a coal-fired power plant. J.Aerosol Sci. 15 (1983), 325-327

JAENICKE, R.: Aerosol Physics and Chemistry. Volume "Meteorology" G. Fischer (Ed.), Landolt Börnstein New Series (1987)

KRÄMER, M.: Analysen von atmosphärischen Niederschlägen einschließlich der unlöslichen Bestandteile in Mainz, M.S. Thesis, Mainz (1987)

MAMANE, Y.; NOLL, K.E.: Characterization of large particles at a rural site in the eastern United States: Mass distribution and individual particle analysis. Atmos. Environ. 19 (1985), 611-622

PARUNGO, F.; ACKERMANN, E.; PROULX, H.; PUESCHEL, R.: Nucleation properties of fly ash in a coal fired power plant plume. Atmos. Environ. 12 (1978), 929-935

PRUPPACHER, H.R.; KLETT, J.D.: Microphysics of Clouds and Precipitation. D. Reidel Publ. Co., Dordrecht, Holland (1978)

WEBBER, J.S.; DUTKIEWICZ, U.A.; HUSAIN, L.: Identification of submicrometer coal fly ash in a high-sulfate episode at Whiteface Mountain, New York. Atmos. Environ. 19 (1985), 285-292

BELOW CLOUD SCAVENGING BY RAIN AND DRIZZLE

Brendan Thomas McGann and S. Gerard Jennings

University College Galway, Ireland.

The scavenging of aerosol particles suspended in the atmosphere by precipitation is one of the major mechanisms for maintaining a balance between the sources and sinks of atmospheric aerosol particles.

The efficiency E(a,r) with which aerosol particles of radius r are collected by water droplets of radius a depends on the combined action of; Brownian diffusion, thermo- and diffusiophoretic forces, inertial impaction and electric forces. For aerosol particles with radii <.5 μm inertial impaction can be ignored and the collection efficiency can be determined from the flux model of Wang *et al.* (1978). Knowing the collection efficiency E(a,r) we can determine the precipitation scavenging rate Λ(r);

$$\Lambda(r) = \int_0^\infty A(a)\ E(a,r)\ V(a)\ N(a)\ da$$

where A(a) is the effective cross-sectional area of the precipitation particle, V(a) is the terminal velocity of a precipitation particle and N(a) da is the concentration of precipitation particles with radii between a and a + da.

At some time t during a scavenging event the concentration (X(r)) of aerosol particles with radii between r and r + dr, is related to the initial (t = 0) concentration (X_o (r), by the precipitation scavenging rate;

$$X(r) = X_o(r)\ \exp(-\Lambda(r)\ t)$$

Radke *et al.* (1980) describe field studies of the scavenging of aerosol particles by precipitation. The aerosol size distribution was measured just prior to, and just following scavenging by a rain shower. The scavenging time and the rainrate were also recorded.

Assuming a Marshall-Palmer distribution for the raindrop spectrum we calculated precipitation scavenging rates for various sized aerosol particles. The scavenging rates displayed in Table 1, corresponds to atmospheric conditions of; 900mb, 10°C, 50% relative humidity. For each aerosol radius the scavenging rate has been calculated with and without electric charges of $+2a^2$ and $-2r^2$ on the raindrop and aerosol particle respectively.

Table 1: Scavenging rates for various aerosol radii.

aerosol radius (μm)	scavenging rate with charges (s^{-1})	scavenging rate without charges (s^{-1})
0.001	1.025×10^{-4}	1.027×10^{-4}
0.002	4.061×10^{-5}	4.084×10^{-5}
0.005	1.298×10^{-5}	1.322×10^{-5}
0.01	6.243×10^{-5}	6.528×10^{-6}
0.02	3.733×10^{-6}	4.103×10^{-6}
0.05	2.844×10^{-6}	3.394×10^{-6}
0.1	2.652×10^{-6}	3.372×10^{-6}
0.2	2.389×10^{-6}	3.455×10^{-6}
0.5	1.629×10^{-6}	3.782×10^{-6}

The percentage of particles removed by scavenging for varying aerosol particle radius is diplayed in Figure 1, where a scavenging time of 1 hour has been assumed.

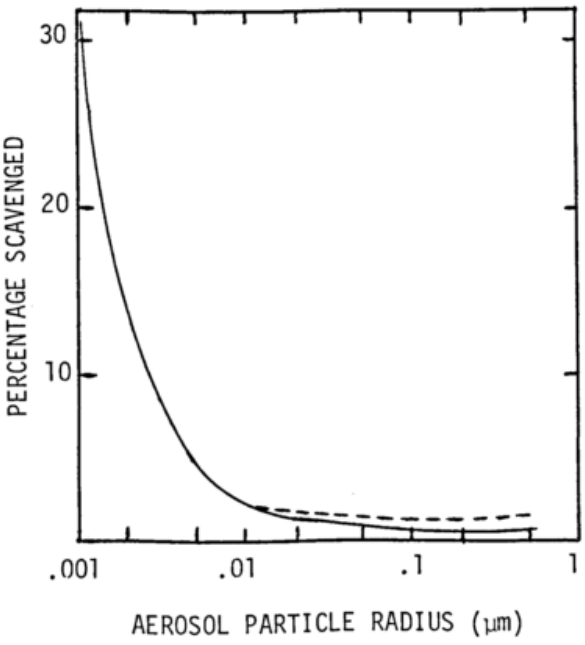


Figure 1: Percentage of aerosol particles scavenged by a Marshall-Palmer distribution for a rainrate of 10.2 mm/hr.

These results support the existence of the so-called "Greenfield Gap" in agreement with the results of Radke *et al.*(1980), however, for smaller aerosol particles ($r \sim 0.01\mu m$) the flux model predicts atmospheric half-lives 200 - 300 times those measured by Radke *et al.*(1980).

REFERENCES

Marshall, J.S., and Palmer, W.M. 1948; The distribution of raindrops with size, *J. Meteorol.*,5,165.

Radke, L.F., Hobbs, P.V., and Eltgroth, M.W., (1980); Scavenging of aerosol particles by precipitation, *J. Appl. Meteorol.*,19,715.

Wang, P.K., Grover, S.N., and Pruppacher, H.R., (1978); On the effect of electric charges on the scavenging of aerosol particles by cloud and small raindrops, *J. Atmos. Sci.*,35,1735.

STUDIES OF CLOUD MICRO-CHEMICAL PHYSICS

Richard L. Pitter and William G. Finnegan

Desert Research Institute, Reno, Nevada

1. INTRODUCTION

There are very few linkages between chemistry and hydrometeor growth and behavior in cloud microphysics theories. Two exceptions include the roles of chemistry in cloud condensation and the solute effect to reduce the equilibrium vapor pressure over a water surface.

The only generally-recognized effect of chemistry in the ice phase is that of some sort of chemical requirement must be fulfilled for heterogeneous ice formation to occur.

At the Desert Research Institute (DRI), we have investigated several intriguing chemical aspects relevant to the ice phase. The DRI 6.7 m^3 cloud chamber was used to conduct isothermal and isobaric studies of ice crystal formation and early growth. Water clouds were generated with ultrasonic nebulizers, using 10^{-4} N solutions of salts commonly associated with cloud and precipitation water. The concentrations are similar to those found in clouds and precipitation. We nucleated ice by adiabatic expansion of moist air as per Vonnegut (1948).

Our observations indicate that the solute present in the supercooled water is incorporated into the growing ice crystals and subsequently plays important roles in microphysical processes which are highly pertinent to the formation of precipitation. Three such topics presented herein are ice crystal habit, aggregation, and secondary ice formation.

2. ICE CRYSTAL HABIT

Crystal habit has been studied in solution crystallization for several hundred years. It is recognized that crystal habit is determined by three factors: temperature, supersaturation, and impurities. The role of impurities is not well characterized, except that it is postulated that they act to poison certain surfaces and slow their rates of growth.

Ice crystals were analyzed using microphotographs of crystals which fell onto glass slides within three minutes of ice nucleation. No replication techniques were used. The glass slide was maintained in a chilled chamber (-10 C) and the photography was conducted immediately after collection of the ice crystals on the glass slide to minimize metamorphosis.

Several solute-related effects were noted. In one series, we examined the effects of solutes on morphology of dendrites at -16 C. Several morphological details are solute-dependent. When distilled, deionized water is used, the central region is a large, simple hexagonal plate, while the dendritic branches consist of straight, parallel sides terminated by straight,

angular tips with 120 degree apex angles. A central rib, without lateral ribs, is generally present on each dendritic branch.

When 10^{-4} N solution of NaCl is used to form the cloud, the crystal forms broad sector branches. Each branch contains a central and two lateral ribs, with straight leading edges and an apex angle of 110 to 120 degrees. The central hexagon is smaller than with deionized water, and exhibits a variety of features including six-petaled steppes and 3-dimensional centers, where some dendritic branches are offset from the others along the c-axis.

When the cloud water contains an ammonium carbonate solution, the dendrites have very small central regions and wavy-edge branches which often terminate with high curvature or acute angle tips. Frequently, three ribs diverge from a broad, thick trunk on each branch; the lateral ribs diverge at angles of 60 to 90 degrees from each other. The central crystal is often composed of multiple-tiered crystals, consisting of two or more sets of dendritic branches offset on the c-axis.

4. AGGREGATION

Ice crystal aggregation is an important phenomenon in the formation of hail embryos and precipitation. The major questions involving aggregation relate to the onset of aggregation and the aggregation efficiency. Our study focused on the orientations of aggregated ice crystals.

The appearance of T-shaped aggregates has been noted in snowflakes by several researchers (Odencrantz et al., 1968; Smith-Johanson, 1969; Magono and Tazawa, 1972). These aggregates are not to be confused with spatial crystals (Lee, 1972).

Laboratory studies were conducted on aggregation of ice crystals in the cloud chamber, which allowed the crystals to grow for 3 to 5 minutes before settling out. At -12 C, we observed and counted a variety of orientations of crystal aggregates, including T-shaped (point-to-center); sloppy T's, which we called lambdas; point-to-point; vees; and other configurations. Table 1 presents the results.

TABLE 1

-12 C (PLATES)

SOLUTE	A	B	C	D	E	F	G
$(NH_4)_2SO_4$	15	0	0	5	3	65	0
NaCl	9	4	20	13	4	18	44
Dual	18	16	9	8	1	35	89

A: Tees; B: point-to-point; C: vees; D: lambdas; E: other; F: percent Tees; G: ratio of point-to-point to Tees. Dual consists of two clouds: one of NaCl solution, the other of $(NH_4)_2SO_4$.

In the needle regime (-4 to -6 C), similar results were obtained, as shown in Table 2.

TABLE 2

-4 to -6 C (COLUMNS & NEEDLES)

SOLUTE	A	B	C	D	E	F	G
$(NH_4)_2CO_3$	36	9	5	18	8	47	25
$(NH_4)_2CO_3$	9	1	5	3	3	43	11
Dual	31	29	4	40	4	29	94

Columns are as in Table 1. First row of data are at -4 C, others at -6 C.

The fraction of aggregates which are tees is higher for the ammonium salt solutions, and lower for NaCl. When two nebulizers are used, with different salt solutions, the ratio of point-to-point aggregates to point-to-center aggregates greatly increases. The results are similar at both temperatures studied. The results were consistent for different runs of the same solution, but differed when different salt solutions were used.

The results indicate that the solutes in the cloud water somehow become incorporated in the growing ice crystals and affect the manner in which ice crystals aggregate.

4. SECONDARY ICE FORMATION

Secondary ice formation was studied in the cloud chamber. During ice crystal growth and aggregation, the formation of smaller ice crystals was frequently observed, a phenomenon analogous to crystal breeding, or false grain, in solution crystallization literature (Van Hooke, 1961). Newly-formed ice crystals were not fragments, but complete crystals. They were identified as secondary ice formation on the basis of their delayed appearance, smaller size, and their occasional repeated appearance within single experimental runs. Table 3 indicates that secondary ice formation was observed from -4 to -30 C, and was more readily observed with ammonium salt solutions than with deionized water or sodium nitrate solutions.

TABLE 3 -- SECONDARY ICE FORMATION

Cloud Solution:	$NaNO_3$			NH_4^+ Salts		
Temp (C)	N	SIF	%	N	SIF	%
-4 to -8	18	12	67	14	13	93
-9 to -12	5	2	40	4	2	50
-13 to -30	0	0	--	7	7	100

N: experimental runs with aggregation.
SIF: secondary ice formation observed.

5. CONCLUSIONS

The phenomena studied were found to be affected by the presence of dilute aqueous solutions in the cloud water in which the ice crystals grow. We have noted elsewhere that the freezing potentials of such solutions (Workman and Reynolds, 1950) provides a basis for theoretical development.

6. ACKNOWLEDGEMENTS

The Office of Naval Research (Paul Twitchell, program manager) and the National Oceanic and Atmospheric Administration (NOAA) Federal-State cooperative program (Roger Reinking, program manager) supported this study.

7. REFERENCES

Lee, C.W., 1972. **J. Meteor. Soc. Japan, 50**, 171-180.

Magono, C., and S. Tazawa, 1972. **J. Meteor. Soc. Japan, 50**, 489-495.

Odencrantz, F.K., W.S. McEwan, P. St. Amand, and W.G. Finnegan, 1968. **Science, 160**, 1345-1346.

Smith-Johanson, R.I., 1969. **J. Atmos. Sci., 26**, 523-534.

Van Hooke, A., 1961. **Crystallization Theory and Practice.** Reinhold Publ. Co., New York.

Vonnegut, B. 1948. **J. Appl. Phys., 19**, 959.

Workman, E.J., and S.E. Reynolds, 1950. **Phys. Rev., 78**, 254-259.

KINETICS AND MECHANISM OF THE Fe-CATALYZED AUTOXIDATION OF S(IV)-OXIDES IN AQUEOUS SOLUTION

J. Kraft, M. Dellert, P. Braun and R. van Eldik

Institute for Inorganic Chemistry, University of Witten/Herdecke, Stockumer Str. 10, 5810 Witten, FRG

1. INTRODUCTION

The mechanism of the autoxidation of S(IV)-oxides remains unresolved notwithstanding the fact that numerous studies have been devoted to this system (CHANG 1987, HOFFMANN 1985). This is partly due to the undefined way in which impurities such as metal ions and complexes can catalyse the oxidation process substantially (HUSS 1978). Available data suggests that the Fe(II/III)-catalyzed autoxidation of S(IV)-oxides can account for up to 80% of the overall oxidation rate at pH 4 to 7 in aqueous solution. We have undertaken a detailed study of the Fe(III)-catalyzed process (KRAFT 1987) using fast kinetic and spectroscopic techniques. In addition, a few model Fe(III) complexes were selected to investigate their interaction with S(IV)-oxides and the catalytic nature of the produced sulfito complexes.

2. COMPLEX FORMATION REACTIONS

Aqueous solutions of $Fe^{III}(ClO_4)_3$ contain various aquated species which can be summarized by the following equilibria at pH ≤ 3:

$$Fe(H_2O)_6^{3+} \rightleftharpoons Fe(H_2O)_5OH^{2+} + H^+ \qquad K_1 = 6.4\times10^{-3}\ M \quad (1)$$

$$Fe(H_2O)_5OH^{2+} \rightleftharpoons Fe(H_2O)_4(OH)_2^{+} + H^+ \qquad K_2 = 3.2\times10^{-4}\ M \quad (2)$$

$$2Fe(H_2O)_4(OH)_2^{+} \rightleftharpoons Fe_2(OH)_2(H_2O)_8^{4+} \qquad K_3 = 1.7\times10^{2}\ M^{-1} \quad (3)$$

The concentration of dimeric species can be reduced to below 2% when [total Fe(III)] is kept at 5×10^{-4} M. Under such conditions, $Fe(H_2O)_6^{3+}$ and $Fe(H_2O)_5OH^{2+}$ are the main species present in solution at pH ≤ 3. Aqueous solutions of dissolved SO_2 exhibit the following equilibria:

$$H_2O + SO_2 \rightleftharpoons HSO_3^- + H^+ \qquad K_4 = 1.3\times10^{-2}\ M \quad (4)$$

$$HSO_3^- \rightleftharpoons SO_3^{2-} + H^+ \qquad K_5 = 5.0\times10^{-7}\ M \quad (5)$$

$$2HSO_3^- \rightleftharpoons S_2O_5^{2-} + H_2O \qquad K_6 = 8.8\times10^{-2} \quad (6)$$

At [total S(IV)] ≤ 0.1 M and pH < 4, $SO_2(aq)$ and HSO_3^- will be the main S(IV)-oxides in solution.

The reaction of $Fe^{III}(aq)$ with $SO_2(aq)/HSO_3^-$ is characterized by the rapid formation of yellow/red coloured Fe(III)-S(IV) species. The formation and decomposition of these transients can be followed using stopped-flow and rapid-scan techniques with UV-VIS detection. A schematic representation of the change in absorbance at 390 nm is given in Figure 1,

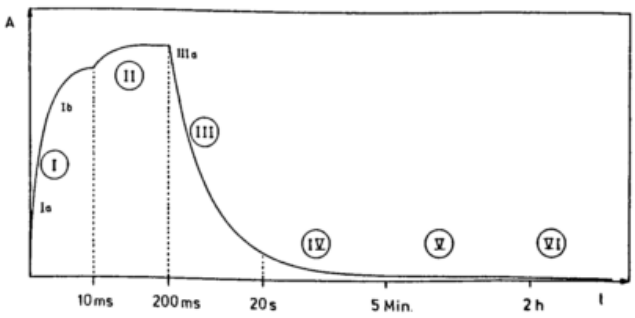


Figure 1 Schematic representation of absorbance at 390 nm versus time for the reaction of Fe(III) with S(IV)-oxides
[Fe(III)]= 5×10^{-4} M; [S(IV)]= 1×10^{-2} M; pH= 2.5; Temp.= 25° C

which demonstrates the occurence of at least four consecutive reactions. The first two steps are ascribed to complex formation, whereas the following two are due to redox decompostion to produce Fe(II), SO_4^{2-} and $S_2O_6^{2-}$. Step I occurs within a couple of milliseconds and only qualitative spectral data could be recorded. A detailed kinetic and spectroscopic study of steps I and II as a function of pH, [Fe(III)] and [S(IV)] revealed that different Fe(III)-S(IV) species (in the ratio 1:1, 1:2 and 1:3) are produced, an overall scheme is given in Fig. 2. Important aspects are:

- $Fe(H_2O)_5OH^{2+}$ and HSO_3^- are the main reactive species
- The 1:2 complex can exist as cis- or trans-$Fe(H_2O)_4(SO_3)_2^-$
- Both bissulfito complexes produce the trissulfito species
- Product distribution strongly depends on pH.

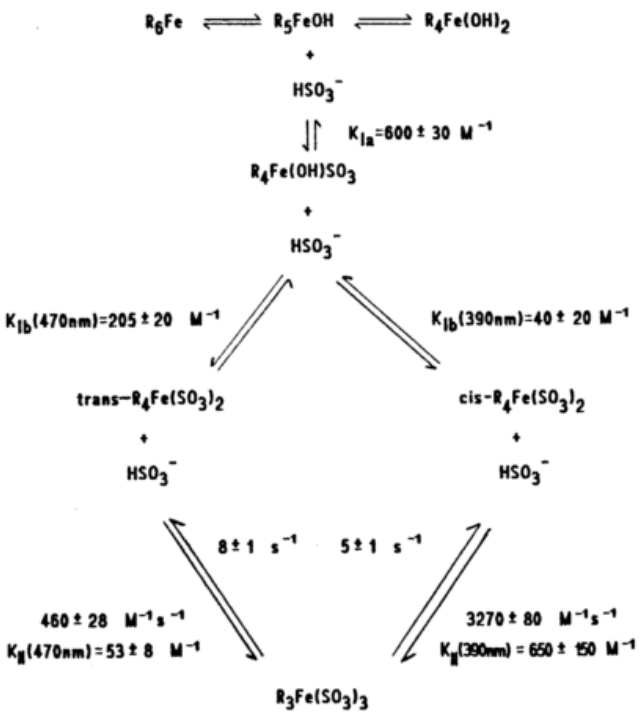


Figure 2 Overall reaction scheme for the formation of various Fe(III)-sulfito complexes (R=H_2O; Fe=Fe ; charges and protons have been omitted for simplification).

Typical kinetic and thermodynamic data are included in Figure 2. Trans labilization effects of coordinated sulfite account for the significantly faster reaction of the cis-bissulfito complex. This is also accompanied by a remarkably more positive $\Delta S^{\#}$ value. Small spectroscopic and kinetic differences are detected in the presence of O_2, which could point toward the formation of an oxo-sulfito intermediate.

Similar reactions were studied using stopped-flow and T-jump techniques for the complex formation of Fe(edta)$^-$ and Fe(nta)$(H_2O)_2$ with S(IV)-oxides. In these cases the metal complex has one or two labile water molecules that are substituted by sulfite, and the formation reactions are less complicated than in the case of aquated Fe(III). Such model complexes enable a systematic variation of all parameters, identification of transient species, as well as kinetic measurements in a pH range not accessible for the aquated Fe(III) system. It is our objective to gain detail insight into the catalytic role of such Fe(III)-sulfito species with the aid of these investigations (VAN ELDIK 1986).

3. REDOX REACTIONS

Immediately after the formation of the Fe(III)-S(IV) species, at least two decompositon reactions occur (see Fig. 1) within the time frame of 5 minutes under the selected conditions. Spectroscopic and ion chromatographic analyses demonstrate that Fe(II), $S_2O_6^{2-}$ and SO_4^{2-} are the reaction products. Up to 90% of the Fe(III) is reduced to Fe(II) during step III, the rest during step IV. The concentration ratio of $S_2O_6^{2-}$ to SO_4^{2-} strongly depends on [total S(IV)], pH, [Fe(III)] and [O_2]. The rate-determining step involves electron-transfer on the 1:2 and 1:3 Fe(III)-S(IV) complexes (see previous section) to produce Fe(II) and SO_3^-, where the sulfite radical can either undergo a subsequent redox reaction or produce $S_2O_6^{2-}$ through radical pairing.

The difference in reactivity of steps III and IV is ascribed to the participation of dimeric species, which can be sulfite or hydroxy bridged species produced by the bis- and trissulfito complexes. Such species are expected to show a significantly lower redox activity. An additional reaction step (IIIa) is observed in the presence of O_2, which is approximately six times faster than step III and is ascribed to the participation of the mentioned oxo-sulfito complexes.

Two more reaction steps have been identified following step IV. These involve the oxidation of the excess of S(IV) to S(V/VI) and are controlled by the [O_2] of the solution. The latter affects the oxidation of Fe(II) to Fe(III), which then rapidly coordinates the excess sulfite and undergoes the redox cycle. A schematic presentation of the overall cycle is given in Figure 3.

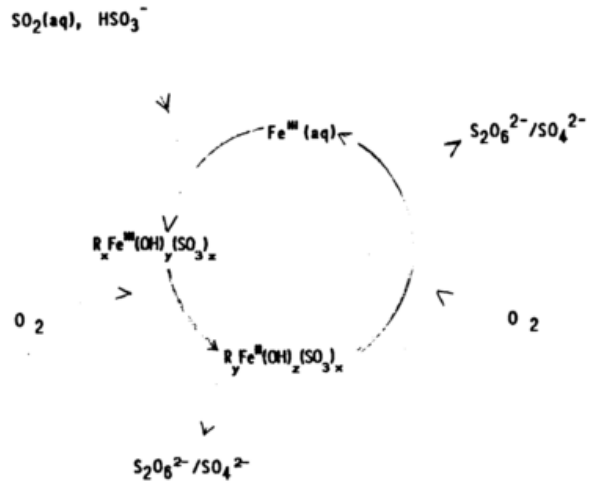


Figure 3 Schematic representation of the catalytic autoxidation cycle (x+y+z=6).

4. OVERALL COMPARISON

A comparison of the obtained data with those published in the literature is complicated by the fact that most studies did not consider the various reaction steps and only reported an overall rate constant. These data correspond to those found for steps IIIa and III in this study. The participation of four reaction steps was also recently reported by CONKLIN (1986).

5. LITERATURE

CHANG, S.G.; LITTLEJOHN, D.; HU, K.Y.: Science, 237 (1987) 756 and literature cited in ref. 1 of this paper.

CONKLIN, M.H.: Ph. D. Thesis, California Institute of Technology (1986).

HOFFMANN, M.R.; CALVERT, J.G.: Chemical Transformation Modules for Eulerian Acid Deposition Models, Vol. II, The Aqueous Phase Chemistry, U.S.E.P.A.-N.C.A.R. Interagency Agreement DW 930237, 1985.

KRAFT, J.: Doctoral Dissertation, University of Frankfurt (1987).

VAN ELDIK, R.: in "Chemistry of Multiphase Atmospheric Systems", Jaeschke, W. (Ed.), Springer Verlag, (1986) 541.

THE EFFECT OF AEROSOLS ON pH OF SNOWFALLS

Motoi Kumai

U.S. Army Cold Regions Research and Engineering Laboratory
Hanover, New Hampshire U.S.A.

1. INTRODUCTION

Chemical analysis of aerosols, aerosol concentration, pH, and electrolytic conductivity of fresh snowfalls were measured during five winters from 1972-1973 to 1983-1987 in Hanover, New Hampshire. The relation between pH values and wind direction during snowfalls was examined. Fly-ash particles and other kinds of atmospheric aerosols in fresh snow were examined by scanning electron microscope (SEM), and the elemental compositions were measured by energy dispersive X-ray (EDX) analyzer to identify the minerals and their origins. The results on snow from New Hampshire were compared and discussed with those obtained from snow accumulated from 1981 to 1983 at Dye-3, Greenland.

2. EXPERIMENTAL PROCEDURE

Fresh snow samples were melted in a microwave oven under cleanroom conditions. The pH and electrolytic conductivity of each sample was measured at 25°C about 10 minutes after melting. A pH meter (Solution Analyzer Model 4505A) was used and calibrated by two buffer solutions of pH 4.00 and 7.00 at 25°C. Electrolytic conductivity measurements were made with the Solution Analyzer and calibrated with a standard solution of 0.005-N KCl (720 ± μs/cm) at 25°C.

The known volume of snow meltwater was filtered through a 0.4 μm pore diameter polycarbonate membrane filter. Particles remaining on the filters were dried in a vacuum oven and the mass was measured. The particles were coated by Au and Pd vapor in a vacuum chamber for scanning electron microscopy.

3. EFFECTS OF WIND DIRECTION ON SNOW pH

Emissions of SO_2 and NO_x in states south of New Hampshire are several times higher than those in states north of N.H. (National Research Council, 1983). Fresh snow was sampled following snowfalls in a rural area, Hanover, N.H. About one-third of annual precipitation occurs as snow, and the ten-year average maximum depth of snow cover in Hanover is 47 cm. Measurements of pH and electrolytic conductivity were performed on precipitation collected during five winters; the results are shown in Table 1. The pH of snow or rain in midwinter ranged from 3.56 to 5.63 and the electrolytic conductivity from 2.52 to 104.5 μS/cm. The acidity of the precipitation increased with the electrolytic conductivity

Table 1. pH and μS/cm values of fresh snowfalls from Hanover, N.H., U.S.A.

Winter	No. of snowfalls	Total precip. mm	pH range	Mean H^+ concentration mol/L	Total H^+ deposition/m^2 mol	Range μS/cm	Mean μS/cm
1972-73	22	207.0	3.96-5.45	$10^{-4.79}$	0.0033	4.02-53.30	11.93
1983-84	16	152.1	4.04-5.27	$10^{-4.66}$	0.0032	3.58-46.50	12.21
1984-85	22	199.3	3.56-5.63	$10^{-4.29}$	0.0101	2.52-56.00	16.64
1985-86	29	285.7	3.72-5.11	$10^{-4.18}$	0.0189	8.15-104.5	21.22
1986-87	17	232.5	3.71-4.86	$10^{-4.49}$	0.0075	4.23-64.00	11.39

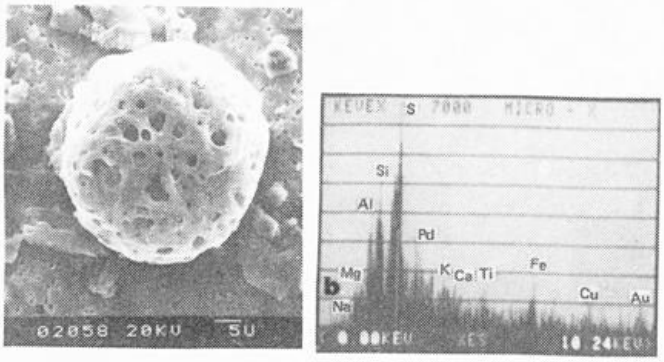


Fig. 1. SEM image (left) of a fly ash in fresh snow from Hanover, N.H. Its shape and elemental compositions (right) indicate that it originated from an oil-fired plant.

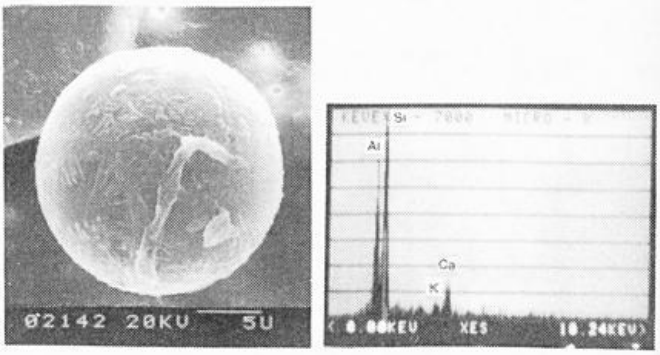


Fig. 2. SEM image (left) of a fly ash in fresh snow from Hanover, N.H. Its shape and elemental compositions (right) indicate that it originated from a coal-fired plant

in general. However, pH and electrolytic conductivity varied considerably among samples. The variation is considered to be caused by several factors, such as wind direction, atmospheric pollution, and amount of precipitation. The relationship between the pH of the snow associated with southerly winds and the amount of precipitation was examined. The pH of snow with southerly wind was almost constant within a narrow range, regardless of the amount of precipitation. This indicates that atmospheric pollution over Hanover, N.H., was not being diluted by precipitation during southerly winds from densely populated areas. The pH of snow with northerly winds increased with the amount of precipitation, indicating that atmospheric pollutants over Hanover, N.H, were being diluted by the water vapor from less populated areas. The mean snow pH associated with northerly winds was higher than that of southerly winds. The mean H^+ concentration of precipitation during winter 1972-1973 (the period of the oil embargo) was the minimum in the 5 winter measurements as shown in Table 1. The total H^+ deposition/m^2 during the 5 winters ranged from 0.0033 to 0.0101 mol (Table 1). The H^+ deposition during winter 1972-1973 was the lowest for the amount of precipitation.

Microparticles in the fresh snow were examined with the SEM and EDX. Typical SEM images of fly ash from an oil-fired plant (Fig. 1) and from a coal-fired plant (Fig. 2) are shown. More fly-ash particles were found in the lower pH snow associated with southerly winds from densely populated areas.

The pH values of snow (1981-83) from Dye-3, Greenland, ranged from 4.65 to 5.23. The electrolytic conductivity ranged from 2.99 to 9.31 μS/cm. The fly-ash concentration was much smaller than that of the Hanover snow.

REFERENCES

NATIONAL RESEARCH COUNCIL: Acid Deposition, Washington, D.C.: National Academy Press (1983) p. 113-116.

IONIC CONCENTRATINS OF RIME ICE AND SNOW AND BERGERON PROCESS

Huang Shi-hong
(Department of Atmospheric Sciences, Nanjing University, Nanjing, China)
R.A.Castillo
(Western Connecticut State University, Danbury, CT 06810 U.S.A.)
V.K.Monhen
(Department of Atmospheric Sciences, State University of New York at albany NY,12222. U.S.A.)

1. INTRODUCTION

The chemical composition of cloud water is of interest since the role of clouds is one of transforming trace atmospheric constituents and delivering the resulting products as precipitation. Measurement of cloud water ion concentrations should allow one to separate nucleation and intracloud scavenging from below cloud scavenging processes. Castillo, et al., (1983) found that the ion concentrations of cloud water at the summit of Whiteface Mountain (WFM) were able to account for 75% to 100% of the concentrations found in rain at a point 1.0 km below. Snow is the main water source at high and middle latitudes and is considered to exert a major pH shock to watersheds during the spring runoff. The ice crystals in a supercooled cloud undergo more complex processes as they grow into snowflakes. The effect of the Bergeron process in a supercooled cloud on snow ion concentrations is described in this paper.

2. DATA AND ANALYSES

2.1 WHITEFACE MOUNTAIN

The rime ice samples of 8 supercooled clouds were collected at the WFM summit (1600 m elevation) during November, 1981 to March, 1982 while event snow samples were collected at base (800 m elevation). The average value of $[SO_4^{2-}]$, $[NO_3^-]$ and total ion concentrations, including $[Na^+]$, $[K^+]$, $[Mg^{2+}]$, $[F^-]$ and $[Cl^-]$ are presented in Table 1. All ion concentrations were measured by ion chromatography.

2.2 YELLOW MOUNTAIN (YLM)

The rime ice and snow samples of 2 supercooled clouds were collected at the YLM (1840 m elevation),

China in January, 1987. The average ion concentrations are presented in Table 2.

The feature shown in Tables 1 and 2 is that the rime ion concentrations generally exceed the snow ion concentrations. Xiong, et al., (1984) found the same results.

The dominant ions in both samples were SO_4^{2-} and NO_3^- at WFM, and SO_4^{2-}, NO_3^-, Ca^{2+} and NH_4^+ at YLM. The average total snow ion concentration accounts for 20% to 30% of that found in the rime. The fact that there was a discrepancy between the rime ice and the snow ion concentrations cannot be explained by the below cloud scavenging of trace atmospheric constituents by snow. It is necessary to take into account the mechanism responsible for the discrepancy of the ion concentratrations between both samples. The Bergeron process (1935) occurring in a supercooled cloud is required for ice crystals to develop into snow. It is possible that the growth of ice crystals by sublimation of water vapor from droplets results in a dilution of the chemical composition in snow.

3. A FIELD EXPERIMENT

In order to confirm the effect of the Bergeron process on the snow ion concentrations, samples were obtained at WFM. Temperatures on WFM summit were about $-25^{\circ}C$ outside and $-15^{\circ}C$ inside a ventilated summit house in the winter.

The sublimation of water vapor to the inside stone surfaces provided natural frost crystals. Only $[SO_4^{2-}]$ were measured in the frost crystal samples; the other ions were below the detection limits of the ion chromatograph. The $[SO_4^{2-}]$ is presented in Table 3. Rime ice concentrations exceeded those found in the frost crystals by an order of magnitude or more. These results support the contention that ice crystals growing by the Bergeron process will have a low $[SO_4^{2-}]$.

4. CONCLUSION

The data from WFM and YLM have shown that the ion concentrations in the snow were generally lower than those measured in rime ice with a lower pH value. The WFM results demonstrated that the

Bergeron process occurring in supercooled clouds may be the main reason for this ion concentration difference. The variation of ion concentrations in precipitation may in part be due to a higher percentage of solid precipitation.

Table 1

Ion Concentrations of the Rime and the Snow at WFM(ppm)

	PH	$[SO_4^{2-}]$	$[NO_3^-]$	total ions
Rime	3.8	6.6	5.2	12.6
Snow	4.3	1.6	1.0	3.1

Table 2

Ion Concentrations of the Rime and Snow at YLM(ppm)

	PH	$[SO_4^{2-}]$	$[NO_3^-]$	$[Ca^{2+}]$	$[NH_4^+]$	total ions
Rime	6.0	11.1	2.6	3.5	2.5	22.9
Snow	7.3	1.0	0.2	2.0	0.9	6.1

Table 3

The Frost $[SO_4^{2-}]$ and The Ice $[SO_4^{2-}]$ at WFM Range of Summit Rime

Samples	$[SO_4^{2-}]$ (ppm)
frost 1	0.07
2	0.10
3	0.09
rime ice	1.92-12.48×

× over four years

Reference

Bergeron. T(1935), On the physics of cloud and precipitation. Pro. 5th Assemly U. G. G. I. Lisbon. Vol. 2. P. 156.

Castillo, R. A., et al, (1983), The ρ H and Ionic Composition of stratisform cloud water. Atmospheric Environment, Vol. 17, No. 8, pp1497-1505.

Xiong Jiling, et al, (1984), The study of Chemical Composition and Distribution of snowfalls in Guiyan. J. Chinese Soc. Env. Sci. Vol. 4, No. 3, p31.

CHEMICAL NATURE OF PRECIPITATION AT VISAKHAPATNAM

Syed Nizamuddin

Department of Meteorology and oceanography
Andhra University, Waltair, India

1. INTRODUCTION

The study of impact industralization and urbanization on global as wellas local climate and its environs occupy major emphasis all over the world. Atmosphere is loaded with several chemical particles and they are interacting with the cloud process and its precipitation. The chemical nature of clouds and precipitation is greatly by these products. In the present study an attempt has been made to see the change in chemical nature of precipitation at Visakhapatnam.

2. METHODOLOGY

Chemical nature of a solution is expressed in terms of pH. When a solution shows 7, it is called as neutral solution. If pH of a solution is more than 7, it is called as basic solution. If pH of a solution is less than 7, it indicates acidic nature. The common measure of pH 7 for neutrality is not applicable to rain water. Atmosphere contains carbon dioxide which dissolves in rain water forming carbonic acid. Because of this pH of even uncontaminated rain water lowers down to 5.6 at 20 deg.C The criterion for acidic nature of precipitation is considered as pH 5.6 in both Europe (Barrett and Brodin, 1955) and USA (Likens et al. 1979). Rain water is collected in clean polythene bottles The pH analysis is carried by pH electrometer. Using ion-chromatography technque, concentrations of cl, Fl, No_2 No_3 ions are determined.

Table 1. Chemical composition of rain water at Visakhapatnam in 1987.

Sample	pH	cl	Fl	No_3	No_2
	Constitution parts per milli				
1.	6.45	7.22	0.03	5.2	0.06
2.	6.75	6.55	0.02	7.0	0.056
3.	7.1	6.75	0.03	10.2	0.033
4.	6.67	6.80	0.02	4.5	0.125
5.	6.71	6.60	0.03	6.5	0.066
6.	6.75	6.70	0.03	6.5	0.055
7.	6.69	6.75	0.03	6.75	0.022
8.	6.70	6.80	0.02	6.70	0.122

3. RESULTS AND DISCUSSIONS

Table 1 shows chemical composition of rain water collected at Visakhapatnam In the light of above discussion, the chemical nature of precipitation at Visakhapatnam is not so acidic. In seventies pH values of rain water at Visakhapatnam are more than 7 (Krishna Nand 1984) where as in 1987, pH values of all samples are less than 7. It indicates the precipitation at Visakhapatnam is tending towards acidic nature. Visakha patnam is coastal city. Sea salt particles consist of calcium, magnesium, potassium and sodium. Soil particles are usually alkaline in nature. They act as as condensation centres for cloud formation and also swept by precipitation. When they are dissolved, they usually form corresponding anion or negative ion and thus pH value is raised. After seventies Visakhapatnam emerged as major industrial centre with petro-chemical, fertilizer, zinc smelter, polymer and other plants. They are injecting sulphur and nitrogen oxides in to the atmosphere. They are interacting with the cloud process and its precipitation. Because of this precipitation is becoming more acidic and acidic constituents are increasing.

3. REFERENCES

BARRETT, E; BRODIN, G: The acidity of scandinavian precipitation, Tellus, 7 1955, P. 251-257.

KRISHNA NAND: Prospects of acid rain over India, Mausam, 35, 1984, P. 225-232.

LIKENS, G.E; WRIGHT, R.F; GALLOWAY, J.N; BUTLER, T.J: Acid rain, Scientific American, 24, 1979 P. 39-47.

A ONE - DIMENSIONAL NUMERICAL MODEL TO SIMULATE LIQUID PHASE CHEMICAL REACTIONS WITHIN RADIATION FOG

Renate Forkel and Winfried Seidl
Meteorologisches Institut der Universität München
Theresienstr. 37, D - 8000 München 2, FRG

1 INTRODUCTION

An important aspect of atmospheric chemistry concerns reactions that occur in cloud and fog droplets. Ionic concentrations and acidity in cloud and fog water can reach quite high values (e.g., Jacob et al., 1984), which raised concern regarding potential damage to vegetation, materials and human health. In this connection, fogs are of special importance due to their lifetimes up to several days and due to the high concentrations of aerosol particles and gaseous reactants near the ground.

A number of cloud water chemistry models has been developed recently. Among others, Jacob and Hoffmann (1983) have published a very detailed chemical model for fog. However, these models did not account for meteorological processes in so far as variables as temperature and liquid water content were prescribed. The increasing number of dynamical models including liquid phase chemistry mainly treats convective clouds (e.g., Walcek and Taylor, 1986) or long range pollutant transport and transformation.

In the following sections, a one - dimensional model for fog prediction is described, which includes liquid phase chemical reactions. The fog chemistry is treated by a hybrid kinetic and equilibrium model for the bulk liquid phase. The model predicts vertical profiles of temperature, water vapor, liquid water and gas - and liquid phase reactant concentrations.

2 DESCRIPTION OF THE MODEL

2.1 FOG MODEL

The one - dimensional atmospheric model predicts the potential temperature, specific humidity, liquid water content, horizontal wind speed and the mass fractions of the chemical reactants in the gas phase (SO_2, H_2O_2, NH_3, O_3) as well as in the liquid phase ($H_2O_2(aq)$, NH_4^+, $O_3(aq)$, S(IV), S(VI), Fe^{3+}, Mn^{2+} and the sum of all other dissolved ions).

The turbulent fluxes in the prognostic equations are parameterized by gradient laws, using a mixing length formulation for the exchange coefficient. The influence of thermal stratification is treated by stability - functions which depend on the local Richardson number (for details see Forkel, 1987). The radiation flux in the heat equation is calculated with the two - stream model of Zdunkowski et al. (1982). The average sedimentation velocity of the fog droplets and of the constituents in the liquid phase is taken as proportional to the liquid water content. To calculate the condensation and evaporation of fog water, McDonald's (1963) adjustment is used. For relative humidities below 100% the amount of liquid water attached to the aerosol particles is parameterized and depends on relative humidity and aerosol composition. The source terms of the chemical constituents are calculated by the chemistry model.

The atmospheric model is coupled to a soil model, which predicts temperature and liquid water content within the soil (Sievers et al., 1983).

2.2 CHEMISTRY MODEL

To calculate concentrations of dissolved aerosol material and trace gases in the fog water, a hybrid equilibrium and kinetic aqueous chemistry model (Jacob and Hoffmann, 1983, Walcek and Taylor, 1986) is used.

Solution and dissociation processes are assumed to occur fast enough to be treated by equilibrium relations. Besides of S(IV) and S(VI) equilibria and dissociation of water, equilibria of NH_4^+, H_2O_2, O_3, Fe^{3+}, Mn^{2+} and CO_2 are calculated, taking into

account ionic strength effects.

The oxidation of S(IV) is calculated by empirical rate laws. For S(IV) – oxidation by H_2O_2 and O_3 relations given by Martin (1984) and Hoigne et al. (1984) are applied, the Fe^{3+} – and Mn^{2+} – catalysed oxidation is calculated according to Freiberg (1975) and Martin (1984), respectively.

In fog free layers (i.e. relative humidity < 100%) the amount of liquid water attached to the aerosol particles is very low. In this case, oxidation rates are assumed to be negligible and only equilibria are calculated.

3 MODEL CALCULATIONS

As an example, a calculated fog event which is typical for midlatitude autumnal situations, is discussed in this section. The model calculations start at 18:00h with an initial temperature profile as given in Fig. 1. The relative humidity near the ground is 65%. The geostrophic wind is 5m/s, the roughness height is 0.01m and the soil is assumed to be moderately moist loam. The pollutant concentrations near the ground are given in Table 1.

Table 1: Initial pollutant concentrations in $\mu g/m^3$ at a height of 1.5m above the ground.

SO_2	O_3	NH_3	H_2O_2
25.0	100.0	2.7	1.5
SO_4^{2-}	NH_4^+	Fe^{3+}	Mn^{2+}
14.6	3.6	0.08	0.01
nonreacting ions		unsoluble material	
4.9		4.7	

To give an impression of the life cycle of the fog, calculated temperature profiles at selected times are given in Fig. 1. Fog forms at 1:30h of the second day. In Fig. 1 the fog top is marked by arrows. In agreement with observations (e.g., Jiusto and Lala, 1983), the strong ground inversion moves upward to fog top as the fog grows during the night and an adiabatic to slightly unstable lapse rate establishes below the inversion. The calculated liquid water content reaches a maximum value of nearly $0.4 g/m^3$ at 7:00h. At around 8:30h the fog begins to lift due to the heating of the ground after sunrise. The fog has completely dissipated at 11:00h.

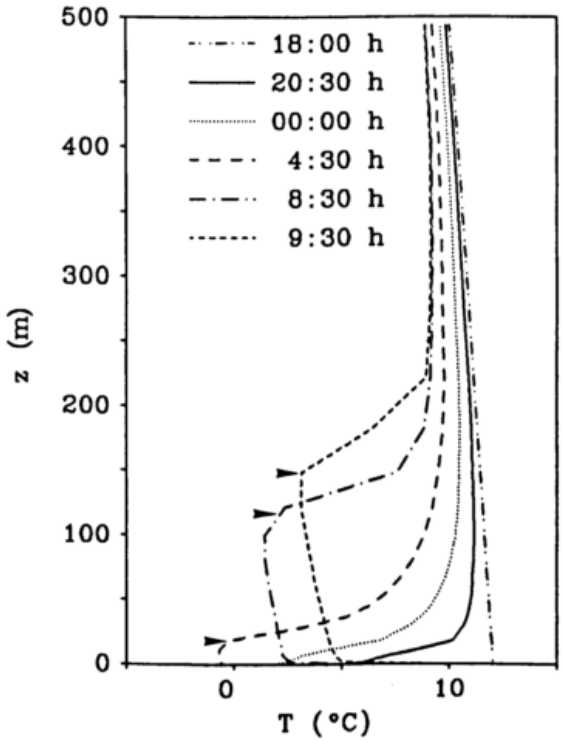


Figure 1: Calculated temperature profiles at various times. The arrows at the curves mark the fog top.

The concentration of S(VI) and the fog water pH during this fog event are given by the solid lines of Figs. 2 and 3. Even though S(IV) is oxidized to S(VI) within the fog, the amount of S(VI) decreases due to sedimentation of the fog droplets. This result agrees with measurements by Jacob et al. (1984). The loss of S(VI) by sedimentation and the increasing dissolution with growing liquid water content during the first hours of the fog result in an increase of the fog water pH.

For the situation given here, oxidation mainly occurs by H_2O_2, however, this oxidant is consumed rather quickly. Half an hour after fog formation its concentration is reduced to 1% of its initial value. Entrainment from aloft is only small during the night.

To get more information on the relative importance of sedimentation and S(IV) – oxidation, the model calculations were repeated, first with the assumption of no oxidation (dashed curves in Figs. 2 and 3) and then with no sedimentation of pollutants (dash – dotted curve in Figs. 2 and 3). In the case of no oxidation, only equilibria of the chemical constituents are calculated within the fog. These sensitivity studies confirm that sedimentation overcompensates the formation of sulfate by oxidation in

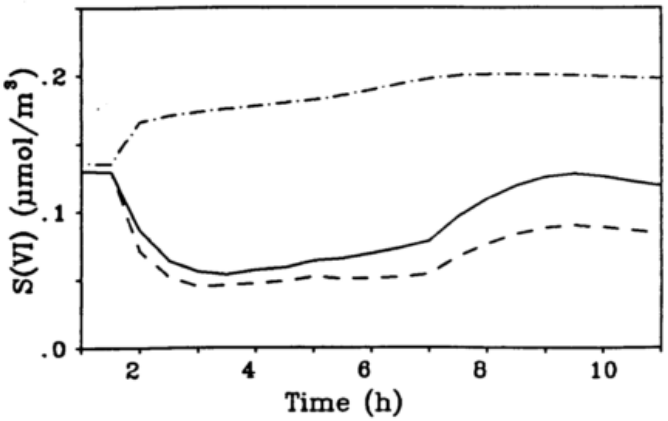


Figure 2: Mass of S(VI) 1.5m above the ground during the fog event. ——— complete treatment, – – – no oxidation, –·–· no sedimentation.

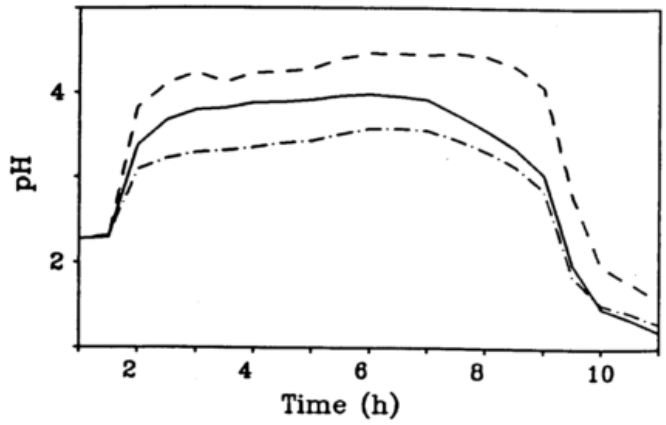


Figure 3: pH – values 1.5m above the ground during the fog event. ——— complete treatment, – – – no oxidation, –·–· no sedimentation.

the case described above and that, although oxidation contributes significantly to the concentration of S(VI) in fog water, the major part of S(VI) in the fog droplets is due to nucleation.

4 CONCLUDING REMARKS

A one – dimensional fog – chemistry model was presented, which permits to estimate the role of liquid phase chemical reactions, initial pollutant concentrations and vertical transport on pollutant concentrations in fog. Sedimentation plays an important role for pollutant removal in fog. For the case discussed above, the total deposition of S(VI) due to sedimentation is 1.5mg/m^2 during the fog event.

Since only the bulk properties of the liquid phase are calculated by the model, no size dependence of the aerosol composition can be taken into account. For aerosol types, which are acidic over the full range of size, the bulk model can yield reliable results. However, if for example, large basic aerosol particles are present, the oxidation rates calculated by the bulk model are not correct anymore (Seidl, 1988). For this reason it is intended to introduce droplet microphysics into the model. This increases the range of application for the model, as it will then be possible to account for size dependent aerosol composition and oxidation rates within the droplets.

REFERENCES

Forkel, R., 1987: Numerische Modellierung von Strahlungsnebel. Wiss. Mitt. Nr. **56** des Met. Inst. München, 135 – 143

Freiberg, J., 1975: The Mechanism of Iron Catalysed Oxidation of SO_2 in Oxygenated Solutions. Atmos.Environ., **9**, 661 – 672

Hoigne, J., H. Bader, W.R. Haag, J. Staehlin, 1984: Rate Constants of Reactions of Ozone with Organic and Inorganic Compounds in Water, Inorganic Compounds and Radicals. Water Res., **18**

Jacob, D.J., M.R. Hoffmann, 1983: A Dynamic Model for the Production of H^+, NO_3^- and SO_4^{2-} in Urban Fog. J. Geophys. Res., **88**, 6611 – 6621

Jacob, D.J, J.W. Munger, J.M. Waldman, M.R. Hoffmann, 1984: Aerosol Composition in a Stagnant Air Mass Impacted by Dense Fog. Proc. 77th Ann. Meeting of the Air Pollution Control Ass., San Francisco

Jiusto, J.E., G.G. Lala, 1983: Radiation Fog Field Programs – Recent Studies. ASRC – SUNY, Pub. No. 869

Martin, L.R., 1984: Kinetic Studies of Sulfite Oxidation in Aqueous Solution. In: SO_2, NO and NO_2 Oxidation Mechanisms: Atmospheric Considerations (J.G.Calvert, Ed.), Butterworth Publ., Boston

McDonald, J.E., 1963: The Saturation Adjustment in Numerical Modelling of Fog. J. Atmos. Sci., **20**, 476 – 478

Seidl, W., 1988: Ionic Concentrations in Droplets During the Condensational Stage of Cloud. Tellus, submitted for publication

Sievers, U., R. Forkel, W. Zdunkowski, 1983: Transport Equations for Heat and Moisture in the Soil and Their Application to Boundary Layer Problems. Beitr. Phys. Atmosph. **56**, 58 – 83

Walcek, C.J., G.R. Taylor, 1986: A Theoretical Method for Computing Vertical Distributions of Acidity and Sulfate Production Within a Cumulus Cloud. J. Atmos. Sci. **43**, 339 – 355

Zdunkowski, W., W.G. Panhans, R. Welch, G. Korb, 1982: A Radiation Scheme for Circulation and Climate Models. Beitr. Phys. Atmosph. **55**, 215 – 237

THE EFFECT OF FREEZING ON THE COMPOSITION OF CLOUD DROPLETS

J.V. Iribarne and T. Pyshnov

McLennan Physical Laboratories, University of Toronto

1. INTRODUCTION

Freezing is involved in the microphysical mechanisms of precipitation development, in particular, in the riming process. It is known that when ice grows from an aqueous solution, the solutes are rejected in higher or lesser proportion by the growing ice lattice (JACCARD and LEVI 1961; DEMICHELI and IRIBARNE 1963). If the solute is non-volatile (e.g. a salt), it will remain entirely in the frozen droplet, and segregation by the ice will result in a very inhomogeneous distribution; but volatile compounds can, in principle, be lost during freezing, due to a displacement of equilibria (IRIBARNE et al. 1983); e.g.:

$$H^+ + Cl^- \rightarrow HCl\ (g)\uparrow$$
$$H^+ + HSO_3^- \rightarrow H_2SO_3 \rightarrow H_2O + SO_2\ (g)\uparrow$$

Cloud chemistry models must take into account the transfers of chemical compounds among air and the different species of hydrometeors. Therefore a knowledge of the fraction of solutes retained by frozen droplets is necessary. This fraction is here called the retention coefficient Γ and the work presented tends to obtain information about this coefficient.

2. RETENTION COEFFICIENT OF HCl, HNO_3, NH_3 AND H_2O_2

2.1 EXPERIMENTAL ARRANGEMENT

Fig. 1 shows schematically the chambers used for the experiments, inside a walk-in cold room. The upper chamber was kept just above 0°C by a thermostatic circuit. A spray was produced with an ultrasonic transducer; it fell through an orifice to the lower chamber at the temperature of the cold room, acquired thermal

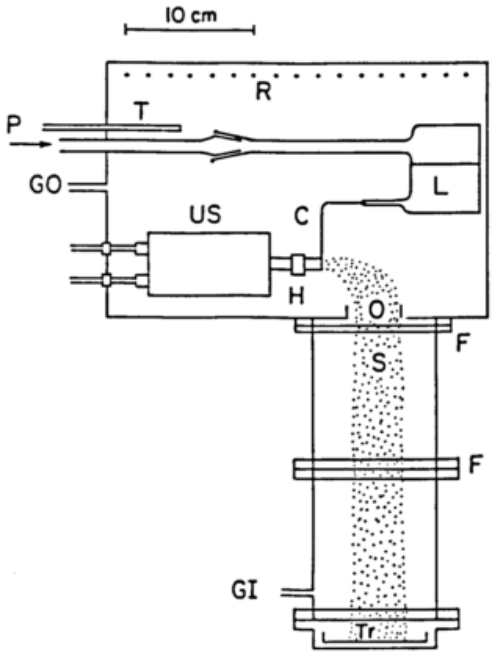


Fig. 1 - Chambers -R: heating resistance; T: thermometric sensor; L: liquid reservoir; P: pressure; C: capillary; US: ultrasonic transducer; H: horn; O: orifice; S: spray; GI: gas inlet; GO: gas outlet; Tr: tray; F: flange.

equilibrium and froze on an ice surface in a tray. The average diameter of droplets was 39 μm.

Samples of 0.5 to 1 g were collected and analyzed. The retention coefficient was obtained by comparing the concentration of the studied ion or compound in the frozen droplets with that in the initial solution.

The experiments described in this section were performed at temperatures varying between -5 and -12°C. Growth occurred in the dry growth regime, except for the highest temperatures.

2.2 HCl

Solutions containing H^+, Cl^- and $SO_4^=$ were tested. The analysis was done by ion chromatography, comparing the peaks corresponding to Cl^- and to $SO_4^=$ (non-volatile reference). If the ratios of peak heights are r_o for the initial solution and r for the sample, $\Gamma = r/r_o$. The results of 21 experiments gave an average $\bar{\Gamma} = 1.004$, with a root mean square error of the average $\mu = 0.008$.

2.3 HNO_3

Solutions containing H^+, NO_3^- and $SO_4^=$ were tested. NO_3^- and $SO_4^=$ chromatographic peaks were compared. The overall result of 18 experiments was $\bar{\Gamma} = 0.995$, with $\mu = 0.004$.

2.4 NH_3

A solution containing NH_4^+, Na^+ and Cl^-, of pH 6.3, was tested. Both NH_4^+ and Na^+ (reference) were determined with specific ion electrodes.

The overall result of 8 experiments was $\bar{\Gamma} = 1.03$, with $\mu = 0.03$.

2.5 H_2O_2

Two series of experiments were performed. In one of them, solutions with various concentrations between 39 and 159 ppm of H_2O_2 were used, and the fluorometric analysis was based on the reaction with horseradish peroxidase and p-hydroxyphenylacetic acid. The overall result of 17 experiments was $\bar{\Gamma} = 1.012$, with $\mu = 0.023$.

A second series was run with a solution 1.045 M H_2O_2, and the analysis was performed with permanganimetry. The result of 10 experiments was $\bar{\Gamma} = 1.016$, with $\mu = 0.008$.

3. RETENTION COEFFICIENT OF S(IV)

3.1 EXPERIMENTAL ARRANGEMENT

The same chambers described in 2. were used for experiments in which spray droplets were collected on an ice surface by gravitation. However, some experiments indicated that the results were influenced by the ventilation conditions during freezing. Therefore, a separate series of experiments was made using a jet of gas with the appropriate concentration of SO_2, which caught the falling spray droplets and projected them over a target, at velocities of the order of several meters per second. The conditions were then similar to those prevailing in the riming of graupel or ice pellets of sizes of several mm. The arrangement was obtained with a modification of the lower chamber, as indicated in Fig. 2.

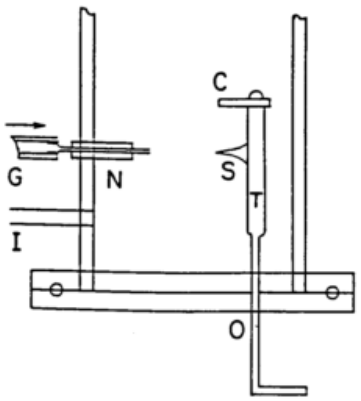


Fig. 2 - Arrangement for ventilation experiments - T: target; C: cover; O: orifice; N: hypodermic needle; G: gas; I: gas inlet; S: collected rime.

3.2 PROCEDURE

The experiments with SO_2 required circulation of a controlled atmosphere through the airtight chambers. N_2 with a known SO_2 concentration (between 25 and 99 ppm (V)) was used. It was estimated that the spray droplets acquired solubility equilibrium with the SO_2 in the atmosphere during their fall in the lower chamber. The chambers were continuously flushed with the gas, and the experiments were initiated only after adsorption equilibrium with the walls had been attained ($\geq$ 1.5 hours).

The liquid sprayed was usually pure water, but in the ventilation experiments a solution of 2×10^{-2} N NaF was also used as a reference in order to check on any possible evaporation of the highly ventilated rime.

The samples were treated with a solution of H_2O_2, which oxidizes SO_2 to H_2SO_4. After bringing the samples to a known volume, the concentration of H_2SO_4 was determined with a conductivity bridge. When NaF was used, a specific ion electrode for F^- was applied, and the contribution of NaF to conductivity was calculated taking into account the equilibrium constants for $HF \rightleftarrows F^- + H^+$ and $F^- + HF \rightleftarrows F_2H^-$.

3.3 RESULTS

a) COLLECTION BY GRAVITATION

Fig. 3 shows the results of a set of 50 experiments, with 30 ppm (v) (crosses) and 99 ppm (v) (circles) of SO_2. Another set of 37 experiments using a stagnant (rather than flushing) atmosphere, during sample collection, gave similar results. The overall result can be expressed by

$$\Gamma = 0.25 - 0.012\ T;\ r = 0.50$$

where T is the temperature in °C and r is the regression coefficient.

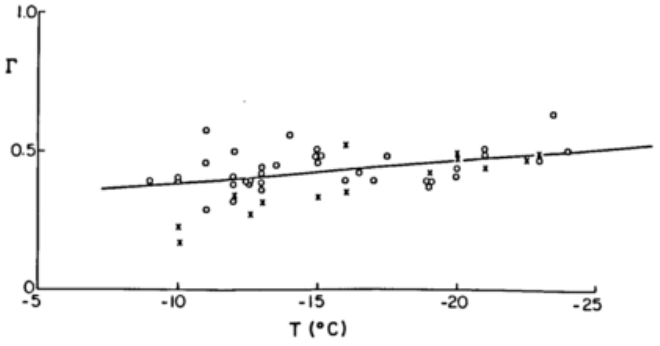


Fig. 3

b) VENTILATION EXPERIMENTS

The results are collected in Fig. 4. Variation of the jet velocity between 2 and 10 m/s did not have any significant influence. The overall result is expressed by

$$\Gamma = 0.82 + 0.011\,T;\ r = -0.45$$

In view of the small temperature dependence and the dispersion of data, an average $\bar{\Gamma} = 0.66$ ($\mu = 0.02$) taken as independent of T, could also be accepted as reasonable approximation.

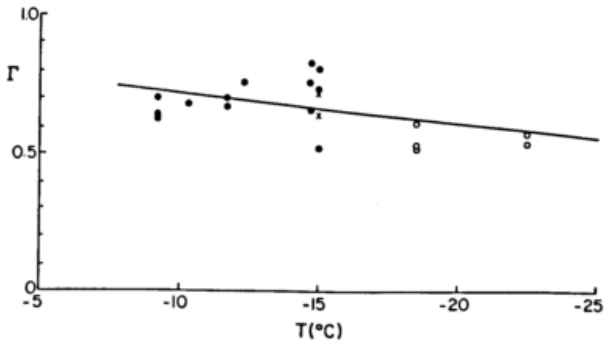


Fig. 4

4. CONCLUSIONS

The experiments regarding possible losses of HCl, HNO_3, NH_3 and H_2O_2 during freezing indicate that these chemical species are totally retained by the ice.

The experiments with SO_2 which are relevant to cloud chemistry are those producing riming conditions. The values of Γ indicated above for these conditions should be used in chemistry models. About two thirds of the S(IV) contained in droplets remain in the ice after freezing, the remaining third being transferred to the interstitial air; there is only a slight dependence of the retention coefficient between -8 and -23°C.

REFERENCES

JACCARD, D.; LEVI, L.: Ségrégation d'impuretés dans la glace. Z. f. angew. Math. u. Phys. 12 (1961) 70-76.

DEMICHELI, S.M.; IRIBARNE, J.V.: La solubilité des electrolytes dans la glace. J. Chimie Phys. (1963) 767-774.

IRIBARNE, J.V.; BARRIE, L.A.; IRIBARNE, A.: Effect of freezing on sulfur dioxide dissolved in supercooled droplets. Atm. Env. 17 (1983) 1047-1050.

SOME EFFECTS OF CLOUD MICROPHYSICS ON CLOUD CHEMISTRY

Dean A. Hegg and Peter V. Hobbs
Atmospheric Sciences Department, University of Washington, Seattle, WA 98195 USA

1. INTRODUCTION

Modeling studies (e.g., Hegg and Hobbs, 1979; Scott, 1982; Chaumerliac et al., 1987; Flossmann et al., 1987; Tremblay and Leighton, 1986) and field measurements (e.g., Borys et al., 1983; Raynor and Hayes, 1983; Daum et al., 1984; Parungo et al., 1988) indicate that microphysical processes in clouds can have a significant influence on chemical reactions in clouds and on the deposition of trace chemical species from clouds. Thus, cloud microphysical processes need to be considered in studies of the geochemical cycles of species that interact strongly with cloud systems (e.g., SO_2, $SO_4^=$, NO_3^-, NH_3).

Here we identify and discuss some cloud microphysical processes of potential significance to cloud chemistry.

2. NUCLEATION SCAVENGING

The first microphysical process of chemical consequence in clouds is the nucleation of cloud droplets on discreet nuclei. This produces a spectrum of cloud droplets containing differing types and amounts of various chemical species. As first pointed out by Hegg and Hobbs (1979), such inhomogeneities can have a significant impact on the aqueous phase chemistry of a cloud system. Hegg and Larson (unpublished manuscript, 1988) have examined the consequences of these inhomogeneities on aqueous sulfate production utilizing an explicit microphysical cloud model. For comparison, a bulk parameterized model was run with the same initial conditions. Depending on the initial conditions, the explicit model predicts up to three times more sulfate production in the cloud during the condensational stage of growth than does the bulk model.

The explicit model also predicts acidification of cloud water relative to the precloud aerosol. The reason is a skewed, non-equilibrium distribution of NH_4^+ ions across the droplet spectrum (Fig. 1). Because the peak supersaturation achieved in the model run was ~ 0.64%, it can be seen that the cloud droplets would have been relatively acidic compared to the unactivated (interstitial) aerosol. The explanation for this, in brief, is that rapid condensational growth after nucleation on the largest CCN "produces" H^+ by progressive ionization of the bisulfate ion with decreasing solution strength. While NH_3 is absorbed into these droplets as a consequence of the H^+ "production", the rapidity of droplet growth precludes the attainment of gas-aqueous equilibrium. By the time that smaller CCN are activated and grow, the driving forces for NH_3 redistribution between drops has decreased significantly and the NH_4^+

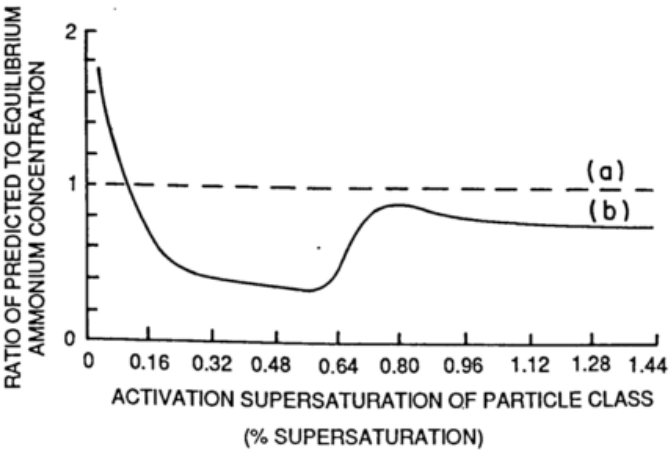


Fig. 1: Ratio of ammonium concentrations in a droplet to the concentrations predicted by Henry's Law as a function of the supersaturation at which the droplet is activated. S(IV) oxidation in the droplet is ignored. (a) Bulk (equilibrium) parameterized model. (b) Explicit model. The simulation time is 465 sec. The discontinuity at a supersaturation of ~ 0.64% represents the peak supersaturation achieved in the simulation (i.e., particle classes to the right of this point are unactivated).

distribution is essentially fixed for the remaining lifetime of the drops.

We believe this effect has been observed in field studies, although it has generally been attributed to acid production by aqueous-phase chemical reactions. For example, Daum et al. (1984), in a study of the chemical composition of stratiform clouds, noted that the bulk ratio of H^+ to NH_4^+ in cloud water samples was always higher than the same ratio in unactivated haze particles measured roughly simultaneously. The H^+/NH_4^+ ratio in the cloud water ranged from 1.9 to > 35, whereas, the ratio in the interstitial particles, when measurable, ranged from < 0 (net basicity after blank correction in Gran titration) to 0.9. For comparison, values for the H^+/NH_4^+ ratio predicted by the Hegg and Larson explicit model range from 1.25 to 11.50 for the activated drops and 0.2 to 0.3 for the unactivated particles. Clearly, the skewed NH_4^+ distribution predicted by the model provides a partial explanation for Daum et al.'s observations, and it illustrates the significance of cloud microphysics on cloud chemistry.

3. SOME EFFECTS OF ICE

Another microphysical process of importance in cloud chemistry is the initiation of ice and interactions between ice and liquid water hydrometeors. These processes can have a profound impact on precipitation efficiency (Hobbs and Matejka, 1980) and both modeling studies (e.g., Hegg et al., 1986) and field experiments (e.g., Borys et al., 1983; Raynor and Hayes, 1983) suggest they can have a substantial influence on wet chemical deposition. The latter effect is attributable to the generally "cleaner" composition of ice relative to water hydrometeors, which, in turn, is due to the insoluble (and generally alkaline) nature of ice nuclei and the depositional growth of cloud ice. The influence of these processes is illustrated below by a case study.

On 6 March 1986 a wide cold-frontal rainband passed over Cape Hatteras, North Carolina. Samples of cloud ice and cloud water were collected from an aircraft flying in the band and analyzed for chemical composition. Sulfate and nitrate concentrations were significantly lower, and the pH significantly higher, in the cloud ice than in the cloud water (Table I). The importance of this dichotomy can be demonstrated by examining the chemical scavenging efficiency (E_c) of the rainband. E_c is defined as the ratio of the mass per unit time of a species advected into the rainband to the deposition of the species on the ground per unit time. We have calculated the chemical scavenging efficiencies from a numerical rainband model (Rutledge et al., 1986) initialized on the measurements for the 6 March 1986 case study.

The model results are shown in Table 2. With the exception of H_2O_2, the chemical scavenging efficiencies are about one-half of the precipitation efficiency. The model calculations also showed the ratio of accretional growth to total growth of the precipitation particles in the rainband to be ~ 50%, the residual being due to depositional growth of the ice. Clearly, such depositional growth, coupled with the initial "cleanliness" of the ice, acted to reduce the chemical scavenging efficiencies.

TABLE I. Measurements of Chemical Concentrations (in ppm) of Hydrometeors in the Rainband on 6 March 1986.

Sample	pH	$[NO_3^-]$	$[SO_4^{=}]$	$[Na^+]$	$[K^+]$	$[Mg^{+2}]$	$[H_2O_2]$
Cloud water 1	4.4	2.10	2.80	0.15	0.66	0.02	0.17
Cloud water 2	4.1	8.10	8.29	0.20	0.89	0.11	0.27
Cloud water 3	3.9	7.89	10.00	0.21	1.08	0.12	0.24
Cloud water & rain 1	4.6	4.65	2.46	0.18	1.13	0.08	--
Cloud ice 1	5.6	0.18	0.21	0.16	0.82	0.04	0.17
Cloud ice 2	5.5	0.16	1.15	--	--	--	--

TABLE II. Model Results for Chemical Scavenging Efficiencies for the Rainband on 6 March 1986.

Species	Fraction Scavenged (%)
Condensed H_2O	8.0*
SO_2	5.0
$SO_4^=$	5.0
NO_3^-	4.0
H_2O_2	2.5

*This is the precipitation efficiency.

ACKNOWLEDGMENTS. Research supported by NSF Grant ATM-8419000.

4. REFERENCES

BORYS, R. D.; DEMOTT, P. J.; HINDMAN, E.; FENG, D.: The significance of snow crystal and mountain-surface riming to the removal of atmospheric trace constituents from cold clouds. In Precipitation Scavenging, Dry Deposition and Resuspension, Eds. Pruppacher, H., Semonin, R., and Slinn, W. New York: Elsevier 1983.

CHAUMERLIAC, N.; RICHARD, E.; PINTY, J.; NICKERSON, E.: Sulfur scavenging in a mesoscale model with quasi-spectral microphysics: Two-dimensional results for continental and maritime clouds. *J. Geophys. Res.*, 92 (1987), 3114-3126.

DAUM, P. H.; SCHWARTZ, S. E.; NEWMAN, L.: Acidic and related constituents in liquid water stratiform clouds. *J. Geophys. Res.*, 89 (1984), 1447-1458.

FLOSSMANN, A.; PRUPPACHER, H.; TOPALIAN, J.: A theoretical study of the wet removal of atmospheric pollutants. Part II: The uptake and redistribution of $(NH_4)_2SO_4$ particles and SO_2 gas simultaneously scavenged by growing cloud drops. *J. Atmos. Sci.*, 44 (1987), 2912-2923.

HEGG, D. A.; HOBBS, P. V.: The homogeneous oxidation of SO_2 in cloud droplets. *Atmos. Environ.*, 13 (1979), 981-987.

HEGG, D. A.; RUTLEDGE, S.; HOBBS, P. V.: A numerical model for sulfur and nitrogen scavenging in narrow cold-frontal rainbands. II: Discussion of chemical fields. *J. Geophys. Res.*, 91 (1986), 14403-14416.

HOBBS, P. V.; MATEJKA, T. J.: Precipitation efficiencies and their potential for artificially modifying extratropical cyclones. 3rd WMO Scientific Conference, Vol. 1 (available from WMO, Geneva, Switzerland.): 1980.

PARUNGO, F.; NAGAMOTO, C.; MADEL, R.: A study of the mechanisms of acid rain formation. *J. Atmos. Sci.*, 44 (1988), 3162-3174.

RAYNOR, G.; HAYES, J.: Differential rain and snow scavenging efficiency implied by ionic concentration differences in winter precipitation. In Precipitation Scavenging, Dry Deposition and Resuspension, Eds. Pruppacher, H., Semonin, R., and Slinn, W. New Elsevier 1983.

RUTLEDGE, S. A.; HEGG, D. A.; HOBBS, P. V.: Numerical model for sulfur and nitrogen scavenging in narrow cold-frontal rainbands. I: Model description and discussion of microphysical fields. *J. Geophys. Res.*, 91 (1986), 14385-14402.

SCOTT, B. C.: Predictions of in-cloud conversion rates of SO_2 to SO_4 based upon a simple chemical and kinematic storm model. *Atmos. Environ.*, 16 (1982), 1735-1752.

TREMBLAY, A.; LEIGHTON, H.: A three-dimensional cloud chemistry model. *J. Clim. Appl. Meteor.*, 25 (1986), 652-671.

PROCESSES DETERMINING CLOUDWATER COMPOSITION: FIELD EVIDENCE FOR IN-CLOUD REACTIVE SCAVENGING OF SO_2

Peter H. Daum
Environmental Chemistry Division
Brookhaven National Laboratory
Upton, New York 11973

1. INTRODUCTION

A major process by which sulfate is incorporated into cloudwater and precipitation is aqueous-phase oxidation of SO_2. The oxidation of gaseous SO_2 to aqueous H_2SO_4 is highly favored thermodynamically in the presence of O_2, O_3 or H_2O_2. Kinetic evaluations indicate that although O_2 and O_3 can cause appreciable in-cloud oxidation of SO_2 under some conditions, H_2O_2 is thought to be the principal in-cloud oxidant of SO_2 at representative pH values, with SO_2 lifetimes as short as a few minutes. The amount of cloudwater H_2SO_4 produced by this reaction appears to be limited by either SO_2 or H_2O_2, whichever reagent is present in a lesser amount. This implies that the spatial and temporal characteristics of sulfate wet deposition will be determined not only by the concentration of SO_2, but also by the amount of H_2O_2 available for aqueous-phase oxidation of S(IV).

2. EXPERIMENTAL

Observations were performed using aircraft and surface networks at a number of locations in the eastern U.S. and southeastern Canada during various field studies. Instrumentation and procedures utilized in these programs are described in detail in other publications (e.g., Daum et al., 1988).

3. RESULTS

3.1 IN-CLOUD CONCENTRATIONS

The concentrations of H_2O_2 we have found in cloudwater have ranged from less than 0.1 μM to over 100 μM; the median value was less than 10 μM. The highest concentrations were measured in the summer; winter concentrations were typically less than 0.5 μM. Equivalent gas-phase concentrations were typically <0.01 to 1 ppb gas phase during the summer, and <0.01 to 0.05 ppb during the winter, suggesting a strong seasonal dependence of cloudwater H_2O_2 concentrations. Cloud interstitial SO_2 concentrations varied greatly and frequently exhibited quite low concentrations, often in the presence of much higher concentrations of cloudwater sulfate. Moreover, it has been noted that in non-precipitating clouds, SO_2 concentrations appear to be related to cloudwater H_2O_2 concentrations in a manner that suggests in-cloud reaction of SO_2 and H_2O_2. This is illustrated in Figure 1.

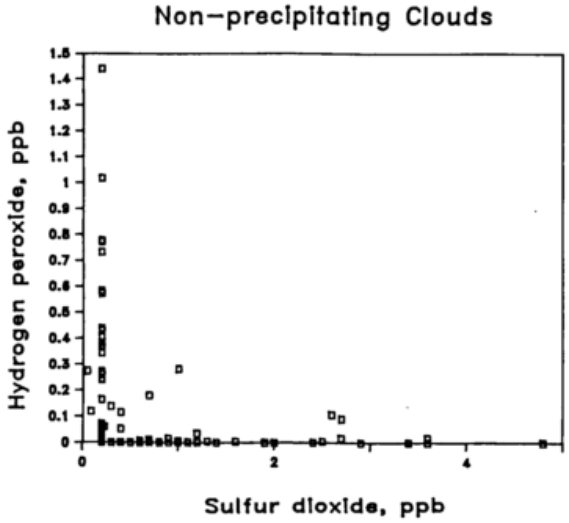


Figure 1. $H_2O_2(aq)$ and $SO_2(g)$ in non-precipitating clouds H_2O_2 concentrations are in equivalent gas-phase units.

3.2 SURFACE PRECIPITATION

H_2O_2 concentrations in surface precipitation have shown the same broad variability and

seasonal trend exhibited by cloudwater concentrations with concentrations in summer occasionally exceeding 100 μM, and in winter frequently below 0.1 μM (Lee et al., 1986). Concentrations of S(IV) in precipitation have been typically below 1 μM; only a small fraction of samples (mostly in winter) was found to contain S(IV). Similar to cloudwater, S(IV) and H_2O_2 were rarely found to co-exist in surface precipitation samples.

3.3 CLEAR-AIR MEASUREMENTS

Vertical profiles of gas-phase H_2O_2 and SO_2 concentrations were made in central Ohio during the month of June 1987. Measurements typically extended over an altitude range of 0.5 to 5.5 km, msl. The H_2O_2 concentration profiles exhibited significant variability, with concentrations higher under moist polluted conditions than under clean dry conditions. For the most part H_2O_2 concentrations were quite variable within the boundary layer, reached a maximum at the top of the boundary layer and then smoothly decreased with altitude. Sulfur dioxide profiles in contrast, exhibited the highest concentrations in the boundary layer and very low concentrations above the boundary layer. Typical concentration profiles are shown in Figure 2.

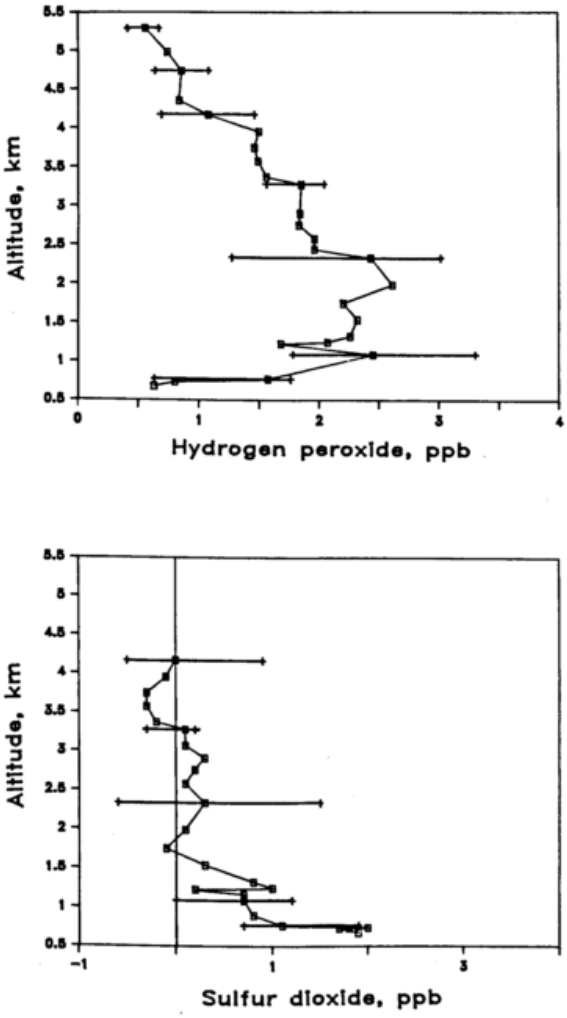


Figure 2. Vertical profiles of H_2O_2 and SO_2 on 6/21/87 in the vicinity of Columbus, OH. Dark symbols and horizontal lines represent the median and range at altitudes where multiple measurements were made.

4. DISCUSSION

We consider the mutual exclusivity observed between cloudwater H_2O_2 concentrations and interstitial SO_2 concentrations in non-precipitating stratiform clouds to constitute perhaps the strongest available field evidence for the in-cloud oxidation of SO_2 by H_2O_2 to produce cloudwater sulfate. These observations imply that this reaction proceeds rapidly and quantitatively in the atmosphere to the extend determined by the availability of H_2O_2 or SO_2. The cloudwater and surface precipitation data also imply that H_2O_2 concentrations are seasonably variable with concentrations higher in summer than in winter. Furthermore, a significant fraction of the cloudwater and precipitation samples collected under summer conditions show an excess of H_2O_2; in contrast, excess H_2O_2 is seldom observed in the winter, suggesting that there is insufficient H_2O_2 in winter to oxidize the available SO_2. This is supported by the occasional observation in winter samples of residual S(IV). Additional information on the relative availability of H_2O_2 and S(IV) can be obtained from the

concentration profiles measured during June 1987. These profiles show that for the most part, SO_2 was confined to the lower part of the boundary layer, while H_2O_2 was more evenly distributed through the troposphere. The observation of generally higher concentrations of SO_2 than H_2O_2 within the boundary layer and vice versa above the boundary layer suggests a reservoir of H_2O_2 available for oxidation of SO_2 if mixing processes can bring these species together under appropriate circumstances. One potential mechanism that could accomplish this is mixing associated with the development of convective clouds.

5. CONCLUSIONS

i. Reactive scavenging of SO_2 by H_2O_2 is an important atmospheric process.

ii. The amount of H_2O_2 available for this reaction appears seasonally dependent with concentrations lower in winter than summer.

iii. SO_2/H_2O_2 vertical profiles suggests that SO_2 is largely confined to the lower part of the boundary layer whereas H_2O_2 is present at significant concentrations over a much wider range of altitudes.

6. ACKNOWLEDGEMENT

The author gratefully acknowledges support of the DOE PRECP program for this work. Vertical profile data of June 1987 were measured by J. Boatman and colleagues of NOAA, under subcontract to BNL. Work was conducted under auspices of the U.S. Department of Energy under contract DE-AC02-76CH00016.

7. REFERENCES

Daum, P.H. Processes determining cloudwater composition: Inferences from field measurement. In: Proceedings of the NATO Workshop: Acid Deposition Processes at High Elevation Sites, D. Fowler, Ed., 1988, in press.

Lee, Y.-N, Shen, J., and Klotz, P. J. Chemical composition of precipitation at Long Island, NY. Water, Air, Soil Pollut. 30, 43-52 (1986).

ACIDIFICATION OF STRATIFORM CLOUDS AND THEIR AEROSOL SCAVENGING PROPERTIES

R. Castillo
Western Connecticut State University, Danbury, CT. 06810

J. DeLuisi
United States Department of Commerce, NOAA/ERL, Boulder, Co. 80303

1. INTRODUCTION

While a monitoring program was not attempted during the summer of 1985 at the Atmospheric Sciences Research Center's (Whiteface Mountain, New York) Schaefer Observatory, sufficient data were obtained to study the acidification of non-precipitating stratiform clouds.

2. DATA AND ANALYSIS

2.1 AIR MASS

Selected trajectories for 1985 were obtained from Joyce Harris (1982) at NOAA/GMCC/ERL in Boulder, Colorado. These trajectories with appropriate scattering data from a 4λnephelometer (Bodhaine, 1985), and with Pollak measurements were used to define the air masses arriving at Whiteface Mountain. The data is for unpolluted continental air masses.

2.2 AEROSOL CONCENTRATIONS

From normal supersaturations expected in the atmosphere, $S\% < .2\%$, and theory, the activated aerosol which would form a cloud was estimated to be in the accumulation mode, $0.1\ \mu m < d < 1.0\mu m$ and larger sizes. An automated CCN (thermal diffusion) instrument was operated at four different $S\%$.

2.3 GAS AND AEROSOL ION CONCENTRATIONS

The water from the filters, for soluble sulfate and nitrate ion concentrations and bulk H_2O samples were sent to Boulder, Co. for ion analysis. The water samples were analyzed at the U.S. Geological Survey Water Laboratory, Arvada, Colorado. They were refrigerated between collection and analysis. Anions were measured by ion chromatography (Fishman and Pyen, 1979).

3. RESULTS

3.1 SCAVENGING OF CLOUD CONDENSATION NUCLEI

Figure 1 depicts the activation of Cloud Condensation Nuclei (CCN) prior to a cloud event at Whiteface Mountain. These aerosols are in accumulation mode, $0.1 < d < 1.0$ um, and larger sizes and are thought to be the main mechanism for the sulfate acidification of non-precipitating, stratiform cloud water.

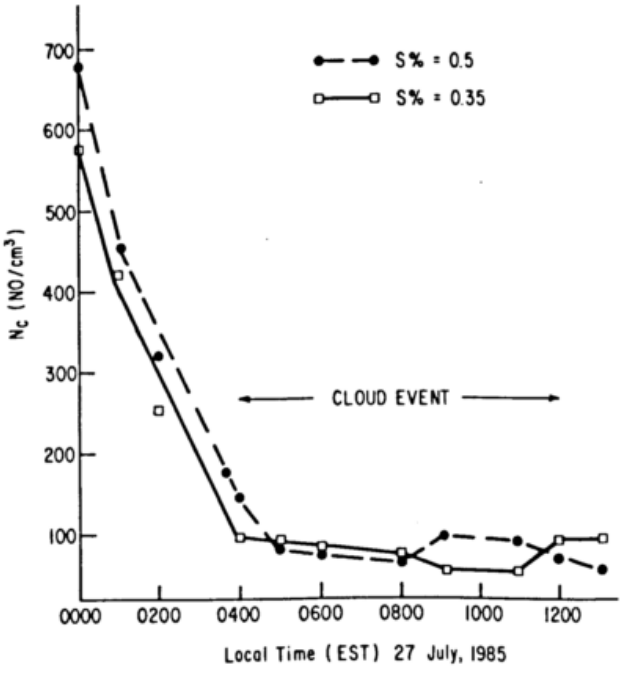


Figure 1. CCN number concentration versus time for Whiteface Mountain Summer, 1985.

3.2 AMBIENT AEROSOL

The TSP for pre-event aerosol is greater than post-event conditions on the average. The interstitial aerosol, indicates that the soluble fraction increases by an order of magnitude. The TSP and soluble fractions both decrease in the post event situation which may last 4-8 hours before a new air mass is established.

3.3 SULFATE ION CONCENTRATIONS

The events to be presented are July 15, July 26 and August 15, 1985 for which the measured cloud water pH was 3.8, 4.2 and 3.4 respectively. For the summer of 1985 the cloud water pH ranged from 3.2 to 4.2.

In each instance the sulfate cloud water and interstitial ion concentrations exceed the post event soluble sulfate concentrations.

3.4 NITRATE ION CONCENTRATIONS

For two events the NO_x mean is $3.2 \pm .93\ \mu g/m^3$ which yields a cloud water concentration of over 10 mg L^{-1} (which exceeds all the measured nitrate cloud water ion concentrations range 1.3 to 6.5 mg L^{-1}). Even though the interstitial and post-event nirate ion concentrations agree closely, (within a factor of 2.0), the cloud water ion concentrations are an order of magnitude greater. Kelly (1985) indicates that the NO_3^- aerosol is low with a summer value of $.13\ \mu g\ m^{-3}$. This back ground nitrate aerosol would convert to 0.43 mg L^{-1} which is an order of magnitude lower than the average ion concentration

found in the cloud water.

4.0 CONCLUSIONS

The activation of cloud condensation nuclei to form a cloud is the predominant acidification process of the cloud water for nonprecipitating stratiform clouds. The ambient aerosol had a mean free acidity of pH ~4.0 and this was most likely associated with $(NH_4)HSO_4$. There is a consistent disagreement between the sum of the cloud water and interstitial sulfate concentrations when compared to the post event sulfate aerosol.

TABLE 1. Filter Averages of Total Suspended Particles (TSP) and Soluble Mass in $\mu g\ m^{-3}$ for Clean Air Mass

CATEGORY	PRE EVENT	INTERSTITIAL	POST EVENT
TSP	14.4 ± 2.1	24.4 ± 16	8.9 ± 4.4
Soluble	1.4 ± .4	14.5 ± 4.7	2.5 ± 1.5

TABLE II ION CONCENTRATIONS mg L-1

DATE	PRE EVENT	EVENT		POST EVENT
July 26, 1985		Cloud	Interstitial	
*SO_2	1.2	---	1.3	---
SO_4^{-2}	66.7	8.4	3.0	1.3
August 15, 1985				
**SO_2	11.7	11.7	---	---
SO_4^{-2}	22.7	29	15	11
July 15, 1985				
SO_2	3.3	3.3	1.0	---
SO_4^{-2}	15.3	15	4.1	3.5

* Assuming a liquid water content of $0.3g\ m^{-3}$ which is used for all calculations

** Using a mean summer SO_2 concentration of $3.5\ \mu g\ m^{-3}$ (Kelly, 1985)

5. REFERENCES

Bodhaine, B.A., et. al.: Light Scattering, Condensation Nuclei, and Air Mass Trajectories at Whiteface Mountain: Summers of 1983 and 1985. NOAA Data Report ERL/ARL-8 Silver Spring, Maryland (1986), pp 82.

Fishman, M.J. and Pyen, G.: Determination of Selected Anions in Water by Ion Chromatography. Water - Resources Investigations, U.S. Geological Survey, Lakewood, Co. (1979) 79-101.

Harris, J.M.: The GMCC Atmospheric Trajectory Program. Tech. Memo ERL/ARL-116, NOAA, Boulder, Co. (1982).

Kelly, T.: Trace Gas and Aerosol Measurements at Whiteface Mountain, New York. Prepared for Empire State Electrical Energy Research Corporation. (1985), pp 97.

6. ACKNOWLEDGEMENTS

I wish to thank NOAA for supporting this research under grants 40 RANR 506003 and 40 RANR50885L. Also thanks go to Dr. John Kadlecek of ASRC for sharing his Whiteface, MT MAP3S and gas measurements with me, Joyce Harris for her trajectory analysis and L. Hussain for sharing his sulfate concentration data.

MICROPHYSICAL, DYNAMICAL AND CHEMICAL ASPECTS OF SCAVENGING PROCESSES DURING WINTER PRECIPITATION

A. Waldvogel, T. Schumann and B. Zinder

Atmospheric Physics ETH, CH-8093 Zürich, Switzerland

1. INTRODUCTION

The scavenging of aerosol particles by cloud droplets, ice crystals, snowflakes and raindrops is investigated in a field experiment. Three ground stations and a mobile measuring platform (cable car) are instrumented, see Figs. 1 and 2. The measuring sites are along a mountain slope between 430 and 1620 meters a.s.l. The mountain is an isolated precursor of the Alps giving a "vertical profile" of the incoming weather systems, which are mostly weak cold fronts.

The main purpose of the measuring program is to study scavenging processes under different meteorological conditions. Specific questions are the quantitative contributions of in-cloud versus below-cloud scavenging, the efficiency of snow versus rain scavenging and the distinction between dynamical and microphysical effects both influencing the scavenging process as a whole.

2. INSTRUMENTATION

Microphysical, meteorological and chemical measurements are made at the three stations; see Fig. 2, WALDVOGEL et al. (1987), SCHUMANN et al. (1988) and ZINDER et al. (1988). The chemical analysis of size dependent aerosol samples and precipitation probes can be used to give more insight into the transfer process of aerosols into precipitiation than the analysis of number or mass concentration changes of aerosols only. A mobile platform (cable car) connecting the middle and the bottom station is instrumented also. This facility can produce a highly resolved vertical profile in about 10 minutes.

3. MEASUREMENTS

A total of 16 case studies have been made during the winter seasons 1984/85, 1985/86 and 1986/87. Normally a case study is defined by a weak cold front, producing weak to medium pre-

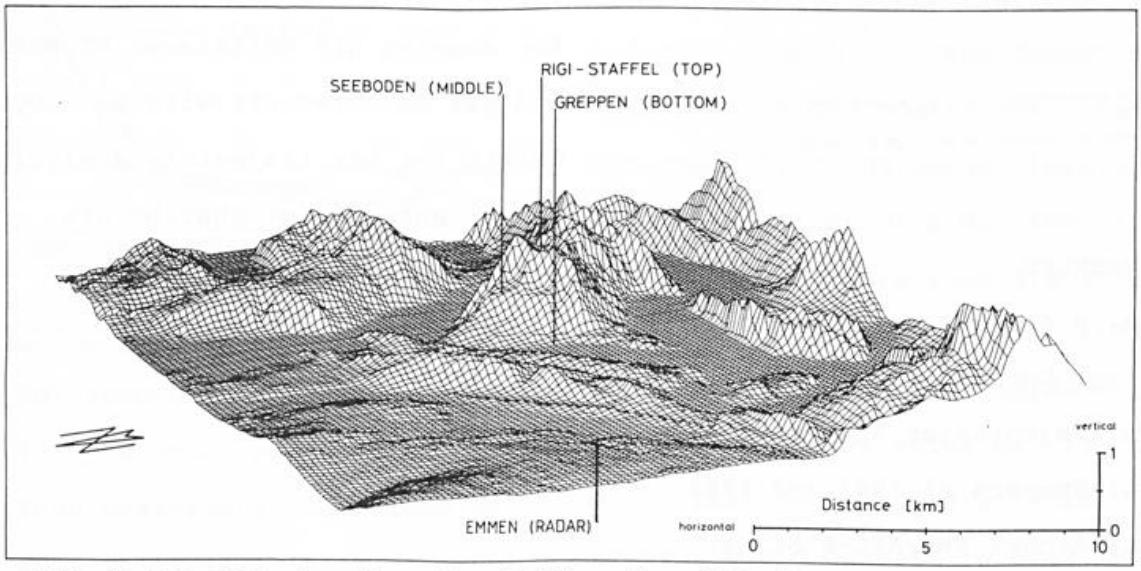


Fig. 1: The measuring sites: Top (1620 masl), middle (1030 masl) and bottom (430 masl). The instrumentation of the stations is given in Fig. 2.

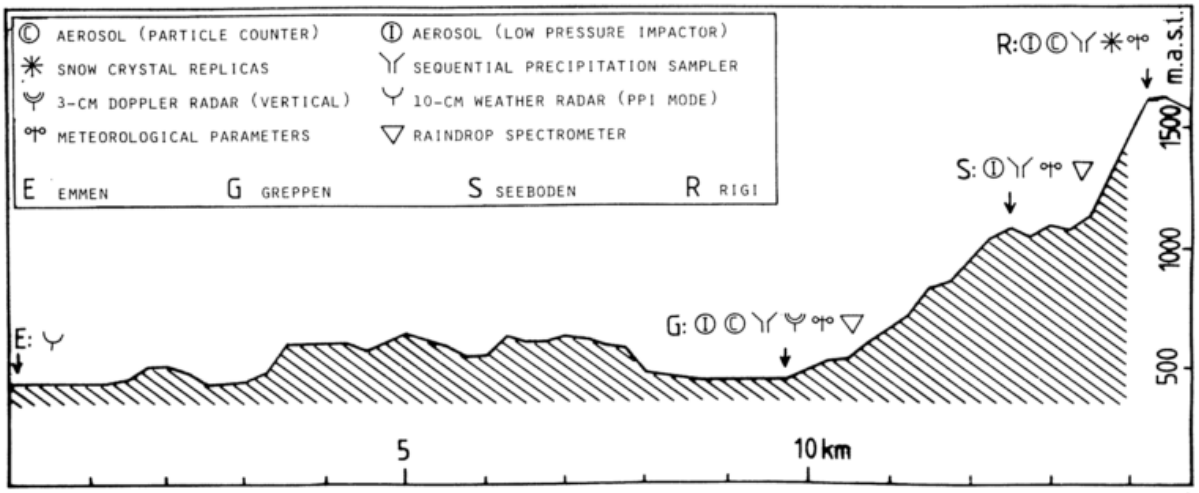


Fig. 2: The instrumentation of the three stations: Top (R), middle (S) and bottom (G).

cipitation (≈ 1 mm/hr) during six hours. Mostly there is snow at the top station and rain at the bottom station. The middle station very often is just within the melting layer. It has been found that about half of the cases are characterized by a strong inversion layer. The air within such a layer can accumulate very high pollution loadings, as it usually remains in place for several days before a frontal passage. The altitude of the inversion is often below the middle station. Scavenging of pollutants is drastically different in the presence of a stable inversion layer, as compared to cases with a well-mixed boundary layer. This fact is illustrated in the next section.

4. INVERSION (Case study)

The existence of the temperature inversion can be measured very easily with the mobile platform. An increase of the air temperature of several degrees over 100 meters can be found. The inversion is characterized by a sudden decrease of the aerosol concentration just above the temperature increase. Such a situation is illustrated in Fig. 3, showing the aerosol concentration of particles between 0.3 and 15 μ between the bottom and the middle station. Within the polluted layer the air humidity is very high, resulting in aerosol particles of larger diameter, or even activated cloud droplets. The effect of such a heavily polluted layer of air on the pollution of precipitation is given in Fig. 4. The upper picture shows the nitrate load found in the precipitation at the three stations B, M and T for the situation without inversion. The bottom station has the largest load because both in-cloud and below-cloud scavenging contribute. The lower picture of Fig. 4 shows the same type of measurements but for an inversion. Now the loads for the top and middle station are about the same, because there is no below-cloud scavenging in the clean air, whereas the bottom station has a load several times larger due to the strong below-cloud scavenging of the large, humid aerosols within the cold polluted airmass.

5. GENERAL FINDINGS

The following general results have been found from our case studies:

- Microphysical processes (scavenging due to nucleation, impaction, etc) dominate the changes of aerosol concentrations at the beginning of the precipitation (first mm of precipitation).



Fig. 3: Number concentration of aerosols (0.3-15 μ) between M and B station during an inversion (17. February 1988). Total measuring for profile: 10 minutes.

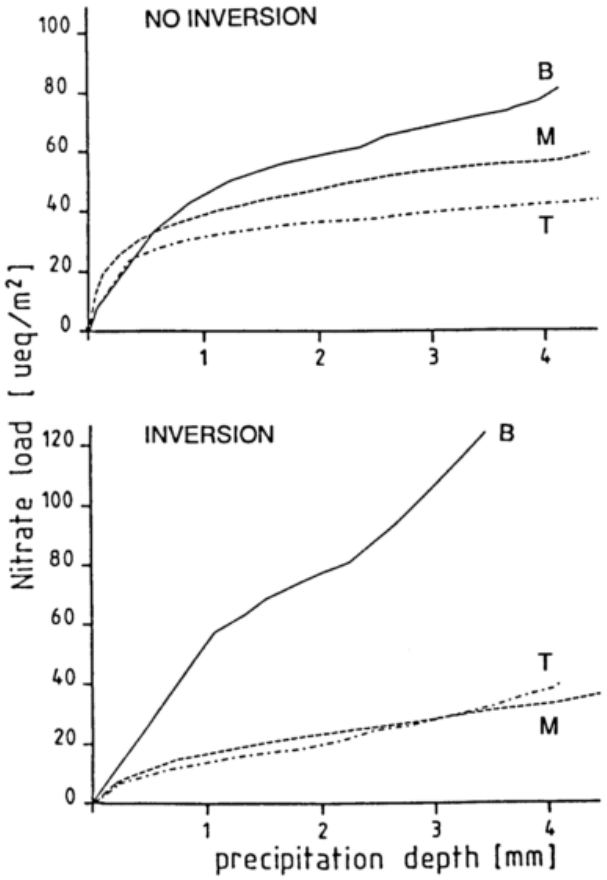


Fig. 4: Nitrate load and precipitation depth for the three stations B, M and T.

- Airmass changes govern the aerosol concentration later.
- In-cloud scavenging is the dominant removal process; the below-cloud scavenging is relatively small under normal conditions (no inversions).
- Very large "below-cloud rates" are found below inversions. This is due to large aerosol particles in the humid cold air mass.

The scavenging process is influenced by many different effects. Therefore there is a large scatter in scavenging coefficients (up to 2 decades) obtained under different meteorological conditions. However, it seems that the very large variations can be reduced and the understanding of the processes can be increased under certain easily definable meteorological conditions.

6. REFERENCES

SCHUMANN, T.; WALDVOGEL, A.: Meteorological effects on ambient aerosol size distributions. J. Aerosol Sco. 18 (1987), 821-824.

SCHUMANN, T.; ZINDER, B.; WALDVOGEL, A.: Aerosol and hydrometeor concentrations during winter precipitation. Part I: Aerosol, Microphiysical and meteorological conditions. Atmos. Environ. 22 (1988), in press.

WALDVOGEL, A.; KLEIN, L.; MUSIL, D.; SMITH, P.L.: Characteristics of radar-identified big drop zones in Swiss hailstorms. J. Climate and Appl. Meteor. 26 (1987), 861-877.

ZINDER, B.; SCHUMANN, T.; WALDVOGEL, A.: Aerosol and hydrometeor concentrations during winter precipitation. Part II: In-cloud versus below-cloud scavenging. Atmos.Environ., to be published.

VERTICAL PROFILES OF POLLUTANTS INSIDE AND OUTSIDE OF CLOUD

by

G.A. Isaac and W.R. Leaitch

Atmospheric Environment Service

4905 Dufferin Street, Downsview, Ontario, Canada M3H 5T4

1. INTRODUCTION

This paper provides information on the vertical profiles of pollutants from several field projects which have been conducted to characterize some physical and chemical properties of clouds in different regions and during different seasons. Projects were conducted as follows: 1.) North Bay, Ontario, during June/July of 1982, 2.) North Bay, Ontario, during January/February of 1984, 3.) Syracuse, New York, during October 1984, 4.) Dartmouth, Nova Scotia, during January to March 1986, and 5.) Alert, Northwest Territories, during April 1986.

2. INSTRUMENTATION

The National Aeronautical Establishment Twin Otter aircraft was used for all projects, and a Canada Centre for Remote Sensing DC-3 aircraft was added for the North Bay 84 and Dartmouth 86 projects. The instrumentation and some of the results have been previously described by Isaac et al. (1986), Leaitch et al. (1986a,b), and Isaac and Daum (1987).

Aerosol particles between 0.17 and 2 μm were obtained using a Particle Measuring Systems (PMS) ASASP-100X. Leaitch et al. (1986b) have shown that $SO_4^=$ is highly correlated with aerosol between 0.2 and 0.6 μm for the North Bay studies reported here. Cloud droplet data (2 - 30 μm) and ice crystal concentrations (25 - 800 μm) were obtained using PMS FSSP and 2D-C probes respectively. NO_y concentrations were obtained using a Monitor Labs Model 8840 monitor. Warm and supercooled cloudwater samples were acquired onboard the aircraft using rod or mesh collectors. The cloudwater samples were analyzed for major ions by ion chromatography.

3. PROFILES IN CLEAR AIR

The average out-of-cloud profiles of aerosol particles and NO_y concentrations for the two North Bay and Syracuse projects (Fig. 1) tend to decrease with increasing height. Isaac et al. (1986) and Isaac and Daum (1987) show that the highest and lowest concentrations tend to come with 48 hour back trajectories from the south and north respectively, at these two locations.

4. PROFILES IN CLOUD

Fig. 2 shows the average in-cloud profiles of interstitial aerosol particles and cloud droplets as measured with the ASASP and FSSP respectively, for 4 different projects. The profiles show the interstitial aerosol is on average a significant fraction of the total number of particles > 0.17 μm. The continental North Bay and Syracuse cases have higher droplet and particulate concentrations than the more maritime Dartmouth case.

Comparisons of the North Bay summer and winter particle concentration profiles generate the following conclusions. First, the ratio of the cloud droplet concentration to the aerosol concentration is lower during the summer. Since supersaturations should not be lower in the summer versus winter, this suggests there are more "holes" due to entrainment of drier air in the summertime clouds. Second, at all pressures, the ratio of the total particle number concentrations

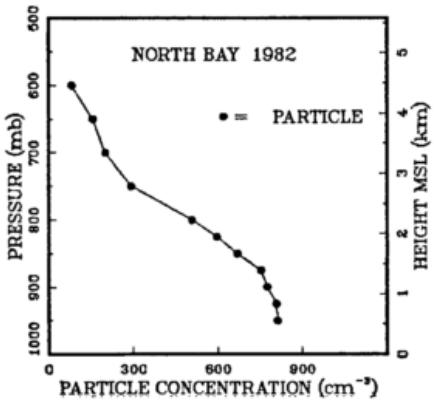


FIG. 1A

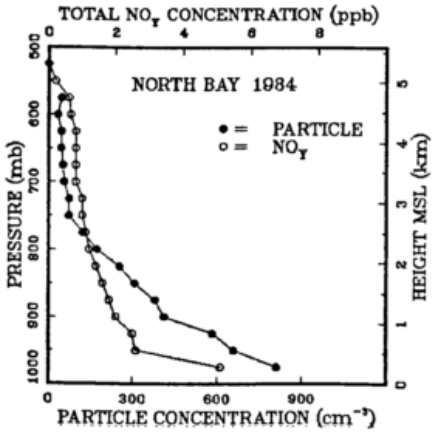


FIG. 1B

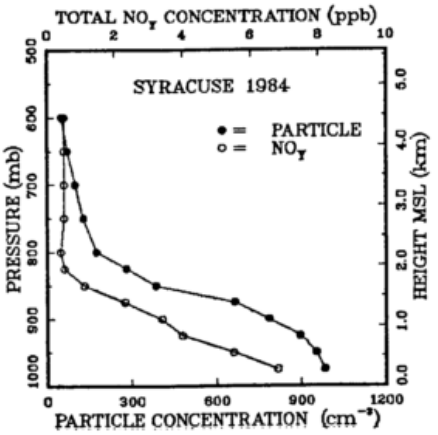


FIG. 1C

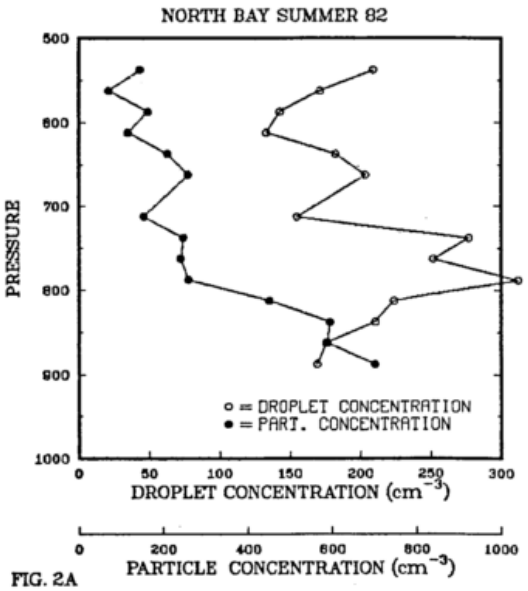


FIG. 2A

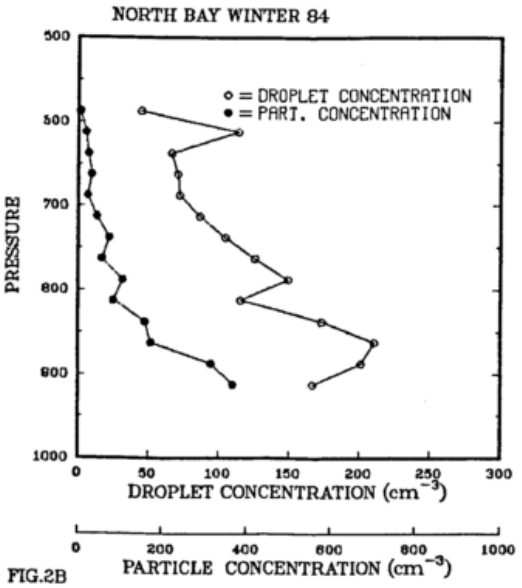


FIG.2B

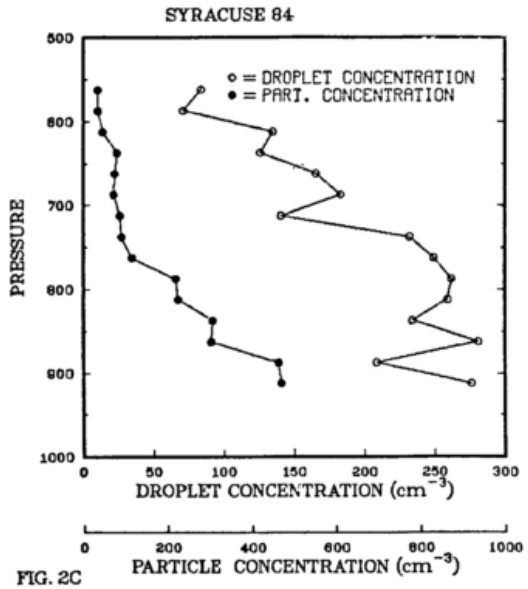


FIG. 2C

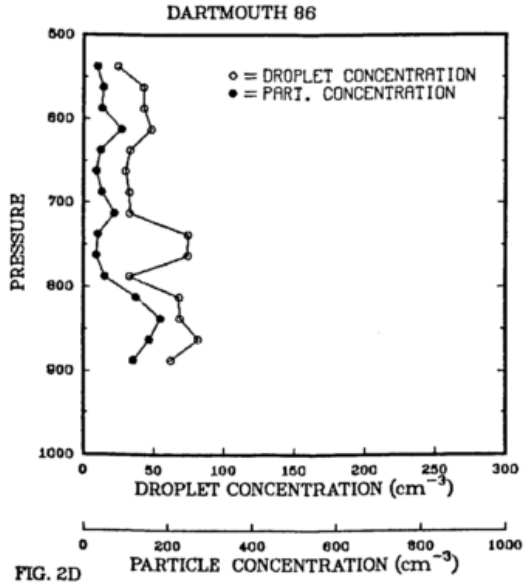


FIG. 2D

(i.e. ASASP+FSSP) to that at the highest pressure or lowest elevation is always greater for the summer. This is evidence for an increase in the effectiveness of vertical transport mechanisms during the summertime.

Measurements made near Alert in the Northwest Territories are shown in Fig. 3. Note that the FSSP and 2D-C ice crystal concentration profiles parallel the aerosol particle number concentration profile very closely, suggesting that the concentration of ice nuclei is increasing with the total aerosol population.

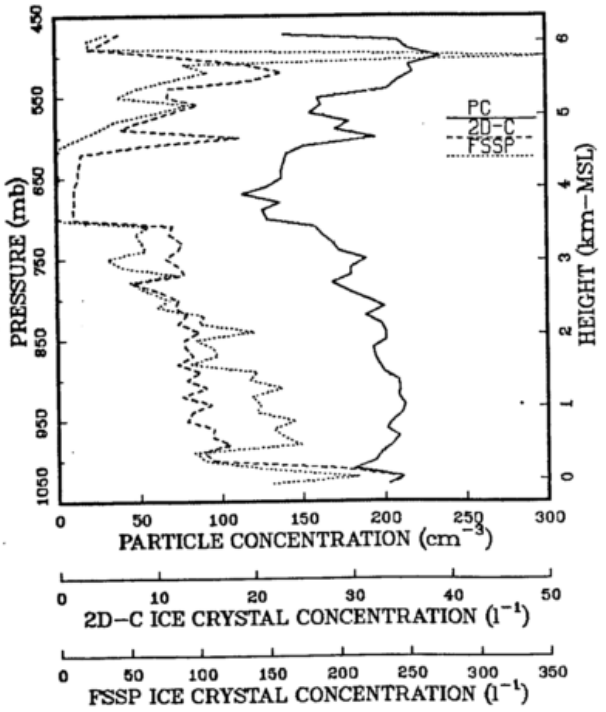


FIG. 3

Fig. 4 shows the average profile of $SO_4^=$ and NO_3^- concentrations found in the North Bay and Syracuse cloudwater samples. The cloudwater concentrations have been multiplied by the liquid water contents. Profiles done for individual locations are similar to these diagrams. The cloudwater $SO_4^=$ and NO_3^- profiles demonstrate similar trends to the profiles of Fig. 1; cloudwater collected at lower levels in the boundary layer will usually contain much higher $SO_4^=$ and NO_3^- air equivalent concentrations. Fig. 4c also shows that $NO_3^-/SO_4^=$ is generally much higher in the boundary layer.

5. REFERENCES

Isaac, G.A., Daum, P.H.: A winter study of air, cloud and precipitation chemistry in Ontario, Canada. Atmospheric Environment, 21 (1987), 1587-1600.

Isaac, G.A., Leaitch, W.R., Strapp, J.W., Anlauf, K.G.: Summer aerosol profiles over Algonquin Park, Canada. Atmospheric Environment, 20 91986), 157-172.

Leaitch, W.R., Strapp, J.W., Wiebe, H.A., Anlauf, K.G., Isaac, G.A.: Chemical and microphysical studies on nonprecipitating summer cloud in Ontario, Canada. J. Geophys. Res., 91 (1986), 11821-11831.

Leaitch, W.R., Strapp, J.W., Isaac, G.A., Hudson, J.G.: Cloud droplet nucleation and cloud scavenging of aerosol sulphate in polluted atmospheres. Tellus, 38B (1986), 328-344.

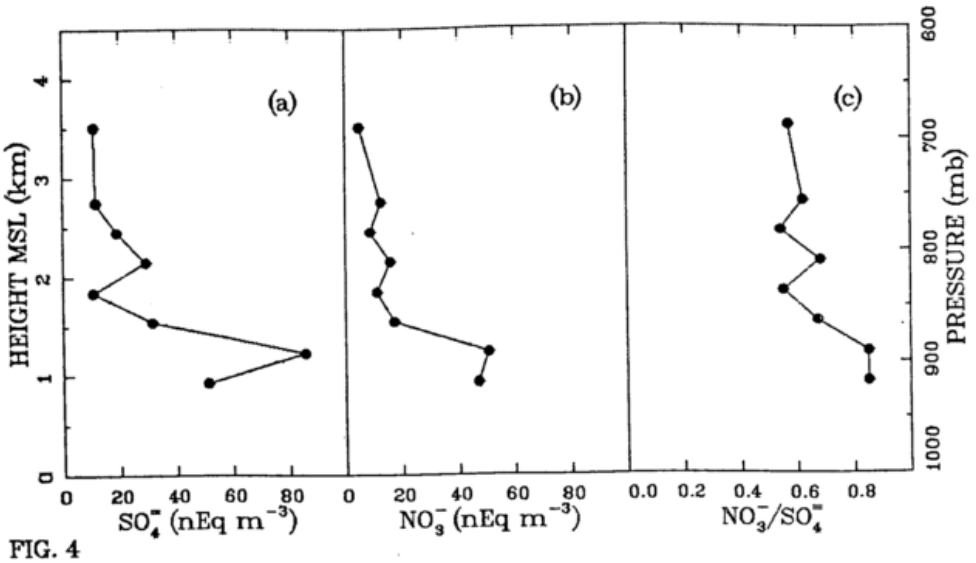


FIG. 4

RESULTS OF TIME AND HEIGHT RESOLVED SCAVENGING EXPERIMENTS

Lucia Kins*, Franz X. Meixner**, Klaus-Peter Müller
Kernforschungsanlage Jülich
Institut für atmosph. Chemie
Postfach 1913
D-5170 Jülich

1 INTRODUCTION

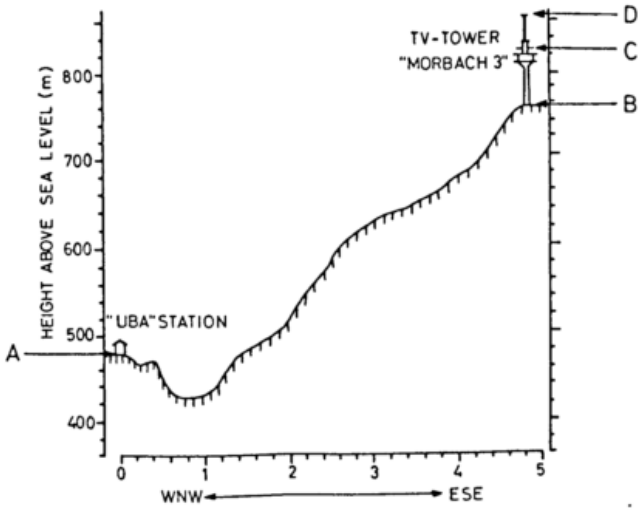
The importance of the potential mechanisms responsible for the accumulation of trace substances in atmospheric hydrometeors is one of the most interesting questions in precipitation chemistry. The mechanisms which have to be considered are: a) nucleation scavenging of aerosol particles, b) uptake of particles and gases by cloud droplets, and c) scavenging of aerosol particles and highly soluble gases by falling rain.

2 EXPERIMENTAL

In 1985 we performed extended field experiments to investigate the significance of these processes for the chemical composition of rainwater. The studies comprised the simultaneous collection of cloud and rain water for chemical analysis, the determination of gaseous and particulate precursors of the substances analyzed in the liquid samples, and measurements and evaluation of the meteorological parameters associated with the rain event.

The examinations were concentrated on case studies of rain from stratiform clouds, which are believed to be essentially univorm at least in the horizontal scale (Hobbs 1981). Consequently, the temporal variability of cloud and rain water concentrations reflect the horizontal variability of a rainband moving over the sampling site.

The experiments were performed at Deuselbach, FRG in the Hunsrück mountains, a hill region in Central Europe. Fig. 1 shows a schematic diagram of the experimental set up. A detailed description of the experiment design and the instrumentation was given elsewhere (Kins et al. 1988).



A "UBA" STATION (480 m a.s.l.):
SO_2, NO, NO_2, O_3, CO_2, HNO_3, HCl, NH_3, aerosol filter*, impactor*, size distribution, sequential rain sampling*, windspeed,-direction, temperature, rel humidity

B TV-TOWER BASE (754m a.s.l.):
sequential rain sampling*

C TV-TOWER PLATFORM (821m a.s.l.):
SO_2, NO, NO_2, O_3, HNO_3, HCl, NH_3, aerosol filter*, cloudwater collector*

D TV-TOWER TOP (861m a.s.l.):
windspeed,- direction, temperature, rel humidity, cloudwater collector*

* lab analysis: H^+, NH_4^+, Cl^-, NO_3^-, SO_4^{2-}, $HCOO^-$, CH_3COO^-, $(COO^-)_2$, (S(IV)), H_2O_2)

Fig. 1: Design and set up of the scavenging experiments

There it was possible to take simultaneously cloud water samples on the TV-tower (821 m and 861 m a.s.l.) and rain samples at the cloud base (480 m a.s.l.).

3 RESULTS

Here, we present the results regarding in-cloud scavenging processes. Each

precipitation event showed an individual character but also some characteristic features common to all events:
a) concentrations of cloud water, collected near the cloud base exceeded those of rain water collected 60 resp. 100 m below, by a factor of 1.5-4,
b) a significant concentration decrease with height was observed inside the clouds, c) trace gas concentrations (with exception of HNO_3) and chemical composition of aerosol particles showed only little decrease during the events if any, and no significant difference in temporal behaviour below and inside clouds. As an example for cloud and rain water results, Fig. 2 shows sulfate concentrations measured during three different events.

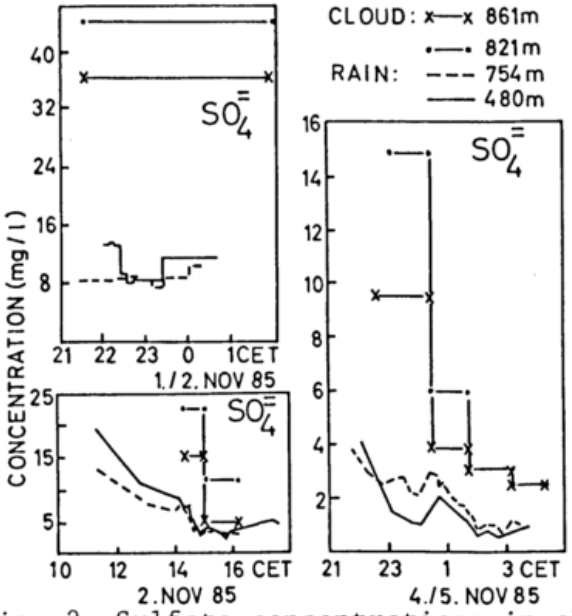


Fig. 2: Sulfate concentrations in cloud and rain water during 3 different events

4 DISCUSSION

The most striking feature of our measurements is the concentration difference between cloud water and rain uninfluenced by below-cloud scavenging. This observation has to be explained by assuming a concentration gradient inside the clouds, with decreasing concentrations with increasing height. To confirm this assumption we considered the vertical structure of the clouds from radiosonding data. Evidence is given that the upper parts of the clouds must have consisted of supercooled water droplets and ice particles. In clouds like that rain droplets form either by aggregation of ice crystals or by accretion of supercooled water to ice (Pruppacher and Klett 1978). For this kind of clouds sulfur chemistry was modelled by Hegg et al. (1984). Their results showed that droplets grown via an ice process are less concentrated than pure liquid water droplets. Our rain water certainly had an ice phase origin whereas the cloud water was collected in the warm (> 0°C) regions of the cloud. Thus the difference between cloud and rain water composition can be explained.

Another question of interest is whether trace gas absorption determines the composition of cloud and rain water. The results of trace gas monitoring give only little hints on gas scavenging. So, we calculated the ion balance ($H^+ + NH_4^+ / 2SO_4^= + NO_3^- + Cl^-$) for aerosol particles, cloud and rain water samples. As an example the results for one event are given in table 1.

tab.1: Ion balance ($H^+ + NH_4^+ / 2SO_4^= + NO_3^- + Cl^-$) for the event 2.Nov.1985

Aerosol (821 m)	Cloud (821 m)	Cloud (861 m)	Rain (754 m)
0.84	0.81	0.8	1.1

These calculations suggest that the cloud water composition is mainly the result of particle scavenging, whereas the rain water has a significantly different composition. Absorption of NH_3 can hardly explain this neutralization. The question rises whether the rain composition reflects a selection of aero-

sol particles during the condensation process.

5 ACKNOWLEDGEMENTS

The authors would like to thank A. Waayers, A. van Wensveen, A. van Westen, C. Schoonebeek, F. Bakker, P. Fonteijn, G. Kos, F.P. Jongejan, M. Langen, N. Beltz, H. Obenlauf, and H. Franken for chemical analysis and assistance during the fild experiments.

6 REFERENCES

Hegg, D.A.; Rutledge,S.A.; Hobbs, P.V.: A numerical model for sulfur chemistry in warm-frontal rainbands. J. Geophys. Res. 89 (1984), 7133-7147.

Hobbs, P.V.: Scales involved in the formation and organization of clouds and precipitation. in: P.V. Hobbs and A. Deepak (eds.), Clouds, their formation optical properties and effects, pp 1-14, Academic Press New York London Toronto 1981.

Kins, L.; Müller, K.P.; Ehhalt, D.H.; Meixner, F.X.: Experiment ALSDAN (1985): Some preliminary results of height resolved measurements of trace gases, aerosol composition, cloud and precipitation water. Paper presented at NATO Advanced research workshop. Acid, Deposition Processes at High Elevation Sites, Edinburgh, Scotland Sept. 1986 (in press).

Pruppacher, H.R.; Klett, J.D.: Microphysics of clouds and precipitation. D. Reidel Publ. Comp., Dordrecht, Boston, London 1978.

---

* present affiliation: Meteorologisches Institut der Universität München, Barbarastr.16, 8000 München 40
** present affiliation: FhI für atm.Umweltforschung, Kreuzeckbahnstr.19, D-8100 Garmisch-Partenkirchen

Oxidation Regimes In Orographic Capping Cloud

P.A. Clark, G.P.Gervat, T.A.Hill, A.R.W.Marsh
Central Electricity Research Laboratories, Central Electricity Generating Board,
Kelvin Avenue, Leatherhead, Surrey. England KT22 7SE
A.S.Chandler, T.W.Choularton, M.J.Gay
Atmospheric Physics Research Group, UMIST, Manchester, UK

1 Introduction

The rate of oxidation of SO_2 in clouds is strongly dependent on ambient atmospheric conditions: not only must the relative abundance of different oxidants be considered (together with their rates of replenishment), but the presence of other species and the time available for reaction are also important. The two major oxidation routes, involving H_2O_2 and O_3, show very different behaviour. In the case of H_2O_2, the overall reaction rate is insensitive to cloud water composition, and the production of SO_4^{2-} is largely determined by the availability of the oxidant. In contrast, O_3 concentrations are usually in excess of SO_2 concentrations, and instead, the most important factor is the acidity of cloud water. These factors are illustrated by the results of a series of experiments that have been conducted at Great Dun Fell, UK.

2 Experimental Results

Great Dun Fell, (847m asl, 54°41'N, 2°27'W) forms part of an approximately two-dimensional ridge in the northern Pennine hills of England. The experiments involved the controlled release of both SO_2 and SF_6 (as a reference tracer) approximately 5km upwind of the summit into an airstream forming capping cloud over the Fell. Comprehensive measurements of cloud physics, meteorological and chemical parameters were performed within the cloud and comparison made with upwind measurements of air composition (Gervat et al, 1986). Three release experiments have been performed, two in spring (1985,1986), and one in winter (December 1985).

2.1 Winter 1985

The winter experiment has been reported by Gervat et al (1988) and contrasts markedly with the spring experiments. The conclusions from this experiment may be briefly summarised as follows:

1. No production of SO_4^{2-} could be detected above natural fluctuations in background concentrations.

2. Background H_2O_2 concentrations were too low (0.6 μM at the summit, 0.8pptv equivalent gas phase) to significantly increase SO_4^{2-} in cloud water, although depletion of H_2O_2 by reaction with S(IV) *could* be detected and the effective rate of reaction estimated.

3. O_3 did not produce a significant increase in SO_4^{2-}, in spite of ample availablity of O_3, (22 ppbv). This was concluded to be a consequence of the cloud water pH (4.75 at the summit) inhibiting reaction.

2.2 Spring 1986

The results from the spring 1985 experiment largely supported conclusions drawn from the second, in spring 1986, so this paper will concentrate on the latter. The main features are illustrated in Figure 1, which shows the response of cloud water composition at the summit to the SO_2 release. Similar results were obtained at the mine road van site. The influence of the plume can be distinguished from changes in background composition by comparison with concentrations measured at the other mine road site which remained outside the plume throughout the SO_2 release. Figure 2 shows the ratio of sulphate concentrations in bulk samples at the summit to the concentration in those collected at the mine road site.

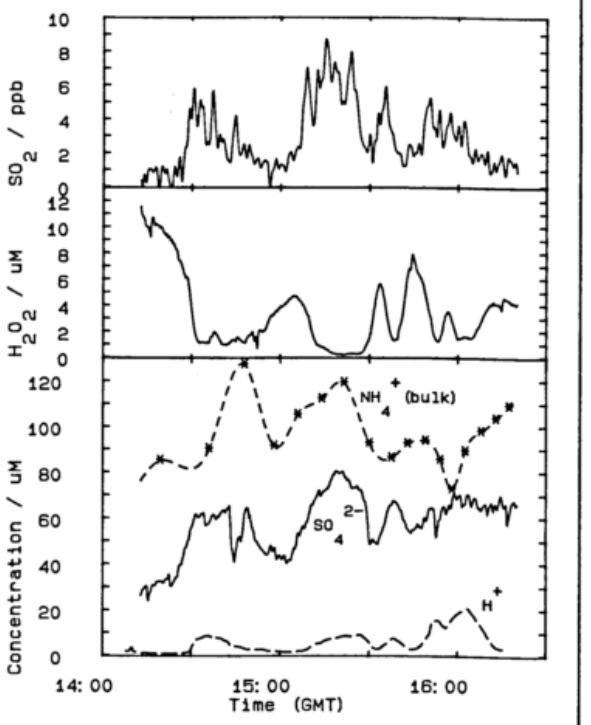


Figure 1. Results from the summit site from the 30 April 1986 experiment.

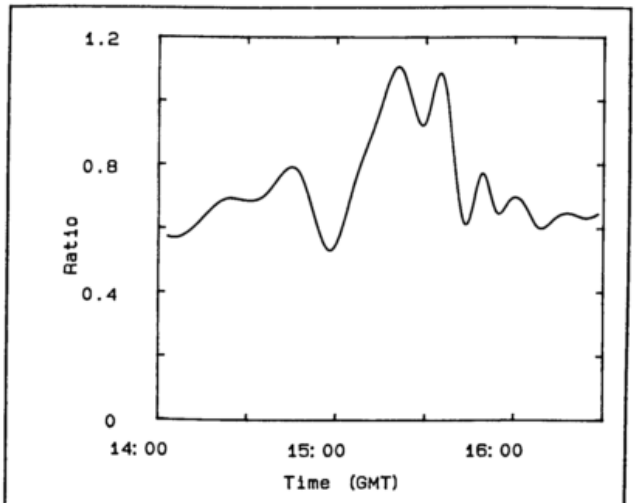


Figure 2. The ratio of SO_4^{2-} at the summit to that outside the plume on the mine road

While the data is smoothed as a result of the averaging time of the bulk samples, the production of SO_4^{2-} is clear. The results may be summarised as follows:

1. There is clear evidence of SO_4^{2-} production in the cloud water as a result of the SO_2 release.

2. Background H_2O_2 levels were high enough to produce some, but not all, of the SO_4^{2-} observed in cloud water, and the consequent depletion of H_2O_2 is clear.

3. It appears that one or more additional oxidants other than H_2O_2 were contributing to the production of SO_4^{2-}. (However, at this time, we are uncertain as to how much HSO_3 in collected cloudwater may have contributed to the observed SO_4^{2-}.)

4. Measured changes in SO_4^{2-} are not quantitatively matched by increases in H^+ in cloud water: instead increases in NH_4^+ are evident.

These results may be compared with calculations of the physical and chemical development of air parcels travelling over the hill using the model of Hill et al (1986), modified to take into account entrainment of non-plume cloud into the plume and reaction rates from Maahs (1983) for O_3 and Martin and Damschen (1981) for H_2O_2. In running the model, input parameters were fixed by matching the observations (liquid water content, cloud water and air composition) made in the absence of the SO_2 plume. Calculations were then repeated using the SO_2 concentration observed as the plume was advected over a measurement site.

Figure 3 shows the calculated time history of SO_4^{2-} production within the plume. It is evident that on this occasion, the model predicts that O_3 contributed markedly to the total production. The reasons for this are twofold. First, ambient air concentrations lead to a high cloud water pH, thus enhancing SO_2 solubility and the oxidation rate by O_3.

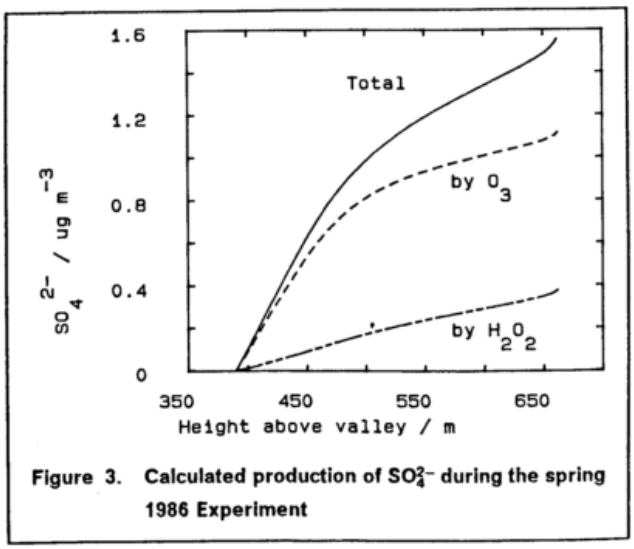


Figure 3. Calculated production of SO_4^{2-} during the spring 1986 Experiment

Second, ambient NH_3 levels were sufficiently high to ensure that, at the resulting cloud water pH, a small but significant proportion of NH_3 remained in the interstitial air within the cloud, available to be taken up by cloud water as plume SO_2 was oxidised and cloud water acidity increased. The SO_4^{2-} production calculated by the model is in close agreement with measured SO_4^{2-} in cloudwater. It should be noted, however, that while the concentration of other species could be accounted for entirely by the measured upwind aerosol composition, there remains a slight discrepancy between the mine road and summit measurements of NH_4^+ which may suggest the additional influence of NH_3 sources on the hill side.

3 Concluding Remarks

The results from these experiments illustrate the importance of considering the full mix of species involved in determining cloud water composition when considering aqueous phase reactions. It is the imbalance of cations and anions which determines the cloud water pH, and hence the importance of oxidants such as O_3. This imbalance may be very sensitive to small changes in the concentration of different species.

In a broader context, it is clear that models which attempt to simulate chemical reactions in cloud systems must take account of sources of species that determine acidity or alkalinity, such as NH_3 and HNO_3, on *appropriate* spatial and temporal scales if they are to have any hope of success.

4 References

Gervat G.P., Clark P.A., Marsh A.R.W., Choularton T.W., Gay M.J., 1986, Controlled Chemical Kinetic Experiments in Cloud; A Review of the CERL/UMIST Great Dun Fell Experiment, proceedings of the NATO workshop on cloud deposition at high elevation sites, Edinburgh, 8-12 Sept 1986

Gervat G.P., Clark P.A., Marsh A.R.W., Teasdale I., Chandler A.S., Choularton T.W., Gay M.J., Hill M.K., Hill T.A., 1988, Field Evidence for the Oxidation of SO_2 by H_2O_2 in Cap Clouds, Nature, in press.

Hill, T.A., Choularton, T.W. and Penkett, S.A., 1986, A Model of Sulphate Production in a Cap Cloud and Subsequent Turbulent Deposition onto the Hill Surface, Atmos. Environment 20, 1763-1771

Maahs, H.G., 1983, Kinetics and Mechanism of the oxidation of S(iv) by ozone in aqueous solution with particular reference to sulphur dioxide conversion in non-urban tropospheric clouds. J.Geophys. Res. 88, 10721-10732

Martin, L.R. and Damschen, D.E., 1981, Aqueous Oxidation of Sulphur Dioxide by Hydrogen Peroxide at low pH, Atmos. Environment 15, 1615-1621

AN EXAMINATION OF THE CHEMICAL AND PHYSICAL VARIABILITY OF CLOUDS AT A MOUNTAIN-TOP SITE IN CENTRAL SWEDEN

Kevin J. Noone, John A. Ogren, Jost Heintzenberg

Department of Meteorology
Stockholm University
S-106 91 Stockholm, Sweden

1) INTRODUCTION

Variations in physical parameters such as liquid water content and droplet number in clouds have long been observed (SQUIRES, 1958; WARNER, 1969.) These variations indicate that clouds are sub-adiabatic, and this sub-adiabaticity has been attributed to the mixing of subsaturated environmental air into the clouds. A considerable body of literature now exists in which the consequences of this mixing between clouds and the surrounding air are discussed, particularly in terms of the effect of mixing on droplet size spectra (BLYTH and LATHAM, 1985; HUDSON and ROGERS, 1986.) Relatively less attention has been paid, however, to the variation in the chemically related parameters such as the amount of solute in different droplet sizes, or the influence of condensation and coagulation processes on the chemical composition and concentration in cloud droplets. While there have been some modelling investigations into the size dependence of cloud droplet chemistry (HOWELL, 1949; JENSEN and CHARLSON, 1984; FLOSSMANN, ET AL., 1985, 1987), few actual measurements have been made. HUDSON and ROGERS (1986) compared measurements of total cloud condensation nuclei (CCN) spectra (nuclei that formed both the cloud drops and the unactivated haze droplets) with CCN spectra taken after selectively removing various fractions of the cloud droplets. They concluded that the larger nuclei showed progressively greater involvement in the cloud droplets (especially for the larger droplets), and that despite the occurrence of mixing, there was still a dependence of the droplet spectrum on the original CCN spectrum. NOONE, ET AL. (1988) used a counterflow virtual impactor (CVI) to sample marine stratus clouds and found that the larger droplets in the cloud had mass concentrations that were a factor of three greater than the smaller droplets. They also presented visual evidence that the larger droplets in the cloud formed on the larger CCN. In this paper, we present time series measurements of various cloud parameters showing that despite large changes in parameters such as liquid water content and droplet number, the distribution of the non-volatile solute mass in two different droplet size classes remains relatively constant.

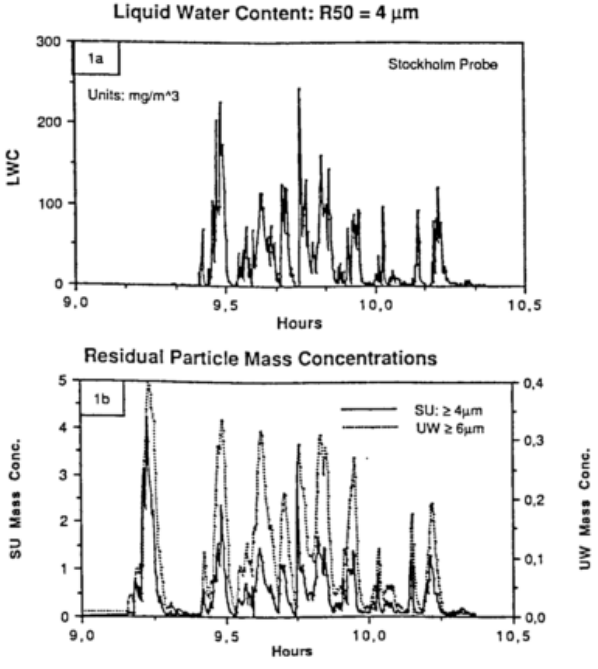
2) EXPERIMENTAL DESCRIPTION

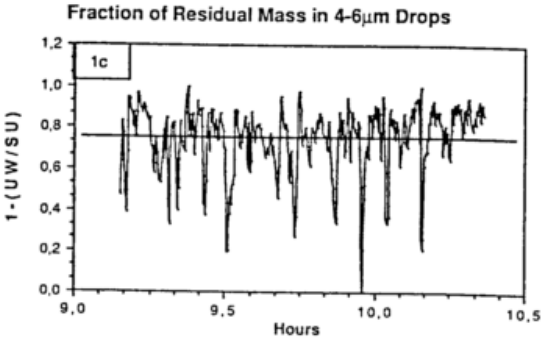
The experiments were carried out at a mountaintop site in central Sweden (Mt. Åreskutan, 63°25' N,13°10' E, alt. 1250 m.) Two CVI probes were operated simultaneously at the site by the University of Washington (UW) and Stockholm University (SU). The two probes were essentially identical in construction. The CVI probes sampled cloud droplets larger than a certain size, while rejecting cloud droplets, unactivated haze droplets and "interstitial" aerosol particles smaller than the cut-off size (OGREN, ET AL. 1985; NOONE ET AL., 1988.) This cut-off size is taken to be the droplet radius at which the collection efficiency of the CVI is 50% (R_{50}, NOONE, ET AL., 1988.) This cut-off radius for each CVI could be varied between a minimum of ca. 4 μm to ca. 15 μm, depending upon the configuration of the probe. Once sampled, the droplets were evaporated; the liquid water associated with the droplets became water vapor, and the non-volatile solute and insoluble material that was dissolved or suspended in the droplets became residual aerosol particles. It was assumed that one droplet releases one particle upon evaporation. The water vapor concentration (previously liquid water associated with the droplets larger than the cut-off size) was then measured with a specially constructed Lyman-alpha hygrometer (ZUBER and WITT, 1987), the scattering coefficient of the residual aerosol particles (which is proportional to residual submicrometer aerosol mass concentration; WAGGONER, ET AL., 1981) was measured using a

nephelometer, and the number concentration of residual aerosol particles (thus the number of droplets greater than the cut-off size) was measured using a condensation nucleus counter (TSI Model 3020.)

During part of the sampling campaign, the two CVI probes were operated at different cut-off sizes. One probe (SU) sampled droplets larger than 4 μm radius, while the second probe (UW) sampled droplets larger than 6 μm radius. For simplification, the droplet range sampled by the SU probe shall be referred to as 'all droplets', while the range sampled by the UW probe shall be referred to as 'larger droplets', with the realization that the 'larger' droplet category is actually a subset of the 'all' droplet category. The upper droplet size limit for both probes was ca. 15 μm radius. By operating the two probes at different cut-off sizes, information regarding the distribution of solute within the two different droplet size classes was obtained. A comparison of the scattering coefficient signals from the two systems can be taken as an example. First, the residual aerosol scattering coefficient signal from each of the CVI probes was transformed to give the mass concentration of the residual aerosol particles (units: $\mu g/m^3$ air, ambient conditions.) Next, the ratio of the residue particle mass concentrations derived from the UW CVI relative to the SU CVI systems was taken. This is the ratio of the amount of non-volatile material in the larger droplets relative to the amount of non-volatile material in all the droplets. This is illustrated in the time series obtained on 23 July 1986, shown in Figure 1. The first plot, Fig. 1a, shows the variation in the liquid water content as measured with the SU probe. The sampling period began at 09:08 local time, and ended at 10:25. Note that the Lyman-α instrument was not on line until 09:19, such that the first peak in the time series shown in Fig. 1b is not shown in the LWC curve. Over this time period, the liquid water content (LWC) of the droplets larger than 4 μm radius varied between ≈ 0 and ca. 0.25 g/m^3. As representative values, at 09:45, the liquid water content measured by the SU probe was 0.14 g/m^3, and the droplet number concentration was 68 cm^{-3}. The spatial scale of the peak-to-peak variation in the LWC was on the order of 1 km. Figure 1b is the corresponding time series of the residue particle mass concentrations measured in the two CVI systems. The mass of non-volatile material in all the droplets varied from essentially 0 to ca. 4 $\mu g/m^3$, while the mass of non-volatile material in the larger droplets varied between 0 to ca. 0.4 $\mu g/m^3$. Comparison of the LWC and dissolved mass curves shows that the variations in these quantities were quite similar - factors of ten variation over spatial scales of roughly 1 km. Figure 1c shows the corresponding time series of the fraction of the amount of dissolved material in the 4-6 μm size interval. This ratio reflects the temporal variation in the distribution of non-volatile material dissolved in the two size categories. Unlike the LWC and particle mass curves, this mass ratio was relatively constant and did not exhibit the same order-of-magnitude variations over the same spatial scale. The fine-scale structure in this plot is probably not physical. This structure is likely due to the two CVI systems not being perfectly synchronized with each other. The line drawn through the data represents the mean value for the time series of 0.74 (± 0.02 at the 95% confidence level.) This shows that there was a factor of five more mass in the droplets 4 μm radius and larger as compared to the mass in the droplets 6 μm radius and larger. Further, this mass ratio did not vary with the same magnitude or spatial scale as the parameters of LWC or dissolved mass.

Figure 1: 23/7/86 Time Series





3) DISCUSSION

Visual observations of the cloud during this period indicated that the variations in LWC were probably not due to entirely different clouds moving past the site, but rather to parts of the same cloud that had different LWC values. This type of variation within a cloud indicates that some mixing of environmental air was taking place. The constancy of the dissolved mass ratio for the two droplet size classes indicates that all of the cloud droplets were behaving in a similar fashion. Apparently, the variations in LWC were caused by all of the droplets evaporating or being diluted by environmental air, and not the smaller droplets evaporating with the large droplets remaining essentially unaffected. If the latter were the case, then one would expect the ratio shown in Fig. 1c to behave similarly to the LWC curve. This constant ratio also indicates that, at least in this cloud, the distribution of non-volatile material *within* the population of cloud droplets studied was robust with respect to those processes causing changes in the droplets themselves.

4) REFERENCES

BLYTH, A.M., and LATHAM, J.: An Airborne Study of Vertical Structure and Microphysical Variability Within a Small Cumulus. Quart. J. R. Met. Soc. **111** (1985), 773-792.

FLOSSMANN, A. I., HALL, W.D., and PRUPPACHER, H.R.: A Theoretical Study of the Wet Removal of Atmospheric Pollutants. Part i: The Redistribution of Aerosol Particles Captured through Nucleation and Impaction Scavenging of Growing Cloud Drops. J. Atmos. Sci. **42** (1985), 583-606.

HOWELL, W.E.: The Growth of Cloud Drops in Uniformly Cooled Air. J. Meteor. **6** (1949), 134-149.

HUDSON, J. G., and ROGERS, C. F.: Relationship Between Critical Supersaturation and Cloud Droplet Size: Implications for Mixing Theory. J. Atmos. Sci. **43** (1986), 2341-2359.

JENSEN, J.B. and CHARLSON, R.J.: On the Efficiency of Nucleation Scavenging. Tellus **36B** (1984), 367-375.

NOONE, K.J., CHARLSON, R.J., COVERT, D.S., OGREN, J.A., and HEINTZENBERG, J.: Cloud Droplets: Solute Concentration is Size Dependent. J. Geophys. Res. (1988), in press.

NOONE, K.J., CHARLSON, R.J., COVERT, D.S., OGREN,J.A., and HEINTZENBERG, J.: Design and Calibration of a Counterflow Virtual Impactor for Sampling of Atmospheric Fog and Cloud Droplets. Aerosol Sci. and Tech. (1988), in press.

OGREN, J.A., HEINTZENBERG, J., and CHARLSON, R.J.: In-Situ Sampling of Clouds with a Droplet to Aerosol Converter. Geophys. Res. Lett. **12** (1985), 121-124.

SQUIRES, P.: The Spatial Variation of Liquid Water and Droplet Concentration in Cumuli. Tellus **10** (1958), 372-380.

WAGGONER, A.P., WEISS, R.W., AHLQUIST, N.C., COVERT, D.S., WILL, S. and CHARLSON, R.J.: The Optical Characteristics of Atmospheric Aerosols. Atmos. Env. **15** (1981), 1891-1909.

WARNER, J.: The Microstructure of Cumulus Cloud. Part I. General Features of the Droplet Spectrum. J. Atmos. Sci. **26** (1969), 1049-1059.

ZUBER, A., and WITT, G.: Optical Hygrometer Using Differential Absorption of Hydrogen Lyman-α Radiation. Appl. Optics **26** (1987), 3083-3089.

INFLUENCES OF CLOUD MICROPHYSICS ON CONTINENTAL AND MARINE PRECIPITATION CHEMISTRY

Farn Parungo and Clarence Nagamoto

Environmental Sciences Group, NOAA/ERL

Boulder, Colorado 80303 U.S.A.

1. INTRODUCTION

Recently acid rain has become an environmental problem in industrial regions. To investigate the mechanisms of acid rain formation and distribution, we investigated air chemistry and cloud microphysics in both continental and marine environments. Here, we report the results of chemical analyses of aerosol, cloud condensation nucleus, atmospheric cloudwater, snow, and rain samples. The data have been interpreted as stepwise incorporations of impurities into precipitation systems.

2. CONTINENTAL PRECIPITATION

Since 1980 we have collected rain and snow samples in Boulder, Colorado, U.S.A. Regional precipitation frequently develops in an upslope system in which air flow moves upward along the eastern slope of the mountain, forming orographic clouds. We reported (NAGAMOTO ET AL. 1983) that the local precipitation acidity depends on synoptic weather patterns. The most acidic precipitation is generally from southeasterly flow that mixes with Denver air pollution. The least acidic snow occurs during a cold front passage of polar air. However, we have also observed acidity and chemical composition varying from one stage to another of the same storm. This suggests that precipitation chemistry is not controlled only by air chemistry but is also affected by cloud microphysics processes. We collected samples of local soil, atmospheric aerosols, CCN, and cloudwater as well as rain and snow. The methods of sampling and the chemical analyses were reported by PARUNGO ET AL. (1987). Table 1 lists the results. Water in Colorado lakes is generally alkaline ($\overline{pH}$ = 8.23), which agrees with the fact that local soil is generally alkaline ($\overline{pH}$ = 7.84). However, atmospheric aerosol solutions were slightly acidic ($\overline{pH}$ = 6.26) (1 g of water was used to treat 1 m^3 air samples. The solution simulated a cloud with liquid water content of 1 g/m^3.) The data indicate that anthropogenic air pollutants, mainly SO_2 and NO_x gases and sulfate and nitrate aerosols, probably mixed with and neutralized wind-blown soil particles and increased the acidity by 2 orders of magnitude. Anthropogenic secondary aerosols are formed either by homogeneous nucleation as fine particles ($d < 0.1$ μm) or by heterogeneous nucleation as a coating on existing particles. In both cases, the number of CCN is enhanced (sulfate and nitrate particles are hygroscopic). Thus, cloud formation and cloud duration may be modified by the excess CCN. The average acidity of CCN solutions collected at ground level (by passing ambient air through a cloud chamber regulated at 1% supersaturation) was ~6, similar to that of the aerosol solution. However, cloudwater samples collected in-flight over Colorado showed $\overline{pH}$ of

Table 1. Average pH and ion concentrations in samples collected in Colorado, U.S.A.

Sample	n	pH	$SO_4^=$ (mg/L)	NO_3^- (mg/L)
Rain	84	4.79	2.91	1.85
Snowmelt	92	5.29	2.12	1.8
Precipitation	201	5.13	2.50	1.83
Cloudwater	23	4.02	15.0	7.41
CCN Solution	17	6.06	4.50	0.22
Aerosol*	21	6.26	2.02	2.68
Soil†	24	7.84	0.77	0.48
Lake Water	139	8.23	130	--

n = sample number
* Aerosols in 1 m^3 air with 1 g of water.
† 1 g of soil extracted with 100 g of water.

4.02, which is 2 orders of magnitude more acidic than CCN or aerosol solutions. The data suggest that cloud drops continuously adsorbed gases (e.g., SO_2, NO_x) that subsequently oxidized to acids. Our analyses (Table 1) also show that the average $SO_4^=$ concentrations in cloudwater was about 3 times that in CCN and the average NO_3^- concentration in cloudwater was ~34 times that in CCN. The data further demonstrated that acidity as well as sulfate and nitrate was incorporated into the continental precipitation system mainly through in-cloud scavenging of gases followed by liquid-phase oxidation.

Analyses showed that rain and snow had an average acidity ~10 times less, $SO_4^=$ ~6 times less, and NO_3^- ~4 times less than in cloudwater. To understand our measurements one must study cloud microphysics. We examined precipitation hydrometeors microscopically and correlated chemical composition with the characteristics of individual hydrometeors. The classification in Fig. 1 is based on several years' observations, Most precipitation is initiated by ice nucleation. Once ice crystals appear in a cloud, they grow at the expense of liquid drops because of the vapor pressure gradient between ice and water (BERGERON 1935; FINDEISEN 1938). When small drops evaporate, the dissolved gases and

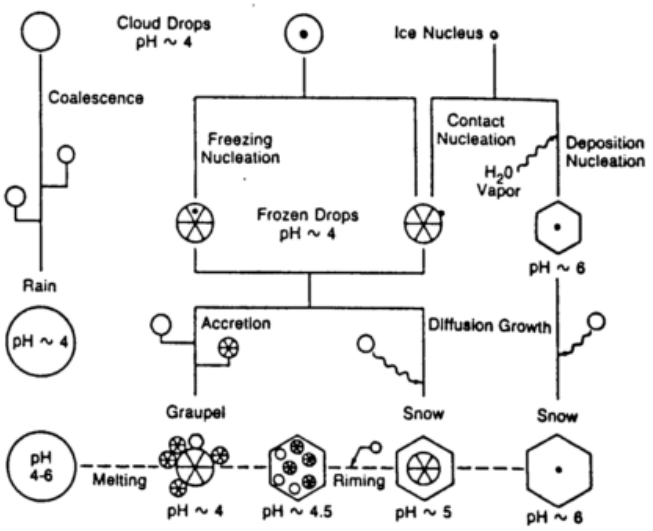


Fig. 1. Diagram of acid precipitation formation.

embedded particles are released into the surrounding air. Gases (e.g., SO_2, NO_x, CO_2, HNO_3), being less soluble in ice than in water, may not be adsorbed by growing ice crystals. As a result, the ice crystals grown by diffusion are purified by distillation and thus less acidic than cloud drops. When ice crystals fall into a liquid-drop layer, they accrete droplets and freeze them upon contact. These rimed crystals may have the chemical composition of both ice crystals (less acidic) and collected cloud droplets (more acidic). Our observations that rimed snow crystals are generally more acidic (pH < 5) than unrimed crystals (pH > 5.5) agree with the finding of BORYS ET AL. (1982) that the heavier the riming, the more acidic the snow sample. At temperatures >-10°C and humidity is at water saturation, frozen drops or ice crystals are covered with a quasi-water layer, which prevents diffusion growth but enhances accretion growth (PARUNGO and WEICKMANN 1983). Thus, the chemical composition of graupel grown by accretion resembles that of cloudwater. In summer convective showers, raindrops may be formed by collision and coalescence of cloud drops without going through glaciation. This physical merging does not dilute the drops' chemical concentration. The rain drops can be as acidic as cloud drops. Therefore we concluded that cloud microphysics has an important role in precipitation chemistry.

3. MARINE PRECIPITATION

In recent years we collected rain and aerosol samples on several research cruises. Table 2 shows some of the analytical results. The ratio of Mg^{++}/Na^+ is the same for rain and aerosols as for seawater, indicating that Mg^{++} and Na^+ have the same source and deposition mechanisms. Rain and aerosols are more acidic than seawater. Ratios $SO_4^=/Na^+$ and NO_3^-/Na^+ are greater in rain and aerosols than in seawater, indicating enrichments of H^+, $SO_4^=$ and NO_3^- in the marine atmosphere. The ratio of Cl^-/Na^+ is smaller in rain and aerosol than

Table 2. Average pH and ion-mass ratio of marine samples.

	pH	$\frac{Mg^{++}}{Na^{+}}$	$\frac{Cl^{-}}{Na^{+}}$	$\frac{SO_4^{=}}{Na^{+}}$	$\frac{NO_3^{-}}{Na^{+}}$
Global Seawater	8.0	0.12	1.80	0.25	$<10^{-5}$
Gulf of Mexico					
Aerosols	5.5	0.12	1.62	0.81	0.43
Rain	4.9	0.12	1.40	0.93	0.54
Pacific Ocean					
Aerosols	6.1	0.11	1.68	0.35	0.05
Rain	5.9	0.12	1.65	0.48	0.05

in seawater, indicating Cl^- loss in seasalt particles, probably replaced by $SO_4^=$ and NO_3^- ions. These phenomena are more severe in the Gulf of Mexico than in the remote Pacific Ocean because the Gulf is highly contaminated with anthropogenic air pollution.

Particles containing Na^+, Cl^-, $SO_4^=$, and NO_3^- are generally hygroscopic particles and thus are active cloud condensation nuclei. If all ions in rain were incorporated through condensation nucleation, the ion ratios in rain and in aerosols should be identical. The fact that $SO_4^=/Na^+$ and NO_3^-/Na^+ are greater in rain than in aerosols suggests that enrichments have occurred in the precipitation processes, most likely through gas adsorption by cloud droplets, followed by liquid-phase oxidation as discussed for continental precipitation. Nevertheless, the enrichment factors in marine systems are <30% for $SO_4^=$ and <20% for NO_3^-. The data indicate that the major portions of $SO_4^=$ and NO_3^- are incorporated in rain through condensation nucleation of aerosol particles and only a minor portion through gas adsorption. The result is contrary to the case of continental precipitation where the dominant mechanism of incorporation is gas adsorption by cloud drops where SO_2 is oxidized to $SO_4^=$ and NO_x to NO_3^-. The difference can be explained by different environments. In a marine atmosphere, abundant wet alkaline seasalt particles can adsorb acidic gases, e.g., SO_2 and NO_x. Following oxidation on the surface, the gases are converted to $SO_4^=$ and NO_3^- respectively, forming a layer of solid coating. Therefore, little of the gases remains to be lifted to the cloud level to be scavenged by cloud drops. On the other hand, in the dry continental air mass, gases probably have longer life and thus remain in high concentration at cloud levels. In conclusion gases have a greater effect on cloud acidification in continental air than in the marine environment.

4. REFERENCES

BERGERON, T.: On the Physics of Clouds and Precipitation. Proc. 5th Assembly UGGI Lisbon, 2, 156-160 (1935).

BORYS, R.D.; DEMOTT, P.J.; HINDMAN, E.E.; and FENG, D.: A Comparison of Unrimed and Rimed Snow Crystals. Preprints Conf. on Cloud Physics, Chicago. Amer. Meteor. Soc. Boston 52-61 (1982).

FINDEISEN, W.: Die Kolloidmeteorologischen Vorgane beider Wieder-schlagsbiludng. Meteor. Z. 55, 121-132 (1938).

NAGAMOTO, C.; PARUNGO, F.; REINKING, R.; PUESCHEL, R., and GERISH, T.: Acid Clouds and Precipitation in Eastern Colorado. Atmos. Environ. 17, 1073-1082 (1983).

PARUNGO, F.; NAGAMOTO, C.; and MADEL, R.: A Study of the Mechanisms of Acid Rain Formation. J. Atmos. Sci. 44, 3162-3174 (1987).

PARUNGO, F.; and WEICKMANN, H.: Ice Crystal Growth at (-8 ± 2)°C. J. Rech. Atmos. 17, 139-156 (1983).

"CONCENTRATIONS IN RAIN EVENTS COLLECTED SEQUENTIALLY: MEASUREMENTS VS RESULTS OF A SIMPLE SCAVENGING MODEL"

JAFFREZO J.L. and COLIN J.L.

Laboratoire de Physico-Chimie de l'Atmosphère, Université Paris VII,
2, Place Jussieu - 75 251 PARIS CEDEX 05, France.

INTRODUCTION

There are at present several theoretical scavenging models for aerosols scavenging by precipitations but they have rarely been tested against field works (STENSLAND and de PENA, 1975 ; HEGG et al., 1984). In this study we have attempted to reconcile the two approaches by making a simple scavenging model compatible with detailed experimental results.

Firstly, we have carried out a sampling campaign with a view to studying the scavenging of particulate nonreactive mineral aerosol by precipitations: sequential event-by-event sampling of wet deposition only; parallel aerosol collection with a short time period (6h). It is shown (JAFFREZO, 1987) that by these techniques interacting media are collected. Sequential sampling of precipitation (with 0.1 mm increments) allows to follow precisely the variations of concentrations during a single event. We have also measurements of volume and rain-rate on each of the sampling steps.

Next, these physical and chemical data about the sequential events are compared with the results of simple scavenging model. this is developed to determined more closely the effect on the chemical concentrations of parameters which vary during the precipitation, in particular the rain-rate.

DISCUSSION

This model is constructed on the basis of the equation describing interaction between raindrops and particles, proposed by CHAMBERLAIN (1960):

$$dcp / dt = -k * ng * cp \qquad (1)$$

where cp is the particles concentration and ng the number of drops. Classically, this equation is integrated (for k and ng = constants):

$$cp(t) = cp(0) * \exp(-Xt) \qquad (2)$$

where cp(0) is the initial concentration of aerosol particles and X the washout coefficient. One obtains then:

$$Cp(t) = H * cp(0) * (1-\exp(-Xt)) \qquad (3)$$

where cp(t) is the total particle mass in the precipitation at time t for the scavenging of the air column of height H, in which cp(0) is taken constant with altitude.

Equation (1) can now be integrated with k and ng constant no longer over the whole event but over each of the sampling step of duration T(i). In order to avoid problems related to the difference in fallspeed between large and small raindrops, we shall consider a single drop size of median diameter (as far as rain-rate is concerned). This size is calculated by the MARSHALL-PALMER relation (1948) relating drop size spectrum and rain-rate. One can then calculated a different scavenging coefficient X(i) for each of the sampling step, with:

$$I = ng * 4/3 * \pi * Rg^3 * Vg \quad (4)$$

$$X = ng * \pi * Rg^2 * Vg * E(a,Rg) \quad (5),$$

$$X(i) = 3/4 * I(i) * E(a,Rg(i)) / Rg(i) \quad \text{(SLINN, 1983)} \quad (6),$$

where I is the rain-rate, Vg the terminal fallspeed of drop of radius Rg and E(a,Rg) the collection efficiency for a particle of radius a by a drop of radius Rg.

A recurrence relationship is easily obtained, similar to (3), giving the variations of the concentrations in the different fractions n constituting of the rain event:

$$Cp(n) = \left(cp(0) - \sum_{i=1}^{n-1} Cp(i) \right) * \left(1-\exp(-X(n)T(n)) \right) \quad (7)$$

and:

$$CT(n) = H * Cp(n) \quad (8),$$

where Cp(n) is the mass of aerosol in the precipitation for step n, per unit volume, and CT(n) for scavenging of height H.

Figure 1 presents the evolution of concentration measured for Zinc, against volume for an event collected in Paris the 24th March 1984. This figure shows an example of the results obtained with this parameterization. It can be seen that this type of calculation makes it possible to encounter:

1- the order of magnitude of the concentrations in the rain for a plausible scavenging height (here 3500m for a ground level concentration cp(0) = 0.145µg/m3);

2- the general evolution of the concentrations decreasing with the volume fallen;

3- certain second-order variations which shows that they are clearly related in part to the rain-rate evolutions.

This example indicates that the preliminary results are encouraging. This comparison will be extended to the large number of sequential sampling performed during this campaign. One could then attempt to develop this type of calculation with more precise parameterizations, particularly as regards the spectra of raindrops and particles.

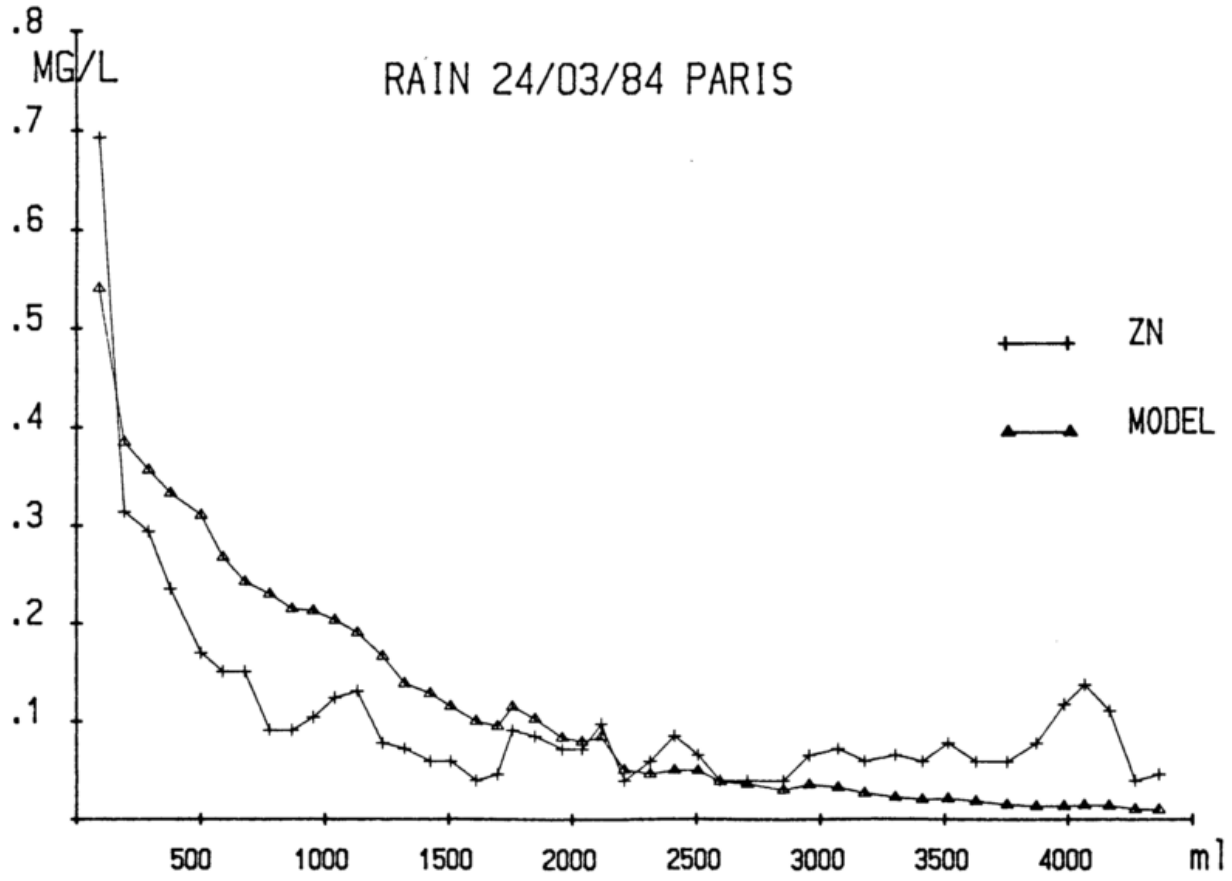


FIGURE 1: concentrations of Zn for a sequential sampling and results of the model.

REFERENCES

Chamberlain A.C. (1960) Aspects of the deposition of radioactive and other gases and particles. Int. J. Air Poll. 3, 63-68.

Hegg D.A., Rutledge S.A. and Hobbs P.V. (1984) A numerical model for sulfur chemistry in warm-frontal rainbands. J. of Geo phys. Res. 89, 7133-7147.

Jaffrezo J.L. (1987) Etude du lessivage des aérosols atmosphériques par les précipitations. Thèse de doctorat, Université Paris VII, 183 pp.

Marshall J.S. and Palmer W. Mck. (1948) The distribution of raindrops with size. J. Meteor. 5, 165-166.

Slinn W.G.N. (1983) Air-to-Sea transfer of particles. In: Air-sea exchange of gases and particles. P.S. Liss and W.G.N. Slinn (eds.), D. Reidel, 299-405.

Stensland G.J. and de Pena R.G. (1975) A model of Below-Cloud scavenging of NaCl. J. of Geophy. Res. 80, 3410-3418.

EXPERIMENTS ON MICROPHYSICS AND CHEMISTRY OF RADIATION FOGS

Karl-Heinz Enderle, Herbert Obenland, Wolfgang Jaeschke

Zentrum für Umweltforschung
Johann Wolfgang Goethe-Universität Frankfurt/Main

1 INTRODUCTION

Since 1985 we have been performing radiation fog experiments in collaboration with FISBAT (Sandro Fuzzi, Bologna), the University of Vienna (Institute for experimental physics, Axel Berner), the TU Vienna (Hans Puxbaum) and a lot of other institutes. The purpose of these experiments is to study the time resolved behaviour of the chemical specimen with respect to the microphysical properties of a radiation fog system. One of the points we are interested in is the possible sulfate production within the fog droplets during the life cycle of a radiation fog. In order to detect analytical errors we use two independent methods (ion chromatography, chemiluminescence technique) to determine S(IV) (all sulfur species where sulfur is in the +4 oxidation state) in the fog water. As expected unexplainable discrepancies occured, especially at pH-values higher than 5. The exciting point was that this was obviously correlated to the intensity of an unidentified peak occuring in the chromatogram when using the method described by Munger et al. (1986, p. 247) to analyze HMSA (hydroxymethanesulfonate). They also reported the presence of an unidentified peak in many samples.

2 ANALYZED SULFUR SPECIES

To study the problem mentioned above we analyzed the following species:

- $S(IV)_{aq}$ (sum of dissolved and dissociated SO_2
- $S(IV)_{HMSA}$
- $S(IV)_{tot}$ (sum of all sulfur species in the oxidation state +4)
- $S(IV)_x$ (unknown S(IV) compound of fog water)

The $S(IV)_{aq}$ was analyzed by our chemiluminescence technique (Meixner, Jaeschke 1981, p. 51). With the same method $S(IV)_{tot}$ was analyzed by shifting the pH-value above 13. This is done by adding NaOH. So the HMSA-adduct is decomposed and the HMSA bonded S(IV) contributes to the $S(IV)_{aq}$ which can be analyzed by the chemiluminescence technique. As

$$S(IV)_{tot} = S(IV)_{HMSA} + S(IV)_{aq}$$

the $S(IV)_{HMSA}$ can be determined as the difference between $S(IV)_{tot}$ and $S(IV)_{aq}$. Independently of the chemiluminescence method $S(IV)_{tot}$ was analyzed by ionchromatography (HPIC) and $S(IV)_{HMSA}$ by ion-pairing chromatography (MPIC). This was done about 7 weeks after the event, while the chemiluminescence method was applied during the fog experiment. The problem was to determine the concentration of the unknown $S(IV)_x$ in the collected water. This was only possible by a lucky chance! Once we found the same unidentified peak in the chromatogram of a HMSA standard solution (solution No. 1) as in the fog samples. As this peak in the standard solution was not present the day before, a check with a fresh HMSA standard solution (solution No. 2) was made. We found out that the HMSA peak in solution No. 1 was lower than it should be. So the unknown S(IV) compound obviously results from the decomposition of the HMSA. With this assumption and by dilution of solution No. 1 a two point calibration was done for the $S(IV)_x$ and used for this presentation. It is worth mentioning that the unidentified peak in solution No. 1 was no more present the next day and the HMSA peak reached again its nominal value!

3 THE RESULTS

The data shown in this paper result from the radiation fog event of the 17th/18th November 1987 at S. Pietro Capofiume (Po Valley, Italy). In that region fogs typically show relative high pH-values which is favorable for HMSA formation. In fig. 1 the timely course of the fog water pH is plotted which was measured immediately after collection.

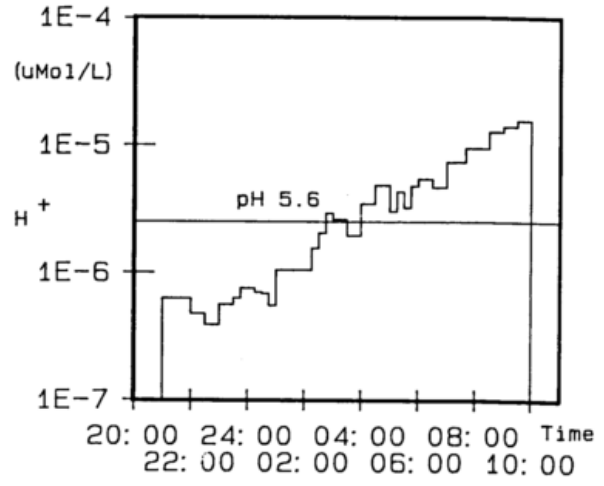


Fig. 1 Timely course of the pH-value, radiation fog event 17./18.11. 1987, S. Pietro Capofiume (Po Valley, Italy)

Until 2:00 o'clock in the morning the pH was higher than 6. Then it decreased continously and reached a value of 4.8 when the fog vanished. The gas phase SO_2 concentration during the event was measured with our chemiluminescence technique. The concentrations were rather low and out of the range (~1.4 ppb) of continous measuring instruments. It is interesting to compare fig. 1 with the $S(IV)_{aq}$-concentration found in the fog water. As shown in figure 2 there is a significant increase in $S(IV)_{aq}$ at 5:00 o'clock in the morning which practically coincides with the time when the pH-value drops below 5.6. A correlation with the gas phase concentration of SO_2 could not be detected.

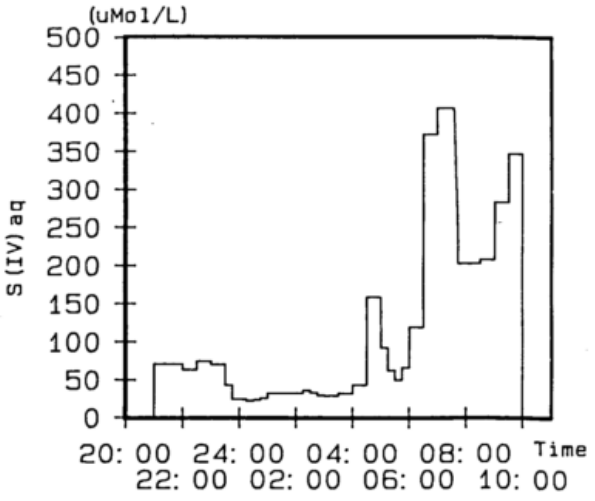


Fig. 2 Timely course of the $S(IV)_{aq}$-concentration in the fog water

It should be pointed out that the $S(IV)_{aq}$ shown in fig. 1 does not include the $S(IV)_x$ concentration as the chemiluminescence method is not sensitive to this compound. It is also important to mention that the analysis of the specimen shown in the figures above was done in the field during the event and the following day.

After about seven weeks the samples were analyzed in our laboratory for $S(IV)_{HMSA}$, $S(IV)_x$ and $S(IV)_{tot}$ by ion-chromatography. Assuming that meanwhile the $S(IV)_{aq}$ concentration did not change, it follows that

$$S(IV)_{tot} - S(IV)_{aq} = S(IV)_{HMSA} + S(IV)_x$$

But our results suggest that at the time when this analysis was done there was not any $S(IV)_{aq}$ in the samples of this fog period. It is likely that this $S(IV)_{aq}$ has been transformed into $S(IV)_{HMSA}$ and $S(IV)_x$, as the high pH-value favorizes this. An oxidation to sulfate can be excluded, as no H_2O_2 was found in the fog water. This is proofed by fig. 3, in which $S(IV)_{tot}$ is plotted against the sum of $S(IV)_{HMSA}$ and $S(IV)_x$. So only analytical values are compared which are practically analyzed at the same time.

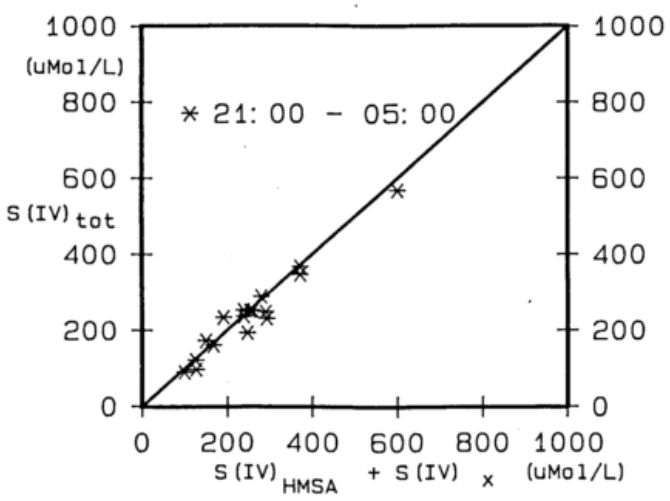


Fig. 3 Balance of $S(IV)_{tot}$ and the sum of $S(IV)_{HMSA}$ and $S(IV)_x$

Only two points (13%) don't ly on the ideal curve when respecting the appropriate error bars ($\pm$10 µMol/L for $S(IV)_{tot}$, $\pm$18 µMol/L for the sum of $S(IV)_{HMSA}$ and $S(IV)_x$). For the time period 05:00 - 10:00 o'clock, when the pH-value drops below 5.6 other results are obtained. During this time the $S(IV)_{aq}$ concentration increased considerably (see fig. 2) while the rate constant of the HMSA-formation decreased due to the decreasing pH-value. As additi-

onally oxidants could not be found, neither in the gas phase (O_3) nor in the liquid phase (H_2O_2), there probably was a good chance for the relative high $S(IV)_{aq}$ concentrations to be stable for a longer time. Fig. 4 shows the balance between $S(IV)_{tot}$ - $S(IV)_{aq}$ and the sum of $S(IV)_{HMSA}$ and $S(IV)_x$.

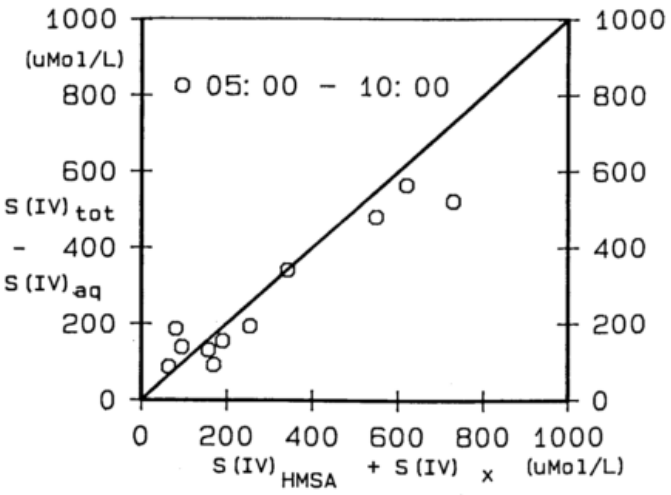


Fig. 4 Balance of the S(IV) compounds of fog water in the time period 05:00-10:00

The scattering of the data around the ideal curve may be due to the incomparability of the concentration of $S(IV)_{aq}$ with the other S(IV) concentrations. Nevertheless reasonable results are obtained.

4 SUMMARY

An unidentified peak in the chromatograms of fog samples, which was below the detection limit in samples of a pH-value of less than 5.4, was found in a one day old HMSA standard solution. So the assumption was made that this peak originates from a decomposition of the HMSA solution. A two point calibration for the unknown $S(IV)_x$ concentration was done. Our analytical results show that this compound of fog water significantly contributes to the S(IV) budget at high pH-values. It is worth noting that the concentrations of $S(IV)_x$ and $S(IV)_{HMSA}$ are in the same order of magnitude and both may contribute to $S(IV)_{tot}$ by up to 100%. A fact which is very important when Henry's law equilibrium is calculated. This work, of course, is not a straightforward proof and additional laboratory studies are necessary. Unfortunately the column (DIONEX ISR) needed for ion-pairing chromatography is no longer commercially available, so that we have to build it ourselves.

5 ACKNOWLEDGEMENTS

We thank Dr. Sandro Fuzzi for his excellent collaboration and the possibility to take advantage of the equipment of the FISBAT measuring site at S. Pietro Capofiume (Po-valley, Italy). This work was funded by the german "Bundesministerium für Forschung und Technologie" (BMFT) under project No. 07vnd01 0.

RERERENCES:

MEIXNER, F.X.; JAESCHKE, W.: The detection of low atmospheric SO_2- concentrations with a chemiluminescence technique. Int. J. Environ. Anal. Chem., 10 (1981), p. 51-67.

MUNGER, J.W.; TILLER, C.; HOFFMANN, M.R.: Identification of hydroxymethanesulfonate in fog water. Science, Vol. 2 (1986), p. 247-249.

Chemical Evolution Within A Cloud Model Featuring A Polydisperse Droplet Size Spectrum

T.A.Hill U.M.I.S.T, Manchester, U.K
now at
Central Electricity Generating Board
Central Electricity Research Laboratories
Kelvin Avenue,Leatherhead,Surrey,U.K

Introduction

There have been many cloud chemistry models developed in order to examine the dependence of sulphate production on the concentration of oxidants, acidic species, alkaline species and SO_2 present within the cloud . However, most have assumed that an equilibrium is maintained between the gas and aqueous phase at all times. In addition, it is assumed that there is no concentration variation of species within the liquid water occupying a volume of cloud. It is well known that droplets form on hygroscopic particles of varying mass and that therefore in reality the concentrations of ions such as NH_4^+ or SO_4^{2-} will vary by orders of magnitude depending on the mass of aerosol on which the droplet formed. This paper discusses the results of a model which features a realistic aerosol size spectrum on which droplets grow and within which solution chemistry takes place. Gases are absorbed or desorbed at a finite rate and the rate of production of SO_4^{2-} by SO_2 oxidation compared with the results of a model in which all the chemistry takes place in bulk water.

Model Formulation

This model follows a system of droplets as it rises as part of some much larger convective structure. The cloud condensation nucleus size spectrum on which the droplets form is assumed to be of mixed origin and consists of a mixture of two distributions, one consisting of NaCl particles (maritime) and the other $(NH_4)_2SO_4$ particles (continental). The size and concentration of particles is calculated using the formula

$$N_i = CS_i^k$$

Where k and C depend on the origin of the aerosol, i is the number of categories. In this case there are 8 maritime and 6 continental size categories. Starting at just below 100% humidity the parcel ascends at 3 ms-1 to the condensation level, at which point some or all of the aerosol particles activate and become droplets. These droplets continue to grow during further ascent according to the standard droplet growth equations (see eg. Pruppacher and Klett 1978). The chemical system employed in this model includes the following chemical species: In the gas and aqueous phases: CO_2, HNO_3, SO_2, H_2O_2, O_3, NH_3 ,in the aqueous phase only: HCO_3^-, NO_3^-, HSO_3^-, NH_4^+, Na^+, Cl^- . At the condensation level, the aerosol material in those categories activated goes into solution. In order to avoid the highly complex interactions between ions in non-ideal solutions, the chemistry within the model is not initiated until a droplet has reached a radius of 0.5 μ m at which time the ionic concentrations are typically less than 0.01M. This is typicaly achieved in less than ten seconds. The rate of uptake of a gas by these droplets is then given by

$$\frac{4}{3}\pi\lambda\sqrt{\frac{8kT}{M_x\pi}}\,r\,\frac{(N_g - N_{ge})}{(1+(0.7+\frac{4(1-\alpha)}{3\alpha})\frac{\lambda}{r})}$$

where M_x is the molecular mass of the gas, r droplet radius, λ mean free path of gas molecule, α the sticking coefficient, N_g the no. of molecules in the gas phase per unit volume, N_{ge} the number of molecules in the gas phase if the concentration in solution were in equilibrium with the gas phase. (after Chameides and Davies 1982). S(iv) in solution is oxidised to S(vi) by O_3 and H_2O_2 so that:

$$\frac{d[S(vi)]}{dt} = K_{H_2O_2}[H_2O_2][HSO_3^-][H^+]$$

$$+ (K_1 + \frac{K_2}{[H^+]})[O_3][HSO_3^-]$$

and the oxidation rate constants are those used by Martin and Damschen 1981 and Maahs 1983. After 250 seconds a mixing event occurs in which the gases are diluted in proportion to the volume entrained and more gas from outside the cloud may be introduced. We assume that a fraction of droplets evaporate completely such the humidity is maintained at 100% .The humidity of environmental air was taken as 85% and the ratio of cloud to outside air was 1:1. The gases in solution are returned to the gas phase and any excess cations ie. NH_4^+ are neutralized by NO_3^- ions and the remaining anion or cation returned to the gas phase as NH_3 or HNO_3. This allows us to estimate the composition and mass of the aerosol in order to calculate which aerosol will reactivate during subsequent ascent. The net result of the mixing event is to treble the number of categories. The chemistry again starts in the newly activating droplets once they have reached 0.5 μm.

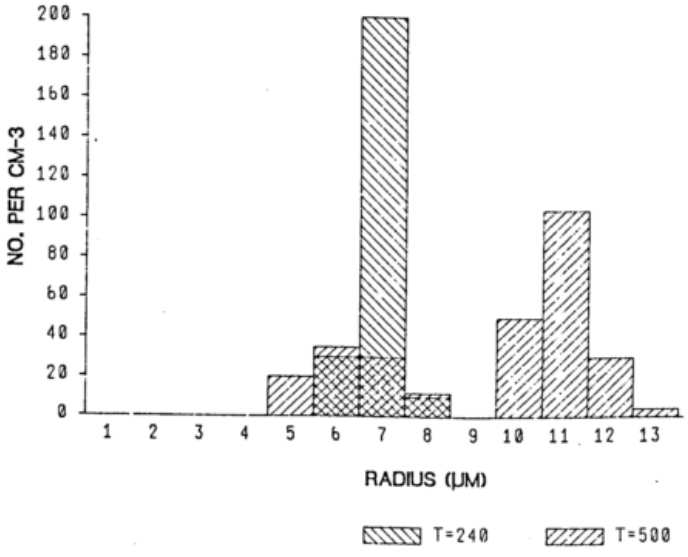


Fig. 1 size distribution

Results

Fig.1 shows the droplet size distribution at 240 secs (just before mixing event) and 500 secs. As is the case in real clouds, the spectrum becomes bi-modal as aerosol activate following the event. Fig. 2 shows the concentration of SO_4^{2-} as a function of time.The starting gas phase mixing ratios were 1ppbv H_2O_2, 1 HNO_3, 1 NH_3, 5 SO_2, and 30 O_3.Concentrations in the entrained air were 1 pbbv H_2O_2 , 0HNO_3 , 0 NH sub 3, 0 SO sub 2 and 30 O sub 3. It is immediately clear that the concentrations vary enormously between droplets even though the radii are similar.Note that initially, some droplets have no SO_4^{2-} in them (the sea-salt nuclei) and the SO_4^{2-} therefore comes from SO_2 oxidation. Fig. 3 shows the departure from equlibrium of NH_3 between gas and aqueous phases for each droplet category as defined by the ratio of $(NH_3 + NH_4^+)_{aq}$ in the droplet to that expected if in equilibrium with the gas phase. Not all the droplets are in equilibrium and this suggests that for some species equilibrium is not always established in clouds because of continual changes in H^+ , droplet size and entrainment. Some of the larger $(NH_4)_2SO_4$ aerosol droplets outgas NH_3 whilst the NaCl based droplets absorb it. Fig 4. shows the mass of SO_4^{2-} produced in the cloudy volume by the two reactions as a function of time compared with that produced in a model in which the chemistry takes place in bulk water - no droplets included. There is very little difference between the two cases as far as oxidation by H_2O_2 is concerned.However, following the entrainment event the O_3 reaction is inhibited in the polydisperse case. This is because the evaporated droplets form more acidic nuclei. These nuclei have a greater mass because of the sulphate produced within them and therefore re-activate preferentially. Since the O_3 reaction is inhibited at low pH the net mass of sulphate produced is reduced. This cannot be reproduced in the bulk water model.

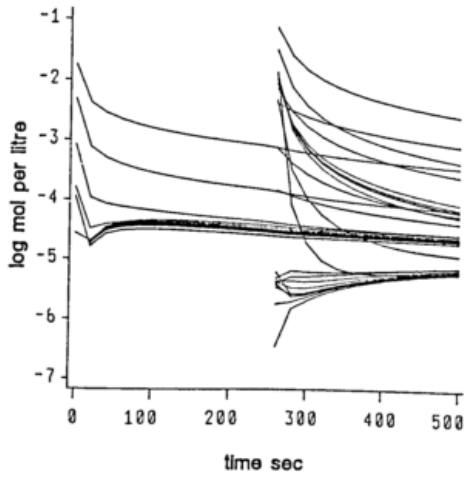


fig 2. sulphate concentrations

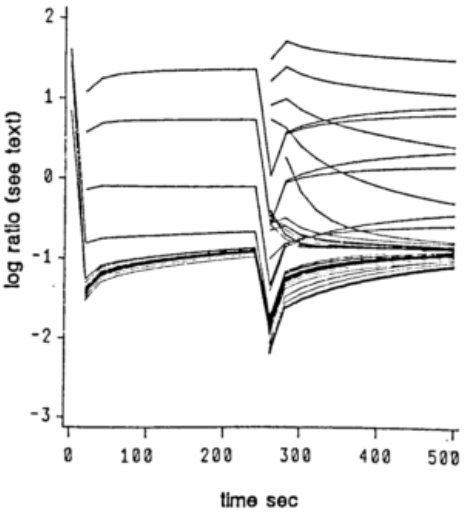


fig 3. Departure of NH3 from equilibrium

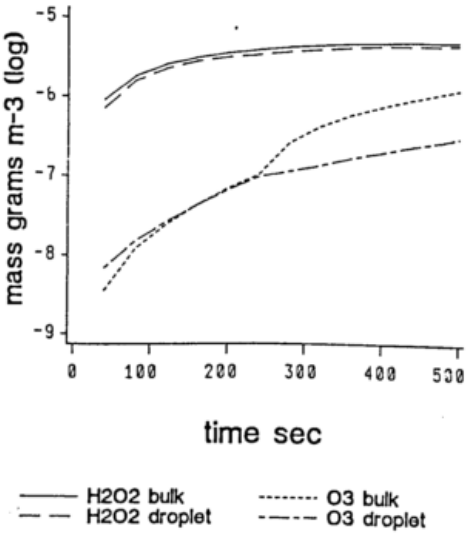


fig 4. SO4 produced by O3 and H2O2

Conclusions

1. Concentrations of many species vary by orders of magnitude from droplet to droplet.

2. Gas/aqueous equilibrium for NH_3 is not necessarily established for all droplets within a cloud system simultaneously.

3. The CCN mass distribution will change as sulphate is produced.

4. The re-activation of the nuclei already involved in the sulphate generation process will take precedence over those entrained with the external air, thus maintaining a lower average pH within the cloud and hence inhibiting the O_3 reaction.

References

Chameides W.L and Davies D.D 1982
The free radical chemistry of cloud droplets and its impact on the composition of rain.J.Geophys.Res 87 4863-4877.

Pruppacher H.R and Klett J.D 1978
Microphysics of clouds and precipitation. D Reidel Pub Co London

Martin L.R and Damschen D.E 1981
Aqueous Phase Oxidation of sulphur dioxide by hydrogen peroxide at low pH. Atmos Env 15 1615-1621

Maahs H.G 1983
Kinetics and mechanism of the oxidation of S(iv) by ozone in aqueous solution with particular reference to sulphur dioxide conversion in non-urban tropospheric clouds. J.Geophys Res 88 10721-10732.

MODELING STUDIES ON THE FORMATION, GROWTH, DISSIPATION, AND ACIDIFICATION OF CUMULUS CLOUDS

Shyam K. Nair* and Leonard K. Peters
Department of Chemical Engineering
University of Kentucky
Lexington, KY 40506, U.S.A.

1. INTRODUCTION

Cumulus cloud acidification depends on the physical and transport properties of the wet phases, including liquid water content, concentration and size distributions of the cloud condensation nuclei, and vertical motions. Any chemistry model to simulate cumulus acidification processes should include realistic cumulus parameters. Two- and three-dimensional models can most realistically link cumulus dynamics to the thermodynamical and microphysical processes and thereby predict cumulus properties. On the other hand, one-dimensional models can capture many of the significant aspects of cumulus clouds while at the same time greatly reducing computational requirements.

In this paper, a one-dimensional approach is adopted so that both transport and chemistry of the gas- and aqueous-phase species can be considered in detail. The one-dimensional model that is used as the basis for cumulus cloud acidification simulations is described. Detailed gas- and aqueous-phase chemical kinetics are coupled to the cloud model. The chemical processes during the formation, growth, and dissipation periods of an entire cloud cycle are considered.

2. MODEL DESCRIPTION

The cloud model simulates a parcel of air being advected upward, following a parabolic velocity profile in the z-direction. This updraft structure allows lateral entrainment and detrainment causing cumulus formation. After the cloud has reached a steady depth at the peak updraft level, a downdraft is introduced causing cloud dissipation as it penetrates into the cloud.

Since the model is one-dimensional, the velocity changes in the x- and y-directions by the prescribed updraft/downdraft in the z-direction are lumped into a lateral entrainment/detrainment term E. A material balance equation can be written for the total water, rain, and snow concentrations, and for other chemical species as

$$\frac{\partial c}{\partial t} = -\frac{\partial (wc)}{\partial t} + \frac{\partial}{\partial z}\left[D_m c^* \frac{\partial (c/c^*)}{\partial z}\right] + \frac{1}{c^*} E\,(\delta_1 c_b + \delta_2 c) + G, \quad (1)$$

where c is the concentration of the species; and D_m is the eddy diffusion coefficient of the species in air. The background concentration of the species is c_b, and $\delta_1 = 1$ when entrainment into the parcel occurs and is zero otherwise.

Similarly, $\delta_2 = 1$ when there is detrainment from the parcel and is zero otherwise. G is the mass generation/loss term accounting for chemical transformation in a particular phase, for mass transfer to/from a phase, and for water category transformations during phase changes. The water species parameterizations have been taken directly from the PLUVIUS model (Eastes and Hales, 1984), including rate equations for accretion, auto-conversion, riming, sublimation, and deposition. The energy balance equation, in addition to considering the normal convection, diffusion, and phase transformation terms, also incorporates the addition/loss of energy due to the entrainment/detrainment processes. It is analogous to Equation (1) but with the addition of latent heat effects.

The system of equations for species and energy conservation is solved using an operator splitting scheme with a finite element method for the transport terms.

3. CHEMICAL MECHANISMS

Detailed gas-phase and aqueous-phase reaction mechanisms are adopted to simulate the chemical transformations. The gas-phase reaction mechanism is based on Atkinson et al. (1982), with amplification to include several reactions involving nitric acid, ammonia, and methane according to Carmichael et al. (1986). The aqueous-phase reactions are adopted from the research of Chameides (1984) and Seigneur et al. (1984).

Aerosol particles are assumed to be present in the form of NH_4NO_3, $(NH_4)_2SO_4$, and H_2SO_4. Upon nucleation, they dissolve into droplets in stoichiometric proportions.

4. RESULTS AND DISCUSSION

Figure 1 shows the relative magnitudes of the entrainment flux and vertical convective flux for a cloud simulation with maximum updraft velocity of 7.5 m/s being attained at 2400 s. Arrows pointing to the right indicate entrainment into the parcel, and those pointing to the left indicate detrainment. Figure 2 shows contours of the cloudwater content as functions of altitude

*Present address - Bechtel Environmental, Inc., Oak Ridge, TN 37831, USA.

and time for this simulation. The maximum cloudwater content occurs slightly above mid-cloud level and is about 2.2 g/m^3 at 2400 s. The cloud base remains roughly constant throughout at 1.8 km, whereas the cloud top grows to about 3 km before eventual dissipation.

This cloud and two others were used for a series of runs at two different initial and background species concentrations. Figure 3 shows vertical gas-phase SO_2 profiles for one run. The profiles show greater decreases in gas-phase concentration as the cloud grows in time until it begins to dissipate. Similar profiles are noted for other soluble species. Graphs of cloudwater pH are shown in Figure 4. All runs indicate cloudwater pH around 4 as the average value. Onset of cloud dissipation lowers the pH somewhat.

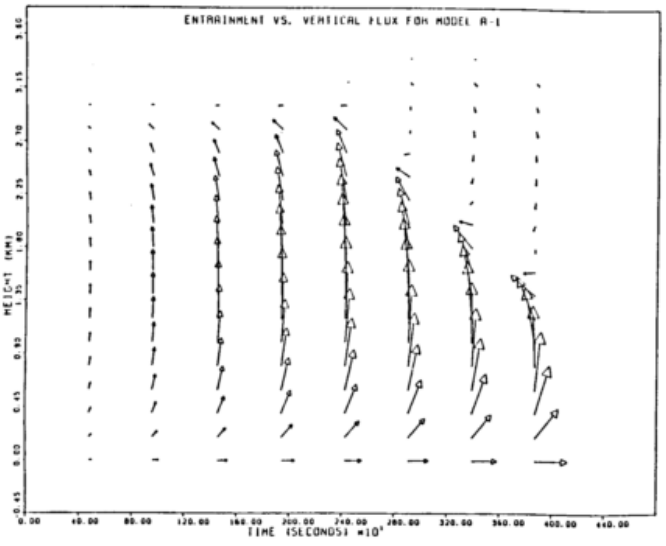


Figure 1. Relative magnitudes of the entrainment and vertical convective fluxes at different altitudes for Run A-1.

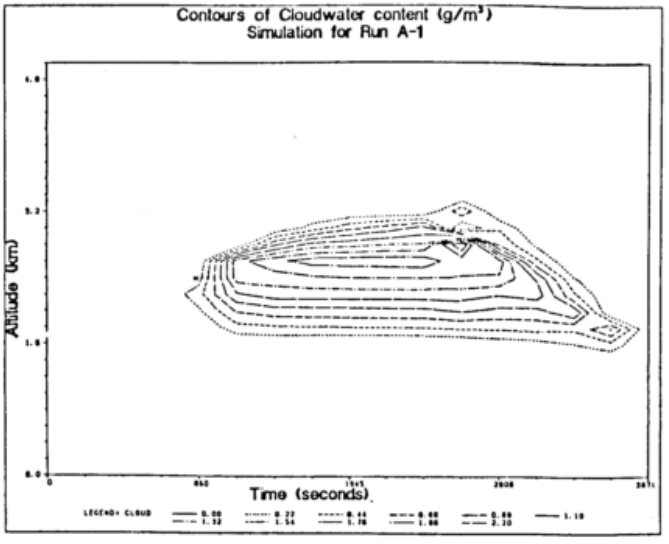


Figure 2. Contours of cloudwater content for Run A-1.

Contours of the first-order rate constant for the overall conversion of SO_2 to S(VI), follow the cloudwater content contours, with higher cloudwater contents showing higher rate constants. The conversion rate constants range from about 1%/min to greater than 30%/min, which can be compared to gas-phase rate constants that are typically on the order of 1%/hr.

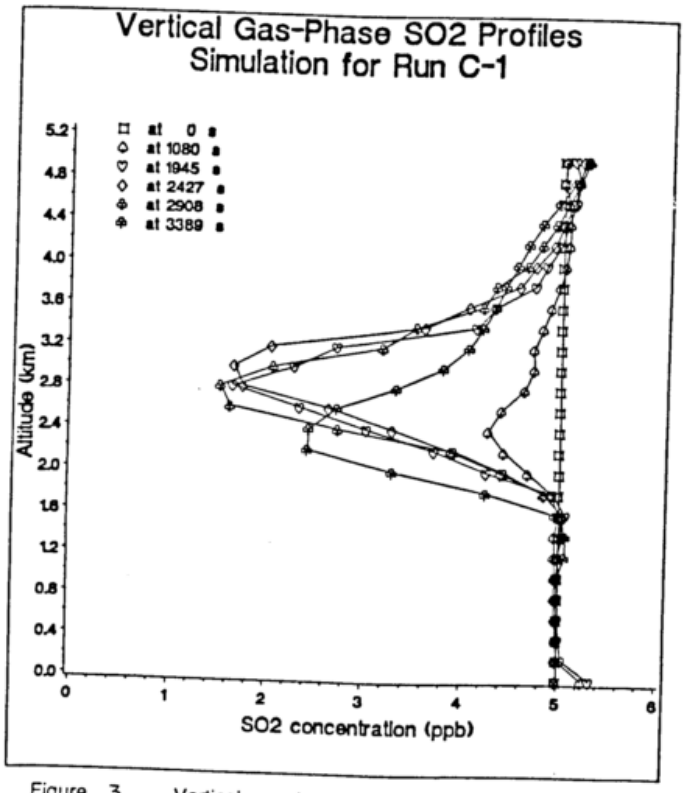


Figure 3. Vertical gas-phase SO_2 profiles for Run C-1.

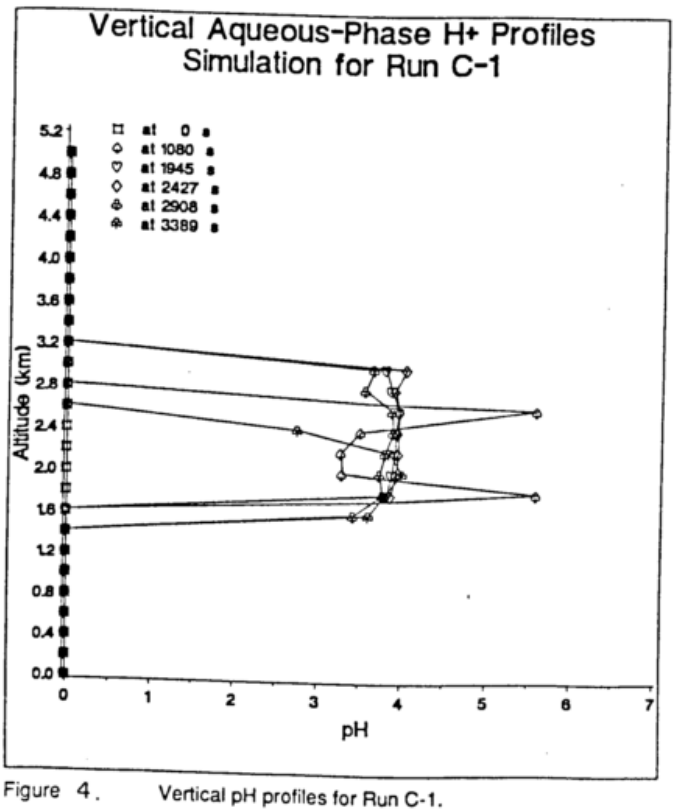


Figure 4. Vertical pH profiles for Run C-1.

In Figure 5, material balances are presented for SO_2, H_2O_2, and HNO_3 during the lifetime of the cloud. The model domain is split into sub-cloud, in-cloud, and above-cloud regions. The maximum conversion of SO_2 to sulfate is in the in-cloud region. This cloud processes ten times as much SO_2 in its lifetime of approximately 40 minutes as is oxidized in the other two regions, even though the cloud depth is always less than 28% of the modeled domain during its lifetime.

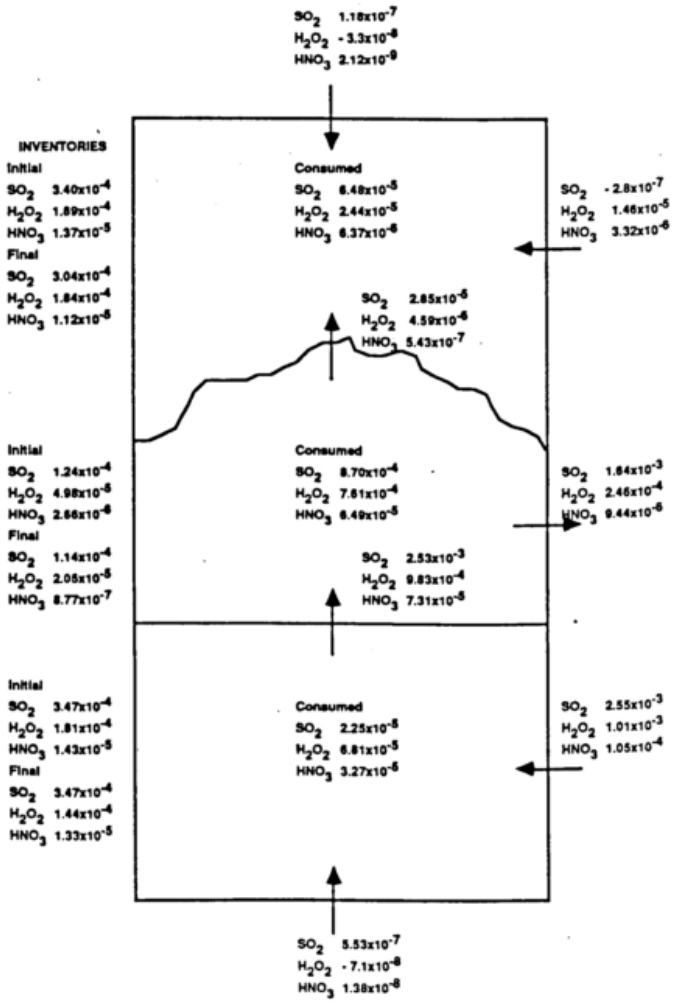


Figure 5. Material balance schematic for the sub-cloud, in-cloud, and above cloud regions in Run C-1. The balances are expressed in moles/m^2.

Overall, the cumulus cloud runs with comprehensive gas-phase and aqueous-phase chemistries indicate that the final cloudwater pH depends primarily on the degree of oxidation of S(IV) to S(VI) by H_2O_2, and hence on the background H_2O_2 concentration. In these runs, H_2O_2 is the most important oxidant of S(IV) in the aqueous phase. HO_2, OH, O_3, and other species make lesser contributions. Cumulus clouds can be considered to behave like giant variable volume reactors with entrainment of background air from below-cloud and above-cloud regions and release of processed air from the sides. These simulations show S(IV) to S(VI) conversion rates ranging from 1%/min to greater than 30%/min in the presence of clouds.

5. ACKNOWLEDGEMENTS

The authors acknowledge the valuable suggestions made by Dr. J.M. Hales of Battelle Pacific Northwest Laboratories. This work was supported in part by the U.S. Department of Energy and Environmental Protection Agency through the PRECP and NAPAP programs.

6. REFERENCES

Atkinson, R.; Lloyd, A.C.; Winges, L.: An Updated Chemical Mechanism for Hydrocarbon/NO_x/SO_2 Photooxidations Suitable for Inclusion in Atmospheric Simulation Models. Atmos. Environ. 16 (1982) 1341-1355.

Carmichael, G.R.; Peters, L.K.; Kitada, T.: A Second Generation Model for Regional-Scale Transport/Chemistry/Deposition. Atmos. Environ. 20 (1986) 173-188.

Chameides, W.L.: The Photochemistry of a Remote Marine Stratiform Cloud. J. Geophys. Res. 89 (1984) 4739-4755.

Easter, R.C.; Hales, J.M.: PLUVIUS: A Generalized One-Dimensional Model of Reactive Pollutant Behavior, Including Dry Deposition, Precipitation Formation, and Wet Removal. PNL Report 4046 ED 2 (1984).

Seigneur, C.; Saxena, P.: A Study of Atmospheric Acid Formation in Different Environments. Atmos. Environ. 18 (1984) 2109-2124.

A NUMERICAL INVESTIGATION OF SULFATE PRODUCTION AND DEPOSITION IN MIDLATITUDE CONTINENTAL CUMULUS CLOUDS

Gregory R. Taylor
Geophysics Program, AK-50
University of Washington
Seattle, WA 98195 U.S.A.

1 INTRODUCTION

In this abstract I will briefly describe a time dependent cloud model cloud model developed for use in cloud chemistry and wet deposition studies, and used here to examine the sensitivity of sulfate oxidation and deposition to the physical processes important in the development of midlatitude continental cumulus clouds.

2 CLOUD MODEL

The cloud model is a 1.5 dimensional axisymmetric Eulerian cumulus model (Asai and Kasahara, 1967; Yau, 1980; Taylor, 1987) which incorporates: (a) two in-cloud regions and the environment, (b) a bulk water parameterization including the ice phase (Cheng, 1981), (c) an entrainment formulation based on the local turbulent kinetic energy, (d) a sustained sub-cloud forcing, and (e) a parameterization of the scavenging and production of sulfate. This model formulation was chosen in order to provide a simple dynamic framework which permits simultaneous up- and downdrafts in-cloud and specifies the mixing of cloud and environmental air in terms of a simple physical model.

The pressure perturbation in each cloud region is approximated by a single mode of a Fourier-Bessel series. The flux-corrected transport algorithm, *ETBFCT* (Boris et al., 1981), is used to advect momentum, total energy, the water and chemistry fields in each region of the model domain.

3 COMPARISON WITH OBSERVATIONS

Two cumulus clouds observed during the Cooperative Convective Precipitation Experiment (CCOPE) held in South-Central Montana during the summer of 1981 were used to test the cloud model. Table 1 lists observations from Dye et al., 1986 for a small, weak-shear cumulonimbus studied on July 19, 1981 and model predicted values of these observations. The sounding used to initialize the cloud model is shown in figure 1. Figure 2 shows a composite Paluch (1979) diagram of four cloud penetrations at about 480 mb and model predicted values at the penetration pressure.

These case studies indicate that this cloud model is able to match the general dynamic and microphysical characteristics of the midlatitude continental cumulus congestus and small isolated cumulonimbus. The aircraft observations provided detailed information on a much finer horizontal resolution than contained within the model, but repeated penetrations at the same level within cloud offer a means of comparing the aircraft measurements with the model predictions. Plotting the time series from the cloud model at the penetration levels for these two clouds on a Paluch (1979) diagram demonstrated that the computed cloud properties were in general agreement with those obtained by multiple aircraft penetrations.

Tests of the sensitivity of the cloud model results to variations in the adjustable dynamical and microphysical parameters were performed.

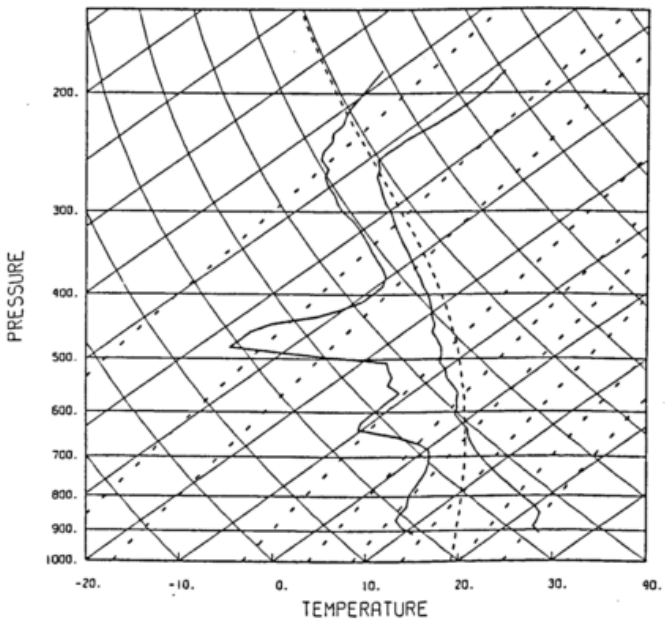


Figure 1. Miles City 1440 MDT sounding. θ_e shown corresponds to observed cloudbase.

Overall, it appears that the cloud properties are highly sensitive to variations in the subcloud forcing. Three cloud types, i.e., fair weather cumulus clouds about 1 km in depth, non-precipitating cumulus congestus about 3 km in depth, and precipitating storms which reached the tropopause, corresponded to differences in the mean cloud base vertical velocity of 1.5 to 2 ms^{-1}.

Three entrainment formulations were tested. The Asai and Kashara (1967) formulation yielded a much weaker, dryer cloud than observed. This is due to the entrainment of large amounts of dry environmental air in order to satisfy mass continuity, and is necessary as a result

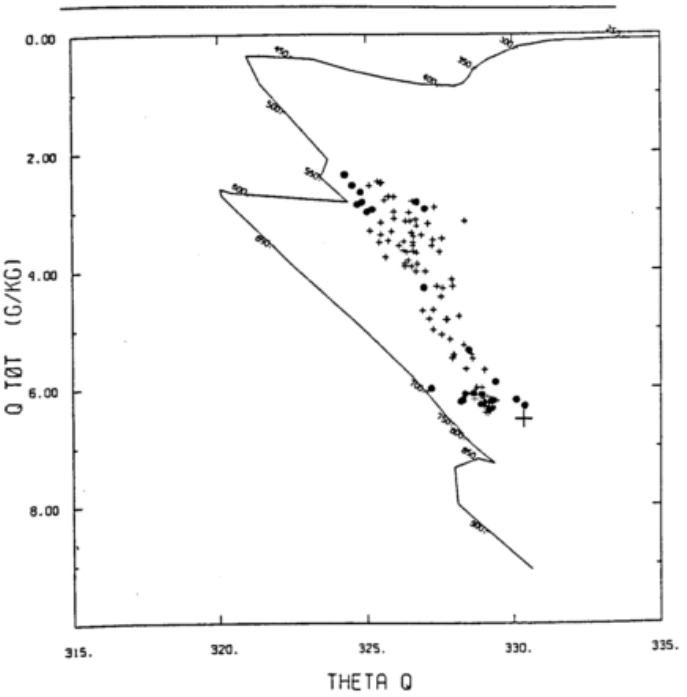


Figure 2. Paluch diagram of observed and model computed points. '+' are observed 1 Hz averaged values from the University of Wyoming King Air. '•' are model predicted points at the penetration level (480 mb). Cloudbase is indicated by '+'.

of geometrical constraints of the model. The Cotton (1975) flux-weighted formulation resulted in a less dilute cloud than observed, and showed little mixing in either the inner or outer cloud region. The entrainment formulation based upon the turbulent kinetic energy (Taylor, 1987) yielded a cloud with an inner region which agreed well with the observed updraft properties and an outer cloud region which exhibited a mixing pattern consistent with that observed by repeated aircraft penetrations. This entrainment formulation requires the specification of an eddy mixing length at the cloud edge. Tests indicate that the model response was not extremely sensitive to the value of the mixing length. A mixing length equal to about half the difference between the inner and outer cloud radii was used for the cloud base runs.

Table 1
Comparison of Observations and Model Results for CCOPE July 19 Cloud

	Observed	Model	
Cloud base height	3.9	3.9	km MSL
Max. cloud top	10.5	11.0	km MSL
Liquid cloud height	6.5	≈ 7	km MSL
First graupel	5.8	6.5	km MSL
max. vertical velocity	10-15	12	ms^{-1}
Cloud base updraft	1-5	3-6	ms^{-1}
First radar echo	7	6.8	km

4 SULFATE CHEMISTRY

SO_2, SO_4^{-2}, NH_4^+, and H_2O_2 fields are advected simultaneously with the dynamic and microphysical fields. The aqueous concentrations of gas phase fields are assumed to follow Henry's law. Sulfate chemistry is incorporated into the cloud model using a parameterization similar to Rutledge et al. (1986). The S(IV) oxidation (via H_2O_2) rate of Martin (1984) is used. A pressure correction is applied to the S(IV) oxidation (via O_3) found in Rutledge et al. (1986).

The cloud model discussed above was used to model a small midlatitude continental cumulonimbus from July 19, 1981 during CCOPE. The chemistry was initialized with several distributions of SO_2, and both NH_4HSO_4 and $(NH_4)_2SO_4$ aerosol to examine the relative importance of oxidation to scavenging, the linearity of sulfur deposition to cloudbase sulfur flux, the influence of entrainment and the ice phase upon in-cloud chemistry and deposition, and the effect of an environment previously modified by cumulus activity. The main points are summarized here.

4.1 OXIDATION / SCAVENGING

For all cases studied, in-cloud scavenging of SO_4^{-2} aerosol mass contributed between 30% and 50% of the total sulfur mass deposited at the surface. Sub-cloud scavenging accounted for about 25% of the total sulfur mass deposited for these cases. In-cloud oxidation of SO_2 contributed from 10% to 15% of the total sulfur mass deposited, and was a function of the aerosol type. Oxidation of SO_2 accounted for between 20% and 45% of the in-cloud SO_4^{-2}.

4.2 DEPENDENCE ON CLOUD BASE FLUX

The ratio of sulfur deposited to the cloud base sulfur flux (**r**) varied significantly as the cloud base sulfur flux was changed. For an order of magnitude increase in the cloud base sulfur flux (relative to the continental background base run initialization), **r** decreased to 0.64-0.78 $\mathbf{r}_{\text{cont.back.}}$.

4.3 ROLE OF ENTRAINMENT

The influence of entrainment in these clouds upon deposition was tested with simulations run in chemical environments in which the SO_2, SO_4^{-2} and NH_4^+ aerosol and H_2O_2 environmental concentrations were set to zero above cloud base. These tests indicate that about 10% of the deposited NH_4^+ results from entrainment, but that the effect upon sulfur deposition is less (around 8%) due to SO_2 oxidation.

This result is somewhat surprising in light of the importance of entrainment for the microphysics and dynamics, but is understandable in terms of the relatively low environmental aerosol and SO_2 concentrations above cloud base.

For other environmental conditions, e.g., vertical gradients of O_3 or H_2O_2 coupled with high SO_2 oxidation rates, or clouds which entrained more air at mid-levels,

the effects of entrainment may be much more noticeable.

4.4 ROLE OF THE ICE PHASE

The ice phase is important in the dynamical and microphysical development of these clouds. Tests of the ice phase impact upon in-cloud chemistry and deposition indicated that the total sulfur mass deposited is increased by about a factor of two relative to the base run case, and suggest that, for some environmental conditions, models of midlatitude cumuli which neglect the ice phase may tend to overpredict deposition.

4.5 MODIFIED ENVIRONMENT

One series of tests was designed to examine the effect of clouds growing in an environment modified by fair-weather, non-precipitating cumulus. These non-precipitating cumuli tend to remove SO_2, sulfate aerosol and H_2O_2 from the sub-cloud layer and increase the SO_2 and SO_4^{-2} and NH_4^+ aerosol concentrations in the mid-cloud region. However, precipitating clouds which subsequently grow in an environment modified by non-precipitating cumulus deposit less total sulfur and NH_4^+ than those initialized with the unmodified environment. This is a consequence of the relatively low importance of entrainment upon sulfur deposition for these cases.

5 SUMMARY

The model results for a small cumulonimbus indicate that for a continental background or moderately polluted atmosphere; aerosol scavenging accounts for between 50 and 80% of the in-cloud sulfate ultimately deposited; that ozone oxidation of sulfur dioxide may be important in the upper regions of the cloud; that although entrainment of environmental air is important in the cloud dynamics and microphysics, it is relatively unimportant in the chemistry for these clouds, and that neglect of the ice phase when considering chemistry in these clouds may lead to overestimates up to 200% in sulfate deposition.

REFERENCES

Asai, T. and A. Kasahara, 1967: A Theoretical Study of the Compensating Downward Motions Associated with Cumulus Clouds, *J. Atmos. Sci.*, **24**, 487-496.

Book, D.L., J.P. Boris and S.T. Zalesak, 1981: Flux-Corrected Transport, in *Finite-Difference Techniques for Vectorized Fluid Dynamics Calculations,* David L. Book, ed., Springer-Verlag, 240 pp.

Cheng, C.P., 1981: Numerical Simulation of the Dynamics, Cloud Microphysics and Radar Echo Structures of Tropical and Mid- Latitude Convection, Ph.D. thesis, University of Washington, 217 pp.

Cotton, W.R., 1975: On Parameterization of Turbulent Transport in Cumulus Clouds, *J. Atmos. Sci.*, **32**, 548-564.

Dye, J.E., B.E. Martner and L.J. Miller, 1983: Dynamical-Microphysical Evolution of a Convective Storm in a Weakly-Sheared Environment. Part I: Microphysical Observations and Interpretations, *J. Atmos. Sci.*, **40**, 2083-2096.

Martin, L.R., 1984: Kinetic Studies of Sulfite Oxidation in Aqueous Solution, in SO_2, NO and NO_2 Oxidation Mechanisms: Atmospheric Considerations, Jack Calvert, ed., Butterworth Pub., pp. 63-101.

Paluch, I.R., 1979: The Entrainment Mechanism in Colorado Cumuli, *J. Atmos. Sci.*, **36**, 2467-2478.

Rutledge, S.A., D.A. Hegg and P.V. Hobbs, 1986: A Numerical Model for Sulfur and Nitrogen Scavenging in Narrow Cold-Frontal Rainbands. 1. Model Description and Discussion of Microphysical Fields, *J. Geophys. Res.*, **91**, 14385-14402.

Taylor, G.R., 1987: A Numerical Investigation of Sulfate Production and Deposition in Midlatitude Continental Cumulus Clouds, Ph.D. Dissertation, University of Washington, 296 pp.

Yau, M.K., 1980: A Two-Cylinder Model of Cumulus Cells and Its Application in Computing Cumulus Transports, *J. Atmos. Sci.*, **37**, 2470-2485.

A NUMERICAL SIMULATION OF THE ACIDIFICATION PROCESS OF RAIN WATER BELOW THE CLOUD AND THE MECHANISM OF ACID RAIN FORMATION IN AREA OF CHONGQING

Huang Meiyuan and Liu Shuairen
(Institute of atmospheric Physics, Academia Sinica)

1.INTRODUCTION

There are two processes,in the cloud and below the cloud,for formation of acid rain,but the relative importance of these processes is different in various regions. The observations[1] in the Chongqing region by aircraft indicate that PH of cloud water is about 5.6,but the average PH of rain water in city is 4.06.So the acidification of rain water below the cloud is predominat in typical local pollution region of Chongqing.

Many scientists had investigated the acidification under the cloud. But these researches didn't consider the aerosols and only considered $[SO_2]_g$ with concentration no more than 20 ppb. We discuss $[SO_2]_g$ with concentration till 100ppb,consider together pollution gases and aerosols so as to investigate the mechanism for acidification of rain water.

2.THE MODEL

There are two parts,upper and lower parts,in atmosphere. The upper is cloud region where rain drops have formed. The lower is pollution region where there are pollution gases of $[SO_2]_g$, $[HNO_3]_g$, $[NH_3]_g$, $[CO_2]_g$, $[O_3]_g$, $[H_2O_2]_g$ et al. and aerosols.The diffusion and absorbtion processes of gases into raindrops are considered.

There are 13 equations of chemical reactions. Equations 1-8 are the reversible reactions for the CO_2-SO_2-HNO_3-NH_3-H_2O system. Equations 9-11 are for sulfate production by ozone oxidation.Equation 12 is the irreversible S(IV) oxidation by H_2O_2. Equation 13 is the manganese-catalyzed S(IV) oxidation reaction.

According to observations we obtain simple Gamma-Junge size distribution of the aerosols which don't change with height and time. but their concentration decreases logarithmically with height. The maximum of aerosol radius is 10 μm. and the minimum is 0.001 μm. The collection efficiency E with which the aerosols particles collide with raindrops is divided into three parts According to Friedlan-der's formula for r<0.1 μm, the experimental results from Hample et al. for 0.1<r<1 μm [2] and numerical simulation by P.K. Wang et al.[3] and experimental results for r>1 μm. We may write the aerosol mass which is collected by raindrops per unit distance is following:

$$dM_r/dz=4/3\,\pi\rho\int E(R,r)(R+r)^2 r^3 n(r)\,d\log r$$

We consider aerosol contents are composed of five ions H^+,OH^-,NH_4^+, NO_3^-, SO_4^{2-} and other contents. if $m=dM_r/dz$, we have

$$d[SO_4^{2-}]/dz=U_{S\,O_4^{2-}}\,m$$
$$d[H^+]/dz=U_{H^+}m$$
$$d[OH^-]/dz=U_{O\,H^-}\,m$$
$$d[NH_4^+]/dz=U_{N\,H_4^+}\,m$$
$$d[NO_3^-]/dz=U_{N\,O_3^-}\,m$$

where u_s is the proportion of a certain ions to the whole aerosols mass.Considering the combined action of pollution gases,aerosols and chemical reactions, we get 14 non-linear equations for determing the $[H^+]$, $[OH^-]$, $[CO_2]$, $[HCO_3^-]$, $[SO_2]$, $[HSO_3^-]$, $[SO_3^{2-}]$, $[NH_3]$, $[NH_4^+]$, $[NO_3^-]$, $[O_3]$, $[H_2O_2]$, $[SO_4^{2-}]$, $[HNO_3]$.

3. RESULTS AND DISCUSSIONS

The range of raindrops radius is from 0.1 to 1.5mm. There are two cases, 1mm/hr and 5mm/hr, for rain rate. Except special indication,the falling distance is 1000m.The initial parameters are PH=5.6, $[CO_2]_g=330$ppm,$CO_2=12$ μM, $HCO_3^-=2.4$μM,$OH^-=4.2$nM,$SO_4^{2-}=75$μM, $NO_3^-=10$μM and $NH_4^+=50$μM. The concentrations of SO_4^{2-},NO_3^-,NH_4^+ are consistent with the average values of cloud water in Chongqing region. We consider precipitation times for five minites at the beginning.

3.1 *The Acidification of Raindrops by Absorbing Pollution Gases*

The results show that PH and the concentration of SO_4^{2-} change obviously with $[H_2O_2]_g$ for various $[SO_2]_g$. PH decreses as $[H_2O_2]_g$ increases. The oxidant $[H_2O_2]_g$ can produce serious acid rain for high $[SO_2]_g$ concentration. As $[SO_2]_g$ concentration is 100 ppb , $[H_2O_2]_g$ of 1ppb makes PH below 4. For high $[H_2O_2]_g$ concentration PH

is lower.For low $[SO_2]_g$ concentration the effect of $[H_2O_2]_g$ on the acidification is weaker. SO_4^{2-} concentration incraeases quickly with $[H_2O_2]_g$ or $[SO_2]_g$. There is nonlinear relationship between $[SO_2]_g$ and SO_4^{2-}.It is able to conclude that PH is nonlinearly relative with $[SO_2]_g$ too. For 1mm/hr H^+ and SO_4^{2-} concentration are larger than that for 5 mm/hr. The result is consistent with observations[1,4].

The oxidation effects of $[O_3]_g$ is proportional to PH. The oxidation of H_2O_2 doesn't decrease with PH. The serious acid rain can be produced by oxidation of H_2O_2 but cann't be produced by O_3. NH_3 is alkaline gas and makes PH increase so that for $[NH_3]_g$=5 ppb the oxidation of ozone is stronger and the factor become smaller. It can be seen from the simulations that an amount of oxidants can acidify rain water within a short distance.As falling distance is 500m PH is 4.18 for 1 mm/hr and 4.38 for 5 mm/hr. As falling distance is 2000m PH is below 4. For PH=4.6 the distance is 230m for 1mm/hr and 350m for 5mm/hr.The larger the distance is, the longer washout time is, the smaller PH is. SO_4^{2-} increases with the distance. At the beginning it increases fast, but after the distance beyond 500m the change becomes slower.

3.2 *Acidification of Rain Water Considering Together Aerosols and Pollution Gases*

Accoding to the data of observations the proportion of NH_4^+ or NO_3^- to the whole aerosol mass is between 0.01 and 0.03. So we choose $U_{NH} = U_{NO} = 0.02$. The proportion of SO_4^{2-} to the whole aerosol mass is 0.222 in city and 0.099 in suburb. we select $U_{SO} = 0.2$ for $r<1.6\mu m$ and $U_{SO} = 0.05$ for $r>1.6\mu m$. To choose U_H and PH for two cases: the aerosols concentration on ground is 1300/cm in case 1 and is 650/cm in case 2. PH and U_H change with radius for two cases. There are in the range of PH=4.3-6.7, $u_H = 4\times10^{-3} - 2\times10^{-5}$. The case without aerosols (case 3) is also considered for The same initial parameters.Figure 1 and Figure 2 show that PH and SO_4^{2-} change with $[H_2O_2]_g$ in case 1, case 2 and case 3. It can be seen that in three cases PH or SO_4^{2-} change inversely with $[H_2O_2]_g$.But the decrement of PH with $[H_2O_2]_g$ in case 1 or case 2 is smaller than in case 3, eg. as $[H_2O_2]_g$ is from 1 to 10ppb PH decreases by 0.457 in case 1, 0.717 in case 2 and 0.736 in case 3.The difference of PH between case 1 or case 2 and case 3 change with $[H_2O_2]_g$. In the absence of $[H_2O_2]_g$ it is very small and PH in case 1 or case 2 is lower than in case 3. But after $[H_2O_2]_g$>1ppb, PH in case 1 or case 2 is larger than in case 3. The diffirence of PH become larger as $[H_2O_2]_g$ increases, It indicates aerosol has adjusting effect on acidification of rain water. For $[H_2O_2]_g$<4.8ppb PH in case 1 is larger than in case 2. The result is opposite for $[H_2O_2]_g$>4.8ppb. The aerosols which dissolve in raindrops has definite PH. It makes PH of rain water which is lower (higher) than aerosols to decrease (increase). Moreover, the larger the aerosol concentration is, the more raindrops collect aerosols, the stronger the adjusting effect is. Because of high concentration of aerosols in case 1,PH in case 1 decreases more than in case 2 while PH is high. But as PH goes below 4.5, the aerosols in case 1 makes PH to increase more than in case 2.

3.3 *The Mechanism on the Acidification of rain Water in Chongqing Region*

The observations by aircraft and on ground show that the average PH of the rain water on ground is between 3.6 and 4.6 and PH of the cloud water (includes rain water) in the air is between 5.0 and 7.4 in Chongqing region. This indicates that the acidification below cloud is predominant during the falling process of rain water. The ion conponments of the cloud and rain water, $[SO_2]_g$ and $[NH_3]_g$ concentrations in the air or on ground and the physical-chemical features of the aerosols had been measured. It is able to carry out calculation and analysis by the above mentioned model. The average value on Sept. 9, 1985 is selected, namely 5.93 for PH of cloud water, 4.37 for rain water. The initial SO_4^{2-} and NO_3^- are 75 μM and 10 μM. The ratio of SO_4^{2-} to NO_3^- is 15 in the cloud and 10.1 in rain water on ground.The falling distance is 2000 m. The concentration of aerosols on ground is 1000/cm^3. The average PH is 0.1 larger than the PH at biginning during a rain event according to our observation, So the simulated value should be 0.1 lower than the real value. $[NH_3]_g$ concentration on ground is very low,it is lower in the air. So it doesn't be considered. According to observations at height of 600-3000m $[SO_2]_g$ concentration is usually between 1 and 20 ppb, so the average $[SO_2]_g$ concentration is selected as 10 ppb. Without oxidants and catalysts the PH of rain water

will be 5.463 for falling distance 2000m, for which it is unable to make serious acid rain. The effect of aerosols has been discussed, the difference of PH between the case in which the aerosols is considered and the case without aerosols is very small for low oxidants. So without oxidants and pollution gases the rain water cann't be efficiently acidified owing to the effect of aerosols. We also calculate oxidation of catalyst Mn^{2+}, discussing the relative effectiveness of Mn^{2+} and O_3. The oxidation of Mn^{2+} is small for usual concentration of 1 μM, so Mn^{2+} has less effect on the acidification than $[O_3]_g$. Mn^{2+} for real condition cann't produce acid rain of PH=4.2. Our observations show that the concentration of $[O_3]_g$ in daytime is between 20 and 80 ppb. So 50 ppb is obtained for $[O_3]_g$ in the region of Chongqing. $[H_2O_2]_g$ concentration doesn't measure regularly in that region. According to a few measurements it is sevral ppb. The relative effectiveness of $[O_3]_g$ and $[H_2O_2]_g$ has been discussed. As PH is below 4.5, for $[O_3]_g$ beyond 10 ppb PH changes very small with $[O_3]_g$, It is impossible for that $[O_3]_g$ can make PH of rain water to fall down to below 4.2. When $[H_2O_2]_g$=3 ppb, $[O_3]_g$=50 ppb, $[SO_2]_g$=10 ppb and $[HNO_3]_g$= 1 ppb, the real PH and the ratio of SO_4^{2-} to NO_3^- in rain water on ground can be simulated. In order to discuss effect of increasing pollution gases, the cases for $[SO_2]_g$=20 ppb and for $[HNO_3]_g$=10 ppb are calculated. Besides, The cases for $[SO_2]_g$=5 ppb ,for $[NH_3]_g$=10 ppb and for which aerosols concentration increases by six times also discussed. For above the cases $[H_2O_2]_g$ and $[O_3]_g$ don't change. As $[SO_2]_g$ concentration increases double, PH decreases by 0.044 for 1 mm/hr and by 0.049 for 5 mm/hr, namely the increment of $[SO_2]_g$ has less effects. As $[HNO_3]_g$ goes from 1 to 10 ppb PH decrease by 0.234 for 1 mm/hr and 0.216 for 5 mm/hr so that increment of $[HNO_3]_g$ has important effect on the acidification of rain water. As $[SO_2]_g$ decreases from 10 to 5 ppb, PH increases by about 0.2, which indicates the decrement of $[SO_2]_g$ makes PH to decrease evidently for low $[SO_2]_g$ concentration. $[NH_3]_g$ softens evidently the acidification of rain water. PH for $[NH_3]_g$=10ppb is 0.70 larger than without $[NH_3]_g$. The increment of aerosol concentration makes PH to increase, but the concentration of N=5000/cm³ is too large to compare with the usual value in atmosphere.

4. REFERRENCES

[1] Huang Meiyuan, Shen Zhilai and Wu Yuxia; 1988: The observations and analysis for acidification of cloud and rain water and chemical contents in Chongqing region, *Scientia Atmospherica Sinica*, 12(2).

[2] Pruppacher, H.R. and J.D.Klett; 1978: Microphysics of clouds and precipitation, 231-361.

[3] Wang,P.K. et al.; 1978: On the effect of electric chargs on the scavenging of aerosol particles by clouds and small rain-drops, *J. Atmos. Sci.*, 35:1735-1743.

[4] He Zhengzheng et al.; 1985: The relation of acidity of rain water and physical characters of precipitation, *Scientia Atmospherica Sinica*, 9(4): 442-446.

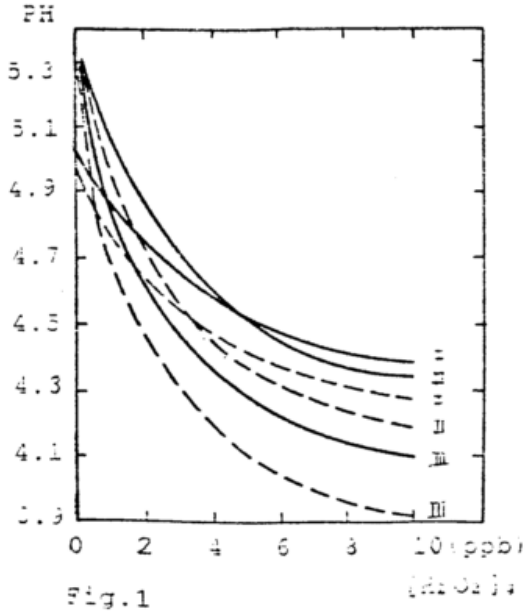


Fig.1

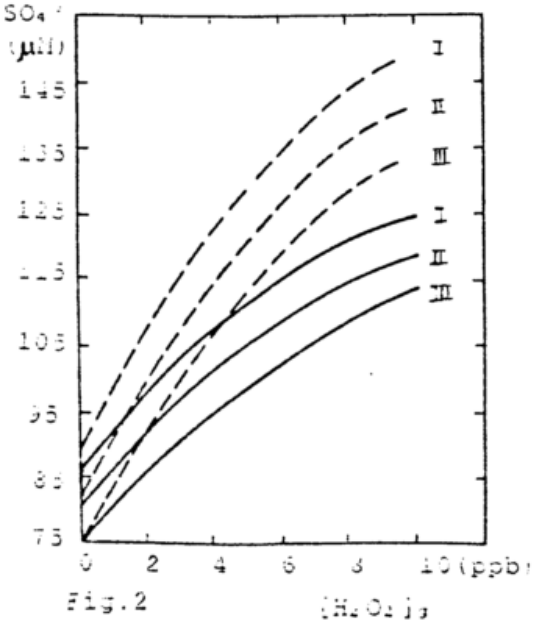


Fig.2

EFFECTS OF CLOUD MICROPHYSICAL PROCESSES ON TRACE CHEMICAL REMOVAL EFFICIENCIES

Dennis Lamb and Jen-Ping Chen

Department of Meteorology
The Pennsylvania State University
University Park, PA, 16802, USA

1. INTRODUCTION

The detailed microphysical processes responsible for cloud and precipitation formation influence not only the precipitation efficiency but also the efficiencies with which trace chemicals are removed from the atmosphere. Clouds represent those places in the atmosphere where the conversion of water vapor to precipitable water takes place. Likewise, clouds permit a host of chemical and physical transformations to take place that are not possible elsewhere in the atmosphere. It should not be surprising, given the dependence of the chemistry on certain cloud properties (e.g., liquid water content), that the removal efficiencies of the water substance and of the trace chemicals should be closely related.

The wet removal of trace constituents from the atmosphere takes place over a range of time and space scales. Clouds that yield precipitation form under certain synoptic-scale weather patterns that allow for the influx and uplift of relatively moist air, air that also contains substances picked up from sources distributed over regional-scales. Superimposed on this large-scale setting are the various cloud-scale flows and microphysical processes which are responsible for bringing the pollutants into contact with the various cloud particles. While the actual precipitation scavenging phenomena necessarily take place on the microscale, data that are based on storm- or event-scale averages can be used to identify the most important or dominant mechanisms of action. Such averaging in effect filters out the numerous microscale or transient phenomena which may be active in the storm but which contribute little to the overall removal of material from the atmosphere. For this reason primary attention is focused here on "event" data and storm-scale concepts.

In this paper we first review the evolution of ideas related to wet deposition of trace chemicals. Then, we show how the concept of scavenging ratio has been modified to improve our understanding of storm-scale removal efficiency.

2. DEVELOPMENT OF THE CONCEPTS

On the storm scale air can be thought of as being "processed" by the cloud. Some of the water vapor is condensed out into liquid and solid forms and converted into large particles that eventually fallout as rain, snow or hail. Similarly, some fraction of the trace chemicals contained in the inflowing air interact with the cloud and precipitation elements and are removed from the atmosphere.

Key elements in this simplified concept of a storm are the inflow, the deposition flux, and the outflow. The inflow provides the chemical and moisture inputs to the system, which are linked in specific ways to the deposition flux by the precipitation microphysics. As the cloud forms by condensation of the water vapor, the various trace chemicals will tend to be incorporated into the condensate with a certain species-dependent efficiency ε_i, where subscript i specifies the chemical in question. JUNGE (1963, p. 291) used simple mass conservation arguments to show that the concentration c_i of a compound in the condensate should be directly proportional to the concentration n_i in the air prior to cloud formation. Thus, in our terminology,

$$c_i = \frac{\varepsilon_i}{\nu_L} n_i \qquad (1)$$

where the inverse proportionality on the liquid water concentration ν_L shows a simple dilution effect when it can be assumed that the attachment or incorporation efficiency ε_i ("rainout" efficiency in Junge's terminology) is independent of the liquid water concentration. When soluble gases are in Henry's Law and ionic equilibrium with the dissolved components, however, ε_i will depend on ν_L.

When the concentration of a particular chemical species in cloud condensate can be linearly related to the concentration of the parent species in the pre-cloud air, then a clear predictive tool is made available, since measurements or model calculations of the air concentration n_i permit ready computation of the concentration in the precipitation. Toward this end numerous workers have made field estimates of storm scavenging ratios c_i/n_i (e.g., ENGELMANN 1971; SCOTT 1981; BARRIE 1985).

If the air flowing into a storm system can be identified and is in any reasonable sense homogeneous, then scavenging ratio measurements can be made meaningful,

especially when comparisons are made between different species. Despite complexities in the airflow patterns and in the structure of most storms, each component in the air mixture is advected into and through the system in the same way. Fractionation of these components tends to take place only during species-dependent microphysical processing within the cloud, not through meteorological transport. Thus, MESZAROS AND SZENTIMREI (1985) calculated enrichment factors, using lead as a reference element, to estimate the relative removal by precipitation of gaseous and particulate forms of sulfur and nitrogen compounds. Used in this way, enrichment factors can be viewed as the ratio of two separate scavenging ratios or as a removal efficiency of one compound compared to that of another.

Earlier, ENGELMANN (1971) had qualitatively noted that some substances tended to be removed more efficiently than others, but the data were not obtained from a common system. However, he did point out the value of comparing the removal efficiency of a trace chemical with the removal efficiency of water vapor. Recently, ENGELMANN (1988) developed this concept more fully by forming a water vapor-normalized scavenging ratio. The traditional difficulties of estimating cloud precipitation efficiencies or specific chemical removal efficiencies, dependent as they are on determining storm mass budgets or knowing storm inflow fields (MARWITZ 1974; SCOTT 1982), are largely avoided when using enrichment factors or any ratio of removal efficiencies since many of the complexities of the storm structure cancel out.

The normalized scavenging ratio of ENGELMANN (1988) is essentially an enrichment factor with H_2O used as the reference substance. This is particularly valuable because water is the primary ingredient of cloud and precipitation and the effective agent of wet deposition. Thus, the simultaneous comparison of the concentrations of two substances (a trace chemical and water) in two phases (gas and condensate) provides a direct measure of the differences with which the storm processes each substance. In this, we have a direct link between the concepts of microphysical fractionation of chemicals during precipitation formation and atmospheric removal efficiency. By application of Eq. (1) to both the substance in question (i) and water (H_2O),

$$\frac{\varepsilon_i}{\varepsilon_{H_2O}} = \frac{c_i \nu_L / n_i}{c_{H_2O} \nu_L / n_{H_2O}} = \frac{c_i / c_{H_2O}}{n_i / n_{H_2O}} \equiv E_i \qquad (2)$$

where E_i is defined as the enrichment factor, the quantitative measure of fractionation, and is clearly identifiable with the efficiency with which component i is removed from the air relative to that with which water vapor is removed. We shall henceforth refer to this special enrichment factor E_i as a "relative removal efficiency."

3. APPLICATION OF THE CONCEPTS

The concept of a relative removal efficiency, being identifiable with chemical fractionation arising from precipitation formation, finds ready application in both theoretical and observational cloud chemistry. A variety of microphysical processes must take place in sequence or in parallel to transform water vapor into precipitation. Examples include cloud drop nucleation and growth by condensation and collision-coalescence, ice nucleation and growth by vapor deposition, aggregation and riming. Each microphysical process has the potential for fractionating the various trace chemicals; in general, each substance will be taken up by the cloud elements at rates which differ from each other and from the rate at which water itself is taken up. An extreme example of fractionation is the classical Bergeron process of ice crystal growth by vapor deposition in mixed-phase clouds; except for possible phoretic capture of interstitial aerosol particles (VITTORI AND PRODI 1967), water vapor is transferred from the cloud drops to the ice readily, almost to the total exclusion of the solute content of the cloud water. By contrast, highly soluble gases tend to become enriched relative to H_2O in liquid cloud drops during condensation. Each process and each chemical must be considered independently to ascertain the true fractionation potential.

At this point we provide a quantitative example of gaseous absorption into cloud water as simulated by an idealized equilibrium cloud model. Specified concentrations of NH_3 (0.5 ppb), SO_2 (10 ppb), and CO_2 (332 ppm) are introduced into a parcel which ascends adiabatically from near the surface to almost 200 mb. Above the condensation level the concentrations of dissolved gases in the liquid phase are calculated in accord with known temperature dependences to the various Henry's Law constants and ionic equilibrium constants. Fig. 1 shows the results of these calculations in terms of the relative removal efficiency, or enrichment factor relative to water, as given by Eq. (2). The abscissa represents the liquid water mixing ratio, a non-linear measure of altitude. The solution pH is shown by the dashed curve, while the horizontal dashed line indicates the condition of no fractionation, i.e., when $E_i = 1$. Particularly noteworthy in a presentation such as this is the great spread in removal efficiencies relative to water, a direct result of the differences in solubilities between NH_3, SO_2, and CO_2. The cloud water can be enriched in ammonia up to 100 times relative to H_2O, whereas CO2 is in effect "rejected" relative to water condensation by a factor

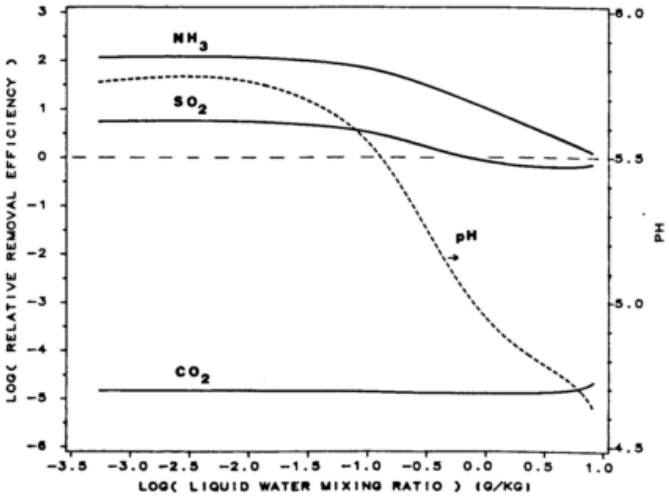


Fig. 1: Relative removal efficiencies and pH as functions of liquid water mixing ratio.

close to 10^5. As the cloud water content continues to grow, the most soluble gases eventually become depleted from the gas phase, leading to a characteristic dilution effect and reduction in relative removal efficiency. Taken to an idealized limit all gases, including H_2O, condense out, causing all enrichment factors to approach unity.

Via such examples it becomes evident that physio-chemical fractionation can be linked quantatively to discrete processes of cloud and precipitation formation. The coupling of the discrete-process analyses from a particular model permits an overall removal efficiency to be computed, which may then be compared with the outputs from other models or with values determined from field observations. Comparison of NH_3 relative removal efficiencies determined from field observations (SHIMSHOCK AND DE PENA 1986) and computed as shown above suggests that the rain from synoptic scale systems in eastern North America tends not to be derived from the simple collection of cloud water in the lower parts of the cloud; the measured relative removal efficiencies tend to be at least a factor of 10 lower than those computed using any reasonable cloud water content. There appears to be a microphysical limit to the transfer of cloud-dissolved NH_3 to the rain. We are exploring the possibility that a substantial fraction of the rain mass was acquired during ice-phase growth processes.

4. CONCLUSION

In this paper we have tried to show the conceptual links between scavenging ratios, enrichment factors, and relative removal efficiencies. A simple theoretical example shows that specific microphysical processes responsible for the growth of cloud and precipitation elements also lead to chemical fractionation and relative removal efficiencies which can vary by orders of magnitude. A real understanding of the wet deposition of trace chemicals cannot be achieved without a detailed study of traditional cloud and precipitation microphysics.

5. ACKNOWLEDGEMENTS

This work was sponsored in part by NOAA (Contract No. 50-EANR-6-00011), DOE (Contract No. DE-FG02-85ER60294) and NSF (Grant Nos. ATM-8520123 and ATM-8716166). Appreciation is also expressed to John Shimshock for early use of data and to Raja ElSalem for help with data analysis.

6. REFERENCES

BARRIE, L.A., 1985: Scavenging ratios, wet deposition, and in-cloud oxidation: An application to the oxides of sulphur and nitrogen. J. Geophys. Res., 90, 5789-5799.

ENGELMANN, R.J., 1971: Scavenging prediction using ratios of concentrations in air and precipitation. J. Appl. Meteor., 10, 493-497.

ENGELMANN, R.J., 1988: The scavenging ratio normalized to remove the effect of humidity. Atmos. Environ., 22, 137-146.

JUNGE, C.E., 1963: Air Chemistry and Radioactivity. New York, Academic Press, 382 pp.

MARWITZ, J.D., 1974: An airflow case study over the San Juan Mountains of Colorado. J. Appl. Meteor., 13, 450-458.

MESZAROS, E.; SZENTIMREI, T., 1985: On the wet removal of gaseous and particulate sulfur and nitrogen species from the atmosphere. J. Atmos. Chem., 2, 405-413.

SCOTT, B.C., 1981: Sulfate washout ratios in winter storms. J. Appl. Meteor., 20, 619-625.

SCOTT, B.C., 1982: Predictions of in-cloud conversion rates of SO_2 to SO_4 based upon a simple chemical and kinematic storm model. Atmos. Environ., 16, 1735-1752.

SHIMSHOCK, J.P.; DE PENA, R.G., 1986: Assessment of the role of tropospheric ammonia as a neutralizing agent in rain. In Meteorology of Acidic Deposition, J. Laznow and G.J. Stensland (eds.), Trans. Air Pollut. Contr. Assoc., 402-410.

VITTORI, A.; PRODI, V., 1967: Scavenging of atmospheric particles by ice crystals. J. Atmos. Sci., 24, 533-538.

DYNAMIC, RADIATIVE, AND CHEMICAL EFFECTS OF CLOUDS ON TROPOSPHERIC TRACE GASES

Chris J. Walcek
Atmospheric Sciences Research Center,
State University of New York, Albany, NY

1. Introduction

Observations (DICKERSON et al., 1987) have suggested that vertical motions in clouds can efficiently transport air between the boundary layer and free troposphere. Also, models of radiative transfer (MADRONICH, 1987) show that photolysis rates within and above the upper levels of clouds can be 2 - 5 times higher than corresponding clear air values, leading to more efficient production of O_3 and H_2O_2 via gas-phase chemical interactions.

In the following discussion, results are presented showing the sensitivity of a tropospheric chemistry model to the presence of clouds. Sulfuric acid and ozone production rates are calculated using the CHANG et al. (1987) tropospheric chemistry model run with and without the effects of cloud mixing included. While the parameterization of these cloud effects used in this study is relatively crude compared to more detailed treatments of these effects, it represents a relatively sophisticated treatment of cloud effects in a regional or global tropospheric chemical model. The purpose of the following discussion is to demonstrate that calculations of regional or global tropospheric chemistry models are sensitive to the treatment of the microphysical and dynamical structure of clouds, suggesting the need for accurate models of these cloud effects in global and regional chemical models.

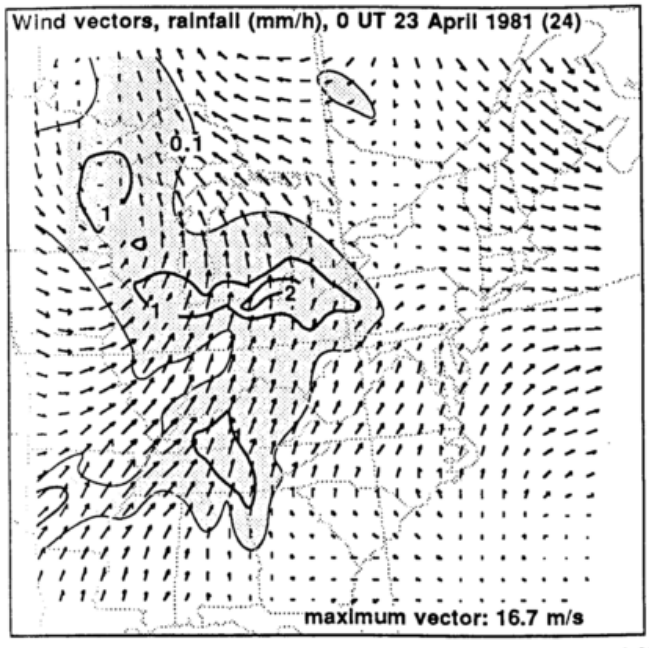


Fig. 1: Hourly precipitation rate and velocity vectors in the layer 0.15 - 0.55 km above surface at 0 UT, 23 April 1981. Shaded areas denote grid-average precipitation rate > 0.1 mm h^{-1}. Darker contour intervals are 1 mm h^{-1}.

2. Vertical redistribution of trace species

Modeling the vertical mixing accomplished by clouds in a regional or global-scale model is complicated since horizontal scales associated with cloud updrafts or downdrafts (<10 km) are significantly smaller than the horizontal grid resolution of most chemical models (>50 km). Therefore, these mixing effects must be parameterized. In the cloud mixing parameterization used in this study (CHANG et al., 1987), the effects of all clouds above a grid area are characterized by an "representative" cloud with a depth and fractional area of coverage determined by larger-scale meteorological factors. The vertical distribution of cloud microphysical properties (liquid, ice, and rainwater contents) and the amount of subcloud-layer air lifted to each cloud layer are determined using a simple entrainment hypothesis (WALCEK and TAYLOR, 1986). Air lifted to each cloud layer is released to the corresponding model level after a typical cloud lifetime. This "mass adjustment" is performed at hourly intervals during the execution of the larger-scale chemical model.

Simple tests of this parameterization show that clouds covering only a small fractional area will accomplish the same vertical mixing throughout a cloudy layer as that found in a fully turbulent boundary layer. Figs. 1 - 3 show model calculations of how surface-derived non-methane hydrocarbons (NMHC) are rapidly transported into the middle and upper troposphere during passage of frontal cloud systems over urban areas. Fig. 1 shows

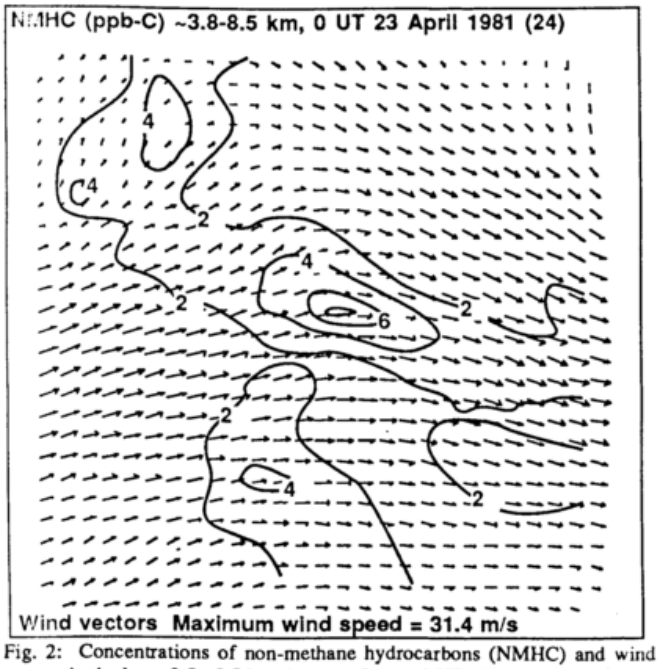


Fig. 2: Concentrations of non-methane hydrocarbons (NMHC) and wind vectors in the layer 3.5 - 8.5 km above surface at 0 UT, 23 April 1981.

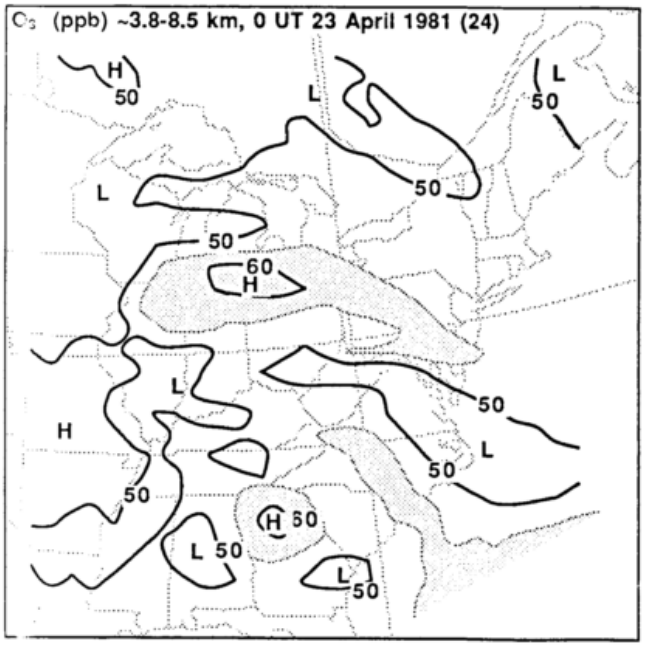


Fig. 3: Ozone concentrations in the layer 3.5 - 8.5 km above surface at 0 UT, 23 April 1981. Shaded areas denote concentrations > 55 ppb.

the distribution of wind fields and rainfall rates in the lower troposphere over the NE U. S. during a spring-time simulation period. Patterns of rainfall are associated with areas of deeper cloud fields in the domain. Fig. 2 shows the distributions of wind fields and concentrations of NMHC in the upper troposphere. Areas of elevated pollutant concentrations in the upper troposphere are strongly associated with the presence of deep cloud systems over pollutant emission regions.

Since NMHC and NO_x ($NO + NO_2$) are significant precursors to the formation of O_3 in the troposphere, Fig. 3 shows that "plumes" of O_3 are produced in upper troposphere downwind of these cloud systems as they pass over the major urban areas of the NE U. S.. As shown in Fig. 4, the average concentration of ozone within the domain is significantly higher when the effects of cloud mixing are allowed. Fig. 5 shows the actual production rate of O_3 due to photochemical interactions averaged over the model domain. Without cloud mixing, surface-emitted NO_x and NMHC are confined to the boundary layer, where dry deposition removes these precursors, and O_3 is produced less efficiently. With vertical mixing by clouds, the chemical production of O_3 is calculated to be significantly enhanced.

3. Radiative Effects

Tropospheric photolysis rate coefficients (j_i) can be evaluated from the expression

$$j_i = \int_{\lambda} \sigma_i(\lambda)\, \phi_i(\lambda) \int_{\varphi} \int_{\theta} I(\lambda,\varphi,\theta) \sin\theta \, d\theta \, d\varphi \, d\lambda \quad , \qquad (1)$$

where $\sigma_i(\lambda)$ and $\phi_i(\lambda)$ are the molecular absorption cross section and quantum yield for each reaction, and $I(\lambda,\varphi,\theta)$ is the radiance at a particular atmospheric location, calculated using the δ-Eddington radiative transfer technique of JOSEPH et al. (1976). The integrals are over all wavelengths λ and directions φ, θ.

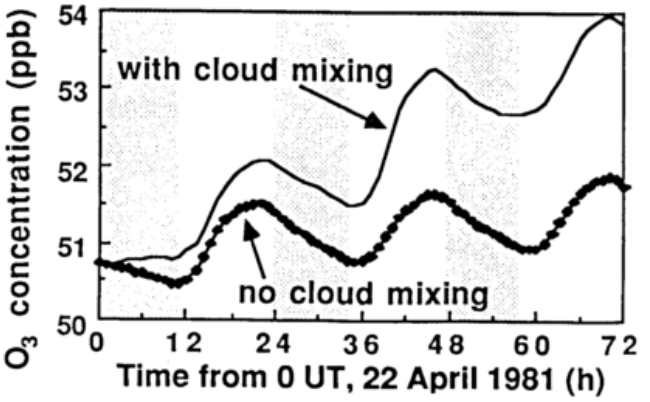


Fig. 4: Ozone concentrations averaged over the troposphere in the domain shown in Fig. 3 vs. time during the 72 h period beginning at 0 UT, 23 April 1981. Model used to generate these data was run with and without a vertical cloud mixing parameterization. Shaded areas denote night-time periods.

Ambient light and photolysis rates are significantly modified in the presence of clouds. For this application, clear air photolysis rate constants (j_{clear}) computed using Eq. (1) are multiplied by a correction factor to account for these effects

$$j = j_{clear}[1 + a\,(F_{cld} - 1)] \quad , \qquad (2)$$

where j is the photolysis rate in the grid column containing clouds, a is the fractional area of cloud coverage, and F_{cld} is ratio of the cloudy-sky to clear-sky photolysis rate coefficient, computed using the radiative transfer model described above. For solar zenith angles $\chi_0 \leq 60°$, the results of the sophisticated model can be approximated very well by the following expression

$$F_{cld} = \begin{cases} 1 + \alpha_i(1 - t_r)\cos\chi_0 & \text{above cloud layer,} \\ 1.4\cos\chi_0 & \text{in cloud layer, and} \\ 1.6 t_r \cos\chi_0 & \text{below cloud layer.} \end{cases} \qquad (3)$$

For $\chi_0 > 60°$, values for F_{cld} evaluated at $\chi_0 = 60°$ are used. In this expression, α_i is a species-specific coefficient ranging between 0.7 - 1.2, and t_r is the energy transmission coefficient for normally incident light, derived from the δ-Eddington theory of JOSEPH et al. (1976)

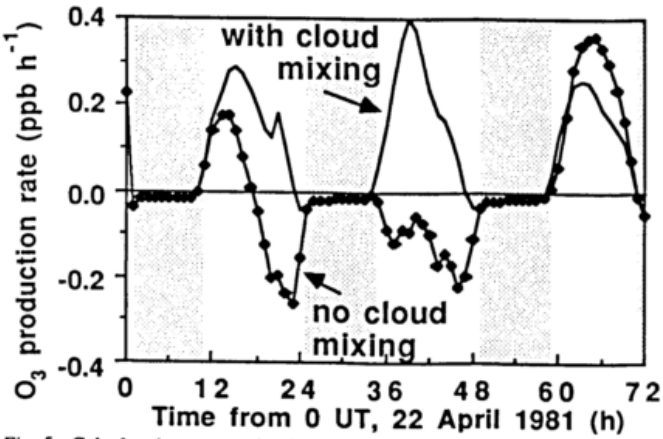


Fig. 5: Calculated ozone production rate due to chemical processes averaged over the troposphere in the domain shown in Fig. 3 vs. time during the 72 h period beginning at 0 UT, 23 April 1981. Model was run with and without a vertical cloud mixing parameterization. Shaded areas denote night.

$$t_r = \frac{5 - e^{-\tau}}{4 + 3\tau(1 - f)} \quad . \qquad (4)$$

Here f is a scattering phase function asymmetry factor, estimated to be 0.86 for typical cloud particle size ranges, and τ is the cloud optical depth, approximated as

$$\tau = \frac{3\, L \Delta z_{cld}}{2 \rho_{H2O} r} \quad . \qquad (5)$$

Here, L is the mean condensed water content (g m^{-3}) of the cloud, Δz_{cld} is the mean depth of the cloudy layer, r is the mean cloud drop radius, and ρ_{H2O} is the density of water. For optically thin clouds ($\tau < 5$), clear air photolysis rate coefficients are used.

This radiative parameterization shows that photolysis rates, and therefore overall tropospheric chemical interactions, are sensitive to the microphysical structure of cloud fields in the troposphere. Fig. 6 shows the sensitivity of photolysis rates to the mean cloud drop size above and below a 2 km deep cloud. Above cloud top, photolysis rates are about 1.6 times greater than the "clear air" value, irrespective of the cloud liquid water content. Photolysis rates in the layer below cloud base are sensitive to the mean cloud drop size as well as the liquid water content of the cloud.

4. Aqueous chemistry

It is well known that SO_2 is converted to sulfuric acid in the troposphere by both gas-phase (SO_2 + HO radical) and aqueous-phase reactions ($SO_2 + H_2O_2$, O_3 and other oxidants). The CHANG et al. (1987) model calculates that during a 3 day, spring-time period over the NE U. S., approximately 70% of this conversion occurs in clouds. Therefore, it is expected that the overall rate of sulfate production in polluted regions will be sensitive to the tropospheric cloud amount. Fig. 7 shows the correlation between the hourly-averaged, domain-averaged, in-cloud sulfate production rate with amount of cloudiness over the domain shown in Fig. 1 during a 72 h springtime period. When cloud amount over the NE U. S. exceeds approximately 1 - 3 % of the tropospheric volume, Fig. 7 shows that the aqueous-phase reaction pathway producing sulfuric acid becomes more important than the gas-phase pathway.

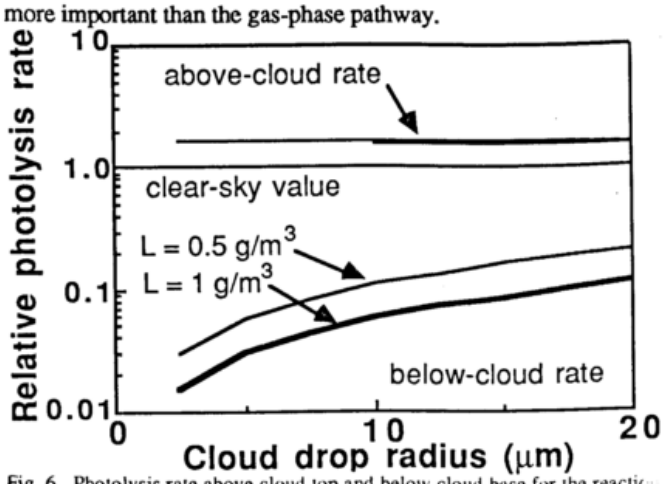


Fig. 6. Photolysis rate above cloud top and below cloud base for the reaction $O_3 \rightarrow O(^1D) + O_2$ relative to a clear-sky value vs mean cloud drop radius in a 2 km deep cloud covering 100% of a grid area. Solar zenith angle is 20°.

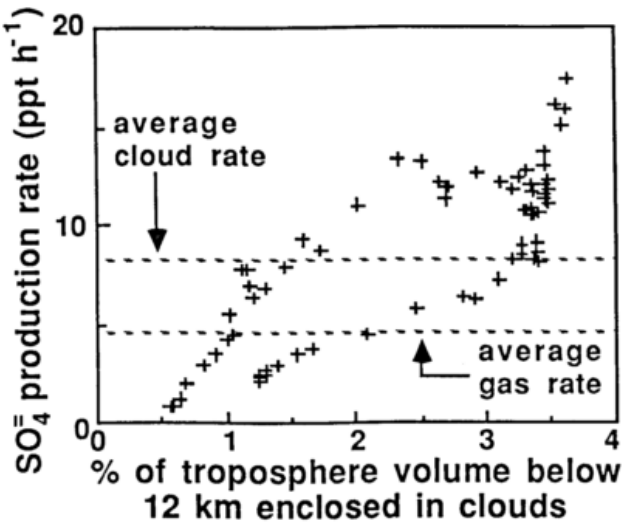


Fig. 7. Hourly-averaged rates of sulfate production within tropospheric clouds over the domain shown in Fig. 1 vs. the amount of clouds in the domain evaluated during the 72 h period beginning at 0 UT, 23 April 1981.

5. Conclusions

These model results suggest that vertical motions associated with mid-latitude cyclones over high NO_x and organic compound emission areas can contribute significantly to the global formation of O_3 since the necessary precursors are efficiently transported into the upper troposphere, where the lifetimes of these O_3 precursors are much longer, and photolysis rates are significantly enhanced due to lower-level cloud fields. Regional-scale O_3 production rates are extremely sensitive to the vertical and horizontal extent of cloudiness, as well as the microphysical structure of these clouds. Calculations of a radiative transfer model show that photolysis rates above clouds may be significantly enhanced, while below clouds, photolysis rates can be reduced to near zero. Since photolysis rates determine the rate at which tropospheric photochemistry is occurring, it is clear that models of tropospheric chemistry must accurately quantify the microphysics and dynamics of tropospheric cloud fields.

6. References

CHANG, J.; BROST,R.; ISAKSEN, I.; MADRONICH, S.; MIDDLETON, P.; STOCKWELL, W.; WALCEK, C.: A three-dimensional Eulerian acid deposition model: physical concepts and model formulation. J. Geophys. Res. **92**, (1987), 14681-14700.

DICKERSON, R. ; HUFFMAN, G.; LUKE, W; PICKERING., K; LESLIE, A;. LINDSEY, C;. SLINN, W.; KELLY, T.; DAUM, P.; DELANY,A.; GREENBERG, J.; ZIMMERMAN, P.; BOATMAN, J.; RAY,J.; STEDMNAN,D: Thunderstorms: and important mechanism in the transport of air pollutants. Science, **235**, (1987), 460-465.

JOSEPH, J.; WISCOMBE, J.; WEINMAN, J.: The delta-Eddington approximation for radiative flux transfer. J. Atmos. Sci., **33**, (1976), 2452-2459.

MADRONICH, S.: Photodissociation in the atmosphere 1: actinic flux and the effects of ground reflections and clouds. J. Geophys. Res. **92**, (1987), 9740-9752.

WALCEK, C; TAYLOR, G.: A theoretical method for computing vertical distributions of acidity and sulfate production within cumulus clouds. J. Atmos. Sci., **43**, (1986), 339-355.

PARAMETERIZATIONS OF MICROPHYSICAL PROCESSES IN CLOUDS FOR APPLICATION IN MODELS OF REGIONAL ATMOSPHERIC DEPOSITION*

In Young Lee

Center for Environmental Research
Biological, Environmental, and Medical Research Division
Argonne National Laboratory Argonne, IL 60439

1. INTRODUCTION

The performance and predictive skill of models of atmospheric transport and deposition depend strongly on how adequately they represent cloud physics. The microphysics of clouds and precipitation in conjunction with macroscale storm dynamics are of fundamental importance in determining changes in the distributions of temperature, moisture, aerosols, and chemical species. The evolution of water substances plays a basic role in determining how trace substances are taken up by cloud water, chemically transformed, and accumulated by precipitation.

Our objectives here were to comprehensively review cloud physics parameterizations in order to examine their theoretical basis and evaluate their applicability to regional models, and to obtain more efficient, improved parameterizations by optimization upon results of a detailed cloud model that incorporates treatments of microphysical processes and cloud dynamics too detailed for routine use in a regional model.

2. TECHNICAL APPROACH

Our scientific approach consisted of three steps: [1] evaluating initial phase interaction schemes based on formulas currently available, [2] deriving optimized formulas from data generated by numerical simulations of clouds in a variety of atmospheric conditions, and [3] performing comparison studies and sensitivity analyses.

We evaluated the cloud microphysics parameterizations currently available (Asai, 1965; Berry and Reinhardt, 1974; Kessler, 1967; Lin et al., 1983; Scott, 1982) for their conformation to the theoretical basis of cloud and precipitation physics and their applicability to regional models.

We obtained parameterized formulas for cloud microphysics from optimization methods. Developing parameterizations by optimization requires many data, either from observations or from numerical calculations. The data sets were produced by numerical calculations from a detailed cloud model that simulates cloud dynamics and the sophisticated microphysics associated with vapor-liquid interactions. The microphysical processes associated with development of cloud and rain are mainly condensation, evaporation, autoconversion, and accretion (Fig. 1). (The ice phase was neglected in this stage of the study.) Cloud droplet and raindrop distributions were described, the former in nine size categories ranging from 1.0 to 40.3 μm in radius and the latter in nine larger sizes up to 2.6 mm in radius.

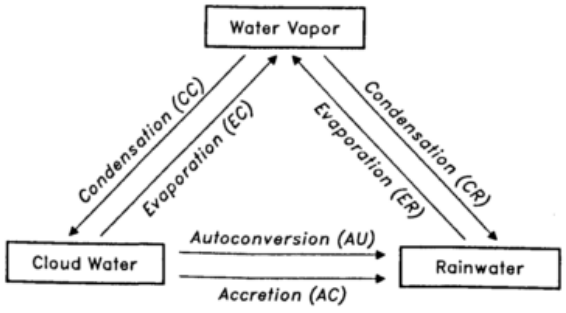


Fig. 1: Schematic diagram of microphysical interactions among hydrometeors.

*Work supported by the U.S. Department of Energy, Office of Health and Environmental Research, under contract W-31-109-ENG-38.

Our cloud model consists of an inner cylindrical cloud column and an outer concentric annular clear region. Interactions between cloudy and clear regions take place through the net buoyancy force, which depends on the difference in virtual temperature, the amount of liquid water produced during cloud development, dynamic entrainment, and lateral eddy mixing at the cloud boundary.

The mixing ratios for water vapor (Q_v), cloud water (Q_c), and rainwater (Q_r); saturation water vapor mixing ratio (Q_s); and air density (ρ_a) were calculated after adiabatic processes only. The macroscale rates for condensation of cloud droplets (CC), evaporation of cloud droplets (EC), condensation of raindrops (CR), evaporation of raindrops (ER), autoconversion of cloud droplets (AU), and accretion of cloud droplets (AC), and the teminal velocities for cloud droplets (V_c) and raindrops (V_r) were calculated after the microphysics computations. The latter rates are defined as:

$$CC = \frac{\rho_w}{\rho_a} \sum_{i=1}^{I} v_i \frac{\partial}{\partial r_i}\left(n_i \frac{\partial r_i}{\partial t}\right), \; s > 0 \; , \qquad (1)$$

$$EC = -\frac{\rho_w}{\rho_a} \sum_{i=1}^{I} v_i \frac{\partial}{\partial r_i}\left(n_i \frac{\partial r_i}{\partial t}\right), \; s < 0 \; , \qquad (2)$$

$$CR = \frac{\rho_w}{\rho_a} \sum_{i=I+1}^{J} v_i \frac{\partial}{\partial r_i}\left(n_i \frac{\partial r_i}{\partial t}\right), \; s > 0 \; , \qquad (3)$$

$$ER = -\frac{\rho_w}{\rho_a} \sum_{i=I+1}^{J} v_i \frac{\partial}{\partial r_i}\left(n_i \frac{\partial r_i}{\partial t}\right), \; s < 0 \; , \qquad (4)$$

$$AU = \frac{\rho_w}{\rho_a} v_i \left[-n_i \sum_{j=1}^{I} K_{Ij} n_j - K_{II} n_I^2 + \sum_{j=1}^{I} K_{Ij} n_I n_j (v_I + v_j)\left(\frac{v_{I+1} - v_I - v_j}{v_{I+1} - v_I}\right) \frac{1}{v_I}\right] - \frac{\rho_w}{\rho_a} v_I \frac{\partial}{\partial r_I}\left(n_I \frac{dr_I}{dt}\right) \; , \qquad (5)$$

$$AC = \frac{\rho_w}{\rho_a} \sum_{k=1}^{I} v_k \left[-n_k \sum_{j=I+1}^{J} K_{kj} n_j\right] \; , \qquad (6)$$

$$V_c = \sum_{i=1}^{I} n_i v_i V_i \Big/ \sum_{i=1}^{I} n_i v_i \; , \text{ and} \qquad (7)$$

$$V_r = \sum_{i=I+1}^{J} n_i v_i V_i \Big/ \sum_{i=I+1}^{J} n_i v_i \; , \qquad (8)$$

where I denotes the number of cloud droplet bins; J the number of cloud droplet and raindrop bins combined; r_i, n_i, v_i and V_i the radius, number density, volume, and terminal velocity, respectively, of a droplet in the size bin i; ρ_w and ρ_a the density of water and air, respectively; and K the collection kernel.

The data from two simulations with different initial moisture conditions were used to derive from multiple regression the first-order rates as functions of bulk variables.

3. RESULTS AND DISCUSSIONS

The cloud model computes changes in moisture content before and after spectral evolution caused by condensation, evaporation, and coagulation. It then saves those values, along with bulk dynamic parameters at each dynamic-scale time step, to produce the macroscale rates associated with the cloud microphysical processes. Our new parameterizations are summarized in Table 1. In general, the rates computed from the regression formulas compare closely with those derived from detailed treatments. The correlation coefficients range from about 0.72 for the rate of condensation of rain to almost 1.0 for the rate of accretion of cloud water. Figures 2 and 3 present the scatter diagrams for regression and detailed parameterizations of accretion of cloud water and condensation of rain. The high correlation for accretion rates was expected because these rates are determined mainly by collision and coalescence processes.

We examined the behavior of the parameterization formulas proposed by different investigators by using a simple cloud model. An air

Table 1. Summary of the new parameterizations.

Rate	Data Source: Detailed Treatment	Regression Parameterization	Correlation Coefficient
Condensation of cloud droplets	Eq. 1	$e^{-4.926}\, Q_c^{0.417}\, (Q_v - Q_s)^{0.537}$	0.90
Evaporation of cloud droplets	Eq. 2	$-e^{-6.153}\, Q_c^{0.743}\, (Q_s - Q_v)^{0.323}$	0.82
Condensation of raindrops	Eq. 3	$e^{-2.167}\, Q_r^{0.490}\, (Q_v - Q_s)^{1.129}$	0.72
Evaporation of raindrops	Eq. 4	$-e^{-6.601}\, Q_r^{0.420}\, (Q_s - Q_v)^{0.746}$	0.80
Autoconversion of cloud droplets	Eq. 5	$e^{0.363}\, Q_c^{2.184}\, (Q_v - Q_s)^{0.173}$, $s>0$	0.87
		$e^{-2.824}\, Q_c^{1.878}\, (Q_s - Q_v)^{0.076}$, $s<0$	0.97
Accretion of cloud droplets	Eq. 6	$e^{2.025}\, Q_c^{1.029}\, Q_r^{1.042}$	0.997
Terminal velocity of cloud droplets	Eq. 7	$e^{2.562}\, Q_c^{0.236}\, (1000\rho_a)^{-2.175}$	0.94
Terminal velocity of raindrops	Eq. 8	$e^{10.90}\, Q_r^{0.604}\, (1000\rho_a)^{4.466}$	0.83

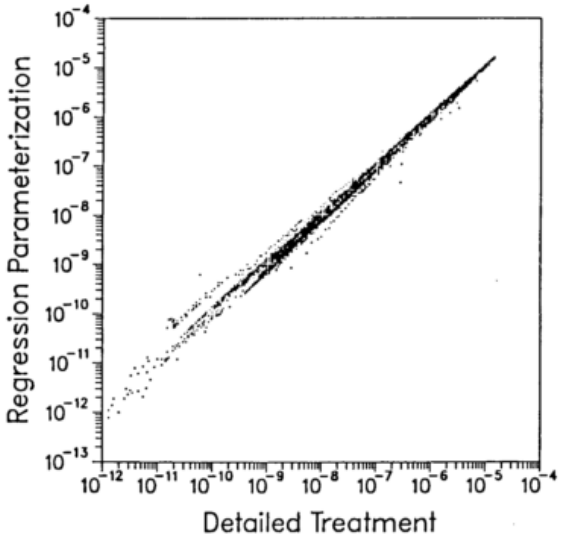


Fig. 2: Comparison of calculations of accretion rates in g g^{-1} s^{-1}.

parcel saturated at 283 K and located initially at the 1000-mb level was assumed to rise adiabatically with a vertical velocity of 1 m s^{-1}. We used the saturation adjustment scheme of Asai (1965) and our parameterized formula (Table 1) to compare evolution of the cloud water mixing ratio. The formulas give similar results; however, our formula is more efficient, since Asai's

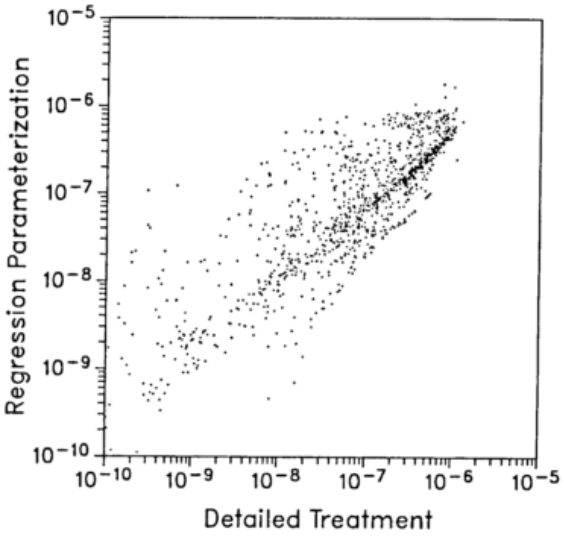


Fig. 3: Comparison of calculations of condensation rates of rainwater in g g^{-1} s^{-1}.

formula requires saturation adjustment through iteration within the macroscale time step. The condensation rate for rainwater is smaller by one to two orders of magnitude than that for cloud water under similar atmospheric conditions.

For autoconversion rates, formulas by Kessler (1967) and Berry and Reinhardt (1974) were compared with our formula (see Table 1). The Kessler formula reduces the water content by 45% in 30 min, while the formula of Berry and Reinhardt results in little change in water content. Our formula has an intermediate result, a 12% reduction after 30 min of cloud development. For accretion rates, we compared formulas by Scott (1982) and Lin et al. (1983) with our formula. Our results agree closely with those of Scott, while Lin et al. predict a more rapid depletion of cloud water. Most of the cloud water can be transformed into rainwater within 20 min in all of the cases.

Finally, we examined the combined effects of condensation, autoconversion, and accretion on cloud water and rainwater mixing ratios (Fig. 4). During the initial stages of cloud development, the cloud water mixing ratio increases rapidly from condensation, closely following the adiabatic line. Thereafter,

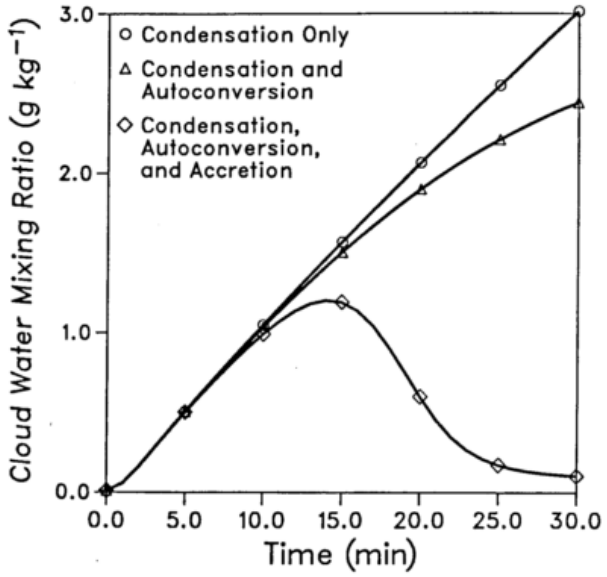


Fig. 4. Examination of the relative contributions of the parameterized formulas to the evolution of the cloud water mixing ratio.

the combined processes of autoconversion and accretion start to control the distribution of water substances. Cloud water reaches a maximum value after 14 min, decreases rapidly during the next 11 min, and decreases very slowly thereafter.

The currently available rates for cloud microphysical interactions were generally derived under assumed size distribution functions for various hydrometeors. Such parameterizations must therefore be applied with caution, because the spectral evolution of both cloud droplets and raindrops may depart significantly from the assumed spectra.

In 1989, we expect to complete an improved scheme for vapor-liquid-solid interactions that is now in the preliminary stages of development. The parameterization problem becomes more complicated with the inclusion of the ice phase, which is crucial in the life cycle of convective storms, because the growth processes for various types of ice crystals are not sufficiently well known for accurate modeling of multiphase cloud microphysics interactions.

4. CONCLUSIONS

Our new parameterizations, in general, compare favorably with those currently available; they are more efficient and are applicable to regional models. The largest discrepancies occur in the autoconversion rates, whereas the accretion rates agree closely when the assumed collection efficiencies in other formulas are smaller than unity.

REFERENCES

Asai, T., 1965: A numerical study of the air mass transformation over the Japan Sea in winter. J. Meteor. Soc. Japan, 43, 1-15.

Berry, E.X, and M. Reinhardt, 1974: An analysis of cloud drop growth by collection: Part IV. A new parameterization. J. Atmos. Sci., 31, 2127-2135.

Kessler, E., 1967: On the continuity of water substance. ESSA Technical Memorandum IERTM-NSSL 33, National Severe Storms Laboratory, Norman, Okla., 125 pp.

Lin, Y.L., R.D. Farley, and H.D. Orville, 1983: Bulk parameterization of the snow field in a cloud model. J.Climate Appl. Meteor., 22, 1065-1092.

Scott, B.C., 1982: Prediction of in-cloud conversion rates of SO_2 to SO_4 based upon a simple kinetic and kinematic storm model. J. Atmos. Environ., 16, 1735-1752.

A MODEL OF WET DEPOSITION TO COMPLEX TERRAIN BY THE SEEDER-FEEDER PROCESS

Andy Jones and Tom Choularton
Dept. Pure and Applied Physics
University of Manchester Institute of Science and Technology
PO Box 88
Manchester M60 1QD

INTRODUCTION

The seeder-feeder mechanism for the orographic enhancement of rainfall was first proposed by Bergeron (1965). This involves the accretion of cloud droplets formed in low level feeder clouds (formed by the forced ascent of moist low level air) by raindrops falling from higher level seeder clouds (typically frontal clouds). Field experiments have supported this mechanism (eg. Hill et al.1981), showing that 80% of the orographic enhancement occurred in the lowest 1.5km above the ground. This model is based on the work of Carruthers & Choularton (1982 & 1983) and Hill et al.(1987) which models orographic rainfall enhancement over a single hill incorporating the effects of a stratified atmosphere and the wind-drift of precipitation. In addition the deposition of aerosol material nucleation scavenged by the feeder cloud was included, and also parameterisations of the oxidation of sulphur dioxide by hydrogen peroxide and ozone. The predictions of this model have recently been quantatively confirmed by field measurements (eg Choularton et al.1988).

2 MODEL FORMULATION

The air in the lowest layers of the atmosphere has a specified relative humidity, and cloud base is defined when this air becomes saturated. For air initially following streamlines above the specified cloud base, condensation occurs as soon as this air suffers a vertical displacement. It is assumed that the aerosol particles form the cloud condensation nuclei and so become incorporated into the feeder cloud by nucleation scavenging. For the cloud base updraughts present in this model (typically 1 ms-1) it is reasonable to assume that all the aerosol size categories will be activated and so all the aerosol material will become incorporated in the cloud water. The model does not include explicit microphysics, as this has been shown not to affect the modelling of this process (Storebø 1976).

A streamline following grid is used, with the top of the feeder cloud being the top edge of the grid, and the terrain surface the lower edge. Beginning with the most upstream element of the top row of the grid, the liquid water content of the element is increased by condensation as the air parcel travels adiabatically across the grid. It is simultaneously depleted by the scavenging of the cloud droplets (and the aerosol they contain) by raindrops falling through the element. The liquid water content of the element is budgeted between these two competing effects. This process is repeated along all the elements of the top row of the grid. The distance drifted by the rain drops is calculated (from a knowledge of their terminal velocity and the windspeed) and the drops re-allocated to the appropriate element on the next row of the grid, and so on down to the surface. There the rainfall rate and the rate of deposition of aerosol material is calculated by integrating across all the raindrop size categories. Two main factors can be seen to govern the rainfall and deposition patterns. Firstly there is the path length of the raindrops through the cloud, which is dependent on the hill length and the wind speed; and secondly there is the rate at which the cloud water scavenged can be replenished by condensation, dependent on the updraught. Consequently short steep hills, having high updraughts near the summit, will

have cap clouds not so seriously depleted of water as longer less steep hills of the same height. The temperature, pressure and relative humidity of the approach flow are the input parameters in the current model, as opposed to specifying the cloud base itself. The model can subsequently determine the extent of cloud depending on the terrain under consideration. Another important effect included in this model is the evaporation of raindrops falling through under-saturated air, which often occurs in the lee of hills where the water content of the air has been depleted by scavenging. This reduction in rainfall rate is often referred to as a rain-shadow. Any changes occurring in the concentration of sulphate in the cloud water due to the oxidation of sulphur dioxide by hydrogen peroxide and ozone were parameterised in line with the detailed cloud chemistry model of Hill et al. (1986).

3 RESULTS

The terrain modelled in this study consisted of two parallel hill ridges separated by a valley of comparable size. To investigate the effects on the rainfall and deposition patterns of differnt hill sizes, these parameters were modelled for hills of characteristic lengths 2km and 20km. The distributions were also modelled for conditions of potential and supercritical flow. The supercritical case is denoted in all cases by the solid line, and the potential flow case by the broken line. Airflow is from left to right in all cases.

3.1 2km Hills

The rainfall distribution over the two ridges is shown in figure 1. Over both hills the effect of wind drift is dominant and the regions of maximum rainfall rate are downstream of the summits. The rainfall rates under the two flow regimes are similar over the first hill, however the strong downdraughts present on the lee side under supercritical flow strongly curtails the extent of the cap cloud on the second hill and so reduces the rainfall enhancement observed. The distribution of the aerosol deposition (and rainfall concentration) is shown in figure 2. As there is no serious depletion of the cloud water by scavenging over short hills the rainfall concentration stays fairly constant and the deposition pattern essentially follows the rainfall distribution.

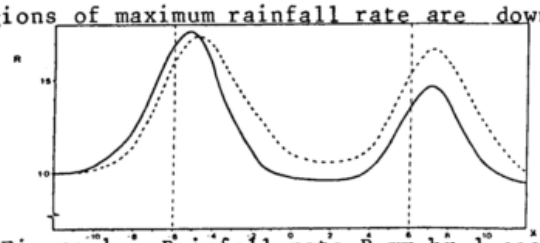


Figure 1. Rainfall rate R mm hr-1 against distance X km for two 2km ridges; summits are at ± 6km.

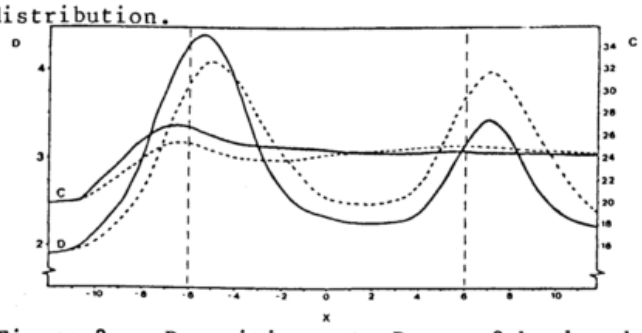


Figure 2. Deposition rate D mg m-2 hr-1 and rainwater concentration CμM against distance X km for two 2km ridges.

3.2 20km Hills

The rainfall distribution is shown in figure 3. Over both ridges the maximum rainfall enhancement occurs upwind of the summit, as expected for the scale lengths under consideration. Under such conditions the rain is scavenging the orographic cloud faster than it can be replenished by condensation because of the relatively low updraughts. Supercritical flow causes enhancements which are both lower and further upstream than under potential flow due to the strong lee-side downdraughts present under supercritical flow, which tend to begin somewhat upstream of the ridge summits. A large rain-shadow is evident in the lee of both hills, with the rainfall rate being reduced by about 15% to 20% of its upstream value. The effect is much more noticeable for hills of this size due to the substantial depletion of atmospheric water in the feeder cloud. The aerosol deposition distribution and variation in rainwater concentration are shown

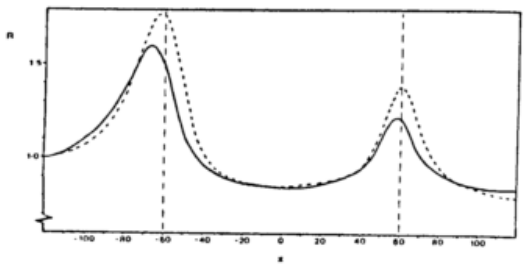


Figure 3. Rainfall rate R mm hr-1 against distance X km for two 20km ridges; summits are at ± 60km.

in figure 4. The differences in the distributions under the two airflow regimes are fairly small, except near the hill summits, and once more there is a close link between the rainfall and the deposition distributions. The

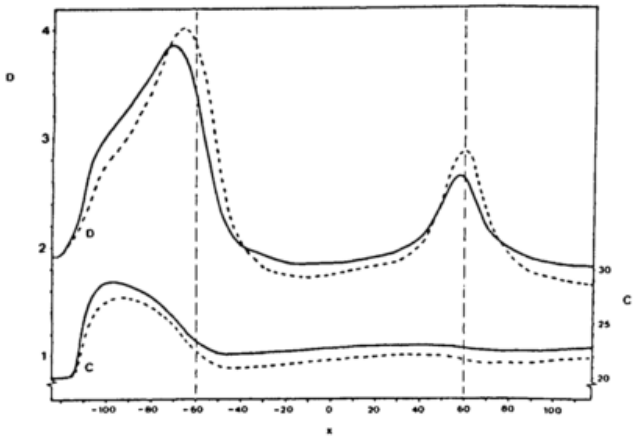


Figure 4. Deposition rate D mg m-2 hr-1 and rainwater concentration CμM against distance X km for two 20km ridges.

exception to this is on the upwind slope of the first hill, where there is a sharp increase in rainfall concentration as the rain scavenges the highly concentrated cloud droplets at the edge of the cloud. As the cloud droplets grow during ascent they become diluted and so the rainwater concentration falls off. This effect produces a large increase in the deposition rate on the upwind face of the first hill which is much faster than the increase in rainfall rate in this region. Due to the large depletion of aerosol material during passage over the first ridge there is no corresponding large increase in deposition on the upwind side of the second ridge, and the rainwater concentration stays fairly constant.

REFERENCES

Bergeron, T.: On the low-level redistribution of atmospheric water caused by orography. Suppl.Proc.Int.Conf.Cloud Physics, Tokyo, 1965 96-100.

Carruthers, D.J.; Choularton, T.W.: Airflow over hills of moderate slope. Q J Roy Met Soc, 108 (1982) 603-624.

Carruthers, D.J.; Choularton, T.W.: A model of the seeder-feeder mechanism of orographic rain including stratification and wind drift effects. Q J Roy Met Soc, 109 (1983) 575-588.

Choularton, T.W.; Gay, M.J.; Jones, A.; Fowler, D.; Cape, J.N.; Leith, I.D.: The influence of altitude on wet deposition: Comparison between field measurements at Great Dun Fell and the predictions of a seeder-feeder model. Atmos. Environment (in press).

Hill, F.F.; Browning, K.A.; Bader, M.J.: Radar and raingauge observations of orographic rain over South Wales. Q J Roy Met Soc, 107 (1981) 643-671.

Hill, T.A.; Choularton, T.W.; Penkett, S.A.: A model of sulphate production in a hill cap cloud and subsequent turbulent deposition onto the hill surface. Atmos.Environment, 20 (1986) 1763-1771.

Hill, T.A.; Jones, A.; Choularton, T.W.: Modelling sulphate deposition onto hills by washout and turbulence. Q J Roy Met Soc, 113 (1987) 1217-1236.

Storebø, P.B.: Small scale topographical influences on precipitation. Tellus, 28 (1976) 45-59.

METEOROLOGICAL AND CHEMICAL INFLUENCING FACTORS ON ACIDITY PRODUCTION IN A MESOSCALE MODEL WITH QUASI-SPECTRAL MICROPHYSICS

Nadine Chaumerliac and Robert Rosset

LAMP/OPGC, Clermont-Ferrand

1. INTRODUCTION

To study gas and aerosol wet removal,we have used an extended version of the mesoscale numerical model of CHAUMERLIAC and al (1987). In particular, concentrations of aqueous phase oxidants are now explicitely predicted, neutralizing agents (NH_3) are considered and an ionic balance equation has been added to predict cloud and rain acidity. Figure 1 displays the processes involved in the gas removal by clouds and rain.

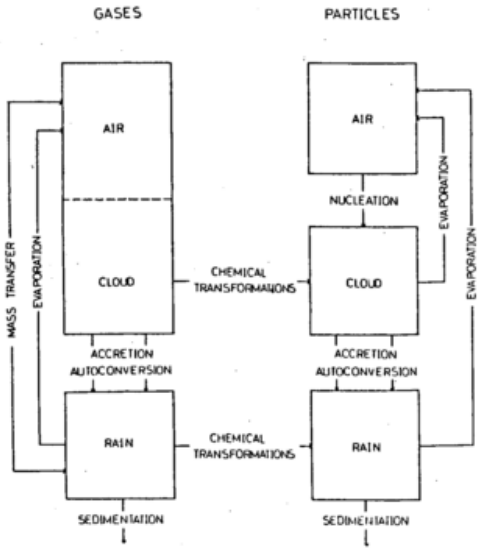


Fig. 1 : Synopsis of the microphysical and chemical processes.

2. CONDITIONS FOR MODEL RUNS

The meteorological scenario defined to test the chemical parameterizations of the model consists in a two-layer atmosphere with an initial horizontal wind speed of 20 m/s and 80 % relative humidity below 3 km.

Gas and particle variables are initialized with exponential profiles (RUTLEDGE et al., 1986).

All the gases are initially set to 1 ppb at the ground-level with the same vertical profiles except for ozone (O_3 = 30 ppb uniformly).

Figure 2 shows vertical cross-sections of cloud water and rainwater mixing ratios, typical of maritime conditions after a 6 h model run. The maritime cloud precipitates with a maximum of precipitation located at the mountain summit.

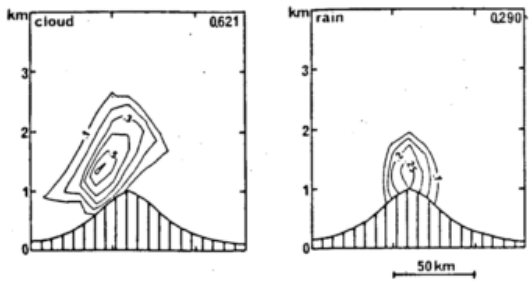


Fig. 2 : Vertical cross sections of cloud water and rainwater mixing ratios (in g/kg) after 6 h.

Figure 3 provides the corresponding vertical cross-sections for pHs associated respectively to cloud water and rainwater. Acidities are not well correlated with the microphysical fields. Stronger gradients in cloud water pH appear at the top of the upwind edge of the cloud. Rain is found to be less acidic than the cloud and rainwater pH is not distributed symmetrically apart from the mountain top.

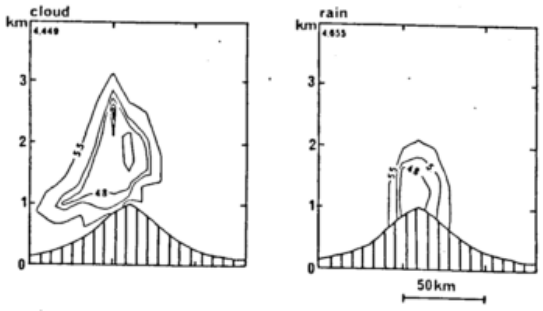


Fig. 3 : Vertical cross sections of cloud water and rainwater pHs.

3. CLOUD ACIDITY

Strong sensitivity of cloud pH to sulfate aerosol loading has been discussed in detail by WALCEK and TAYLOR (1986) for the case of cumulus clouds.

In Figure 4, the lower sulfate load value (curve 1) produced a higher pH in the upwind region, and as the parcel rises along the mountain slope, in-cloud production of sulfate acidifies the cloud water. In the two other cases, pH is found to be much more acidic than without sulfate load while increasing with height due to dilution by increasing liquid water content across the mountain.

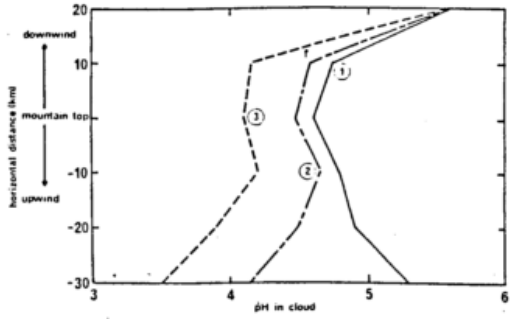


Fig. 4 : Cloud water pH as a function of horizontal distance after 1h model time
Curve 1 : sulfate load excluded
Curves 2 and 3 : sulfate load of 10 µg/m³ and 25 µg/m³

Nucleation mechanism is competing with chemical oxidation effects to produce cloud acidity and its vertical distribution. An evidence is given in Figure 5, where cloud acidity is plotted at two levels as a function of initial SO_2 gas concentration, in the presence of NH_3 and oxidants. Without any SO_2, acidity is greater at higher levels (K = 12) because of aerosol loading through nucleation while increasing SO_2 implies more oxidation and as a consequence more acidity production at lower levels (K = 14) due to advective replenishment at the cloud base.

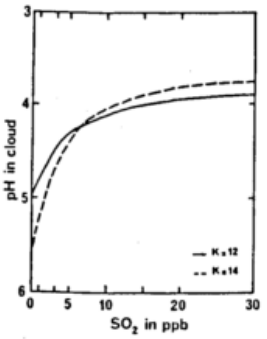


Fig. 5 : Cloud water pH as a function of initial SO_2 gas concentrations for two vertical levels (K = 14 near the ground and K = 12 at 2 km).

4. RAIN ACIDITY

Some ot the rain acidity comes from cloud acidity through autoconversion and accretion. Then, intrinsic processes will act as sinks for species in rainwater (chemical oxidation by O_3 and H_2O_2) and as either source or sink (direct scavenging of gaseous species through mass transfer). At last, loss of species in rainwater arises from sedimentation and total evaporation of the raindrops. Calculated values of these terms as a function of height are illustrated in Figure 6 successively for SO_2, H_2O_2 and NH_3 and after six hour model time. Profiles in Figure 6b for H_2O_2, which has an effective solubility around 10^5 M/atm are quite comparable to the results early obtained by YU QIN and CHAMEIDES (1986).

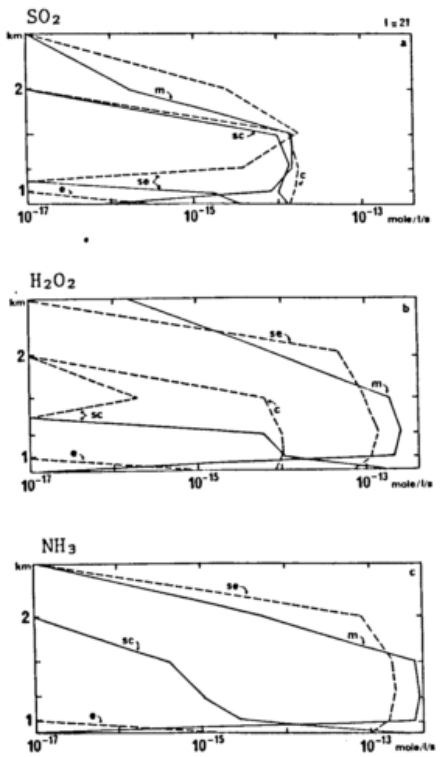


Fig. 6 : Calculated rates of change in concentrations in rainwater (in mole/l_{water}/s) as a function of height.
"m" stands for microphysical coalescence "se" for sedimentation, "e" for evaporation "sc" for mass transfer and "c" for chemical sink. Dashed lines refer to sink terms while solid lines correspond to source terms.

5. CONCLUSION

Very tight and complex interactions have been found between microphysical, dynamical and chemical processes leading to acidity production in cloud and rain. Both acidity load from nucleating particles and acidity production through SO_2 oxidation are competing to determine spatial cloud water pH distribution. Part of this cloud acidity is transferred to the rain through coalescence processes in the case of soluble species. This transfer is limited by the chemical reactivity of the species. The fate of insoluble species is less dependent on coalescence processes and depends on chemical and direct scavenging mechanisms.

6. REFERENCES

CHAUMERLIAC, N.; RICHARD, E.; PINTY, J.P.; NICKERSON E.C. : Sulfur scavenging in a mesoscale model with quasi-spectral microphysics : two dimensional results for continental and maritime clouds. J. Geophys. Res., Nr 92 (1987), P. 3114-3126

RUTLEDGE, S.A.; HEGG, D.A.; HOBBS, P.V. : A numerical model for sulfur and nitrogen scavenging in narrow cold-frontal rainbands. 2-Discussion of chemical fields. J. Geophys. Res., Nr 91 (1986), P. 14,403-14,416.

WALCEK, C.J.; TAYLOR G.R. : A theoretical method for computing vertical distributions of acidity and sulfate production within cumulus clouds. J. Atmos. Sci., Nr 43 (1986), P. 339-355

YU QIN; CHAMEIDES, W.L.: The removal of soluble species by warm stratiform clouds. Tellus, Nr 38B (1986), P 285-299

A COMPARISON OF RADIOMETRIC AND IMMERSION TEMPERATURE MEASUREMENTS IN WATER CLOUDS

S Nicholls, E L Simmons, N C Atkinson and S D Rudman

Meteorological Office, Bracknell

1 INTRODUCTION

The accurate measurement of temperature in clouds has long been a problem for observational cloud physics. Latent heat exchange accompanying water phase changes can significantly alter the heat balance of many designs of thermometer, rendering the measurements at best uncertain, at worst, misleading. Commonly used immersion type thermometers, which assume a certain heat balance between a sensing element and the fluid in which it is immersed are particularly at risk. This is especially true for airborne devices where compression heats free stream air by several degrees. The temperature sensed will then depend on the generally unknown partial evaporation during compression and the equally undetermined effectiveness of the inertial shielding provided by the element housing which protects the sensor from direct drop impacts.

An alternative, fast response method for measuring temperature in clouds (the In-Cloud Temperature Probe, ICTP, described in Ref 1) has recently been installed on the MRF C130 aircraft. This measures temperature radiometrically and avoids the problems associated with ill-defined heat balances entirely. This paper describes some initial comparisons between the ICTP and a standard platinum resistance, cold wire thermometer, widely used in meteorological research.

2 THE INSTRUMENTS

The ICTP employs a Peltier-cooled cadmium mercury telluride detector to measure radiance in a narrow, 0.1μm wide interval centred near 4.3μm. This lies within a strong CO_2 absorption band which ensures that the weighting function peaks close to the aircraft and is spatially compact (Fig 1).

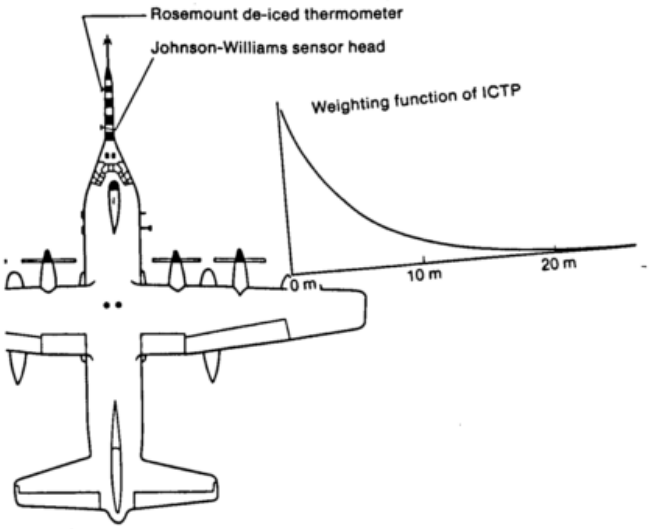


Fig 1. ICTP installation and clear air weighting function

The ICTP is mounted in an underwing pod and has a beamwidth of ±3°, looking slightly forward and downwards (7.5° below horizontal) This ensures the sensing volume is shielded from viewing the hot engines and exhaust plumes. Contamination due to back-scatter from these sources is thereby minimized. The separation between the sensing volume and the *in-situ* sensors located at the noseboom tip is calculated to be ~20m. The lateral separation from the aircraft roll axis induces a significant roll sensitivity, especially in cloud-free air. For the intercomparison purposes, all data with roll angles exceeding 5° were excluded.

The immersion thermometer, constructed by Rosemount Engineering, consists of a shielded open-wire type 102BL platinum resistance element in a de-iced housing (type 102BX).

3 CALIBRATION AND DATA REDUCTION

The incoming ICTP signal is chopped at 24kHz and compared with a reference black body at a known temperature. The resistance-temperature calibration of the Rosemount element is carried out periodically by the supplier. Corrections for compressive heating are carried out during data reduction using the known recovery factor (0.985) and the true airspeed, but no account is taken of cloud conditions. The housing is regularly cleaned, especially after low level flight. The inaccessible element is only cleaned during recalibration.

4 FLIGHT RESULTS AND DISCUSSION

There is typically a strong correlation between liquid water content and the immersion-radiation temperature difference (Fig 2. These data are unfiltered and sampled at 32Hz).

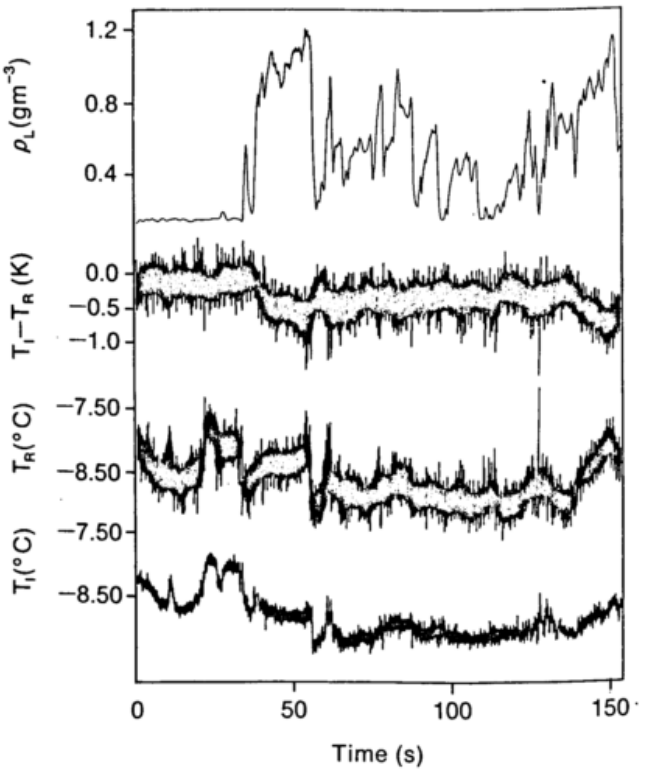


Fig 2. Immersion (T_I), ICTP (T_R) & J-W liquid water data from a flight thro' marine Cu

The correlation is clearer in Fig 3, which indicates a sensitivity of ~0.4°C per g/m³. Horizontally averaged data from ~50km long

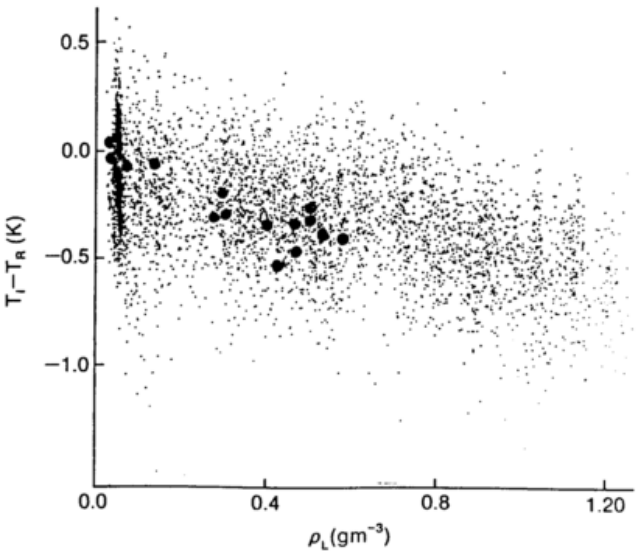


Fig 3. Same data as in Fig 2 plus run average data from FIRE (●).

runs on flights in very uniform marine stratocumulus during the recent FIRE experiment (Ref 2) show a similar sensitivity. The sign is consistent with evaporative cooling depressing the Rosemount temperature. Under certain conditions, simple parcel thermodynamics may also be used to show that these temperatures are lower than expected by a similar amount.

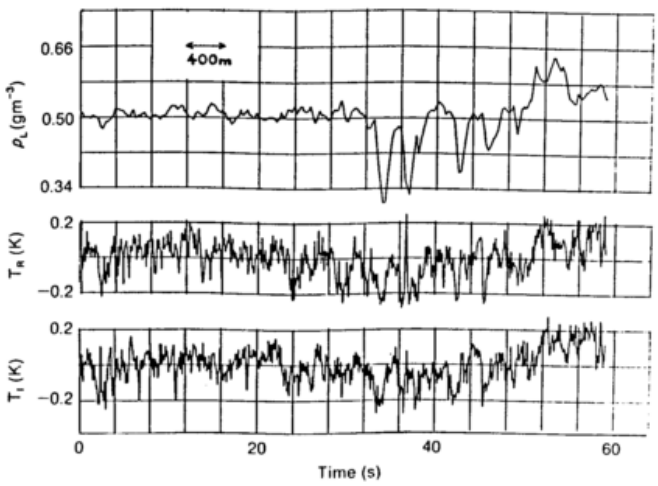


Fig 4. Part of a run just below cloud top in marine SCu during FIRE.

However, when liquid water fluctuations are relatively small, eg within stratiform cloud, the temperature fluctuations measured by both instruments are very similar (Fig 4. Here, noise has been reduced by low-pass filtering). Larger features in these time series are clearly well correlated, smaller scales less well so. This reflects the spatial separation of the samples, as shown by the coherence (Fig 5). At high frequencies instrumental noise dominates and the coherence falls to zero.

This agreement suggests that heat fluxes within cloud may be measured by eddy correlation using either thermometer, provided liquid water fluctuations are not too large. In general, heat fluxes in stratocumulus are found to be slightly larger using the Rosemount data. This apparently reflects the separation between the velocity sensors and the ICTP sampling volume. Near cloud top, a significant amount of the flux is carried on scales of the same order as the separation distance (Fig 5) which is not captured using the ICTP data.

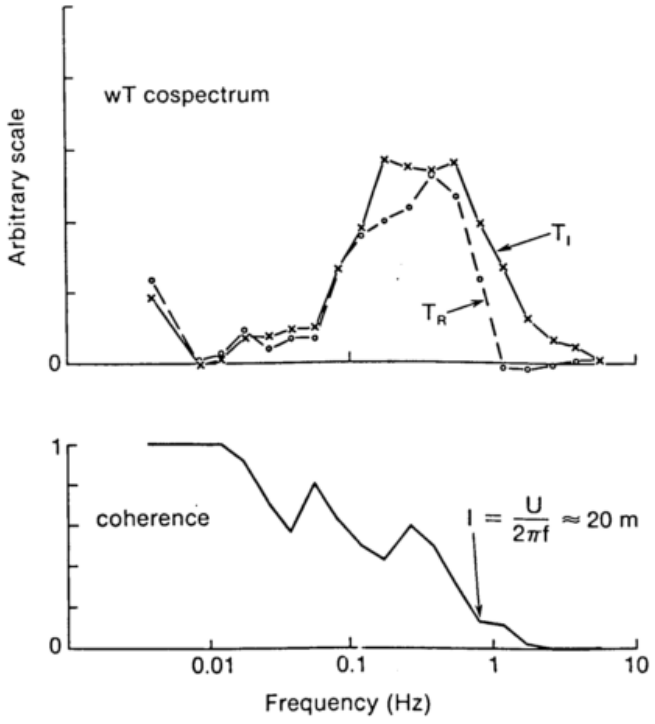


Fig 5. wT cospectra and $T_I T_R$ coherence from the same run as Fig 4.

Currently, it is not known whether the cool immersion temperatures reflect incorrect compressive heating corrections, wetting of the sensing element or a combination of both. However, the smooth time variation of the error which closely follows the mean liquid water content (eg Fig 2) and the lack of high frequency spikes which might be expected to accompany the direct impact of drops onto the element, favour the former. If all the liquid water were to be evaporated on compression, the correction could be reduced by up to 3°C per g/kg *ie* partial evaporation could easily explain the observed sensitivity.

4 CONCLUSIONS

1. Commonly used airborne immersion thermometers may be significantly in error in water clouds because of undetermined partial evaporation. One fitted to the MRF C130 shows errors of about 0.5°C per g/kg of liquid water. The precise cause is still unknown, but the compressive heating correction is a prime suspect. Data from these instruments should be used with extreme care in studies of cloud thermodynamics.

2. No large short period spikes or other disagreements are apparent in high resolution fluctuation data, even in fairly high liquid water clouds provided liquid water fluctuations remain fairly small. Heat flux measurements can probably be made with confidence in these conditions, although the spatial separation of the ICTP sampling volume from the other sensors should be remembered.

5 REFERENCES

1. *Atkinson N C et al, 1984, Proc. Ninth Int. Cloud Physics Conf., Tallinn, USSR, 3, 811-813*
2. *Randall D A et al, 1984, Bull Amer Met Soc, 65, 1290-1301*

CALIBRATION OF PMS FSSP AND 1D-C PROBES FOR CLOUD DROPLET MEASUREMENTS

Jean-François Gayet

LAMP, University of Clermont II, B.P. 45, 63170 Aubière (France)

1. INTRODUCTION

The measurements provided by the FSSP and 1D-C probes are often subject to discussion due to a large source of uncertainties inherent to the working characteristics. Despite different experimental and theoretical methods of correction mostly devoted to the FSSP undercounting (BAUMGARDNER et al., 1985) and diameter calibration (PINNICK et al., 1981 ; CERNI, 1983), the results generally suffer from a lack of absolute comparisons for a wide range of conditions of use (airspeed, liquid water content ...). The purpose of the paper is to propose a method of absolute FSSP diameter calibration, then to confirm the results with simultaneous holographic measurements carried out in a wet wind tunnel for various airspeeds ranged from 25 to 130 m s^{-1}. These comparisons also show the airspeed dependence of the undercounting of the 1D-C first five channels.

2. DIAMETER RESPONSE OF THE FSSP PROBE

2.1 DESCRIPTION OF THE METHOD

PINNICK et al. (1981) proposed a diameter calibration method based on the Mie calculations. In order to link the theoretical results with the probe output, they compared the theoretical and experimental latex particle responses from which they deduced a normalized constant C = 2.8 x 10^6 V m^{-2}. This constant, which is a proper characteristic of each probe, may be subject to caution due to the uncertainties on the latex particle characteristics. We propose an absolute diameter calibration so as to reduce these uncertainties. The probe output voltage V(D) is related to the diameter D of a droplet passing through the laser beam with the following expression :

$$V(D) = G \times T_p \times T_o \times (I_o/S) \times Se(D) \quad (1)$$

with G the total gain of the signal amplifier ; T_p the photodiode conductance (in V/mW) ; T_o the transmission of the optical system ; I_o the laser beam energy (in mW) ; S the cross-section of the laser beam (in μm^2) and Se(D) the diffusion cross-section of a droplet (D diameter) (μm^2). A series of optical/electronical measurements has been carried out in laboratory for the determination of the constant terms of eq. (1) : G, T_p, T_o, I_o and S. According to the experimental results and for the range # 0 and a mean laser beam diameter of 180 µm, eq. (1) becomes :

$$V(D) = 5.0 \times 44.22 \times 0.25 \times 7.25/(\pi \times 90^2) Se(D) \quad (2)$$

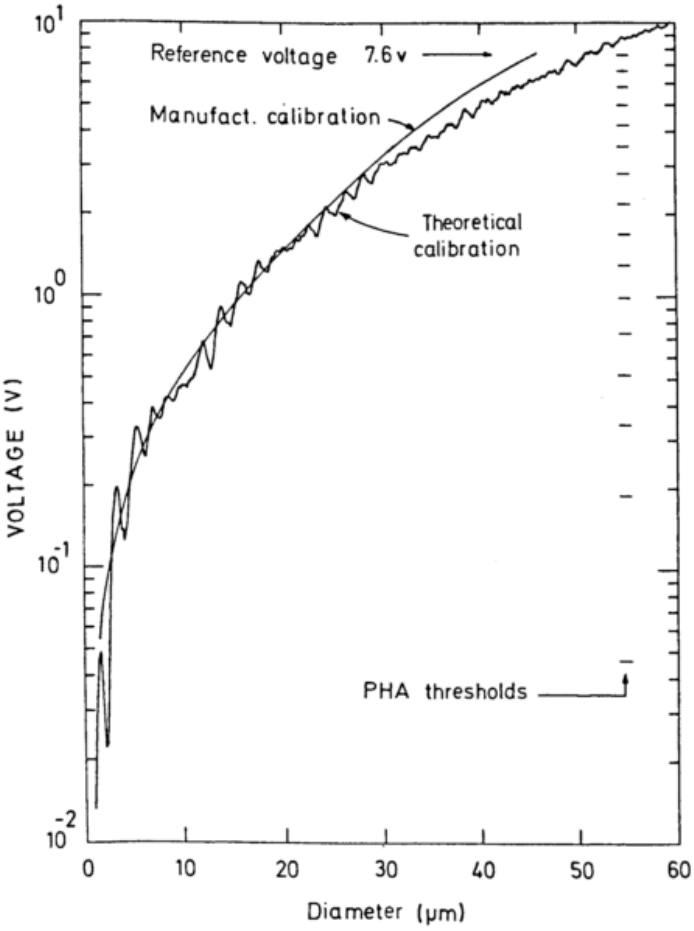


Fig. 1 : Theoretical and manufacturer diameter calibrations (range ≠ 0)

As for the theoretical diffusion response Se(D), it has been obtained from the Mie calculation by using collecting solid angles of 3° and 14°, a water refractive index (m = 1.33) and a laser wavelength of 0.6328 µm. Figure 1 displays our results (output voltage V(D) as a function of D), the manufacturer calibration and the PHA thresholds by taking into account a reference voltage of 7.6 V. This figure shows that for a droplet diameter greater than 20 µm, the theoretical curve progressively deviates from the manufacturer calibration as the diameter increases. This conducts to a maximum measuring diameter much larger than the proposed one (about 52 µm against 47 µm). The curve presented on Figure 1 corresponds to droplets which intercept the laser beam at the depth of field center. When the droplets intercept the beam on both sides of the focusing point, the collecting solid angles and the laser beam diameter take different values. In order to take into account these two combined effects, the diameter variations which correspond to the output voltage variations V(D,x) along the beam axis (x) (in the depth of field limits) has been calculated.

Channel number	Manufacturer calibration (µm)	Proposed calibration (µm)	Channel width (µm)
1	3	3,00	3,00
2	6	6,00	3,00
3	9	9,00	3,00
4	12	12,00	3,00
5	15	15,00	3,00
6	18	18,00	3,00
7	21	21,125	3,25
8	24	24,575	3,65
9	27	28,30	3,80
10	30	32,15	3,90
11	33	36,05	4,00
12	36	40,00	4,00
13	39	44,00	4,00
14	42	48,00	4,00
15	45	52,00	4,00

Table I : FSSP diameter calibration (range O)

For example, the diameter response relative to the upper limit of channel 15 varies from 53.0 to 52.0 then 55.5 µm, when x changes from -1.3 to 0 then +1.3 mm (current depth of field limits). From these results, we have deduced the mean values of the diameter for each channel and we propose the calibration diameter (of our FSSP) in Table I together with the channel width and the manufacturer calibration for comparison. For the other FSSP size ranges, the diameter calibration does not need any correction, the theoretical and manufacturer calibrations being very similar.

2.2 CONFIRMATION OF THE RESULTS OF THE METHOD

During a series of tests carried out in a wet wind tunnel, the FSSP (and 1D-C) probes were simultaneously used with an holographic technique. The main advantage of this technique (ROYER, 1986) is to give very accurate measurements of the droplet diameter (larger than 20 µm) whatever the airspeed. Figure 2 displays typical comparisons of normalized droplet spectra issued from the holography and the FSSP (corrected) for two airspeeds (40 m s^{-1} (a) and 100 m s^{-1} (b)).

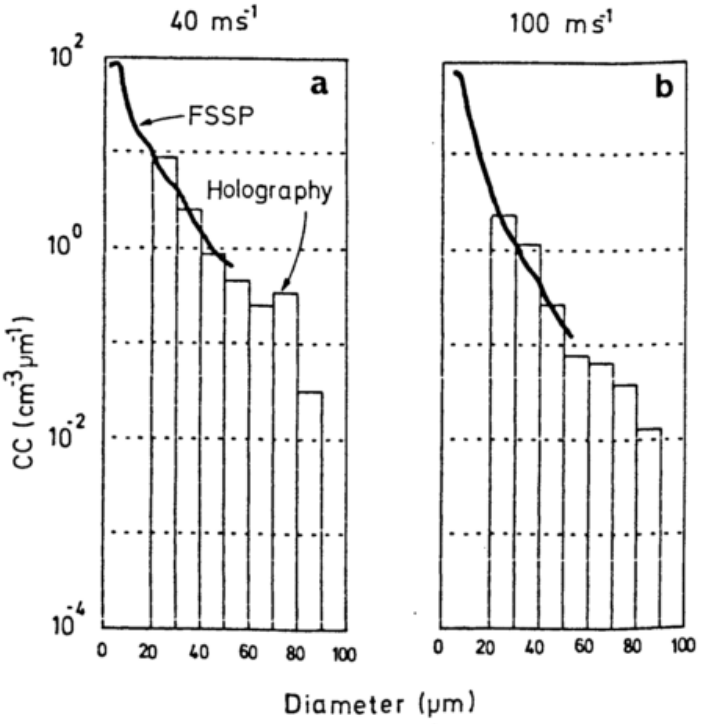


Fig.2 : Comparison of normalized droplet spectra obtained from the holographic technique and the FSSP (corrected) during wet wind tunnel tests for two airspeeds : 40 m s^{-1} (a) and 100 m s^{-1} (b).

The results on Figure 2 show a good agreement between the two independent spectra measurements wathever the airspeed. This result confirms our absolute method of diameter calibration and that the airspeed does not induce a noticeable effect on sizing as shown from electronical measurements (FOURNOL, 1986).

3. THE UNDERCOUNTING OF THE FIRST CHANNELS OF THE 1D-C PROBE

During the wind tunnel experiment, the water cloud characteristics were set in order to cover a wide range of median volume diameter (MVD) (from 10 to 100 µm). For MVD values larger than about 30 µm, the complete description of the droplet spectra needed the use of the 1D-C probe (20-300 µm diameter range). The comparisons of 1D-C and holographic measurements have shown a systematic undercounting of the first five channels of the 1D-C, which increases with the airspeed. We have determined from about seventy tests performed with different airspeeds (from 25 to 130 m s^{-1}), the airspeed dependent correction factors of channels 3 (60 µm), 4 (80 µm) and 5 (100 µm) (labelled F3, F4 and F5 on Fig. 3).

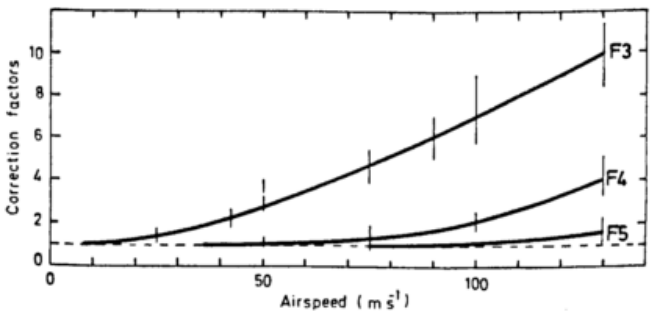


Fig.3 : Correction factors of channels 3 (F3), 4 (F4) and 5 (F5) of the 1D-C probe as a function of the airspeed.

The coefficient factors of channels 1 and 2 are not proposed due to unreliable responses. The vertical bars on Fig.3 represent the measurements dispersion. The correction factors for channels 3, 4 and 5 are respectively 7.0, 2.0 and 1.1 for an airspeed of 100 m s^{-1}. When applying these results, the droplet spectra comparisons show a very good reliability between the three independent probe measurements (FSSP, 1D-C and holography) as shown on Fig. 4 whatever the airspeed.

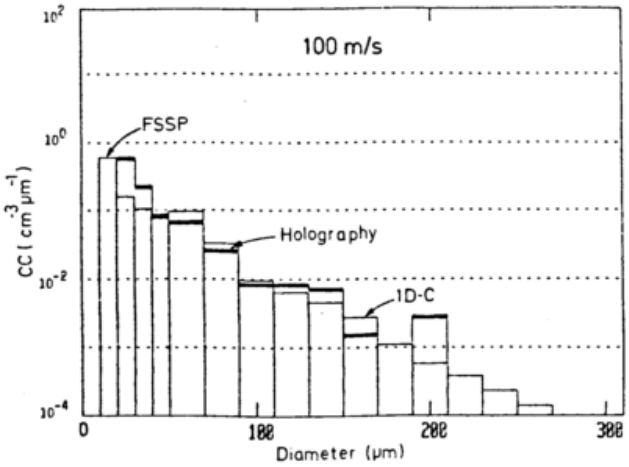


Fig.4 : Comparison of the droplet spectra obtained from the holography, FSSP and 1D-C probes for an airspeed of 100 m s^{-1}. The FSSP and 1D-C measurements are corrected.

4. ACKNOWLEDGEMENTS

This research was supported by the grant CEPr/ADER n° 86/00020. I hereby express my gratitude to Pr. R.G. Soulage for the confidence and support he provided. I would like to thank H. Royer for his help in the holographic data interpretation and C. Duroure, J-F Fournol and M. Soulage for their assistance during the tests.

5. REFERENCES

BAUMGARDNER, D., W. STRAPP and J.E. DYE, 1985 : Evaluation of the forward scattering spectrometer probe. Part II : corrections for coincidence and dead-time losses. J. Atmos. Ocean. Tech., 2, 626-632.

CERNI, T.A., 1983 : Determination of the size and concentration of cloud drops with a FSSP. J. Climate Appl. Meteor., 22, 1346-1355.

DYE, J.E. and D. BAUMGARDNER, 1984 : Evaluation of the forward scattering spectrometer probe. Part I : Electronical and optical studies. J. Atmos. Ocean. Tech., 1, 329-344.

FOURNOL, J-F, 1986 : Etude de la bande passante électronique des sondes PMS. Rapport technique n° 47 du LAMP.

PINNICK, R.G., D.M. GARVEY and L.D. DUCAN, 1981 : Calibration of Knollenberg FSSP light-scattering counters for measurement of cloud droplets. J. Appl. Meteor., 20, 1049-1057.

ROYER, H., 1986 : Microholographie. Une méthode de référence pour l'étude des petites particules. 4ème Symp. Inter. sur les visualisations d'écoulement. Paris, 26-29 août.

Radar Observations of Precipitation Microstructure: The Morphology of Linear Depolarization Measurements in Cloud

Paul H. Herzegh
National Center for Atmospheric Research
P. O. Box 3000, Boulder CO 80307

Arthur R. Jameson
Applied Research Corporation
8201 Corporate Drive, Landover, MD 20785

1. Introduction

Dual-polarization radar measurements are primarily influenced by the size, shape, orientation and phase of scattering hydrometeors. As a result, these data can serve as a tool for remote identification of hydrometeor characteristics. Differential reflectivity (Z_{DR}) measurements in highly-oriented media such as rain yield a measure of the reflectivity-weighted mean axis ratio of hydrometeors in the radar sample volume (Jameson, 1983). Measurements of this type now form the basis for a reliable discriminator between rain and solid precipitation. However, in media which are less highly-oriented or lower in dielectric constant, such as solid precipitation, Z_{DR} measurements may yield little information. In these situations, radar depolarization measurements, which are sensitive to the degree of hydrometeor alignment and the occurrence of mixed-phase regions in cloud, can provide useful information to aid interpretation of hydrometeor characteristics.

2. Radar-Measured Parameters

The data discussed were obtained using the National Center for Atmospheric Research CP-2 radar. Z_{DR} measurements were obtained at S-band (10 cm wavelength), while LDR measurements were obtained at X-band (3.2 cm wavelength). Z_{DR} is given by the relation

$$Z_{DR} = 10\ log\left(\frac{Z_{hh}}{Z_{vv}}\right) \qquad (1)$$

where Z is radar reflectivity, and the first and second subscripts refer to the linear polarization state (horizontal or vertical) for transmission and reception, respectively. Both Z_{DR} and Z are functions of range. For transmitted waves of horizontal linear polarization, LDR at range R can be defined as

$$LDR = 10\ log\left(\frac{Z_{hv}}{Z_{hh}}\right). \qquad (2)$$

3. LDR Propagation Corrections

In heavy precipitation, LDR measurements at wavelengths shorter than 10 cm can be significantly affected by differential attenuation. At X-band (used in this study), differential attenuation must be taken into account in moderate to heavy rain and in solid precipitation containing hail. In these situations, direct radar observations of Z_{hh} and Z_{hv} will yield measured values of LDR which are positively biased. The magnitude of this bias is shown in Eq. (3), which relates LDR_m (*measured* LDR) to differential attenuation as

$$LDR_m = 10\ Log\left(\frac{Z_{hv}}{Z_{hh}}\right) + \int_0^R (A_h - A_v)\,dr \qquad (3)$$

where A_h and A_v are the one-way X-band attenuation rates at horizontal and vertical polarizations, respectively.

Since its effects accumulate with range, strong differential attenuation in a convective core, for example, will likely become evident through monotonic increasing values of LDR_m within the core. The elevated values of LDR_m will persist in measurements obtained behind the core as well.

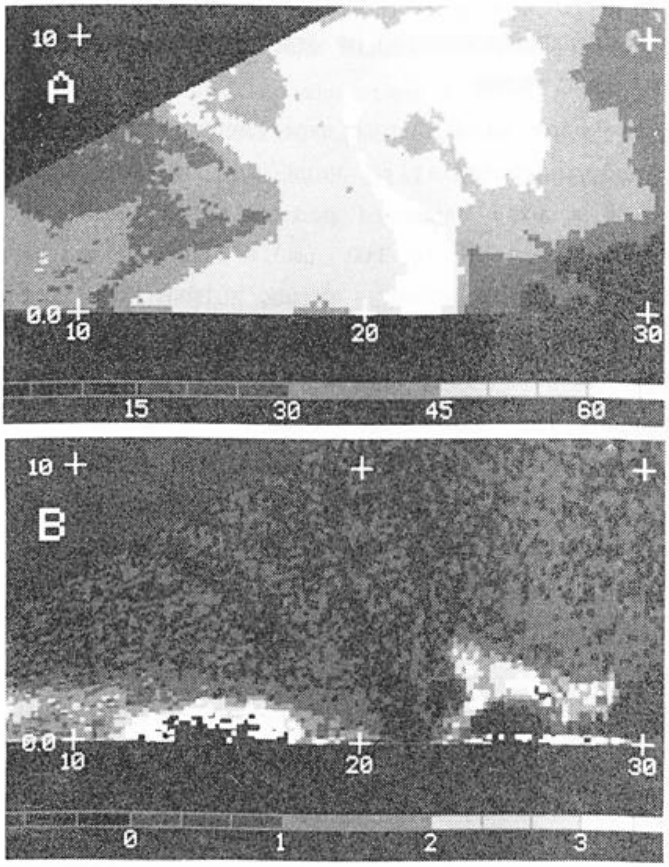


Fig. 1 Radar measurements for a vertical section through the 13 June 1984 convective storm. (a) Reflectivity in dBZ. (b) Z_{DR} in dB.

LDR_m can be corrected for the effects of differential attenuation in a manner similar to that used by Jameson and Heymsfield (1980) to correct for X-band attenuation encountered in dual-wavelength hail studies. The correction technique (for either parameter) relies upon the monotonic increase with range of the attenuation-related measurement error. Through piecewise least-squares linear curve-fitting, the monotonic increasing component of LDR_m (obtained as a function of range) can be determined and subtracted from the measurements. The resulting (corrected) data are then representative of true LDR, and can be interpreted as an indicator of particle characteristics related to depolarization.

4. Observations and Discussion

Radar measurements obtained in a severe convective storm over Denver, Colorado, on 13 June 1984 are shown in Figs. 1-3. The vertical section of S-band radar reflectivity Z_h in Fig. 1a indicates the presence of a 60 to 65 dBZ_e precipitation core at a range of about 23 km from the CP-2 radar. As is typical of con-

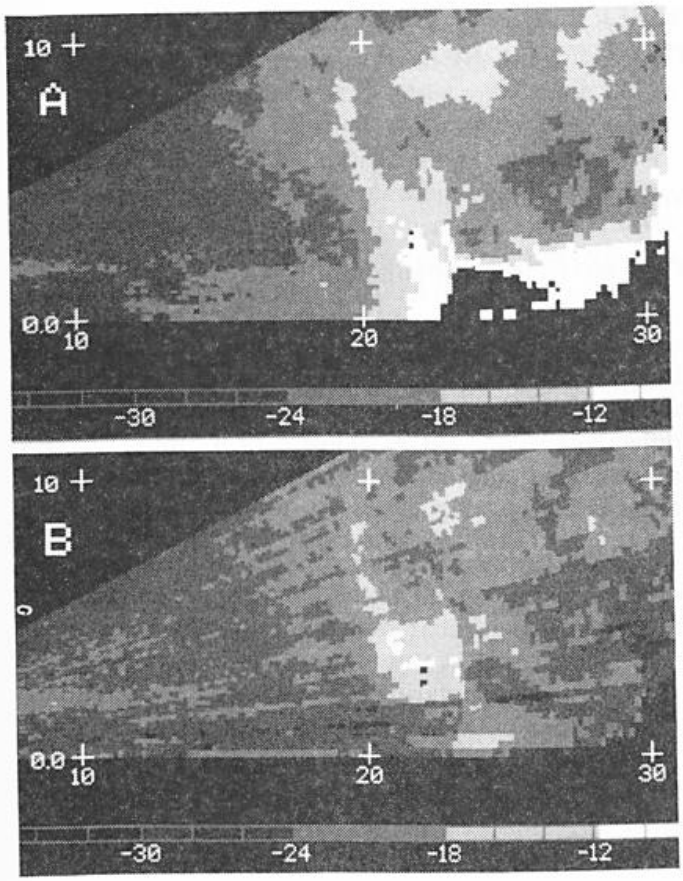


Fig. 2 LDR measurements (in dB) for the vertical section shown in Fig. 1. (a) Raw measurements. (b) Corrected for propagation effects.

vective situations, Z_{DR} (Fig. 1b) varies between about 0 to 0.5 dB above the freezing level (2 km agl). The transition from solid precipitation to rain is evident, however, in the higher values of Z_{DR} observed below 2 km height. A well-defined hail signature marked by low Z_{DR} and high Z_h values is associated with the convective core at the surface (23 km range).

Observations of LDR_m for the same vertical section reveal interesting sub-structure in the precipitation and clear evidence of strong propagation effects (Fig. 2). The high values of LDR_m shown behind the main precipitation shaft at the surface and aloft result from differential attenuation of the X-band signal. As expected, the strongest differential attenuation effects result from propagation through rain and are most visible near the surface. Propagation effects are largely removed in the data shown in Fig. 2b, which were processed using the correction technique discussed in §3. Correction of the extreme attenuation effects shown within and behind the main shaft at the surface improperly suppressed LDR in the surface hailshaft. Improvements to the scheme are in development.

Regions of light precipitation within 15-18 km range in Fig. 2b show low depolarization values of -25 to -27 dB in the solid precipitation above the freezing level and in the rain below. High values of LDR_m are present in the high-reflectivity precipitation core at 20-23 km range, indicating a significant change in hydrometeor characteristics. The strong depolarization observed suggests that particles in the precipitation shaft are less-uniformly aligned in orientation and/or higher in dielectric constant than the lighter precipitation outside the shaft. This interpretation suggests

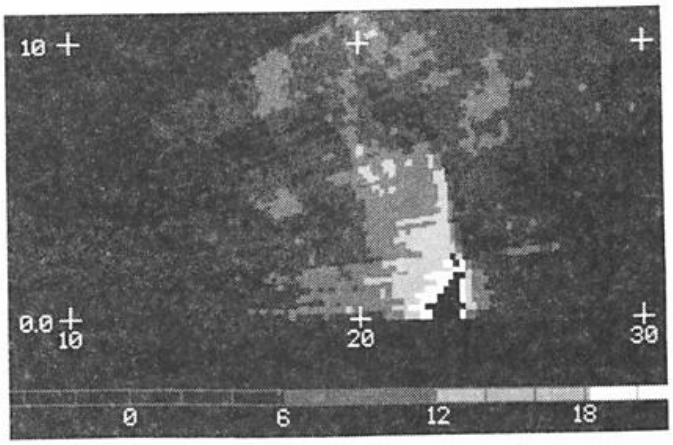


Fig. 3 Dual-wavelength hail signal (in dB) calculated for the vertical section shown in Fig. 1.

that the shaft contains large, tumbling hail, possible water-coated. The effect of water coating would be to increase the effective dielectric constant of the scattering particles, resulting in greater depolarization by asymmetric hail particles.

For comparison, the structure of the precipitation in this case was also examined using dual-wavelength techniques for hail detection (Jameson and Heymsfield, 1983; Bringi *et al.*, 1986). These techniques are based upon the concept that hail can behave like a Rayleigh-Gans scatterer with strong size dependence at long radar wavelengths (such as S-band) and like a Mie scatterer with weaker size dependence at shorter wavelengths (such as X-band). The dual-wavelength hail signal shown in Fig. 3 supports the interpretation of LDR_m posed above by showing good correspondence between maxima in LDR_m and hail signal in the precipitation shaft aloft.

Acknowledgements

Support for ARJ was provided by the National Science Foundation through grant ATM-86-01257. Partial support for data collection and analysis by PHH was provided by the U.S. Army Research Office.

References

Bringi, V.N., J. Vivekanandan and J.D. Tuttle, 1986: Multi-parameter radar measurements in Colorado convective storms. Part II: Hail detection., *J. Atmos. Sci.*, **43**, 2564-2577.

Jameson A. R., and A. J. Heymsfield, 1980: Hail growth mechanisms in a Colorado storm. Part I: Dual-wavelength radar observations. *J. Atmos. Sci.*, **37**, 1763-1778.

Jameson, A.R., 1983: Microphysical interpretation of multi-parameter radar measurements in rain. Part II: Estimation of raindrop distribution parameters by combined dual-wavelength and polarization meaurements. *J. Atmos. Sci.*, **40**, 1803-1818.

MULTIPARAMETER DOPPLER RADAR OBSERVATIONS OF A SQUALL LINE WITH THE POLARIMETRIC DFVLR RADAR

P. Meischner, V.N. Bringi and T. Jank

Institut für Physik der Atmosphäre, DFVLR, 8031 Oberpfaffenhofen, F.R.G.

1 Introduction

Deep convection, its initiation and forcing, the dynamical structure and the precipitation formation process has been a main topic of research by the Institute for Atmospheric Physics of DFVLR, the German Aerospace Research Establishment during summer 1987. This was the first year of operation of the newly installed polarimetric Doppler C-band radar in the Oberpfaffenhofen area some 80 km north of the Alps (SCHROTH, CHANDRA and MEISCHNER, 1988). This system combines sophisticated processing and display techniques of Doppler measurements and polarimetric measurements as well.

The polarimetric versatility includes the transmitting of arbitrary elliptical polarizations -for meteorological applications circular or linear polarizations are most common- and the dual channel receiving of the backscattered co- and cross-signals. Further, the transmitting polarization may be switched between orthogonal states from pulse to pulse. This way, depolarization ratios due to radar scattering at hydrometeors can be estimated for any transmitting radiation as well as the well established differential reflectivity $Z_{DR}(dB) = 10\log(Z_H/Z_V)$ and Z_H, Z_V representing the horizontal and vertical reflectivities respectively.

The three Doppler moments reflectivity, velocity and spectral width as well as the polarimetric parameters are computed in near real time and displayed on a color screen. It is this unique combination of the most advanced polarimetric measurement capabilities together with the Doppler moments estimation which give us new insights into the precipitation formation process within deep convective cloud systems.

2 Measurements

Some dynamical and microphysical structures of a squall line, observed on July 1, 1987 and measured with the new radar are going to be discussed.

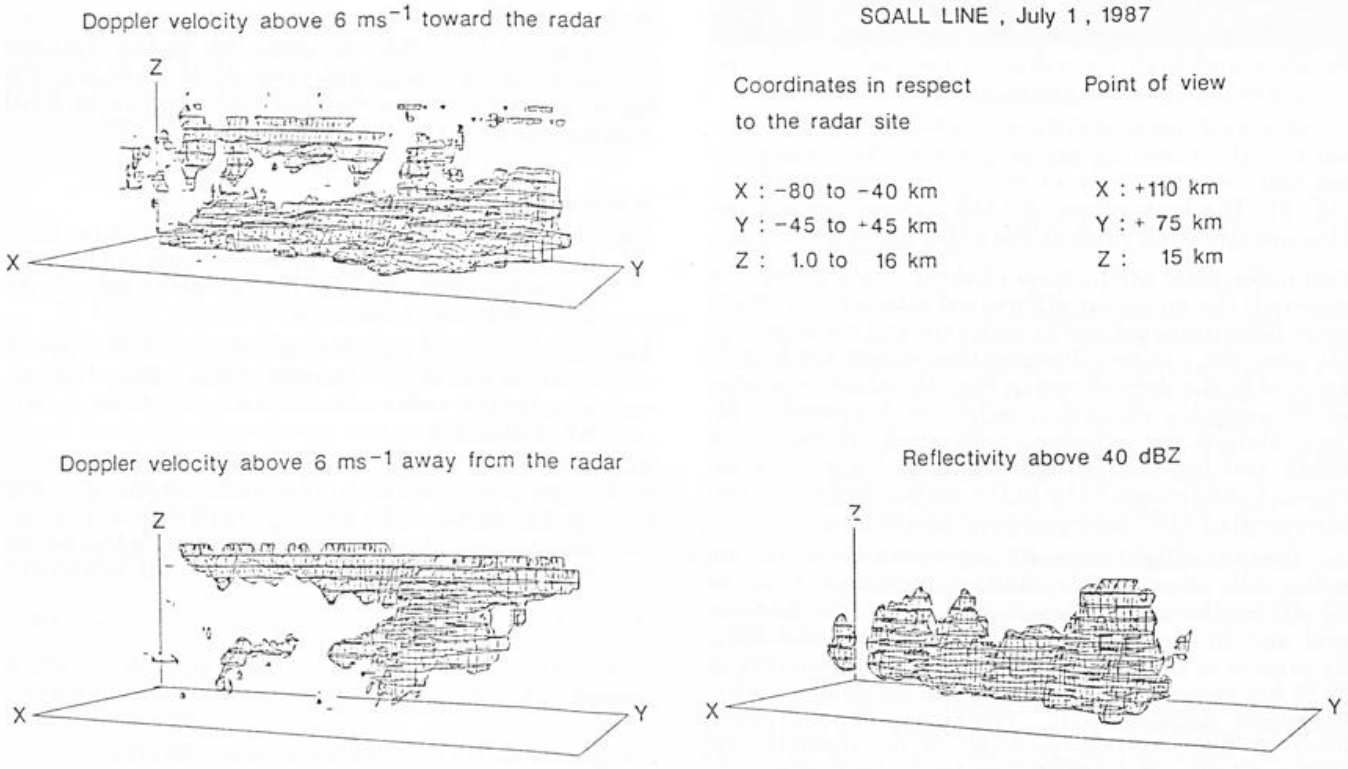


Figure 1. Structure of the squall line advancing from the west towards the radar.

The squall line developed at a line of convergence advancing a cold front approaching the site of observation from the west with a velocity of 30 km/h. The air in front of the system was rather warm and humid. The approaching cooler and more stable air flowing eastward caused lifting and destabilisation, which initiated deep convection to form the squall line. This squall line, oriented SW-NE had a length of approximately 200 km. It was observed for about 5 hrs and it reached its maximum activity 2 hrs after the first recognition. At that time hail was reported on the ground connected with strong local downdrafts.

The main flow structure across the squall line system is given in Fig. 1 for a selected area typical for the system during the whole observation time. Displayed are those volumes which have either a Doppler velocity of more than $6ms^{-1}$ towards the radar, or Doppler velocities more than $6ms^{-1}$ away from the radar. Areas of reflectivity values above 40 dBZ are also depicted. This presentation in a Cartesian frame was carried out with a NCAR radar software package (MOHR et al., 1986). The figure clearly shows the eastward moving surface air of a wedge-shaped volume increasing in depth towards the west, the upgliding westerly inflow at mid-level, as well as the high level outflows towards the east at the top of the deep convection. This cirrus shield preceeds the leading edge of the squall line by about 10 km at least from those areas that tower highest up to 14 km AGL.

Two microphysically interesting observations have been made with the polarimetric measurements.

1. In front of the leading edge, at mid-level within the westerly inflow, isolated small cumulus clouds developed beneath the advancing cirrus shield. They continually merged with the main system during their individual growth. Fig. 2 shows a RHI depicting such a typical situation. Displayed are the reflectivity Z and Z_{DR}. The extreme high Z_{DR} values are beyond the values known for big raindrops of a Marschall-Palmer distribution (see Fig. 4 of BRINGI and MEISCHNER , 1988). One possible explanation is, that in fact extremely large raindrops are produced during the rigorous growth of these cumulus clouds. ILLINGWORTH (1987) has discussed it similarly, although no such high Z_{DR} values were observed with the Chilbolton radar used, arguing that giant nuclei may have caused such big drops. See also JOHNSON (1982), discussing giant and ultragiant nuclei causing big drops. We may speculate that the release and recirculation of ice particles from the cirrus shield may have played a similar role. Another explanation is the existence of uncommon drop size distributions. We have performed electromagnetic scattering calculations for single drops and the radar wavelength of $\lambda = 5.5cm$.

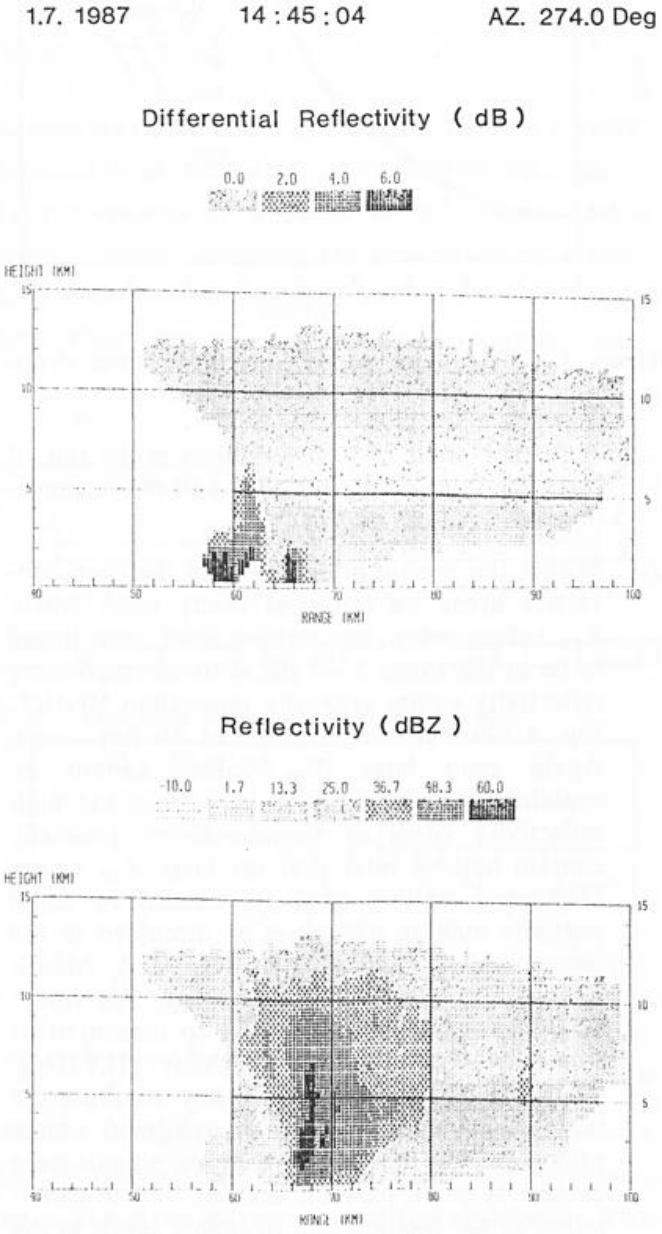


Figure 2. **Cross Section of the squall line.** Very high Z_{DR} values appear within merging cell in front and within the main precipitation shaft.

These calculations show some resonances for equivalent diameters around 6 mm. The Z_{DR} values increase up to nearly 8 dB in dependance of temperature, see Fig 3.

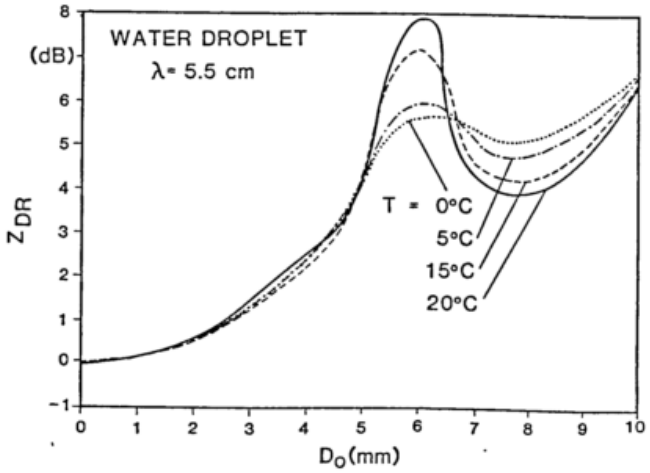


Figure 3. Z_{DR} calculations for simple water droplets and different temperatures.

A further point of future interest is the role of these merging 'feeder cells' as hail embryo producers.

2. Within the precipitation shafts of the deep convective areas we observed many cases where Z_{DR} values below the melting level were found to be in the range 5 - 7 dB with corresponding reflectivity values generally more than 50 dBZ. Fig. 2 illustrates such areas at 66 km range. Again such large Z_{DR} values cannot be explained with common rain. Since the high reflectivity cores of thunderstorms generally contain hail we infer that the large Z_{DR} values below the melting level are caused by small partially melting hailstones as discussed in the corresponding paper (BRINGI and MEISCHNER, 1988). We note that large Z_{DR} values in the range 5 - 8 dB were also measured at S-band by the Chilbolton radar (ILLINGWORTH at al., 1987) while they attribute the large Z_{DR} values to "super" deformed oblate raindrops it is more likely that the signals were caused by small partially melting hail. Recirculation of the melting hail to higher levels in the storm by beeing caught in the updraft can also cause the high Z_{DR} values to occur at higher levels in a storm, in some cases even above the $0°C$ level.

3 Conclusion

Polarimetric and corresponding Doppler measurements performed simultaneously will permit more insight into the precipitation formation process of deep convection, coupled to the dynamics on all scales. During summer 1987, the first year of operation of the advanced DFVLR radar, a number of case studies showed that squall line systems of different scales were frequent during the period of observation. High Z_{DR} signatures like those presented, were observed rather frequently for different deep convective systems. Radar observations well coordinated with aircraft measurements as well as cloud modelling and electromagnetic scattering modelling work will be continued.

4 Acknowledgements

The authers are greatly indebted to J. Vivekanandan for performing scattering computations as well as to F. Ritenberg who operated the radar anytime with great enthusiasm.

5 References

BRINGI, V.N.; MEISCHNER, P: Radar Remote Sensing of Melting Hail. 10th Intern. Cloud Physics Conf., Bad Homburg, FRG, 1988.

ILLINGWORTH, A.J.; GODDARD, J.W.F.; CHERRY, S.M.: Polarization Radar Studies of Precipitation Developement in Convective Storms. Q. J. R. Met. Soc. 113 (1987), p. 469 - 489.

JOHNSON, D.B.: The Role of Giant and Ultragiant Aerosol Particles in Warm Rain Initiation. J. Atmos. Sci. 39 (1982), p. 448 - 460.

MOHR, C.G.; MILLER, L.J.; VAUGHAN, R.L.; FRANK, H.W.: The Merger of Mesoscale Datasets into a Common Cartesian Format for Efficient and Systematic Analysis. J. Atm. Ocean. Techn. 3 (1986), p. 143 - 161.

SCHROTH, A.; CHANDRA, M.; MEISCHNER, P.: A C-Band Polarimetric Radar for Propagation and Cloud Physics Research. To appear in J. Atmos. Ocean. Techn.

A POOR MAN'S OPTICAL FOG DETECTOR

Ronald K.A.M. Mallant,
Netherlands Energy Research Foundation, ECN
P.O. Box 1, 1755 ZG Petten
The Netherlands.

1. INTRODUCTION

An optical device for fog detection is developed at ECN. The arrangement of optical components in this detector is not obvious, yet enables the use of low-cost components. Tests were done in a large fog-producing facility, and at two field sites.

2. INSTRUMENT DESCRIPTION

The detector responds to the light that is near-forward scattered by fog droplets. Mie theory predicts that the light confined to scattering angles smaller than approximately 5°, is by orders of magnitude more intense than the light scattered at larger angles. An unusual configuration of light source and detector was chosen to be able to detect this near-forward scattered light, without the use of highly collimated optics (Fig.1). The ECN-Optical Fog Detector (ECN-OFD) uses a low-cost commercially available source-receiver combination. A beam stopper prevents activation of the detector in the absence of fog. The sides of the stopper have slots, to prevent erroneous signals of particles deposited on the stopper. The light source uses a pulsed LED (880 nm). The receiver electronics responds to pulsed signals only, so there is no influence of stray light. It is a switching device, with adjustable threshold.

An algorithm (BOHREN 1983, p. 477) to compute the Mie scattering coefficients, and a numerical integration method to calculate the contribution of various droplet sizes to the total signal reaching the receiver, were used to compute the response of the OFD (Fig.2).

3. EXPERIMENTS

The OFD was first tested in the CHamber for Investigations with Equilibrated Fog (CHIEF) available at ECN (MALLANT 1986[a,b]). This facility consists of a large 20 m^3 vessel and a wind tunnel. Droplets are generated by spraying water in saturated air. An optical probe (PMS FSSP-100) is used to size the droplets.

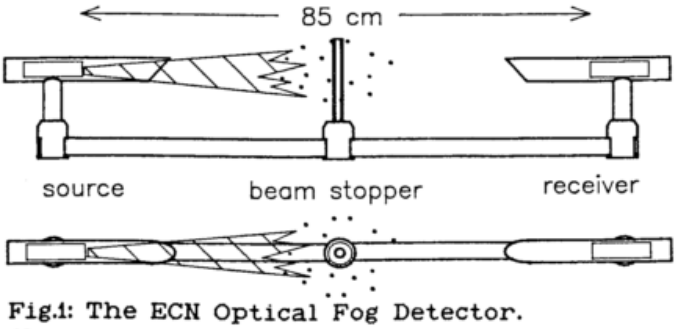


Fig.1: The ECN Optical Fog Detector.

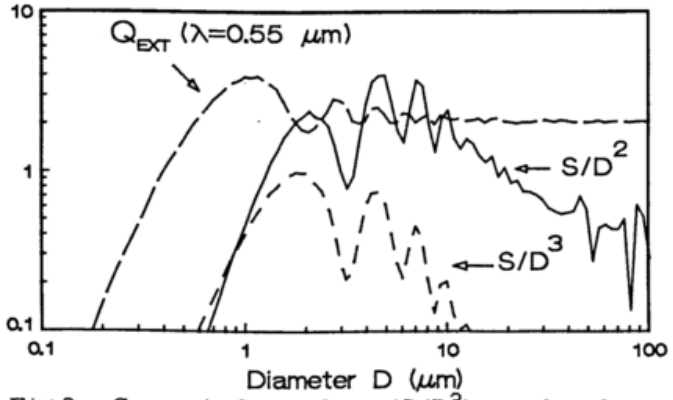


Fig.2: Computed surface (S/D^2) and volume (S/D^3) normalized signals S at the receiver, as a function of water droplet diameter. The graph of the extinction coefficient for visible light is given to enable a comparison with the effect of droplets on visibility.

During a field-test at the ECN site in Petten, many different meteorological conditions were encountered. Snow produces random spike signals that can be easily rejected by a RC-filter. In rain, fewer similar signals occur. In May 1987 the instrument was placed at Whitetop Mountain (VA, USA). There it was run in a performance test of various ground based LWC

and cloud detector instruments (VALENTE, 1988). The reference instrument for cloud occurrence was a commercially available (Qualimetrics, Inc.) reflectometer. The ECN-OFD performed well compared to the (much more expensive) reflectometer (FIG.3).

4. RESULTS

In the facility CHIEF the OFD was tested using two droplet size distributions, characterized by their Mass Median Diameter (MMD) and Geometric Standard Deviation (GSD). At maximum sensitivity setting, the threshold Liquid Water Content (LWC) was 5 mgr/m^3 (MMD=7.4 μm, GSD=1.35). The OFD was adjusted to trigger at a LWC of 15-20 mgr/m^3 for this droplet spectrum. When using larger droplets, (MMD=13 μm, GSD=1.6), the OFD triggered at 25-30 mgr/m^3.

5. DISCUSSION OF RESULTS

Meteorologists use the word fog for those atmospheric conditions in which the presence of water droplets, not being rain, reduces the visual range to less then 1 km. Hence, a fog detector should have a relation to visibility and a maximal sensitivity for droplets in the size range of about 2-20 μm. Visibility is inversely proportional to light extinction which in turn is linked to D^2 by a coefficient Q_{EXT}, being more or less constant for water droplets in the range of 2-20 μm (Fig.2). Therefore, it is desirable for the response of a fog detector to have a one-to-one relationship to D^2 in this range. The ECN-OFD meets this demand quite reasonably. Outside the fog droplet size range, the sensitivity to visibility reductions (e.g. by fine aerosol or rain) decreases rapidly. The tests in CHIEF demonstrated the effect of MMD on the LWC-level at which the OFD triggers. The calculated visual ranges associated with the above given small and large drop spectra are approximately 510 and 570 m (Atlas 1953). This once more indicates that the OFD is triggered by the visibility reduction due to the presence of fog.

The ECN-OFD however has poor qualities as a LWC-indicator as has been demonstrated by the experiments and the computations (Fig.2).

6. CONCLUSION

The ECN-OFD supplies the need that exists at ECN; to have a low-cost, fast responding device to control fog samplers. It can also be used to obtain statistics on fog occurrence or for traffic control.

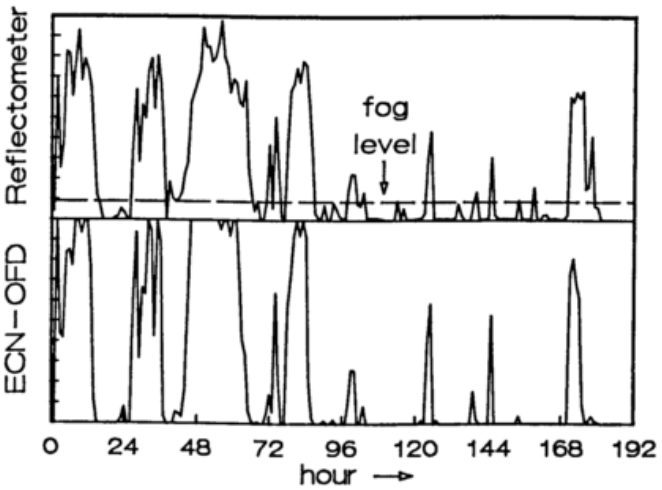


Fig.3: The ECN-OFD signal (expressed as the fraction of an hour that fog is detected), and the signal of the reflectometer. Inherent to the difference in output signal, only the temporal development must correlate.

7. REFERENCES

ATLAS, D.; BARTNOFF, S.: Cloud Visibility, Radar Reflectivity, and Drop-size Distribution. J. of Meteorol. 10 (1953) p. 143-148

BOHREN, C.F.; HUFFMAN, D.R.: Absorption and Scattering of Light by Small Particles, John Wiley & Sons (1983)

MALLANT, R.K.A.M.: A Fog Chamber and Wind Tunnel Facility for Calibration of Cloud Water Collectors. proceedings of the NATO workshop 'Acid deposition processes at high elevation sites' Edinburgh, Sept. 1986 (in press).

MALLANT, R.K.A.M.: Design and Characterization of Fog Water Collectors", proc. workshop on Fog Chemistry, Frankfurt, Dec. 1986 (in press)

VALENTE, R.J.; GERBER, H.; MALLANT, R.K.A.M.; McLAREN, S.E.; SCHEMENAUER, R.S.; STOGNER, R.E.: Field Intercomparison of Ground Based Cloud Physics Instruments at Whitetop Mountain, Virginia. Submitted to Journal of Atmospheric and Oceanic Technology (1988)

APPLICATIONS OF THE NCAR ELECTRA DOPPLER RADAR FOR THE STUDY OF PHYSICAL PARAMETERS OF CLOUDS

Craig Walther, Charles Frush, and Peter Hildebrand

National Center for Atmospheric Research
Boulder, Colorado

1. INTRODUCTION

NCAR is building an airborne Doppler radar to be mounted in the tail of a Lockheed Electra. This project has been named ELDORA for ELectra DOppler RAdar. While the radar has primarily been designed for storm scale and mesoscale meteorological observations, it will also have some interesting measurement capabilities which will be useful for cloud physics investigations. This paper will summarize the design of the ELDORA system, then will discuss the possibilities for application of ELDORA to cloud physics research.

2. ELDORA RADAR DESIGN

2.1 ELDORA SAMPLING CONSIDERATIONS

The ELDORA system will be a dual-beam X-band radar. The specifications of the radar are given in Table 1. The radar antennas will be mounted in the tail and rotated about the longitudinal axis of the aircraft (Fig 1). One antenna will point slightly in front of the aircraft, the other will point slightly to the rear. The radar beams will thus sweep out conical helixes as the aircraft flies forward. With this design, dual Doppler data can be taken from one pass along an area of interest (Fig 2).

TABLE 1
ELDORA RADAR PARAMTERS

WAVELENGTH:	3.2 cm
BANDWIDTH:	+/- 200 MHz CENTERED @ 9.5 GHz
ANTENNA BEAMWIDTH:	1.7 DEGREES FWHP
FIRST SIDE LOBE POWER:	<30 dB DOWN
PEAK RADIATED POWER:	15 Kw PER BEAM AT ANTENNA
AVERAGE RADIATED POWER:	200 w PER BEAM
PULSE WIDTH:	.1 TO 10 MICROSECONDS
PULSE REPETITION RATE:	MAXIMUM OF 5 KHz
EXPECTED SENSITIVITY:	0 dBZ AT 25 Km RANGE
MAXIMUM ROTATION RATE:	40 RPM

The radar is designed such that the radar's measurement or sampling density can be adjusted to match the scientific needs. In its normal, storm scale operating modes, the pulse length will be able to be adjusted between about 50 m and 1.5 km. The spin rate of the antenna will be able to be adjusted such that one complete revolution will occur every 180 m to 1 km. The maximum range of data collection will be adjusted in concert with other sampling parameters such that large domains will be sampled using lower resolution data collection and small domains can be sampled with moderately high resolution. The range bins, which can be as narrow as 15 meters, can be averaged to provide higher quality data having range resolution matched to the sampling in the other two dimensions.

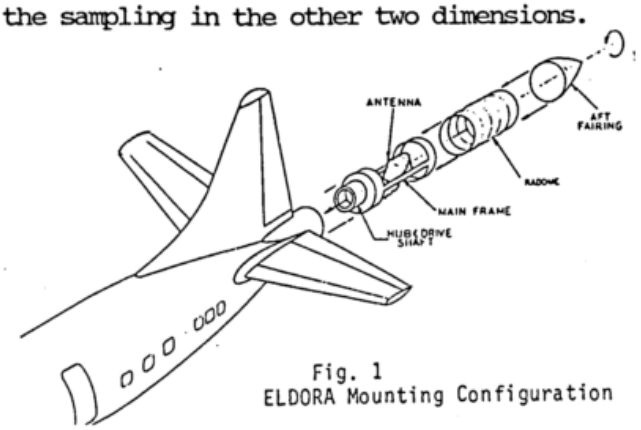


Fig. 1
ELDORA Mounting Configuration

If the antenna is rotated at the proper speed, each beam pattern can be overlapped slightly, hence the entire cylinder, with the aircraft flight track as its center, can eventually be filled with radiated energy. This illumination and sampling strategy will be especially useful for the study of wind patterns in storm and mesoscale weather structures. For instance, an entire storm front could be studied in a few hours as the aircraft flies along the front, adjusting its position as the front progresses.

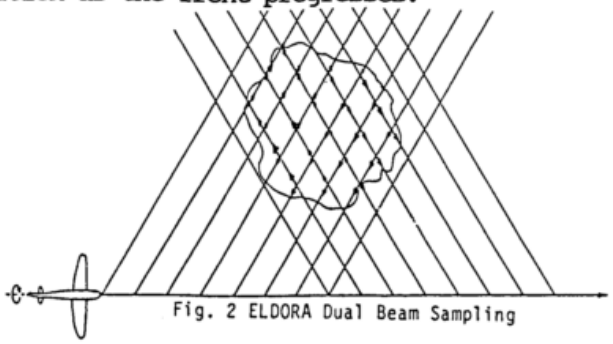


Fig. 2 ELDORA Dual Beam Sampling

2.2 ROTODOME DESIGN

The ELDORA antenna mounting structure will have the antennas rigidly attached to a rotating structure (rotodome) which also contains the radome (Fig 3). This design will allow for larger antennas and better sidelobe characteristics.

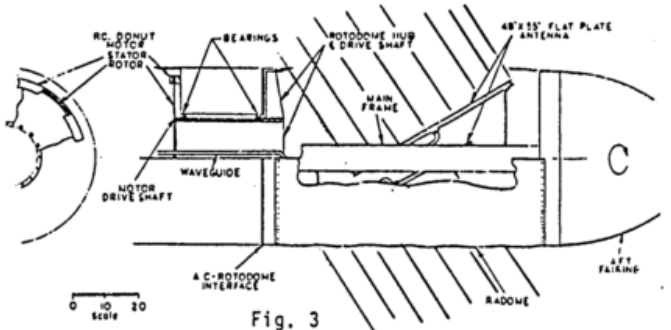


Fig. 3
ELDORA Rotodome Detail

The scanning hardware can rotate the antennas at a fixed rate or hold them in a fixed pointing position. The actual position of the antennas, hence radar beams, will be measured with inertial navigational equipment mounted in the aircraft tail section.

2.3 THE TRANSMITTER AND RECEIVER

Each antenna will be driven by a coherent X-band transmitter unit, which will transmit a complex, multiple frequency waveform. The complex waveform is needed to provide adequate signal statistics when the radar is operated for high resolution data collection. The received signals from each antenna will be processed by a receiver and passed to a channel of the data system for processing and display.

2.4 THE DATA SYSTEM

The data system will be designed to process, record and display the data from both antennas. The radar and data system are being designed to sample every 50 m. This range resolution is limited by radar sensitivity and sample statistics considerations. The standard processing algorithm used will be autocovariance pulse pair processing of quadrature signals. However, other algorithms will be available, including spectral analysis. The sampling, recording and display of the radar data will all be controlled in real time by the user on the aircraft.

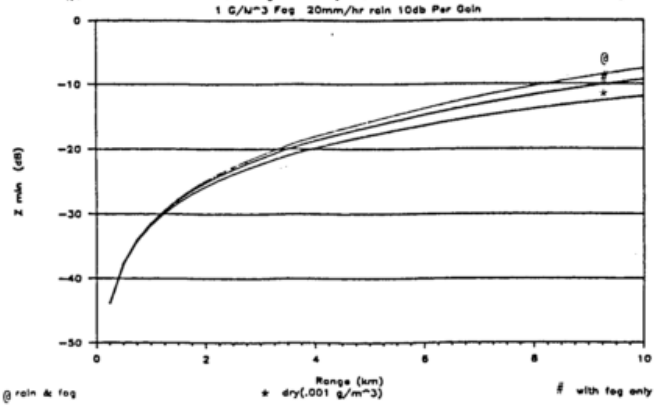
3. RADAR STUDY OF CLOUD PHYSICAL PARAMETERS

As noted above, the ELDORA system was designed with storm and mesoscale measurements in mind. However, the system has capabilities which could easily be applied to cloud physics measurements. Two modes of operation should be discussed: high resolution scanning mode operation of the radar, and use of a special vertically pointing, nonscanning antenna to gather special cloud physics information.

3.1 SCANNING MODE DATA COLLECTION

In scanning mode, ELDORA will be able to collect radar data having 50 meter range resolution. At close ranges, the radar will be very sensitive (Fig 4) and data with slightly higher spatial resolution can be collected. Since the aircraft can be positioned very precisely with respect to clouds, it should be possible to examine many aspects of three dimensional cloud structure far more completely than was previously possible. Studies which may find these capabilities valuable include: the dynamics of small cumulus, coherent downward mixing structures, turbulent mixing processes, cloud edge entrainment, hydrometer development and evolution of precipitation. The study of any of these phenomena requires high spatial and temporal resolution and excellent sensitivity.

Fig. 4 ELDORA Sensitivity: 25Kw, 1.2m Antenna, 50m Data Density



These studies could be performed with data densities around 50 meters and sensitivities near -20 dbZ. The width of the 1.8 degree ELDORA beam will be approximately 50 meters across at 1600 meters from the aircraft. This means that the user could select range gate spacings of 50 meters, ranging from 0.5 km to 2.5 km from the

aircraft. The maximum rotodome rotation rate limits the along track resolution to 180 m. This combination of narrow beam width and infrequent sampling will produce "picket fence" sampling (Fig 5), which will complicate data analysis, particularly at close ranges.

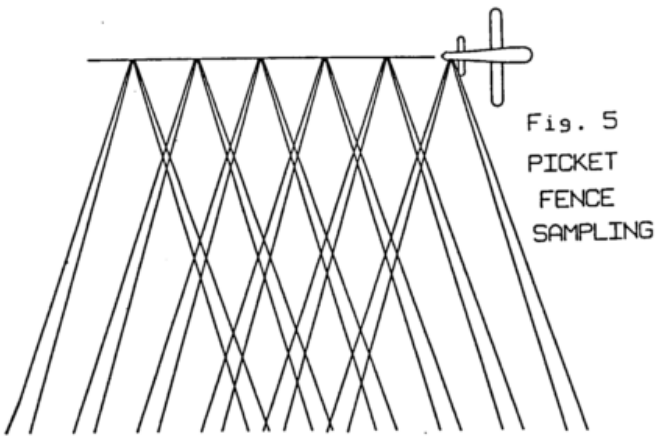


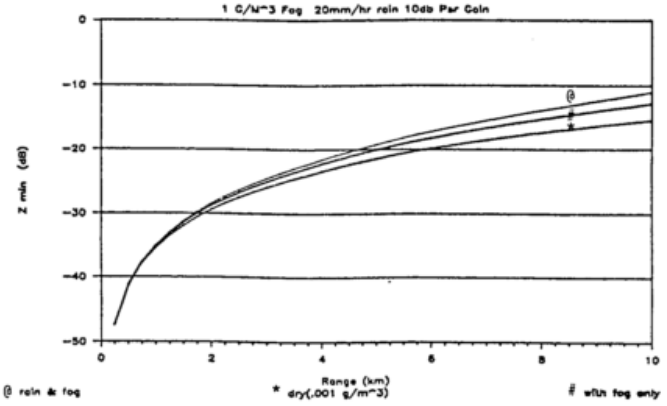
Fig. 5
PICKET
FENCE
SAMPLING

Because the ELDORA radar can be moved so close to the phenomena of interest, temporal sampling problems are also mitigated. The time for the ELDORA to get two distinct looks at a point in space that is 2.5 km away is only 15 seconds. Points closer to the aircraft are observed in even a shorter time frame.

3.2 ADDITION OF A VERTICALLY POINTING CLOUD PHYSICS ANTENNA

As was mentioned earlier, the ELDORA antennas will have beam width limitations when trying to measure physical parameters of clouds. To alleviate this problem, a larger, vertically pointing antenna could be mounted on the Electra aircraft. This antenna would have no scanning capabilities but would simply look directly up or down. During a cloud physics mission on the aircraft, the ELDORA could be reconfigured to radiate energy through this antenna, either continuously, or possibly intermittently while the scanning antennas are also collecting data. It is believed that an antenna 1.8 m in diameter could be mounted in this way, resulting in a 1.2 degree beamwidth. The width of the principal lobe of this antenna would be 50 m at 2400 m from the aircraft. With this antenna and a data density of 50 m the ELDORA radar can provide sensitivities of -20 dbZ or less out to 5 km (Fig 6). Since this antenna would not be scanned, many uncorrelated data points can be retrieved from the same volume in space, with a reasonable PRF. One or both of the scanning antennas could also be operated to provide a lower resolution, larger scale view of the meteorological phenomenon being observed.

Fig. 6 Vertically Pointing Antenna Sensitivity:
25Kw, 1.8m Antenna, 50m Data Density



4. CONCLUSION

The NCAR ELDORA radar is being designed with a primary emphasis on the study of storm and mesoscale weather phenomena. However, the radar will also be very useful for the study of cloud physical parameters. Because the aircraft can be positioned close to the area of interest, reasonably fine scale data can be taken in a very short length of time. Since these types of measurements have not been performed before, there is much to be learned even with the moderately course resolution of the ELDORA. The use of a larger, vertically pointing antenna will further enhance the ability of the ELDORA to measure these properties. Once this effort has been completed, the information obtained will greatly enhance the cloud physics community's ability to determine what specific properties of airborne radar are necessary to measure their various phenomena of interest.

INTERCOMPARISONS OF AIRCRAFT MEASUREMENTS WITH LIDAR RETURNS FOR AEROSOL, ICE CRYSTALS, AND WATER DROPLETS

W.R. Leaitch and R.M. Hoff, Atmospheric Environment Service
4905 Dufferin Street, Downsview, Ontario, Canada M3H 5T4

A.I. Carswell, S.R. Pal, and A.G. Cunningham, Department of Physics
York University, 4700 Keele Street, Downsview, Ontario, Canada M3J 1P3

1. INTRODUCTION

Lidar is a tool for the study of the scattering of electromagnetic radiation by aerosol and cloud particles. Ultimately, the intensity and polarization of the backscattered radiation may be used to diagnose microphysical properties of aerosols and clouds (e.g. Dubinsky et al., 1985). Here in-situ observations of aerosol and cloud particles are compared with remote observations from ground-based lidars.

2. EXPERIMENTAL

The airborne measurements were made from the National Research Council of Canada Twin Otter near Alert, Northwest Territories during April 1986, and near Cambridge, Ontario during October 1986. Particle spectra were measured with Particle Measuring Systems ASASP-100X (0.17-2.0 μm dia.), FSSP-100 (1.0-35 μm), and 2D-C (25-800 μm). The aerosol volume scattering coefficient (b_{sp}) was measured with a Meteorology Research Inc. Model 1550 integrating nephelometer. Ruby lidars (0.694 μm) were used on the ground to profile backscattering by the aerosol and clouds. An excimer lidar (0.308 μm) was also used at Cambridge. One ice crystal case at Alert, and 3 water droplet cases at Cambridge are presented.

3. THEORETICAL

For the Cambridge cases, the lidar backscatter profiles are inverted to give profiles of the extinction coefficient ($b_e = b_{sp}+b_{ap}+b_r+b_{ag}$, where b_{ap}, b_r, and b_{ag} represent absorption by particles, Rayleigh scattering, and gaseous absorption respectively) as described below. To facilitate comparisons among all the data, b_e (NO_2 profiles indicate b_{ag} is negligible for wavelengths appropriate to the nephelometer and ruby lidars) and b_{sp} have been calculated for the particle spectra.

3.1 b_e FOR LIDAR RETURNS

The lidar backscatter power (P(r)) as a function of range (r) can be written as

$$P(r) = C\,\{\beta(r)/r^2\}\,\exp\{-2\int b_e(r')dr'\} \qquad (1)$$

where C is the system constant, and β(r) is the backscatter coefficient. The inversion technique of Klett (1981) is used to obtain $b_e(r)$ from P(r).

3.2 $b_{e/sp}$ FOR AEROSOL PARTICLES

The aerosol is assumed to be a homogeneous internal mixture of concentric spheres. The inner and outer spheres each represent 50% of the total particle mass, and are composed of a water-insoluble substance (index of refraction of 1.6-i0.1), and NH_4HSO_4 respectively. The equilibrium size of the particles at the measured relative humidity is computed using a model described in Leaitch et al. (1986). The extinction and scattering coefficients are then determined using Mie scattering.

3.3 $b_{e/sp}$ FOR CLOUD DROPLETS

Since scattering is the dominant extinction factor in liquid water clouds, b_e is calculated from the FSSP spectra using Mie scattering for a single sphere with a refractive index of 1.33.

4. RESULTS

4.1 CAMBRIDGE

Fig. 1-3 show aircraft-data profiles of

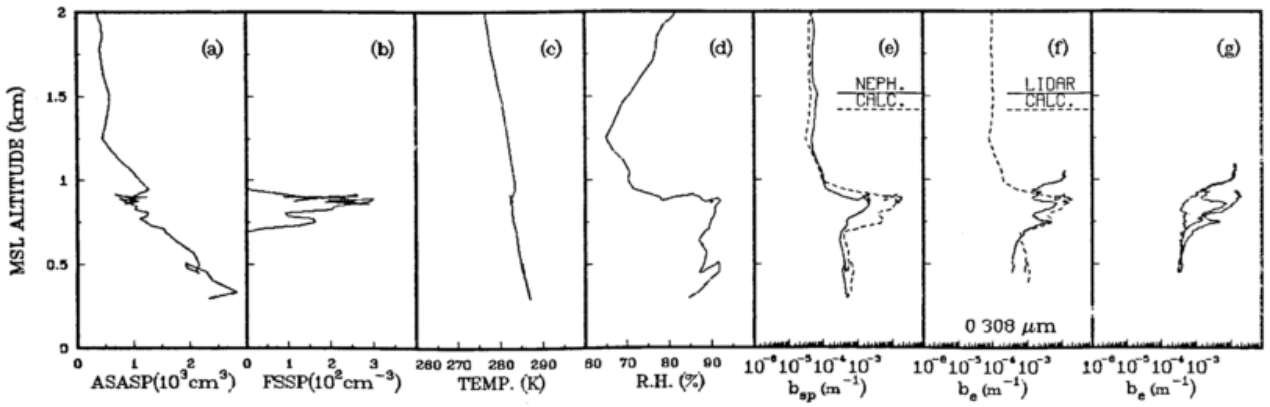


FIG.1 PROFILES FOR CAMBRIDGE 23/10/86

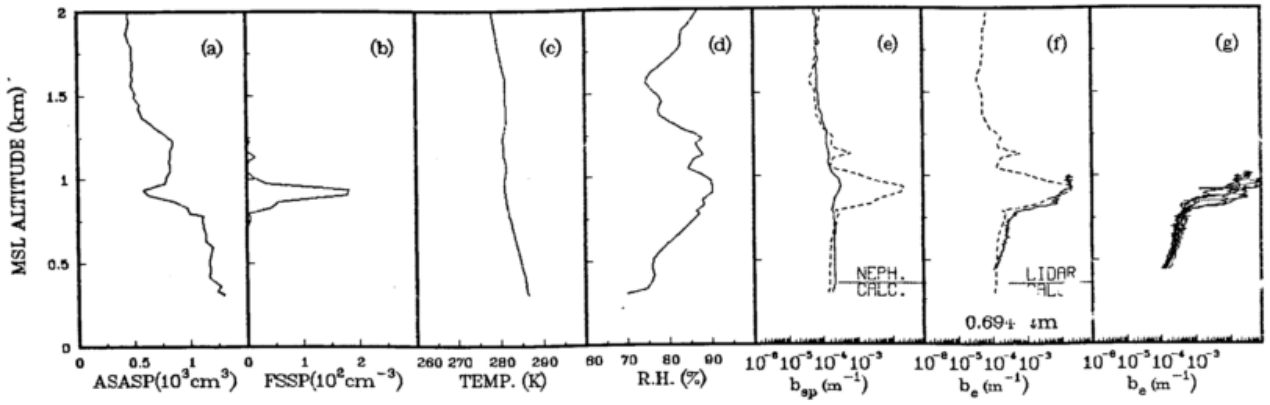


FIG.2 PROFILES FOR CAMBRIDGE 29/10/86

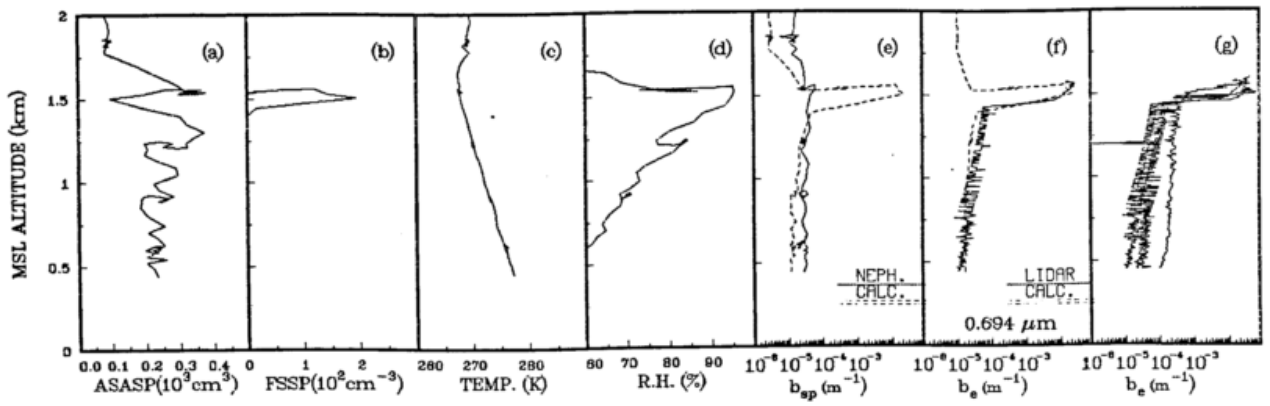


FIG.3 PROFILES FOR CAMBRIDGE 30/10/86

aerosol particle (a) and cloud droplet (b) number concentrations, temperature (c), relative humidity (d), and the nephelometer b_{sp} (e). Profiles of b_{sp} calculated from the particle spectra for a wavelength of 0.55 μm are also shown in Fig. 1e-3e. Profiles of b_e from the inversion of the lidar data collected near the time the aircraft was overhead the lidar, and b_e calculated from the particle spectra at the lidar wavelength are shown in Fig. 1f-3f. Variability in the lidar b_e profiles is illustrated in Fig. 1g-3g with data collected within ±20 minutes of the aircraft profiles.

Losses of cloud droplets in the intake of the nephelometer permit only aerosol comparisons to be drawn with the data from this instrument. For the 2 cases with the highest aerosol concentrations (i.e. 23/10/86 and 29/10/86) the comparison of the measured and calculated aerosol scattering coefficient is very strong. At much lower concentrations (i.e. 30/10/86) the comparison is worse, because the b_{sp} values are near the detection limit of this particular nephelometer (≈ 1×10^{-5} m^{-1}). These comparisons indicate the model to be a suitable gauge for the lidar measurements.

The Cambridge clouds discussed here were not homogeneous. Given this, the in-cloud lidar profiles of b_e agree very well with the calculated b_e. The large discrepancy between the below-cloud lidar and calculated b_e on the 23rd is partially due to NO_2 absorption, which is about 1×10^{-4} m^{-1} for this case. The below-cloud lidar and calculated b_e profiles for the 29th agree very well. Some of the below-cloud lidar profiles of b_e on the 30th compare well with the calculated b_e profile, however, the noise level is high because the b_e is near the detection limit of this lidar. One example of a lidar b_e profile from the 30th which compares poorly is shown in Fig. 3g. It is not known if this indicates a problem with the inversion technique. Overall, these results indicate promise for the simultaneous monitoring of aerosol and cloud extinction coefficients using lidar, however, much more research is needed.

4.2 ALERT

Fig. 4 shows aircraft-data profiles of aerosol number concentration (a), ice crystal number concentration as measured with the FSSP and 2D-C (b and c respectively), and b_{sp} measured with the nephelometer (d). Lidar profiles of β are shown in Fig. 4e. The lidar and aircraft profiles are separated by about 2 hours, and 1 km.

The concentration of aerosol particles is nearly uniform up to about 3 km. The FSSP and 2D-C profile data indicate ice crystals present between 1 and 3 km with the concentration increasing with altitude in this range. The b_{sp} profile parallels very closely the ice crystal profiles, demonstrating the nephelometer to be responsive to the ice crystals, however, some sublimation and deposition of crystals in the inlet is likely. Estimates of b_{sp} for the ice crystal spectra, assuming non-absorbing spherical particles, are 1.5×10^{-4} m^{-1}, and

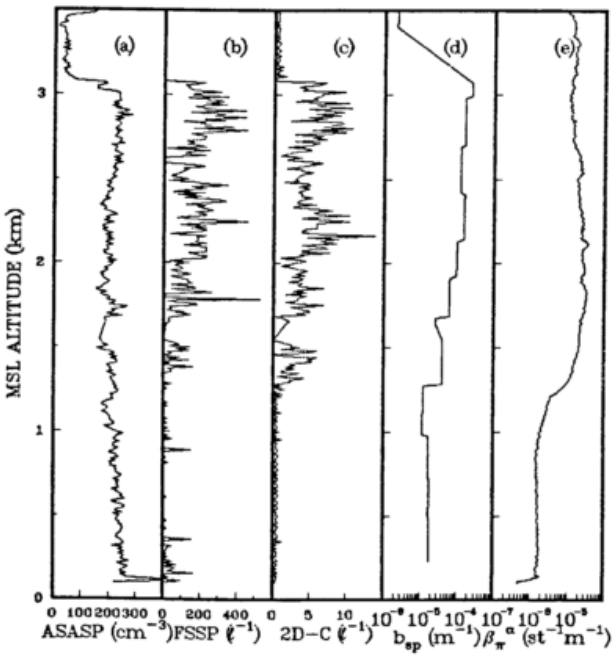


FIG.4 PROFILES FOR ALERT 12/4/86

4.5×10^{-4} m^{-1} for 1.2 km, and 3.0 km respectively. Scattering from the larger crystals (2D-C) is about an order of magnitude greater than from the smaller crystals (FSSP). The lidar backscatter profile indicates about an order of magnitude increase in the backscatter from the ice crystals plus aerosol versus just the aerosol, and is consistent with the value of b_{sp} estimated for the ice crystals compared with the measured aerosol b_{sp}. Temporal variations contribute to the discrepancies between the shapes of the lidar and aircraft-data profiles.

5. REFERENCES

Dubinsky. R.H.; Carswell. A.I.; Pal, S.R. Determination of Cloud Microphysical Properties by Laser Backscattering and Extinction Measurements. Appl. Opt. 24 (1985), 1614-1622.

Klett. J.D.: Stable Analytical Inversion Solution for Processing Lidar Returns. Appl. Opt. 20 (1981), 211-220.

Leaitch, W.R.: Strapp, J.W.; Isaac, G.A.; Hudson, J.G.: Cloud Droplet Nucleation and Cloud Scavenging of Aerosol Sulphate in Polluted Atmospheres. Tellus 38B (1986), 328-344.

A NEW AIRBORNE DEVICE FOR MEASUREMENT OF CLOUD PARTICLES USING VIDEO-MICROSCOPE

T.Tanaka‡,T.Matsuo‡,K.Okada‡,I.Ichimura‡
S.Ichikawa‡‡ and A.Tokuda‡‡

‡ Meteorological Research Institute, 1-1 Nagamine, Tsukuba, 305 Japan
‡‡ Sankei Co. Ltd., 3-20-12 Yushima, Bunkyou-ku, Tokyo, 113 Japan

1. INTRODUCTION

Size distribution and phase of cloud particles as well as liquid water content of clouds are of fundamental knowledge in cloud and radiation physics.

Techniques for measuring cloud particles on board aircraft have advanced significantly owing to the development of PMS probes: FSSP and 2D-C probe (Knollenberg,1981). The probes use light scattering or shadow techniques. Although the FSSP probe can measure cloud particles of 2 to 30 μm in diameter, it has some difficulty in phase discrimination of the particles. The 2D probe could not catch cloud particles smaller than 25 μm in diameter.

Liquid water content of clouds has been measured widely and easily by the use of Johnson-Williams hot-wire device. However the device underestimates the mass of droplets with diameters grater than 30 μm.

To overcome these difficulties, we have designed and developed a new-type airborne cloud particle measuring system combining an impactor with a video-microscope. In this paper we will describe the new device and a result of comparative measurements with J-W hot wire device in natural clouds.

2. SYSTEM DESCRIPTION

The system consists of three parts: cloud particle detection unit, image display and recording units, and control unit.

The detection unit consists of three components as shown in Fig.1: two shutters, a rotating optical hollow drum, and a video-microscope.These components are regulated by the control unit in a cabin.

The first shutter(hood shutter) protects the second shutter against the deposition of cloud particles . Synchronizing with opening of the hood shutter, the second shutter (sampling shutter) provides an exposure time with a rectangular window (7x14 mm) . In normal operation the exposure time is fixed to be 1/100 sec. Cloud particles passed through the window of the sampling shutter are captured on the surface of a glass stage. After the sampling, the rear side of the shutter reflect the light and serves as a light source to illuminate cloud particles on a glass stage.

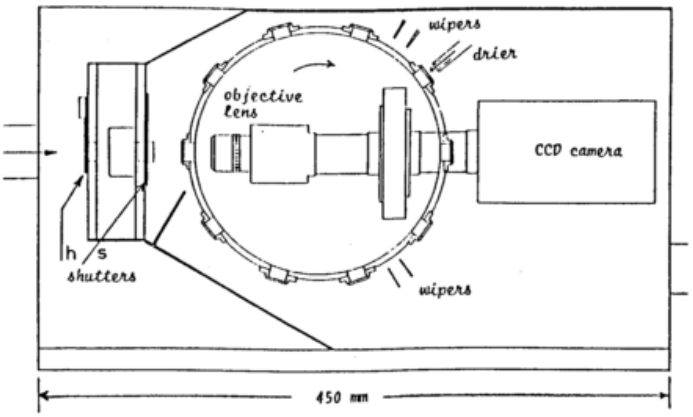


Fig.1: Airborne video-microscope for CP measurement

Ten glass stages were mounted at regular intervals on the frame surface of optical hollow drum of 180 mm in diameter. One of the stages has a 100 μm grid mesh as a reference object.

The glass stages of 15mm in diameter serve as a collecting surface of cloud particles at 25mm behind the sampling shutter. The surface of the stage was treated with hydrophobic chemicals to minimize the spreading of cloud droplets on the stage. Collection efficiency of particles larger than 5 μm in diameter are evaluated to be 100% in the situation of flight speed grater than 50 m/sec. The optical drum is

driven intermittently with an interval of 1.4 sec by controlled stepping motor.

Cloud particles on the stage can be seen through the glass plate from the rear side of the stage with an optical microscope. The optical system used in the present study consists of an objective lens x5 (Nikon M Plan5), a crank shape optical tube with two right-angle prisms, and CCD Video-camera(HITACHI KP-130).

The video signal of cloud particles is transmitted to a CRT and a VTR through a video time generator on the coaxial cable of 5m length. Phase, size, shape, and number of cloud particles are immediately identified visually from their images on the CRT. The images of cloud particles are simultaneously recorded on the VTR.

3. SYSTEM OPERATION

Some tests of the system performance were made in wind tunnel and in natural clouds. The detection unit was mounted on shock absorbers in the nose of aircraft Cessna 404.

In flight, the sample air was introduced into a pipe protruded from the nose of the aircraft and impinged on the hood shutter. The air flew down through the detection unit to the suction pipe connected to the skin of the aircraft.

An example of each images of cloud droplets on CRT is shown in Fig.2 (a) which was taken by the replay of video tape recorded on the flight of 24 Dec.1986. Fig.2 (b) shows images of ice crystals found in flight on 20 Sept.1987.

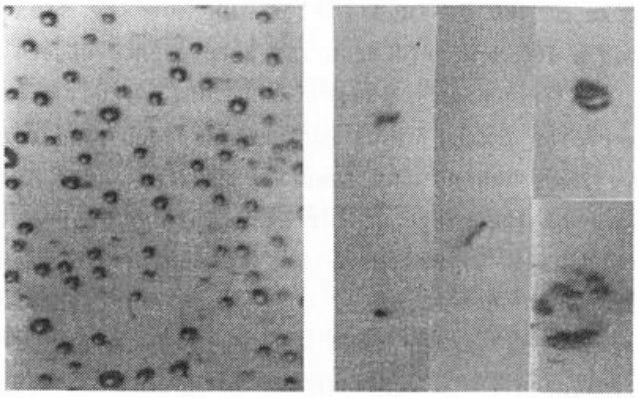


Fig.2 (a): Cloud droplets (b): Ice crystals

Full measurements of size and number of particles on each stage were made automatically on images by using a Particle Image Analyzing System (PIAS LA-500). Fig.3 shows an example of size distribution calculated by the following formula;

$$n = \Sigma n_i / E_i \cdot U_p \cdot S \cdot t \qquad (1)$$

where n_i stands for the number of particles of size i , E_i collection efficiency for size i, U_p air speed in the pipe ($U_p=1.09U_a$, U_a means TAS). S is the area of examination (16×10^{-2} cm^2), and t means the sampling time of 1/100 sec.

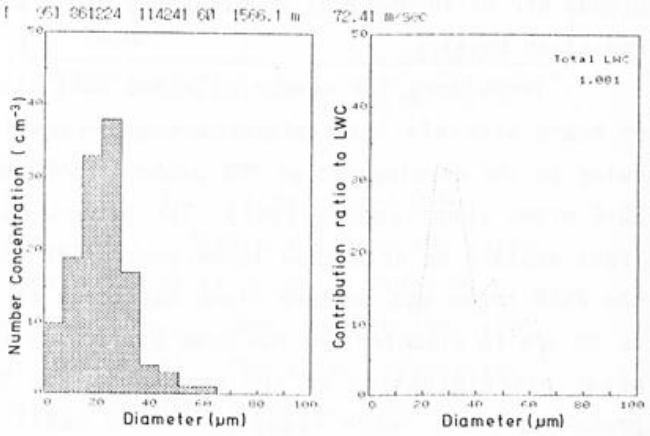


Fig.3: Size distribution and contribution rate to LWC

The liquid water content is integrable from the droplet size spectra obtained above.

$$LWC=4/3\cdot\pi\cdot\rho\cdot n\ \Sigma\ (F\cdot D_i/2\beta)^3 \qquad (2)$$

where F means the conversion factor of 0.673 for the stages used in the observation of 1986, β total of optical and electrical magnifications (by using the mesh scale on the stage, β becomes to unity), D_i diameter of particle image for size i on the stage.

4.FLIGHT MEASUREMENTS

A flight for the study of cloud and radiation physics was carried out on 24 Dec. 1986 over the Hachijo Island situated at 300 km S of Tokyo. Immediately after the instrumented aircraft began to pass through the clouds from the base to the top, the screen of CRT started successively to project images of cloud particles as shown in Fig.2(a) at an interval of 1.4 sec.

Liquid water contents were calculated by the formula (2) from droplet spectra and plotted

in Fig.4. The rapid change was also observed by J-W hot wire device. A scatter plot of LWC

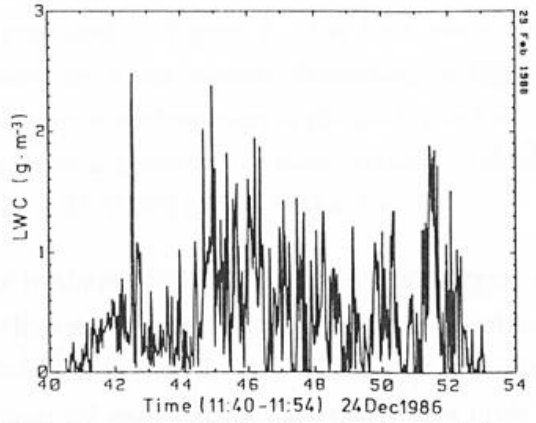


Fig.4: Time series of LWC obtained by the new device

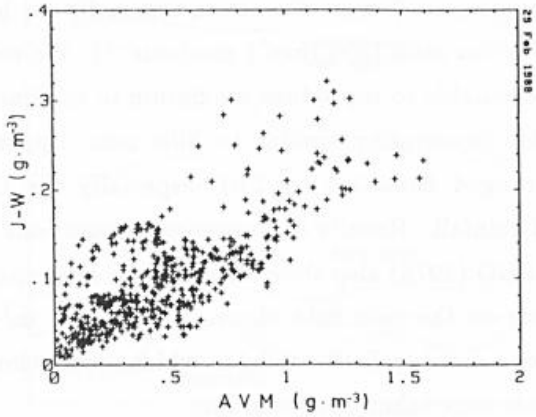


Fig.5: Scatter plot of data for Fig.6(total) and Fig.7(J-W)

measured by J-W device versus LWC of the new device are shown in Fig.5. Data used are of 10 sec running means. The figure shows that the LWC obtained by the new device are about 5 times higher than those of J-W hot wire device.

In order to consider the reason of discrepancy in liquid water contents between two devices, cloud particles were classified into three ranges of size (0-30, 0-40 μm and total of particles). LWC was recalculated with each

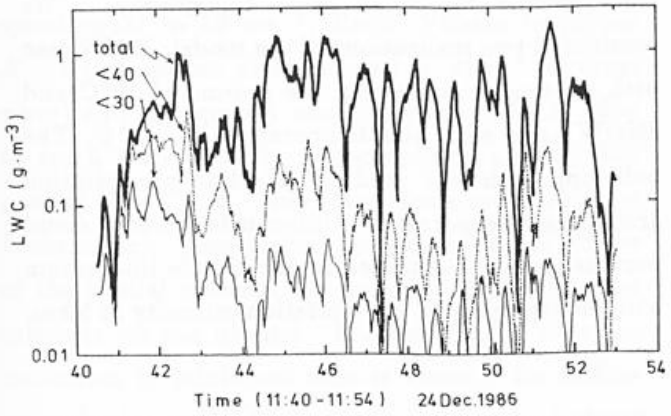


Fig.6: Timeseries of LWC and two partial LWC(<30,<40 μm)

size range and plotted in Fig.6 as 10 sec running means.Fig.7 shows the liquid water contents calculated from the limited cloud particles up to 40 μm in diameter is in agreement with those obtained by J-W device.

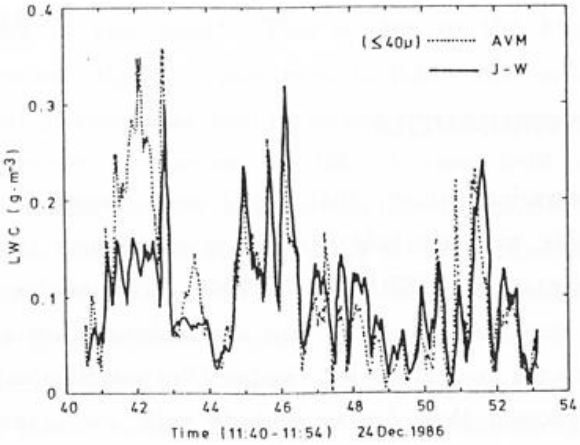


Fig.7: Comparison of LWC(J-W) with Partial LWC(<40 μm)

The agreement suggests that the J-W device underestimates the mass of cloud particles larger than 40 μm in diameter.

5.CONCLUSIONS

The new airborne device provided high quality image of cloud particles in the size range of 5 to 150 μm with time resolution of 1.4 sec. The LWC of clouds were calculated on the basis of the size distribution of particles. The result of calculation suggested that the LWC measured by J-W hot wire device was closely related to particles up to 40 μm in diameter .

It is the most important features of the new device that the phase, shape, size and number of cloud particles can be confirmed visually on board aircraft.

ACKNOWLEDGMENTS

Authors are deeply grateful to Drs.M. Asano, M.Shiobara, and Mrs. M.Ikegami, a crew of WCRP project in Meteorological Research Institute. They wish to thank a chief director T. Koga, of NHK-TV Nagoya station and a director K.Kitahara of Shouwa Aviation Co. who gave a chance of test flights. Pilot and copilot of the observation aircraft Messrs. M.Siratsuchi and C.Minato supported the operation of the new device.

REFERENCE

Knollenberg,R.G.: Techniques for probing cloud microstructure. CLOUDS Their formation, optical properties, and effects, ed. Hobbs & Deepak. Academic Press 1981.

ON THE SMALL SCALE TOPOGRAPHICAL INFLUENCES ON PRECIPITATION

Wojciech W. Grabowski[1]

NCAR[2], Boulder, USA

1. INTRODUCTION

Observations show, that small scale topography is able to remarkably influence continuous type precipitation. BERGERON (1968, 1973) analysed fine structure of spatial rain accumulations in the hilly area near Uppsala, Sweden (Project Pluvius). He showed that during periods with continuous type precipitation those small hills (5 – 10 km of horizontal scale and less than 100 m height) receive on average of 40 to 100% more rain than nearby areas. BERGERON (1965) put forward a mechanism for the small scale orographical influences on precipitation, the "seeder–feeder" mechanism. We investigated the redistribution of precipitation in hilly terrain similar to that of Uppsala area assuming idealized two dimensional topography in the form of one period of sine function with the spacing of ridges of about 10 km and amplitude of about 100 m. The maximum to minimum ratio of precipitation intensity distribution at the surface was used as a measure of orographic influence on rainfall or snowfall. Using a simple approach (i.e. we assumed unperturbed seeding precipitation at 2 km AGL in the form of rain/snow for the case of rainfall/snowfall) we showed that: 1) for both rainfall and snowfall the maximum to minimum ratio increased as the amplitude (i.e. relative height) and horizontal scale of topography increased; the ratio was higher for smaller seeding precipitation intensity; 2) for snowfall the ratio was a strong function of ground temperature (with the highest ratio for ground temperature close to 0°C) and weakly depended on the snow particle size distribution; 3) for rainfall the ground temperature had a small effect on the ratio but raindrop size distribution was crucial (the ratio increased as concentration of drizzle size droplets increased); 4) the ratio was higher for snowfall than for rainfall when other model parameters (scale of topography, seeding rate, etc.) were the same, especially for low precipitation rates (less then 1 mmhour^{-1}). We were however unable to reproduce maximum to minimum ratio for topography similar to hills near Uppsala (that ranged from 1.4 to 2.0), especially for the case of rainfall. Results of numerical simulations of STOREBO (1976) also show rather weak orographic influence on the rain field alone. This forced us to consider a more realistic model in which seeder cloud processes were taken into account.

2. THE MODEL

The model is kinematic (prescribed airflow) and two dimensional ($x - z$). Two separate scales of motion are considered (see Fig. 1): the larger scale responsible for seeder cloud formation and the small scale responsible for precipitation redistribution. A seeder cloud is a deep stratiform cloud with a weak updraft (maximum of 15 cms^{-1} at 3.5 km AGL) which may be considered as horizontally homogeneous for small scale topography. We considered two realizations of the model: RAIN case with air temperature near the ground of 12°C and SNOW case with the temperature of −5°C. The bulk approach was used to calculate precipitation growth and evaporation. Unperturbed seeder cloud parameters were obtained in the simple integration without topography. Precipitation intensity at 5 km,

[1] On leave from Institute of Geophysics, Polish Academy of Science, Warsaw, Poland.
[2] NCAR is sponsored by the National Science Foundation

updraft profile and the ground temperature formed initial conditions for this integration and results are presented in Figure 2. For both cases growth of snow by water vapour deposition in the water subsaturated environment is the basic mechanism of precipitation growth. For more details of the model see GRABOWSKI (1985, 1988a, 1988b).

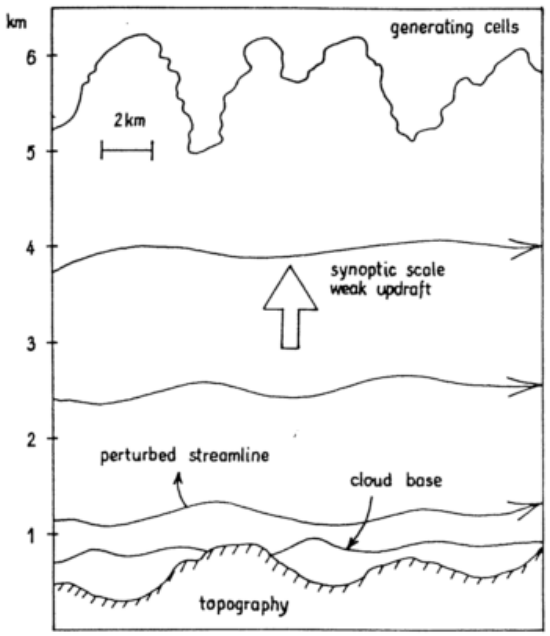


Fig.1. Schematic picture of the model idea.

3. SOME RESULTS

As mentioned before we considered topography in the form of one period of the sine function. Airflow pattern was assumed in the form of internal gravity wave for atmosphere with constant stability or evanescent perturbation for neutrally stratified atmosphere. Examples of results are presented in Fig. 3 for spacing of ridges equal to 20 km, wind speed equal to 10 ms^{-1}, Brunt–Väisäla frequency $N = 0$ (evanescent perturbation) or .01 s^{-1} (internal wave) and topography amplitude $h = 100$ m (due to small amplitude the topography is actually not presented in Fig. 3 – only wave crests are marked by broken line). Also shown are positions and values of the spatial maxima and minima of precipitation intensity on the ground. For the SNOW case the maximum to minimum ratio is about 2 for airflow perturbation in the form of internal wave and about 1.6 for $N = 0$ case. Due to strong wind drift of the snowflakes precipitation redistribution occurs in the shallow layer close to the ground. For the RAIN case the ratio is about 3.6 and 2.4 for internal wave and evanescent perturbation, respectively, and precipitation redistribution occurs in a much deeper layer in this case. This is due to the higher terminal velocity of raindrops. In RAIN case airflow perturbations near melting level are very important. There are two reasons for this: 1) snow field just above the melting level is the most sensitive to airflow perturbations (and more sensitive than rain field below – see 2 and 4 in the introduction) and 2) precipitation intensity is smaller there, so precipitation field is more sensitive again (see 1 in the Introduction). The maximum to minimum ratio is the measure of sensitivity. Due to wind drift, airflow perturbations much above melting level are not important. After melting, rain continues to grow in the layer between melting level and the ground. The difference between internal wave and evanescent perturbation for RAIN case is due to different airflow perturbations near melting level (about 2 km AGL) and upstream shift of perturbation for internal wave that reduces wind drift of raindrops. Thus both wave amplitude and phase near melting level with respect to the underlaying topography are important for rain distribution. Simulations with topography amplitude of 50 m (similar to that in Uppsala field) gave the ratio for RAIN case of about 1.6 – 2.0, i.e. close to observed. However, those results should be treated as qualitative rather then quantitative since real topography near Uppsala is definitely three dimensional.

4. DISCUSSION

Our results support Bergeron's idea that observed influence of small scale topography on precipitation may be explained in terms of the "seeder–feeder" mechanism. However, since raindrops are not very efficient in removing condensate that appears due to small vertical displacements of air parcel the influences on the snow stage of precipitation growth are very important. From the point of view of maximum to minimum ratio of precipitation intensity, the region just above melting level is the

most sensitive to airflow perturbations. Although it is difficult to treat those results as qualitative for the region of Uppsala, we believe that they represent a basic mechanism in which small scale topography influences the precipitation field.

REFERENCES

BERGERON, T.: On the low level redistribution of atmospheric water caused by topography, Supp. Proc. Int. Conf. Cloud Phys.,Tokyo, 96–100, 1965.

BERGERON, T.: Studies of oreigenic effects on the areal fine structure of rainfall distribution, *Uppsala Met. Inst. Rep. No. 6*, 1968.

BERGERON, T.: Mesometeorological studies of precipitation. Part V: Monthly rainfall in Uppsala field, *Uppsala Met. Inst. Rep. No. 38*, 1973.

GRABOWSKI, W.W.: On the influence of microphysics parameterization on rainfall rates in numerical models of clouds, *Pure Appl. Geophys.* **123** (1985), 941-950.

GRABOWSKI, W.W.: On the bulk parameterization of snow and its application to the quantitative studies of precipitation growth, *Pure Appl. Geophys.* **128** (1988a), in press.

GRABOWSKI, W.W.: On the redistribution of precipitation by small scale topography., *Quart. J. R. Met. Soc.* (1988b), submitted.

STOREBO, P.B.: Small scale topographical influences on precipitation, *Tellus* **28** (1976), 45-59.

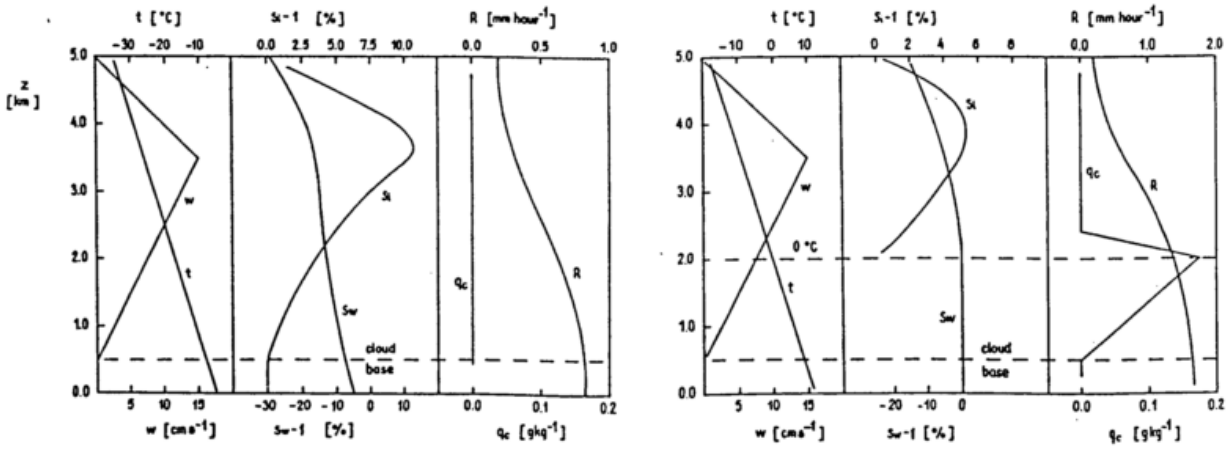


Fig. 2. Parameters of the seeder cloud as a function of height for SNOW and RAIN simulations.

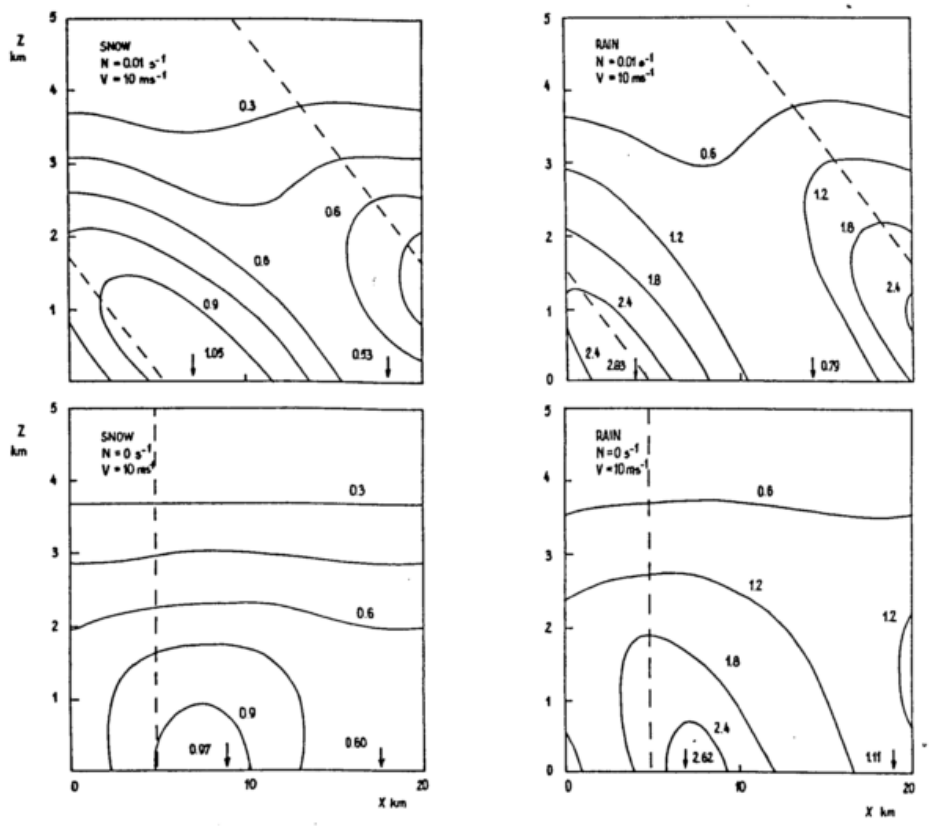


Fig. 3. Precipitation intensity isolines for RAIN and SNOW cases when seeder cloud and subcloud layer are modified by internal gravity wave or evanescent airflow perturbation. See text for details.

A NUMERICAL INVESTIGATION OF AN OROGRAPHIC PRECIPITATION EVENT

Michael P. Meyers and William R. Cotton
Dept. of Atmospheric Science
Colorado State University
Dept. of Atmospheric Science
Fort Collins, CO 80523

1 Introduction

A prolonged orographic precipitation event, in a relatively steady-state synoptic environment, occurred over the Sierra Nevada range in central California on 12-13 February 1986. Extensive observational data for this case were collected and analyzed by Sierra Cooperative Pilot Project (SCCP) personnel (Reynolds and Dennis, 1986). Marwitz (1986) notes that deep stable orographic clouds produce a majority of the precipitation over the Sierra Nevada range. A numerical investigation will be employed which should reveal the dominant physical controls on orographic precipitation and cloud processes. In this paper we will discuss the main features of the model, describe the case study data and discuss the preliminary results obtained with the model.

2 Model Description

The numerical model employed is the two-dimensional non-hydrostatic option of Colorado State University's RAMS (Regional Atmospheric Modeling System) similar to that reported by Tripoli and Cotton (1982) and Cotton *et. al.* (1982; 1986). The topography has been rotated to a cross-barrier horizontal component to maximize the greatest orographic lifting. Full microphysics including vapor, cloud water, rainwater, pristine ice crystals, graupel, and aggregates was used. The microphysical processes, including the liquid and ice phase precipitation processes, are modeled following the parameterizations described in Tripoli *et. al.* (1988a) and a summary of the approach is given in an accompanying paper in this proceedings (Tripoli *et. al.*, 1988b). Horizontal and vertical turbulence are parameterized in the eddy viscosity closure as described by Tripoli and Cotton (1982). The equations are integrated numerically by a time-splitting procedure for a non-hydrostatic, compressible system (Tripoli and Cotton, 1982) with a large timestep of 10 seconds and a small timestep of 5 seconds.

The model domain is 450 km long and 14.5 km deep with a horizontal grid resolution of 1.5 km and a stretched vertical grid resolution of 0.25 km up to crest level to 0.5 km at the top of the boundary. The model is initiated with a horizontally-homogeneous wind, temperature, and moisture sounding for 12 February 1986. The observed winds are added incrementally during the first 30 minutes (Cotton *et.al.*, 1986) and then the model is allowed to adjust to these winds for a 3.0 hour period during which time all microphysical tendencies are deactivated .

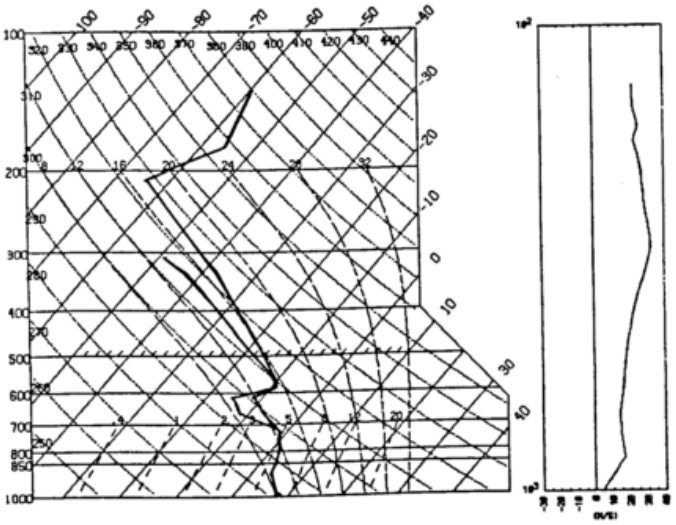


Figure 1: Skew-T log-p diagram of Sheridan sounding at 1500 GMT 12 February 1986. Temperature and dew point are displayed. Wind speeds are displayed to the right of the diagram.

3 Synoptic Environment

The storm system which affected the central California region originated over the south-central Pacific and was characterized by seasonably warm temperatures. The synoptic scale flow was southwesterly at 850 mb slightly veering to west-southwesterly at 500 mb. The 500 mb analysis showed weak ridging occurring over the state throughout the period. The 500 mb temperature was -16°C, shown in the sounding for 12 February 1986 in Figure 1, reflecting the warm nature of the storm. Weak trough passage and its associated humidity front occurred at 1200 GMT. Middle tropospheric subsidence occurred behind the passage of the trough drying the layer between the 0°C and -12°C . Potential instability was present at the top of the deep moist layer which extended up to the 0°C level. By 2100 GMT, the effects of subsidence diminished, and the moist layer extended from the surface to -15°C.

4 The Simulation

Preliminary results thus far have agreed quite well with observations. The dynamic and microphysical structures of the simulation exhibit many of the features of the orographic precipitation event. Figure 2 shows the simulated vertical velocity fields after 5 h of simulation. The vertical velocity field shows the strongest positive vertical velocities occurring in the lower troposphere on the windward side of the crest. Vertically propagating hydrostatic mountain waves existed just to the lee of the crests of both the

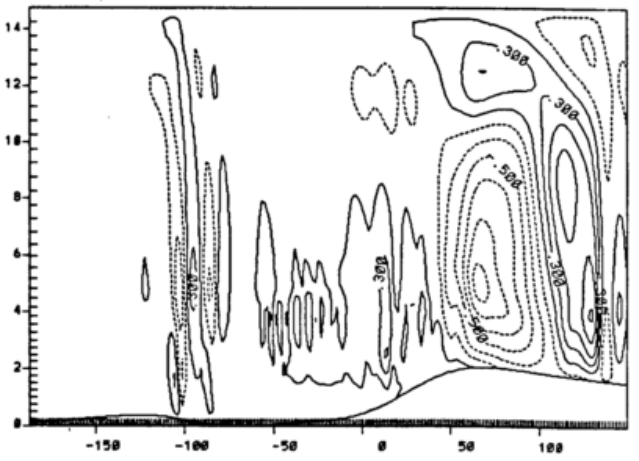


Figure 2: Vertical velocity after 5 h of integration time. The contour interval is 0.2 $m\ s^{-1}$. Coordinates are in kilometers.

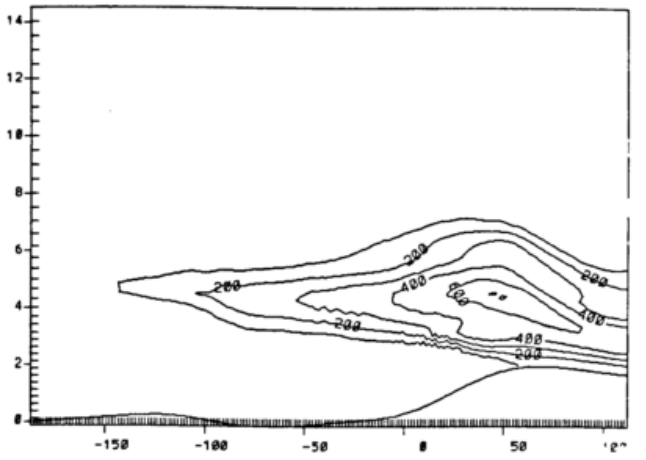


Figure 4: Mixing ratios of pristine ice crystals after 5 h of integration time. The contour interval is 0.1 $g\ kg^{-1}$.

Sierra Nevada Range and the Coastal Range which extends through most of the troposphere.

A conceptual model of the observed growth and evolution of precipitation processes is shown in Figure 3 (Huggins *et. al.*, 1986). The primary source region of ice crystals must have been near cloud top, based on the large number of dendrites present throughout the upper levels of the cloud system. These ice particles advected eastward as they fell and converged with large liquid particles originating from cloud base. Figure 4 shows the simulated pristine ice crystal mixing ratios at 5 h which agrees well with the observed structure with a maximum just above the crest. The subsequent riming and secondary ice multiplication enhanced the fall velocities of the ice crystals and led to higher precipitation rates in the middle elevations of the foothills a feature commonly observed in Sierras. The simulated graupel field shown in Figure 5 shows a peak where this convergence of cloud water droplets and large crystals

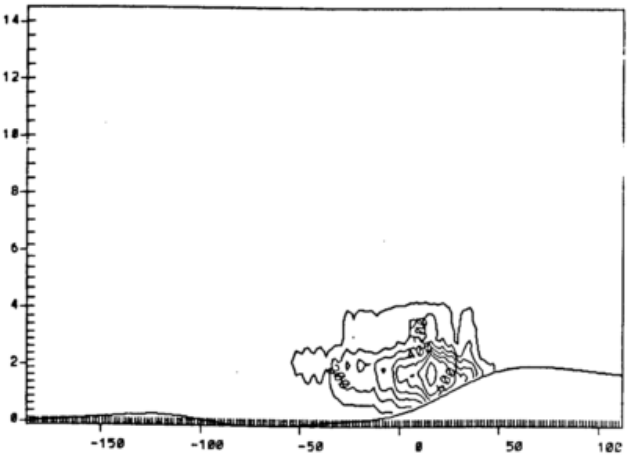


Figure 5: Mixing ratios of graupel after 5 h of integration time. The contour interval is 0.01 $g\ kg^{-1}$.

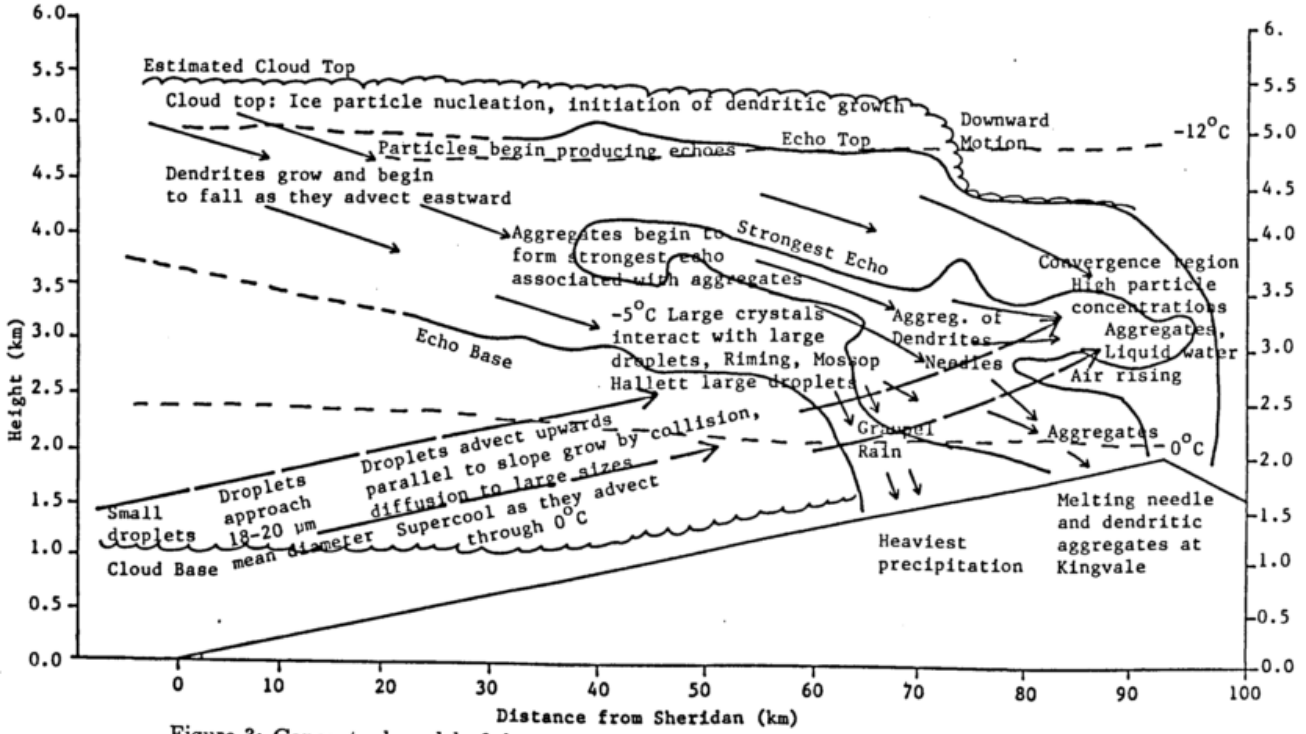


Figure 3: Conceptual model of the growth and evolution of cloud and precipitation particles in the cloud system. (From Huggins *et. al.*, 1986).

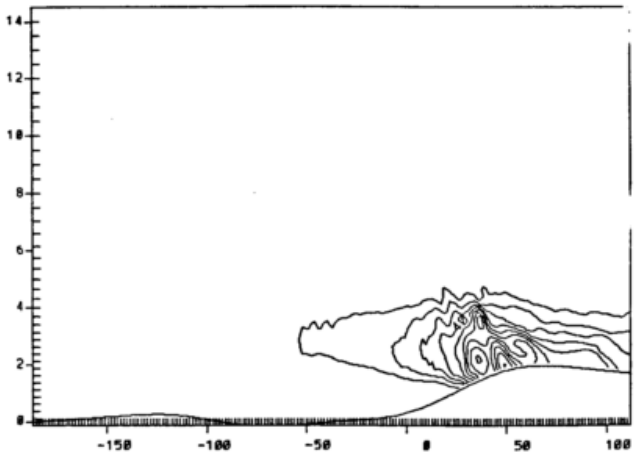


Figure 6: Mixing ratios of aggregates after 5 h of integration time. The contour interval is 0.01 $g\ kg^{-1}$.

occurs. The simulated aggregate field, shown in Figure 6 shows peak values near the upper third of the crest. This maximum coincides quite well with downwind location of dendritic and needle production which favors aggregation.

5 Summary

The control simulation was very consistent with the data observed. The dynamical and microphysical structure of the simulation exhibited the same basic features as the observed characteristics. To further reveal the dominant physical processes occurring in an orographic precipitation event, sensitivity tests will be run. Individual mechanisms such as the sensitivity of orographic cloud behavior to longwave radiation, melting and evaporation processes, warm rain, and ice phase heating will be examined. These results will be presented at the conference.

Acknowledgements

The authors wish to acknowledge Craig Tremback, Dr. Robert Walko and Dr. Gregory Tripoli for their many helpful suggestions in developing the model. Thanks are also extended to Ray McAnelly for valuable suggestions. Brenda Thompson helped with the manuscript. This research was supported by the Army Research Office under contract #DAAL03-86-K-0175. Computations were performed at the National Center for Atmospheric Research (NCAR). NCAR is sponsored by the National Science Foundation.

References

Cotton, W.R., M.A. Stephens, T. Nehrkorn, and G.J. Tripoli, 1982: The Colorado State University three-dimensional cloud/mesoscale model - 1982. Part II: An ice phase parameterization. *J. de Rech. Atmos.* **16**, 295-320.

Cotton, W.R., G.J. Tripoli, R.M. Rauber, and E.A. Mulvihill, 1986: Numerical simulation of the effects of varying ice crystal nucleation rates and aggregation processes on orographic snowfall. *J. Clim. Appl. Met.*, **25**, 1658-1680.

Huggins, A.W., *et.al.*, 1986: Interim progress report, Vol I, SCPP Meteorological and Statistical Support for period 1 September 1985-31 August 1986. Prepared for Div. of Atmos. Resources Res., Dept. of Interior, Bureau of Reclamation, Contract No. 4CR-81-038360.

Reynolds D.W., and A.S. Dennis, 1986: A review of the Sierra Cooperative Pilot Project. *Bull. Amer. Meteor. Soc.*, **67**, 513-523.

Tripoli, G.J., and W.R. Cotton, 1982: The Colorado State University three-dimensional cloud/mesoscale model - 1982. Part I: General theoretical framework and sensitivity experiments. *J. de Rech. Atmos.*, **16**, 185-220.

Tripoli, G.J., W.R. Cotton and P.J. Flatau, 1988: Generalized microphysics scheme for use in mesoscale/cloud models. 10*th* International Cloud Physics Conference, 15-20 August 1988, Bad Homburg, FRG.

Tripoli, G.J., W.R. Cotton and P.J. Flatau, 1988: Generalized microphysics scheme for use in mesoscale/cloud models. Technical Report, Colo. State University, Fort Collins.

COMPLEX MICROPHYSICAL INTERACTIONS WITHIN A CENTRAL SIERRA NEVADA OROGRAPHIC CLOUD SYSTEM

Robert M. Rauber
Department of Atmospheric Sciences
University of Illinois
105 S. Gregory Ave, Urbana, IL. 61801

1. INTRODUCTION

Precipitation processes in cloud systems over the mountains of the western United States have been investigated for many years because of the importance of these cloud systems to the water resources of the area. Recent investigations (Rauber, 1987; Marwitz, 1987) have shown that the microphysical interactions within these clouds can be quite complicated.

This paper describes microphysical interactions that were observed within a shallow, stable wintertime orographic cloud system over the central Sierra Nevada Mountains. Measurements of the physical structure and microphysical characteristics of the cloud system were made during the Sierra Cooperative Pilot Project (SCPP). The SCPP was a U.S. Bureau of Reclamation Project designed to evaluate the potential for precipitation enhancement from Sierra Nevada clouds through cloud seeding.

Data sources for this analysis include a 5 cm scanning radar, a vertically pointing 0.8 cm radar located near the mountain crest, the University of Wyoming King Air, a surface microphysical laboratory also located near the mountain crest, and a network of precipitation gages across the mountain. The SCPP has been reviewed recently by Reynolds and Dennis (1986) and the instruments used in this study have been described in detail by Marwitz (1987) and Huggins and Rodi (1985).

2. 12 FEBRUARY 1986 CLOUD SYSTEM

The cloud system which affected central California during 12 February was characterized by warmer than usual temperatures. At the time of first observation, the cloud extended 130 km upwind of the Sierra Nevada crestline, was 4 km deep, had a base temperature of +5°C and a top temperature of approximately -14°C. Fig. 1 displays a radar reflectivity RHI at 1638 GMT over the mountain along with the aircraft track. These data and similar data taken upwind of of the radar site indicated that the ice particle cloud extended eastward in a narrow mid-level layer, deepening to the surface 25 km west of the mountain crest near the town of Blue Canyon. Reflectivity and aircraft measurements indicated that ice particles within the cloud were confined primarily to elevations between the -5°C and -15°C levels westward of a point about 40 km upwind of the crestline .

3. CLOUD SYSTEM MICROSTRUCTURE

The flight track, radar reflectivity measurements along the 66° radial near the flight path, and the atmospheric thermal structure for the period 1605 -1650 GMT are shown on Fig. 1. The conceptual model shown on Fig. 2 and the discussion below are based on aircraft measurements in the microphysically distinct regions A-Q, and other measurements collected at the surface.

Processes near cloud base

Cloud base over the valley was located at +5°C. Near cloud base, cloud droplets were small (4-6 μm mean diameter (D)). Using the average measured cross-barrier component of the wind (u) in the 0°C to +5°C layer (~10 ms^{-1}) and an estimate of the mean vertical velocity from the slope of the underlying terrain (0.1 to 0.3 ms^{-1}), these droplets had the potential to rise upward along the terrain slope, advect eastward and grow for as long as 83 minutes by diffusion and later by collision, prior to advecting upward through the 0°C level. At +2°C over the valley, droplets with D=18-20 μm were observed. Within this region of the cloud, droplet collisions were likely to initiate and contribute to the production of larger cloud droplets. Such large droplets (D=25-35 μm diameter, maximum droplet size ≈ 100 μm) were observed near -5°C near region Q on Fig. 1. These droplets, now supercooled, continued advecting eastward and upward along the slope into the region where they encountered ice particles falling from higher elevations. The region of large droplets near -5°C observed by the

aircraft near region Q was most likely the result of long growth times and active coalescence occurring throughout the cloud base region.

Cloud top

Dendrites were common throughout the upper levels of the cloud system. Echo cloud top, based on 5 cm radar data, was located at -12°C. The 0.8 cm radar data indicated that cloud top was higher, at least near the mountain crest. The actual cloud top probably extended well into the temperature range characteristic of dendritic growth (-13°C to -15°C). Therefore, cloud top must have been a primary source region for the ice particles within the echo region of the cloud on Fig. 1.

Particle growth processes

As particles formed in the upper levels of this cloud, they advected eastward through the cloud system, grew and began to fall. The slope of the echo pattern upwind of 55 km on Fig. 1 corresponds well to the path a dendrite would take if it advected eastward at 15-20 ms^{-1} (value of u component on 12 February within echo layer) and fell at 0.2 to 0.3 ms^{-1} average velocity (0.4 ms^{-1} is the terminal velocity of a large unrimed unaggregated dendrite in still air). Aggregation was observed in the cloud, particularly in regions of strong echo. Based on aircraft observations, it is likely that aggregation initiated around the -12°C level and continued to the ground. The change in the slope of the echo east of 55 km reflects a change in fall velocity due to aggregation as well as a decrease in the u component as larger particles approached the surface.

Particular regions of importance in this cloud system were areas where large particles falling from cloud top encountered the large droplets originating at cloud base. One region where such collisions occurred was near the -5°C level, approximately 50 km east of the radar (see Fig. 1). This point coincides with a marked change in the slope of the reflectivity pattern. During penetrations of this region, the aircraft encountered several areas where large drops (D=25-35 μm) coincided with ice particles with sizes > 200 μm in concentrations of 1-20 L^{-1}. The coexistence of large ice particles and large water drops in these areas suggest that the water and ice particles arrived from two separate regions of the cloud. Riming occurred in this region, leading to enhanced fall velocities of the ice particles. The heaviest precipitation was observed at the middle elevations of the foothills, approximately 40 km upwind of the crestline. A potential consequence of riming in the region where large drops encountered ice particles was secondary ice multiplication by rime splintering. The appropriate conditions for the Hallett-Mossop (1974) process were all present. Needles, the expected habits that would be observed due to rime splintering at -5°C, were observed in several locations in this region of the cloud. Visual records of precipitation near the mountain crest indicated that some aggregates in the precipitation contained both dendrities and some needles. The aggregates of dendrites, falling from above, apparently incorporated the needles as they fell through the -5°C level downwind of the region where droplets first enountered the falling ice particles.

Two additional features of note in this cloud system were the descent region upwind of the crest evident near cloud top and the apparent convergence region in the flow between 3.0 and 3.5 km elevation near the crest. The convergence region was suggested by the very high ice particle concentrations and high reflectivity. This region corresponds to the location where forced descent from higher elevations (rapid net particle fall velocity) would converge with rising air from lower elevations (slow net particle vertical velocity).

4. DISCUSSION

Shallow orographic cloud systems over the Sierra Nevada can produce considerable precipitation near the crest of the mountain despite the clouds characteristic warm temperatures. This study provides new information concerning the precipitation growth processes that occur in such cloud systems. Of particular importance to the precipitation is the existence of an intersection region in the cloud where droplets advecting upward from cloud base encounter ice particles falling from cloud top. Within this region, secondary ice multiplication can occur and particle growth by diffusion, accretion and aggregation all occur rapidly. These processes lead to rapid development of precipitation particles and lead to more effective precipitation processes in the cloud system.

5. REFERENCES

Hallett J. and S.C. Mossop, 1974: The production of secondary ice particles during the riming process. *Nature, 249,* 26-28.

Huggins A.W. and A.R. Rodi, 1985: Physical response of convective clouds over the Sierra Nevada to seeding with dry ice. *J. Clim. Appl. Meteor., 24,* 1082-1098.

Marwitz, J.D., 1987: Deep orographic storms over the Sierra Nevada. Part II: The precipitation processes. *J.Atmos. Sci., 44,* 174-185.

Rauber, R. M., 1987: Characteristics of cloud ice and precipitation during wintertime storms over the mountains of northern Colorado. *J. Clim. Appl. Meteor., 26,* 488-524.

Reynolds D.W. and A.S. Dennis, 1986: A review of the Sierra Cooperative Pilot Project. *Bull. Amer. Meteor Soc., 67,* 513-523.

6. ACKNOWLEDGEMENTS

The author would like to thank all the participants of the SCPP program for their input to this research. Part of this research was conducted while the author was with Electronic Techniques Inc., under contract to the U.S. Bureau of Reclamation, Division of Atmospheric Water Resources Research.

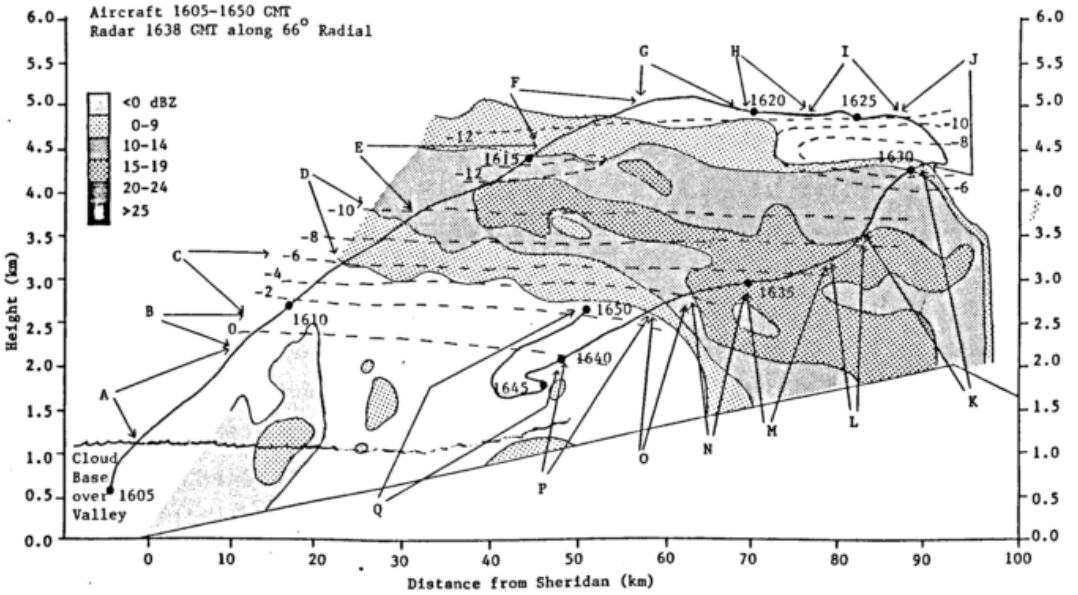


Fig. 1. Cross-section along 66° radial from radar site showing radar reflectivity, aircraft flight track, isotherms, terrain and cloud features. Points A-T denote microphysically distinct regions of the cloud.

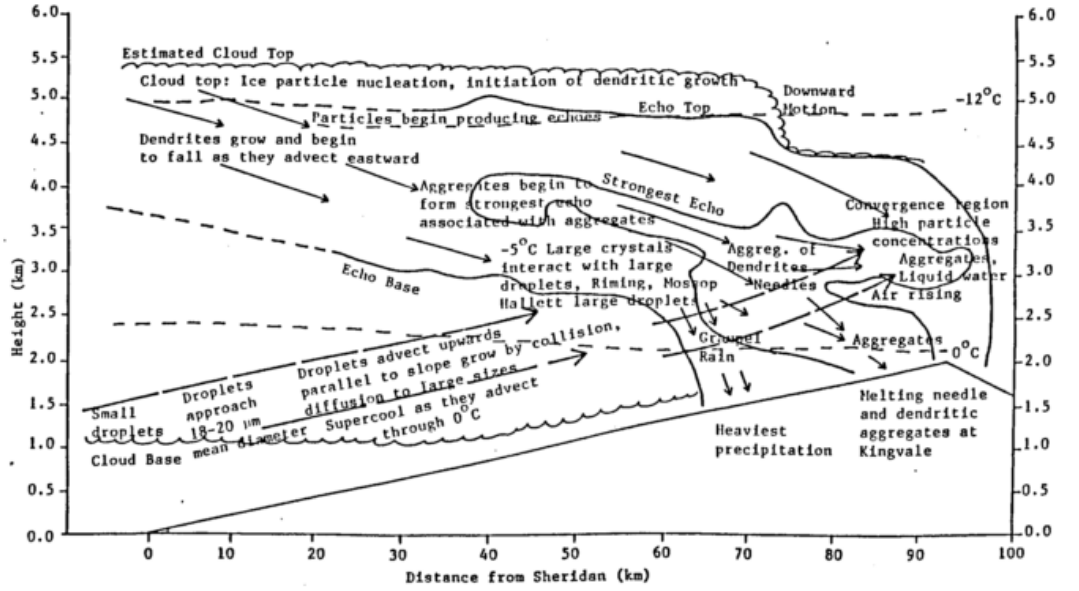


Fig. 2. Conceptual model of the microphysical processes occurring in the cloud system shown on Figure 1, based on aircraft measurements within the cloud system.

Comparison of Orographic Cloud and Precipitation Development of Three Different Geographic Locations Using a 3-D Nested Grid Cloud Model

Roy M. Rasmussen[1], P. Smolarkiewicz[2], W.D.Hall[2], and T.Clark[2]

[1]Bureau of Reclamation
Denver Federal Center
PO Box 25007
Denver CO

[2]National Center for Atmospheric Research
Boulder CO 80301

1. INTRODUCTION

A significant fraction of the world's useable water is created when moist air interacts with mountain barriers to form precipitation. In this study, we use the Clark (1977) three dimensional cloud model with interactive nesting (Clark and Farley,1984) to study in more detail the exact nature of this interaction at three different geographic locations. Precipitation development in the model is simulated using the Kessler (1969) formulation for warm rain, and the Koenig and Murray (1976) parameterization for ice phase precipitaion. This paper will consider precipitation formation over the island of Hawaii, USA, the Sierra Nevada mountains in California, USA, and over the mountains in the Northern part of Thailand.. These three orographic barriers represent a wide range of climates and physical situations. By using the nested grid version of Clark's model we are able to first establish the proper large scale flow field for each of the different terrain types, and then use the higher resolution inner models to focus on the details of the cloud and precipitation process in more localized regions.

2. PRECIPITATION OVER HAWAII

A numerical simulation of the airflow around the island of Hawaii was conducted for August 1, 1985 in order to determine the effect of a relatively simple large barrier(over 4 km high) on the development of precipitation over and close to the island. Details of this simulation are presented in Smolarkiewicz et. al. (1988ab)and Rasmussen et. al. (1988), Figure 1 shows horizontal flow vectors and contours of vertical velocity every 0.0625 m/s for the second nested model, which has 5.08 km horizontal resolution and 0.25 km vertical resolution. In Rasmussen et. al. we showed that the vertical velocity near cloud base (typically 0.5 km) was well correlated to the climatological patterns of precipitation. Significant updrafts are located at the Northern and Southern tips of the island, as well as just offshore the eastern portion of the island. Note, however the abscence of any significant updraft over the eastern side of the island, at least at this low level, despite the oncoming flow at this level being 10 m/s from the east-northeast. The reason for this behavior is that the island is so large that the oncoming air does not have enough kinetic energy to overcome the atmospheric stability and go over the obstacle. Rather, most of the flow goes around the obstacle, as evidenced from the horizontal wind vectors. As the air goes around the island, it encounters a small mountain range on the Northern end of the island, and a ridge near the Southern edge, which are evidently small enough for the air to go over and produce the lifting required to create clouds and precipitation(cloud and precipitation figure not shown). The air also has additional kinetic energy because of its acceleration around the island. The wind vectors show that the air speed has increased at both locations to nearly 15 m/s, which is 50% faster than the far offshore flow, increasing the kinetic energy by over a factor of two. The lower barrier and increased kinetic energy make it relatively easy for the air to go over, rather than around these barriers. Climatologically these two locations both produce nearly 400 cm of rain per year and are known for their high winds. Since the most common wind direction is from the east-northeast to the northeast, the above described behavior is a likely cause for the large amounts of precipitation at these locations. In order to quantify the above described behavior, consider the Froude number, which can be

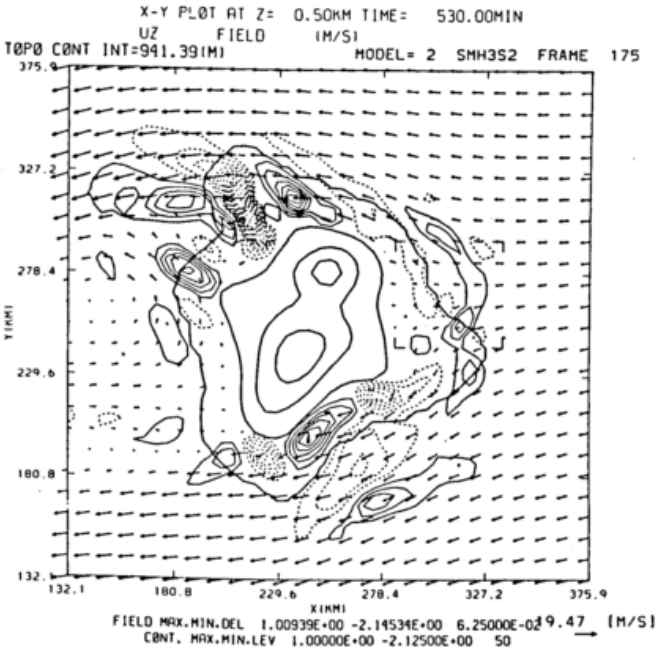


Figure 1

considered as the ratio of the kinetic energy of the oncoming air to the energy required to go over the obstacle:

$$Fr = U/(N \cdot H)$$

In this equation, U is the mean upstream wind speed, N is the Brunt-Vaisala frequency, and H is a characteristic height of the obstacle. Small Froude numbers (<<1.0) indicate that the air will more likely go around, rather than over an obstacle. For the entire island of Hawaii, the Froude number for a 10 m/s trade wind and typical Brunt-Vaisala frequency of 0.01 sec^{-1}, and island height of 4000m is 0.25, which is consistent with flow mostly going around, rather than over the island. The lower barriers to the North and South have a height of only 1500 meters, and the oncoming flow is 15 m/s, giving a Froude number of 1.0. Thus, the smaller mountains have a four times larger Froude number than the overall island, making it much more likely that air will go over these smaller barriers than around them.

Another important factor effecting cloud and precipitation development in the current simulation was solar heating. The physical time which figure 1 was meant to simulate was 7:50 a.m., at which time solar heating had just started. Solar heating has the effect of decreasing the stability of the air on the eastern side of the island, resulting in a local increase in the Froude number, and consequently more upslope flow. This results in the formation of an orographic cloud on the eastern slope by about 10:00 a.m. This cloud is limited in height by the prescence of a trade wind inversion typically 2-3 km above mean sea level. This inversion also has a strong influence on precipitation formation, since warm clouds require a depth of at least 2.0 km to from rain. Although the low level moist air may be forced upward, it may not form a deep enough cloud if a strong inversion is present capping the convection.

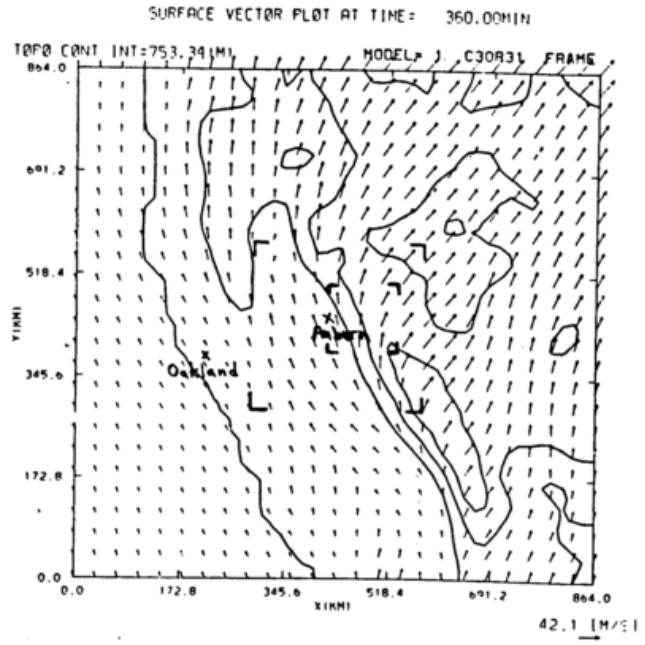


Figure 2

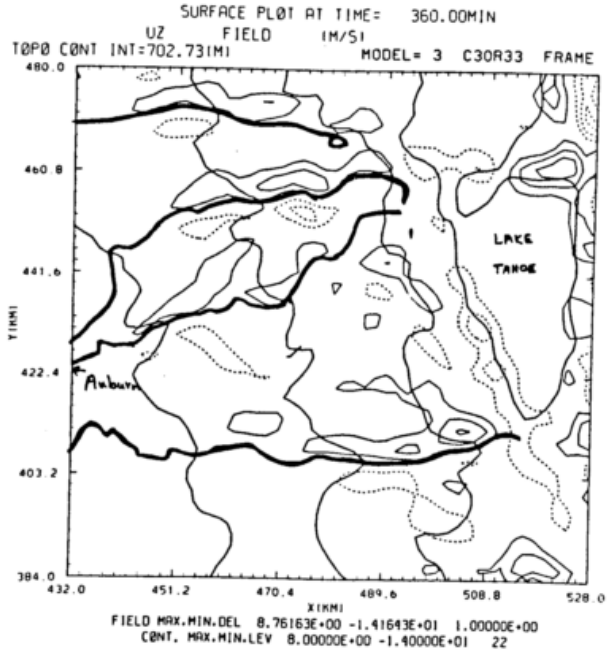


Figure 3

Another factor in the formation of precipitation over this island is the updraft band which forms just upstream of the eastern portion of the island. This band forms in response to the deceleration of the flow as it approaches a large barrier under the low Froude number flow regime, creating a region of low level convergence upstream of the island. Band clouds form over this low level convergence region,and in some cases they propogate onshore and produce over 50 minutes of continuous precipitation. In our companion paper in this conference (Smolarkiewicz et. al.(1988b), we discuss a numerical simulation of this long lived propogating band cloud, and show that its behavior is in many respects similar to a mini squall line.

Figure 1 also shows updrafts existing on the lee side of the island. These updrafts are a result of the onshore flow associated with a lee side vortex, evident just to the west of the island. Afternoon heating enhances the upslope component, and produces significant amounts of clouds and precipitation on the western side of the island.

The above results show some fundamental ways in which airflow interacts with a large relatively simple obstacle to produce clouds and precipitation. In the following we will apply some of these principles to investigate the formation of clouds and precipitation in the more complicated orographic situations of the Sierra Nevadas in California, and the mountains in Northern Thailand, giving only basic results due to the limitation of space.

3. SIERRA NEVADA MOUNTAINS, CALIFORNIA,

The Sierra Nevadas are a tall northwest to southwest oriented mountain range extending over 600 km. A numerical simulation was conducted for the synoptic conditions of February 12,1986, for which the main feature was a deep trough located off the coast of California. More detailed discussion of the synoptic and other conditions associated with this storm are given by Huggins et. al. (1986). The reason this storm was chosen was because of its weak time evolution, allowing the use of a single sounding for the simulation. An upstream sounding from Oakland,California was chosen to initialize the model. Three nested models were run, the outer model had 18 km horizontal resolution and 900 meters vertical, the second model had 6 km horizontal resolution and 450 meters vertical, and the third had 2 km horizontal resolution and 450 meter vertical. The outer model covered the entire state of California in order to establish the proper large scale flow, while the second and third models were centered over Auburn California, which was the headquarters for the Bureau of Reclamations Sierra Cooperative Pilot Project(SCPP). Figure 2 presents horizontal wind vectors averaged between the surface and 900 meters above the surface for a six hour run of the model including clouds and warm precipitation. The outer model was run for 2 hours, then the next inner model spawned and run together with the outer model for another 2 hours, and then finally the third inner model was spawned and run together with the other two models for another 2 hours. Also indicated are the relative locations of the three models, and the location of Oakland and Auburn California. The solid contours represent topography contours every 753 meters, with the leftmost line representing the coastline. South-southeasterly flow parallel to the 753 meter contour line closest to the coastline is evident almost the entire length of the barrier. This is in agreement with a sounding taken close to Auburn, and with climatology, which indicates that a barrier parallel flow develops when a cold front and/or an upper level trough approaches the mountains from the west (Waight(1984). The sounding showed the wind speed to be south-southeasterly at 20m/s at the 850mb(1.8km) pressure level, which is consistent with the wind speeds and directions predicted by the model at this pressure and location. The barrier parallel flow becomes stronger the further North along the barrier one goes. This airflow is in contrast to the airflow pattern shown in figure 1 for the island of Hawaii. In that case the air flow was defected both to the North and to the South of the barrier. In the California case, the airflow is deflected mainly in one direction, that is to the North. The cause of this deflection has been attributed to the Coriolis force acting on air which is accelerated away from the barrier due to the formation of an adverse pressure gradient by the adiabatic cooling of air lifted up the barrier(Marwitz,1983). The Froude number in the present case is more complicated to calculate than in the Hawaii case because the oncoming wind is not uniform over the height of the mountain. Taking the average wind speed at Oakland from the surface to the top of the barrier(4 km), we obtain an average wind speed of 15 m/s. Using a barrier height of 4000 meters and a Brunt-Vaisala frequency of 0.01, the Froude number is 0.38, which is relatively low, suggesting that a significant amount of the air flows around rather than over the barrier, as in the Hawaii case. The difference in the two cases, however, is that the Corolis force is much stronger in the California case, and the barrier is much longer, allowing time for the Coriolis force to be active. The barrier parallel flow also encounters ridges associated with river valleys

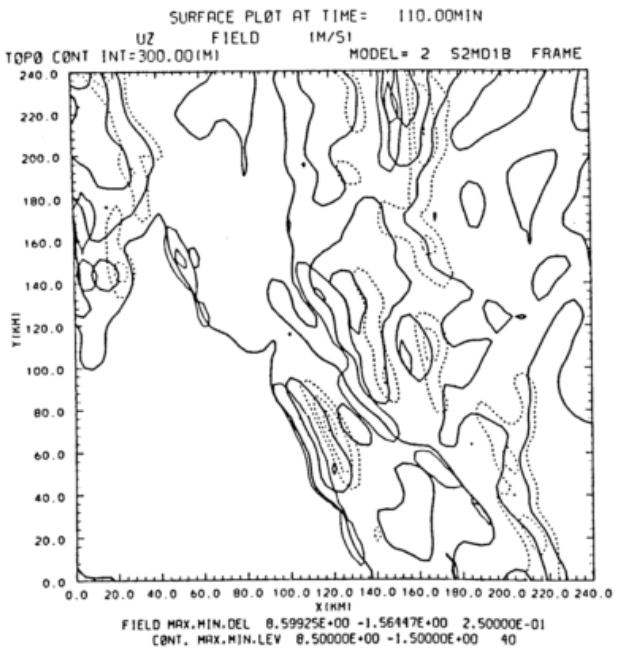


Figure 4

and updrafts form in response to the lifting of the air over these ridges, similar to the lifting over the smaller ridges in the Hawaii case. Figure 3 presents updraft contours every 1 m/s from the third inner model. The heavy superimposed lines represent the major rivers flowing down from the upper catchment area. The updraft regions are seen to occur just downwind of the rivers, consistent with the concept that updrafts are created by these smaller ridges as air flows over them(the horizontal flow in this figure is essentially from south to north). The Froude number is relatively large for flow over these ridges, and the air can easily go over, especially with the extra kinetic energy it has from the formation of a barrier jet.

Eventually the air flow in the California case has to go over the larger barrier, unlike the Hawaii case, and this occurs in the Northern part of the domain(figure 2). The barrier is lower in the North, and the flow stronger, resulting in a larger Froude number, and thus making it more probable that the flow will go over rather than around the barrier. This cross barrier flow results in strong lifting, and produces a high condensate supply rate resulting in the production of extensive clouds and precipitation at this location. Indeed, the climatological maximum of precipitation in California is located just in those regions where the up-valley flow is forced to go over the Northern part of the Sierra Nevada mountains, especially the area just south of Mt.Lassen and the area near Mt. Shasta.

3. CLOUDS OVER THE MOUNTAINS IN NORTHERN THAILAND

The mountains over Northern Thailand are relatively small compared to the mountains in Hawaii and California, with the tallest mountains reaching only 2.5 km above sea level. During the summer monsoon, the low level airflow is from the southwest, while the upper level flow is from the northeast. Two nested models were used to simulate the cloud and precipitation development on July 11,1982 using a far upwind sounding from the Andaman Islands, located 400 km upwind. The horizontal resolution used was 4 km, and 600 meters resolution in the vertical, and 4 km horizontal resolution and 300 meters vertical resolution for the second model.. The model was started at 7:00 a.m., and solar heating was simulated. The southwest corner of the model was located at 16.75 degrees north latitude, and 97 degrees east longitude. Figure 4 shows the model domain, with contours of average updraft speed betwwen the surface and 600 meters as the thin lines, and the topographic contours as the thicker lines. The air flow in this figure is from the southwest to the northwest. Note that the updrafts are located just upstream of the major ridges and downdrafts on the lee, consistent with the air going over, rather than around these relatively small ridges. The Froude number in this situation, using as average upstream velocity of 8.5 m/s, stability of $0.01s^{-1}$, and an average elevation of 1200 m, is 0.71. This relatively large value of Froude number makes it relatively likey that a large fraction of the flow goes over, rather than around these ridges.

4. CONCLUSIONS

Cloud and precipitation development has been investigated at three different geographic locations using a three dimensional nested cloud model. An important finding was that in many cases, the local Froude number could predict the likelyhood of precipitation at a particular locality because it gives a good indication as to whether air will go over or around an obstacle. If the air goes over an obstacle, significant lifting can occur, resulting in the formation of clouds and precipitation. If air goes around an obstacle, it is not significantly lifted, but does experience horizontal acceleration. If the flow then encounters smaller obstacles, it has a larger local Froude number, and a better probability of going over the obstacle and producing clouds and precipitation. In some cases, low Froude number flow was found to produce low level convergence regions upstream of obstacles that produced significant amounts of clouds and precipitation. Additional factors which were shown to be important to cloud and precipitation formation at these three locations were the strength of the solar heating,the height and strength of inversions, and the cloud base temperature. Obviously, any synoptic scale forcing will also effect the formation of precipitaion over these obstacles. For instance, large scale lifting will decrease the atmospheric stability, leading to a smaller Brunt-Vaisala frequency, and a larger Froude number, making it easier for the air to be lifted over the obstacle.

REFERENCES

Clark,T.L.,1977: A small scale dynamic model using a terrain-following coordinate transformation. *J. Comput. Phys.,24,186-215.*

Clark,T.L.and R.Farley,1984: Severe downslope windstorm calculations in two and three spatial dimensions using anelastic interactive grid nesting: A possible mechanism for Gustiness. *J. Atmos. Sci.,41,329-350.*

Huggins,A.W.,R.M.Rauber,T.F.Lee,A.P.Kuciauskas,G.L.Hemmer,C. J.Wilcox,R.D.Elliott,D.A.Griffith,J.A.Flueck,1986:*SCPP Meteorological and Statistical Support for Period 1 September 1985-31 August 1986.* Available from the U.S.Bureau of Reclamation,Division of Atmospheric Resources Research,Denver Federal Center, Denver, Colorado.

Kessler,E.,1969: On the distribution and continuity of water substance in atmospheric circulations. Meteor. Monogr., No. 32, Amer. Meteor. Soc.,84 pp.

Koenig,L.R. and F.W.Murray,1976: Ice-bearing cumulus cloud evolution: Numerical simulation and general comparison against observations. *J. Appl. Meteor. ,15, 747-762.*

Marwitz,J.D.,1983: The kinematics of orographic airflow during Sierra storms., *J. Atmos. Sci.,40,1218-1227.*

Rasmussen,R.M.,P.Smolarkiewicz, and J.Warner,1988:On the Dynamics of Hawaiian Cloud Bands: Cloud Scale Aspects.(in preparation).

Smolarkiewicz,P.,R.M.Rasmussen,and T.L.Clark,1988a:On the Dynamics of Hawaiian Cloud Bands:Island Forcing(Accepted for publication in JAS).

Smolarkiewicz,P.,R.M.Rasmussen,and T.L.Clark,1988b:Long Lived Hawaiian Rainbands,1988b:1988 Preprints of the 1988 Cloud Physics Conference,Bad Hamburg,Germany.

Waight,K.T.,1984:A numerical study of the Sierra Nevada barrier jet,Masters Thesis,University of Wyoming,Laramie,Wyoming.120 pp.

Microphysical Observations Over the Atlas Mountains in Morocco

Omar Baddour Meteorologie Nationale Division
de Developpement et de Recherche
- - Casablanca Royaume du Maroc

Roy M. Rasmussen Bureau of Reclamation - Denver,
Colorado, U.S.A.

I. Introduction

Morocco's climate is Mediterranean, with most of its precipitation occurring during the winter months as a result of frontal pass-ages. The High Atlas Mountains, which extend from the southwest end of the country to the northeast end, are a formidable barrier to the oncoming fronts, with peaks over 4 km elevation at some locations (fig. 1). Consequently, there is a significant enhancement of precipitation due to orography. In the current paper we present cloud physics data collected during the winter of 1985 by the University of North Dakota Citation II aircraft as part of the Al Ghait Snowpack Enhancement Programme in Morocco. The data were collected over the portion of the Atlas mountains 200 km southeast of Casablanca.

The goal of the present paper is to determine some of the natural precipitation processes active over the Atlas mountains. Two case studies during winter are presented. The focus is on SLW (supercooled liquid water), and ice crystals analysis for the 8 and 9th December, 1985.

II. December 8 and 9th Case Studies

A. Synoptic weather description:

The 1200 GMT surface analysis from December 7 to December 9, 1985 shows the passage of a cold front over Morocco.

1. December 8th

The 12 GMT sounding made at Beni Mellal weather station (located 80 km upwind of the crest line of the High Atlas mountains, see fig. 2a) and satellite photos show the passage of a cold front at this time. The airmass below 550 mb produced two stratiform cloud layers: The lower one was 2700 m thick with 7 °C as cloud base temperature (CBT) and -11 °C as cloud top temperature (CTT). The higher layer was thinner and separated from the lower layer by a relatively dry layer of about 500 m thickness. The CTT for the upper cloud layer was estimated to be -16 °C.

2. December 9th

A sequence of satellite picture for this day showed the penetration of a cold air mass from the northwest in the morning following the frontal passage. The 12 GMT sounding (fig. 2b) showed a saturated and relatively cold air mass below 600 mb associated with a stratiform layer and embedded convection. The CBT and CTT for these clouds were +2 °C and -17 °C respectively, from the Beni Mellal sounding. The northwest wind and subsidence at upper levels indicated an approaching ridge and the end of the storm. These two days experienced a typical winter air mass crossing Morocco from the western coast to the east, which generally produces significant rainfall over the plains and snowpack over the mountains.

*The Al Ghait Snowpack Enhancement Programme is currently running and using a Moroccan instrumented King Air for microphysical data collection.

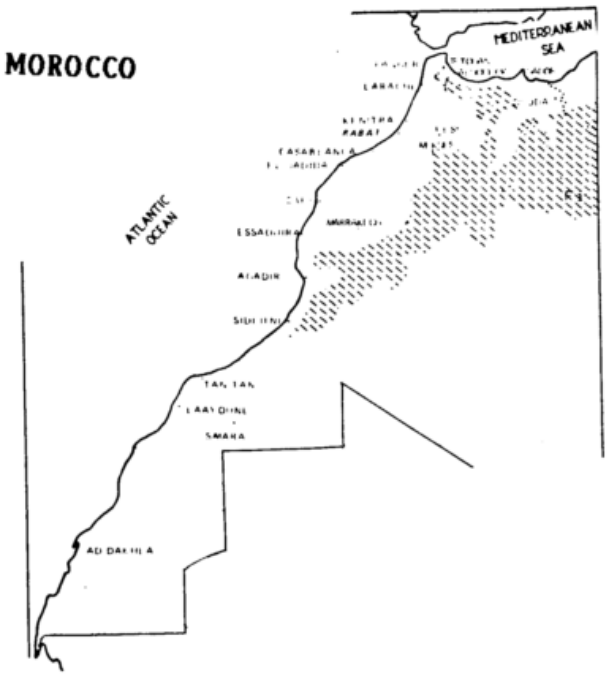


Figure 1 Map of Morocco

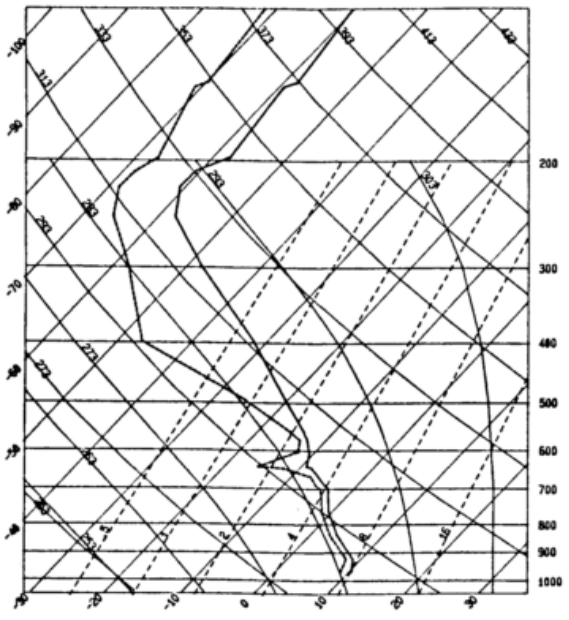


Figure 2a Beni Mellal sounding 12/8/85,12Z

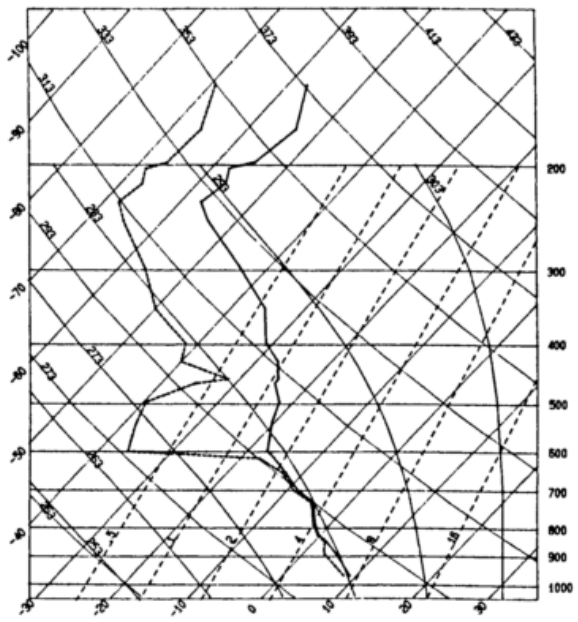


Figure 2b Beni Mellal sounding

12/9/85,12Z

B. Microphysical observations

1. December 8th

After taking a sounding the aircraft flew to the Atlas Mountains and made several penetrations near the top of the lower stratiform cloud at -11 °C. Low concentrations of aggregates consisting of dendritic crystals were observed in this region, with patches of LWC up to 0.3 g/m^3. These observations suggest that the upper layer was seeding the lower stratiform cloud. Later penetrations of stratiform clouds 25 km south-southwest of Beni Mellal over the lower portions of the Atlas mountains shows no significant concentrations of ice crystals near cloud top (-11 °C). The analysis shows a super cooled water band (0.2 gm^{-3} over 10 km of flight) lasting more than 10 minutes, which suggests the absence of an efficient depletion process, as observed in the previous penetration (see fig.3).

In the earlier afternoon convection was developing over the plains 60 km downwind of the coast. Data analysis from six successive penetrations through a developing cumulus shows sustained LWC of 3 gm^{-3}, which is near the adiabatic value (recalling that the estimated cloud base temperature was about +7 °C.) Drops as large as 500 microns diameter were evident at the -8 °C level near cloud top without any significant ice concentration or evidence of frozen drops. The high LWC lasted for more than 10 minutes despite the depletion of LWC by the large drops. The moderate updraft observed (3-4 ms^{-1}) and high LWC are consistent with a coalescence process.

2. December 9th

For this day the cloud system was post-frontal, with embedded convection in stratiform layers just upwind of the mountains. While the ice-phase growth of stellar and dendritic crystals and subsequent aggregation dominated the stratiform part of the clouds, the coalescence process followed in many cases by drop freezing and growth to graupel by riming governed the convective parts. In literature this mechanism has been called the CRG (coalescence-riming-graupel) process (Silverman, 1986; Braham, 1986). In embedded convective regions just upwind of the mountains, high LWC was encountered at the -10 °C level in regions of 4 to 6 ms^{-1} updraft. The 2D-C images in this region show the presence of large drops up to 800 microns diameter (fig. 4). Frozen drops coexisting with graupel particles were also evident in other penetrations. Figure 5 shows a penetration through a typical region of embedded convection, with aggregates of dendrites and stellars in the non-convective portions of the penetration, and more spherical graupel particles in the convective portions.

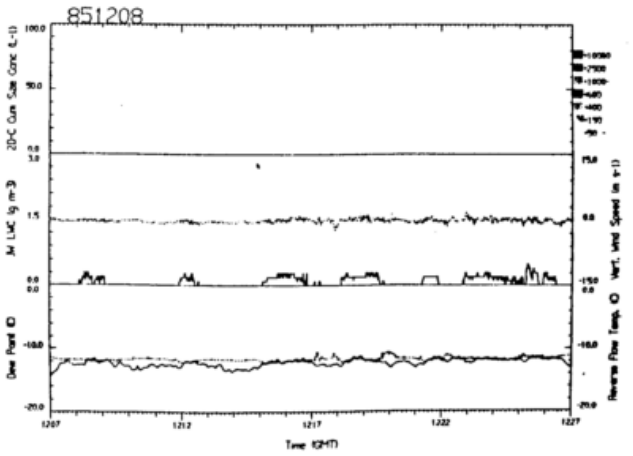


Figure 3 UND aircraft data

Discussion:

The clouds observed with the UND aircraft on December 8 and 9, 1985 represent a fairly typical winter storm event in Morocco. These types of storm systems leads to significant rainfall over the plains and snowpack over the mountains. The microphysical observations during the main frontal passage (Dec. 8) shows the presence of stratiform cloud layers, with an active seeder-feeder mechanism over the mountains. The seed crystals were aggregates of dendrites falling from an upper level cloud layer into a lower supercooled liquid water layer. The laboratory results of Lew et al. (1986) suggest that the riming of aggregates can lead to rapid growth by accretion, and may be an important process depleting low-level SLW in Morocco. In regions without an active seeder mechanism aloft, SLW (up to 0.3 gm^{-3}) regions were sustained without significant depletion for long periods of time. In the present case these regions occurred over the lower regions of the Atlas Mountains.

During the post frontal period of the storm (Dec. 9), stratocumulus clouds were penetrated by the UND aircraft just upwind of the mountains. In the stratiform regions of the cloud (cloud top near -13 °C), aggregates of dendrites and stellars were observed at -10 °C, suggesting an efficient primary nucleation process near cloud top in these clouds. In the convective portions of these clouds at -10 °C, drops, frozen drops, and spherical graupel were observed, suggesting an active coalescence process, followed by drop freezing and subsequent riming. High liquid water contents close to adiabatic were observed for significant periods of time in many of these clouds,

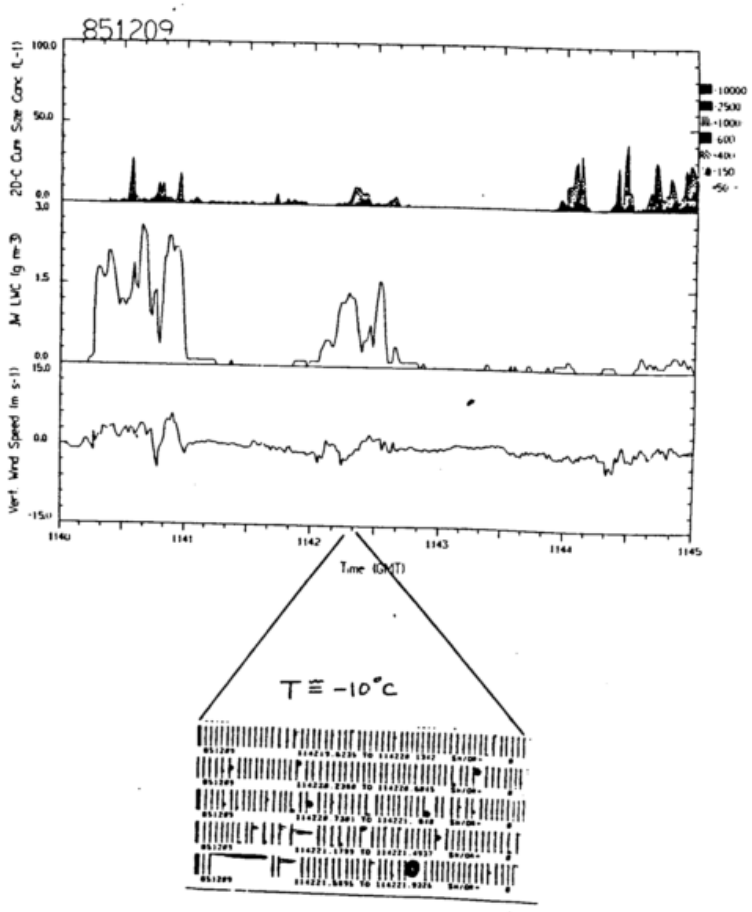


Figure 4 UND aircraft data and 2DC images

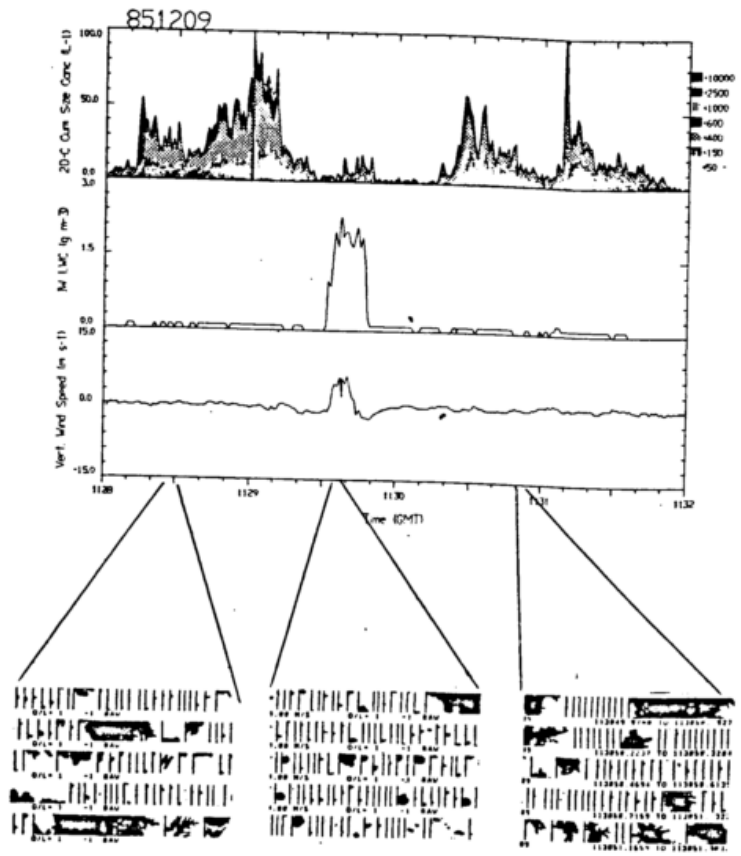


Figure 5 UND aircraft data and 2DC images

suggesting that depletion of LW by entrainment and growing ice particles was not very efficient. Updraft velocities were moderate (4-6 m/s), allowing the upward moving cloudy air sufficient time to develop drops by coalescence in these high LWC's. Despite the relatively cold cloud base temperature (+3 °C), the coalescence process was still active due to the nearly adiabatic cores.

V. Conclusions

The above observations represent only one wintertime storm in Morocco, and therefore caution must be taken in extrapolating to other winter storms. These results do, however, show a typical winter storm sequence, and reveal some of the basic cloud physics occurring.

During the frontal passage, a seeder-feeder type mechanism was active in the clouds over the Atlas mountains, with an upper level stratiform deck feeding aggregates of dendrites and stellars into a lower level supercooled cloud layer. Some regions of the system had lower cloud top heights, and and no upper level cloud to provide ice crystals, allowing for long-lived regions of supercooled liquid water. Post frontal stratocumulus clouds had an active coalescence process in convective regions, leading to drop freezing and subsequent riming. Aggregation of dendrites and stellars were observed in the stratiform regions.

Acknowledgments. The authors gratefully acknowledge the support of the U.S. agency for International Development for making this research possible. The data collection efforts by the UND (University of North Dakota) Citation crew are well appreciated. We also acknowledge the tireless efforts by Dr. David Matthews (resident scientific advisor in Morocco) to coordinate the data collection by the UND Citation in Morocco. We also acknowledge the steering committee of the Al Ghait Snowpack Enhancement Programme for their support of this study.

References.

Braham, R.R., 1986: The cloud physics of weather modification. Part I: Scientific basis. World Meteorological Organization Bulletin, 35, 215-221.

Lew, J.K., D.C. Montague, H.R. Pruppacher, and R.M. Rasmussen, 1986: A wind tunnel investigation on the riming of snowflakes. Part I: Porous disks and large stellars. J. Atmos. Sci., 43, 2392-2409.

Silverman, B.A., 1986: Static mode seeding of summer cumuli - a review, Precipitation Enhancement - A Scientific Challenge, Meteor. Monog., No. 21, Amer. Meteor. Soc., 7-24.

MICROPHYSICAL AND DYNAMICAL INTERACTIONS IN COLORADO FRONT RANGE UPSLOPE STORMS

Douglas A. Wesley, Michael J. Weissbluth, Roger A. Pielke, and William R. Cotton
Department of Atmospheric Science
Colorado State University
Fort Collins, Colorado 80523 USA

1. INTRODUCTION

Previous modeling and observational investigations of the physical processes operating in upslope cloud systems along the east slopes of the Rocky Mountains have shown that the microphysical and dynamical aspects are coupled to a broad extent (e.g., Weissbluth *et al.*, 1988 and Reinking and Boatman, 1986). Topographical and synoptic-scale influences frequently create low-level convergence zones associated with cold air damming (Dunn, 1987) as well as in-cloud regions of enhanced vertical motions associated with gravity waves (Weissbluth *et al.*, 1988). Such circulations can occur both in the shallow anticyclonic storm systems and the deeper cyclonic disturbances. Other mechanisms for snow production include supercooled water regions in the cloud enhancing the formation of precipitation-sized particles. Crystals reaching the ground along the Front Range during heavy snowfall are predominantly heavily rimed and usually exhibit dendritic growth, resulting in significant aggregation. The resulting snowfall distributions for most heavy events exhibit bands of enhanced precipitation extending onto the plains. These mechanisms are investigated using a combination of extensive observations and mesoscale model simulations of several winter storm events in the Front Range region.

2. OBSERVATIONS

During the winters of 1986-87 and 1987-88, researchers at Colorado State University have conducted an extensive observational program to isolate the important physical processes occurring in upslope storms along the Front Range. This has included a network of spotters providing microphysical information about the snowfall, as well as various synoptic and mesoscale data provided by standard radiosonde releases at the National Weather Service in Denver, the PROFS Mesonet, the NCAR CP-2 Doppler radar in Boulder, and special soundings in the Fort Collins area using the CLASS system provided by the ONR. Preliminary results have uncovered many interesting aspects of these storms relating to their tendency to produce localized regions of very heavy snow.

The presence of cold air damming is common during these storms. Fig. 1 is a temperature, wind and moisture profile for the Fort Collins area during the upslope storm of February 9-10, 1988, which produced more than 22 cm of snow just to the west of the city. Moderate snow, in the form of heavily-rimed spatial dendrites, was falling as the radiosonde was launched, and more than 20 cm of snow had already fallen. Cloud base was visually observed at approximately 790 mb, or 550 m above the ground. As shown, a strong cold pool was present near the ground in response to the passage of an arctic cold front during the previous evening. The depth of the cold pool at this time was approximately 65 mb, or about 600 m. This cold pool has formed in response to the blocking effects of the 2 km high Rocky Mountain barrier to the west. Since cloud base was apparently located just above the top of the cold pool, and heavily-rimed spatial dendrites were the primary crystal habit observed at the ground, it is probable that ice crystals produced above the cold pool (in the near-saturated layer to about 500 mb) fell through layers of supercooled water in and above the strong inversion at the top of the cold pool (where temperatures range from about -10° to -20° C), and continued to grow (via the dendritic habit) in the relatively moist cold pool, where temperatures were -13° to -14° C). Such a seeder-feeder type process may be very important in these types of storms for the production of precipitation-sized particles.

The deflection by the barrier, along with the extremely stable conditions at the top of the cold pool, produced relatively strong meridional flow in the surface wind direction along the Front Range during this storm, as shown in Fig. 2. The post-frontal easterlies are blocked by the topography and cannot rise due to the stable lower troposphere; hence south-southeasterlies existed along the northwestern portion of the mesonet (the geostrophic flow was from the east-southeast). In Figs. 3 and 4 are two more cases of blocking-induced convergence during upslope precipitation events. In the first case (Fig. 3), moderate to heavy rain and snow showers were occurring along the northern portion of the blocking-induced convergence line outlined in heavy black. For the case of Fig. 4, this convergence is again most pronounced along a line roughly from the western suburbs of Denver to just east of Fort Collins; heavy snow was occurring in Fort Collins at this time and a total of about 20 cm fell. These flow characteristics are analogous to those reported by Dunn (1987) for the heavy snowstorm of December 8-9, 1985 along the Colorado Front Range.

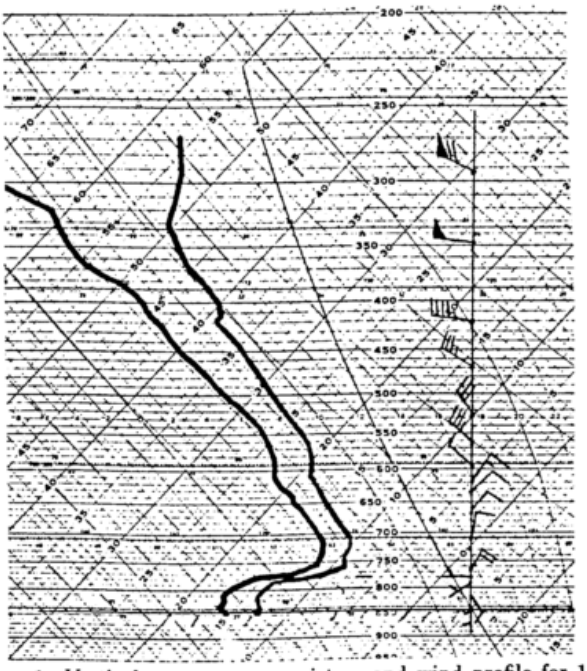


Figure 1: Vertical temperature, moisture and wind profile for 1454 GMT, 10 February 1988. One wind barb equals 10 knots.

3. MODEL DESCRIPTION

In order to numerically investigate the physical processes occurring in the upslope events, the Colorado State University RAMS (Regional Atmospheric Modeling System) is being utilized (see Cotton *et al.*, 1982 and Tripoli and Cotton, 1982). The version used here (see also Weissbluth *et al.*, 1988) employs the non-hydrostatic primitive equations expressed in a terrain-following coordinate system. Rain and graupel are predicted by allowing condensation of water vapor into both the liquid and ice phases. The surface layer energy balance is achieved by the method presented by Mahrer and Pielke (1977). The lateral boundary conditions are the radiative boundary conditions introduced by Klemp and Lilly (1978) with a mesoscale compensation region (Tripoli and Cotton, 1982).

The model domain and topography are identical to that of Weissbluth *et al.*, (1988), except that cyclic conditions are not employed meridionally. The domain size is approximately 1000 km by 600 km by 18 km, with a constant horizontal grid spacing of 14 km and a stretched vertical grid of resolution 500 m near the ground increasing to a constant 1.5 km aloft.

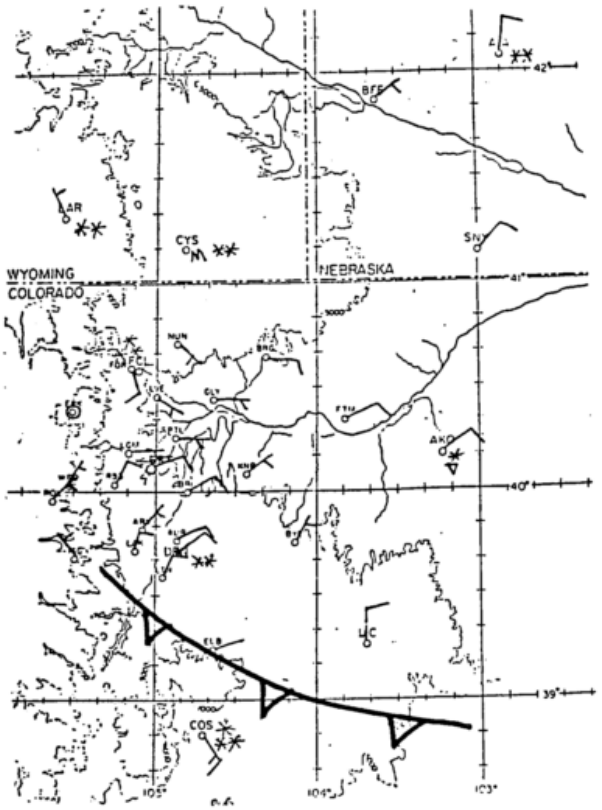


Figure 2: Surface observations for the PROFS Mesonet and surrounding NWS reporting stations; 1500 GMT 10 February 1988. One wind barb equals 10 knots. Cold front shown in southern portion of Mesonet. Terrain contours are shown.

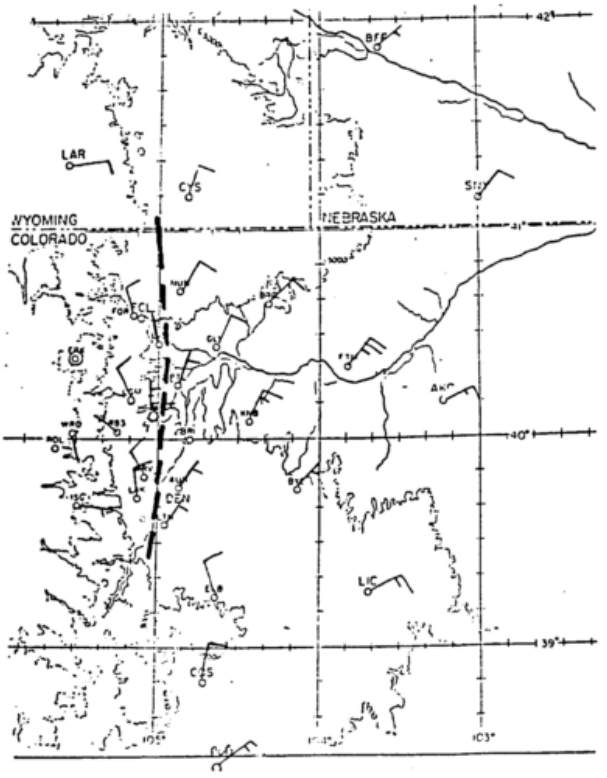


Figure 3: As in Figure 2 except for 0300 GMT 2 March 1988. Thick dashed line indicates location of convergence line mentioned in text.

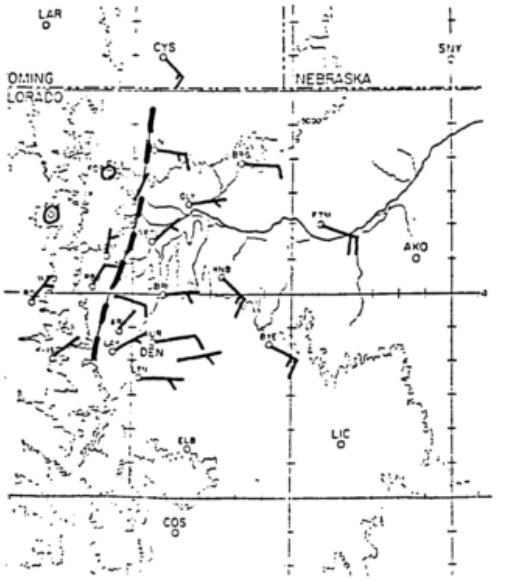


Figure 4: As in Figure 2 except for 1200 GMT 16 March 1987.

The initialization of the model is horizontally homogeneous. The input sounding is shown in Fig. 5. The sounding represents a typical situation for the Front Range during an upslope storm, with low-level easterlies veering to the southwest aloft and a moist lower troposphere. The atmosphere is absolutely stable and thus may induce cold air damming. The model was run without the computationally expensive ice phase for the first two hours and with the ice phase thereafter.

4. MODEL RESULTS

This section discusses preliminary results of the initial model simulation of the upslope flow. Fig. 6 presents the vertical motion field at 2.5h of simulation for an x-z cross section at a latitude just north of the Denver area. A significant region of cloud has developed at and east of the crest in the low levels. The strongest upward vertical motion (~12 cm/s) is immediately above the steepest topography on the east slope. A significant secondary maximum in the w field is located east of the barrier at about 1.5 km above the ground in the eastern portions of the cloud. This is apparently caused by transient disturbances forming in response to the easterlies impinging on the barrier (see Weissbluth *et al.*, 1988, Pierrehumbert and Wyman, 1985). These are observed to propagate upstream and weaken. During some upslope events, snow bands oriented north to south are observed to do the same. As shown by the model cloud extent and the ice mixing ratio field at 2.5h (Fig. 6b), these disturbances are enhancing the formation of the ice phase, and thus could have an impact on the formation of snow over the plains.

Fig. 7 shows the same fields for a different x-z cross section approximately 90 km south of the Denver area. The transient disturbance is weaker, but evident in the form of upward motion above the more gen-

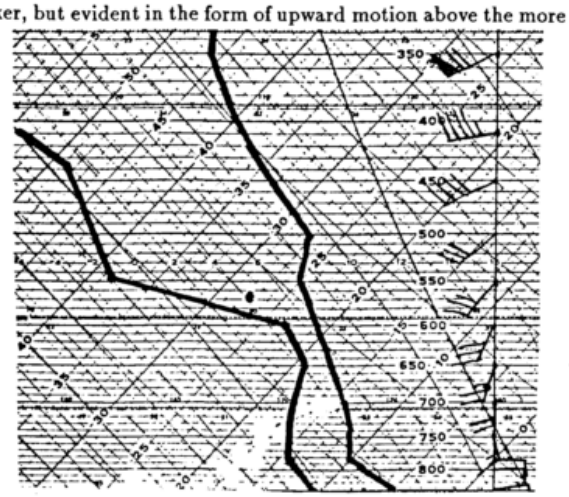


Figure 5: Model input sounding. One wind barb equals 5 m/s.

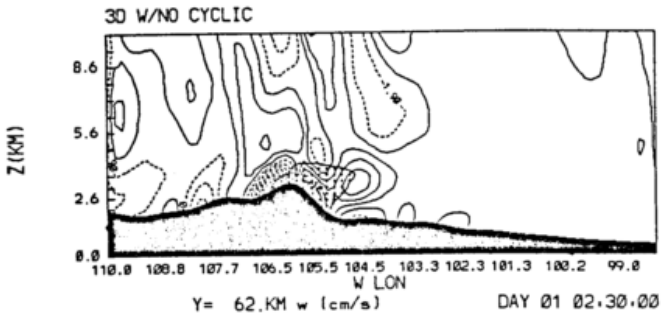


Figure 6a: Vertical motion field after two and one-half hours of simulation. Cloud area is marked with dots. Contour interval is 2 cm/s.

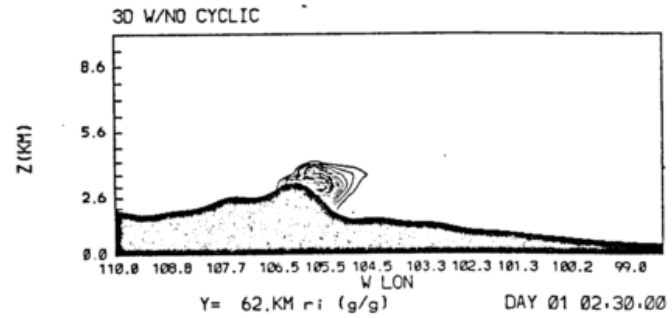


Figure 6b: Pristine ice crystal mixing ratio after two and one-half hours of simulation. Contour interval is 0.008 g/kg.

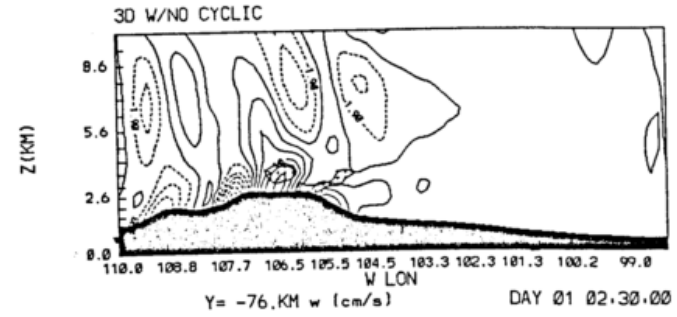


Figure 7a: As in Figure 6a except for cross-section location, which is 138km south of that of Figure 6a.

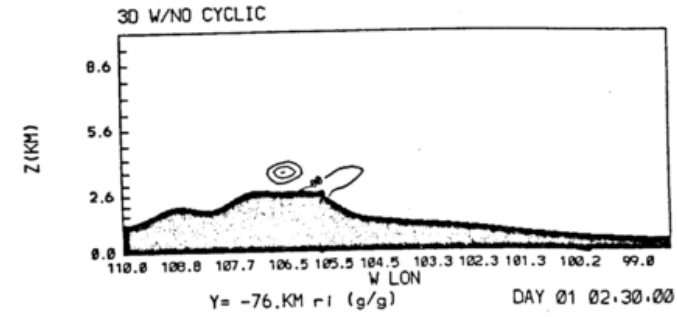


Figure 7b: As in Figure 6b except for cross-section location, which coincides with that of Figure 7a.

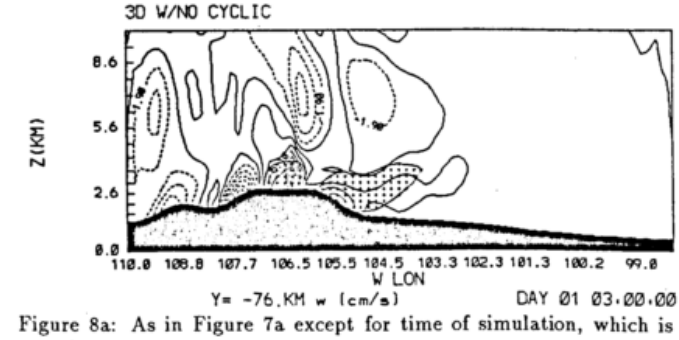


Figure 8a: As in Figure 7a except for time of simulation, which is three hours.

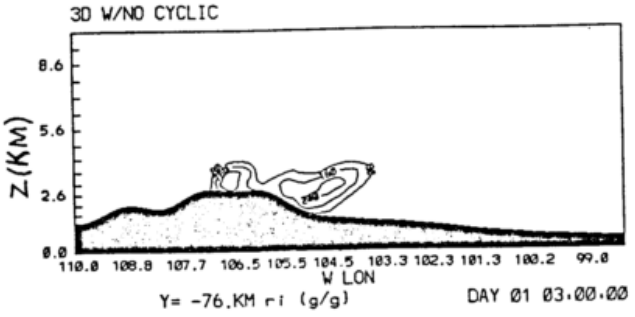


Figure 8b: As in Figure 7b except for time of simulation, which is three hours.

tle slope just east of the barrier. The appearance of the disturbance, however, is distinctly different than that of Fig. 6 due to the marked difference in the east slope topography for this latitude. At 3h (Fig. 8), again the cloud has grown eastward significantly over the plains and appears to have responded to the eastward-propagating transient disturbance. Strong upward motion remains over the steepest east slope as well as at the top of the barrier.

5. SUMMARY

This ongoing investigation combines an observational program with mesoscale model simulations to assess the various physical processes which control microphysical and dynamical interactions in upslope snowstorms. Evidence and interaction of the roles of cold air damming, transient internal gravity wave disturbances, and seeder-feeder processes are the current emphases. Current and future simulations will attempt to isolate these phenomena and assess their relative importance in the formation of snowfall along the Front Range.

Acknowledgements

Special CLASS sounding facilities provided by the Office of Naval Research under contract N00014-87-K-02281/P00001. Mr. John Kleist and Mr. Jim Wirshborn provided assistance with the observational program. Ms. Dallas McDonald and Ms. Brenda Thompson are thanked for drafting the manuscript. This research was supported by the Army Research Office under contract #DAAL03-86-K-0175. Computations were performed at the National Center for Atmospheric Research (NCAR). NCAR is sponsored by the National Science Foundation.

References

Cotton, W.R., Stephens, M.A., Nehrkorn, T., and Tripoli, G.J., 1982: The Colorado State University three-dimensional cloud mesoscale model - 1982. Part II: An ice phase parameterization. *J. Rech. Atmos.*, **16**, 295-320.

Dunn, L., 1987: Cold air damming by the Front Range of the Colorado Rockies and its relationship to locally heavy snows. *Wea. Forecasting*, **2**, 177-189.

Klemp, J.B. and Lilly, D.K., 1978: Numerical simulation of hydrostatic mountain waves. *J. Atmos. Sci.*, **35**, 78-107.

Mahrer, Y. and Pielke, R.A., 1977: The effects of topography on the sea and land breezes in a two-dimensional numerical model. *Mon. Wea. Rev.*, **105**, 1151-1162.

Pierrehumbert, R.T. and Wyman, B., 1985: Upstream effects of mesoscale mountains. *J. Atmos. Sci.*, **42**, 977-1003.

Reinking, R.F. and Boatman, J.F., 1986: Upslope precipitation events. Chapter 19 in *Mesoscale Meteorology and Forecasting*. Ed. P.S. Ray, AMS, Boston, MA, 437-471.

Tripoli, G.J. and Cotton, W.R., 1982: The Colorado State University three-dimensional cloud/mesoscale model, 1982. Part I: General theoretical framework and sensitivity experiments. *J. Rech. Atmos.*, **16**, 185-219.

Weissbluth, M.J., Wesley, D.A., Pielke, R.A. and Cotton, W.R., 1988: A numerical simulation of possible mechanisms contributing to Front Range snowfall disparity. Submitted to *Mon. Wea. Rev.*, March 1988.

CHARACTERISTICS OF RADAR ECHO OF SNOW BAND FORMED IN THE LEE SIDE OF A MOUNTAIN

Yasushi Fujiyoshi, Tatsuo Endoh and Gorow Wakahama
Institute of Low Temperature Science, Hokkaido Univ., Sapporo

1. INTRODUCTION

It is widely recognized that vortex-streets develop in the lee of an island and often persist several hundered kilometers(Bowley et al. 1962; Chopra and Hubert 1965; Lyons and Fujita 1968). Studies on vortex-streets have been concentrated on vortex pairs similar to the Kármán vortex-street. However, non-wavy or weakly wavy cloud bands also develop in the lee of an island. As the analysis of cloud bands have been based mainly on satellite photographs, the size, structure and movement of convective clouds composing these cloud bands are unclear until now.

Under the existence of strong temperature inversion over the Sea of Japan, cloud bands are often formed in the lee of mountains. An example of cloud bands is shown in Fig.1, which is taken by LANDSAT at 9h (JST) on 12 Jan., 1987.

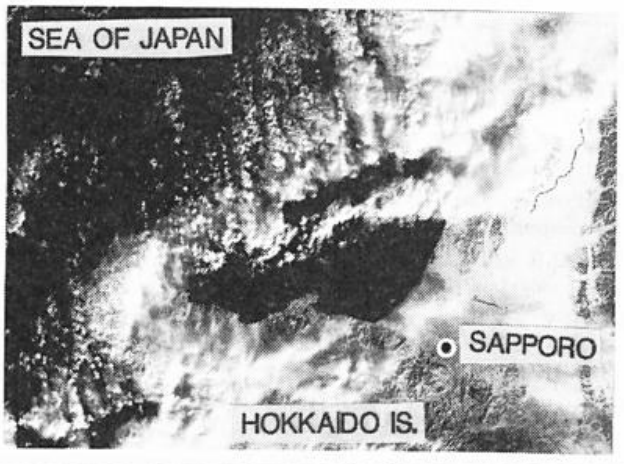


Fig.1: An example of cloud bands formed in the lee of a mountain.

Especially on 26 Dec., 1986, snow bands observed at Sapporo by a single Doppler radar with 3.2 cm in wavelength changed their echo patterns from non-wavy to wavy in a few hours. In this paper we will report the difference in radar echo structure of these cloud bands.

2. IDENTIFICATION OF A TRIGGERED MOUNTAIN

Figure 2 shows map around the observation area and direction of echo cells at typical periods of time. Dotted and solid lines indicate the direction of snow bands. Echo cells moves almost the same direction with that of snow bands.

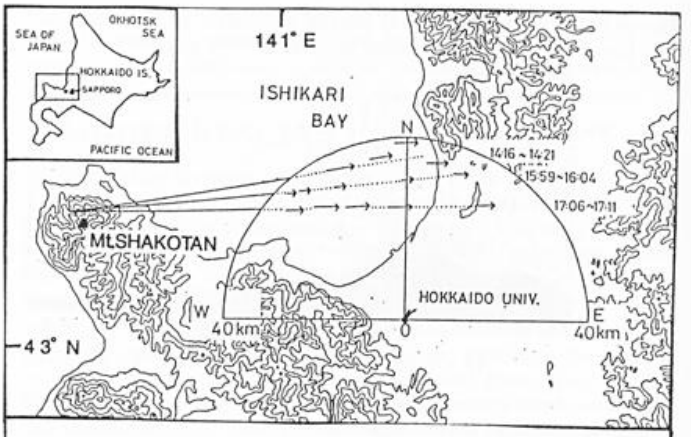


Fig.2: Map around the observation area and direction of snow bands and echo cells.

This figure suggests that snow bands would be formed at the same point, that is, at the north slope of Mt. Shakotan. The height of the point is about 700m. Maximum cross stream dimension of the mountain at this level is 13.5 km. Upper air sounding made at 8:30 JST shows that the temperature inversion existed at the level of 1750 m which is well above the level of summit of the mountain (1255 m).

3. TYPICAL RADAR ECHO PATTERNS OF CLOUD BANDS

Radar echo pattern of the cloud band changed with time in a few hours;

(a)Wavy pattern (14:47-15:13 JST) (Fig.3a)
(b)Non-wavy pattern (15:28-16:04 JST) (Fig.3b)
(c)Weakly wavy pattern (16:56-17:22 JST) (Fig.3c).

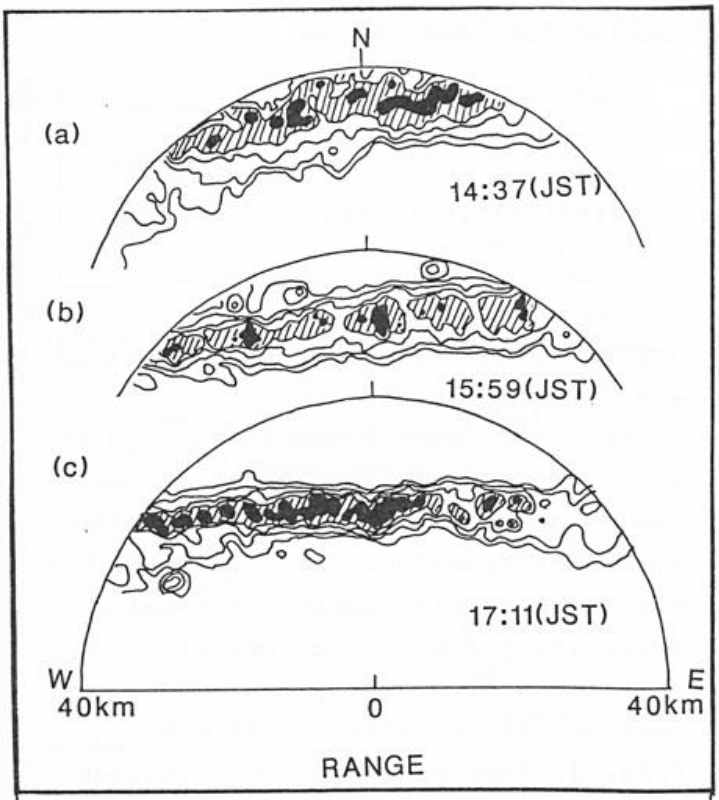


Fig.3: PPI radar echoes which show (a)wavy, (b)non-wavy and (c)weakly wavy patterns.

Table 1 summarizes averaged direction (D) and velocity (U) of echo cells, wavelength (L), amplitude (A) and frequency (T=L/U) of snow bands and Reynold's number (Re=Ud/ν); we assume $\nu = 2 \times 10^{3}$ m^{2}/s and d=13.5 km).

	D(°)	U(m/s)	L(km)	A(km)	T(min.)	Re
(a)Wavy	261	18.1	12.4	3.1	11	122
(b)Non-wavy	264	9.8	9.7*	0	17	66
(c)Weakly wavy	268	14.6	15.4	1.5	18	99

Table1:Characteristic properties of three types of radar echoes.
*Wavelength of the non-wavy snow band is defined as the distance between the large echoes.

As is expected, the snow band bacomes wavy with increase in Reynold's number. We would like to emphasis that radar echo structure is different from each other. The weakly wavy snow band (c) is composed of many small but intense convective echoes. The non-wavy snow band (b) is composed of large and small number of echoes. The wavy snow band (a) has the widest echo area and intermediate features of echo cells.

Figure 4 shows the frequency distribution of radar echo intensity in snow bands. It is found that the frequency of intense echoes is the highest in the weakly wavy snow band, and that of weak echoes is the highest in the non-wavy snow band. The wavy snow band is composed of echo cells with medium intensity. In other words, heavy snowfall tends to concentrate into a small area when the weakly wavy snow band is formed. Snow with medium intensity falls wider area when the wavy snow band is formed. Time change in snowfall intensity is large when the non-wavy snow band is formed.

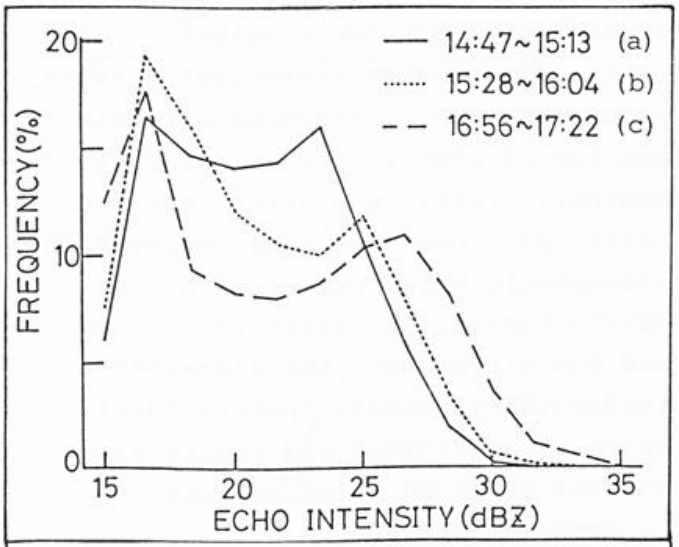


Fig.4: Frequency distribution of radar echo intensity in three kinds of snow bands.

REFERENCES

Bowley, C.J.; Glaser, A.H.; Newcomb, R.J.; Wexler, R.: Satellite observations of wake formation beneath an inversion. J. Atmos. Sci., 19,52-55.

Chopra, K.P.; Hubert, L.F.: Mesoscale eddies in wake of islands. J.Atmos.Sci.,22,652-657.

Lyons, W.A.; Fujita, T.: Mesoscale motions in oceanic stratus as revealed by satellite data. Mon.Wea.Rev.,96,304-314.

STUDY ON CLOUD AND RAIN BY MICROWAVE RADIOMETER OBSERVATION

Zhao Bolin

Department of Geophysics,Peking University,Beijing,

1.The atmosphere is known to be a source of heat noise,to derive the atmospheric properties from remote sensing of microwave radiation is a hopeful method of atmospheric exploration. By means of ground based reception of atmospheric emission constituted mainly by oxygen,water vapor, cloud and rain,we can make a remote sensing of atmospheric temperature-humidity profile and obtain the parameters of cloud and rain. By using atmospheric noise reception of 5mm oxygen band,1.35cm water vapor band and 8mm window band,the atmospheric temperature-humidity profile,total water vapor content and liquid water content of cloud in cloudy sky can be derived.

A set of microwave radiometers from 5mm-3cm waveband of 5 frequencies (9.37,22.235,35.3,52.9 and 54.5GHz) used in meteorology have been developed.

Table 1. Microwave Radiometer

wavelength	frequency	aim
5mm	52.9GHz	temperature (<10km)
5mm	54.5GHz	temperature (< 3km)
1.35cm	22.235GHz	humidity
8mm	35.3GHz	cloud
3cm	9.37GHz	rain

2.The experiments of remote sensing were carried out at Peking University, Beijing,with 5mm-1.35cm band 4 channel radiometers. In this note we present and discuss the experimental results from 8mm and 1.35cm radiometers of remote sensing atmospheric water vapor content,liquid water content of cloud and the process of rain.

The water vapor content and liquid water content of cloud could be derived by means of 1.35cm and 8mm radiometers observation. The results of microwave remote sensing of total water vapor content in comparison with those obtained by radiosonde,the mean deviation between them $<7\%$. (Fig.1). Some cases of precipitation process of Cu-cloud and St-cloud have been studied with microwave radiometer observation. Monitoring the precipitation process of cloud layer continuously. Before rain begin,the total water vapor content and liquid water of cloud increase rapidly. The microwave radiometers can be used to monitor changes and provides some information for nowcasting.(Fig.2).

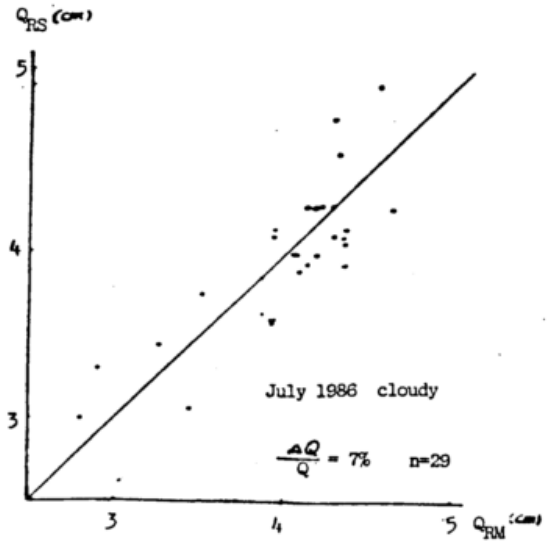


Fig.1.

Total water vapor content obtained by microwave radiometers Q_{RM} in comparison with the results obtained by radiosonde Q_{RS} (in cloudy)

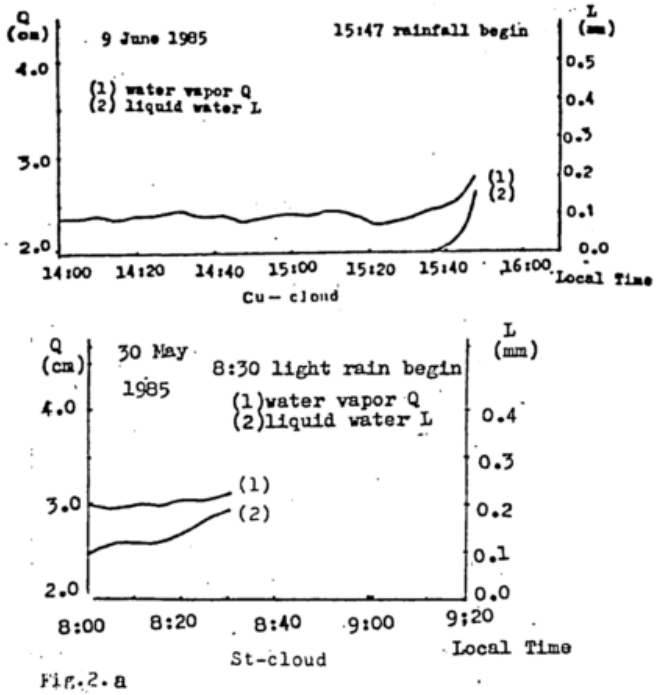


Fig.2.a

The variation of total water vapor content and liquid water content of cloud

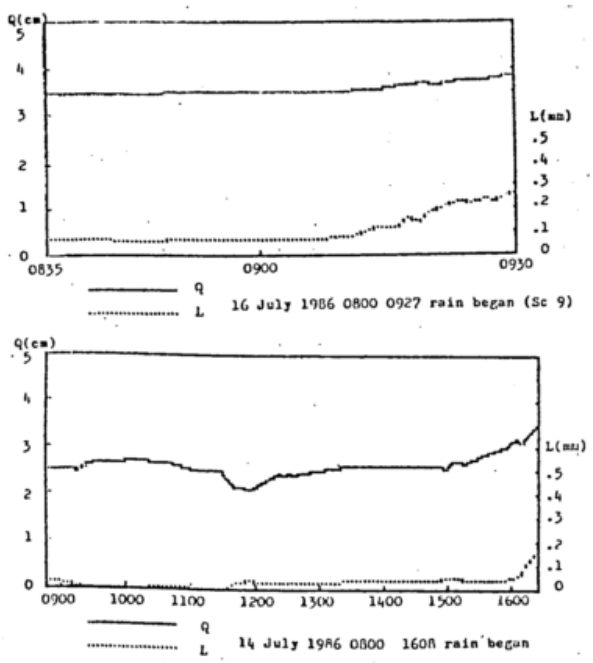


Fig.2.b

The variation of total water vapor content and liquid water content of cloud

3.The measurement of rain intensity by microwave radiometer combined with radar has been stdied. The errors of rain intensity measurement are mainly caused by instability of radar constant and uncertainty of raindrop spectrum. Radar-radiometer system has both good for space resolution and for accuracy of rain intensity measurements. The rain emission,measured by radiometer is used to correct the radar constant instability and the influence of raindrop spectrum uncertainty.

The developed 3cm radiometer has been combined with the chinese built 3cm radar to detect the distribution of rain intensity,which can be improve the precision.(Fig.3). The results of rain intensity measured by radar-radiometer in comparison with those obtained by raingauge,the mean deviation between them is 25%. The rainfall variation on Miyun Reservior area,Beijing was observed.

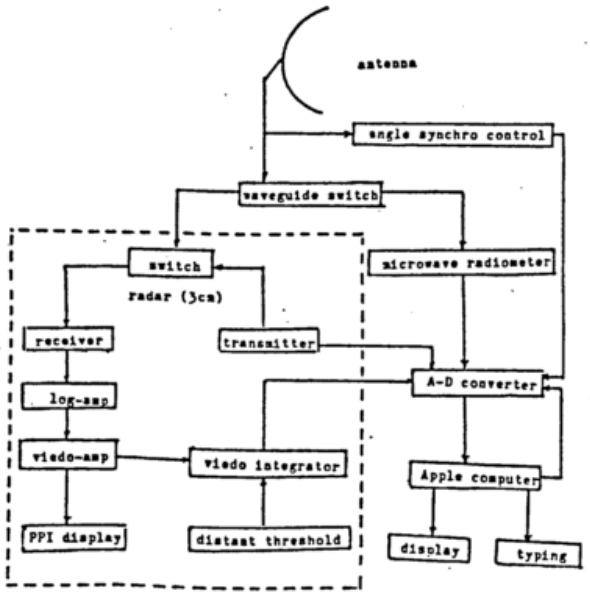


Fig. 3. The block diagram of radiometer-radar

A NEW DROPSONDE FOR CLOUD PROBINGS

Dimiter Gaytandjiev

Institute of Hydrology and Meteorology,
Hydrometeorological Service, blvd.Lenin 66,
Sofia - 1184, Bulgaria

1. INTRODUCTION

At present, the aircraft methods are mostly used for direct measurements inside the clouds. However, laboratory aircraft flights are an expensive solution and even impossible to be carried out in some mature convective clouds. For the purpose of the analysis, in particular of the processes in convective clouds, it is often more useful to know the vertical profile of an atmosphere parameter, instead of its distribution along an aircraft trajectory.

Considering these problems and the observations of clouds, provided by the Bulgarian Meteorological facilities under some hail suppression and precipitation enhancement projects, a new dropsonde has been designed for measuring the air temperature, liquid water content (LWC) and airflow velocity in different types of clouds.

2. DROPSONDE LAUNCHING AND TRACKING

The sonde is designed for measurements along only its descent trajectory, after having been carried aloft in the cloud. After carrier separation (from a balloon, aircraft or a modified anti-hail rocket) the appr. 1 kg weight sonde is dropped inside the cloud and carried downwards by means of a specially designed parachute with a relative-to-ambient air fallspeed varying from 25 m/s at altitude 9 km to 16 m/s at SL.

A standard MARS-type transmitter is used in the dropsonde for tracking by an ordinary, 1782 MHz METEORITE-2 aerological radar. The signals from the air temperature and LWC transducers are telemetered to the ground via such radar channel. The subsequence positions of the dropsonde are registered once per every 5 s on the basis of a transponder method.

3. AIR TEMPERATURE MEASUREMENT

The provided analysis has shown that the thermometer inertia and the cloud water phase transitions on its surface introduce the main inaccuracy in the temperature measurements with the dropsonde and the sensor has been designed to decrease their influence.

A reverse airflow temperature probe has been used in the dropsonde. The efficiency of such devices for separation of the large droplets is rather good. An additional oil protection has been used to avoid the influence of sensors wetting by smaller cloud droplets.

By an estimation of the temperature difference (inertia error) between sonde readings and cloud air medium temperature has been pointed out that, if the time constant of the dropsonde thermometer is about 0,3 - 0,5 s, this error doesn't exceed the values, required by the WMO for the aerological temperature measurement accuracy.

4. AIRFLOW VELOCITY DETERMINATION

The determination of the wind vector is done by tracking with an ordinary radar system, available in Bulgaria, to simplify the sonde construction, as well

as to reduce its size and total mass, unlike the Bushnell et al.(1973) system, especially designed for similar purposes.

The airflow velocity correct measurement is possible, when the following requirements for the sonde-parachute system are met :
- constant parachute frontal (side) air drag along the sonde total trajectory;
- no parachute side slip;
- stability of the parachute-sonde system, i.e. rapidly restored equilibrium after swinging;
- negligible changes of the sonde total mass due to wetting or icing.

The dropsonde parachute has been designed with a "disk-gap-band" canopy, strained on a retractable plastic carcass, the last being connected "rigidly" with the sonde body. The power supply and the radiotelemetric unit are placed in the lowest part of the sonde body to acquire the lowest center of gravity. All stream-lined surfaces of the parachute and the sonde are covered with a hydrophobe material. In addition, antifreezing measures have been taken to protect the surfaces, subject to the most intensive depositing and water icing.

5. LWC MEASUREMENT

The basic construction of the proto - type-dropsonde LWC measuring device, based on a variation of the "hot-wire" method, is shown on Fig.1(Gaytandjiev, 1980).It contains two identical, electrically equally heated and equally ventilated collectors 1 and 2, made of profiled kanthal band, with an exposure width 0.6 mm. On each collector an area thermometer 3 is cemented. Both collectors are energized by a 3 V-12 Ah silver-zink battery 11. The open collector 1 is mounted on a collapsible bracket 5 and evaporates the water elements, collected by its surface. The screened collector 2 is located in the screen 4. The airflow around collector 2 is caused by the Venturi tube 6 suction effect through the hole 7. The cloud elements in airflow inside the screen 4 are inertially separated through the inlet hole 10. The measuring transducer 8 transforms the collectors temperature difference $T'_к - T_к$, which is transmitted via radar channel. The whole device is mounted rigidly on the parachute 9.

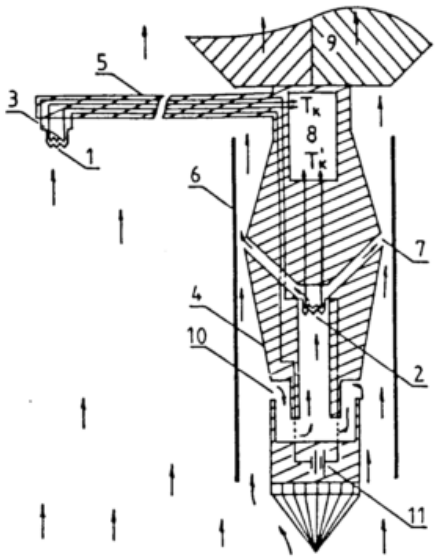


Fig. 1 Schematic cross section of dropsonde LWC measuring device.

Some of the distinctive peculiarities of this device are the identity of both collectors and the aerodynamic method of balanced ventilation of the compensation wire. On Fig.2 is shown the result of screened wire ventilation adjustment. The disadvantageous necessity for deicing heating of Venturi's tube orifices is avoided in the latest dropsonde version.

In sufficiently rapid evaporation of cloud droplets by the open wire, the LWC can be determined in a simple way as a linear function of dropsonde col-

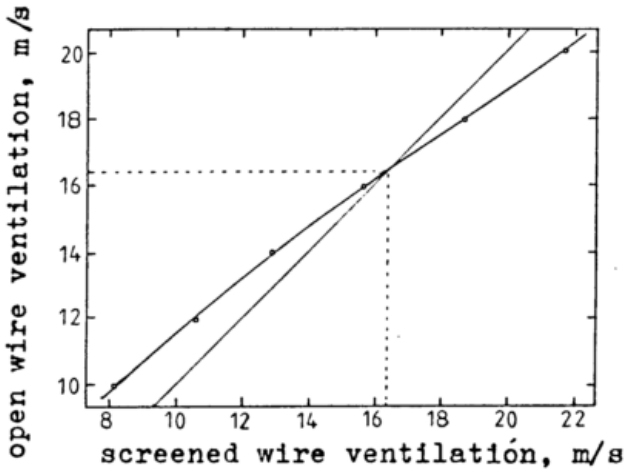


Fig. 2 Wind tunnel data of dropsonde collectors ventilation. The flow velocity is isokinetic at both wires for the mean dropsonde fallspeed at altitude H=0.58 km above MSL (Sofia level).

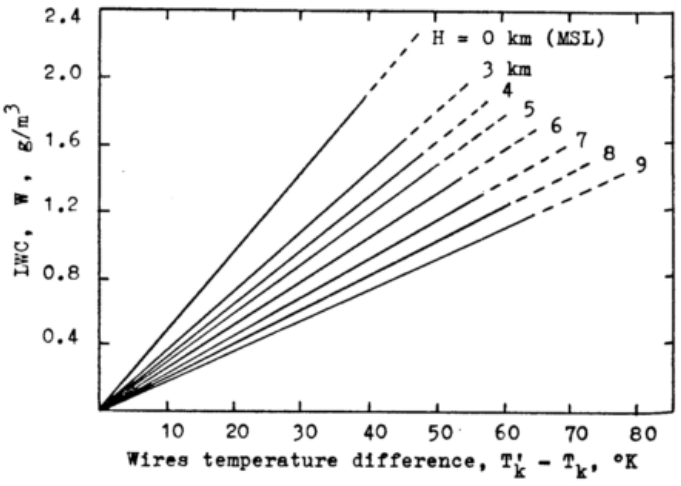


Fig. 3 Tentative LWC calibration graph of the dropsonde

lectors difference $T'_k - T_k$, depending implicitly on the altitude of the measurement point H above MSL via the parameter A_H:

$$W \simeq A_H.(T'_k - T_k).const$$

In October 1986 the dropsonde collectors were calibrated at Riga's (USSR) wet wind tunnel (Gaytandjiev et al., 1987). Measurements were conducted at LWC values ranging from 0.06 to 2.17 g/m^3, at atmospheric pressure 1026.6 hPa and temperature 12 °C with airspeed 65 m/s. The water droplet spectrum hasn't been controlled in the experiments. On the basis of this empirical calibration and an extrapolation for the typical dropsonde fallspeed at MSL, a linear dependance $W = A_{H=0}(T'_k - T_k)$ for H=0 has been obtained.

Considering the possible variations of the parameter A_H in an actual dropsonding : I) at fixed level H as well as II) with the altitude H, it is possible to find the A_H relative deviations : I) from an average value A^*_H for the level H and II) of A^*_H with the altitude. The dependence of A^*_H/A^*_o on the altitude coincide with the dependence of the air density ρ_H/ρ_o ratio on H, which is a result, to a great extent, of dropsonde fallspeed dependence on air density ρ_H. On the basis of A^*_H/A^*_o ratio, the total LWC calibration graph of the sonde has been determined - Fig. 3.

Acknowledgments : The author would like to thank V.P.Korneev for his assistance during many stages of the work; and Dr.A.N.Nevzorov for the helpful discussions and providing of the wet wind tunnel calibrations.

R E F E R E N C E S :

BUSHNELL R.,GLOVER V.,CHU R.: Engineering report on a dropsonde for measuring vertical wind velocity in thunderstorms - NCAR Tech. Note - EDD 83, Boulder, Co, 60 pp., 1973

GAYTANDJIEV D.: Cloud water content measuring device - Patent appl. No 29100, IRR Bul. No 9, 1980

GAYTANDJIEV D.,KALAYDJIEV J.,KORNEEV V., NEVZOROV A.: Results of the development and tests of dropsondes for measuring some cloud parameters - All Union Conference on Weather Modifications, Kiev, USSR, November 17 - 21, 1987, (in Russian).